

T. Entwistle PhD Thesis



**The Development of a High-Throughput,  
Microwave-Assisted Synthesis Process for  
Nickel-Rich Cathodes**

Thomas Entwistle  
Chemical Engineering  
Prof. Serena Cussen

19<sup>th</sup> September 2023

# Abstract

The commercial demand for high-capacity batteries is driven by the 300-mile driving range that is expected for electric vehicles, which equates to a cell-energy density of  $300 \text{ Wh kg}^{-1}$  and a material specific capacity of  $\sim 200 \text{ mAh g}^{-1}$ . Nickel-manganese-cobalt (NMC-811) is a cathode material that can achieve a practical capacity of  $180\text{-}200 \text{ mAh g}^{-1}$ , but one obstacle to its commercialisation is the long synthesis durations and its sensitivity to reaction conditions. This thesis investigates alternative synthesis methods for NMC-811 using microwave technology to reduce the reaction time, energy consumption during the reaction and increasing the throughput of NMC-811 synthesis making its synthesis procedure more environmentally friendly. Specifically, the application of a microwave reactor to the synthesis of  $\text{Ni}_{0.8}\text{Mn}_{0.1}\text{Co}_{0.1}(\text{OH})_2$  precursor is investigated, as well as the application of a microwave furnace during the calcination of the precursor to form the cathode active material,  $\text{LiNi}_{0.8}\text{Mn}_{0.1}\text{Co}_{0.1}\text{O}_2$ . Due to the alternative mechanism behind the heating of the system, the crystallographic, morphological, and electrochemical properties of the resultant materials were examined to establish any differences between the conventional and microwave syntheses.

In this thesis, Chapters 1 and 2 introduces the background literature behind lithium-ion batteries, microwave heating, experimental techniques, and other related topics. Chapter 2 also details the experimental methods conducted in this work. Chapter 3 investigates an alternate calcination procedure that utilises a microwave furnace and an alternative lithium source,  $\text{Li}_2\text{O}_2$  to optimise the synthesis pathway for microwave heating. Chapter 4 validates this alternative calcination pathway using electrochemical half-cell testing to evaluate the capacity yielded from the cells, the capacity retention, impedance, and diffusivity of samples to evaluate the optimised microwave calcination procedure. Chapter 5 discusses the hydrothermal synthesis of  $\text{Ni}_{0.8}\text{Mn}_{0.1}\text{Co}_{0.1}(\text{OH})_2$  using a microwave reactor and the optimisation of this reaction. Chapter 6 develops the novel microwave-assisted co-precipitation synthesis of  $\text{Ni}_{0.8}\text{Mn}_{0.1}\text{Co}_{0.1}(\text{OH})_2$ , involving the design and commissioning of the Microwave Stirred Tank Reactor (MiSTR). Chapter 7 and 8 concludes the findings in this work and discusses the future work associated with this research; namely the addition of oxygen to the microwave furnace system during calcination and further development of the microwave stirred tank reactor and developing the design and operating procedure.

## II. Preface & Declaration of Authorship

I hereby declare that this thesis and the work within was the result of my own efforts except where appropriately referenced and acknowledged.

## III. Coronavirus Pandemic Impact Statement

My PhD research began in September 2019, with my lab work starting in early 2020. The UK government lockdown in March 2020 hindered progress from an experimental perspective, with no lab access until August 2020 followed by partial/ limited access to laboratory equipment and no access to training due to the social distancing rules. The second lockdown in November 2020 coincided with an industrial placement to PV3 technologies (now TFP Hydrogen) in Launceston, Cornwall. This placement went ahead and lab work was completed, but the third lockdown in January 2021 resulted in further disruption to the PhD schedule and a change in project scope to focus on microwave synthesis routes as opposed to conventional high-throughput synthetic routes. This caused the abandonment of the collaboration with PV3 technologies, which resulted in an incomplete project that was not included in this thesis.

The subsequent third lockdown ran from January-April 2021, with limited access to the laboratory and training during this time but with social distancing rules in effect. The resultant back-log of training requirements by students across the department/faculty resulted in a delay in training post-COVID, causing further delays in analysis of results. As a whole, the coronavirus pandemic caused a significant delay in lab work during the early stages of the project, a change in scope of the project and consequent 'catch-up' that delayed the write up of the project, which resulted in additional mental health challenges. I was fortunate to have a 6-month financial extension to the project and the CDT timeline gave 4 years to conduct the PhD.

## IV. Acknowledgements

I would like to profoundly thank my supervisor, Prof. Serena Cussen, for her support, patience, guidance, and opportunities she has arranged throughout my PhD. I would also like to extend a special appreciation to Dr Enrique Sanchez-Perez, Dr Innes McClelland, Dr Nirmallesh Anthonisamy, Dr Marco Amores, Dr Beth Johnston, and Dr Samuel Booth for their guidance and help throughout the project. Prof. Eddie Cussen, Seb Altus and the remainder of the Cussen group have also supported me socially and academically, so many thanks to them. I'd also like to thank Calum Clenahan has also been instrumental in keeping my sanity with philosophical conversations and support while we lived together the last 3 years.

The CDT for Energy Storage and its Applications and the University of Sheffield have been instrumental in allowing me to conduct the work I have done and providing me with laboratory space, funding, and opportunities to develop professionally; and for that I thank them. Specifically, I would like to thank Tracey McNeilly for organising multiple fantastic opportunities and support (including trips to Dublin, New York, and Canada), and Andrew Hutchinson, Jethro Pryke, and Flora Biggins their support and friendship throughout this experience. I would also like to thank TFP Hydrogen Products of Launceston, Cornwall for accommodating me during the placement I spent with them in November 2020, and the advice of Nick van Dijk, David Hodgson, and the team.

My family and friends have been outstandingly supportive throughout my undergraduate and postgraduate pursuits, and I would like to thank them prolifically. My parents specifically have been fantastic at encouraging and supporting me throughout the process, especially during the bleak times of the COVID pandemic! A special thanks to my close friends Samuel Gittins, Joe Delahunty, Nathan Lawson, Mary Fleming, Alice Rigby, Sam Higginbotham, Daniel Hartmann and Chris Williamson and Joe Woodley for their advice and being the receiving ends of many rambles during our runs, races, and social gatherings.

Finally, I would like to show my appreciation for my late grandfather William Henry Shaw for his support throughout my life, inspiring me before I could walk. A successful engineer with Tate & Lyle, he inspired me to follow chemical engineering as a career path, which has led me to this PhD and all experiences to follow.

## V. Contents:

<b>ABSTRACT</b> .....	<b>2</b>
<b>II. PREFACE &amp; DECLARATION OF AUTHORSHIP</b> .....	<b>3</b>
<b>III. CORONAVIRUS PANDEMIC IMPACT STATEMENT</b> .....	<b>3</b>
<b>IV. ACKNOWLEDGEMENTS</b> .....	<b>4</b>
<b>V. CONTENTS:</b> .....	<b>5</b>
<b>A) LIST OF ACRONYMS</b> .....	<b>8</b>
<b>B) LIST OF FIGURES</b> .....	<b>9</b>
<b>C) LIST OF TABLES</b> .....	<b>16</b>
<b>D) LIST OF PUBLICATIONS AND TALKS</b> .....	<b>17</b>
<i>Publications</i> .....	<b>17</b>
<i>Review of Publications</i> .....	<b>18</b>
<i>Conference Presentations</i> .....	<b>18</b>
<b>1. INTRODUCTION</b> .....	<b>19</b>
<b>1.1 – LITHIUM-ION BATTERY PRINCIPLES</b> .....	<b>20</b>
1.1.1 – <i>Battery Components</i> .....	<b>22</b>
1.1.2 – <i>Battery Operation</i> .....	<b>26</b>
<b>1.2 – DEVELOPMENT OF NICKEL-RICH CATHODE MATERIALS</b> .....	<b>28</b>
1.2.1 – <i>Development of NMC Materials</i> .....	<b>30</b>
1.2.2 – <i>NMC-811 as a Commercial Goal</i> .....	<b>37</b>
1.2.3. – <i>Future Advances to NMC-811</i> .....	<b>40</b>
1.2.4. – <i>The NMC Precursor</i> .....	<b>42</b>
<b>1.3. – SYNTHESIS TECHNIQUES</b> .....	<b>45</b>
1.3.1. – <i>Particle Nucleation and Growth</i> .....	<b>46</b>
1.3.2. – <i>Co-precipitation Synthesis Route</i> .....	<b>47</b>
1.3.3. – <i>Hydrothermal synthesis route</i> .....	<b>53</b>
1.3.4. – <i>Lithiation and Calcination of the <math>Ni_xMn_yCo_z(OH)_2</math> precursor</i> .....	<b>56</b>
<b>1.4. STIRRED TANK REACTORS – A GATEWAY TO HIGH-THROUGHPUT SYNTHESIS</b> .....	<b>64</b>
1.4.1. - <i>Stirred Tank Reactors</i> .....	<b>65</b>
1.4.2. – <i>The Design and Operation of a STR</i> .....	<b>66</b>
<b>1.5. – MICROWAVE TECHNOLOGY</b> .....	<b>69</b>
1.5.1 – <i>Microwave Heating</i> .....	<b>69</b>
1.5.2 – <i>Microwave Technology Applications &amp; Benefits</i> .....	<b>71</b>
<b>1.6. AIMS &amp; EXPERIMENTAL OBJECTIVES</b> .....	<b>75</b>
<b>2. EXPERIMENTAL METHOD</b> .....	<b>76</b>
2.1. – <b>MATERIALS</b> .....	<b>76</b>
2.2. – <b>EXPERIMENTAL EQUIPMENT</b> .....	<b>77</b>
2.3. – <b>SYNTHESIS PROCEDURES</b> .....	<b>79</b>

2.3.1. – Optimisation of the microwave calcination of $Ni_{0.8}Mn_{0.1}Co_{0.1}(OH)_2$ .....	79
2.3.2. – Hydrothermal synthesis of $Ni_{0.8}Mn_{0.1}Co_{0.1}(OH)_2$ .....	81
2.3.3. – Microwave Co-precipitation synthesis of $Ni_{0.8}Mn_{0.1}Co_{0.1}(OH)_2$ .....	87
<b>2.4. – CHARACTERISATION TECHNIQUES</b> .....	<b>91</b>
2.4.1. – X-Ray Diffraction Analysis .....	91
2.4.2. – Electron Microscopy .....	98
2.4.3. – Electrochemical Testing .....	102
2.4.4. – Further Characterisation Techniques .....	108
<b>3. INVESTIGATING OXYGEN-RICH ALTERNATIVE CALCINATION APPROACHES FOR NMC-811 CATHODES</b> .....	<b>110</b>
3.1. – THE $Ni_{0.8}Mn_{0.1}Co_{0.1}(OH)_2$ PRECURSOR .....	110
3.2. – LITHIATION OF THE $Ni_{0.8}Mn_{0.1}Co_{0.1}(OH)_2$ PRECURSOR .....	114
3.3. – OPTIMISATION OF THE MICROWAVE CALCINATION PROCEDURE .....	115
3.3.1. – Optimisation of the Calcination Temperature .....	119
3.3.2. – Optimisation of the Calcination Duration .....	122
3.3.3. – In-situ XRD studies of the calcination of NMC-811 .....	133
3.3.4. – Increasing the Throughput for the Microwave Calcination of NMC-811 .....	138
3.4. – CONCLUDING REMARKS FOR CHAPTER 3 .....	149
<b>4. VALIDATION OF AN OPTIMISED MICROWAVE CALCINATION PROCEDURE</b> .....	<b>152</b>
4.1. – Validation of Microwave Heating for the Calcination of $Ni_{0.8}Mn_{0.1}Co_{0.1}(OH)_2$ .....	152
4.2. – Validation of the Application of $Li_2O_2$ in the Calcination of $Ni_{0.8}Mn_{0.1}Co_{0.1}(OH)_2$ .....	154
4.3. – Electrochemical Analysis of Microwave Calcination Procedures .....	157
4.4. – Post-Mortem Analysis of Microwave-calcined Cells .....	166
4.5. – Mechanical Testing of oxygen- and microwave- calcined particles .....	170
4.5. – CONCLUDING REMARKS FOR CHAPTER 4 .....	172
<b>5. OPTIMISING A MICROWAVE-ASSISTED HYDROTHERMAL SYNTHESIS PATHWAY FOR <math>Ni_{0.8}Mn_{0.1}Co_{0.1}(OH)_2</math></b> .....	<b>173</b>
5.1. OPTIMISATION OF THE MICROWAVE-ASSISTED HYDROTHERMAL METHODOLOGY .....	173
5.1.1. Optimisation of the Reaction Duration .....	173
5.1.2. Optimisation of the Reaction Temperature .....	177
5.1.3. Investigating the Effect of Pressure on the Reaction .....	180
5.1.4. Optimisation of the urea ratio .....	183
5.2. ELECTROCHEMICAL ANALYSIS OF HYDROTHERMALLY SYNTHESISED $LiNi_{0.8}Mn_{0.1}Co_{0.1}O_2$ .....	187
5.2.1. Effect of Temperature and Duration on the Electrochemical Performance .....	187
5.2.2. Effect of pressure on the capacity of microwave-assisted hydrothermal $LiNi_{0.8}Mn_{0.1}Co_{0.1}O_2$ .....	191
5.3. SYNTHESIS OF THE A- $Ni_{0.8}Mn_{0.1}Co_{0.1}(OH)_2$ POLYMORPH .....	194
5.4. CONCLUDING REMARKS .....	197
<b>6. THE DEVELOPMENT OF A CO-PRECIPITATION SYNTHESIS PATHWAY FOR NMC-811 IN A MICROWAVE REACTOR</b> .....	<b>198</b>
6.1. – DESIGN OF THE MICROWAVE STIRRED TANK REACTOR (MISTR) SYSTEM .....	198
6.1.1. Design of the stirred tank reactor vessel .....	199

6.1.2. Agitator design – Stirrer bar vs Overhead stirrer .....	201
6.2. – OPERATION OF THE MICROWAVE STIRRED TANK REACTOR (MISTR) SYSTEM .....	204
6.3. – EVALUATION OF THE CO-PRECIPITATION SYNTHESIS PRODUCT SYNTHESISED FROM THE MISTR SYSTEM .....	208
6.3.1. Material Characterisation of $Ni_{0.8}Mn_{0.1}Co_{0.1}(OH)_2$ .....	208
6.3.2. Material Characterisation of $LiNi_{0.8}Mn_{0.1}Co_{0.1}O_2$ .....	210
6.3.3. Electrochemical Characterisation of $LiNi_{0.8}Mn_{0.1}Co_{0.1}O_2$ .....	213
6.4. CONCLUDING REMARKS .....	215
<b>7. CONCLUSIONS.....</b>	<b>216</b>
<b>8. FUTURE WORK .....</b>	<b>218</b>
<b>9. APPENDICES.....</b>	<b>222</b>
<b>REFERENCES.....</b>	<b>245</b>

## A) List of Acronyms

BR – Batch Reactor

CIF – Crystallographic Information Framework (file type)

(C)STR – (Continuous) Stirred Tank Reactor

DOD – Depth Of Discharge

EDS – Energy Dispersive X-ray Spectroscopy

EIS – Electrochemical Impedance Spectroscopy

EV – Electric Vehicle

FTIR – Fourier Transform Infrared Spectroscopy

GITT – Galvanostatic Intermittent Titration Technique

LCO – Lithium Cobalt Oxide,  $\text{LiCoO}_2$

LDH – Layered Double Hydroxide

LFP – Lithium Iron Phosphate,  $\text{Li}_{1-x}\text{FePO}_4$

LiB – Lithium Ion Battery

LNO – Lithium Nickel Oxide,  $\text{LiNiO}_2$

MiSTR – Microwave Stirred Tank Reactor

MW – Microwave

NCA-xyz – Lithium Nickel-Cobalt-Aluminium(x:y:z) oxide,  $\text{LiNi}_x\text{Co}_y\text{Al}_z\text{O}_2$

NMC(OH)<sub>2</sub> – Nickel-Manganese-Cobalt Hydroxide

NMC-xyz – Lithium Nickel-Manganese-Cobalt (x:y:z) oxide,  $\text{LiNi}_x\text{Mn}_y\text{Co}_z\text{O}_2$

OCV – Open Circuit Voltage

SEI – Solid Electrolyte Interface

SBFR – Semi-Batch Fed Reactor

SEM – Scanning Electron Microscopy

SOC – State Of Charge

TM – Transition Metal

XRD – X-Ray Diffraction

## B) List of Figures

<b>Figure 1.1:</b> A Ragone Plot depicting the relative energy and power densities of different energy storage mechanisms, where PHS is ‘Pumped Hydroelectric Storage’, VRFB is ‘Vanadium Redox Flow Battery’, and SMES is ‘Superconducting Magnetic Energy Storage’. Reproduced due to CC BY 4.0 licensing [6].	20
<b>Figure 1.2:</b> A schematic of a Li-ion battery, with a lithium cobalt oxide (LiCoO <sub>2</sub> ) cathode and graphite as the negative anode. The figure shows the electronic and ionic direction of flow during charge (green) and discharge (black). Reprinted with permission from [10], Copyright 2015, American Chemical Society.	22
<b>Figure 1.3:</b> The crystalline structure of <b>(a)</b> layered LiNi <sub>0.8</sub> Mn <sub>0.1</sub> Co <sub>0.1</sub> O <sub>2</sub> , [11]; <b>(b)</b> olivine LiFePO <sub>4</sub> , [12]; and <b>(c)</b> spinel LiMn <sub>2</sub> O <sub>4</sub> , [13]. Green atoms are lithium, red atoms are oxygen, blue atoms are the nickel-manganese-cobalt mixture, brown atoms are iron, grey atoms are phosphorous and purple atoms are manganese. All figures were visualised using Vesta version 3.5.8 [14] using CIF files.	24
<b>Figure 1.4:</b> The crystallographic structure of lithium nickel-manganese-cobalt 8:1:1 oxide, which has a layered α-NaFeO <sub>2</sub> structure and may also be applied to LiNiO <sub>2</sub> , LiCoO <sub>2</sub> and LiNi <sub>x</sub> Co <sub>y</sub> Al <sub>z</sub> O <sub>2</sub> . The lithium ions are depicted as green, whereas the transition metals are the grey-purple-blue balls in the dark blue octahedral sites (in this circumstance, nickel is grey, manganese is purple, and cobalt is pale blue).	29
<b>Figure 1.5:</b> An X-ray diffraction pattern of NMC-811 with each Bragg peak labelled according to the <i>hkl</i> Miller indices.	33
<b>Figure 1.6:</b> A depiction of the lithium-ion migration mechanisms during cycling, namely ‘oxygen dumbbell hopping’ (ODH) and ‘tetrahedral site hopping’ (TSH) [64].	34
<b>Figure 1.7:</b> A high-resolution TEM image of NMC-811 depicting (a) the layered LiNi <sub>0.8</sub> Mn <sub>0.1</sub> Co <sub>0.1</sub> O <sub>2</sub> crystalline structure, identified by the parallel lines at site A and B; and (b) the change in crystalline structure from layered LiNi <sub>0.8</sub> Mn <sub>0.1</sub> Co <sub>0.1</sub> O <sub>2</sub> at site B to rocksalt LiNi <sub>0.8</sub> Mn <sub>0.1</sub> Co <sub>0.1</sub> O at site A. Reproduced with permission from [82].	36
<b>Figure 1.8:</b> SEM images of <b>(a)</b> NMC-811 primary particles within the secondary assembly; <b>(b)</b> NMC-811 secondary particles with a quasi-spherical morphology <b>(c)</b> agglomerated ‘clusters’ of secondary NMC-811 particles. These materials were synthesised in-house at the University of Sheffield by Thomas Entwistle and Dr Nirmalesh Anthonisamy.	37
<b>Figure 1.9:</b> A LiNi <sub>0.8</sub> Mn <sub>0.1</sub> Co <sub>0.1</sub> O <sub>2</sub> particle that has undergone an extreme cracking event post-cycling. Microcracks can be seen on the right side of the particle, with a larger crack on the upper side of the image. These materials were synthesised in-house at the University of Sheffield by Thomas Entwistle and Dr Nirmalesh Anthonisamy.	38
<b>Figure 1.10:</b> A crystallographic representation of <b>(a)</b> α Ni(OH) <sub>2</sub> , which can be appropriated as the layered double hydroxide structure; and <b>(b)</b> β Ni(OH) <sub>2</sub> . These images were prepared using Vesta version 3.5.8 [14] using appropriate CIF files.	43
<b>Figure 1.11:</b> The XRD pattern for alpha- and beta- Ni(OH) <sub>2</sub> with key peaks labelled. The peaks labelled with an asterisk in the alpha polymorph are attributed to aluminium of the XRD stage.	44
<b>Figure 1.12:</b> A schematic of the co-precipitation synthesis pathway for NMC materials, including the chemical reaction to form the ‘green’ Ni <sub>x</sub> Mn <sub>y</sub> Co <sub>z</sub> (OH) <sub>2</sub> and the calcination to form the ‘blue’ LiNi <sub>x</sub> Mn <sub>y</sub> Co <sub>z</sub> O <sub>2</sub> ( <i>n.b.</i> these colours are not representative of the actual colours of the materials) [83].	47
<b>Figure 1.13:</b> Pourbaix diagrams depicting the different Nickel <b>(a)</b> [153] and Manganese <b>(b)</b> [154] species present at different pH and redox states.	49

<b>Figure 1.14:</b> An XRD profile showing the presence of $\text{Li}_2\text{CO}_3$ between the (003) and (101) peaks in a sample of $\text{LiNi}_{0.8}\text{Mn}_{0.1}\text{Co}_{0.1}\text{O}_2$ .	59
<b>Figure 1.15:</b> A graphical depiction between the interaction between polar molecules and the alternating electric field generated by microwave radiation. The changing of alignment was highlighted to cause resistance between adjacent particles, which was the cause of microwave heating technology.	70
<b>Figure 2.1:</b> A picture of the CEM Mars6 Synthesis with 4 EasyPrep Plus vessels installed with the quartz thermocouple and pressure sensor. The two waveguides that emit the microwave radiation from their respective magnetrons are annotated in red and the temperature and pressure sensors are indicated in blue and green respectively.	77
<b>Figure 2.2:</b> A technical drawing of the EasyPrep Plus control vessel, complete with stirrer bar, volume of reactants and fibre optic temperature sensor. All dimensions are quantified in millimetres (mm).	85
<b>Figure 2.3:</b> A process flow diagram depicting the layout of the batch microwave reactor system.	88
<b>Figure 2.4:</b> An image depicting the variation in intensity of the Bremsstrahlung radiation with photoenergy. Characteristic ' $K_\alpha$ ' and ' $K_\beta$ ' x-ray peaks from the electron energy level transitions are clearly seen within the Bremsstrahlung profile. Reproduced from PhysicsOpenLab website [235].	92
<b>Figure 2.5:</b> A visualisation of x ray diffraction within a lattice structure and its relation to Bragg's law.	94
<b>Figure 2.6:</b> (a) The exploded schematic of the construction of the coin cell, and (b) An image of the Kapton window half-cell during <i>operando</i> XRD.	97
<b>Figure 2.7:</b> A schematic of a scanning electron microscope, depicting the formation, refinement, and impact of the electron beam onto the sample, and the resultant electrons and photons that result from the interactions.	100
<b>Figure 2.8:</b> The current and voltage profiles for GCPL cycling. Current was constant during cycling, whereas voltage increases/decreases to a maximum/ minimum.	103
<b>Figure 2.9:</b> An example Nyquist plot, with examples of characteristic cell features and degradation mechanisms highlighted.	105
<b>Figure 2.10:</b> A GITT plot that demonstrates the current and voltage profiles over the course of 2 charging current pulses, with the gradual increase in potential observed.	108
<b>Figure 3.1:</b> XRD profiles of experimentally acquired $\text{Ni}_{0.8}\text{Mn}_{0.1}\text{Co}_{0.1}(\text{OH})_2$ (red), with ICSD standards of $\text{Ni}(\text{OH})_2$ (green), $\text{Ni}_{0.6}\text{Mn}_{0.2}\text{Co}_{0.2}(\text{OH})_2$ (black), and a manufactured CIF file of $\text{Ni}_{0.8}\text{Mn}_{0.1}\text{Co}_{0.1}(\text{OH})_2$ (red). a) depicts the full range 10-80° XRD profile, with b) showing a close-up of the (001) peak between 17-22°, and c) showing the (102) peak at 50-54°.	111
<b>Figure 3.2:</b> SEM images of $\text{Ni}_{0.8}\text{Mn}_{0.1}\text{Co}_{0.1}(\text{OH})_2$ precursor at 1000x (a), 20,000x (b), and 120,000x (c) magnification.	113
<b>Figure 3.3:</b> A histogram depicting the particle size distribution from the $\text{Ni}_{0.8}\text{Mn}_{0.1}\text{Co}_{0.1}(\text{OH})_2$ sample, from a 200x SEM image with a population of 11,563 particles with at least 50% circularity.	113
<b>Figure 3.4:</b> (a) XRD profiles of $\text{LiNi}_{0.8}\text{Mn}_{0.1}\text{Co}_{0.1}\text{O}_2$ lithiated with 1, 3, 5 and 7 mol% excess $\text{Li}_2\text{O}_2$ and calcined in a microwave furnace (750 °C for 5 hours); (b) an enlargement of the (101) and (006)/(012) doublet; (c) evidence of residual $\text{Li}_2\text{CO}_3$ exhibited by the peaks in the 20-35° 2 $\theta$ range, with peaks labelled with a grey circle.	114
<b>Figure 3.5:</b> XRD profile of $\text{LiNi}_{0.8}\text{Mn}_{0.1}\text{Co}_{0.1}\text{O}_2$ calcined with 7 mol% excess of $\text{Li}_2\text{O}_2$ . Additional lithium peaks are compared to ICSD patterns for $\text{LiOH}$ , $\text{Li}_2\text{CO}_3$ and $\text{Li}_2\text{O}$ confirm the presence of $\text{Li}_2\text{CO}_3$ .	115
<b>Figure 3.6:</b> A depiction of the two calcination mechanisms within the conventional, oxygen-fed tube furnace (left) and microwave furnace with $\text{Ni}_{0.8}\text{Mn}_{0.1}\text{Co}_{0.1}(\text{OH})_2$ calcined with $\text{Li}_2\text{O}_2$ with an added crucible lid to avoid oxygen loss (right).	116

<b>Figure 3.7: (a)</b> XRD profiles for $\text{LiNi}_{0.8}\text{Mn}_{0.1}\text{Co}_{0.1}\text{O}_2$ calcined at 850 °C in a microwave furnace for 3 hours and an oxygen-fed tube furnace for 10 hours. Peak analysis of the (104) and (108)/(110) doublet are enclosed in <b>(b)</b> and <b>(c)</b> respectively. ....	117
<b>Figure 3.8: (a)</b> XRD profiles for $\text{LiNi}_{0.8}\text{Mn}_{0.1}\text{Co}_{0.1}\text{O}_2$ calcined with $\text{Li}_2\text{O}_2$ for 3 hours at a range of temperatures 650-850 °C. The (104) and (108)/(110) peaks can be seen in <b>(b)</b> and <b>(c)</b> respectively. ....	120
<b>Figure 3.9:</b> The variation in $c/a$ ratio and (003)/(104) peak ratio for various microwave calcination temperatures (650-850 °C) when calcined with a $\text{Li}_2\text{O}_2$ salt. ....	121
<b>Figure 3.10:</b> XRD profiles for $\text{LiNi}_{0.8}\text{Mn}_{0.1}\text{Co}_{0.1}\text{O}_2$ calcined with $\text{Li}_2\text{O}_2$ and LiOH for 3 hours at 775 and 800 °C. A full-range XRD pattern can be seen in <b>(a)</b> , with a magnification of the (104) peak in <b>(b)</b> . .	122
<b>Figure 3.11: (a)</b> XRD profiles of $\text{LiNi}_{0.8}\text{Mn}_{0.1}\text{Co}_{0.1}\text{O}_2$ calcined with 3 mol% excess $\text{Li}_2\text{O}_2$ in a microwave furnace over a range of durations, ranging from 90 minutes to 6 hours. The (104) peak <b>(b)</b> and (108)/(110) doublet peak <b>(c)</b> are magnified for analysis. ....	123
<b>Figure 3.12:</b> The XRD profile <b>(a)</b> and magnification of the (104) peak <b>(b)</b> of $\text{LiNi}_{0.8}\text{Mn}_{0.1}\text{Co}_{0.1}\text{O}_2$ calcined with 3 mol% excess $\text{Li}_2\text{O}_2$ or LiOH in a microwave furnace for 5-6 hours. The $c/a$ ratios for both LiOH and $\text{Li}_2\text{O}_2$ over the range of calcination durations and displayed in <b>(c)</b> .....	125
<b>Figure 3.13:</b> SEM images of $\text{LiNi}_{0.8}\text{Mn}_{0.1}\text{Co}_{0.1}\text{O}_2$ calcined at 750 °C in a microwave furnace with 3 mol% excess LiOH or $\text{Li}_2\text{O}_2$ that depict the secondary (left) and primary (right) morphology. The calcination periods for each calcination experiment are indicated on the left-hand side. ....	127
<b>Figure 3.14:</b> Capacity retention over 100 cycles of half-cells cycled with a voltage window of 3.0-4.2 V, with 2 cycles at C/20 followed by 98 cycles of C/2. The NMC-811 cathode active material was calcined for different durations with two lithium salts, LiOH <b>(a)</b> and $\text{Li}_2\text{O}_2$ <b>(b)</b> .....	129
<b>Figure 3.15:</b> Voltage profiles for half-cells cycled at 3.0-4.2 V in their 1 <sup>st</sup> , 5 <sup>th</sup> , 10 <sup>th</sup> , 50 <sup>th</sup> and 100 <sup>th</sup> cycle. <b>(a)</b> , <b>(c)</b> , <b>(e)</b> , <b>(g)</b> , <b>(i)</b> and <b>(k)</b> represent the cathode materials calcined with LiOH at 1.5, 2, 3, 4, 5 and 6 hours respectively; with their $\text{Li}_2\text{O}_2$ counterparts seen in <b>(b)</b> , <b>(d)</b> , <b>(f)</b> , <b>(h)</b> , <b>(j)</b> and <b>(l)</b> respectively.....	130
<b>Figure 3.16:</b> Differential capacity ( $dQ\ dV^{-1}$ ) profiles for the half-cells cycled at 3.0-4.2 V in their 1 <sup>st</sup> , 5 <sup>th</sup> , 10 <sup>th</sup> , 50 <sup>th</sup> and 100 <sup>th</sup> cycle. <b>(a)</b> , <b>(c)</b> , <b>(e)</b> , <b>(g)</b> , <b>(i)</b> and <b>(k)</b> represent the cathode materials calcined with LiOH at 1.5, 2, 3, 4, 5 and 6 hours respectively; with their $\text{Li}_2\text{O}_2$ counterparts seen in <b>(b)</b> , <b>(d)</b> , <b>(f)</b> , <b>(h)</b> , <b>(j)</b> and <b>(l)</b> respectively.....	132
<b>Figure 3.17:</b> High temperature XRD of $\text{Ni}_{0.8}\text{Mn}_{0.1}\text{Co}_{0.1}(\text{OH})_2$ heated with LiOH between 20-400 °C at 100 °C-intervals, captured using a Anton Parr BTS-500 XRD stage on a benchtop Rigaku Miniflex 6 diffractometer. Peaks are labelled for each potential phase (blue, $M(\text{OH})_2$ ; green, $M_3\text{O}_4$ ; red, $MO$ ). ....	134
<b>Figure 3.18:</b> XRD patterns of $\text{Ni}_{0.8}\text{Mn}_{0.1}\text{Co}_{0.1}(\text{OH})_2$ heated with LiOH in the 100-850 °C temperature range with $\text{Li}_2\text{CO}_3$ indicated with a green square; $\text{Li}_2\text{O}$ indicated with a blue circle. This was captured using a PANalytical X'Pert <sup>3</sup> X-ray diffractometer with a HTK 1200N high temperature stage. ....	134
<b>Figure 3.19:</b> High temperature XRD study of $\text{Ni}_{0.8}\text{Mn}_{0.1}\text{Co}_{0.1}(\text{OH})_2$ heated with $\text{Li}_2\text{O}_2$ between 20-500 °C at 100 °C intervals, Peaks are labelled for each potential phase (blue, $M(\text{OH})_2$ ; green, $M_3\text{O}_4$ ; red, $MO$ ). ....	135
<b>Figure 3.20:</b> XRD patterns of $\text{Ni}_{0.8}\text{Mn}_{0.1}\text{Co}_{0.1}(\text{OH})_2$ heated with $\text{Li}_2\text{O}_2$ in the 200-300 °C temperature range with reference patterns of three common lithium species in the system: $\text{Li}_2\text{O}_2$ , $\text{Li}_2\text{CO}_3$ and LiOH acquired from ICSD. ....	136
<b>Figure 3.21:</b> XRD patterns of $\text{Ni}_{0.8}\text{Mn}_{0.1}\text{Co}_{0.1}(\text{OH})_2$ heated with $\text{Li}_2\text{O}_2$ between 100-850 °C, with the different Bragg peaks highlighted for each phase and the $\text{Li}_2\text{O}$ peaks indicated with a blue circle...	137
<b>Figure 3.22: (a)</b> XRD patterns of $\text{LiNi}_{0.8}\text{Mn}_{0.1}\text{Co}_{0.1}\text{O}_2$ , calcined with LiOH in a 2.5 mL crucible for 5 hours at 750-850 °C. The (104) peak and (108)/(110) peak doublet are enclosed in <b>(b)</b> and <b>(c)</b> . ....	138
<b>Figure 3.23: (a)</b> XRD patterns of $\text{LiNi}_{0.8}\text{Mn}_{0.1}\text{Co}_{0.1}\text{O}_2$ , calcined with $\text{Li}_2\text{O}_2$ in a 2.5 mL crucible for 5 hours at 750-850 °C. The (104) peak and (108)/(110) peak doublet are enclosed in <b>(b)</b> and <b>(c)</b> . ....	139

<b>Figure 3.24:</b> (a) XRD patterns of $\text{LiNi}_{0.8}\text{Mn}_{0.1}\text{Co}_{0.1}\text{O}_2$ , calcined with LiOH in a 2.5 mL crucible for 3-5 hours at 775 °C. The (104) peak and (108)/(110) peak doublet are enclosed in (b) and (c). .....	140
<b>Figure 3.25:</b> (a) XRD patterns of $\text{LiNi}_{0.8}\text{Mn}_{0.1}\text{Co}_{0.1}\text{O}_2$ , calcined with $\text{Li}_2\text{O}_2$ in a 2.5 mL crucible for 3-5 hours at 775 °C. The (104) peak and (108)/(110) peak doublet are enclosed in (b) and (c). .....	140
<b>Figure 3.26:</b> The Rietveld refinement results for the optimisation experiment conducted in the 2.5 mL alumina crucible, featuring the $c/a$ ratio (a, b); the fraction of Ni in the Li layer (c, d); and the unit cell volume (e, f) for samples calcined with LiOH (a, c, e) and $\text{Li}_2\text{O}_2$ (b, d, f). Error bars are present for all graphs but may not be visible due to the small magnitude of the standard deviation. ....	141
<b>Figure 3.27:</b> SEM images of $\text{LiNi}_{0.8}\text{Mn}_{0.1}\text{Co}_{0.1}\text{O}_2$ secondary particles calcined with LiOH or $\text{Li}_2\text{O}_2$ for 5 hours at a range of temperatures 750-850 °C. ....	142
<b>Figure 3.28:</b> SEM and EDS images of $\text{LiNi}_{0.8}\text{Mn}_{0.1}\text{Co}_{0.1}\text{O}_2$ secondary particles calcined with LiOH or $\text{Li}_2\text{O}_2$ for 5 hours at 750 °C, with an amorphous material indicated by a blue oval in (a). EDS analysis was also conducted in (b), with each of the elements indicated by colour-key. ....	143
<b>Figure 3.29:</b> SEM images of $\text{LiNi}_{0.8}\text{Mn}_{0.1}\text{Co}_{0.1}\text{O}_2$ secondary particles calcined with LiOH or $\text{Li}_2\text{O}_2$ for 5 hours at a range of temperatures 750-850 °C, labelled. ....	144
<b>Figure 3.30:</b> Capacity retention over 100 cycles of half-cells cycled with a voltage window of 3.0-4.3 V, the first two cycles at C/20, the following 98 conducted at C/2. The NMC-811 cathode material was calcined for 5 hours with a $\text{Li}_2\text{O}_2$ lithium source at a temperature of 750, 775 or 800 °C. ....	145
<b>Figure 3.31:</b> Voltage profiles of half-cells cycled at 3.0-4.3 V in their 1 <sup>st</sup> , 5 <sup>th</sup> , 10 <sup>th</sup> , 50 <sup>th</sup> and 100 <sup>th</sup> cycle for samples calcined at 750, 775 and 800 °C with $\text{Li}_2\text{O}_2$ . ....	146
<b>Figure 3.32:</b> Differential capacity profiles of half-cells cycled at 3.0-4.3 V in their 1 <sup>st</sup> , 5 <sup>th</sup> , 10 <sup>th</sup> , 50 <sup>th</sup> and 100 <sup>th</sup> cycle for samples calcined at 750, 775 and 800 °C with $\text{Li}_2\text{O}_2$ . ....	146
<b>Figure 3.33:</b> Capacity retention of two cycles at C/20 followed by 98 cycles at C/2 over a voltage window of 3.0-4.3 V. The NMC-811 cathode active material was calcined for 4-5 hours with either LiOH or $\text{Li}_2\text{O}_2$ at a temperature of 775 °C.....	147
<b>Figure 3.34:</b> Voltage profiles of half-cells cycled over a voltage window of 3.0-4.3 V in their 1 <sup>st</sup> , 5 <sup>th</sup> , 10 <sup>th</sup> , 50 <sup>th</sup> and 100 <sup>th</sup> cycle for samples calcined 775 °C with LiOH or $\text{Li}_2\text{O}_2$ . Samples were calcined for 4 hours (a) and 5 hours (b). ....	148
<b>Figure 3.35:</b> Differential capacity profiles of half-cells cycled over a voltage window of 3.0-4.3 V in their 1 <sup>st</sup> , 5 <sup>th</sup> , 10 <sup>th</sup> , 50 <sup>th</sup> and 100 <sup>th</sup> cycle for samples calcined 775 °C with LiOH or $\text{Li}_2\text{O}_2$ . Samples were calcined for 4 hours (a) and 5 hours (b).....	149
<b>Figure 4.1:</b> (a) XRD profiles of $\text{LiNi}_{0.8}\text{Mn}_{0.1}\text{Co}_{0.1}\text{O}_2$ calcined with 3 mol% excess LiOH in a microwave furnace, air-fed tube furnace and oxygen-fed tube furnace at 775 °C for 4 or 12 hours. Magnification of the (104) peak (b) and (108)/(110) peak doublet (c) are included.....	153
<b>Figure 4.2:</b> SEM images of $\text{LiNi}_{0.8}\text{Mn}_{0.1}\text{Co}_{0.1}\text{O}_2$ calcined using different calcination procedures in a microwave furnace, air fed tube furnace or an oxygen fed tube furnace.....	154
<b>Figure 4.3:</b> (a) XRD profiles of $\text{LiNi}_{0.8}\text{Mn}_{0.1}\text{Co}_{0.1}\text{O}_2$ calcined with 3 mol% excess LiOH or $\text{Li}_2\text{O}_2$ at 775 °C. Microwave calcined samples were calcined for 4 hours, whereas an air-fed or oxygen-fed tube furnace samples were calcined for 12 hours. Magnification of the (104) peak (b) and the (108)/(110) doublet peaks (c) are also included. ....	155
<b>Figure 4.4:</b> SEM images of $\text{LiNi}_{0.8}\text{Mn}_{0.1}\text{Co}_{0.1}\text{O}_2$ calcined with LiOH and $\text{Li}_2\text{O}_2$ using an optimised microwave-heated calcination procedure and equivalent air-fed and oxygen-fed conventionally-heated calcination procedures. ....	157
<b>Figure 4.5:</b> Capacity retention data for the half-cell cycling of $\text{LiNi}_{0.8}\text{Mn}_{0.1}\text{Co}_{0.1}\text{O}_2$ over 100 cycles at 3.0-4.2 V at a rate of C/2. Oxygen-fed furnace with LiOH (green), microwave furnace with a LiOH or $\text{Li}_2\text{O}_2$ salt (black and red respectively), and air-fed furnace with $\text{Li}_2\text{O}_2$ (blue) are compared. ....	158

**Figure 4.6:** Long-term capacity retention data for half-cells consisting of  $\text{LiNi}_{0.8}\text{Mn}_{0.1}\text{Co}_{0.1}\text{O}_2$  cycled over 400 cycles at 3.0-4.2 V at a rate of C/2. Oxygen-fed furnace with LiOH (green), microwave furnace with a LiOH or  $\text{Li}_2\text{O}_2$  salt (black and red respectively), and an air-fed furnace with  $\text{Li}_2\text{O}_2$  (blue) are compared..... 159

**Figure 4.7:** Capacity retention data for the half-cells of  $\text{LiNi}_{0.8}\text{Mn}_{0.1}\text{Co}_{0.1}\text{O}_2$  cycled twice at a rate of C/20 followed by 98 cycles at C/2, over a voltage window of 3.0-4.3 V. Microwave-calcined samples with LiOH or  $\text{Li}_2\text{O}_2$  salt (black and grey respectively), an air-fed sample calcined with LiOH (red) and oxygen-fed calcination samples with LiOH and  $\text{Li}_2\text{O}_2$  (blue and cyan respectively) are compared.... 160

**Figure 4.8:** Voltage profiles of half-cells cycled over a voltage window of 3.0-4.3 V. The 1<sup>st</sup>, 5<sup>th</sup>, 10<sup>th</sup>, 50<sup>th</sup> and 100<sup>th</sup> cycles are included for samples calcined 775 °C with LiOH or  $\text{Li}_2\text{O}_2$ , in either a microwave furnace for 4 hours (top row) or 12 hours in a conventional furnace (bottom row). .... 161

**Figure 4.9:** Differential capacity profiles of half-cells cycled at 3.0-4.3 V. The 1<sup>st</sup>, 5<sup>th</sup>, 10<sup>th</sup>, 50<sup>th</sup> and 100<sup>th</sup> cycles for samples calcined 775 °C with LiOH or  $\text{Li}_2\text{O}_2$  in either a microwave furnace for 4 hours (top row) or 12 hours in a conventional furnace (bottom row). ..... 162

**Figure 4.10: (a)** XRD profiles of a  $\text{LiNi}_{0.8}\text{Mn}_{0.1}\text{Co}_{0.1}\text{O}_2$  cathode calcined in a microwave furnace at 775 °C for 4 hours with  $\text{Li}_2\text{O}_2$ . Magnification of the (003), (101), and (110) peaks are seen in **(b)**. ... 163

**Figure 4.11:** A chromatic ‘heat map’ of the XRD profile for the  $\text{LiNi}_{0.8}\text{Mn}_{0.1}\text{Co}_{0.1}\text{O}_2$  cathode analysed *via* XRD *in-operando* over a voltage range of 3.0-4.3 V. **(a)** depicts the whole angle range (0-35°) of the XRD profile, with **(b)** showing a magnification of the (003) peak at 6-7°.  $\theta$ ..... 163

**Figure 4.12:** Nyquist plots for uncycled, 1<sup>st</sup>, 5<sup>th</sup>, 10<sup>th</sup> cycles of  $\text{LiNi}_{0.8}\text{Mn}_{0.1}\text{Co}_{0.1}\text{O}_2$  calcined using the optimised microwave calcination **(a)** and oxygen-fed calcination procedures **(b)** cycled over a voltage window of 3.0 – 4.3 V, with two cycles at C/20 followed by 8 cycles at a rate of C/2. .... 164

**Figure 4.13:** GITT analysis of the optimised microwave and oxygen-fed calcination procedures during the charge profile, cycled between 3.0–4.5 V at a rate of C/20. .... 165

**Figure 4.14:** A rate capability test of the optimised microwave-calcined oxygen-calcined samples *via* a series of rates: C/20, C/10/ C/5, C/2, 1C, 2C, 5C and 10C; cycled at 3.0-4.3 V. .... 166

**Figure 4.15:** XRD profiles of a  $\text{LiNi}_{0.8}\text{Mn}_{0.1}\text{Co}_{0.1}\text{O}_2$  cathode disc with aluminium foil. **(a)** depicts the effects of refining the sample displacement of crystalline Al; **(b)** demonstrates how scaling a peak can remove aluminium peaks without impacting the intensity of the NMC peaks. .... 167

**Figure 4.16:** XRD profiles of the microwave-calcined samples with LiOH or  $\text{Li}_2\text{O}_2$  **(a and b)**, air-calcined sample with  $\text{Li}_2\text{O}_2$  **(c)**, and the oxygen-calcined sample with LiOH **(d)**. Two profiles are included for the uncycled powder (red) and cycled cathode (black). .... 168

**Figure 4.17:** SEM images of the cycled cathode materials, featuring the two microwave samples calcined with LiOH **(a)**, **(c)**, and  $\text{Li}_2\text{O}_2$  **(b)**, **(d)**; the air-calcined sample with  $\text{Li}_2\text{O}_2$  **(e)**, and the oxygen-calcined sample with LiOH **(f)**. Images **(c)** and **(d)** depict the extreme cracking event that some microwave-calcined particles underwent during cycling..... 169

**Figure 4.18:** SEM images of  $\text{LiNi}_{0.8}\text{Mn}_{0.1}\text{Co}_{0.1}\text{O}_2$  calcined *via* a microwave procedure (left) or oxygen-calcined procedure (right). The micro-indenter applies pressure, with images depicting the secondary particles before (top) and after (bottom) particle failure. .... 170

**Figure 4.19:** The mechanical strength of  $\text{LiNi}_{0.8}\text{Mn}_{0.1}\text{Co}_{0.1}\text{O}_2$  secondary particles relative to the particle diameter. Error bars are included for all datapoints, but some are too small to be visible.. 171

**Figure 5.1:** XRD profiles of  $\text{Ni}_{0.8}\text{Mn}_{0.1}\text{Co}_{0.1}(\text{OH})_2$  samples synthesised in four hydrothermal vessels within the Mars6 Synthesis (200 °C, 3 hours), with labelled Bragg peaks. The potential phase impurities,  $(\text{Ni}_{0.6}\text{Mn}_{0.2}\text{Co}_{0.2})_3\text{O}_4$  spinel and  $\text{Ni}_{0.6}\text{Mn}_{0.2}\text{Co}_{0.2}\text{O}$  rocksalt, are also included. .... 174

**Figure 5.2:** XRD profiles of  $\text{Ni}_{0.8}\text{Mn}_{0.1}\text{Co}_{0.1}(\text{OH})_2$  synthesised *via* a microwave-assisted hydrothermal method at 200 °C with a reaction period of 30 minutes, 45 minutes, 1 hour, 2 hours and 3 hours.. 175

<b>Figure 5.3:</b> SEM images of $\text{Ni}_{0.8}\text{Mn}_{0.1}\text{Co}_{0.1}(\text{OH})_2$ synthesised <i>via</i> a microwave-assisted hydrothermal method at 200 °C with a reaction duration of 30 minutes, 45 minutes, 1 hour, 2 hours and 3 hours.	175
<b>Figure 5.4:</b> (a) XRD profiles of $\text{LiNi}_{0.8}\text{Mn}_{0.1}\text{Co}_{0.1}\text{O}_2$ , calcined in an oxygen-fed tube furnace with LiOH (775 °C, 12 hours). The (104) peak (b) and (108)/(110) peak doublet (c) are enclosed.	176
<b>Figure 5.5:</b> SEM images of $\text{LiNi}_{0.8}\text{Mn}_{0.1}\text{Co}_{0.1}\text{O}_2$ calcined in an oxygen-fed tube furnace (775 °C, 12 hours). Samples were synthesised using a microwave-assisted hydrothermal method at 200 °C for 1 hour, 2 hours and 3 hours.	177
<b>Figure 5.6:</b> XRD profiles of $\text{Ni}_{0.8}\text{Mn}_{0.1}\text{Co}_{0.1}(\text{OH})_2$ synthesised <i>via</i> a microwave-assisted hydrothermal method at 180, 200 and 220 °C for 2 hours, with labelled Bragg peaks.	178
<b>Figure 5.7:</b> SEM images of $\text{Ni}_{0.8}\text{Mn}_{0.1}\text{Co}_{0.1}(\text{OH})_2$ synthesised <i>via</i> a microwave-assisted hydrothermal method for 2 hours at 180, 200 and 220 °C.	178
<b>Figure 5.8:</b> (a) XRD profiles of $\text{LiNi}_{0.8}\text{Mn}_{0.1}\text{Co}_{0.1}\text{O}_2$ , calcined with LiOH for 12 hours in an oxygen-fed tube furnace at 775 °C. The (104) peak and (108)/(110) peak doublet are enclosed in (b) and (c).	179
<b>Figure 5.9:</b> SEM images of $\text{LiNi}_{0.8}\text{Mn}_{0.1}\text{Co}_{0.1}\text{O}_2$ calcined at 775 °C for 12 hours. These samples were synthesised using a microwave-assisted hydrothermal method for 2 hours at 180, 200 and 220 °C.	180
<b>Figure 5.10:</b> XRD profiles of $\text{Ni}_{0.8}\text{Mn}_{0.1}\text{Co}_{0.1}(\text{OH})_2$ synthesised <i>via</i> a microwave-assisted hydrothermal method for 3 hours at a variety of pressures: 200 °C with a volume of 20 mL, 200 °C with a volume of 40 mL; and at 400 PSI.	181
<b>Figure 5.11:</b> SEM images of $\text{Ni}_{0.8}\text{Mn}_{0.1}\text{Co}_{0.1}(\text{OH})_2$ synthesised <i>via</i> a microwave-assisted hydrothermal method for 3 hours in 20 mL of solvent (left), 40 mL of solvent (centre), and in 20 mL solvent at a fixed pressure of 400 PSI with variable temperature.	181
<b>Figure 5.12:</b> (a) XRD profiles of $\text{LiNi}_{0.8}\text{Mn}_{0.1}\text{Co}_{0.1}\text{O}_2$ , calcined with LiOH for 12 hours in an oxygen-fed tube furnace at 775 °C. The (104) peak and (108)/(110) peak doublet are enclosed in (b) and (c).	182
<b>Figure 5.13:</b> SEM images of $\text{LiNi}_{0.8}\text{Mn}_{0.1}\text{Co}_{0.1}\text{O}_2$ synthesised <i>via</i> a microwave-assisted hydrothermal method for 3 hours at different pressures: the hydrostatic pressure head for a 20 mL reaction (left) and 40 mL (centre), as well as a fixed pressure of 400 PSI with variable temperature. Samples calcined in an oxygen-supplied tube furnace at 775 °C for 12 hours.	183
<b>Figure 5.14:</b> XRD profiles of $\text{Ni}_{0.8}\text{Mn}_{0.1}\text{Co}_{0.1}(\text{OH})_2$ synthesised <i>via</i> a microwave-assisted hydrothermal method at 200 °C for 45 minutes using a range of urea: transition metal ratios (1: 1, 5: 2, 2.9: 1, 3: 1 and 5: 1). The Bragg's peaks for the $\beta$ -polymorph $\text{Ni}_{0.8}\text{Mn}_{0.1}\text{Co}_{0.1}(\text{OH})_2$ are labelled.	184
<b>Figure 5.15:</b> SEM images of $\text{Ni}_{0.8}\text{Mn}_{0.1}\text{Co}_{0.1}(\text{OH})_2$ synthesised <i>via</i> a microwave-assisted hydrothermal method for 45 minutes at 200 °C using a variety of urea: transition metal (M) ratios, ranging from 1:1 to 5:1.	185
<b>Figure 5.16:</b> (a) XRD profiles of $\text{LiNi}_{0.8}\text{Mn}_{0.1}\text{Co}_{0.1}\text{O}_2$ , calcined with LiOH for 12 hours in an oxygen-fed tube furnace at 775 °C. The (104) peak and (108)/(110) peak doublet are enclosed in (b) and (c).	186
<b>Figure 5.17:</b> SEM images of $\text{LiNi}_{0.8}\text{Mn}_{0.1}\text{Co}_{0.1}\text{O}_2$ synthesised <i>via</i> a microwave-assisted hydrothermal method for 45 minutes at 200 °C using a range of urea: transition metal (M) ratios, 1:1 to 5:1.	187
<b>Figure 5.18:</b> Capacity retention plot for the $\text{LiNi}_{0.8}\text{Mn}_{0.1}\text{Co}_{0.1}\text{O}_2$ samples with a precursor synthesis reaction duration of 1-, 2- and 3- hours and a reaction temperature of 200 and 220 °C. The half-cells were cycled at 3.0-4.3 V for 52 cycles (2 cycles of C/20, 50 cycles of C/2).	188
<b>Figure 5.19:</b> Voltage profile plots of the $\text{LiNi}_{0.8}\text{Mn}_{0.1}\text{Co}_{0.1}\text{O}_2$ samples with a precursor synthesis reaction duration of 1- (a-b), 2- (c-d) and 3- (e-f) hours and a reaction temperature of 200 °C (a, c, e) and 220 °C (b, d, f). The voltage profiles include the 1 <sup>st</sup> , 2 <sup>nd</sup> , 5 <sup>th</sup> , 10 <sup>th</sup> and 50 <sup>th</sup> cycles.	189
<b>Figure 5.20:</b> Differential capacity profiles for the $\text{LiNi}_{0.8}\text{Mn}_{0.1}\text{Co}_{0.1}\text{O}_2$ samples with a precursor synthesis reaction duration of 1- (a-b), 2- (c-d) and 3- (e-f) hours and a reaction temperature of	

200 °C **(a, c, e)** and 220 °C **(b, d, f)**. The profiles for the 1<sup>st</sup>, 2<sup>nd</sup>, 5<sup>th</sup>, 10<sup>th</sup> and 50<sup>th</sup> cycles are included. .... 190

**Figure 5.21:** Capacity retention plot for the LiNi<sub>0.8</sub>Mn<sub>0.1</sub>Co<sub>0.1</sub>O<sub>2</sub> samples with a precursor synthesis reaction duration of 1-, 2- and 3- hours, reaction temperature of 200 °C and a reaction volume of 20 or 40 mL. This was also compared to a 20 mL sample that was reacted at 400 PSI for 3 hours. The half-cells were cycled over a voltage window of 3.0-4.3 V, with 2 cycles of C/20, 50 cycles of C/2. . 191

**Figure 5.22:** Voltage profile plots of the 1<sup>st</sup>, 2<sup>nd</sup>, 5<sup>th</sup>, 10<sup>th</sup> and 50<sup>th</sup> cycles for LiNi<sub>0.8</sub>Mn<sub>0.1</sub>Co<sub>0.1</sub>O<sub>2</sub> samples with a precursor synthesis reaction duration of 1- **(a-b)**, 2- **(c-d)** and 3- **(e-f)** hours with a reaction volume of 20 mL **(a, c, e)** and 40 mL **(b, d, f)**. The sample that was synthesised at 400 PSI for 3 hours is included in part **(g)**. .... 192

**Figure 5.23:** Differential capacity profile plots for the 1<sup>st</sup>, 2<sup>nd</sup>, 5<sup>th</sup>, 10<sup>th</sup> and 50<sup>th</sup> cycles of LiNi<sub>0.8</sub>Mn<sub>0.1</sub>Co<sub>0.1</sub>O<sub>2</sub> samples with a precursor synthesis reaction duration of 1- **(a-b)**, 2- **(c-d)** and 3- **(e-f)** hours with a reaction volume of 20 mL **(a, c, e)** and 40 mL **(b, d, f)**. The sample that was synthesised at 400 PSI for 3 hours is included in part **(g)**. .... 193

**Figure 5.24:** The XRD profiles of the LiNi<sub>0.8</sub>Mn<sub>0.1</sub>Co<sub>0.1</sub>O<sub>2</sub> samples calcined from the α- and β-Ni<sub>0.8</sub>Mn<sub>0.1</sub>Co<sub>0.1</sub>(OH)<sub>2</sub> precursors, with the Bragg peaks labelled accordingly below the profiles. .... 194

**Figure 5.25:** A capacity retention plot for the LiNi<sub>0.8</sub>Mn<sub>0.1</sub>Co<sub>0.1</sub>O<sub>2</sub> samples with the α- and β-Ni<sub>0.8</sub>Mn<sub>0.1</sub>Co<sub>0.1</sub>(OH)<sub>2</sub> precursor. Half-cells were cycled over a voltage window of 3.0-4.3 V for 52 cycles (2 cycles of C/20, 50 cycles of C/2). .... 195

**Figure 5.26:** Voltage profiles of the LiNi<sub>0.8</sub>Mn<sub>0.1</sub>Co<sub>0.1</sub>O<sub>2</sub> calcined from with the α- or β-Ni<sub>0.8</sub>Mn<sub>0.1</sub>Co<sub>0.1</sub>(OH)<sub>2</sub> polymorphs represented in parts **(a)** and **(b)** respectively. The voltage profiles include the 1<sup>st</sup>, 2<sup>nd</sup>, 5<sup>th</sup>, 10<sup>th</sup> and 50<sup>th</sup> cycles. .... 196

**Figure 5.27:** Differential capacity profiles of the LiNi<sub>0.8</sub>Mn<sub>0.1</sub>Co<sub>0.1</sub>O<sub>2</sub> calcined from with the α- or β-Ni<sub>0.8</sub>Mn<sub>0.1</sub>Co<sub>0.1</sub>(OH)<sub>2</sub> polymorphs represented in parts **(a)** and **(b)** respectively. The voltage profiles include the 1<sup>st</sup>, 2<sup>nd</sup>, 5<sup>th</sup>, 10<sup>th</sup> and 50<sup>th</sup> cycles. .... 196

**Figure 6.1:** A technical drawing of the Microwave stirred tank reactor (MiSTR) vessel design, including the baffles and agitator, as an overhead stirrer. All dimensions are in millimetres (mm). 200

**Figure 6.2:** A photo of the two 3D-printed stirred tank reactor vessels: the filament-printed vessel (left) and resin-printed vessel (right). .... 201

**Figure 6.3:** A 3D visualisation of the design for the MiSTR impellor blade using Autodesk Inventor. .... 202

**Figure 6.4:** A 3D model rendered in Autodesk Inventor for the tube separator device designed for the throat of the I/O port of the CEM Mars6 Synthesis. The model was shortened to 100 mm in length for clarity, but was printed to a length of 300 mm. .... 203

**Figure 6.5:** A piping and instrumentation diagram (P&ID) of the microwave stirred tank reactor (MiSTR) system. .... 206

**Figure 6.6:** A picture of the microwave stirred tank reactor (MiSTR) system during a reaction. .... 207

**Figure 6.7:** **(a)** XRD profiles for the Ni<sub>0.8</sub>Mn<sub>0.1</sub>Co<sub>0.1</sub>(OH)<sub>2</sub> precursors synthesised in the (MiSTR) system, featuring three MiSTR trial runs and a benchmark sample. **(b)** and **(c)** depicts the (104) peak and (108)/(110) peak doublet respectively. .... 209

**Figure 6.8:** SEM images of the Ni<sub>0.8</sub>Mn<sub>0.1</sub>Co<sub>0.1</sub>(OH)<sub>2</sub> during trials 1, 2 and 3 (depicted in a, b, and c respectively). .... 209

**Figure 6.9:** X-ray diffraction profiles of LiNi<sub>0.8</sub>Mn<sub>0.1</sub>Co<sub>0.1</sub>O<sub>2</sub>, synthesised from the calcination of the three MiSTR trials conducted in an oxygen-supplied tube furnace, compared to a benchmark sample. **(a)** depicts the full XRD profile range of 10-80° with labelled *hkl* planes, with **(b)** and **(c)** depicting peak analysis of the (104) peak and (108)/(110) peak doublet respectively. .... 210

**Figure 6.10:** SEM images of calcined LiNi<sub>0.8</sub>Mn<sub>0.1</sub>Co<sub>0.1</sub>O<sub>2</sub> secondary particles in an oxygen-atmosphere tube furnace. The three trials (1-3) are included left to right. .... 211

<b>Figure 6.11:</b> SEM/EDS images of the three MiSTR trial experiment samples (1-3, left to right), with an elemental overlay as well as individual images for nickel, manganese and cobalt EDS mapping. ....	212
<b>Figure 6.12:</b> Capacity retention plot for the three MiSTR commissioning trials calcined in an oxygen-fed tube furnace. The half-cells were cycled over a voltage window of 3.0-4.3 V for 100 cycles (2 cycles of C/20, 98 cycles of C/2). .....	213
<b>Figure 6.13:</b> Voltage profile of the three MiSTR commissioning trials (1-3), calcined using an oxygen-fed tube furnace (left to right respectively). Profiles of cycles 1, 5, 10, 50 and 100 displayed. ....	214
<b>Figure 6.14:</b> Differential capacity profiles for the three MiSTR commissioning trials (1-3) calcined in an oxygen-fed tube furnace, displayed left to right respectively. Profiles of cycles 1, 5, 10, 50 and 100 displayed. ....	214
<b>Figure 8.1:</b> A schematic of a microwave tube furnace, comprised of a commercial microwave with a mullite tube and fibrefrax insulation package with silicon carbide rods to facilitate the high-temperature heating [263]. Reproduced with permissions from Springer Nature, 2023.....	219

## C) List of Tables

<b>Table 1.1:</b> A summary of the most frequently used temperatures for common versions of NMC, accompanied by their sources. ....	62
<b>Table 2.1:</b> The array of conditions tested during the temperature and duration optimisation of the microwave calcination of NMC-811(OH) <sub>2</sub> with LiOH and Li <sub>2</sub> O <sub>2</sub> . The blue cells indicate trials run in the 20 mL and 2.5 mL crucibles; orange indicates trials run in the 20 mL crucible. ....	81
<b>Table 2.2:</b> A table showing the mass values used for the experiments, with each Urea ratio specified. ....	82
<b>Table 2.3:</b> A table depicting the matrix of temperature and reaction duration ranges used to determine optimum values for the reaction. ....	83
<b>Table 2.4:</b> A table describing the masses and volumes of the reactants that are used in the three trials of the batch microwave reactor reaction experiments. ....	89
<b>Table 2.5:</b> A table describing the different reaction times, tube diameters and corresponding flow rates and their effect on the pH range measured throughout the trial. ....	90
<b>Table 3.1:</b> A table of 2θ Bragg peaks for the β-M(OH) <sub>2</sub> phase and corresponding angles for each of the analysed Ni <sub>0.8</sub> Mn <sub>0.1</sub> Co <sub>0.1</sub> (OH) <sub>2</sub> phases, with the difference to the experimental value in brackets. ....	112
<b>Table 3.2:</b> A table of lattice and model fitting parameters from the Rietveld refinement of experimentally acquired Ni <sub>0.8</sub> Mn <sub>0.1</sub> Co <sub>0.1</sub> (OH) <sub>2</sub> compared to three different CIF files. Estimated standard deviations are included in brackets, where refined. ....	112
<b>Table 3.3:</b> Key values from the Rietveld refinement of LiNi <sub>0.8</sub> Mn <sub>0.1</sub> Co <sub>0.1</sub> O <sub>2</sub> calcined at 850 °C with LiOH or Li <sub>2</sub> O <sub>2</sub> in a microwave-assisted furnace for 3 hours; or an oxygen-fed tube furnace for 10 hours. ....	118
<b>Table 3.4:</b> Key values from the Rietveld refinement of LiNi <sub>0.8</sub> Mn <sub>0.1</sub> Co <sub>0.1</sub> O <sub>2</sub> calcined with Li <sub>2</sub> O <sub>2</sub> at temperatures ranging from 650-850 °C in a 2.5 mL crucible. ....	119
<b>Table 3.5:</b> Key values from the Rietveld refinement of LiNi <sub>0.8</sub> Mn <sub>0.1</sub> Co <sub>0.1</sub> O <sub>2</sub> calcined with LiOH or Li <sub>2</sub> O <sub>2</sub> at different temperatures 775-800 °C in a 2.5 mL crucible. ....	121
<b>Table 3.6:</b> Key values from the Rietveld refinement of LiNi <sub>0.8</sub> Mn <sub>0.1</sub> Co <sub>0.1</sub> O <sub>2</sub> calcined with Li <sub>2</sub> O <sub>2</sub> at 750 °C for different durations, including the c/a lattice parameter ratio, the calculated nickel fraction in the lithium 3a layer, and the (003)/(104) peak ratio calculated from the raw XRD data. ....	124

<b>Table 3.7:</b> Key values from the Rietveld refinement of $\text{LiNi}_{0.8}\text{Mn}_{0.1}\text{Co}_{0.1}\text{O}_2$ calcined with LiOH at 750 °C for different durations, including the $c/a$ lattice parameter ratio, the calculated nickel fraction in the lithium $3a$ layer, and the (003)/(104) peak ratio calculated from the raw XRD data. ....	125
<b>Table 3.8:</b> Key values from the Rietveld refinement of $\text{LiNi}_{0.8}\text{Mn}_{0.1}\text{Co}_{0.1}\text{O}_2$ calcined with $\text{Li}_2\text{O}_2$ at 750 °C for 5 and 6 hours with LiOH or $\text{Li}_2\text{O}_2$ in a microwave furnace. Estimated standard deviations are included in brackets, where refined. ....	126
<b>Table 4.1:</b> Lattice parameters from the Rietveld refinement of $\text{LiNi}_{0.8}\text{Mn}_{0.1}\text{Co}_{0.1}\text{O}_2$ calcined using a microwave, air-supplied and oxygen-supplied furnace. Estimated standard deviations are included in brackets, where refined. ....	156
<b>Table 5.1:</b> Key values from the Rietveld refinement of $\text{LiNi}_{0.8}\text{Mn}_{0.1}\text{Co}_{0.1}\text{O}_2$ calcined with LiOH in an oxygen-rich atmosphere at 775 °C for 12 hours, including the lattice parameters, the calculated nickel fraction in the lithium $3a$ layer, and the (003)/(104) peak ratio. The $\text{Ni}_{0.8}\text{Mn}_{0.1}\text{Co}_{0.1}(\text{OH})_2$ precursors were synthesised in a microwave reactor at 200 °C for 30 minutes – 3 hours. ....	177
<b>Table 5.2:</b> Key values from the Rietveld refinement of $\text{LiNi}_{0.8}\text{Mn}_{0.1}\text{Co}_{0.1}\text{O}_2$ calcined with LiOH in an oxygen-rich atmosphere at 775 °C for 12 hours, including the lattice parameters, the calculated nickel fraction in the lithium $3a$ layer, and the (003)/(104) peak ratio. The $\text{Ni}_{0.8}\text{Mn}_{0.1}\text{Co}_{0.1}(\text{OH})_2$ precursors were synthesised in a microwave reactor at 180-220 °C for 2 hours. ....	178
<b>Table 5.3:</b> Key values from the Rietveld refinement of $\text{LiNi}_{0.8}\text{Mn}_{0.1}\text{Co}_{0.1}\text{O}_2$ calcined with LiOH in an oxygen-rich atmosphere at 775 °C for 12 hours, including the lattice parameters, the calculated nickel fraction in the lithium $3a$ layer, and the (003)/(104) peak ratio. The $\text{Ni}_{0.8}\text{Mn}_{0.1}\text{Co}_{0.1}(\text{OH})_2$ precursors were synthesised in a microwave reactor for 3 hours at conditions to provoke different pressures within the hydrothermal vessels. ....	183
<b>Table 5.4:</b> Key values from the Rietveld refinement of $\text{LiNi}_{0.8}\text{Mn}_{0.1}\text{Co}_{0.1}\text{O}_2$ calcined with LiOH in an oxygen-rich atmosphere at 775 °C for 12 hours, including the lattice parameters, the calculated nickel fraction in the lithium $3a$ layer, and the (003)/(104) peak ratio. The $\text{Ni}_{0.8}\text{Mn}_{0.1}\text{Co}_{0.1}(\text{OH})_2$ precursors were synthesised in a microwave reactor at 200 °C for 45 minutes using a range of Urea: transition metal ratios. ....	186
<b>Table 6.1:</b> Key values from the Rietveld refinement of $\text{LiNi}_{0.8}\text{Mn}_{0.1}\text{Co}_{0.1}\text{O}_2$ calcined with LiOH in an oxygen-rich atmosphere at 775 °C for 12 hours, including the lattice parameters, the calculated nickel fraction in the lithium $3a$ layer, and the (003)/(104) peak ratio. The $\text{Ni}_{0.8}\text{Mn}_{0.1}\text{Co}_{0.1}(\text{OH})_2$ precursors were synthesised in the MiSTR reactor, which occurred over three trials and then compared to a benchmark sample. ....	211

## D) List of Publications and Talks

### Publications

- Entwistle, T., Sanchez-Perez, E., Murray, G. J., Anthonisamy, N., & Cussen, S. A. (2022). Co-precipitation synthesis of nickel-rich cathodes for Li-ion batteries. *Energy Reports*, 8, 67–73. <https://doi.org/10.1016/J.EGYR.2022.06.110>
- Grant, P. S., Greenwood, D., Smith, R., Entwistle, T., Cumming, D. J., *et al.* (2022). Roadmap on Li-ion battery manufacturing research. *Journal of Physics: Energy*, 4(4), 042006. <https://doi.org/10.1088/2515-7655/AC8E30>

## Review of Publications

- Li, J., Liang, G., Zheng, W., Zhang, S., Davey, K., Guo, Z., *et al.* (2022). Addressing cation mixing in layered structured cathodes for lithium-ion batteries: A critical review. *Nano Materials Science*. <https://doi.org/10.1016/J.NANOMS.2022.09.001>
- Gao, Z., Zhao, C., Zhou, K., Wu, Z., Deng, X., Li, B., *et al.* (2022). Nucleation chemical synthesis design of high-energy layered oxide cathodes for lithium batteries. *ACS Energy Letters*. *Not currently published*.

## Conference Presentations

- Presentation: MRS Fall Meeting 2023, Boston, USA; “Investigating oxygen-rich alternative calcination approaches for NMC-811 cathodes”
- Poster: IMLB Conference June 2022, Sydney, Australia; “Investigating oxygen-rich alternative calcination approaches for NMC-811 cathodes”
- Presentation: CDT-ESA Conference Apr 2022, Sheffield, UK; “Co-precipitation synthesis of nickel-rich cathodes for Li-ion batteries”
- Presentation: CDT-ESA Conference Jan 2021, Online; “The evolution of nickel-rich cathode synthesis for lithium-ion batteries: a review for future high-throughput research”
- Poster: CDT-ESA Conference Sept 2019, Southampton, UK; “Designing a continuous process for the manufacture of NMC-111 using a microwave synthesiser”

# 1. Introduction

An increase in worldwide energy demand during the ongoing climate crisis has induced a societal pressure to reduce carbon emissions while generating more energy from 'low-carbon' energy sources. According to the Stated Policies Scenario (STEPS), which uses the progress of government policies and targets to predict their energy generation and usage, the share of global renewable electricity generation was expected to increase from 28% to 65% of total electricity generated by 2050. This translates to an increase in generation from 28,334 TWh to 49,845 TWh [1].

Variable renewable energy sources, such as solar or wind, are a key part to this strategy, with the share of solar and wind energy being generated worldwide predicted to increase from 10.1% to 68.9% by 2050, but they require stationary grid scale to support the electrical supply from these intermittent sources [1], [2], [3]. Grid scale electrical energy storage from renewables can be achieved using batteries and aid frequency response, which moderates the frequency of alternating current (AC) power to 50 Hz as well as supplement energy supplies during 30-minute duty periods [4]. Lithium-ion batteries have been a key part of this energy storage movement since their first commercialisation in the 1990s, and currently have 27 GW of global battery storage capacity [1].

While the use of lithium-ion batteries for stationary storage applications is important, they have garnered much more interest publicly in the field of portable electronics and vehicular powertrains as they present an energy dense solution, both with respect to weight and volume. Research into lithium-ion battery electrode chemistries have helped develop the power and lifetime of electronic devices, including mobile phones, laptops, and electric vehicles (EVs). Recent developments into cathode materials have allowed the energy density of Li-ion batteries materials to reach  $760 \text{ Wh kg}^{-1}$  at pack level (or  $180\text{-}200 \text{ mAh g}^{-1}$  at material level), which is the threshold for EVs to have a range of 300 miles, which mitigates some consumer barriers over range anxiety [5]. This coincides with governmental phasing out internal combustion engine (ICE) vehicles and STEPS prediction estimating that transport electrical demand will increase from 441 TWh (1.8% of total demand) to 3,607 TWh (8.3% of total demand) by 2050 and the prediction that there will need to be 1,000 GW of global battery storage to help facilitate this [1].

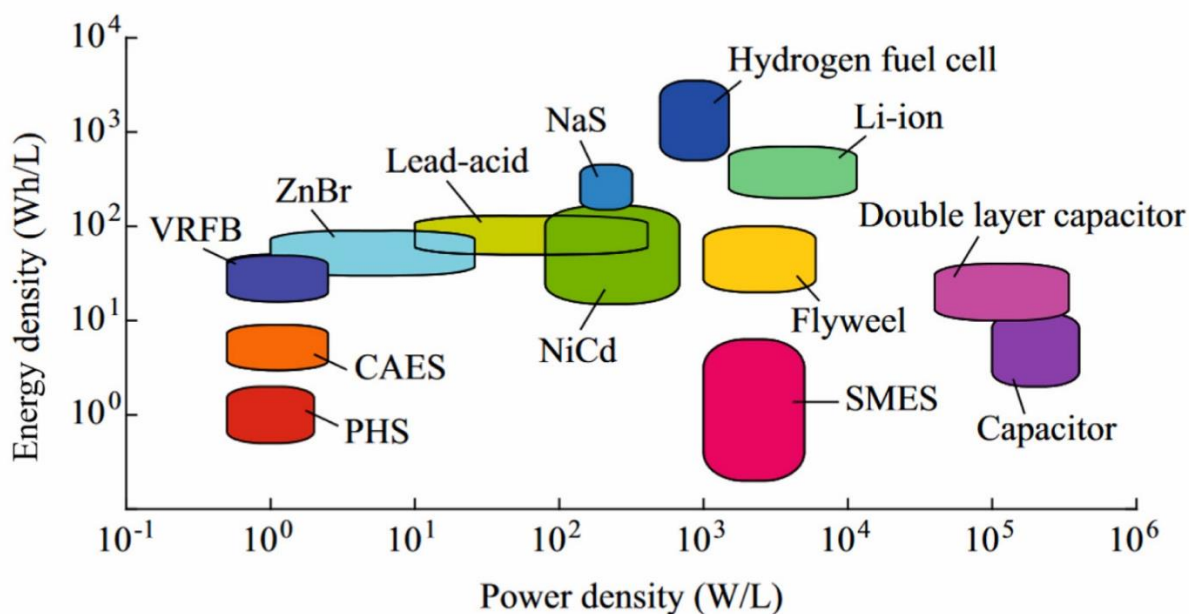


**Figure 1.1:** A Ragone Plot depicting the relative energy and power densities of different energy storage mechanisms, where PHS is ‘Pumped Hydroelectric Storage’, VRFB is ‘Vanadium Redox Flow Battery’, and SMES is ‘Superconducting Magnetic Energy Storage’. Reproduced due to CC BY 4.0 licensing [6].

The demand for these cathode active material batteries drives an increase in manufacture throughput for these materials. Traditional approaches often require high reaction temperatures and long reaction times. For example, the use of kilns in the production of the layered cathode material  $\text{LiNi}_{0.33}\text{Mn}_{0.33}\text{Co}_{0.33}\text{O}_2$  was reported to be the majority contributor to the  $4 \text{ kWh kg}^{-1}$  energy production requirement [7]. One novel way of reducing these costs and potentially delivering high throughput manufacturing is through the use of microwaves, which can theoretically reduce the reaction time and energy consumption due to their rapid heating properties. This thesis investigates nickel rich cathode materials, the common synthesis methods, and how microwave technology during preparation can aid the development of high-throughput synthesis methods for these materials.

## 1.1 – Lithium-Ion Battery Principles

Electrochemical energy storage utilises the energy involved in oxidation and reduction reactions to generate electrical charge which can conduct current through and external electrical circuit, and power devices such as phones, laptops, and electric vehicles. Alkali metals such as lithium (and sodium in the case of sodium-ion batteries) exist within a transition metal positive electrode

(cathode) and can be transferred to a negative electrode (anode) with a higher energy state during charging. This stored energy was released during discharging, with the alkali metals dissociating into ions and electrons, the latter being directed through the external circuit to conduct work, as depicted in Figure 1.2. The ions migrate from the anode, through a porous separator (e.g. glass fibre) using the electrolyte as an ionic medium and intercalate into the cathode, triggering a reduction reaction. This process is reversible in lithium-ion batteries, allowing the cell to be charged and discharged multiple times – *i.e.* a rechargeable battery.

As with the first voltaic cells pioneered by Alessandro Volta in the early 19<sup>th</sup> century, the two electrodes are connected by an ionically conductive and electrically insulative salt bridge, or electrolyte, and a porous separator to force the electrons generated to travel *via* the external electrical circuit whilst allowing the transfer of alkali metal ions through the electrolyte to facilitate the reversible operation of the cell.

Lithium-ion battery technology was first conceived in the 1970s, where lithium was reversibly intercalated into a titanium disulphide ( $\text{LiTiS}_2$ ) layered framework. This concept was later evolved by John Goodenough *et al.* in 1980, who developed the lithiated transition metal oxides ( $\text{LiMO}_2$ , where the transition metal(s) is denoted by 'M') cathodes in the form of lithium cobalt oxide ( $\text{LiCoO}_2$ , LCO). This technology was then commercialised by Sony in the 1990s after research into a safe anode material was successful [8], [9]. The development of the cathode chemistry has been instrumental to commercial success of lithium-ion batteries, due to the contribution to the overall capacity of the battery the cathode has, with the transition metal chemistries and their synthesis being of particular relevance to this work.

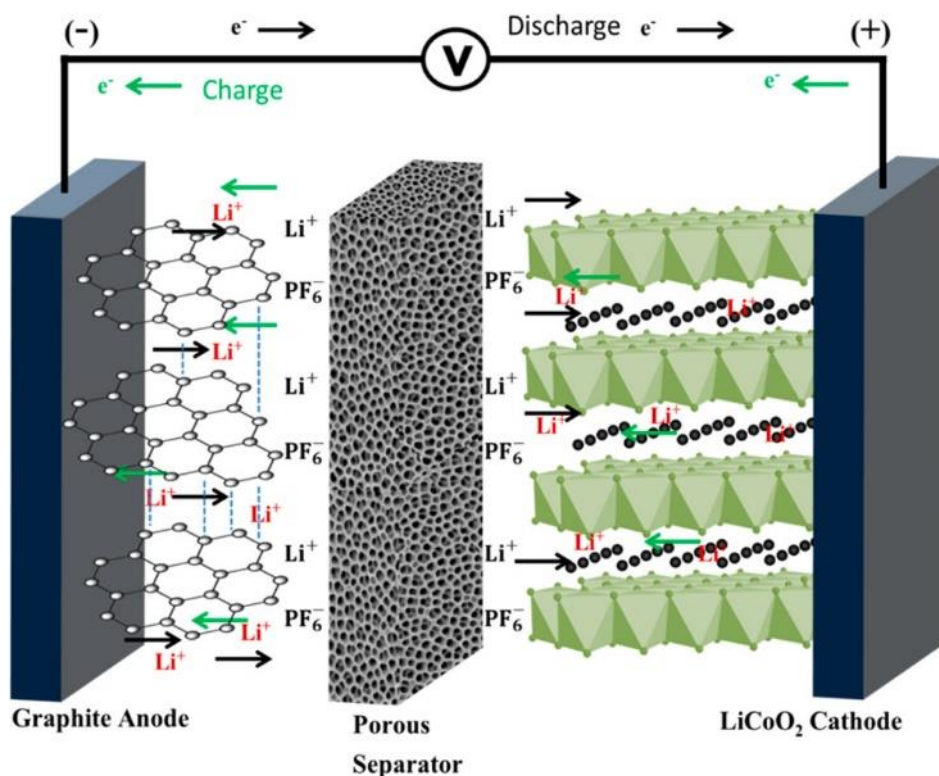


**Figure 1.2:** A schematic of a Li-ion battery, with a lithium cobalt oxide (LiCoO<sub>2</sub>) cathode and graphite as the negative anode. The figure shows the electronic and ionic direction of flow during charge (green) and discharge (black). Reprinted with permission from [10], Copyright 2015, American Chemical Society.

### 1.1.1 – Battery Components

Lithium ions are stored at two electrodes within the cell: the cathode and anode. The cathode often comprises a lithium-transition metal crystal structure that stores lithium ions at low energy in a ‘discharged’ state; whereas the anode was typically made up of a lithium-ion store for the high energy, ‘charged’ state. Both allow the reversible insertion and deintercalation of lithium ions during the cycling process and are adjoined to metal current collectors, which aid conductivity between the electrodes and external electrical circuits. The two electrode terminals are physically separated by a porous membrane soaked in an ionically conductive, electron-insulative electrolyte, typically a lithium salt dissolved in a combination of organic solvents.

Typical cathode active materials consist of a transition metal crystalline structure with lithium intercalated into positions within the lattice. The transition metal composition of the cathode can reversibly undergo oxidation and reduction (redox) reactions to balance the charge indifference in

the discharge (lithiated) and charged (delithiated) states by changing the oxidation states of the transition metals. The stable nature of the lithium within the transition metal structures means that electrical energy is needed to separate the lithium atoms into ions and electrons, which initiates the battery charging process. The crystallography of the cathode can impact the number of lithium ions per unit cell and therefore charge density, with the arrangement of transition metals and anions affecting the size of the migration channels, and consequently the ease of lithium (de)intercalation.

There are three types of crystal structure that are typically used as cathode materials: layered, spinel, olivine and rocksalt [10]. The layered crystal structure, depicted in Figure 1.3.a), has parallel layers of redox-active transition metals (such as Ni, Mn, and Co) or non-redox-active metal dopants and lithium atoms. This structure has 2-dimensional channels between the transition metal layers for the lithium-ion migration during (de)lithiation but incurs greater mechanical stress than olivine and spinel structures during this process due to unit cell expansion/contraction. Olivine and spinel structures have a non-lithium structure that spans the  $a$ -,  $b$ -, and  $c$ - axis, permitting lithium-ions to migrate in/out of the structure *via* 1-dimensional channels. Olivine structures, depicted in Figure 1.3.b), consist of tetrahedron molecular ions (e.g.  $\text{PO}_4$ ) connected by an associated cation (e.g. Fe) and arranged in a close-packed hexagonal array to form an orthorhombic system. Spinel structures consist of two cations (e.g.  $\text{Mn}^{2+}$ ,  $\text{Mn}^{3+}$ ,  $\text{Fe}^{2+}$ ) bound within two sub-lattices: one tetrahedral, one octahedral, resulting in a face-centred cubic symmetry. The rocksalt structure is also a face-centred cubic structure but presents as a '3-dimensional chessboard' with cations and anions alternating in the  $a$ -,  $b$ -, and  $c$ - axes. Due to the absence of sites that can facilitate movement of lithium ions, these materials are not electrochemically active unless they are 'disordered', in which ordering defects are engineered to produce lithium channels within the crystal structure.

The theoretical specific capacity attained from an electrochemically active material is measured by the charge transferred per mass of electrode material, calculated using Equation 1.1 below. This results in a theoretical specific capacity of layered oxide materials such as  $\text{LiCoO}_2$  (LCO) and  $\text{LiNiO}_2$  (LNO) of 273-275  $\text{mAh g}^{-1}$ . Spinel materials such as  $\text{LiMn}_2\text{O}_4$  and olivine materials such as  $\text{LiFePO}_4$ , seen in Figure 1.3.b) and c), have less lithium ions per unit cell than the layered transition metal oxide material and a smaller theoretical specific capacity of 148.2 and 169.9  $\text{mAh g}^{-1}$  respectively [11].

$$\textit{Theoretical capacity (mAh g}^{-1}\text{)} = \frac{\textit{Faraday Constant (C mol}^{-1}\text{)}}{\textit{Molecular weight (g mol}^{-1}\text{)}*3.6 \textit{ (mAh C}^{-1}\text{)}} \quad \text{Equation 1.1.}$$

Spinel materials (*e.g.*  $\text{Li}_x\text{Mn}_2\text{O}_4$ ) and olivine materials (*e.g.*  $\text{LiFePO}_4$ , LFP) are typically cheaper than layered and rocksalt oxides due to the absence of expensive materials such as cobalt [12]. These materials have increased structural and mechanical stability due to the arrangement of transition metals seen in Figure 1.3.b) and c), with minimal movement within the structure during (de)lithiation. Rocksalt materials have a similar structural stability, with the 3-dimensional ‘checkerboard’ crystal structure having minimal movement during (de)lithiation. Transition metal layered structures, depicted in Figure 1.3.a), experience collapsing and swelling between the transition layers during repeated  $\text{Li}^+$  (de)insertion which can cause defects in the structure and degrade the capacity of the cell. To maximise the capacity and lifetime of these materials, a combination of metals substituents has been used to stabilise the layered structure, with two more popular chemistries being nickel-manganese-cobalt (NMC) and nickel-cobalt-aluminium (NCA).

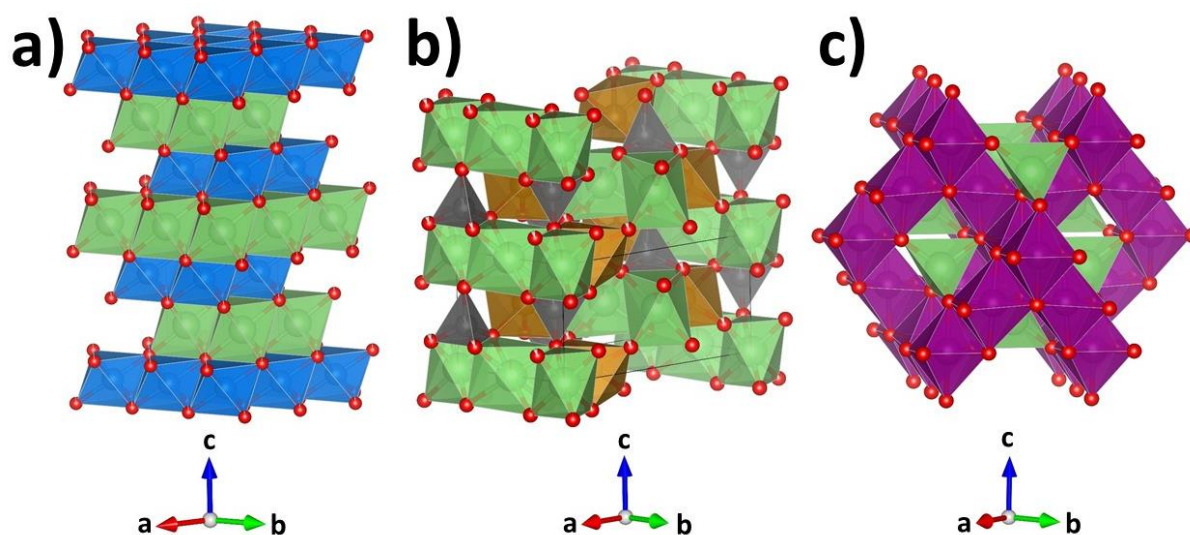


**Figure 1.3:** The crystalline structure of (a) layered  $\text{LiNi}_{0.8}\text{Mn}_{0.1}\text{Co}_{0.1}\text{O}_2$ , [11]; (b) olivine  $\text{LiFePO}_4$ , [12]; and (c) spinel  $\text{LiMn}_2\text{O}_4$ , [13]. Green atoms are lithium, red atoms are oxygen, blue atoms are the nickel-manganese-cobalt mixture, brown atoms are iron, grey atoms are phosphorous and purple atoms are manganese. All figures were visualised using Vesta version 3.5.8 [14] using CIF files.

The anode is the negative electrode that typically consists of lithium metal, graphite, or silicon. Graphite is the most common anode used in commercial settings due to its high theoretical capacity of  $372 \text{ mAh g}^{-1}$  and its ability to recover close to 100% of the charge after the first cycle [15] [16]. Lithium nucleation can occur at the surface of the graphite anode and inhibit its performance by introducing a parasitic side reaction that results in a loss of lithium inventory. Lithium dendrite formation can also occur, lead to a reduction in the cell’s capacity, and the eventual short-circuiting of the cell should the dendrite penetrate the electrode separator [17].

Lithium metal is often used in excessive quantities during research in 'half cells' to measure the capacity and electrochemical qualities of the cathode by acting as the counter and reference electrode [18], [19]. Lithium metal has the potential as a commercial anode due to its low density and high specific capacity of 3,680 mAh g<sup>-1</sup>, but the cathode: anode ratio needs to be moderated to prevent the formation of lithium dendrites [20] [21]. The negative/positive (N/P) ratio used in full cell experimentation was typically 1.09-1.13 which minimises the growth of lithium dendrites and related loss of reversible capacity [19] [22].

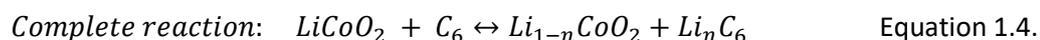
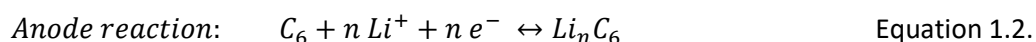
Silicon is an alternative anode chemistry being researched, with it possessing a high specific capacity of 3,579-4,200 mAh g<sup>-1</sup>, depending on the molar ratio of lithium to silicon (with up to Li<sub>4</sub>Si being achieved) [23]. Lithiation of the silicon structure causes a significant volume increase of up to 270-300% which can cause a number of problems including destruction of particles and the SEI layer. The swelling of the silicon during lithiation can disconnect the active material from the electrical contacts and rupture the cell, releasing toxic and flammable components of lithium-ion batteries. The increase in specific capacity was an incentive to investigate this technology, with silicon particle size, morphology and composition being investigated in order to mitigate the detrimental volume changes [24] [25].

The electrolyte generally consists of a lithium salt that permits the migration of lithium ions across the porous separator between electrodes during cycling. The electrolyte can be in solid or liquid phase, the former having poorer ionic conduction but was more resistant to lithium dendrite growth but typically has a poor electrode-electrolyte interface due to the poor contact between the two solid crystalline structures [26], [27]. The latter is more common variation of electrolyte that was applied commercially but aqueous organic compounds are flammable, especially when in contact with oxygen.

Electrolytes can also become unstable at higher voltages and high charge rates, which can cause reactions and ignitions within the cell. At high voltages and charging rates, parasitic reactions between the cathode and electrolyte can occur and produce gaseous products, causing volumetric swelling of the cell. Additionally, at the anode, lithium plating can occur and destabilise the carbonate solvents in the electrolyte, causing reduction and increased impedance [28]. Consequently, managing the operational voltage window and charging rate was important for battery life and safety.

### 1.1.2 – Battery Operation

The anode and cathode material are typically synthesised in their low-energy discharged form, meaning the cathode is fully lithiated and the anode is not (except in the case of lithium metal anodes). Charging the electrochemical cell involves inputting electrical energy to dissociate the lithium atom into a lithium ion and an electron, which migrates through the electrolyte and external electrical circuit respectively to form the high-energy charged lithiated anode, as described in Equations 1.2-1.4 and exemplified by the LiCoO<sub>2</sub>-graphite system depicted in Figure 1.2. The cobalt layer undergoes a Co<sup>3+/4+</sup> redox reaction in the low-energy t<sub>2g</sub> band. Other transition metals used in cathode materials, Ni<sup>3+/4+</sup> and Mn<sup>3+/4+</sup>, undergo the redox reaction in the higher e<sub>g</sub> energy level to minimise the overlap with the O<sub>2p</sub>, which risks oxidising the oxygen, resulting in the loss of chemical stability and oxygen from the crystal structure during cycling [29], [30], [31], [32]. The density of states diagram is included in Appendix A.1 [31]. This potential electrical energy is deployed during discharge where electrons flow from the lithiated graphite anode to the more stable cathode by conducting electrical work in an external electrical circuit [10]. The intercalation of lithium ions (lithiation) back into the cathodic material occurs concurrently and incurs a reduction reaction demonstrated by the reversibility of reactions described in Equations 1.2-1.4 below.



The transfer of stored electronic charge ( $Q$ ) during cycling requires a current ( $I$ , where  $Q = I * t$ ) with the energy density of the cell ( $W$ ) proportional to the electrode potential difference ( $V$ ) within the cell (where  $W = V * Q$ ). The storage of this electronic charge ( $Q$ ) at the electrodes was defined as the capacity and was dependent on the degree of lithium (de)intercalation at the anode and cathode, with the charging capacity and discharging capacity being named accordingly. From a material level, the number of lithium ions that migrate per mole of material correlates to the specific (practical) capacity of a material, which cannot exceed the theoretical specific capacity described in Equation 1.1. This characteristic was critical at a large scale to satisfy the ‘range anxiety’ demanded by current consumers of lithium-ion battery powered devices such as electric vehicles.

One factor that helps determine the energy density of a material is the voltage at which the redox reactions occur. A redox reaction will occur at set voltages depending on the energy levels of the electrons orbiting a transition metal, with different elements and oxidation states transitions occurring at different voltage windows [30], [31]. A cell's voltage window may encompass multiple redox reactions, enhancing the energy density of the cell chemistry, but if the voltage was too high it can cause parasitic reactions between the cathode and electrolyte, causing loss of capacity and hazardous electrolyte decomposition. Consequently, a balance needs to be struck between upper cut-off voltage, which enhances the energy density if a higher voltage was used, and the mitigation of these degrading mechanisms which can hamper cell lifetime capabilities [33].

Typically, this is determined by the level of delithiation and the subsequent effect on the cathode structure, with a maximum state of charge (SOC) or depth of discharge (DOD) being determined. This also relates to over-charging/ over-discharging the battery, when charging occurs after the maximum SOC was achieved and forces lithium ions to be extracted from the cathode, saturating the anode, and causing structural weaknesses in the cathode [34]. Limiting the SOC range from 0-100% DOD to 10-70% can help avoid overpotential and polarization of the voltage profile (which results in the deviation from the electrochemical equilibrium), particularly if the upper cut-off voltage was limited and the lower cut-off voltage was reduced. This has a pronounced effect on increasing the cycling stability of the materials, reducing the capacity loss of  $\text{Li}(\text{Ni}_{0.76}\text{Co}_{0.14}\text{Al}_{0.1})\text{O}_2$  over 2500 cycles from 33.5% to 1.5% (at 25 °C, 1C) [35], [36].

The lifetime of the cell, or capacity retention, is a measure of a cell's ability to retain its capacity over a number of cycles. This characteristic can be affected by the voltage window (as described above), the temperature at which the cell was cycled, and the current applied (*i.e.* cell cycling rate). As temperature increases from 25 °C to 55 °C, it has been observed by Noh *et al.* and Harlow *et al.* that the capacity retention decreases, irrespective of cathode material and whether the cells have been cycling or stored [37] [38]. This increase in temperature facilitates a kinetically favourable environment that allows further delithiation, but encourages side reactions between the cathode and electrolyte, which results in a partially reversible phase transition from the desired O3 phase to the O1 phase, with the contraction of the *c*-axis hindering the re-intercalation of lithium ions into the delithiated structure [39], [40].

Slower charging rates enables high capacities and capacity retentions to be achieved upon charging and discharging [17]. Faster charging rates generate more heat and chemical instability within the cathode material and cathode-electrolyte interfaces, with an increased rate of parasitic reactions and lithium nucleation at the anode occurring [17]. Rate capability is a common test to analyse the performance of a material over a range of charging rates. The test involves cycling a cell for a set number of cycles at a slow cycling rate (known as C-rate) and repeating the cycling regime at faster C-rates to analyse the effect on the specific capacity yielded from the material, which typically decreases with an increase in C-rate [41] [42] [43]. A balance between energy density (i.e. specific capacity yielded from a cell) and power density (i.e. (dis)charging rate) needs to be found to account for the main consumer anxieties, which are the EV range and charging time [5].

## 1.2 – Development of Nickel-rich Cathode Materials

The first commercialised lithium-ion battery used a lithium cobalt oxide ( $\text{LiCoO}_2$ , LCO) cathode centred around the  $\text{Co}^{3+}/\text{Co}^{4+}$  redox reaction at 4-5 V and ignited research into the lithiated transition metal oxide chemistries [8]. The pseudo-cubic array of anions and layered crystalline structure of LCO allows a dense storage of lithium ions whilst allowing 2-dimensional channels for the lithium ions to (de)intercalate into/out of the material between the transition metal layers. This produces an *a-b* layered plane of transition metal oxide and lithium respectively that was stacked in the *c*-plane. This was equivalent to other transition metal oxide layered materials such as  $\text{LiNiO}_2$ ,  $\text{LiNi}_x\text{Mn}_y\text{Co}_z\text{O}_2$  and  $\text{LiNi}_x\text{Co}_y\text{Al}_z\text{O}_2$ , the structure of which can be seen in Figure 1.4.

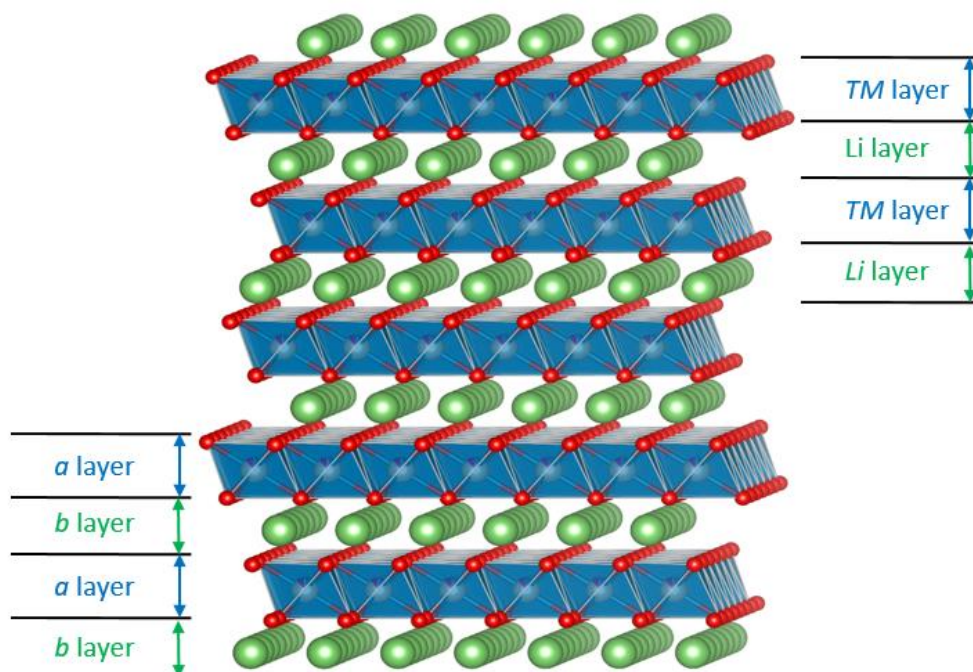


**Figure 1.4:** The crystallographic structure of lithium nickel-manganese-cobalt 8:1:1 oxide, which has a layered  $\alpha$ - $\text{NaFeO}_2$  structure and may also be applied to  $\text{LiNiO}_2$ ,  $\text{LiCoO}_2$  and  $\text{LiNi}_x\text{Co}_y\text{Al}_z\text{O}_2$ . The lithium ions are depicted as green, whereas the transition metals are the grey-purple-blue balls in the dark blue octahedral sites (in this circumstance, nickel is grey, manganese is purple, and cobalt is pale blue).

A theoretical capacity of  $274 \text{ mAh g}^{-1}$  was calculated for LCO but the practical reversible capacity was limited to *ca.*  $140 \text{ mAh g}^{-1}$  by limiting the upper cut-off voltage to 4.2 V due to the low structural stability at low lithiation levels [44]. The capacity limit of  $140 \text{ mAh g}^{-1}$  is due to the hybridisation of  $\text{Co}_{3d}$  and  $\text{O}_{2p}$  electron bands, with the energy required to extract more lithium (capacity) resulting in the oxidation of the  $\text{O}^{2-}$  ions, oxygen loss from the structure, and the resultant formation of a parasitic rocksalt phase [32], [45]. Increasing the cut-off voltage can increase the capacity to  $180 \text{ mAh g}^{-1}$  but imposes significant lattice defects due to phase transformations in the stacking sequences, impeding the cycling lifetime of the material [46], [47]. While LCO revolutionised the portable electronics industry, growing concerns over cobalt's high cost, toxicity, ethical and performance issues have led to further investigations where cobalt content has been reduced [48], [49]. Consequently, research began on alternative materials such as lithium nickel oxide and spinel lithium manganese oxide, the former of which showed high theoretical specific capacity ( $275 \text{ mAh g}^{-1}$ ), but had narrower practical-theoretical discrepancies, lower cost, and toxicity [9].

Lithium nickel oxide became a desirable material due to the increased practical capacity of over 200 mAh g<sup>-1</sup> (3.0-4.5 V), but experienced poor cycling performance when cycled above 4.2 V due to a contraction in the *c*-axis during delithiation [9] [50] [51]. The increased practical capacity for LNO was attributed to the increased electron stabilisation energy of the Ni<sup>3+</sup>/Ni<sup>4+</sup> redox pair in the e<sub>g</sub> energy band. This band has minimal overlap with the oxygen O<sub>2p</sub> band gap, allowing more capacity to be obtained before oxygen evolution and loss from the structure occurs [29], [31], [47]. Above 4.2 V, delithiation results in an absence of lithium in the LNO structure and causes a rapid *c*-axis contraction leading to the abrupt decrease in the cell volume, leading to particle mechanical strain at the grain boundaries between primary particles results in cracking and an irreversible loss of capacity [52].

The stoichiometry of LNO (Li<sub>1-z</sub>Ni<sub>1+z</sub>O<sub>2</sub>) during synthesis is also important, with an increase in off-stoichiometry yielding lower capacities [51]. The off-stoichiometries arise as Ni<sup>3+</sup> ions reduce to Ni<sup>2+</sup> during delithiation, which can irreversibly migrate to the Li layer in a process described as cation mixing. Ni<sup>2+</sup> ions migrate to the Li<sup>+</sup> interslab layer due to the similar ionic radii of (0.69 vs 0.76 Å), with the smaller ion causing a localised shrinkage to the ion site and the adjacent lithium sites, increasing the activation barrier and impeding lithium kinetics [9]. Obtaining stoichiometric LNO is difficult due to Ni<sup>3+</sup> readily reducing to form Ni<sup>2+</sup> in non-oxidising environments, with oxygen gas typically utilised during the calcination of Ni(OH)<sub>2</sub> to prevent this and minimise the value of *z* in Li<sub>1-z</sub>Ni<sub>1+z</sub>O<sub>2</sub>.

Challenges remain with LNO due to electrochemical (surface instabilities), mechanical (volume change during the phase transition above 4.2 V) and thermal (decomposition of LNO when heated in charged state) issues. To combat these, substituents were added to form nickel-manganese-cobalt (NMC) and nickel-cobalt-aluminium (NCA) system, which aimed to improve cycle life and safety. The specific capacity acquired from these materials (180 mAh g<sup>-1</sup> for NMC-622, 200 mAh g<sup>-1</sup> NCA) proved sufficient enough for the manufacture of electric vehicles [9].

### 1.2.1 – Development of NMC Materials

Tertiary systems were devised to stabilise LNO, with cobalt, manganese and aluminium applied to form NMC and NCA cathodes. Cobalt provides structural stability, particularly under deep delithiation conditions where capacity-degrading mechanisms can occur while manganese offers increased mechanical, structural and thermal stability in NMC compounds, with the

electrochemically inactive  $Mn^{4+}$  stabilising the cathode surface, increasing the cycling stability at higher cut-off voltages (4.5 V) [53] [54] [55] [56]. Aluminium in the NCA system is present as electrochemically inactive  $Al^{3+}$ , so is generally doped in small quantities (typically <5%) to minimise the capacity loss, meaning that increased cobalt content of 15% was typically used for commercial NCA-80:15:05. Due to the increased toxicity, expense and ethical issues associated with cobalt, nickel-rich cathode materials with lower cobalt content are preferred and NMC materials will be focussed on throughout this thesis.

Nickel-manganese-cobalt (NMC) chemistries were first synthesised with an equal ratio of Ni: Mn: Co (NMC-111) which yielded a competitive capacity of  $163 \text{ mAh g}^{-1}$  compared to the alternative cathode materials at the time (LFP  $169 \text{ mAh g}^{-1}$  and LCO  $150 \text{ mAh g}^{-1}$ , cycled at 2.5-4.3 V) [11] [38]. Due to the limited practical capacities that can be achieved by cobalt, and the electrochemical inactivity of manganese over a voltage window of 2.5-4.3 V, cathodes with a high nickel content were found to increase the achievable capacity of NMC materials [37]. Reducing the proportion of stabilising manganese and cobalt agents also leads to the thermal and mechanical stability decreasing. This is because as the nickel content exceeds 60%, degradation mechanisms associated with the rapid *c*-axis contraction propagates when the material is cycled above 4.2 V [33]. Increasing the nickel content provides an increased capacity upon first-cycle discharge ( $218 \text{ mAh g}^{-1}$  for  $LiNi_{0.9}Mn_{0.05}Co_{0.05}O_2$  compared to  $176 \text{ mAh g}^{-1}$  for NMC-532 and  $163 \text{ mAh g}^{-1}$  for NMC-111), but the absence of stabilising dopants such as manganese and cobalt results in reduced cycle retention [57].

$LiNi_xMn_yCo_zO_2$  is a layered transition metal oxide phase that forms an  $\alpha\text{-NaFeO}_2$  structure, visualised in Figure 1.3. Six oxygen atoms form an octahedral site occupied by a transition metal ion, which assemble along the *ab* plane to form a transition metal '3a' layer. Lithium intercalates into octahedral '3b' sites in the interslab layer, with empty tetrahedral sites situated between the adjacent octahedral sites. The transition metal '3a' and lithium '3b' layers stack along the *c*-axis in an ABAB formation as the layered transition metal oxide structure forms.

During delithiation, the quantity of lithium in the NMC structure decreases, consequently it is denoted as  $Li_fNi_xMn_yCo_zO_2$ , where 'f' is the fraction of lithium. This rhombohedral ' $R\bar{3}m$ ' system organises the octahedral sites into the 3-layer 'ABCABC' stacking sequence seen in  $LiNi_xMn_yCo_zO_2$  and is consequently described as 'O3' [58], [59]. This edge-sharing system experiences a reduction in symmetry during delithiation, forming a face-sharing  $Li_fNi_xMn_yCo_zO_2$  monoclinic  $C2/m$  phase with alternating 'ABAB' octahedral stacking described as 'O1' when  $f < 0.7$  [58], [60].

The transition from 'O3' stacking to 'O1' stacking encompasses four phase transitions during (de)lithiation as the migration of lithium causes structural changes: H1, M, H2 and H3 [59]. Visualisation of these changes can be found in Appendix A.2a) and A.2b). For near-full lithiation states (where  $f > 0.85$ )  $\text{Li}_f\text{Ni}_x\text{Mn}_y\text{Co}_z\text{O}_2$  exists in the first hexagonal 'H1' phase. The monoclinic 'M' phase represents a temporary phase transition to a less symmetrical monoclinic phase at  $0.5 < f < 0.8$  which incurs detrimental O'3 stacking caused by Jahn-Teller distortions, which can cause mechanical strain and micro-cracking [47]. One prominent example of this was the H2-H3 phase transition which occurs at 4.2 V and causes a significant *c*-axis lattice contraction that incurs an irreversible loss of capacity that occurs when  $f \approx 0.25$ . A further H3-H4 phase transition can occur when lithiation levels drop below  $f < 0.06$ , with the O3 stacking forming an O1 stacking fault that minimises oxygen *p* orbitals overlapping. The O1 structure can cause irreversible lithium inventory loss *via* the formation of  $\text{MO}_2$  [9], [50]. Although the H2-H3 and H3-H4 phase changes occur in  $\text{LiNiO}_2$ , there is no evidence of a O3-O1 phase transition in NMC materials [59], [61]

The oxidation of nickel from  $\text{Ni}^{2+}$  to  $\text{Ni}^{3+}$  occurs as lithium is extracted from the compound in order to balance the charge [62]. As oxidation occurs, the transition metal layer contracts due to the smaller ionic radius of  $\text{Ni}^{3+}$  (0.56 Å) compared to  $\text{Ni}^{2+}$  (0.69 Å) and the charge density increases, repelling adjacent transition metal layers with similar positive charge densities [9]. This leads to a gradual increase in the *c/a* ratio during charging until delithiation reaches approximately 75% in  $\text{Li}_f\text{Ni}_x\text{Mn}_y\text{Co}_z\text{O}_2$ , and a significant contraction in the *c*-axis occurs due to the H2-H3 transition, leading to unit cell shrinkage and mechanical strain on the crystal structure [63]. This volume change can facilitate  $\text{Li}^+/\text{Ni}^{2+}$  cation mixing, accelerating the electrochemical capacity degradation over the cell's lifetime.

The *c*-axis distortion within the structure results in a hexagonal structure with the lattice parameters being  $a=b=2.88$  Å and  $c=14.19$  Å. The *c/a* ratio represents this *c*-axis distortion relative to the  $3a$  and  $3b$  layers, with larger *c/a* ratios indicating a more layered material. A cubic system has a *c/a* of 4.9, whereas the *c/a* ratio for a hexagonal structure was slightly larger, in the range of 4.93-4.98, with LNO having a smaller *c/a* ratio of 4.93 compared to NMC materials, with NMC-111 having a ratio of 4.98 [9], [64], [65]. This ratio was typically acquired *via* X-ray diffraction (XRD) analysis, an example of which can be seen in Figure 1.5.

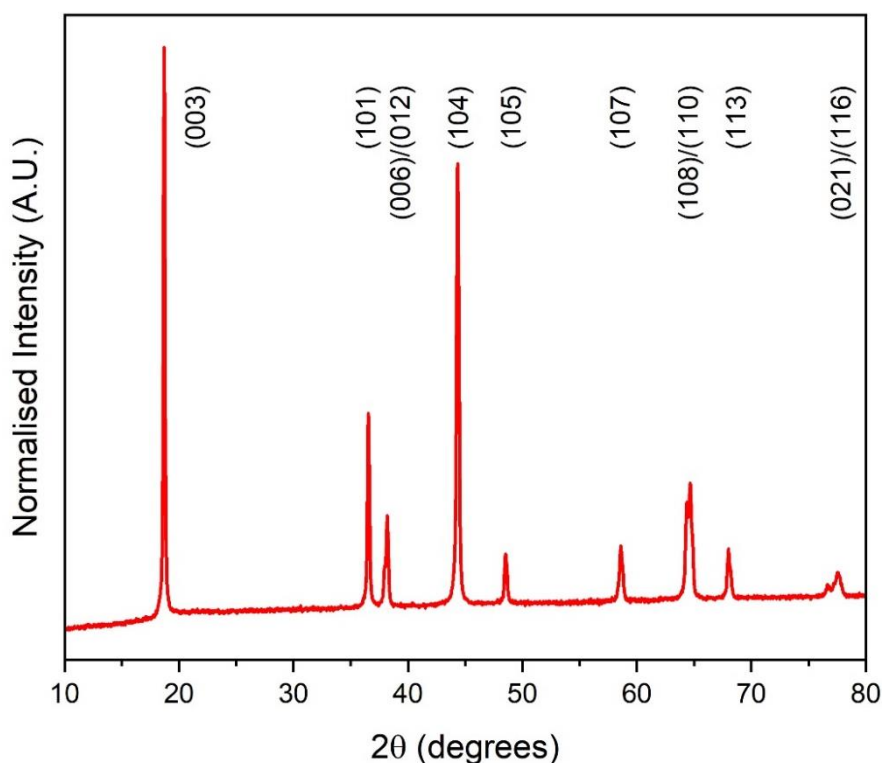


**Figure 1.5:** An X-ray diffraction pattern of NMC-811 with each Bragg peak labelled according to the  $hkl$  Miller indices.

There are indicators within the XRD pattern that can allude to the degree of crystallinity and degree of layering within the crystalline structure. Sharp, narrow peaks generally indicate a structure with good crystallinity, particularly with respect to the separation of peak doublets, for example the (006)/(012) and (108)/(110) doublets. Good peak separation in the (006)/(012) and (108)/(110) doublets can indicate good hexagonal ordering.

The intensity of peaks can qualitatively indicate features of the crystalline structure, for example the ordering of the transition metal layers and the degree of cation mixing. Specifically, the degree of cation mixing is qualitatively represented by the (003)/(104) ratio in transition metal oxides, with a ratio above 1.2 indicating a reduced degree of mixing [66]. Rietveld refinement can be conducted on XRD patterns in order to establish unit cell dimensions and volumes and can quantify the degree of cation mixing within the structure. Cation mixing values for Ni-rich cathodes are typically higher due to the reduction in cobalt content, with NMC-811 showing similar levels of nickel in the lithium 3a sites (2.6%) compared to NMC-622 (2.5%) and NMC-802 having less cation mixing (0.5%) [67]. Doping nickel-rich cathodes such as LNO can reduce the degree of cation mixing, as evidenced by NMC, but other dopants with high valence states (*e.g.* tungsten,  $W^{6+}$ ) can increase the  $Ni^{2+}$  in the system, promoting cation mixing [68], [69], [70].

Lithium ions migrate in and out of a layered transition metal oxide structure in their two-dimensional ab planes through site hopping, typically done by two mechanisms: oxygen dumbbell hopping (ODH) and tetrahedral site hopping (TSH) [71]. The ODH mechanism involves lithium ions hopping directly between octahedral sites *via* the oxygen ‘dumbbell’ bond that makes up one edge of the octahedral site, as seen in Figure 1.6. This typically occurs when an isolated vacancy was available at low levels of delithiation ( $f < 0.25$  in  $\text{Li}_{1-f}\text{MO}_2$ ) due to the electrostatic repulsion between the migrating Li-ion and the adjacent transition metal ions. The alternative mechanism, tetrahedral site hopping, occurs at higher delithiation levels ( $f > 0.25$  in  $\text{Li}_{1-f}\text{MO}_2$ ) when divacancies allow the migrating Li-ion to hop *via* a tetrahedral site, also seen in Figure 1.6 [72], [73].

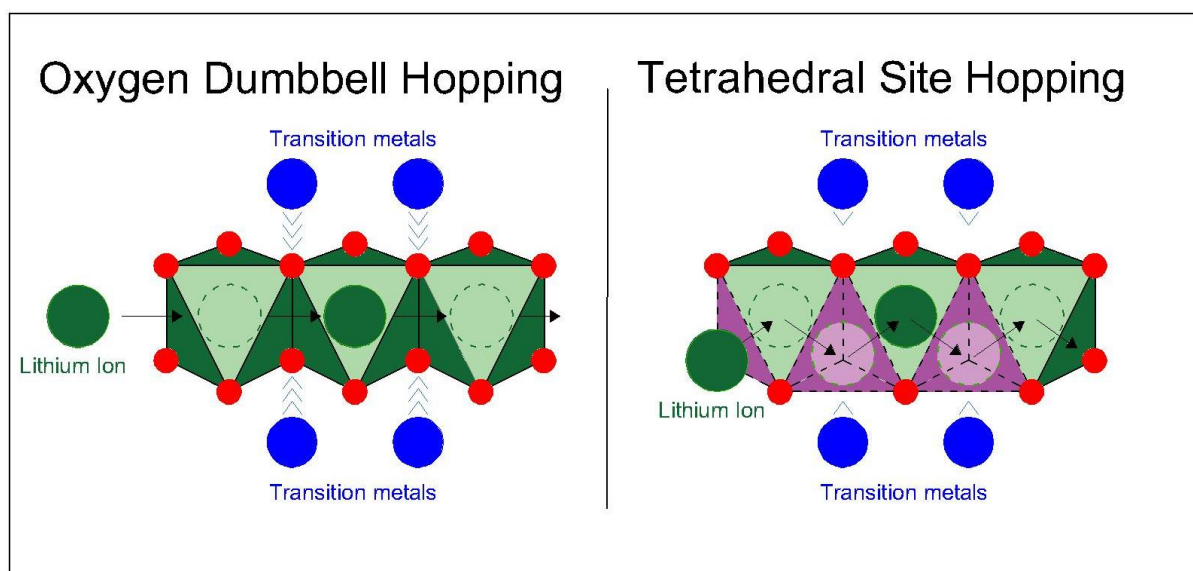


**Figure 1.6:** A depiction of the lithium-ion migration mechanisms during cycling, namely ‘oxygen dumbbell hopping’ (ODH) and ‘tetrahedral site hopping’ (TSH) [64].

As the delithiation level increases, the transition metal oxidation state increases, and the activation barrier to both pathways increase, with this being more significant in the ODH mechanism. This, along with the increase in vacant lithium sites and probability of divacancies occurring, means that the TSH mechanism becomes more favourable. There is a ‘strain effect’ experienced by the transition metal structure during the lithium migration mechanism, which occurs around the length of the oxygen bond (in the case of the ODH mechanism) or the tetrahedral site (in the case of the TSH mechanism). This naturally decreases during delithiation as the transition metal layers repel each other and the lithium interplanar gallery expands, favouring the TSH mechanism [71], [72], [73].

From a particle level, the delithiation process has been observed by Grey *et al.* using optical scattering microscopy. This work shows that as the charging mechanism occurs, delithiation first occurs in the periphery of the particle, with the core of the particle lagging behind. Once the core has approximately 20% level of delithiation, the overall particle delithiation increases uniformly until fully discharged. During discharging, the lithiation rate was uniform across the particle, with the centre having a marginally higher lithiation rate and the peripheral of the particle lagging [74].

The cycling rate at which lithium is extracted from electrodes can result in increased temperatures, chance of overpotential from higher currents promoting the formation, and thickening of solid electrolyte interfaces (SEIs) [75]. SEIs are formed naturally in the first few cycles from reactions between the electrodes and the electrolyte and consist of stable but electrochemically inactive lithium compounds such as lithium carbonate ( $\text{Li}_2\text{CO}_3$ ) and other lithium-based polymers from excess 'residual' lithium during synthesis [9], [76], [77]. Gases such as  $\text{H}_2$ ,  $\text{C}_2\text{H}_4$ ,  $\text{CO}$  and  $\text{CO}_2$  can also be produced as by-products from the SEI formation [78]. Water is sensitive to reduction in this environment, even during SEI formation, with the presence of  $\text{OH}^-$  and  $\text{H}^+$  ions creating additional reaction pathways to lithium polymers and carbonates. The same has been found for  $\text{CO}_2$ , which was an impurity in the system but can react to form lithium carbonates [76], [78].

The formation of this layer protects the cathode active material from further reaction with electrolyte but incurs a 'charge transfer resistance' at the SEI layer that reduces lithium diffusivity and can generate heat as the ions pass through it [47], [79]. If allowed to form appropriately, the SEI will allow metal ions to migrate through without further degradation. Typical cycling programmes have slower cycling rates for the first two cycles, typically called "formation cycles" to denote the formation of the passivating SEI. At the anode, a fully-passivated SEI can mitigate lithium plating and dendrite formation [76], [80], [81]. If the SEI was not formed correctly, it will continue to react and consume lithium inventory in the cathode and electrolyte, limiting the capacity the cell was able to achieve.

Transmission electron microscopy (TEM) and scanning electron microscopy (SEM) are two methods of visualising and analysing the physical structure and morphology of crystals and the resulting primary and secondary particles. TEM works by an electron source firing electrons through a vacuum and passing through the sample, which scatters some of the electrons. The un-scattered electrons reveal a shadow of the crystalline structure. Combined with energy-dispersive spectrometry (EDS), which uses X-rays to determine the elements in the sample, TEM can be used to visually identify the

layers of transition metals and lithium as well as observe the crystalline change to rocksalt structure and the formation of an SEI layer, as seen in Figure 1.6 [82].

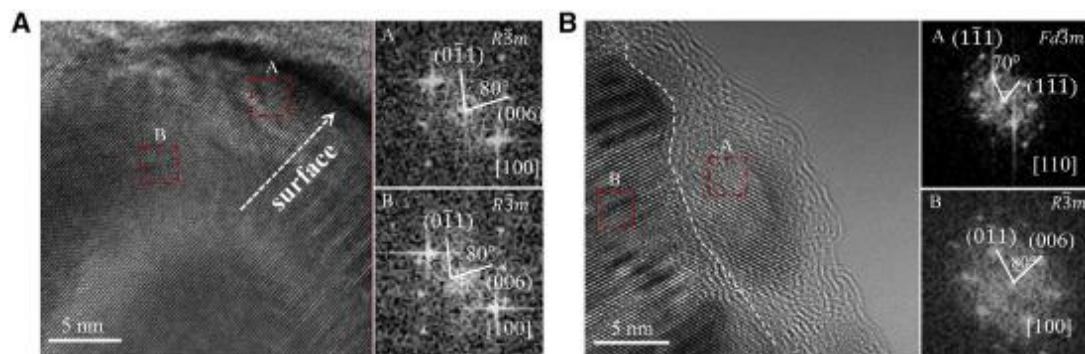


**Figure 1.7:** A high-resolution TEM image of NMC-811 depicting (a) the layered  $\text{LiNi}_{0.8}\text{Mn}_{0.1}\text{Co}_{0.1}\text{O}_2$  crystalline structure, identified by the parallel lines at site A and B; and (b) the change in crystalline structure from layered  $\text{LiNi}_{0.8}\text{Mn}_{0.1}\text{Co}_{0.1}\text{O}_2$  at site B to rocksalt  $\text{LiNi}_{0.8}\text{Mn}_{0.1}\text{Co}_{0.1}\text{O}$  at site A. Reproduced with permission from [82].

SEM is used for the analysis of primary and secondary particle morphology. SEM works by firing electrons at a sample through a vacuum, which then interacts with surface atoms and creates secondary electrons, backscattered electrons and X-rays which are collected, processed, and produce a highly magnified image of the sample.  $\text{LiMO}_2$  particles typically consist of small nanometre-sized primary particles which agglomerate to form quasi-spherical secondary particles, seen in Figure 1.8a. SEM can also be combined with EDS to determine the spatial distribution and quantities of different elements across primary and secondary particles.

Where primary particles tend to be on the order of 10-100 nm, secondary particles form quasi-spherical shapes with sizes typically ranging from 1-20  $\mu\text{m}$ , as seen in Figure 1.8b. Poor control of the synthesis conditions can lead to secondary particles agglomerating to form 3-50  $\mu\text{m}$  irregular ‘clusters’ seen in Figure 1.8c. The size and shape of secondary particles can be tuned during synthesis, with increased control yielding more uniform, quasi-spherical secondary particles. Homogeneous, quasi-spherical particles are preferred due to their uniform shape and subsequent lithium diffusion pathways out of each particle [55], [83]. This is discussed further below in Section 1.3.

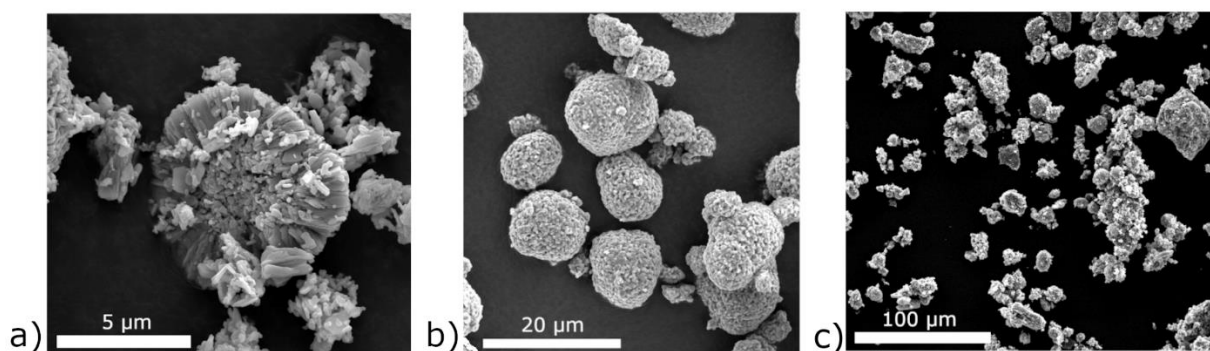


**Figure 1.8:** SEM images of **(a)** NMC-811 primary particles within the secondary assembly; **(b)** NMC-811 secondary particles with a quasi-spherical morphology **(c)** agglomerated ‘clusters’ of secondary NMC-811 particles. These materials were synthesised in-house at the University of Sheffield by Thomas Entwistle and Dr Nirmalesh Anthonisamy.

### 1.2.2 – NMC-811 as a Commercial Goal

Two NMC ratios containing 60% (NMC-622) and 80% nickel (NMC-811) were highlighted as commercially viable materials, being able to produce a capacity of approximately 160 and 180 mAh g<sup>-1</sup> respectively [12], [37], [78], [84], [85]. NMC-622 is the more stable chemistry, with an initial capacity in the region of 150-170 mAh g<sup>-1</sup> but a better capacity retention over 300 cycles (95% retention vs 66% for NMC-811 at 3.0-4.2 V) [33], [37]. However, a material energy density benchmark of 180-200 mAh g<sup>-1</sup> was set by consumers of electric vehicles, who required a range of 300 miles to overcome their range anxiety [5], [84]. NMC-811 was the material with the lowest nickel content to satisfy this, yielding initial capacities of 170-200 mAh g<sup>-1</sup> depending on cycling conditions [33], and was more stable than the 90%+ nickel alternatives and 100% nickel (LNO), yielding a capacity of *ca.* 230 mAh g<sup>-1</sup> (cycled at 0.1C, 2.7-4.3 V) and *ca.* 246 mAh g<sup>-1</sup> (cycled at 0.1C, 2.7-4.3 V) respectively [86], [87].

Reducing the levels of stabilising elements manganese and cobalt within the cathode active material exaggerates the chemical, structural and morphological instabilities, aggravating capacity degradation of the material over its lifetime. High cut-off voltages are evidence of this, with NMC-811 having a reduced capacity retention at higher voltage cut-offs compared to NMC-622 and NMC-111 due to the collapse in the *c*-axis at *ca.* 4.2 V [78] [88] [67]. At this high voltage, the *c*-axis of the lattice structure collapses due to the level of delithiation (approx. 80%) which can lead to irreversible capacity loss [86]. The anisotropic volume expansion and contraction leads to

intergranular mechanical strain that can form and propagate microcracking within the secondary particle, eventually leading to particle pulverisation [88].

Should these penetrate the surface, electrolyte can perforate into the interior of the particle, resulting in more SEI formation, loss of active material, and increased degree of capacity fading. In severe events, cracking can result in the severe reduction in electrical contact of active material from a secondary particle formation, which can be seen below in Figure 1.9. It has been shown that the increase in nickel content can increase the width and surface penetration of the microcracks, particularly at Ni >90% [9], [88]. Dopants have been shown to alleviate microcracking, either by limiting the *c*-axis contraction, with magnesium, or by aligning the primary particles such that the anisotropic expansion causes minimal mechanical strain, such as tungsten or boron [89], [90], [91], [92].

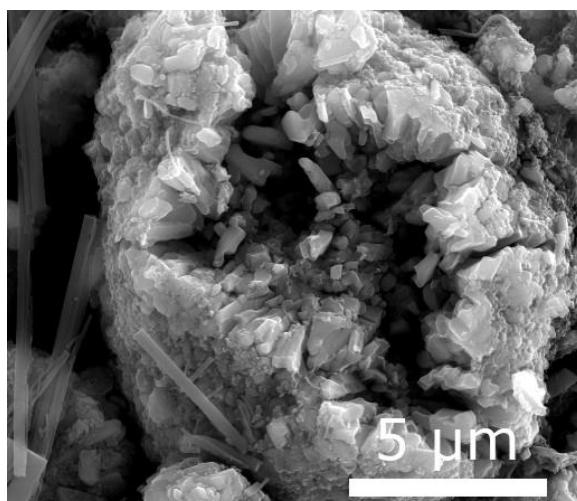


**Figure 1.9:** A LiNi<sub>0.8</sub>Mn<sub>0.1</sub>Co<sub>0.1</sub>O<sub>2</sub> particle that has undergone an extreme cracking event post-cycling. Microcracks can be seen on the right side of the particle, with a larger crack on the upper side of the image. These materials were synthesised in-house at the University of Sheffield by Thomas Entwistle and Dr Nirmalesh Anthonisamy.

Cation mixing is another degradation mechanism that occurs at high degrees of delithiation. The Ni<sup>2+</sup> ion migration can to lithium 3*a* octahedral sites act as a “pillar” to prevent structural collapse through electrostatic repulsions. This is due to the similar ionic radii of Ni<sup>2+</sup> (0.74 Å vs 0.76 Å for Li<sup>+</sup>) of divalent nickel. This mechanism is generally reversible, but as the structure reaches higher levels of delithiation, nickel migration to the intermediate tetrahedral sites becomes energetically favourable but is irreversible [93].

Excessive voltages can cause decomposition of residual lithium compounds (*e.g.*  $\text{Li}_2\text{CO}_3$ ), and electrolytic components such as the lithium salts and organic solvents. Above 4 V, the decomposition of these electrolyte components incurs a thickening of the SEI, which increases electrode diffusion resistances and inhibits the capacity and cycling rate capabilities [94]. One of the salts, lithium hexafluorophosphate ( $\text{LiPF}_6$ ), commonly breaks down in the presence of water to form lithium fluoride ( $\text{LiF}$ ), which can deposit on an electrode to form/thicken an SEI or can react with water to form hydrofluoric acid ( $\text{HF}$ ) [85], [94], [95].  $\text{HF}$  has a detrimental effect on the stoichiometry of the cathode lattice, reacting with the surface to dissolve manganese and cobalt into the electrolyte. The dissolved transition metals can migrate to the anode and poison the anodic SEI and degrade the separator, increasing capacity decay and the potential for short-circuiting and thermal runaway. Different techniques have been employed to mitigate this that revolve around the scavenging water and  $\text{HF}$  from the electrolyte, including lithium phosphate ( $\text{Li}_3\text{PO}_4$ ) coatings and metal-organic framework additives in the electrolyte [96], [97].

The breakdown of electrolyte is exacerbated by the presence of delithiated cathode, with the  $\text{Ni}^{4+}$  being particularly reactive [98]. A parasitic reaction between tetravalent nickel and the electrolyte results in oxygen loss from the lattice structure, causing a surface phase transformation from the layered transition metal oxide to a spinel or rocksalt structure, incurring an increase in electrochemical impedance in the form of surface-film resistances [88], [99]. The spinel-rocksalt formation occurs at high temperatures (above 200 °C depending on the cathode composition) and involves the oxygen loss as the stoichiometry of the lattice changes from  $\text{LiMO}_2$  (layered) to  $\text{LiM}_2\text{O}_4$  (spinel) as delithiation reaches  $x=0.5$ , and  $\text{LiMO}$  (rocksalt) [99], [100].

Thermal decomposition of the cathode material can also result in the detrimental layered-to-rocksalt phase transformation. The decomposition temperature decreases with increasing nickel content due to its chemical instability, and the instability increases during delithiation [101]. When delithiation levels exceed 50%, the rocksalt formation has been shown to become exothermic, increasing the temperature of the system and likelihood of thermal runaway [102]. Both the temperature and the rate of temperature increase are factors that determine the potential for thermal runaway, with temperatures above 130 °C decomposing the electrolyte separator and triggering short-circuiting, and 180 °C triggering the breakdown of the cathode layered materials to rocksalt (in this case,  $\text{LiCoO}_2$ ). Once the temperature increase rate exceeds 10 °C per minute, thermal runaway was decreed [99].

Thermogravimetric analysis (TGA) combined with mass spectrometry (MS) has allowed further insight into the thermal instability of NMC cathode active materials through the identification of material evolution within different NMC ratios as temperature was increased. TGA-MS has shown that at elevated temperatures, there was a mass loss corresponding to oxygen release, with the increase in nickel content within the cathode material indicating a lower temperature of oxygen release and an increased amount of oxygen released from the structure [103]. This corresponds to the formation of the nickel oxide rocksalt phase and the evolution of structural lithium to lithium oxide ( $\text{Li}_2\text{O}$ ), which consequently limits the capacity both by reducing lithium inventory and through structural storage of lithium ions [103].

This process was exacerbated if the NMC material was exposed to moisture ( $\text{H}_2\text{O}$ ) and carbon dioxide ( $\text{CO}_2$ ), which react with lithium to form the surface species of  $\text{LiOH}$  and  $\text{Li}_2\text{CO}_3$  found on cathode materials. There were two main mass-loss temperature periods measured, one between  $150\text{ }^\circ\text{C}$  and  $450\text{ }^\circ\text{C}$  which corresponds to the decomposition of  $\text{LiOH}$  and embedded  $\text{H}_2\text{O}$ ; and one above  $650\text{ }^\circ\text{C}$  which corresponds to the decomposition of  $\text{Li}_2\text{CO}_3$ . It was observed that at  $150\text{-}450\text{ }^\circ\text{C}$  there was a higher mass loss attributed to  $\text{H}_2\text{O}$  through  $\text{LiOH}$  decomposition, which was increased for higher nickel content materials, with 2.13% mass loss observed for NMC-901, whereas NMC-532 observed a 0.4% mass loss [103]. In the same region there was also  $\text{O}_2$  and  $\text{CO}_2$  generated. There was no explanation given for this low-temperature evolution of  $\text{O}_2$  gas, but  $\text{CO}_2$  generation at a temperature below its thermal degradation temperature of  $680\text{-}780\text{ }^\circ\text{C}$  was concluded to be the result of adsorbed  $\text{CO}_2$ , with lower nickel content materials adsorbing more  $\text{CO}_2$ .  $\text{CO}_2$  and  $\text{O}_2$  are also generated at temperatures above  $650\text{ }^\circ\text{C}$ , with this being attributed to the decomposition of  $\text{Li}_2\text{CO}_3$  and oxygen evolution observed in unexposed NMC materials [104]. Higher nickel content materials displaying an increase in mass loss at lower temperatures as a result of the presence (and decomposition) of more  $\text{Li}_2\text{CO}_3$  and oxygen evolution [103].

### 1.2.3. – Future Advances to NMC-811

Doping LNO and nickel-rich NMC can improve the electrochemical performance, typically by improving the structural stability. Replacing cobalt in NMC with other elements that increase thermal and cycling stability could increase performance while simultaneously decreasing cobalt content. Doping 0.7% aluminium into the cobalt sites of NMC-61: 27: 12 has been shown to increase

the capacity retention without sacrificing specific capacity, yielding an 84.5% capacity retention after 3000 cycles compared with the undoped sample (65.1%) [105]. Li *et al.* replaced all cobalt with aluminium in NMC materials to produce a nickel-manganese-aluminium 'NMA' structure [101]. The NMA system was compared to the NMC, NCA, and an Al- and Mg- doped NMC system (NMCAMg). The NMA had a reduced first-cycle capacity (216 mAh g<sup>-1</sup> vs 220 mAh g<sup>-1</sup> for NCA-88: 05: 06 at 2.8-4.4 V, 0.1C) but increased capacity retention after 100 and 1000 cycles (82% vs commercial NMC-622 at 80% and NCA-88 at 54%). The manganese and aluminium appear to increase the thermal stability of NMA relative to NCA-88 by maintaining a high exothermic event temperature and reducing degree of heat flow at the event [101].

Other metals have been investigated to improve cycling stability and capacity attributes of nickel-rich cathode systems. Tungsten has been one such dopant that has shown improved capacity retention of NMC-811 at a higher cut-off voltage (92.1% vs 85% retention at 2.8-4.5 V, 1C charging after 100 cycles), reduced electrolytic attack and HF formation, and suppresses the rocksalt phase transition [106]. Tungsten dopes the Ni<sup>2+</sup> sites with a W<sup>6+</sup> ions, which alters the charge balance of the system, decreasing the capacity slightly through cation mixing and nickel inventory displacement, but capacities of over 200 mAh g<sup>-1</sup> being achieved after 100 cycles [107]. Other dopants include zirconium [93], titanium [9], tin [108] and tantalum [109]; all doping the transition metal layer and increasing the stability of the lattice structure during cycling to extend cycling life. It was important to consider the economic impact when researching dopants however, as the cost of the dopant will impact the financial viability of the product when it reaches commercialisation. Although tantalum may improve the stability of NMC-811 to a greater than magnesium, aluminium, and titanium, it is approximately 100 times more expensive and so poses a reduced commercial potential [109] [110].

Coating nickel-rich materials can also improve the capacity retention of nickel-rich cathodes, with a stable coating acting as an artificial SEI that shields the reactive Ni<sup>4+</sup> ions from electrolytic attack [47]. These materials are electrochemically inactive and include materials like silicon and metal oxides, which ideally have good ionic conductive qualities to minimise the resistances applied to the lithium migration process [111]. Coatings are typically applied by wet or dry processing which involves mixing the cathode materials with the coating material aqueously or *via* milling before an additional calcination stage secures the coating to the cathode. These methods are typical due to their ability to be scaled for high-throughput synthesis, but do not apply the coating evenly across the particles. The inclusion of water may also react with Ni<sup>4+</sup> and cause rocksalt formation from the layered oxide cathode [92], [112]. Alternatively, atomic layer deposition (ALD) can be used to coat

samples with a controllable and uniform thickness but was expensive to scale up to high throughput synthesis [113].

Additionally, core-shell and gradient particles are one method of developing an electrochemically active surface coating. By changing the cathode active material between the core and surface, a high-capacity, nickel-rich cathode can be utilised in the core and a stable cathode material can be grafted to the surface of the particles, maximising the capacity yielded from the cathode materials whilst protecting the nickel-rich material from electrolyte exposure and degradation mechanisms. One consideration with the core-shell and gradient particles, as well as the coatings of these particles, was that they should be able to adjust to the volumetric expansion and contraction that occurs to the particles during cycling [114], [115], [116].

#### 1.2.4. – The NMC Precursor

The  $\text{LiMO}_2$  layered oxide product has a precursor prior to the lithiation and calcination stage of the synthesis pathway. The layered precursor structure is typically synthesised in either a hydroxide form ( $M(\text{OH})_2$ ) or hydroxy-carbonate form ( $M_2(\text{OH})_x(\text{CO}_3)_y$ ) [117]. The transition metal compound was then milled with a corresponding salt,  $\text{LiOH}$  or  $\text{Li}_2\text{CO}_3$  respectively during lithiation prior to calcination and the formation of the  $\text{LiMO}_2$  layered oxide. For nickel-rich cathodes, the transition metal hydroxide calcined with lithium hydroxide ( $\text{LiOH}$ ) is preferred due to the lower thermal decomposition of  $\text{LiOH}$  (400-650 °C) meaning that the lithium salt will fully decompose at the calcination temperature range (750-850 °C for NMC-811) [37], [104], [118]. The higher thermal decomposition of lithium carbonate (680-780 °C) means the lithium salt will not fully decompose over the calcination period. This results in a reduced amount of lithium intercalating into the NMC structure and a lithium deficiency, which would result in a reduced electrochemical capacity [103].

Similar to the lithiated NMC oxide, the transition metal hydroxide (abbreviated to  $\text{NMC}(\text{OH})_2$ ) has a layered structure with trigonal symmetry and is isostructural to  $\text{Ni}(\text{OH})_2$  with regards to crystallographic and morphological properties. There are two polymorphs of  $\text{Ni}(\text{OH})_2$  denoted as ' $\alpha\text{-Ni}(\text{OH})_2$ ' and ' $\beta\text{-Ni}(\text{OH})_2$ '; the latter of which was more commonly involved with the synthesis of NMC cathode materials [119], [120]. The  $\beta\text{-Ni}(\text{OH})_2$  'brucite' polymorph consists of trigonal layers stacked in the *ab* plane that are stacked in parallel, whereas  $\alpha\text{-Ni}(\text{OH})_2$  consists of  $\beta\text{-Ni}(\text{OH})_2$  layers with water intercalated between layers as seen in Figure 1.10 a) and b) respectively [119]. There is a third polymorph prevalent in doped  $\text{Ni}(\text{OH})_2$  that arises from the inclusion of trivalent transition

metals (*i.e.* manganese and cobalt) called layered double hydroxide (LDH). Structurally, it is similar to  $\alpha$ -Ni(OH)<sub>2</sub> that consists of the  $\beta$ -Ni(OH)<sub>2</sub> layers but with anions intercalated between layers. The additional positive charge from the trivalent transition metal needs to be balanced, hence the intercalation of anions, which can be OH<sup>-</sup> (hydroxide), NO<sub>3</sub><sup>-</sup> (nitrate) or CH<sub>3</sub>COO<sup>-</sup> (acetate) ions depending on the solution in which the Ni(OH)<sub>2</sub> was synthesised in [119], [121], [122]. This enlarges the interplanar gallery spacing, just as  $\alpha$ -Ni(OH)<sub>2</sub> does.

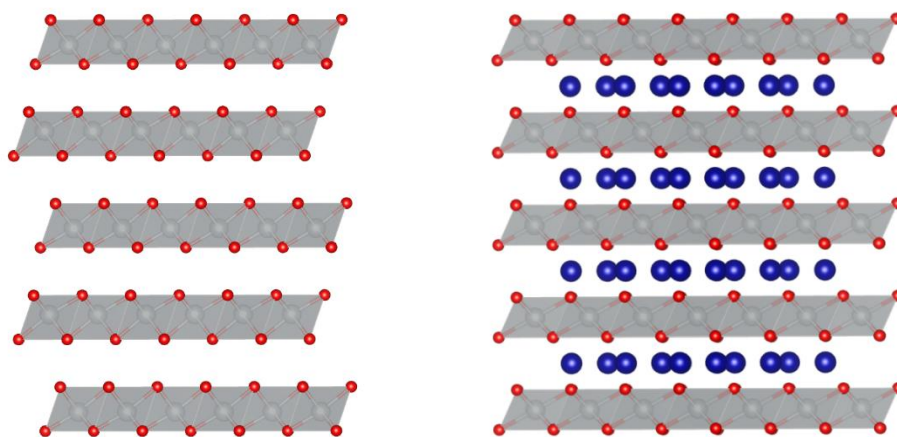


**Figure 1.10:** A crystallographic representation of **(a)**  $\alpha$  Ni(OH)<sub>2</sub>, which can be appropriated as the layered double hydroxide structure; and **(b)**  $\beta$  Ni(OH)<sub>2</sub>. These images were prepared using Vesta version 3.5.8 [14] using appropriate CIF files.

The water and anion intercalation between the transition metal layers mean that  $\alpha$ -Ni(OH)<sub>2</sub> and LDH have a more turbostratic crystallographic structure than the  $\beta$ -Ni(OH)<sub>2</sub> alternative. This is visualised as fewer peaks in the XRD diffraction patterns, seen in Figure 1.11. The splitting of the (001) peak from the beta- to the (001) and (002) alpha- polymorph is indicative of the water/anionic disruption to the crystalline structure between the transition metal layers. This interlayer disruption was also seen by the reduction of lattice planes orientated through the *c*-axis. The unlabelled peaks in the alpha polymorph are attributed to aluminium of the XRD stage [119].

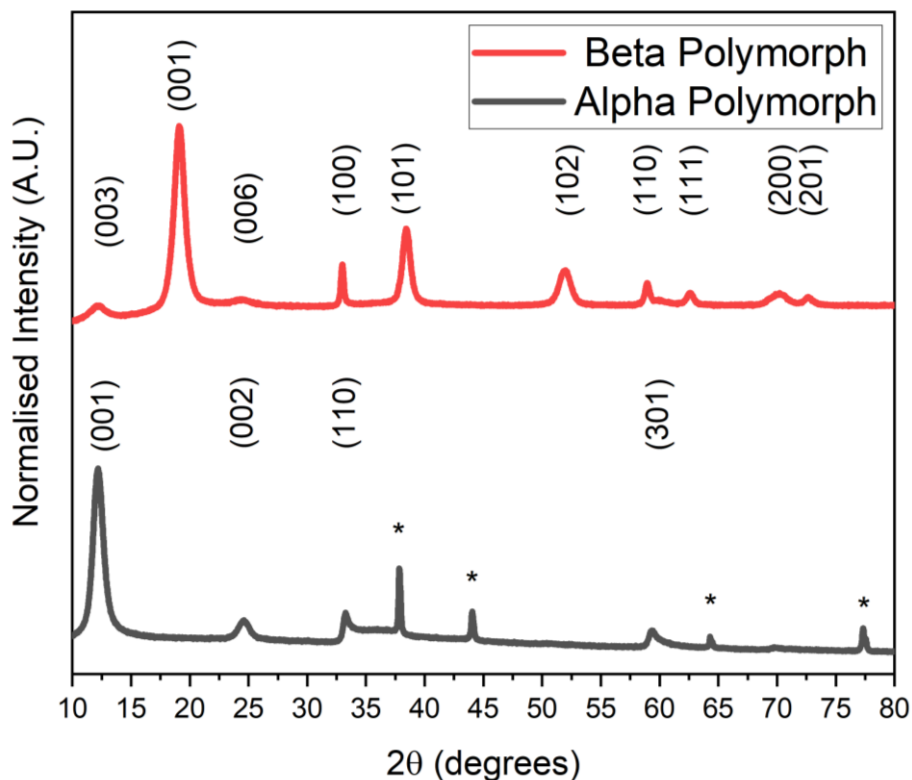


**Figure 1.11:** The XRD pattern for alpha- and beta- Ni(OH)<sub>2</sub> with key peaks labelled. The peaks labelled with an asterisk in the alpha polymorph are attributed to aluminium of the XRD stage.

Structural disorder can occur in both the  $\alpha$ -Ni(OH)<sub>2</sub>,  $\beta$ -Ni(OH)<sub>2</sub> and LDH polymorphs. Rotational and translation stacking faults are prevalent in  $\beta$ -Ni(OH)<sub>2</sub>, and result in the stretching of the O-H bonds and broadening in the (101) and (102) XRD diffraction peaks. The partial intercalation of water and anions can create a hybrid ‘interstratified’  $\alpha/\beta$  Ni(OH)<sub>2</sub>, in which the two polymorphs are present in the same structure and the misalignment of layers can occur as the transition metal layer spacing changes [119], [122], [123]. In these two-phase systems, the two  $\alpha$ -Ni(OH)<sub>2</sub> (00L) peaks can be present in the  $\beta$ -Ni(OH)<sub>2</sub> diffraction pattern, labelled as (003) and (006) accordingly [121]. These samples were prepared with an aluminium XRD stage, with some Al Bragg peaks being detected, identified by cross-referencing with a CIF file from ICSD, and labelled with an asterisk [124]

Ni(OH)<sub>2</sub> and NiCO(OH)<sub>2</sub>, in both polymorphs, have been synthesised using a variety of pathways including sol-gel, hydrothermal and co-precipitation. These methods form thin nanosheet and nanoribbon primary particles that assemble to form secondary assemblies, which depending on the control of the synthesis conditions, the secondary morphology can be controlled to form either a quasi-spherical secondary particle, faceted, or irregular ‘clustered’ morphologies [119], [125], [126], [127].

### 1.3. – Synthesis Techniques

Layered transition-metal oxides have been synthesised *via* many pathways, generally involving chemical mixing or reaction followed by high temperature calcination. Originally, LCO and LNO were synthesised *via* a solid-state route, milling the transition metal salt and lithium salt together and exposing it to a high temperature treatment to form the  $\text{LiMO}_2$  desired [8], [128]. This method had limited control and often resulted in off-stoichiometric product, especially when LNO was being synthesised which yielded lower capacity values both initially and after 10 cycles due to cation mixing of the  $\text{Ni}^{2+}$  ions [51], [129].

Other methods have been used to synthesise layered transition-metal oxides including sol-gel (forming a gel-like mixture before evaporating and calcining) [130], [131] and molten salt synthesis (high-temperature heating of a solution before chemically precipitating the product) [132], [133], [134]. Although effective, the conditions within these reactions were difficult to control, which is particularly important for nickel-rich cathode materials as they are more sensitive to oxygen and water. The increased presence of  $\text{Ni}^{4+}$  can cause structural and chemical instabilities that result in reactions with electrolyte which could generate oxygen gas, a critical substance in the thermal runaway mechanism [78], [88]. These instabilities are present throughout the synthesis process, which needs to be carefully controlled.

Two alternative synthesis pathways, co-precipitation (reacting a solution to produce a precursor, before lithiation and high temperature heat treatment) and hydrothermal (using high temperatures and pressures to synthesize a precursor before heat treatment) [135], [136] have been investigated due to their ability to control the particle growth and morphology as well as their ability to be used for high-throughput synthesis, with many companies using co-precipitation [137], [138].

The commercially desired NMC product has average particle size of  $<0.5\text{-}20\ \mu\text{m}$ , with polycrystalline particles with a quasi-spherical morphology having a secondary particle assembly (*i.e.* multiple primary particles agglomerating together) and a larger diameter of approximately  $5\text{-}20\ \mu\text{m}$ ; and monocrystalline 'single-crystal' particles, which consist of a faceted, primary particle which typically have a particle size of  $<0.5\text{-}5\ \mu\text{m}$ , which is synthesised with the addition of a surfactant agent [139], [140], [141]. Smaller particles ( $0.1\text{-}1\ \mu\text{m}$  diameter) have been shown to have an improved capacity and rate capabilities due to shorter lithium diffusion pathways, but a lower cycling retention compared to larger particles ( $10\ \mu\text{m}$  diameter) [136], [142]. The focus of previous research in literature regarding the synthesis of NMC-811 has been particle size and morphology control, with

quasi-spherical, polycrystalline particles with a particle size diameter of approximately 10  $\mu\text{m}$  desired, with larger particles yielding a higher tap density [142]. Tap density is the density of a material after vibrations (or tapping) has occurred, which results in the optimal positioning of particles to reduce voidage and therefore optimise the effective density or 'packing' of said particles. The synthesis of monocrystalline, 'single-crystal' particles is mentioned out of completeness of this literature review but is beyond the scope of this thesis.

### 1.3.1. – Particle Nucleation and Growth

The construction of a cathode active material particle has been researched, with a high tap density, uniform particle size and quasi-spherical morphology being preferred for  $\text{LiMO}_2$  particles [143], [144]. The development of these particles is typically described by LaMer's mechanism, which consists of two stages of particle formation: nucleation and particle growth. Nucleation involves the formation of a particle from solution and its growth to the critical nucleus (the size above which particle can survive in solution without re-dissolving). This was followed by particle growth, which involves the ripening of the surviving particles that mature to form the desired dense, quasi-spherical morphology in the secondary particles. The synthesis conditions can affect the particle density, morphology and size and should be controlled in order to tailor particles [145].

Nucleation typically occurs in a mass-nucleation event where monomers nucleate to form a solution with an "effectively infinite" concentration, after which nucleation does not frequently occur. Nucleation can occur homogeneously (where the particle forms uniformly through the parent phase) or heterogeneously (where the particle forms at a system abnormality, such as container surface, impurity, or boundary), with the stable surface making heterogeneous nucleation more favourable [145] [146]. Following the nucleation event, ripening and growth occurs, *via* one of Ostwald ripening or digestive ripening. Ostwald ripening involves smaller particles dissolving into the solution to allow the larger particles to grow, leading to a particle size distribution. Digestive ripening involves the larger particles being consumed by the solution to allow the smaller particles to grow, reducing the particle size distribution [145], [147].

The free energy of the system determines whether the particle re-dissolves, which was the sum of the surface free energy and the bulk volume free energy. Once the critical nucleus has been reached, the bulk volume free energy dominates the surface free energy and the particle will grow [145],

[148]. The final stage of nucleation, where the particles were controlled by the diffusion of monomers through Fick's first law of diffusion [145], [149].

### 1.3.2. – Co-precipitation Synthesis Route

A co-precipitation reaction involves the controlled concurrent precipitation of transition metals from their salt precursor *via* the addition of a base solution and a complexing agent. The dissolved salt releases metal cations which form complexes with the complexing agent before its reaction and precipitation due to the basicity of the solution. The reaction conditions within a stirred tank reactor (STR) can be carefully controlled, with the temperature, pH, atmosphere, stirring speed and ratio of transition metal: base: complexing agent all affecting the precipitation mechanism. The metal precipitates formed can be harvested from the waste aqueous solution and washed.

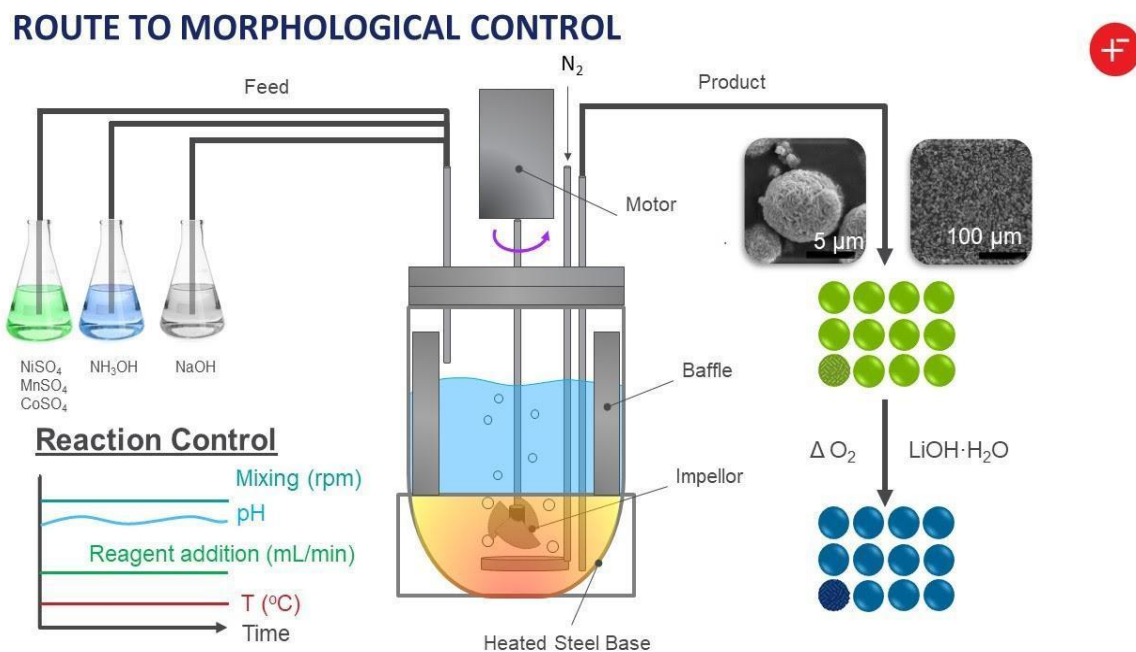


**Figure 1.12:** A schematic of the co-precipitation synthesis pathway for NMC materials, including the chemical reaction to form the 'green'  $\text{Ni}_x\text{Mn}_y\text{Co}_z(\text{OH})_2$  and the calcination to form the 'blue'  $\text{LiNi}_x\text{Mn}_y\text{Co}_z\text{O}_2$  (*n.b.* these colours are not representative of the actual colours of the materials) [83].

For NMC materials, stoichiometric amounts of nickel, manganese, and cobalt sulphates are dissolved in deoxygenated, deionised water and reacted with a base solution typically consisting of either sodium hydroxide or sodium carbonate, depending on the desire for a hydroxide or carbonate NMC

precursor. Sodium hydroxide is the most common choice for nickel-rich materials as it complements the lithium hydroxide salt used in its calcination. The pH, a metric for the proportion of  $H^+$  ions in the system and its acidity, is an important factor that controls the rate of reaction (precipitation) of the acidic component (TM sulphate) and base component (sodium hydroxide) of the co-precipitation reaction.

A complexing agent, ammonia, is also used to agglomerate transition metal ions within the solution prior to the precipitation of the  $Ni_{0.8}Mn_{0.1}Co_{0.1}(OH)_2$  solid [67], [137]. The temperature, ratio of transition metal and pH all impact the development and growth of the particles and need to be tailored to the NMC ratio due to the solubility of each transition metal at each pH [143], [150]. The precipitate is washed and filtered to remove salts formed during the co-precipitation reaction, before introducing lithium to the system *via* milling with a lithium salt (typically lithium hydroxide because of a suitably low thermal decomposition temperature) [151].

An example of the reaction/reactor configuration can be seen in Figure 1.12, with the reaction typically occurring in a stirred tank reactor (STR), which allows the control over temperature, pH, atmosphere, and agitation rate. The transition metal, base and ammonia solutions addition rate can be controlled to cater for desired pH control and reaction times, with the addition of the base solution being used in a feedback loop controlled by the pH meter recordings. Nitrogen gas is added *via* a sparger, which maximises the dispersion of nitrogen within the solution. The vessel was kept at atmospheric pressure, with a condenser unit mitigating losses through evaporation.

#### 1.3.2.1. – Chemical Parameters Affecting the Co-Precipitation reaction

Control over the reaction conditions for nickel-rich NMC materials (*e.g.* NMC-811) is critical due to the readiness for  $Ni^{2+}$  and  $Mn^{2+}$  to oxidise. The reaction solution is basic, which increases the sensitivity for nickel and manganese to oxidise, as evidenced by Pourbaix diagrams in Figure 1.13, which map the transition metal valences at various redox environments. An inert, nitrogen atmosphere and use of deoxygenated water would reduce the redox potential of  $Mn^{2+}$  and  $Ni^{2+}$  and promote the  $Ni(OH)_2$  and  $Mn(OH)_2$  phases at high pH's which form the preferred layered precursor. Oxidation of the  $Mn^{2+}$  and  $Ni^{2+}$  ions can lead to the formation of layered-double hydroxide, metal oxide or spinel  $Mn_3O_4$  phase impurities that disrupts the ordering of the desired  $Ni_{0.8}Mn_{0.1}Co_{0.1}(OH)_2$  layered structure [137], [152].

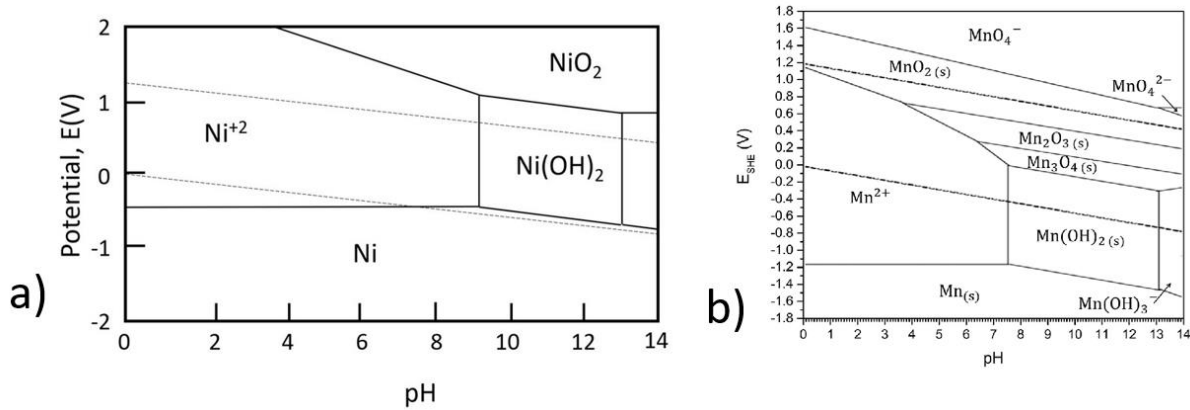
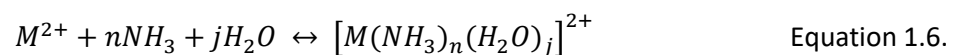


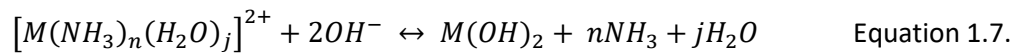
**Figure 1.13:** Pourbaix diagrams depicting the different Nickel **(a)** [153] and Manganese **(b)** [154] species present at different pH and redox states.

The temperature of the precursor synthesis also relates to the oxidation states of nickel and manganese, with an increase in temperature resulting in the increase in redox potential according to the Nernst equation seen in Equation 1.5. below.  $E$  and  $E^0$  represent the cell potential and standard cell potential respectively,  $R$  and  $F$  represent the universal gas constant ( $8.314 \text{ J mol}^{-1} \text{ K}^{-1}$ ) and Faraday constant ( $96,485 \text{ C mol}^{-1}$ ),  $n$  was the number of moles of electrons involved and  $T$  was temperature in Kelvin [155]. As per the Pourbaix diagrams of Figure 1.13, an increase in cell potential can expose the transition metal to the possibility of oxidising and forming undesired phases. For NMC systems, an ideal temperature range of between 50 and 60 °C has been reported without oxidising the manganese, which occurs above 60 °C [118]. It has been found that synthesis of NMC-811 at 45 °C has yielded smaller primary particles and lower tap density [118], [156].

$$E = E^0 - \frac{RT}{nF} \ln(Q) \quad \text{Equation 1.5.}$$

Another conclusion drawn from Figure 1.13 is that the formation of the  $M(\text{OH})_2$  phase requires a high pH of between 9 and 13. This is accomplished through the inclusion of sodium hydroxide and ammonia in the solution. A 2-stage reaction scheme described in Equation 1.6 and 1.7 details the dissolution of the transition metal ions and their subsequent complexation with ammonia and water atoms, before the basicity of the solution allows the  $M(\text{OH})_2$  phase to form through the introduction of  $\text{OH}^-$  ions [137], [157], [158]. The transition metals have a 6-coordination ligand, hence the sum of ‘ $n$ ’ and ‘ $j$ ’ equal 6. An increase in pH would increase the concentration of hydroxyl ions and shift the equilibrium of Equation 1.7 to the right, increasing the yield of the  $M(\text{OH})_2$  phase.





Van Bommel *et al.* reported that an optimal pH range of 10.0-11.5 was preferred for the synthesis of nickel-rich hydroxides with a high tap density (1.5 – 1.75 g cm<sup>-3</sup>), with a pH of 10.6 producing a more uniform, quasi-spherical secondary particle morphology [157]. A pH above 11.4 yielded lower tap densities of 0.7-0.8 g cm<sup>-3</sup> and irregular particle morphologies. This was supported by Lee *et al.*, who found that synthesis of NMC-111 at pH 11.0 produced a higher tap density (1.79 g cm<sup>-3</sup>) and larger, more uniform, and spherical secondary particles than at pH 11.5 and 12.0 (1.12 and 1.11 g cm<sup>-3</sup> respectively) [156]. A pH of 10.6 was compared to 11.4 for the synthesis of NMC-111 to find that the 10.6 pH had a larger, more uniform particle size (modal average particle diameter of 16 μm compared to 8 μm) with increased tap density (1.23 g cm<sup>-3</sup> vs 0.3 g cm<sup>-3</sup>, after 3 hours of reaction and capacity retention (96.5% vs 93.6% for the 11.4 pH sample after 50 cycles, 0.1C) [159].

For nickel-rich materials, Liang *et al.* concluded a pH of 11.2 was optimal for Ni<sub>0.6</sub>Mn<sub>0.2</sub>Co<sub>0.2</sub>(OH)<sub>2</sub>, yielding quasi-spherical particles with a tap density of 1.65 g cm<sup>-3</sup>, with reduced tap densities of 1.47 and 1.08 g cm<sup>-3</sup> at pH 11.5 and 11.8, and a reduction in particle morphology and size control [160]. Vu *et al.* found that for NMC-811 synthesis, larger (average diameter of 16 μm), more spherical, denser (1.91 g cm<sup>-3</sup>) particles were yielded at a pH of 11.5 compared with 11.2 and 11.8. A loss of uniformity and a smaller size was observed with the alternative pH values, with the 11.8 pH sample yielding a tap density of 1.26 g cm<sup>-3</sup> [118].

The complexation qualities of ammonia to form  $[M(NH_3)_n]^{2+}$  allows the agglomeration of dissolved transition metal ions prior to precipitation, encouraging a uniform precipitation rate of all three transition metals to form a single particle [157], [160]. The NaOH: NH<sub>3</sub> ratio in the reactor can help control the particle tap density and morphology. Wang *et al.* have shown that a ratio of 1:1 shows increased tap density (1.5 g cm<sup>-3</sup> vs 0.53 - 0.84 g cm<sup>-3</sup>) and more spherical, uniform particle morphologies [158].

The relationship between nickel, manganese and the water-ammonia system was investigated during the synthesis of Ni<sub>0.3</sub>Mn<sub>0.7</sub>CO<sub>3</sub>, where sodium carbonate acted as the base. It was found that between pH 5.0 and 7.5 the carbonate co-precipitation reaction was dominant and both nickel and manganese exist as a carbonate, but with excess residual ions existing in the solution. Between 7.5 and 9.8, the readiness for nickel and manganese to form ammonium complexes increases, with the

formation of  $[M(\text{NH}_3)_n]^{2+}$  dominating during this range and consequently re-dissolution of transition metal ions back into the solution increases. Above 9.8, hydroxyl ions are sufficiently concentrated to incur the formation of  $M(\text{OH})_2$ , with this causing a reduction in residual ions in the solution with increasing pH values [161].

The transition metal: ammonia ratio was a more common ratio referred to during the optimisation of synthesis pathways, due to the direct influence on the formation of the  $[M(\text{NH}_3)_n(\text{H}_2\text{O})_j]^{2+}$  ligand complex. The equilibrium constant,  $K_n$ , for the complexation of transition metals with ammonia varies for each transition metal due to their varying solubility over the pH range, with the largest equilibrium constant for nickel occurring when it has 6 ammonia compounds complexing with it (i.e.  $n = 6$ ), manganese at  $n = 3$ , and cobalt at  $n = 5$  [157]. The  $M:\text{NH}_3$  ratio can affect the particle morphology and tap density, evidenced by Cheralathan *et al.*, who found that when synthesizing  $\text{Ni}_{0.8}\text{Co}_{0.15}\text{Mn}_{0.05}(\text{OH})_2$  at pH 11.5-11.6, a ratio of 1:1 yielded quasi-spherical, dense particles ( $2.00 \text{ g cm}^{-3}$ ) compared to ratios of 1: 0.6, 0.8 and 1.2 ( $1.50$ ,  $1.58$  and  $1.50 \text{ g cm}^{-3}$  respectively) [162]. The primary particles for all ammonia ratios were needle-like, with the 1:1 ratio yielding larger, more distinct primary particles. Contrarily, Vu *et al.* found that  $M:\text{NH}_3$  ratios of 1: 0.8, 1.0 and 1.2 yielded NMC-811 with quasi-spherical particles at pH 11.5, with nanoplate primary particles, with more uniform secondary particles at the 1:1 ratio [118].

Liang *et al.* found that increasing the concentration of ammonia added to a co-precipitation reaction synthesizing NMC-622 changed the morphology of the primary particles from thin, low-density nanoplates ( $1.29 \text{ g cm}^{-3}$ ) at 0.3 M ammonia to denser, needle-like particles at 0.6 and 1.0 M ( $1.76$  and  $1.66 \text{ g cm}^{-3}$  respectively), where the concentration of transition metal added was 1.5 M and the pH was 11.2 [160]. Lee *et al.* also found that an increase in ammonia concentration relative to a 2 M transition metal solution of NMC-111 with a pH of 11.0 increased the tap density of the resultant hydroxide particles ( $1.42$ ,  $1.57$ ,  $1.70 \text{ g cm}^{-3}$  for 0.12, 0.24 and  $0.36 \text{ mol dm}^{-3}$ ) [156]. Additionally, the secondary particle morphology was more spherical.

A common transition metal concentration was stoichiometrically summed to form a typical concentration of 2.0 M, with the ratio of transition metals varying from NMC-1:1:1 to NMC-95:2.5:2.5 M [157], [159], [163], [164], [165]. This was typically coupled with a 4.0–5.0 M concentration of sodium hydroxide, with an ideal molar flow ratio of 2.0 [87], [88], [152], [166]. Ammonia's role in the can take two forms: all of the ammonia can be added concurrently with the transition metal and base solution; or some of the ammonia can be added concurrently, some of it

acting as an 'initial solution' that was situated in the reactor prior to transition metal addition. The latter, 'initial solution' methodology can involve a 1 M solution of  $\text{NH}_3$  initially, with a concentrated 5 - 10 M solution of  $\text{NH}_3$  added concurrently [67], [157]. If the ammonia was only added to the reaction, a similar, high concentration of 10.5 M was used [167]. The volumes have been inconsistently reported (either as volumes or volumetric flow rates with addition times) therefore molar quantities and ratios cannot be determined.

What can be summarised from this was that pH and ammonia: *TM* ratio are related. Increasing the ammonia concentration within the solution can help agglomerate the transition metals due to the increased amount of the complexing agent. This can increase the tap density, but the ammonia: *TM* ratio should be moderated with the amount of sodium hydroxide in the system to ensure optimal particle sizes can be yielded.

#### 1.3.2.2. – Physical Parameters Affecting the Co-Precipitation reaction

Another factor that increases the tap density was the reaction duration, with Van Bommel *et al.* and Zhu *et al.* finding that the tap density increases with duration as the particles grow and mature until it reaches an asymptotic maximum [157], [163]. Van Bommel *et al.* found that the tap density of synthesised  $\text{Ni}(\text{OH})_2$  plateaued after a residence time 20 hours, specifying a continuous flow system *via* overflow control to keep a constant volume [143], [157]. This concurs with other literature, which reports addition and/or reaction times of 18-27 hours, but they do not specify the system in which the reactions occur [165], [168], [169], [170]. The stirred tank reactor can be operated in a continuous (CSTR) system, where reactants are continuously pumped in and out of the reactor, with a 'residence time' dictating the duration of which they react; or a semi-batch fed reactor (SBFR) system, with gradual addition of reactants occurring over an 'addition time' before the  $\text{Ni}_x\text{Mn}_y\text{Co}_z(\text{OH})_2$  product being yielded after a certain 'maturation time' that sum to produce the 'reaction time'. This terminology needs to be acknowledged when considering quantitative reaction durations to provide suitable context to the reaction system, with a semi-batch reactor system having a transient reactor concentration and volume, whereas a CSTR system contains a constant concentration and volume of reactants. Given the influence of reactant concentration and pH on the system as described above, the operation of a BR or CSTR system may impact the particle growth mechanics, but there was not enough information to form a conclusion [159].

Stirring is another feature of a co-precipitation reaction that affects the reaction mechanism, both with respect to the type of agitator and the stirring speed. Zhu *et al.* investigated the effect of the impellor blade design on the precipitation of NMC-622 in a 4-baffled reactor vessel, with an axial mixing propeller turbine (PT), radially mixing flat blade turbine (FBT) and Rushton turbine (RT), and an axial and radial mixing pitched blade turbine (PBT) being compared [163]. The impellor blade and mixing regime was found to affect the primary particle morphology, particle size, tap density and crystal structure. The PT hydroxide was found to have larger secondary particles than FBT, RT and PBT samples, with an average diameter of 12  $\mu\text{m}$  (vs <5  $\mu\text{m}$ , <5  $\mu\text{m}$  and 8  $\mu\text{m}$  respectively) and a higher tap density of 2  $\text{g cm}^{-3}$  than the other samples, which had a density of <1  $\text{g cm}^{-3}$  [163].

Morphologically, all NMC-622 hydroxides synthesised from the different impellor blades formed quasi-spherical secondary particles, with the main distinction coming from the primary particle morphology, with the PT sample forming needle-like particles, whereas the PBT, FBT and RT samples formed nanoplate primary particles, which displayed a lower tap density. The PBT sample had smaller nanoplate primary particles that were randomly aligned, with these smaller voids between primary particles indicating the minor increase in tap density observed between PBT vs FBT and RT. It was found that radial-dominated turbines (FBT and RT) formed an  $\alpha\text{-Ni}_{0.6}\text{Mn}_{0.2}\text{Co}_{0.2}(\text{OH})_2$  crystal structure, with the axial-dominated turbine (PT) forming the  $\beta\text{-Ni}_{0.6}\text{Mn}_{0.2}\text{Co}_{0.2}(\text{OH})_2$  phase and the PBT forming a combination of the two [163].

The agitation speed was found to have an effect on the size of the resultant secondary particles, with Vu *et al.* finding that an increased stirring speed from 500-800 rpm during the co-precipitation synthesis of NMC-811 reduces the average particle diameter from 20  $\mu\text{m}$  to 13  $\mu\text{m}$ . The lower stirring speed of 500 rpm also observes more agglomeration between particles leading to a larger size distribution [118]. Lee *et al.* concurs, concluding similar findings that during the optimisation of the synthesis of NMC-111, with smaller, denser particles seen at 1000 rpm (vs 400 and 600 rpm), with a tap density of 1.79  $\text{g cm}^{-3}$  (vs 1.45 and 1.68  $\text{g cm}^{-3}$  respectively) [156]. This suggests that agitation speed is independent of NMC chemistry.

### 1.3.3. – Hydrothermal synthesis route

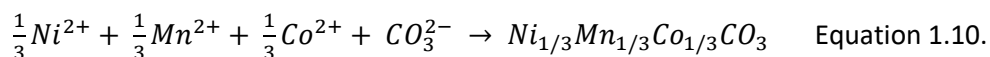
The hydrothermal (using water as a solution) and solvothermal (using a mixed water-organic solution) method are syntheses that promote crystal nucleation and growth through exposure to increased temperature and pressure by heating a solution past its boiling point in a pressurised

vessel, with the resultant vapour head creating pressure within the vessel. These methodologies behave similarly, and can control the particle size, morphology, and crystallinity of the product, with increased temperatures achieving larger particles and improved crystallinity [171].

The exposure to high temperatures during hydrothermal and solvothermal syntheses causes many properties of the solvent (for example water) to change, with density and the dielectric constant decreasing linearly with an increase in temperature until the critical temperature at 374 °C, above which the supercritical properties cause a significant reduction in density and dielectric constant. Above the critical temperature, lower pressures cause a steeper drop in density and dielectric constant [172], [173]. The dielectric constant is the relative permittivity of a substance, and consequently is an indicator of a substance's ability to contain electrical charge. A high dielectric constant in a solvent would be able to hold large quantities of ions dissolved within it, and therefore can be a commentary on the solvent's solubility of salts [173]. Applying this to hydro-/solvo- thermal reactions means reactants can dissolve into the solvent at room temperature, then as the solution is heated and reacted, the solution promotes crystallisation (as opposed to precipitation due to the change in solubility rather than chemical reaction) which yields a highly crystalline product [172].

With respect to the synthesis of NMC materials, hydro-/solvo- thermal reactions involve dissolving transition metal salt reactants (typically acetates or sulphates) into deionised water and/or ethylene glycol, the latter of which can regulate the particle growth [150], [174]. A precipitating agent can be added (*e.g.* urea, ammonium bicarbonate) before the mixture was autoclaved at high temperature (140-200 °C) for 6-24 hours in an oven [171], [174], [175]. The autoclave and hydrothermal 'bomb' reaction vessel allows an increased pressure to be achieved [150], [171], [176]. Once the precursor has formed, the autoclaved precipitate was washed with deionised water.

$\text{Ni}_{0.33}\text{Mn}_{0.33}\text{Co}_{0.33}\text{CO}_3$  was synthesised using nickel, manganese and cobalt acetate precursors dissolved in a 35:45 mL ratio of distilled water to ethylene glycol to form a 1 M solution, with 2.4 g Urea being added as a precipitating agent [174]. This gave a urea: transition metal ratio of 5:1 in the solution. The solution was sealed into an autoclave and annealed at 140 °C for 10 hours. The resulting reaction mechanism could be described by Equations 1.8 - 1.10 and involves the decomposition of urea into ammonia and carbon dioxide [174], [177]. The basic environment promotes the formation of carbonate ions, which react with the transition metal ions to form  $\text{Ni}_{1/3}\text{Mn}_{1/3}\text{Co}_{1/3}\text{CO}_3$ .



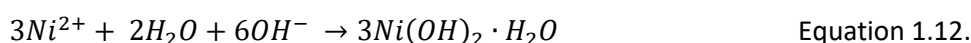
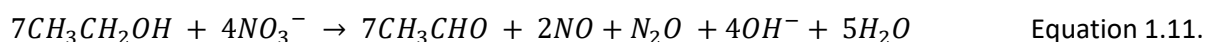
The reaction yields a morphology that consists of quasi-spherical secondary particles comprising of faceted primary particles. After a 700 °C calcination with a stoichiometric quantity of Li<sub>2</sub>CO<sub>3</sub>, the quasi-spherical particles fuse with one adjacent particle to form a ‘dumbbell’ secondary structure, with the developing grains and nodules on their surface as lithium carbonate decomposes and evacuates from the particle, causing densification of the resultant structure [174].

Comparing the solvothermal synthesised NMC-111 (SH-NMC) with an equivalent co-precipitation synthesised NMC-111 (C-NMC, synthesised with ammonia bicarbonate), Brunauer-Emmet-Teller (BET) analysis determined the surface area of SH-NMC was approximately double that of C-NMC (~9.2 vs 4.4 m<sup>2</sup> g<sup>-1</sup>). From an electrochemical perspective, the first cycle discharge capacity of SH-NMC was also greater than the C-NMC, with a capacity of 171 mAh g<sup>-1</sup> compared to 159 mAh g<sup>-1</sup>. The 50-cycle capacity retention for SH-NMC was 87.7% compared to 67.9% for C-NMC, with both Galvanostatic cycling regimes conducted at 0.1C over a voltage window of 2.5-4.5 V [174].

NMC-622 has been synthesised using transition metal acetates (0.1 M), urea (0.2 M), and cetyltrimethyl ammonium bromide (CTAB, 0.1 M) dissolved in a 1:1 ratio of deionised water and ethanol. An autoclaving procedure was conducted over a period of 5 hours at 150 °C before being washed and dried. XRD analysis concluded the solvothermal reaction produced a transition metal hydroxide precursor. Morphological analysis *via* SEM showed quasi-spherical secondary particles with a nanoplate primary particle morphology with three-dimensional pathways, which promotes lithium-ion (de)intercalation during the calcination stage. These pathways are a result of the stabilisation of surface energy caused by CTAB. Calcination caused these nanoplates to thicken and form 100 nm ‘nanobricks’ [178].

A nickel-rich cathode material, LiNi<sub>0.9</sub>Mn<sub>0.05</sub>Al<sub>0.05</sub>O<sub>2</sub> (NMA) was synthesised *via* an ethanol solvothermal process and a co-doped calcination method. The solvothermal method used a Ni(NO<sub>3</sub>)<sub>2</sub>·6H<sub>2</sub>O reactant dissolved in ethanol and autoclaved the solution at 180 °C for 24 hours until an α-3Ni(OH)<sub>2</sub>·2H<sub>2</sub>O was produced, which was washed and dried. This was dissolved with

stoichiometric quantities of  $\text{Al}(\text{NO}_3)_3$  and  $\text{Mn}(\text{NO}_3)_3$ , and a 2 mol% excess amount of  $\text{LiOH}$  in ethanol, stirred and evaporated to form a lithiated  $\text{LiNi}_{0.9}\text{Mn}_{0.05}\text{Al}_{0.05}(\text{OH})_2$  precursor, which was calcined at  $500\text{ }^\circ\text{C}$  for 12 hours in air and  $750\text{ }^\circ\text{C}$  for 20 hours in an oxygen rich atmosphere. The use of nitrates throughout this reaction in combination with ethanol was because ethanol dissolves the metal nitrates and produces hydroxide ions, which facilitate the formation of the desired  $M(\text{OH})_2$  phase, as seen in Equations 1.11 and 1.12 below [179].



The formation of the  $\alpha\text{-}3\text{Ni}(\text{OH})_2 \cdot 2\text{H}_2\text{O}$  layered double hydroxide phase was confirmed *via* XRD, with SEM micrographs displaying quasi-spherical secondary particles. After calcination, the  $\sim 12\text{ }\mu\text{m}$  quasi-spherical morphology remained and XRD analysis showed good peak splitting between (006)/(102) and (108)/(110) doublets, indicating good crystallinity. Rietveld refinement of this material indicated the  $\text{Ni}^{2+}/\text{Li}^+$  cation mixing was approximately 5%. The material underwent electrochemical testing, with cyclic voltammetry testing indicating stable H1-M-H2-H3 phase transitions over the first 5 cycles for voltage windows 3.0–4.3, 3.0-4.4 and 3.0-4.5 V. Galvanostatic cycling for these voltage windows were also conducted at 0.3C, with first cycle discharge capacities of 182, 191 and 200  $\text{mAh g}^{-1}$  being achieved for 4.3 V, 4.4 V and 4.5 V respectively and 83%, 91% and 76% of the capacity being retained after 100 cycles [179].

#### 1.3.4. – Lithiation and Calcination of the $\text{Ni}_x\text{Mn}_y\text{Co}_z(\text{OH})_2$ precursor

Once the NMC precursor was synthesised, it is typically washed with deionised water and filtered and/or dried to remove the residual sodium and sulphur species [158]. The precursor is then mixed with a source of lithium, commonly referred to as lithiation, which can be done *via* hand milling or an aqueous dissolution of a lithium source with the precursor. A high temperature ‘calcination’ heat treatment follows, which initiates a reaction between the lithium and transition metal species until the desired product,  $\text{LiNi}_x\text{Mn}_y\text{Co}_z\text{O}_2$ , is formed. The high temperature and oxygen-rich atmosphere causes the transition metal to oxidise and the evolution of the layered transition metal oxide phase to change to intermediate lithium-deficient rocksalt or spinel oxide phases. As the lithium source thermally decomposes at higher temperatures (above  $473\text{ }^\circ\text{C}$  for  $\text{LiOH}$ ), lithium is released into the

system and incorporates into the transition metal compound, with the oxygen-rich atmosphere providing a source of oxygen to form the final  $\text{LiNi}_x\text{Mn}_y\text{Co}_z\text{O}_2$  phase [152].

Aqueous lithiation of a material involves dispersing the  $M(\text{OH})_2$  precursor and a lithium source in a solution. Belharouak *et al.* achieved this by dissolving the  $\alpha\text{-3Ni}(\text{OH})_2 \cdot 2\text{H}_2\text{O}$  precursor with soluble dopants and 2 mol% excess  $\text{LiOH} \cdot \text{H}_2\text{O}$  in ethanol, before mixing for 2 hours at 40 °C to evaporate the solvent. Water can also be used as a solvent, dissolving  $\text{Ni}(\text{NO}_3)_2 \cdot 6\text{H}_2\text{O}$  and  $\text{LiOH} \cdot \text{H}_2\text{O}$  and mixing it prior to calcination at 800 °C for 12 hours [180]. This methodology was investigated by Arai *et al.* with a 1: 1 and 1: 4 transition metal: lithium ratio being compared. It was found that in order to synthesise near-stoichiometric  $\text{Li}_{1-z}\text{Ni}_{1+z}\text{O}_2$ , optimised conditions involve mixing the 1:1  $M$ : Li solution for 8 hours (which produced LNO with  $z = 0.033$ ) or mixing the 1:4  $M$ : Li solution for 2 hours (LNO with  $z = 0.031$ ) [51].

The more common method for the lithiation of transition metal precursors involves hand milling dried precursor and a lithium source. Typically, an excess of lithium source was used to the stoichiometric amount, with a Li: M ratio of 1.01-1.05: 1 used to ensure integration into the cathode structure and to compensate for loss of lithium at high temperatures as it vaporises to form  $\text{Li}_2\text{O}$ , which results in the formation of a lithium- and oxygen- deficient rock-salt phase [9], [87], [88], [181]. This milling was conducted for 15-30 minutes with a pestle and mortar or mechanical grinding equivalent (*e.g.* ball mill) in order to maximise the surface area to volume ratio of the materials, reducing the lithium pathway during the lithiating calcination mechanism [150], [182], [183]. A small amount of solvent, for example ethanol, can be added to dissolve the lithium hydroxide, allowing it to further reduce the penetrate the transition metal precursor and minimise the lithium pathway [183]. The thermal decomposition temperature range of lithium carbonate was 700-1100 °C, making it potentially unsuitable for the synthesis of nickel-rich cathode materials as not all of the lithium carbonate may decompose and lithiate the NMC/ LNO material [104]. Lithium hydroxide, which decomposes at 400-600 °C, is preferred for the calcination of nickel-rich cathodes.

Should the degree of excess lithium be too high, lithium oxide ( $\text{Li}_2\text{O}$ ) can form on the surface of the secondary NMC particles during calcination [85], [184]. This  $\text{Li}_2\text{O}$  reacts with the  $\text{CO}_2$  or  $\text{H}_2\text{O}$  in air to form  $\text{Li}_2\text{CO}_3$  or  $\text{LiOH}$ , which can increase the pH of the electrode slurry and interact with the polyvinylidene fluoride (PVdF) causing gelation of the electrode slurry, complicating their handling and casting. Furthermore, these impurities such as  $\text{LiOH}$  with can react  $\text{LiPF}_6$  electrolyte to form hydrofluoric (HF) acid, which dissolves metal in the cathode and gasifies the anionic component

during cycling, forming CO, CO<sub>2</sub> or O<sub>2</sub>, which leads to swelling within the cells and a potential safety risk if the cell ruptures [85], [184], [185].

Residual lithium compounds are more present in nickel-rich NMC materials, with Noh *et al.* measuring the quantities of residual lithium *via* titration to find that there was a significant increase in both LiOH and Li<sub>2</sub>CO<sub>3</sub> when the nickel content was above 70%. NMC-111 had a total residual lithium concentration of 1798 ppm, with the concentration increasing for other NMC materials (NMC-622, 4908 ppm; NMC-701515, 11,054 ppm; NMC-811, 23,819 ppm) [37]. One more practical method for identifying these residual lithium compounds was through their presence in XRD profiles of LiNi<sub>x</sub>Mn<sub>y</sub>Co<sub>z</sub>O<sub>2</sub>, as seen in Figure 1.14, where Li<sub>2</sub>CO<sub>3</sub> exists between the (003) and (101) peak as a phase impurity.

In order to remove these residual lithium compounds, the current practice was to wash the lithiated sample post-calcination, but as these compounds are more common amongst nickel-rich cathodes. This risks hampering the electrochemical performance due to the sensitivity of nickel to water and oxygen [37], [85]. One alternative option was investigated by Jo *et al.* who dissolved phosphoric acid (H<sub>3</sub>PO<sub>4</sub>) into ethanol, then added pre-synthesised LiNi<sub>0.6</sub>Mn<sub>0.2</sub>Co<sub>0.2</sub>O<sub>2</sub> and heated to 80 °C to slowly evaporate the solvent. The lithium reacts with the phosphate ion to form a coating of conductive Li<sub>3</sub>PO<sub>4</sub>, which in turn improved the capacity retention of the NMC-622 from 76.1% (bare) to 94.1% (coated) after 150 cycles at 1C (3.0-4.3 V) [186]. A non-aqueous solution to the formation of residual lithium compounds was researched by Seong *et al.* who introduced SO<sub>2</sub> gas into the calcination system of LiNi<sub>0.91</sub>Mn<sub>0.03</sub>Co<sub>0.06</sub>O<sub>2</sub> such that the Li<sub>2</sub>O formed a coating of Li<sub>2</sub>SO<sub>4</sub>, which stabilised the electrode slurry during mixing, preventing gelation, and stabilised the Galvanostatic cycling such that after 100 cycles of 0.1C (3.0 – 4.3 V), the Li<sub>2</sub>SO<sub>4</sub> coated cell retained 91% capacity, whereas the uncoated sample saw a drop off in capacity [184].

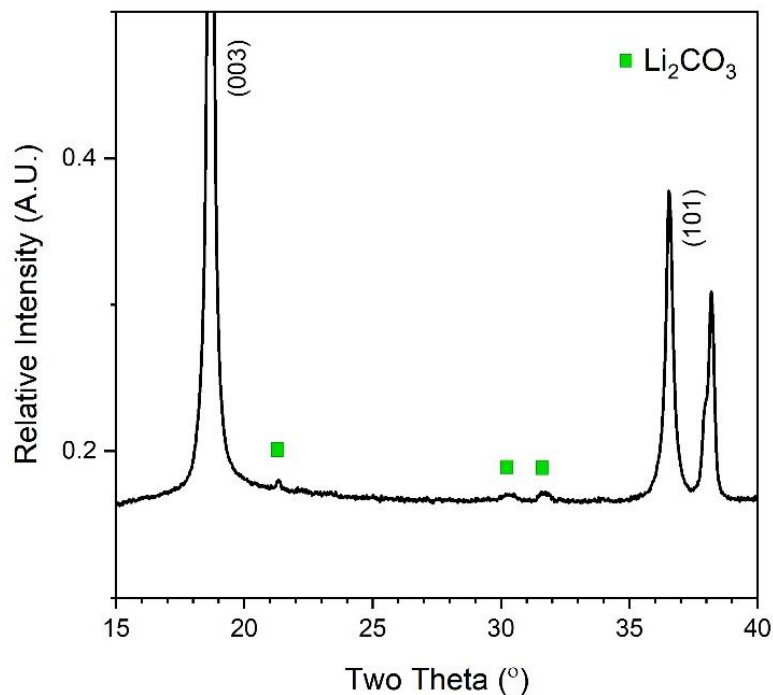
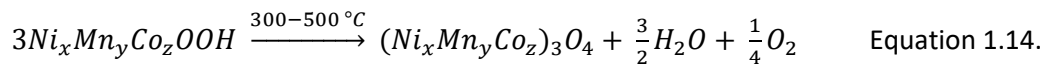


**Figure 1.14:** An XRD profile showing the presence of  $\text{Li}_2\text{CO}_3$  between the (003) and (101) peaks in a sample of  $\text{LiNi}_{0.8}\text{Mn}_{0.1}\text{Co}_{0.1}\text{O}_2$ .

Once the solid lithium and NMC hydroxide mixture is deemed ‘homogenous’, a high temperature treatment of the precursor to allow the incorporation of oxygen and lithium into the structure through the loss of water *via*  $\text{OH}^-$  evolution. The desired phase resulting from this ‘calcination’ of the transition metal precursor was the  $\alpha\text{-NaFeO}_2$  layered transition metal oxide ( $\text{LiMO}_2$ ) described in Section 1.2.1, although poor control over conditions such as temperature could lead to phase impurities such as a lithiated transition metal rocksalt ( $\text{LiMO}$ ), non-lithiated rocksalt ( $\text{MO}$ ) or a spinel-phase transition metal ( $\text{M}_3\text{O}_4$ ) [103], [187], [188].

When calcined alone, the  $\text{M}(\text{OH})_2$  layered structure (P3m) can oxidise *via* a reaction mechanism described in Equation 1.13 to form a  $\text{MOOH}$  phase at approximately 100 °C, which can have to crystal phases: R3m and C2/m. The resulting  $\text{M}(\text{OH})_2$  or  $\text{MOOH}$  species reacts to form a transition metal oxide with a spinel or rocksalt structure between 300 and 500 °C, coinciding with the vaporisation of water from the material, seen in Equation 1.14 [103], [152].  $\text{Co}(\text{OH})_2$  and low-nickel  $\text{M}(\text{OH})_2$  species react to form a dominant  $\text{M}_3\text{O}_4$  spinel phase (Fd3m), but as the nickel content increases within the  $\text{M}(\text{OH})_2$  precursor, the spinel phase was replaced by a  $\text{MO}$  rocksalt phase (Fm3m), with only the rocksalt  $\text{MO}$  phase synthesised for  $\text{Ni}(\text{OH})_2$  [152].

The inclusion of a lithium source, for example lithium hydroxide (LiOH) allows the full reaction to take place and the LiMO<sub>2</sub> layered structure (R3m phase) to dominate, with the overall reaction for this seen in Equation 1.15 [152]. The desired LiMO<sub>2</sub> phase can also be obtained through calcination from any one of the lithiated intermediates and non-lithiated alternatives (calcined with a lithium source) including M<sub>3</sub>O<sub>4</sub> and MO, although due to the higher thermal stability of these reactants, phase dominance of LiMO<sub>2</sub> tends to be achieved at a higher temperature [152], [189]. Consequently, a minimum temperature should be achieved to ensure the layered R3m structure was phase pure, which Lin *et al.* has been reported to be 600 °C (in air) for the formation of LNO from Li<sub>2</sub>CO<sub>3</sub> and NiO reactants. Below this temperature, unreacted NiO and Li<sub>2</sub>CO<sub>3</sub> were present [189].



In order to balance the charge in the LiNi<sub>1-x-y</sub>Mn<sub>x</sub>Co<sub>y</sub>O<sub>2</sub> structure, the transition metals oxidise from their +2 oxidation states (in M(OH)<sub>2</sub>) in the hydroxide precursor to their Ni<sup>2+/3+/4+</sup>, Mn<sup>4+</sup> and Co<sup>3+/4+</sup> during calcination [62], [190]. The manganese (Mn<sup>4+</sup>) and cobalt (Co<sup>3+/4+</sup>) content of the cathode determines the oxidation state of the nickel, with an increase in nickel content promoting the formation of the less stable Ni<sup>3+/4+</sup> ions in favour of Ni<sup>2+</sup> in order to balance the electrostatic charge. The presence of Ni<sup>2+</sup> ions in the final LiNi<sub>x</sub>Mn<sub>y</sub>Co<sub>z</sub>O<sub>2</sub> product can be indicated by the degree of cation mixing within the pristine (*i.e.* uncycled) product. The ratio of the (003) and (104) intensities (I<sub>(003)</sub>/I<sub>(104)</sub> ratio) can be a qualitative indicator of the Ni<sup>2+</sup> ions that intercalate into the Li layer. This compares a purely *c*-axis measurement, (003), with a parameter that cuts diagonally across the unit cell, (104), that is affected by the *a* and *b* axis. An increase in cation mixing would cause a shrinkage in the *ab* plane due to the smaller Ni<sup>2+</sup> ions (0.69 Å, vs 0.76 Å for Li<sup>+</sup> ions), resulting in a smaller I<sub>(003)</sub>/I<sub>(104)</sub> ratio. Rietveld refinement can determine the degree of cation mixing quantitatively.

The instability of Ni<sup>3+/4+</sup> ions create difficulties in maintaining nickel in its tri-/tetra- valent state, introducing the need for oxygen gas or an oxidising agent during the calcination stage to maximise this oxidation reaction and encourage good cation ordering. This was highlighted by Idris *et al.* who calcined NMC-811 in oxygen gas and nitrogen gas at various temperatures [191], [192]. They found

that the presence of oxygen increased the  $I_{(003)}/I_{(104)}$  ratio of oxygen calcined samples (approx. 1.0-1.2, 850-950 °C) compared to nitrogen samples (approx. 0.6-0.4, 850-950 °C). This suggested an increase in cation ordering within the superstructure, which was supported by the unit cell volume, which increases from 101-102 Å<sup>3</sup> for oxygen samples (low cation mixing 3.3-6.2%), to 103-104 Å<sup>3</sup> (11.1-22.3% cation mixing) for the nitrogen calcined samples, which is consistent with literature [191], [193]. Park *et al.* showed that an increase in oxygen gas flow rate during the calcination of LNO increased the  $I_{003}/I_{104}$  ratio, with larger ratios of 1.599-1.616 observed for oxygen flow rates above 500 sccm (standard cubic centimetres per minute). This in turn had an impact on the specific capacity, with the 500 and 800 sccm yielding a first cycle discharge capacity of 139 and 163 mAh g<sup>-1</sup> (compared to a 300 sccm sample producing 56 mAh g<sup>-1</sup>, and a 35-cycle capacity retention of <20%, 95% and 90% for the 300, 500 and 800 sccm samples [194].

Low-nickel content materials such as NMC-111 can be calcined in air due to the tendency for nickel to remain in its divalent state, whereas nickel-rich materials such as NMC-811 and LNO require Ni<sup>3+/4+</sup> ions in order to balance the electrostatic charge and require an oxygen atmosphere due to the lower reduction potential for nickel compared to manganese and cobalt [195]. Shim *et al.* calcined LiNi<sub>0.8</sub>Mn<sub>0.05</sub>Co<sub>0.15</sub>O<sub>2</sub> with oxygen and air and confirmed the increased degree of cation mixing in the air sample *via* Rietveld refinement (3.67% for the air-calcined sample, 3.00% for the oxygen-calcined sample). The effect on the electrochemical performance included an increase in first-cycle discharge capacity for the oxygen sample (193.7 mAh g<sup>-1</sup> vs 185.2 mAh g<sup>-1</sup>), an increased 50-cycle capacity retention (95.6% vs 92.6%, cycled at C/2, 2.8-4.3 V) and an increased rate capability [192].

Excessive temperature can cause oxygen evolution and loss from the layered structure to degrade and form off-stoichiometries (Li<sub>1-z</sub>M<sub>1+z</sub>O<sub>2</sub>) and a rocksalt phase impurity [9], [191]. This evolution begins at different temperatures depending on the nickel content, with Ni<sup>3+</sup> reducing to Ni<sup>2+</sup> in NMC-901 at 625 °C, at ~700 °C in NMC-811, and at 800 °C in NMC-532, which coincides with a spike in oxygen release as Li<sub>2</sub>O and O<sub>2</sub> was formed [9], [103], [196]. The temperature of the heat treatment should vary with the nickel content of the material, with LNO typically being calcined at 650-700 °C and NMC-111 at 900 °C (Table 1.1) [142], [169]. Calcining below 650 °C forms lithium-nickel impurities including lithium carbonate and the rocksalt phase and calcining below 600 °C can leave unreacted NiO in the system [9], [152]. One deviation from this method was to calcine nickel-rich materials in two stages, firstly at 400-500 °C, then at 700-800 °C [88], [187], [197], [198]. The initial 500 °C temperature was to breakdown the lithium hydroxide to form Li<sub>2</sub>O and release any incorporated water and carbonates, indicated by mass loss during the process [101], [152].

**Table 1.1:** A summary of the most frequently used temperatures for common versions of NMC, accompanied by their sources.

Nickel content (with a typical NMC composition)	Optimum temperature (°C)	Literature Reference
33% ( <i>e.g.</i> NMC-111)	850-1000	[37], [156], [199]
50% ( <i>e.g.</i> NMC-532)	900-950	[37], [150]
60% ( <i>e.g.</i> NMC-622)	800-920	[37], [67], [88]
80% ( <i>e.g.</i> NMC-811)	780-850	[37], [118], [200]
90%	700-750	[70], [87], [184]
100% (LNO)	650-700	[9], [52], [187], [201], [202]

From a morphological perspective, secondary particle assemblies remain relatively unchanged throughout calcination, with little change in size and morphology [118], [156]. Primary particles however tend to thicken and densify, regardless of needle-like or nanoplate morphology, to form individual ‘nanobricks’ or fuse together within the secondary structure to form a ‘meatball’ like particle [118], [178], [202]. Temperature can affect the size of the faceted primary particles, and consequently the surface area for the particle/ sample, which in turn can increase the capacity and capacity retention (with an increase in area). Vu *et al.* reported that NMC-811 calcined at 800 °C was found to have a larger surface area and achieve a first-cycle capacity of 193.9 mAh g<sup>-1</sup> (0.1C, 3.0-4.3 V) compared to a capacity of 185.6 and 186.2 mAh g<sup>-1</sup> obtained by calcination at 780 and 820 °C respectively. The capacity retention at 1C after 100 cycles are 84.5% for the 780 °C NMC-811, 90.4% for the 800 °C, and 80.9% for 820 °C [118].

Zheng *et al.* also reported a similar finding for the calcination of LiNi<sub>0.76</sub>Mn<sub>0.14</sub>Co<sub>0.10</sub>O<sub>2</sub> at temperatures ranging from 725-900 °C, with a reduced Ni/Li cation mixing was observed at 775 °C (3.65%, vs 5.16% for 900 °C) and an increased I<sub>(003)</sub>/I<sub>(104)</sub> ratio (1.33, vs 1.23 for 900 °C) indicating increased crystallinity [203]. Morphologically, calcinations at 725-775 °C yielded smaller primary particles of 100-300 nm, with a cuboidal shape and minimal voidage within the quasi-spherical secondary assembly. Above 800 °C, primary particle size increased from ca. 500 nm at 800 °C to 1-2 μm for 850-900 °C. Smaller particle sizes (*i.e.* 725-775 °C) yielded larger capacities of ca. 220 mAh g<sup>-1</sup>, vs ca. 200 mAh g<sup>-1</sup> for samples calcined at 850-900 °C, cycled 2.7-4.5 V at a rate of C/10. Additionally the 725-775 °C calcined samples had higher capacity retentions when cycled at a rate of C/3, with a retention of 80.1-78.7% compared to higher temperatures (72.9%, 56.4% and 41.9% for

800, 850 and 900 °C respectively) when cycled between 2.7-4.5 V. Increased rate performances were also observed, with the 750 °C sample observing a capacity of 168 mAh g<sup>-1</sup> at 10C, compared to 164, 125 and 47 mAh g<sup>-1</sup> for 775, 850 and 900 °C [203]. Lower temperatures tend to produce materials with poor crystallinity, whereas excessive temperatures will sinter the primary particles, decreasing the Li diffusion pathways and reducing the rate performance and coulombic efficiency.

A similar investigation was conducted by Kurzhals *et al.* into the calcination of LNO at 680-720 °C with a range of lithium source content, with 0.98, 1.01 and 1.04 (relative to the Ni(OH)<sub>2</sub> precursor) used. They found that crystalline LNO with a layered, α-NaFeO<sub>2</sub> phase was formed for all three lithium contents, for temperatures of 680, 700 and 720 °C. Cation mixing was reduced in samples with a higher lithium content, with 1.04 lithium content yielding a cation mixing of 1.6% when calcined at 720 °C, compared to 1.01 and 0.98 (2.2% and 3.5% respectively). This is because excess lithium within the system pushes the reaction equilibrium to form LiNiO<sub>2</sub> rather than LiNiO, according to Le Chatelier's principle. The three temperature samples (680, 700 and 720 °C) yielded similar degrees of cation mixing, but the higher temperatures yielded larger primary particles within the secondary particle assembly, due to the higher temperature growing larger crystals [187].

Morphological analysis on this LNO material was conducted by Riewald *et al.*, who concluded that the secondary particle agglomeration occurs during calcination due to the increase in mean average diameter of the particle (d<sub>50</sub>), which occurs more significantly in smaller particles, with 4.3 μm precursor (d<sub>50</sub>) increasing to an average size of 9.1 μm; and 11.1 μm Ni(OH)<sub>2</sub> particles (d<sub>50</sub>) increasing to an average value of 13.6 μm post-calcination. It was confirmed that an increase in calcination temperature increased the mean primary particle size from 200-300 nm at 680 °C to 350-500 nm at 720 °C. Translating this to electrochemical performance, LNO/graphite full cells were constructed and cycled at 1C, with intermittent C/3 and C/10 cycles, with all three samples yielding similar first-cycle discharge capacities (210-220 mAh g<sup>-1</sup>, C/10). Over 120 subsequent cycles, the 680 °C samples saw a larger capacity retention, yielding a capacity of *ca.* 170 mAh g<sup>-1</sup>, whereas 700 and 720 °C samples yielded capacities of *ca.* 145 and 120 mAh g<sup>-1</sup> respectively [202].

The duration of calcination was another parameter that was contested amongst literature. Many reports use a time of 10-15 hours for calcination, irrespective of composition or oxidising atmosphere [37], [88], [118], [167]. An investigation into the effect of calcination duration of NMC-111 was conducted by Habibi *et al.* over a period of 5-15 hours. XRD and Rietveld analysis shows that regardless of temperature (750, 850 and 950 °C), larger peaks, and an increased I<sub>(003)</sub>/I<sub>(104)</sub>

ratio was observed for 15 hours (1.38, 1.36 and 1.09 respectively), indicating greater crystallinity and less cation mixing. Longer calcination times and higher temperatures also increased primary particle size, which reduced particle agglomeration due to less surface energy (relative to shorter calcination times and lower temperatures) [199]. Due to the solution combustion synthesis of the NMC-111 precursor, there was no obvious secondary particle morphology. The 15-hour samples displayed a higher discharge capacity of 160.5 mAh g<sup>-1</sup> (850 °C, 0.05C, 2.5-4.3 V) relative to the shorter calcination periods (15.5 and 47.4 mAh g<sup>-1</sup> for 5- and 10-hour durations respectively). For the 15-hour calcination sample, a temperature of 850 °C was determined to be optimal with a discharge capacity of 160.5 mAh g<sup>-1</sup> (vs 155.9 and 141.4 mAh g<sup>-1</sup>), further evidenced by rate capability (36 mAh g<sup>-1</sup> vs <25 mAh g<sup>-1</sup> for both 750 and 950 °C at 5C cycling rate), and capacity retention (86% retention after 50 cycles of 2.5-4.3 V cycling at 1C, compared to 65% and 43% retention for 750 °C and 950 °C respectively) analysis [199].

$\alpha$ -NMC(OH)<sub>2</sub> and layered double hydroxides can have an adverse effect on the formation of layered transition metal oxides due to irregularities in the layered hydroxide structure. Xu *et al.* synthesised  $\alpha$ -NMC(OH)<sub>2</sub> 6:2:2 precursor using sodium DL lactate in place of ammonia as a chelating agent, which was calcined at 850 °C for 15 hours to form layered NMC-622 oxide [204]. XRD analysis showed samples prepared at a higher pH (11.5) displayed a larger proportion of  $\beta$ -NMC(OH)<sub>2</sub> impurity within the  $\alpha$ -NMC(OH)<sub>2</sub> phase. Calcination gave rise to the desired  $\alpha$ -NaFeO<sub>2</sub> layered structure, with no phase impurities present and the pH 11.5 sample having a higher I<sub>003</sub>/I<sub>104</sub> ratio of 1.575 (compared to the pH 10.5 sample having a ratio of 1.487), indicating a smaller degree of cation mixing. The synthesis of layered double and  $\alpha$ -polymorph hydroxides in the context of NMC- and nickel- based battery structures was rare, and consequently the resultant effect of calcination of these materials was just as rare, but Xu *et al.* confirm that from a crystallographic perspective, the presence of layered double and  $\alpha$ -polymorph hydroxides does not impact the formation of  $\alpha$ -NaFeO<sub>2</sub> layered structure with a low degree of cation mixing [204]. Zhu *et al.* have investigated the effect of calcining Mg/Al-CO<sub>3</sub> layered double hydroxides to form layered double oxides. The X-ray diffraction studies suggested the formation of a low-crystalline structure with no interlayer anions/ water [205].

#### 1.4. Stirred Tank Reactors – A Gateway to High-Throughput Synthesis

Stirred tank reactors (STRs) are vessels that allow great control over the reactions that occur within them through the utilisation of sensors and control loops to accurately maintain parameters. This becomes advantageous for the synthesis of many materials from a biological and chemical perspective, with the earliest use of stirred tank reactors relating to the production of alcohol through the use of yeast and cereals. In a modern chemical landscape, STRs are often used for aqueous reactions that are being upscaled from small, laboratory configurations in beakers such as a round bottom flask, up to industrial production of chemicals.

#### 1.4.1. - Stirred Tank Reactors

Stirred tank reactors can be configured to three different system operations: a batch reaction (BR), a semi-batch fed reactor (SBFR) and a continuous stirred tank reactor (CSTR). A batch reactor system involves inputting all reactants into the reactor before the reaction, allowing the reaction to run to completion without any reactants or products entering/ leaving the system, before the extraction of the product after the reaction has run to its completion. A semi-batch fed reaction (SBFR) involves an open system over the course of the reaction, with reactants continuously added to promote the reaction occurring, but the final reactants being extracted only once the reaction has completed. A continuous stirred tank reactor operates by continuous addition of reactants and removal of products in order to keep the contents of the reactor at a steady-state (*i.e.*, no accumulation of material or change in concentration) [206]. From a reaction perspective, BRs and SBFRs have a changing concentration throughout the reaction due to the absence of product extraction, whereas the CSTR systems have a quasi-constant steady-state concentration [159].

There are two main factors that differentiate between the three operational modes: the transient/ steady-state nature of the system, and the degree of throughput that the configurations allow. Batch and semi-batch systems have a fixed start and end time, limiting the throughput of the reactor vessel due to the downtime that occurs between reactions. Steady-state systems observed in CSTRs are desirable due to the constant conditions that the reaction was conducted under, meaning the product have consistent properties and can operate continuously for periods of time without the product dropping in quality. This can increase the throughput capabilities of the reactor relative to BRs and SBFRs. This also improves product consistency, as there was one continuous batch rather than separate batches for inconsistency to arise [206].

Controlling the conditions within a STR system, regardless of the configuration, can be done using control loops. This is typically done *via* a feedback loop, where a sensor (*e.g.* thermocouple) will

record a parameter (e.g. temperature) within the system in real-time and compare it to a pre-set value. The computer was then connected to another aspect of the system that relates to the control loop parameter (in this case, the reactor heater) in order to alter the output of the unit to guide the parameter closer to the pre-set value.

#### 1.4.2. – The Design and Operation of a STR

The configuration of the STR are key factors to consider when sizing the reactor. For BRs and SFBRs, which have a fixed reaction time (time taken for the reaction to complete) and the throughput is restricted to the operational volume of the reactor; whereas in CSTR systems, the throughput is determined by both the volume and the residence time (the average time taken a particle spends in the reactor).

The shape of a CSTR is typically a domed cylindrical vessel, with either a dished or hemispherical bottom. The type of dome, as well as the operational volume of the vessel can affect the flow regime within the vessel and consequently the agitation within the vessel. These flow regimes indicate the degree of mixing, with laminar flow typically having parallel fluid flow paths and suffering reduced mixing, whereas the turbulent flow regime introduces the formation of eddies and the crossing of fluid flow paths, increasing the mixing within the system [207]. The flow regime within a reactor is described through the Reynold's number ( $Re$ ) executed through the stirring of an agitator applying the force upon the fluid, thus the characteristic length was the diameter of this impellor ( $D_i$ ). The speed of the agitator in revolutions per second ( $N$ ) relative to the dynamic viscosity ( $\mu$ ) can form Equation 1.16. It is worth noting that the dynamic viscosity ( $\mu$ , a metric for force) can be converted to the kinematic viscosity ( $\nu$ , a metric for velocity), which can be more applicable to the STR scenario due to the force exerted by the impellor blade during agitation *via* Equation 1.17 [208].

$$Re = \frac{\rho * N * D_i^2}{\mu} \quad \text{Equation 1.16.}$$

$$\text{Kinematic Viscosity } (\nu) * \text{Density } (\rho) = \text{Dynamic Viscosity } (\mu) \quad \text{Equation 1.17.}$$

The area ( $A$ ) of the impellor blade impacts the inertia imparted onto the system, as denoted in Equation 1.18, where 'u' is the velocity of the blade. This relates to the dispersion of particles, characterised through Froude number ( $Fr$ ), seen in Equation 1.19, which describes the ratio of inertia

(involving the rotational speed of the agitator,  $n$ , in rpm; and impellor diameter,  $D_i$ ) and gravity ( $g = 9.81 \text{ m s}^{-2}$ ). Below this critical velocity, particles begin to settle as the flow becomes tranquil, and above the critical velocity, particles distribute within the fluid under a rapid flow regime [207]. The minimum velocity for particle suspension was investigated first by Zwietering *et al.* and later by Baldi *et al.*, the latter developing Equation 1.20, and describes the minimum velocity for all particles to be suspended within a system [209], [210]. The factors include particle concentration ( $B$ ), particle and liquid density ( $\rho_p$  and  $\rho_L$  respectively), particle diameter ( $D_p$ ) and impellor diameter ( $D_i$ ) [211].

$$\text{Inertial Force } (F_i) = \rho * A * \frac{u^2}{2} \quad \text{Equation 1.18.}$$

$$\text{Froude Number } (Fr) = \frac{n^2 * D_i}{g} \quad \text{Equation 1.19.}$$

$$N_{min} = \frac{B^{0.125} \mu_L^{0.17} [g(\rho_p - \rho_L)^{0.42} D_p^{0.14}]}{\rho_L^{0.58} D_i^{0.89}} \quad \text{Equation 1.20.}$$

Increasing the agitation rate can lead to a turbulent regime during mixing, resulting in the formation of eddy currents and an increased change in momentum and an increase in shear stress ( $R_y$ ) in the system, as described in Equation 1.21, where  $E$  was the eddy kinematic viscosity and,  $u_x$  was the random fluctuations in the fluid perpendicular to the direction  $y$  [207]. Vortexes can also arise from vigorous agitation within a system, limiting the degree of mixing that can occur within this system. Vortex formation increases with depth [212]. To counteract vortex formation, the STR vessel shape can change to a more angular square perimeter; the agitator axle and impellor blade can be positioned off-centre within the reactor vessel; or most commonly, baffles can be added to the reactor vessel [207]. Baffles disrupt the circular motion of fluid, causing dispersion of the quasi-parallel fluid flow lines in the axial and radial direction, thus discouraging the formation of a vortex. Different impellor blades promote different variations of axial and radial flow, as discussed in Section 1.3.2., with propeller turbines (PT) causing axial flow, flat blade turbine (FBT) and Rushton turbine (RT) causing radial flow, and pitched blade turbine (PBT) causing both types of flow [163].

$$R_y = -\left(\frac{\mu}{\rho} + E\right) \frac{d(\rho u_x)}{dy} \quad \text{Equation 1.21.}$$

The type of impellor blade also impacts the power ( $P$ ) needed to drive the agitator, which was described in Equation 1.22 below, where  $N_p$  was the dimensionless power number, attained graphically from power curves, which is exemplified in Appendix A.3 [213]. Agitators act as a pump

during the mixing displacing a volume of fluid displaced ( $V_D$ ) during its rotation. The volume flow pumping rate ( $Q$ ,  $\text{m}^3 \text{s}^{-1}$ ) is described in Equation 1.23 and relates to the efficiency at which the impellor blade pumps fluid ( $\eta$ ), which can also be described as the agitator factor ( $N_Q$ ), visually determined using dimensionless graphs. Correlations between the power number ( $N_p$ ), agitator factor, and Reynolds number found they were independent, resulting in a constant agitator factor across all regimes, which for a  $45^\circ$  pitched propeller, was  $N_Q = 0.87$  [214], [215].

$$P = N_p D_I^5 N^3 \rho \quad \text{Equation 1.22.}$$

$$Q = N_Q D_I^3 N = \eta V_D N \quad \text{Equation 1.23.}$$

The volume flow pumping rate,  $Q$ , for the agitator can be used to determine a mixing time ( $t_t$ ) for the system, defined as the time taken for a particle flow path to return to the agitator. This is typically denoted alongside the agitator speed as  $Nt_t$  due to the correlation between the two factors. There have been a number of models used to determine the mixing time factor ( $Nt_t$ ), one of which was derived experimentally (see Equation 1.24), another model by Fox and Gex used for high efficiency impellers in the turbulent regime (Equation 1.25). The experimental model operates under the basis that the mixing time is approximately one-fifth of the residence time from a 6-blade turbine, determined experimentally from the equalisation of concentration in a tracer experiment, modified for a  $45^\circ$  pitched propeller ( $N_Q = 0.87$ ). The Fox and Gex model accounts for inertial and gravitational forces within the system through the inclusion of Froude number and Reynolds number in its derivation [215], [216].

$$Nt_t = 4.5 \left(\frac{D_T}{D_I}\right)^2 \left(\frac{H}{D_T}\right) \quad \text{Equation 1.24.}$$

$$Nt_t = Fr^{1/6} \left(\frac{K}{Re^{1/6}}\right) \left(\frac{D_T}{D_I}\right)^{3/2} \left(\frac{H}{D_T}\right)^{1/2} \quad \text{Equation 1.25.}$$

It can be seen that in both models there is a reliance on the geometry of the stirred tank reactor, namely the tank diameter ( $D_T$ ), impellor diameter ( $D_I$ ) and the height of the fluid in the tank ( $H$ ). In turbulent systems, the Fox and Gex model can be simplified to Equation 1.26 below. Heuristically, most systems are designed such that the tank diameter and fluid height are equal, and the agitator diameter was one-third of the tank diameter. This gives the value of  $Nt_t$  (dimensionless) to be 40.5 and 105.5 for the experimental and Fox and Gex model respectively.

$$Nt_t = 16.9 \left(\frac{D_T}{D_I}\right)^{10/6} \left(\frac{H}{D_T}\right)^{1/2} \quad \text{Equation 1.26.}$$

## 1.5. – Microwave Technology

The heating properties of microwaves were first discovered by Percy Spencer in 1945 and have since been developed and refined the technology to produce food and chemical processing units. The vacuum tube used by Spencer, called a ‘magnetron’, emits a high frequency microwave radiation that interacts with and heats the target. This has led the purpose of the processing units to be primarily heating, drying and chemical extraction by partial evaporation, with a big commercial advantage of the technology being the reduced time and energy used to conduct the heating. Most commercial applications focus on the interaction between microwave radiation and water molecules, with the interaction typically heating the water to boiling point causing evaporation.

### 1.5.1 – Microwave Heating

The benefit of microwave heating technology to chemical synthesis centres around the precise mechanism of microwave assisted heating. The magnetron emits high frequency microwave radiation in the order of 2.45 GHz which has a corresponding wavelength in the order of molecular bond lengths [217], [218]. In polar molecules, where there is a charge disparity over the length of a bond, the molecule can align with the microwave radiation according to the alternating electric field generated by the radiation, as seen in Figure 1.15. The resulting change in alignment with neighbouring molecules causes resistance between adjacent particles with opposing charges, which generates localised heating [219]. Ionic liquids experience a similar heating effect called ionic conduction, with the charged particles moving spatially to align with the alternating electric field, with the adjacent opposing charges generating heat.

This heating mechanism, known as dielectric heating, is an energy conversion as opposed to heat transfer, and performs molecular-level heating throughout the system with while minimising the need for slower heating mechanisms such as conduction or convection. Dielectric heating relies on two properties of a target material: it’s ‘real’ dielectric constant ( $\epsilon'$ ; how readily a material polarises within an electric field) and the imaginary dielectric loss ( $\epsilon''$ ; is the heat dissipation from a microwave-heated sample). The suitability of a material to convert electromagnetic energy into heat

is determined by the ratio of dielectric loss to the dielectric constant, defined as  $\tan(\delta)$ , in Equation 1.27. This allows for rapid heating to occur, reducing the time needed for reactions to complete, which increases the applicability of microwave technology to high-throughput synthesis pathways.

$$\tan(\delta) = \frac{\epsilon''}{\epsilon'} \quad \text{Equation 1.27.}$$

There are two 'modes' in which this heating can occur, involving the magnetron microwave generator and a waveguide, which guides the waves from the magnetron to the reactor. Firstly, monomode involves the magnetron generating the microwaves, and the reactor was situated within the waveguide. This results in standing waves being formed, with designated hot and cold spots depending on the position of the reactor within the alternating electric field. The reactor / microwave equipment is typically designed such that the sample needing to be heated is positioned in a hot spot.

The second mode, multimode, has the waveguide direct the microwaves into a cavity, where refraction and reflection of the microwave radiation occurs, creating a more homogenous microwave distribution and heating [218], [219]. Although a multimode system provides a quasi-homogeneous distribution of microwaves, inhomogeneities within a system can lead to fluctuations in concentrations and consequently 'hotspots' forming. This is due to the increased polarisation at the higher amplitudes of the microwave, with the excessive temperatures potentially giving rise to parasitic reaction that occurs above the reaction temperature [219].

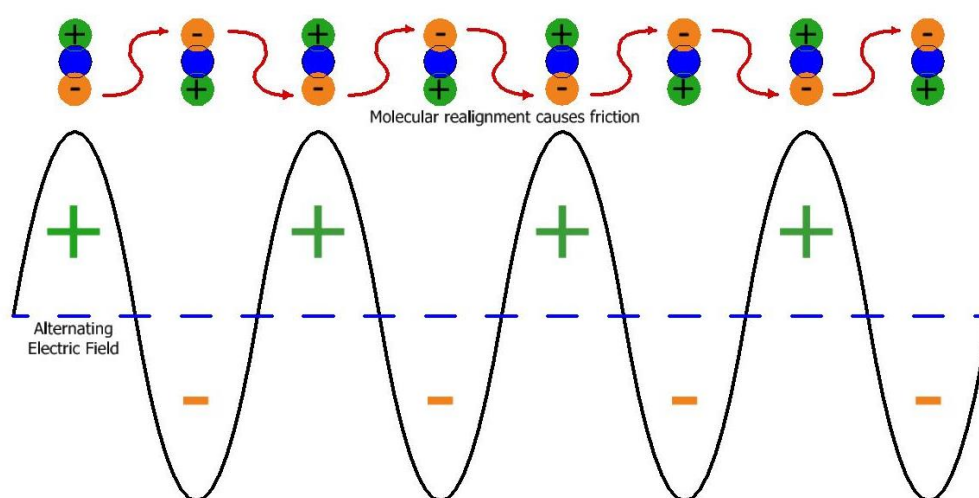


**Figure 1.15:** A graphical depiction between the interaction between polar molecules and the alternating electric field generated by microwave radiation. The changing of alignment was

highlighted to cause resistance between adjacent particles, which was the cause of microwave heating technology.

Power is supplied to the vacuum tube filament to emit electrons, with their electric field interacting with the magnets within the magnetron to curve the accelerating electrons into cavities, which causes a charge disparity across the cavity and the formation of microwave radiation due to the resonant frequencies of the cavities. The power of the microwave can be adjusted *via* pulsed or unpulsed modulation of the power supply to the vacuum tube. In a pulsed power supply, the 'maximum' power is supplied to the vacuum tube filament in pulsed bursts, discretely supplying/ not supplying the 'maximum' power of the microwave, with the proportion of on/off time being proportional to the percentage of max power the desired power was set to. Unpulsed microwave power is used for technical systems to prevent the reactants overheating with the microwave technology due to the excess intensity. This system continuously alters the power supplied to the filament, allowing a percentage of the 'maximum' number of electrons to be produced, allowing a continuous variation of microwave intensity to be produced and thus a more accurate power supply/ heat supply to the system [219], [220]. Unpulsed power supply allows a greater energy efficiency to be achieved due to the low, constant power supply.

With regards to high temperature microwave heating, microwave absorbing materials, known as susceptors, are used to aid the energy conversion of the microwaves. The microwave absorption of some materials has been investigated, with diesel particles, NaY zeolite, and solvents (e.g. water, glycerol, and paraffin oil) only had a microwave absorption of 5.65-14.64%, 10.3% and *ca.* 0.9% respectively. In order to maximise the energy conversion of these materials and increase the heating rate and temperature, microwave absorbing materials such as silicon carbide (SiC) can be used to absorb more microwaves, convert more energy and thus facilitate a greater degree of heating [221]. The power needed to operate a magnetron is also less than a conventional heater/ reactor, meaning that as well as reducing the reaction time, the energy needed to fuel the reaction was also reduced. This was particularly important with respect to the net-zero emissions targets [219].

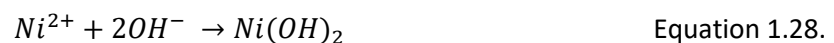
### 1.5.2 – Microwave Technology Applications & Benefits

Microwave technology has been applied in the synthesis of metal oxides and hydroxides, with the hydrothermal synthesis of aluminium oxide and the microwave flow synthesis of silver, copper, and tin oxide [222], [223]. The hydrothermal synthesis of Al<sub>2</sub>O<sub>3</sub> was compared to a conventional (*i.e.*

non-microwave) synthesis route, which confirmed the microwave synthesis was able to synthesise phase pure  $\gamma\text{-Al}_2\text{O}_3$  with a shorter synthesis time of 40 minutes (compared to 3 hours). Microwave synthesis producing smaller particles than conventional synthesis, with a diameter of 0.8-1.2  $\mu\text{m}$  compared to 3-4  $\mu\text{m}$ , meaning the sample had a larger specific surface area (242 vs 148  $\text{m}^2 \text{g}^{-1}$ ) [224]. Nickel hydroxide can also be synthesised through microwave-assisted hydrothermal synthesis, with uniform nanoparticles being formed. Methodologies described by Hall *et al.* involve dissolving a nickel nitrate reactant in a solvent (*e.g.* water, ethanol) and other complexing agents (*e.g.* urea, ammonia and PEG-20,000) to synthesise nickel hydroxide with a nanoflower morphology, consisting of nanoflakes/ nanosheets, with the crystallography ascribed to the  $\beta\text{-Ni(OH)}_2$  phase [119].

NMC materials have also been synthesised *via* microwave-assisted hydrothermal synthesis, with  $\text{Li}_{1.2}\text{Mn}_{0.56}\text{Ni}_{0.16}\text{Co}_{0.08}\text{O}_2$  synthesised using ammonium bicarbonate, ethanol, and water, with the reaction occurring at 200 °C for 30 minutes. The microwave-assisted synthesis of the  $\text{Ni}_x\text{Mn}_y\text{Co}_z\text{CO}_3$  precursor was compared to a conventional (*i.e.* non-microwave) co-precipitation procedure. After a calcination procedure of 800 °C for 16 hours, a layered  $\alpha\text{-NaFeO}_2$   $\text{Li}_{1.2}\text{Mn}_{0.56}\text{Ni}_{0.16}\text{Co}_{0.08}\text{O}_2$  phase was produced with  $\text{LiMn}_6$  impurities. Rietveld refinement confirmed less cation mixing was observed in the microwave hydrothermal sample, with 1.75% nickel in the lithium 3a sites (compared to 4.24% for co-precipitation synthesis). The secondary particle morphology of both samples was quasi-spherical, with less primary particle agglomeration observed in the microwave sample, revealing a narrow primary particle size range of 150-250 nm (compared to 150-450 nm). This yielded an increased first-cycle specific capacity for the microwave hydrothermal sample (229.8  $\text{mAh g}^{-1}$  vs 157.8  $\text{mAh g}^{-1}$ ) but a lower 100-cycle capacity retention (80.6%, 100 cycles at 2.5-4.8 V, 200 mA  $\text{g}^{-1}$ ) [223].

One common precursor in the presence of ammonium bicarbonate and urea is  $\text{Ni}_x\text{Mn}_y\text{Co}_z\text{CO}_3$  due to their degradation to form carbonate ions within the solution [150]. Li *et al.* showed that reducing the urea content from 500% to 200% excess led to a change in phase formation from  $\text{Ni(HCO}_3)_2$  to  $\text{Ni(OH)}_2$  through the hydroxide synthesis mechanism described below in Equations 1.27-1.28 (compared to the mechanism described in equations 1.8-1.10) [225].



An investigation by Shi *et al.* into the urea-based, microwave-assisted hydrothermal synthesis of NMC-532. Using urea as a complexing agent, the temperature, hydrothermal duration, and urea: transition metal ratio were optimised to form a  $\text{Ni}_{0.5}\text{Mn}_{0.3}\text{Co}_{0.2}\text{CO}_3$  precursor. The optimal urea: transition metal ratio was determined *via* ICP elemental analysis, which determined a ratio of 5: 2 produced the most accurate Ni: Mn: Co precipitant ratio of 4.986: 3.012: 2.000 (compared to 2: 1, yielding a 4.60: 2.90: 2.00 ratio; and 3: 1 ratio yielding a 4.71: 2.91: 2.00 ratio). Longer reaction times reduced the residual transition metal content within the solution post-synthesis, with a 6-hour reaction time having  $0.21 \text{ mg L}^{-1}$  relative to a 24-hour reaction time ( $0.13 \text{ mg L}^{-1}$ ) [150].

The optimal synthesis conditions were determined to be  $200^\circ\text{C}$  for 18 hours with a 5:2 urea: transition metal ratio. These conditions produced a sample with the most accurate NMC composition (5.006: 2.994: 2.000), but the tap density and morphology remained similar for samples reacted for greater than 12 hours, with a tap density of  $2.54\text{-}2.56 \text{ g cm}^{-3}$  being achieved and quasi-spherical secondary particle assemblies being yielded. Crystallographic analysis *via* XRD and Rietveld refinement found a longer reaction time of 24 hours to have the smallest degree of cation mixing (4.40% vs 6.39 and 5.87% for 12- and 18- hour syntheses). Electrochemical analysis also reveals the longer reaction time of 24 hours has a greater initial discharge capacity ( $158.6 \text{ mAh g}^{-1}$ , vs  $145.3$  and  $153.9 \text{ mAh g}^{-1}$ ) and capacity retention (92.6%, vs 89.5% and 91.0%) compared to 12- and 18- hour samples, cycled at  $20 \text{ mA g}^{-1}$  between 3.0-4.3 V for 50 cycles. The increased capacity retention was attributed to better nickel penetration into the core of the particle, with the 12-hour synthesis sample having a higher nickel content toward the surface of the particle, which are reactive with the electrolyte and facilitate degradation mechanisms which cause irreversible capacity loss [150].

Microwave-assisted co-precipitation synthesis has been trialled by Liu *et al.* who synthesised  $\text{LiNi}_{0.85}\text{Mn}_{0.1}\text{Co}_{0.05}\text{O}_2$  using a two-hour microwave-assisted co-precipitation reaction (at  $55^\circ\text{C}$ ) in a round bottomed flask followed by either a four-hour conventional hydrothermal reaction (at  $120^\circ\text{C}$ ) or four-hour room temperature stirring reaction. These methodologies were compared to a 12-hour co-precipitation reaction conducted at  $55^\circ\text{C}$ , controlled to a pH of  $11.3 \pm 0.1$ . These samples were then lithiated with 8 mol% excess  $\text{LiOH}\cdot\text{H}_2\text{O}$  at  $550^\circ\text{C}$  for 6 hours followed by  $760^\circ\text{C}$  for 12 hours. XRD analysis of the lithiated NMC oxide showed a higher  $I_{(003)}/I_{(104)}$  ratio for the microwave hydrothermal sample (NMC-MH, 1.44) compared to the microwave-assisted co-precipitation (NMC-MC, 1.37), and the conventional co-precipitation (NMC-CC, 1.23), which suggests a reduced degree of cation mixing for NMC-MH. The three samples had similar quasi-spherical secondary

particle assemblies and tap densities of 2.16, 2.12 and 2.08 g cm<sup>-3</sup> (for NMC-MH, -MC, -CC respectively). Galvanostatic cycling of NMC-MH between 2.75-4.2 V at 0.2C produced a larger initial discharge capacity of 197.1 mAh g<sup>-1</sup> (vs 185.7 and 189.5 mAh g<sup>-1</sup> for NMC-CC and -MC respectively). The capacity retention of this cycling after 100 cycles yielded similar retention values for the microwave samples (84.8% and 83.9% for NMC-MC and -MH respectively) whereas NMC-CC had a retention of 73.0%. Similar trends were observed for Galvanostatic cycling at an increased rate of 1C over the same voltage window with NMC-MH yielding an initial capacity of 169.2 mAh g<sup>-1</sup> (88.3% retention after 200 cycles), compared with NMC-MC (163.9 mAh g<sup>-1</sup>, with 82.1% retention) and NMC-CC (157.5 mAh g<sup>-1</sup>, with 79.7% retention) [226].

## 1.6. Aims & Experimental Objectives

Literature and societal needs have established the relevance of high-throughput synthesis and the need for continuous stirred tank reactors (CSTRs) to synthesise nickel-rich cathode active materials. Nickel-manganese-cobalt 811 (NMC-811) has been identified as a material that can achieve the commercial goals of overcoming 'range anxiety' in consumers while remaining stable enough to yield competitive capacities throughout its lifetime. This thesis will investigate the applicability of microwave heating technology on the synthesis of this NMC-811 material, assessing and validating the use of microwave technology in the two synthesis stages: the NMC hydroxide chemical synthesis and the calcination of the hydroxide to form the lithiated NMC oxide product. Once the viability of microwave technology was assessed, the overall aim of the project was to design and commission a novel co-precipitation reactor vessel that was suitable for the high-throughput, microwave synthesis of the NMC-811 hydroxide precursor *via* a Microwave Stirred Tank Reactor (MiSTR) system.

The synthesis of the NMC-811 hydroxide precursor will be investigated by applying microwave technology to a hydrothermal pathway in an attempt to investigate some of the characteristics of microwave synthesis. The nature of the precipitation and the products formed during the reaction can lead to insights into the microwave synthesis mechanism, and consequently inform the future design of the co-precipitation reactor and reaction conditions. The final objective, is the development of a Microwave Stirred Tank Reactor (MiSTR) system, will be designed to increase the throughput of the NMC-811 hydroxide precursor synthesis *via* a co-precipitation synthesis, with a 1 L vessel placed inside the microwave reactor able to replicate the conventional co-precipitation reaction that was widely used in literature with the aim of decreasing the reaction time and energy usage.

With respect to the calcination aspect of the synthesis pathway, microwave heating technology will be assessed by comparing the crystallographic, morphological, and electrochemical properties of the final lithiated NMC-811 oxide product with samples heated in a microwave furnace compared to that of an oxygen furnace. This set of experiments will use NMC-811 hydroxide precursor obtained through conventional co-precipitation synthesis to maximise the uniformity of the precursor sample and validity of the comparison. The objective was to optimise the synthesis procedure for microwave technology and minimise the cell capacity penalty associated with microwave treatment by generating an oxygen atmosphere during calcination, as a supply of oxygen gas cannot be safely supplied during the reaction.

## 2. Experimental Method

This chapter contains the detail and methodology for each experiment and the corresponding analytical techniques, as well as applicable information regarding the equipment used in the synthesis, for example the microwave furnace and microwave reactor. However, the design and operation of the novel microwave batch reactor system will be included in chapter 5.

### 2.1. – Materials

The following chemicals were purchased and employed without further purification.

$\text{Co}(\text{CH}_3\text{CO}_2)_2 \cdot 4 \text{H}_2\text{O}$  (98%),  $\text{CoSO}_4 \cdot 7 \text{H}_2\text{O}$  (98%),  $\text{LiOH} \cdot \text{H}_2\text{O}$  (>98%),  $\text{Li}_2\text{O}_2$  (95%),  $\text{Mn}(\text{CH}_3\text{CO}_2)_2 \cdot 4 \text{H}_2\text{O}$  (>99%),  $\text{Ni}(\text{CH}_3\text{CO}_2)_2 \cdot 4 \text{H}_2\text{O}$  (>98%), Urea ( $\text{CH}_4\text{N}_2\text{O}$ , >99%) were purchased from Alfa Aesar. Ethanol (99.9%),  $\text{MnSO}_4 \cdot \text{H}_2\text{O}$  (>98%), and NaOH (>98% anhydrous pellets) were purchased from Sigma Aldrich.  $\text{NiSO}_4 \cdot 4 \text{H}_2\text{O}$  (99%) was purchased from Thermoscientific, 2-propanol (99.8%) was purchased from Honeywell and ammonia (28-30 wt%) was purchased from Supelco.

Compressed oxygen and compressed argon were purchased from BOC Ltd.

$\text{Ni}_{0.8}\text{Mn}_{0.1}\text{Co}_{0.1}(\text{OH})_2$  was synthesised in-house by a PDRA, Dr Nirmalesh Anthonisamy, and utilised in the calcination experiments.

Cathode active material slurries were prepared using C-65 carbon black (purchased from Imerys), Polyvinylidene Fluoride (PVDF, purchased from Sigma Aldrich), and N-methyl-2-Pyrrolidone (NMP, 99.5% anhydrous, purchased from Sigma Aldrich), and coated onto carbon-coated aluminium foil. The following materials were used in the manufacture of coin cells: 1 M lithium hexafluorophosphate in ethylene carbonate (EC) and ethylmethyl carbonate (EMC) 3:7 v/v + 2% vinyl carbonate (VC) (electrolyte solution purchased from solivonics), lithium metal ribbon (purchased from Cambridge energy solutions) and a Whatman glass microfiber filter as separator. Stainless steel coin cell components were utilised to make the 2032 cells, including the positive and negative casings, the conical spring and spacer. The *operando* cell assembly method used modified stainless steel 2032 coin cell casings with Kapton/polyimide windows. Dimethyl carbonate (99%, Sigma Aldrich) was used to clean the cathodes during the post-mortem preparation of cycled coin cells.

## 2.2. – Experimental Equipment

The two pieces of microwave equipment used in these methodologies are a microwave furnace (CEM Phoenix) and a microwave reactor (CEM Mars6 Synthesis). The CEM Phoenix is a muffle furnace with a silicon carbide microwave-absorbing heating element surrounded by an insulator, which rapidly heats the interior of the heating zone, as previously described in Section 1.5.1. The CEM Mars6 Synthesis was a microwave reactor that is designed for multiple vessels and methodologies, including hydrothermal reactions (using the EasyPrep Plus vessels) and open-atmosphere reactions, such as co-precipitation reactions (using microwave-transparent vessels and beakers, *e.g.* glass or temperature-resistant plastics).

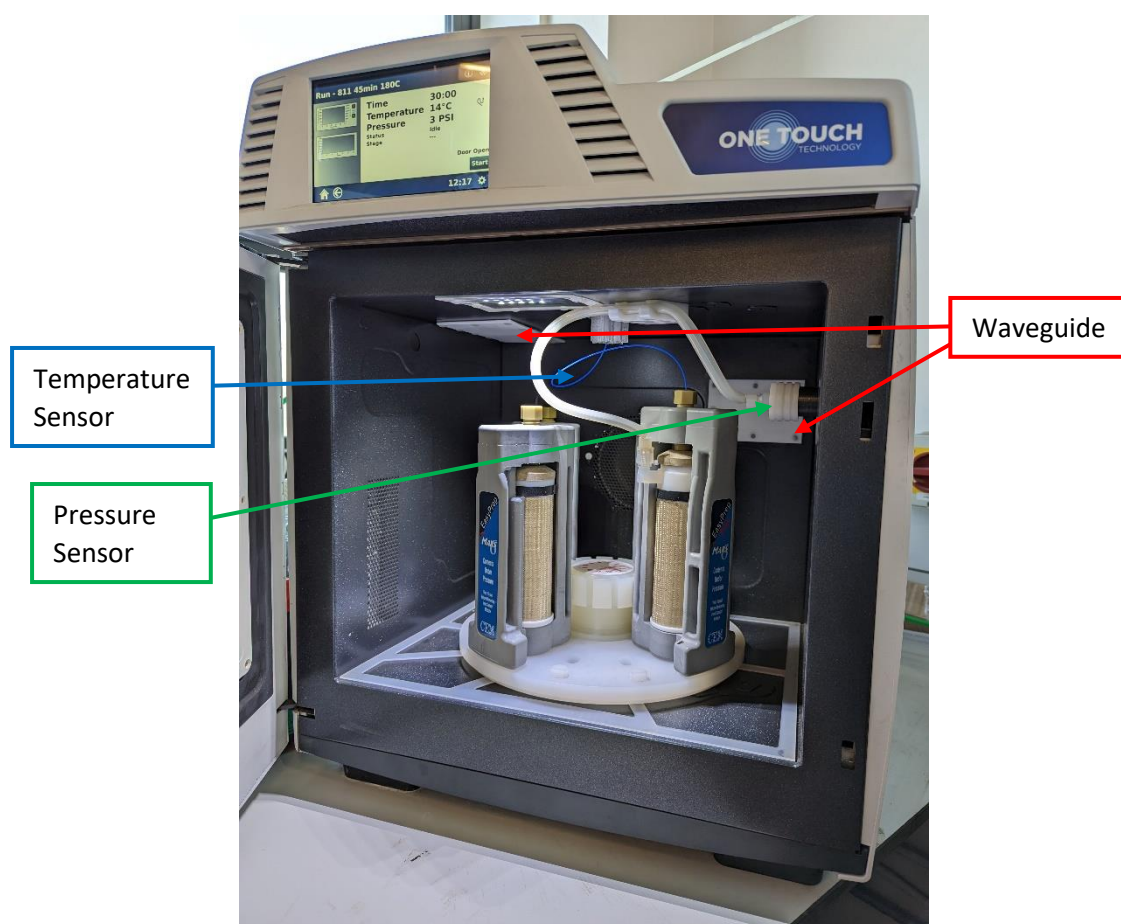


**Figure 2.0.1:** A picture of the CEM Mars6 Synthesis with 4 EasyPrep Plus vessels installed with the quartz thermocouple and pressure sensor. The two waveguides that emit the microwave radiation from their respective magnetrons are annotated in red and the temperature and pressure sensors are indicated in blue and green respectively.

The CEM Mars6 shown in Figure 2.0.1 has a dual-magnetron system, generating microwaves *via* 800 W and 1000 W magnetrons that are guided to the internal cavity by waveguide before irradiating the cavity and sample. The cavity was surrounded by a stainless-steel construction which acts as a Faraday cage to prevent the leakage of microwave radiation. The power and reaction volume needs to be controlled in order to prevent microwave leakage, which was most prevalent in the window of the glass door and should be kept below  $5 \text{ mW cm}^{-2}$  at 5 cm from the surface (as established in the EN 60335-2-25 European Standard). The microwave power output occurs at a frequency of 2.45 GHz, which equates to a wavelength of 12.2 cm. The I/O port that extends out of the top of the microwave was perpendicular to the waveguide and was longer than 12.2 cm, meaning that the microwave radiation cannot travel down the port and leak.

Infrared (IR) temperature sensing works by focusing the IR radiation emitted by the heated reactor vessel using lenses [227]. The lenses transmit the focussed IR radiation outside the faraday cage where thermocouples can measure the temperature of the system by converting the IR energy to a voltage output and comparing it to a standard. There are multiple IR sensors for each EasyPrep Plus reactor vessel that can record IR temperature simultaneously, whereas there was only one fibre optic temperature sensor. The fibre optic sensor was inserted into a sapphire thermowell protection sleeve and contains a gallium arsenide (GaAs) semiconductor, which transmits white light at different wavelengths depending on the temperature. As the temperature increases, the energy of the system increases, which relates to Planck's law such that the wavelength at which the white light was transmitted increases, thus emissivity increases. The wavelength of the transmitted light is sensed by a fibre optic cable and converted to an electronic signal, which is quantified as a numerical temperature value [228]. The pressure was measured using an Electronic Sensor for Pressure (ESP), which measures the pressure as a force applied through a capillary tube connecting the control vessel to a pressure transducer [229]. The resultant electronic signal can be quantified and displayed.

## 2.3. – Synthesis Procedures

### 2.3.1. – Optimisation of the microwave calcination of $\text{Ni}_{0.8}\text{Mn}_{0.1}\text{Co}_{0.1}(\text{OH})_2$

The dependence of oxygen to oxidise nickel to its divalent state during calcination poses a problem to the CEM Phoenix microwave furnace, due to the physical layout of the furnace preventing a safe flow of oxygen through the furnace. To overcome this, it was hypothesised that lithium peroxide ( $\text{Li}_2\text{O}_2$ ) would be able to lithiate the  $\text{NMC-811}(\text{OH})_2$  and generate oxygen gas during its thermal decomposition at 280-400 °C, as per Equation 2.1 below [104].



To exercise this theory, a series of optimisation experiments were conducted to compare the impact of lithium peroxide on the calcination of  $\text{NMC-811}(\text{OH})_2$  to the standard lithium salt used in the calcination of nickel-rich cathode materials, lithium hydroxide ( $\text{LiOH}$ ). This involved investigating the effect of temperature, duration, crucible size, lithium peroxide excess, milling, and heating rate on the material. Samples optimised in these conditions were then compared to samples prepared in oxygen-supplied and air-supplied tube furnaces to gauge the effectiveness of both microwave furnace technology and lithium peroxide.

The  $\text{NMC-811}(\text{OH})_2$  used in this reaction was synthesised in-house by Dr Nirmalesh Anthonisamy using a co-precipitation technique in an Eppendorf BioFlo 320 stirred tank reactor. Stoichiometric quantities of transition metal sulphates, nickel sulphate ( $\text{NiSO}_4 \cdot 6 \text{H}_2\text{O}$ ), manganese sulphate ( $\text{MnSO}_4 \cdot \text{H}_2\text{O}$ ), and cobalt sulphate ( $\text{CoSO}_4 \cdot 7\text{H}_2\text{O}$ ) were weighed and dissolved in 560 mL of deoxygenated, deionised water using the same methodology described in Section 2.3.1. 800 mL of 1 M ammonia was placed in the reactor before the transition metal and 10 M ammonia ( $\text{NH}_4\text{OH}$ ) solution was added concurrently at a rate of  $0.7 \text{ mL min}^{-1}$  and  $0.1 \text{ mL min}^{-1}$  respectively. This equates the molar ratio of transition metal ions to ammonia to be 1: 1.4. 10 M sodium hydroxide ( $\text{NaOH}$ ) solution was added *via* a base cascade with a varying rate to control the pH to 11. This addition time took 14 hours, but the total time for the reaction was 41.5 hours which includes the reaction/particle maturation time after the addition of the reactants. The solution was washed *via* filtration with deionised water and dried in open air.

During the optimisation of different parameters, cylindrical alumina crucibles were used, as seen in Appendix A.4. The heating rate of the oxygen-supplied tube furnaces was kept consistent at  $5\text{ }^{\circ}\text{C min}^{-1}$  and the oxygen flow rate in the furnace was  $50\text{ cm}^3\text{ min}^{-1}$  throughout all experiments. In the microwave furnace, the heating period was 1 hour (equating to a heating rate of  $\approx 12.2\text{ }^{\circ}\text{C min}^{-1}$  depending on operational temperature) unless otherwise stated. These samples are clearly labelled in the discussion. In both furnaces, cooling was natural (i.e. not controlled), and samples were extracted at  $200\text{ }^{\circ}\text{C}$  and placed into a glove box, which stored the samples in an argon atmosphere with  $<0.5$  ppm of  $\text{H}_2\text{O}$  and  $\text{O}_2$ .

Due to the production of oxygen gas during the thermal decomposition of lithium peroxide, a lid was used on all lithium peroxide experiments in an attempt to trap the oxygen in the alumina crucible, but these were not air-tight. To maximise the partial pressure of the oxygen within the crucible, the amount of  $\text{Li}_2\text{O}_2$  was increased from 1 mmol to 4 mmol, which increases the oxygen volume from approximately 46.1 mL to 184.3 mL (at  $850\text{ }^{\circ}\text{C}$ , atmospheric pressure). Additionally, the crucible volume can be decreased from 20 mL to 2.5 mL, in order to maximise the partial pressure and the residence time of oxygen within the crucible, with this exemplified by the cylindrical alumina crucibles (Appendix A.3). The molar excess of lithium peroxide was investigated across a range of 1 - 7 mol%, milled with 4 mmol of  $\text{NMC-811(OH)}_2$  powder and calcined at  $750\text{ }^{\circ}\text{C}$  for 5 hours in the CEM Phoenix microwave furnace. This is based on a lithium excess of 1-5 mol% being used for the calcination of  $\text{LiOH}$  in literature [9], [87], [88], [181].

Temperature and duration are two parameters that were investigated to determine the most suitable conditions for the microwave reaction. Temperatures reported for oxygen-supplied tube furnaces range from  $750\text{--}850\text{ }^{\circ}\text{C}$ , which was extended to  $650\text{--}900\text{ }^{\circ}\text{C}$  in the initial optimisation using 20 mL crucibles, with 1 mmol of  $\text{NMC-811(OH)}_2$  powder being milled with 3 mol% excess of either  $\text{LiOH}$  or  $\text{Li}_2\text{O}_2$ . The duration of the microwave calcination was investigated over a period of 1.5 – 6 hours (based on a 3-hour heuristic) for the 20 mL crucible, with 2 mmol being calcined at  $750\text{ }^{\circ}\text{C}$ . These parameters were refined to the  $750\text{--}850\text{ }^{\circ}\text{C}$  over a period of 3 – 5 hours for the smaller 2.5 mL crucible and the amount of  $\text{NMC-811(OH)}_2$  calcined was increased to 4 mmol. Once the procedure was optimised to a set of conditions for the microwave furnace ( $775\text{ }^{\circ}\text{C}$  for 4 hours), an equivalent procedure was determined for ‘conventional’ tube furnaces, with both air-supplied and oxygen-supplied tube furnaces undertaking the calcination of  $\text{NMC-811(OH)}_2$  milled with either  $\text{LiOH}$  or  $\text{Li}_2\text{O}_2$  in a boat alumina crucible for 12 hours at  $775\text{ }^{\circ}\text{C}$ . The matrix of microwave calcination conditions of which the optimisation was carried out can be seen below in Table 2.0.1.

**Table 2.0.1:** The array of conditions tested during the temperature and duration optimisation of the microwave calcination of NMC-811(OH)<sub>2</sub> with LiOH and Li<sub>2</sub>O<sub>2</sub>. The blue cells indicate trials run in the 20 mL and 2.5 mL crucibles; orange indicates trials run in the 20 mL crucible.

	650 °C	700 °C	750 °C	775 °C	800 °C	825 °C	850 °C	900 °C
1.5 hours			20 mL					
2 hours			20 mL					
3 hours	20 mL	20 mL	20 mL 2.5 mL	20 mL 2.5 mL	20 mL 2.5 mL	20 mL 2.5 mL	20 mL 2.5 mL	20 mL
4 hours			20 mL 2.5 mL					
5 hours			20 mL 2.5 mL					
6 hours			20 mL					

The milling procedure for all trials mentioned involves 15 minutes of hand milling in a pestle and mortar to reduce the particle agglomeration size of the lithium source and NMC-811(OH)<sub>2</sub> to reduce the diffusion pathway of the lithium. During the 20 mL crucible series of reactions, ‘dry-milling’ was conducted, with the lithium salt and NMC-811(OH)<sub>2</sub> milled alone; but it was found that the addition of acetone allowed the partial dissolution of the lithium salt with the transition metal powder, creating a smoother powder and better lithium mixing, while mitigating loss of powders as the wetted mixture contains them. Consequently, the 2.5 mL crucible series introduced ‘wet-milling’, with acetone added to the procedure initially (t = 0 minutes) and at the half-way point (t = 7.5 minutes), allowing two opportunities for the powder mixture to be wetted before its evaporation.

### 2.3.2. – Hydrothermal synthesis of Ni<sub>0.8</sub>Mn<sub>0.1</sub>Co<sub>0.1</sub>(OH)<sub>2</sub>

This optimisation experiment was based on the work of Shi *et al.* in which transition metal acetates (TM(Ac)<sub>2</sub>) were reacted with urea and water under high temperatures of 180-200 °C for 6-24 h in a conventional (*i.e.* non-microwave) hydrothermal bomb reactor to synthesise NMC-532. They concluded that the optimum conditions were reacting a ratio of 5: 2 urea: TM reactants at 200 °C for 24 h due to the reduced cation mixing, increased capacity and rate capabilities [150]. This work needs to be translated to the application of microwave technology and the NMC-811 chemistry, which requires the optimisation of reaction conditions.

Approximately 1 L of deionised water (~16.418 mΩ, Purite Select Fusion) was deoxygenated by bubbling argon through it at a rate of ~1 L min<sup>-1</sup> for 30 minutes. This method was based on the work of Butler *et al.*, who recorded a deoxygenation level of 0.47-0.56 ppm after 5 minutes of bubbling nitrogen at a rate of 25 mL s<sup>-1</sup>, compared to boiling water for 30 minutes, which achieved an oxygen level of 0.87-1.21 [230]. Due to the exposure to air, it was unknown how long the water remains deoxygenated. For clarity, the future use of 'deoxygenated' in the context of water in this experiment and the co-precipitation experiments described in Section 2.3.3. applies the assumption that the water / solution maintains an acceptable level of deoxygenation such that manganese does not oxidise during the transfer between vessels and during laminar (vortex-inducing) mixing. Any turbulent agitation or re-oxygenation of will be clearly notified, and the assumption ceases to apply to that scenario.

Stoichiometric masses of Nickel acetate tetrahydrate (Ni(CH<sub>3</sub>CO<sub>2</sub>)<sub>2</sub> · 4 H<sub>2</sub>O, NiAc), manganese acetate tetrahydrate (Mn(CH<sub>3</sub>CO<sub>2</sub>)<sub>2</sub> · 4 H<sub>2</sub>O, MnAc) and cobalt acetate tetrahydrate (Co(CH<sub>3</sub>CO<sub>2</sub>)<sub>2</sub> · 4 H<sub>2</sub>O, CoAc) were weighed such that 0.002 moles (0.0016 mol, 0.002 mol, 0.002 mol respectively) of transition metal acetate were stirred in 10 mL of the deoxygenated, deionised water until dissolved. This mixing was conducted in an open atmosphere, so it is unknown whether a deoxygenated system was maintained. This was typically mixed with a 2.9:1 molar ratio of Urea (0.0058 mol), based on the hypothesis that NMC-811 needed a higher Urea: *TM* ratio than NMC-532 (optimised to 2.5:1) [150], [157]. The specified urea was also dissolved in deoxygenated, deionised water. The mass values used for the series of experiments can be seen in Table 2.0.2.

**Table 2.0.2:** A table showing the mass values used for the experiments, with each Urea ratio specified.

Column	Reaction volume (mL)	Urea: <i>TM</i> ratio	Mass of Urea (g)	Mass of NiAc (g)	Mass of MnAc (g)	Mass of CoAc (g)
1	20 mL	2.9:1	0.348	0.3982	0.049	0.049
2	20 mL	2.5:1	0.300	0.3982	0.049	0.049
3	20 mL	5.0:1	0.600	0.3982	0.049	0.049
4	20 mL	3.0:1	0.360	0.3982	0.049	0.049
5	20 mL	1.0:1	0.120	0.3982	0.049	0.049
6	40 mL	2.9:1	0.696	0.7964	0.098	0.098

Once the solid reactants had fully dissolved, the two solutions were mixed, forming a transition metal- urea solution, which was repeated 3 times, such that 4 reactor vessels were used, satisfying the minimum cavity volume for the Mars6. The pH of these solutions was measured using a Mettler Toledo FiveEasy Plus meter, which was stored in a 3 M KCl solution and calibrated at room temperature with pH 7.00, 9.21 and 10.00 buffer solution. Once recorded, the solutions were decanted into the EasyPrep Plus hydrothermal vessels and sealed with an 84 PSI torque wrench.

The hydrothermal procedures were experimentally designed to optimise the reaction conditions of the microwave reaction, namely: temperature, duration, volume, urea: *TM* ratio, pH, and pressure. According to literature, temperature and duration are two key parameters that control the outcome of the reaction. The temperatures chosen were based on the heuristic described by CEM that for microwave hydrothermal reactions, the reaction temperature should be approximately double that of the boiling point of the solvent,  $\pm 10\%$  (180 °C, 200 °C and 220 °C), to prevent over-pressurisation. Equally, the range of durations selected was based on recommendations by CEM based on their previous experience. The Mars6 was rated to operate at high power for approximately 1 hour, thus as mid-range power used in these experiments, 3 hours was deemed a suitable maximum value, with appropriate intervals selected below this value. The reaction times quoted for the microwave hydrothermal experiments (1-3 h) are significantly less than those quoted in literature by Shi *et al.* for similar reactions (24 h), indicating the benefits of microwave hydrothermal reactions should this methodology be scaled for high-throughput/ commercial syntheses. The Table 2.0.3 highlights the matrix table for experimental optimisation of temperature and duration, and the volumes used under the corresponding conditions.

**Table 2.0.3:** A table depicting the matrix of temperature and reaction duration ranges used to determine optimum values for the reaction.

Duration (across) / Temperature (below)	30 minutes	45 minutes	1 hour	2 hours	3 hours
180 °C	20 mL, 40 mL	20 mL, 40 mL	20 mL	20 mL	20 mL
200 °C	20 mL	20 mL	20 mL, 40 mL	20 mL, 40 mL	20 mL, 40 mL
220 °C	20 mL				

The volume used in the reaction vessel indicates the power and pressure of the system during the reaction, due to the pressure head generated upon boiling of the solvent. The 100 mL EasyPrep Plus hydrothermal vessels have a working volume for the Mars6 vessels was 20 mL, which is represented by the light blue shaded 'fluid' in the left-hand vessel in Figure 2.0.2. **Figure 2.0.2:** A technical drawing of the EasyPrep Plus control vessel, complete with stirrer bar, volume of reactants and fibre optic temperature sensor. All dimensions are quantified in millimetres (mm). However, given the scope of the project was to target high-throughput synthesis, 40 mL experiments were run to investigate the scalability of the reaction, with the additional volume indicated with the additional dark blue shaded 'fluid' volume in Figure 2.0.2. Mixing within the reaction was conducted by a 13x 2.5 mm magnetic stirrer bar operating with an arbitrary 'high' stirring speed set by the CEM programming.

The hydrothermal vessel with a magnetic stirrer bar and reaction solution was placed (left, Figure 2.0.2) into a Kevlar housing sleeve and a chamber with pressure and thermocouple housing closes the vessel (centre, Figure 2.0.2). These are then placed with a screw well housing unit into the vessel (right, Figure 2.0.2), where it was tightened to 84 PSI. These were then loaded symmetrically into the Mars6 reactor to maximise the uniformity of heating. The magnetic stirrer bar is Teflon-coated, so although it absorbs microwaves, Teflon is thermally insulative, controlling the transfer of heat from the superheated metal to the surrounding water [231].

The chemical parameters of the reaction, urea: *TM* ratio (which corresponds to the ammonia concentration due to the thermal degradation of urea) and the pH, can determine the nucleation and growth of particles, as discussed in Section 1.3.1. [232]. The optimisation of the urea: *TM* ratio investigated ratios ranging from 1:1 to 5:1 and was reacted for 45 minutes at 200 °C. The optimisation of the pH reacted for 3-hour duration at 200 °C and investigated pH values ranging 10.5-11.5. In order to ensure the volume of each reaction vessel of the pH optimisation experiment remained constant, a 0.5 M solution of sodium hydroxide was prepared by dissolving anhydrous pellets into deoxygenated, deionised water and added dropwise to a 10 mL transition metal-urea solution from a pipette, monitoring the volume added. A volume of deoxygenated, deionised water was added to total the volume to 20 mL. pH was measured continuously during this procedure to ensure it was tailored to the desired values of 10.5, 11.0 and 11.5.

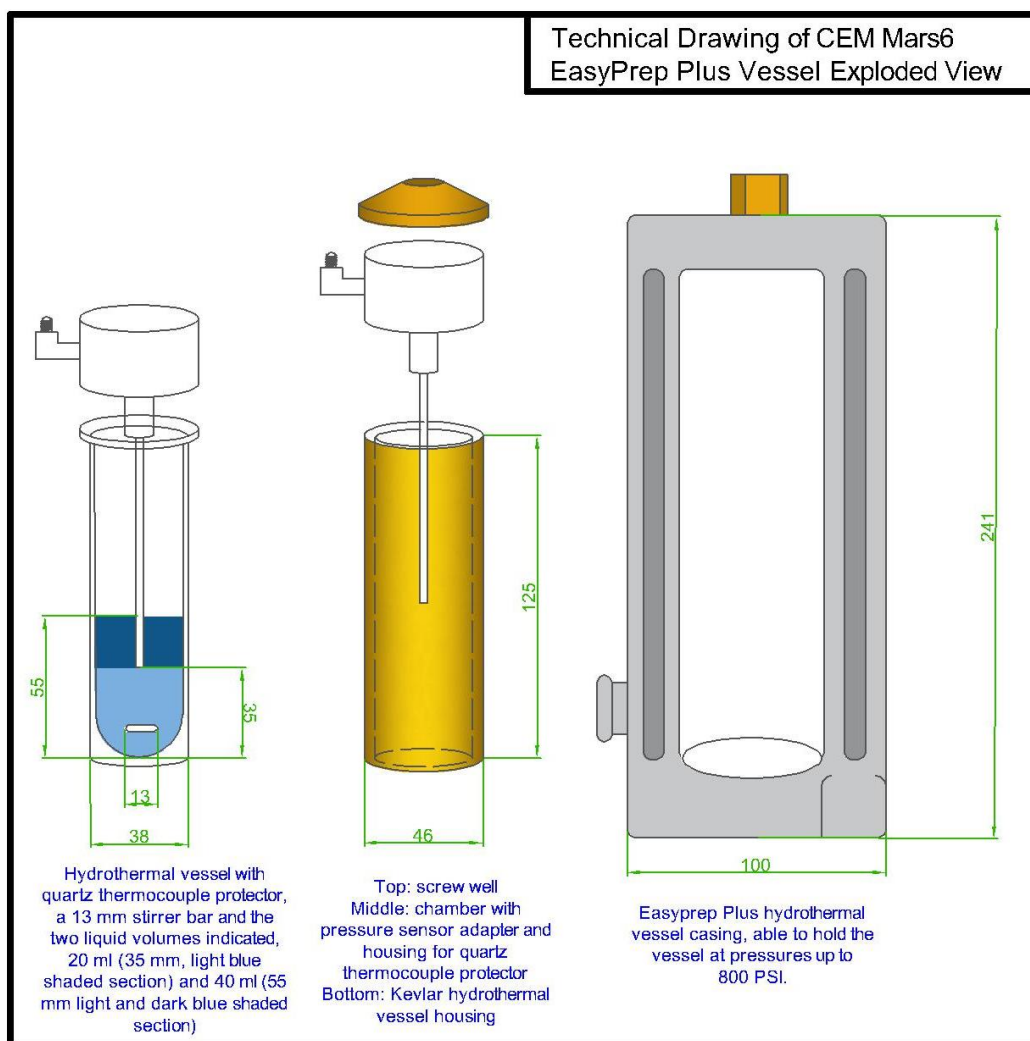


**Figure 2.0.2:** A technical drawing of the EasyPrep Plus control vessel, complete with stirrer bar, volume of reactants and fibre optic temperature sensor. All dimensions are quantified in millimetres (mm).

Typically, the power was automatically tuned to meet a predetermined temperature during experiments due to its relation to reaction kinetics and excessive temperatures driving parasitic-reactions. Due to the hydrothermal vessel being a closed system (i.e. a fixed volume within the vessel), Charles' law dictates that the system pressure and temperature are inversely proportional to one another in order to maintain the constant volume. An experiment was conducted to tune the power ramps the sample to a certain pressure, 400 PSI (50% of the maximum pressure capability of the hydrothermal vessels). 20 mL of solution was measured (see column 1 of Table 2.0.2 for dissolved masses of urea and transition metal), placed in the hydrothermal vessel tightened to 84 PSI, and reacted for 3 hours at 400 PSI.

After each reaction, samples were washed and centrifuged, with each vessel washed in a separate tube. Three washes using 20 mL deionised water were conducted followed by one wash using 10 mL of ethanol. The centrifuge programme involved a 2-minute ramp to 6000 rpm, where it was held at that speed for 4 minutes, before decelerating in 2 minutes to a stop. Prior to centrifuge, the solution and washing medium were placed on a vortex generator for 10 seconds to suitably disperse the two phases. The wetted  $\text{Ni}_{0.8}\text{Mn}_{0.1}\text{Co}_{0.1}(\text{OH})_2$  powder was dried in an oven overnight before undergoing X-ray diffractometry to ensure each of the vessels for each experiment were the same phase before mixing the 4 powders together in order to achieve a greater sample size (0.145-0.165 g yielded per vessel). A portion of the resultant powder was heat treated at high temperature with one of two lithium salts ( $\text{LiOH}$  or  $\text{Li}_2\text{O}_2$ ) to form the lithiated NMC-811 oxide product,  $\text{LiNi}_{0.8}\text{Mn}_{0.1}\text{Co}_{0.1}\text{O}_2$ .

The two lithium salts used ( $\text{LiOH}$  or  $\text{Li}_2\text{O}_2$ ) are the standard lithium source used for nickel-rich cathode materials and the novel Li source that thermally decomposes to form oxygen gas. The  $\text{NMC-811}(\text{OH})_2$  powder was hand-milled with 3 mol% excess of the lithium source for 15 minutes in a pestle and mortar, with the powder wetted with acetone to prevent aerial dispersion of particles and aid mixing through the partial dissolution of the lithium hydroxide. The acetone evaporates off leaving a dried powder. This lithiated powder was placed into a 2.5 mL alumina cylindrical crucible (depicted in Appendix A.4) and placed into one of two furnaces for high temperature heat treatment. An 'oxygen-supplied tube furnace' was supplied with  $50 \text{ cm}^3 \text{ min}^{-1}$  of oxygen gas and heated at  $5 \text{ }^\circ\text{C min}^{-1}$  to a temperature of  $775 \text{ }^\circ\text{C}$ , where it was held for 12 hours. Alternatively, a microwave furnace was heated to  $775 \text{ }^\circ\text{C}$  over a 2-hour period, then held at the high temperature for 4 hours. The sample was then cooled to  $200 \text{ }^\circ\text{C}$ , extracted and placed into a glove box, which stored the samples in an argon atmosphere with  $<0.5 \text{ ppm}$  of  $\text{H}_2\text{O}$  and  $\text{O}_2$ .

### 2.3.3. – Microwave Co-precipitation synthesis of $\text{Ni}_{0.8}\text{Mn}_{0.1}\text{Co}_{0.1}(\text{OH})_2$

In order to increase the scale of synthesis of  $\text{NMC-811}(\text{OH})_2$ , a co-precipitation methodology was developed. This involved using a 3D-printed reactor vessel made from FormLabs Clear Resin (consisting of urethane dimethacrylate, methacryl monomers and diphenyl (2,4,6-trimethylbenzoyl)phosphine oxide) [233]. A lid with seven holes to allow the safe insertion of multiple tubes and sensors, one of which was for the fibre optic temperature sensor, which was protected by a glass capillary tube. Due to the open vessel reaction and contact with the atmosphere, there was oxygen exposure throughout the reaction and evaporation of the content can occur. Peristaltic pumps and a pH probe were utilised from the Eppendorf Bioflo 320 system, with one pump supplying a transition metal sulphate solution, one pump a basic solution and two pumps created a feedback loop pumping reactor solution to a remote pH sensor on a stirrer hot-plate. This system was depicted *via* the process flow diagram in Figure 2.0.3.

The co-precipitation reaction inside the microwave reactor consisted of the addition of a transition metal sulphate solution to an 'initial' ammonia solution alongside a basic solution that consisted of sodium hydroxide and ammonia. This reaction occurs at 60 °C heated through a power rating of 400 W, but with a 'low' stirring speed (based on the arbitrary CEM Mars6 stirring speeds) to minimise the possibility of the stirrer bar smashing the glass capillary tube housing the fibre optic temperature probe. The transition metal sulphate solution was prepared by weighing stoichiometric quantities of nickel sulphate ( $\text{NiSO}_4 \cdot 6 \text{H}_2\text{O}$ ), manganese sulphate ( $\text{MnSO}_4 \cdot \text{H}_2\text{O}$ ), and cobalt sulphate ( $\text{CoSO}_4 \cdot 7\text{H}_2\text{O}$ ) and dissolving them in 200 mL of deoxygenated, deionised water, to form a 0.8: 0.1: 0.1 M (Ni: Mn: Co) solution, aside from the third trial, which formed a 0.4: 0.05: 0.05 M solution, detailed in Table 2.0.4. Deoxygenation was achieved by bubbling argon through a volume of water at a rate of  $1 \text{ L min}^{-1}$  for 30 minutes [230].

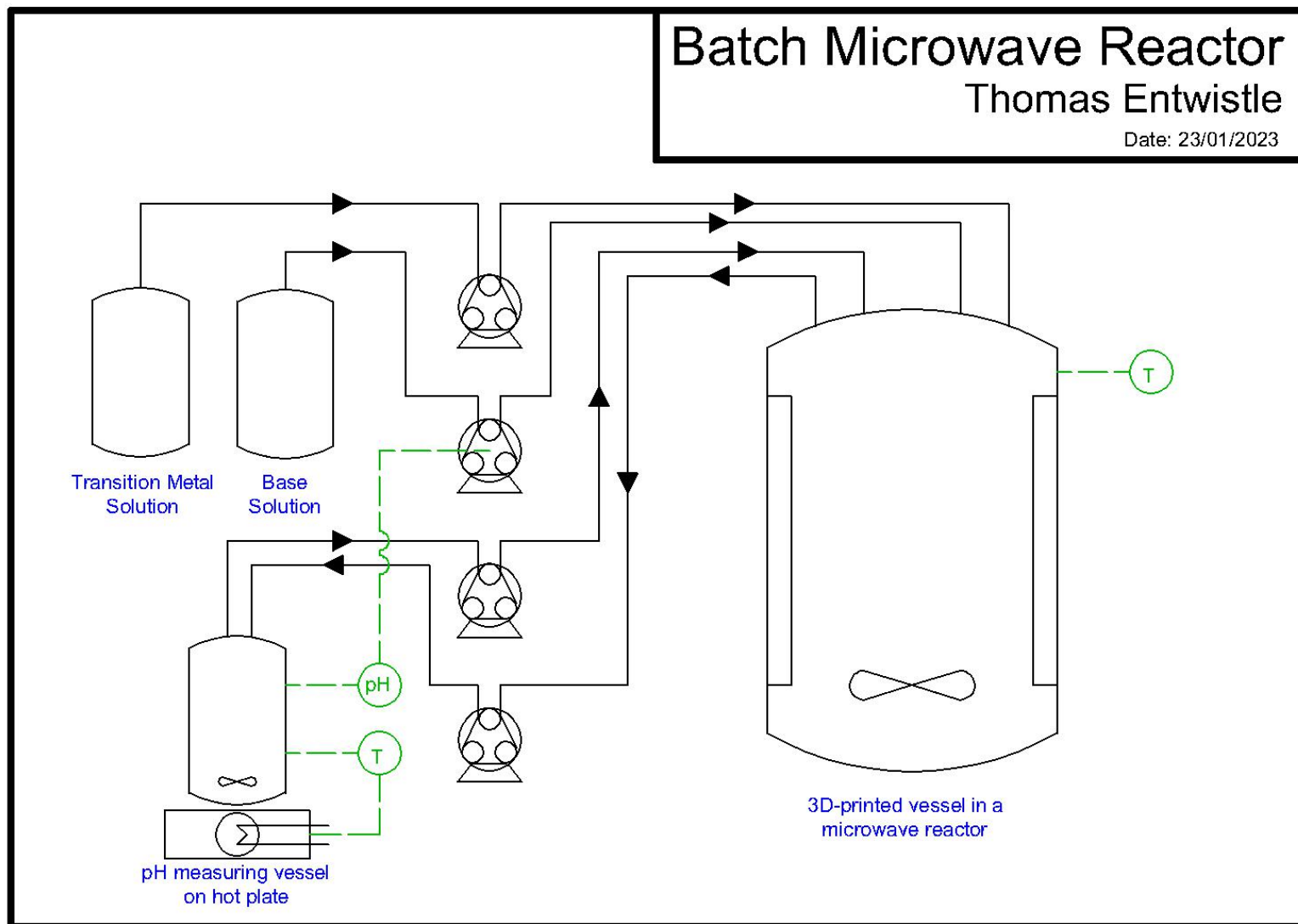


**Figure 2.0.3:** A process flow diagram depicting the layout of the batch microwave reactor system.

An additional 150 mL was added to this solution to account for the loss of water through evaporation over the course of the reaction, leading to an overall concentration of 0.57 M. This was due to a previous test that indicated an evaporation rate of 50 mL h<sup>-1</sup> through heating deionised water to 60 °C at a power rating of 400 W over an extended period of time. A 300 mL, 0.747 M ammonia solution was initially added to the reactor vessel. The molar ratio of ammonia to the three transition metals (Ni, Mn, Co) in the solution was 1: 1.2 to compensate for any ammonia lost through evaporation in the reactor vessel. The base solution consists of varying concentrations of anhydrous sodium hydroxide (5 M, 3 M, and 1 M for each of the three trials respectively) in deoxygenated, deionised water, as detailed in Table 2.0.4.

**Table 2.0.4:** A table describing the masses and volumes of the reactants that are used in the three trials of the batch microwave reactor reaction experiments.

	Trial 1	Trial 2	Trial 3
Moles of nickel sulphate (g)	0.16	0.16	0.08
Moles of manganese sulphate (g)	0.02	0.02	0.01
Moles of cobalt sulphate (g)	0.02	0.02	0.01
Volume of transition metal solution (mL)	350	350	350
Concentration of 'initial' ammonia solution (M)	0.747	0.747	0.373
Total volume of 'initial' ammonia solution (mL)	300	300	300
Concentration of sodium hydroxide in the base solution (M)	5.0	2.0	1.0
Concentration of ammonia in the base solution (M)	0.299	0.299	0.112
Total volume of base solution (mL)	100	150	300

During this proof-of-concept experimental series, three trials were conducted in an attempt to control two characteristics of the co-precipitation reaction: pH control and transition metal addition rate. pH was measured using a Mettler Toledo InPro 3250i probe and initially calibrated using pH 7.00 and 9.21 buffer solutions at room temperature for the first two trials but was calibrated at 60 °C using pH 7.00 and 12.46 buffer solutions for the final trial to improve the accuracy of the readings. The solution in the reactor was continuously pumped in a quasi-steady state nature along 2 m of

tubing to a beaker with the pH probe and back along another 2 m of tubing to the reactor vessel. The beaker with the pH probe was continuously stirred using a stirrer bar to avoid sedimentation, promoting a homogenous temperature for the pH reading (in the first two trials temperature was not controlled, with an ethanol thermometer measuring 35-40 °C; and the third trial the temperature was controlled at 60 °C using the hot plate and thermocouple).

Controlling the pH and transition metal addition rate to maintain a pH of 11.0 was attempted by adjusting different parameters. The first two trials attempted to control pH using a dual acid-base cascade feedback loop, with there being a standard flow rate of transition metal solution (which acted as an acid) of 2.0 mL min<sup>-1</sup> and base solution flow rate of 0.2 mL min<sup>-1</sup>, but these flow rates vary depending on the pH of the system. The minimum and maximum flow rates are indicated in Table 2.0.5. One problem identified from the first trial was the lag in measuring the pH compared to the actual pH in the system causing overcompensation to occur in the response, so in subsequent trials, larger diameter tubing and more dilute base solution were employed to maximise control over the pH, as seen in Table 2.0.5. In the third trial, the transition metal flow rate was fixed at 1.4 mL min<sup>-1</sup> and the base solution flow rate was manually controlled until an equilibrium at pH 11.0 was achieved. A small, weak base cascade was added following this, with the base solution flow rate increasing from 1.0 mL min<sup>-1</sup> to 1.2 mL min<sup>-1</sup> if pH 11.1 was exceeded.

**Table 2.0.5:** A table describing the different reaction times, tube diameters and corresponding flow rates and their effect on the pH range measured throughout the trial.

	Trial 1	Trial 2	Trial 3
Addition Time (hours)	4	5	3.5
Maturation Time (hours)	1	1	2
Base Solution Pump; ID (mm) / flow rate (mL min <sup>-1</sup> )	0.8 mm / 0.0-0.8	1.6 mm / 0.0-0.8	1.6 mm / 1.0-1.4
Transition Metal Solution Pump 2; ID (mm) / flow rate (mL min <sup>-1</sup> )	1.6 mm / 0.0-7.0	1.6 mm / 0.0-4.0	1.6 mm / 1.4
pH Pump (out of reactor); ID (mm) / flow rate (mL min <sup>-1</sup> )	1.6 mm / 3.0	4.8 mm / 15.0	4.8 mm / 15.0
pH Pump (into reactor); ID (mm) / flow rate (mL min <sup>-1</sup> )	1.6 mm / 3.0	4.8 mm / 15.0	4.8 mm / 15.0
pH Range	9.9 – 12.4	10.1 – 12.3	10.5 – 11.7

Once the addition time had been completed, the reaction was left to mature for a ‘maturation time’ before being pumped out and washed *via* vacuum filtration. For this, a wetted Whatman glass microfiber filter with a diameter of 257 mm was used, and the reaction solution was pumped onto

the surface of the filter. Additionally, 1.5-2.0 L of deionised water was added to wash the solution, with the pH of the filtrate measured *via* litmus paper after every 500 mL was added until it was pH 7.0-8. The filter cake produced was then dried in an oven at 80 °C overnight. The lithiation and calcination protocols followed the same procedure as previously mentioned in Section 2.3.2., with 3 mol% excess lithium salt being hand milled with the NMC-811(OH)<sub>2</sub> powder for 15 minutes prior to calcination in an oxygen-supplied tube furnace (at 775 °C for 12 hours) or a microwave furnace (at 775 °C for 4 hours). All samples were removed from the furnace at 200 °C and placed in an argon filled glove box with H<sub>2</sub>O <0.5 ppm and O<sub>2</sub> <0.5ppm.

## 2.4. – Characterisation techniques

Based on the literature and the crystalline products expected from the microwave synthesis methods, crystalline and morphological analysis would be necessary to characterise the reaction products. Electrochemical testing was also conducted to assess the practical characteristics of select materials as well as providing insight into mechanisms present during the electrochemical cycling of the material.

### 2.4.1. – X-Ray Diffraction Analysis

The 3-dimensional crystalline structure of the layered transition metal oxides materials are important to the electrochemical performance of NMC-811 cathodes, with crystal phase degradation mechanisms and cation mixing between the transition metal and lithium layers indicating loss of electrochemical capacity of the cathode active material. One form of analysis that can identify crystallographic information from the product is X-ray diffractometry (XRD), which can identify the crystal phases and qualitative information from a sample, with further Rietveld refinement attaining quantitative lattice parameters of the unit cell.

#### 2.4.1.1. – Powder X-Ray Diffraction (PXRD)

X-rays are a form of electromagnetic radiation that have a wavelength of 0.01 – 10 nm (1-100 Å), which was within the order of magnitude of chemical bonds. This factor allows X-ray radiation to interact with crystalline structures, revealing information on the crystalline phase of the material

and other structural properties. X-ray generation involves a cathode and anode, with the cathode tube containing a tungsten filament (chosen due to its high melting point) which was heated until it produces electrons, which are then accelerated down a vacuum chamber by a potential of 10-60 kV towards an anodic target metal source (e.g. copper, molybdenum, chromium), which generates X-rays upon the collision with a wavelength that corresponds to the target material.

This collision with the target materials produces two types of radiation seen in Figure 2.4: characteristic X-ray radiation and *Bremsstrahlung* radiation. The first, more desirable, ‘characteristic’ X-ray radiation is generated from the collision between the incident cathodic electron and the target material’s anodic electron positioned in an inner shell. Both the cathodic and anodic electron are ejected from the target atom, with an electron in the outer shell filling the space, losing energy in the form of X-ray photons with a discrete energy band and wavelength, typically denoted  $K_{\alpha}$ ,  $K_{\beta}$  or  $L_{\alpha}$  depending on the electron orbital transition (L- to K- electron shell transition, M- to K- electron shell transition and M- to L- electron shell transition respectively) [234]. A common example of this was the use of copper in the anode target material, which produces a  $K_{\alpha}$  radiation with a wavelength of 1.541 Å, and  $K_{\beta}$  radiation with a wavelength of 1.544 Å. The *Bremsstrahlung* radiation is a result of the cathodic incident X-ray passing too close to the nucleus, causing deceleration and the production of broad-spectrum X-ray radiation.

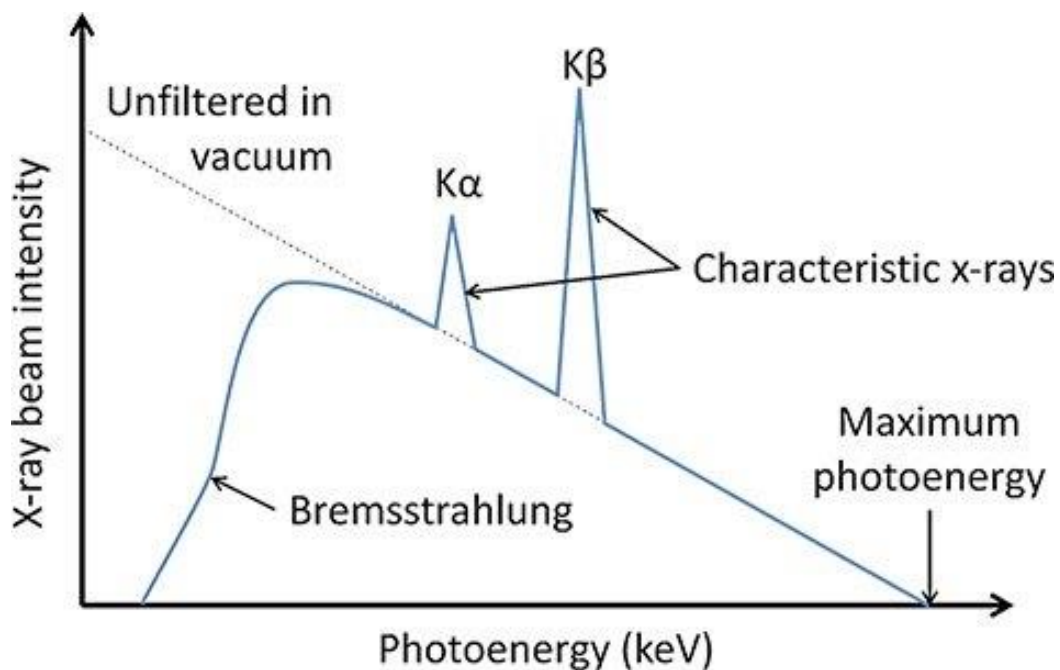


**Figure 2.0.4:** An image depicting the variation in intensity of the Bremsstrahlung radiation with photoenergy. Characteristic ‘ $K_{\alpha}$ ’ and ‘ $K_{\beta}$ ’ x-ray peaks from the electron energy level transitions are clearly seen within the Bremsstrahlung profile. Reproduced from PhysicsOpenLab website [235].

In order to accurately analyse and determine structural characteristics of a crystallite, one wavelength of radiation should be used in order satisfy Bragg's law (see Equation 2.2) and consequently a monochromator is used to filter out unwanted radiation wavelengths, namely the *Bremsstrahlung* and  $K_{\beta}$  radiation. One common monochromator is a single-crystal monochromator, which uses a graphite, quartz or germanium crystal that was rotated such that only the specified  $K_{\alpha 1}$  wavelength undergoes constructive interference [236].

The anodic target source metal has a particular electronic structure with a minimum 'excitation potential' that allows the ejection of a core-shell electron, such as the K-shell electron of  $K_{\alpha 1}$  X-rays. The target source material and excitation potential will generate characteristic X-rays of a particular wavelength and energy, with 'softer', low energy sources such as copper having a lower excitation potential of 8.98 kV and a longer  $K_{\alpha 1}$  wavelength of 1.541 Å and less energy (as per Planck's equation, Equation 2.3); whereas 'harder', high-energy sources such as molybdenum have high excitation potential of 20.0 kV, producing higher energy X-rays with a  $K_{\alpha 1}$  wavelength of 0.709 Å [236]. Softer sources have an increased degree of elastic scattering, leading to a higher resolution and applications in powder X-ray diffraction (PXRD), and for materials with a low atomic number. Harder sources have less scattering, allowing a wider range of angles to be measured at the cost of resolution, and their higher energy decreases the level of absorption, meaning that transmission XRD can be configured.

$$\text{Bragg's Law: } n\lambda = 2 d_{hkl} \sin(\theta) \quad \text{Equation 2.2.}$$

$$\text{Planck's equation: } E = \frac{hc}{\lambda} \quad \text{Equation 2.3.}$$

The resultant monochromatic source X-rays that interact with the sample are absorbed and re-radiated *via* elastic scattering, with the conservation of energy throughout this interaction meaning that only certain angles can constructively interfere and produce high-intensity signals at these angles. These angles are dependent on the crystal structure of the sample, with the synchronisation of 3-dimensional lattice planes allowing the constructive interference of parallel x-rays in accordance with Bragg's law (Equation 2.2); where  $n$  was the absolute value for order of diffraction,  $\lambda$  was the wavelength of the incident x-ray beam,  $d_{hkl}$  was the lattice spacing and  $\theta$  was the incident angle of the x-ray with respect to the sample, as seen in Figure 2.0.5.

The most common configuration of a diffractometer revolves around maintaining a constant  $K_{\alpha 1}$  wavelength over a range of angles. The unit cell of the crystal has multiple lattice planes that are constructively diffracted to produce a 'fingerprint' pattern over the range of angles, which can be analysed against a database (such as the Inorganic Crystal Structure Database, ICSD) of diffraction patterns and can be used to identify phases and materials. The incident and diffracted radiation occur at the same angle,  $\theta$ , as depicted in Figure 2.0.5, with the total diffraction angle of  $2\theta$  also annotated as it was this angle that was denoted in the analysis of diffraction patterns.

For successful powder diffraction analyses, a random alignment of crystalline domains was needed in order to get an accurate representation of each lattice plane in the diffraction pattern, portrayed by comparing the relative intensity of diffraction peaks. 'Preferred orientation' of a sample can occur, particularly in single-crystal particles, resulting from certain morphologies or sample preparations that can lead to an artificial representation of a certain lattice plane. Lighter elements such as lithium and hydrogen do not interact as heavily with X-rays due to the smaller electron shell structure and resultant density, and consequently have lower intensity peaks on diffraction patterns.

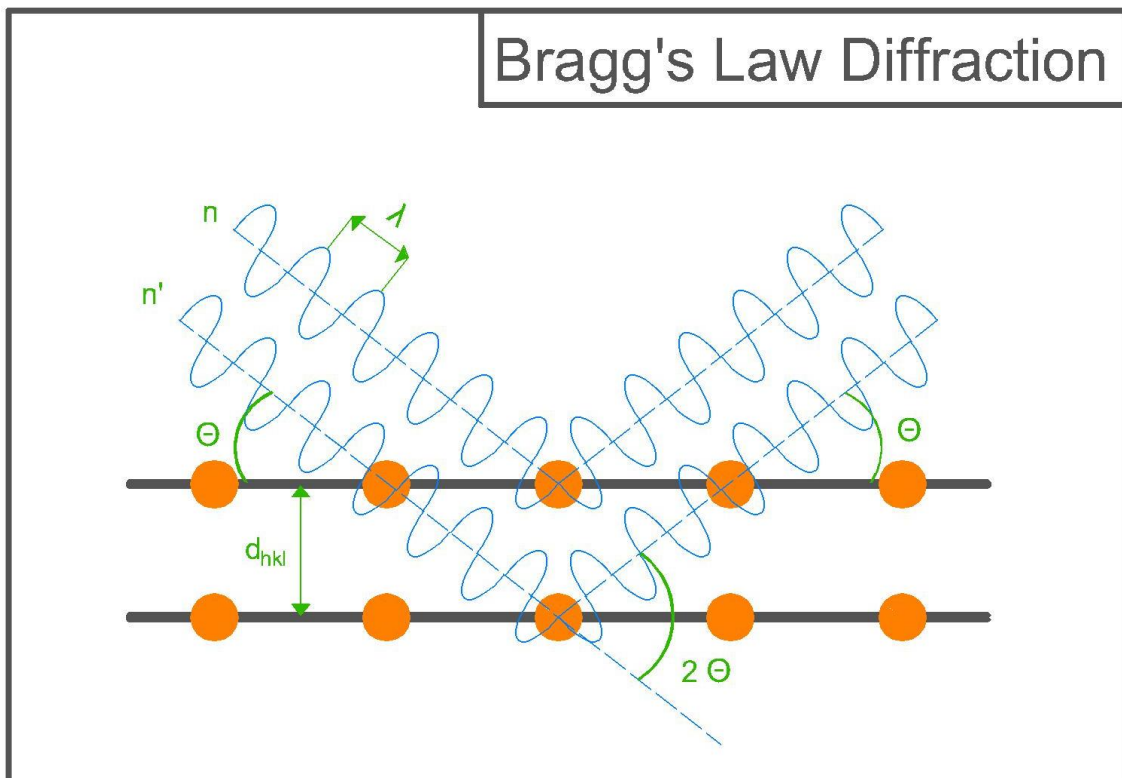


**Figure 2.0.5:** A visualisation of x ray diffraction within a lattice structure and its relation to Bragg's law.

In this work, PXRD was conducted on a Rigaku Miniflex 600 benchtop diffractometer that utilises  $\text{Cu-K}\alpha$  source radiation ( $\text{Cu-K}\alpha = 1.541 \text{ \AA}$ ) with a voltage of 40 kV and a current of 40 mA. Analyses were conducted between  $10$  and  $80^\circ$  with a step size of  $0.02$ . Initial scan rates were  $1.5^\circ \text{ min}^{-1}$ , but this was reduced to  $0.8^\circ \text{ min}^{-1}$  to reduce signal noise when conducting Rietveld refinements. Cathode discs were also analysed using a molybdenum-sourced STOE STADI P diffractometer ( $\text{Mo-K}\alpha = 0.709 \text{ \AA}$ ) in a transmission configuration, where it was operated at a voltage of 50 kV and current of 40 mA. Four consecutive scans were conducted per analysis over a range of  $5$  to  $50^\circ$  using a step size of  $0.495$  and scan rate of  $2.0^\circ \text{ min}^{-1}$ .

#### 2.4.1.2. – Rietveld Refinement Method

The Rietveld method is the computational analysis of an experimentally acquired X-ray diffraction pattern to obtain structural properties of the sample, including unit cell dimensions and site occupancies [237]. An algorithm was used to map a calculated diffraction pattern onto the experimentally acquired diffraction pattern *via* a least-squares method. A number of instrumental and powder parameters are accounted for, including peak width, intensity and shape (using a pseudo-Voigt function, Lorentzian factors, and Gaussian factors), background parameters and lattice parameters. These parameters help fit the calculated data profile,  $y(\text{calc})$ , onto the observed data profile,  $y(\text{obs})$ , through an overall scale factor,  $c$ , modelled through a difference function,  $M$ , described in Equation 2.4. Where  $i$  is the  $i^{\text{th}}$  atom and  $W_i$  is the statistical weighting factor. The iterative nature of the Rietveld method aids the convergence of the  $y(\text{obs})$  and  $y(\text{calc})$  data, thus the difference function should reduce to a minimum. In order to measure the convergence and accuracy of the fit, a weighted profile factor ( $R_{wp}$ ), and expected factor ( $R_{exp}$ ) are used to form the goodness of fit value ( $\chi^2$ ) (Equations 2.5 to 2.7 below). Once these values have reached an iterative minimum, they can be used to evaluate the fit before acquiring the cell dimensions, atomic position, and site occupancies [236].

$$M = \sum_i W_i \left[ y_i(\text{obs}) - \frac{1}{c} y(\text{calc}) \right]^2 \quad \text{Equation 2.4.}$$

$$R_{wp} = \sqrt{\frac{\sum_i W_i \left[ y_i(\text{obs}) - \frac{1}{c} y(\text{calc}) \right]^2}{\sum_i W_i (y_i(\text{obs}))^2}} \quad \text{Equation 2.5.}$$

$$R_{exp} = \sqrt{\frac{N-P}{\sum_i W_i (y_i(obs))^2}} \quad \text{Equation 2.6.}$$

$$\chi^2 = \left[ \frac{R_{wp}}{R_{exp}} \right]^2 \quad \text{Equation 2.7.}$$

In the above equations,  $N$  (number of data points) should greatly exceed  $P$  (number of parameters), indicating that  $\chi^2$  was closely related to  $M$ , with  $R_{wp}$  and  $R_{exp}$  being approximately equal to each other. Good fits have a low  $\chi^2$  value (due to the low difference factor of  $M$ ) and small R-factors [238]. The Rietveld analysis in this thesis was done using the GSAS-II program to refine X-ray diffraction patterns using the least-squares approach to attain lattice parameters and site occupation information [239]. A general procedure was followed to ensure consistency in the results: refinement of (i) the background polynomial, (ii) the unit cell, (iii) the sample displacement / zero parameter, (iv) profile parameters, and (v) the atomic phase parameters.

#### 2.4.1.3. – Operando X-ray Diffraction

In order to observe the changes in phase over the charging cycle, *operando* half-cells with a lithium anode and an NMC-811 cathode were constructed in an argon-filled glove box. The cathode slurry was synthesised by mixing 90% NMC-811 active mass, 5% carbon black and 5% PVDF powders mass percentage in a pestle and mortar before adding approximately 0.2 mL N-methyl-2-Pyrrolidone (NMP) and mixing in a Thinky mixer using the standard coin cell slurry procedure described below in Section 2.4.3.1. This slurry was then cast onto aluminium foil and dried in a vacuum oven before 15 mm discs were punched using a swing arm clicker press. The *operando* cells were constructed by Dr Laurence Middlemiss with a Whatman glass fibre separator between the NMC-811 cathode and lithium metal anode, soaked in a 1 M lithium hexafluorophosphate (LiPF<sub>6</sub>) in ethylene carbonate (EC) and ethylmethyl carbonate (EMC) 3:7 v/v + 2% vinyl carbonate (VC) electrolyte. These were encased in stainless steel 2032 coin cell cases with a Kapton/polyimide window, seen in Figure 2.5.a).

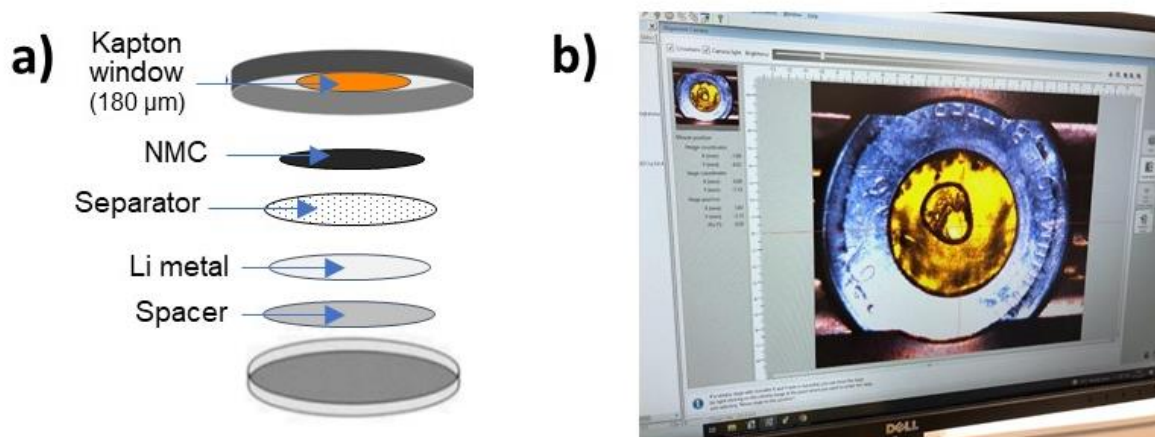


**Figure 2.0.6:** (a) The exploded schematic of the construction of the coin cell, and (b) An image of the Kapton window half-cell during *operando* XRD.

The *operando* coin cell cycling procedure involved cycling the coin cell between 2.0 V and 4.3 V at a rate of C/20 (i.e. at a current that would fully (dis)charge the cell to its theoretical capacity) using a Maccor battery cycler. A PANalytical Empyrean with a silver source ( $\text{Ag-K}\alpha = 0.56 \text{ \AA}$ ) was used to conduct the X-ray diffraction over a range of  $5\text{-}35^\circ$  and step size of 0.01, with measurements taken every 0.1 V, seen in Figure 2.5.b).  $\mu\text{m}$

#### 2.4.1.4. – High Temperature X-ray Diffraction

Powder X-ray diffraction was also conducted at high temperature using an Anton Parr BTS-500 stage and PANalytical X'Pert<sup>3</sup> with high temperature capabilities. The BTS-500 uses an electric heater and a nickel stage to heat the powder sample up to a maximum temperature of  $500 \text{ }^\circ\text{C}$ , with Kapton windows surrounding the stage, which are X-ray transparent. Analytical experiments were conducted using NMC-811(OH)<sub>2</sub> alone, and NMC-811(OH)<sub>2</sub> mixed with 3 mol% excess of lithium salt (either lithium hydroxide or lithium peroxide), lithiation procedure described in Section 2.3.2. being employed. The sample was heated at a rate of  $5 \text{ }^\circ\text{C min}^{-1}$ , with scans completed at room temperature and  $100\text{-}500 \text{ }^\circ\text{C}$  with  $100 \text{ }^\circ\text{C}$  intervals. The BTS-500 stage was compatible with the Rigaku 600 Miniflex (copper source,  $\text{Cu-K}\alpha = 1.541 \text{ \AA}$ ), where measurements were taken over a range of  $10\text{-}80^\circ$  with a step size of  $0.02^\circ$  and scan rate of  $1.5^\circ \text{ min}^{-1}$ .

The PANalytical X'Pert<sup>3</sup> has a copper source ( $\text{Cu-K}\alpha = 1.541 \text{ \AA}$ ) and can reach a higher temperature than the BTS-500, so was able to analyse the complete range of temperatures of the calcination procedure. Samples of NMC-811(OH)<sub>2</sub> were hand-milled with 3 mol% excess LiOH or Li<sub>2</sub>O<sub>2</sub> powder

and measured over a range of 10-80° with a step size of 0.02° at the following temperatures: 100 °C, 500 °C, 600 °C, 700 °C, 750 °C, 800 °C and 850 °C.

## 2.4.2. – Electron Microscopy

### 2.4.2.1. – Scanning Electron Microscopy

One method of analysing the morphology and chemical composition of the bulk specimen was through the use of scanning electron microscopy (SEM). A beam of electrons are fired at a sample, focused on a particular point and depending on the penetration into the sample determines the nature of the scattered product, with secondary electrons being a low-energy scattered electron released near the surface of the sample, back-scattered electrons being high-energy scattered electrons released from up to a few micrometres within the sample, and characteristic X-rays being emitted from the bulk of the sample, all depicted in Figure 2.0.7.

The source of electrons originates from the thermionic release of electrons from a tungsten filament when exposed to high temperatures. These electrons are fired through an aperture through an evacuated chamber in what was colloquially known as an *electron gun*. This beam of electrons passes through ‘condenser’ and ‘objective’ lenses that focus the electron beam onto a point and inverse the image respectively, visualised in Figure 2.0.7. These lenses deflect the electron beam *via* electrostatic or electromagnetic repulsion, with the electrons having a force applied to them perpendicular to the direction of the motion band electric/ magnetic field. The resultant focal length and lens alignment can be adjusted through sample and lens positioning to account for astigmatism and image focus [240], [241].

As the electron beam was being refined, scan coils are utilised to divert the beam across an area of the sample using a cathode ray tube, which scans a rectangular area divided up into an array of square units. Magnification can be calculated by comparing the relative size of the raster area on the sample as it was displayed on the display screen, with a 1 µm x 1 µm sample-raster area being displayed on a 10 mm x 10 mm display screen having a magnification of 10,000x [240], [241].

Backscattered electrons are the result of the elastic scattering of the primary electrons throughout the sample, with the absence of energy loss from the collisions allowing the electrons to penetrate

further into the sample, with the penetration depth depending on the atomic number of the sample, with a heavier atom having a shorter penetration depth. For example, the mean free path of carbon,  $Z = 6$ , was 150 nm; and mean free path of gold,  $Z = 79$ , having a penetration of 5 nm. Secondary electrons are generated from a sample *via* inelastic scattering of a primary sample at the surface of the sample, resulting in energy loss of the primary energy *via* heat transfer to the sample. This results in a short mean free path in the order of  $10^{-9}$  to  $10^{-10}$  m into the sample, hence secondary electron analysis is most commonly used to analyse surface characteristics and topography/ particle morphology [240], [241].

These backscattered and secondary electrons are detected using the Everhart-Thornley scintillator-photomultiplier system that fluoresces upon contact. The phosphorous-based detector emits a light that was transmitted to a photomultiplier, which converts it into pulses of electrons that are relayed onto a display screen, with each portion of the raster array correlating to a pixel. The low energy of secondary electrons can inhibit their ability to cause fluorescence of the scintillator. An aluminium foil coating was applied to the scintillator with a bias voltage across it that causes the secondary electrons to accelerate, increasing their energy such that they overcome the minimum energy needed to scintillate and generate a signal [240], [241].

The practical application of SEM with respect to this project involves preparing a powdered sample onto an adhesive carbon tab stuck to an aluminium stage, which was then sputter-coated with gold for 20 seconds in a vacuum-sealed chamber. The use of carbon and gold both aid the conduction of electrons in the sample, with the gold having the additional benefit of protecting it from damage caused by the electron beam. SEM analysis was conducted on an FEI Inspect F and Inspect F50 microscope. The acceleration voltage (energy) applied to the sample ranged from 5-15 kV to moderate the energy depending on the conductivity and stability of the sample under observation, with a beam spot size of 3.0-4.

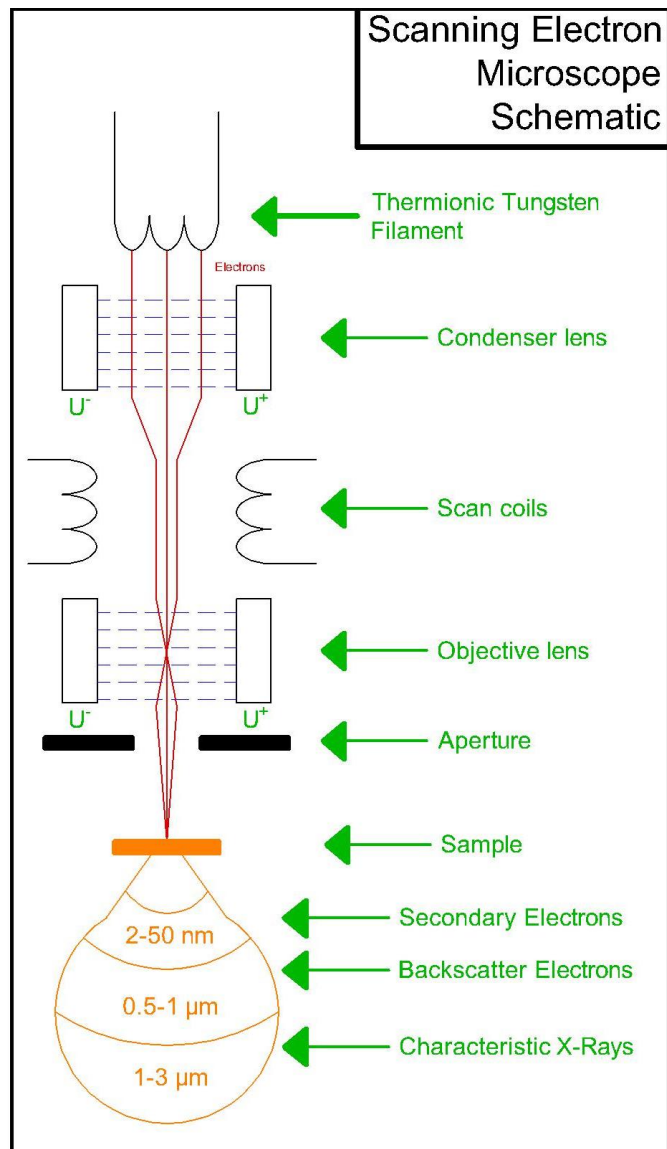


**Figure 2.0.7:** A schematic of a scanning electron microscope, depicting the formation, refinement, and impact of the electron beam onto the sample, and the resultant electrons and photons that result from the interactions.

#### 2.4.2.2. – Particle Size Analysis

Analysis of the primary and secondary particle sizes were measured using ImageJ software that allowed the identification of these particles and sizing them against a scale bar [242]. SEM images of secondary particle populations were loaded and saturated such that they became a two-coloured image, allowing the identification of particles. Once all particles were sized using the relative size of particles relative to a calibrated scale bar, a particle size distribution could be established.

### 2.4.2.3. – Energy Dispersive Spectroscopy (EDS)

Energy dispersive spectroscopy (EDS) harvests the characteristic X-rays released from the SEM sample to provide elemental composition information related to the sample. The accelerated voltage (incident energy) of the incident electrons needs to be sufficiently high to generate enough characteristic X-rays counts to get a quantification of elemental composition. This was selected to be 15 kV, as this was the minimum voltage needed for EDS analysis and limited the damage to the sample. EDS analysis can be done for a single point or for a two-dimensional raster ‘mapping’ of the sample, both of which are employable within the FEI Inspect F50 and coupled with Oxford Instruments Aztec program for data collection and analysis.

The release of characteristic X-rays from the sample occurs at a variety of wavelengths and energies depending on the atomic weight of the sample and which electron was excited (i.e.  $K_{\alpha}$ ,  $K_{\beta}$ ,  $L_{\alpha}$ ,  $L_{\beta}$  etc., as described in Section 2.4.1.1.). The X-rays collide with a detector consisting of a silicon semiconductor, and the energy of the incident X-ray photon excites a particular number of electrons across the 3.8 eV band gap. The resultant voltage from the formation of the electron-hole pairs will induce a current pulse, which processes the magnitude of the current into one X-ray energy category, which forms a profile based on the number of counts and hence can quantify the proportion of elements within a system. As well as developing a quantification of the elemental X-ray signals, the two-dimensional rasterization of the sample allows the visualisation and projection of this quantification onto the SEM image, giving a spatial aspect to the elemental distribution and compositional data.

The difficulty encountered with EDS analysis was the need to keep the detector crystal at 77 K, which requires a significant amount of cooling. Additionally, the energy resolution is poor, resulting in wide peaks which can obscure peaks with similar energies. There was also electronic background noise on the profile, which can not only hide the presence of peaks, but also impact the accuracy of the quantification of elemental composition, which was accounted for in the SEM-EDS analysis in this work.

### 2.4.3. – Electrochemical Testing

#### 2.4.3.1. – Cathode Slurry Synthesis and Coin Cell Manufacture

Electrochemical testing conducted in this thesis used 2032 stainless-steel coin cells, manufactured as half-cells with a synthesised cathode disc and lithium metal chip anode counterpart. 2032 coin cells are 'button cells' that have a 20 mm diameter and 3.2 mm height and consist of a two-part metal casing that is 'crimped' together to form an air-tight seal to protect the sensitive chemicals from the atmosphere. The cathode disc was prepared through the casting of a slurry, which comprised of 90 wt% active material ( $\text{LiNi}_{0.8}\text{Mn}_{0.1}\text{Co}_{0.1}\text{O}_2$ ), 5 wt% polyvinylidene fluoride (PVDF) binding agent and 5 wt% carbon black conductive agent. 150 mg of these materials (with a 125 mg: 7.5 mg: 7.5 mg ratio) were weighed out inside an argon-filled glove box and hand milled in a pestle and mortar for 10 minutes. The resultant powder mix was transferred to a Thinky mixer pot, where approximately 0.2 mL of N-methyl-2-Pyrrolidone (NMP) was added dropwise until the powder was fully mixed and the resultant slurry was glossy. The slurry was then transferred to a Thinky mixer, where it undergoes a mixing regime of 5 minutes at 2000 rpm, followed continuously by a defoaming stage of 30 seconds at 2200 rpm, which was repeated once. The slurry was cast onto carbon coated aluminium foil on a vacuum plate drawdown table. A doctor blade set to 15  $\mu\text{m}$  thickness was used to cast the slurry evenly across the drawdown table. An excess of NMP often led to either the partial or complete gelation of the mixture, producing an uneven, non-uniform slurry, which was undesirable. The cast slurry was then dried at 100 °C for approximately 2 hours, then stored in a vacuum oven overnight at 80 °C for further drying. The dried slurry was cut into 10 mm cathode discs with a swinging-arm hydraulic cutter, with the cathodes stored in an argon-filled glove box for storage.

In the manufacturing of the coin cells, 2032 coin cells were assembled in an argon-filled glove box. A stainless-steel negative casing was used as the base, with a stainless-steel conical spring and spacer added to provide a pressure within the cell to ensure uniform contact between the cathode, separator, and anode. The lithium metal anode disc was placed atop of the spacer, with the 16 mm diameter Whatman glass microfibre separator wetted with 100  $\mu\text{l}$  of electrolyte of 1 M of  $\text{LiPF}_6$  in ethylene carbonate and dimethyl carbonate (3: 7 w/w) with 2% vinyl carbonate (VC). The cathode disc was placed in the centre of the wetted separator, with the active mass facing the separator, and enclosed with the stainless-steel positive casing. The coin cell was then crimped using a hydraulic

press to seal the coin cell, which was then stored in a plastic zip-lock bag to prevent self-discharge prior to the electrochemical tests.

The post-mortem analysis of the 2032 coin cells involved de-crimping of cycled cells in an argon-filled glove box. Once the seal had been broken, each component was sorted, with the cathode disc being recovered and soaked in dimethyl carbonate to clean the cathode ahead of analysis, while the remaining components were removed from the glove box and quenched in ethanol and water until all lithium had reacted. The dimethyl carbonate was drained from the cathode and removed with the waste coin cell components, with the wetted coin cell being left to dry under vacuum in the antechamber overnight.

#### 2.4.3.2. – Galvanostatic Cycling with Potential Limitation

Two common indexes for the success of a cathode active material are their specific capacity and capacity retention. One common method of measuring the specific capacity was through Galvanostatic cycling with potential limitation (GCPL), which involves charging and discharging (cycling) a cell at a constant current until maximum and minimum voltage limits are reached, with the current and voltage profiles indicated in Figure 2.0.8.

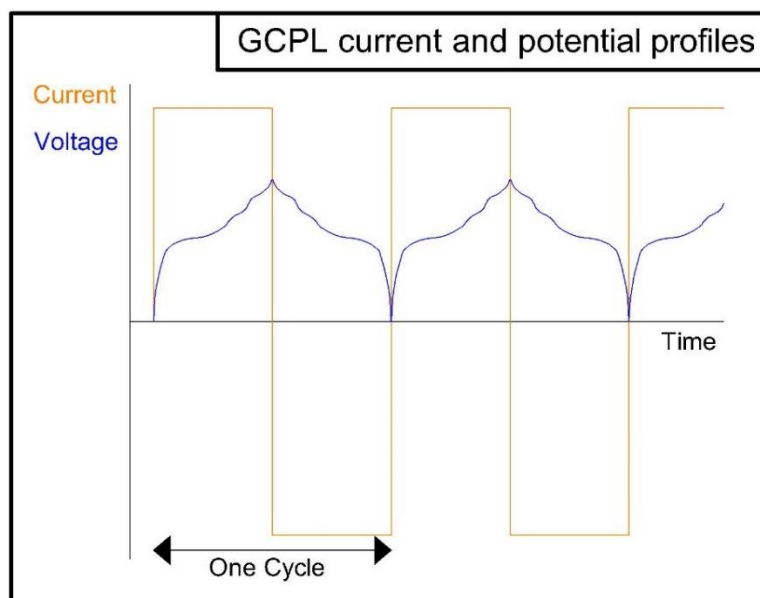


**Figure 2.0.8:** The current and voltage profiles for GCPL cycling. Current was constant during cycling, whereas voltage increases/decreases to a maximum/ minimum.

The specific capacity defined in Equation 1.1 describes capacity the cathode active material can store per mass, hence the units of coulombs per gram ( $C\ g^{-1}$ ) or amp-hours per gram ( $Ah\ g^{-1}$ ). This can be used to determine the current to apply to the cells as the current applied to the cell needs to be normalised to the active mass of the cathode disc to ensure cells being compared are put under consistent electrochemical strain. This is done by calculating ‘C-rates’, which determines how long a current was applied to the cell during cycling (in hours), for a theoretically fully charged /discharged cell, hence determining a normalised current for each coin cell. For example, a 1C current fully charges/ discharges a cell over a period of 1 hour, and C/2 fully charges/ discharges the cell over 2 hours, and so on. The practical specific capacity can be calculated using the applied current along with the time taken to charge/discharge the cell and the active mass of the material, as seen in Equation 2.8 below.

$$\text{Practical Specific Capacity} = \frac{\text{Current} \cdot \text{Time}}{\text{Active Mass}} \quad \text{Equation 2.8.}$$

A standard protocol was established for GCPL experiments that involved two solid electrolyte interphase (SEI) formation cycles at a current of C/20 followed by  $x$  number of cycles (most typically 100 cycles) at a current of C/2. A rest period was included for 2 hours prior to the first charging cycle to allow the cell to reach an equilibrium (hence the charge profile did not start at  $t = 0$  in Figure 2.0.8). The potential limits selected were 3.0–4.2 V and 3.0–4.3 V, with the two limits assessing the impact of the  $c$ -axis contraction at  $\sim 4.2$  V described in Section 1.2.1. These tests were either completed at room temperature, or in a temperature-controlled chamber at 20 °C. Similarly, a rate capability test was deployed to analyse the ability of different materials to cope with increasing cycling rates. This involved cycling a coin cell at C/20 for 5 cycles while the SEI layer was formed, then 5 cycles were completed at the following C-rates: C/10, C/5, C/2, 1C, 2C, 5C and 10C, before a final 5 cycles at C/20 were completed. The voltage window for this test was 3.0 – 4.3 V.

#### 2.4.3.3. – Electrochemical Impedance Spectroscopy

One method of characterising degradation mechanisms that can occur within a cycling cell was through the non-destructive analysis of electrochemical impedance spectroscopy (EIS). When considering Ohm’s law and resistance under an alternating current, practical applications result in inductive and capacitive effects on the sinusoidal waveform and a phase shift,  $\phi$ , desynchronising the voltage ( $E$ ) and current ( $I$ ) profiles. Impedance ‘ $Z$ ’ should therefore be used in place of resistance, which was defined through Ohm’s law in Equation 2.9, where  $\omega$  was the radial frequency. This gives

rise to the Lissajous Figure, which is an oval formed from the I-E plot of Equation 2.10 and can therefore introduce Euler's relationship into the expression, with Equations 2.9 and 2.10 respectively.

$$Z = \frac{E_t}{I_t} = \frac{E_0 \sin(\omega t)}{I_0 \sin(\omega t + \varphi)} \quad \text{Equation 2.9.}$$

$$\exp(j\varphi) = \cos(\varphi) + j \sin(\varphi) \quad \text{Equation 2.10.}$$

$$Z(\omega) = Z_0 \exp(j\varphi) = Z_0[\cos(\varphi) + j \sin(\varphi)] \quad \text{Equation 2.11.}$$

Equation 2.11 gives an expression for Z that introduces complex numbers to the impedance interpretation, with a real and imaginary part. Plotting the real and imaginary components against one another (on the x-axis and y-axis respectively) gives rise to a Nyquist plot depicted in Figure 2.0.9, with each semicircle representing a different form of impedance within the cell, and eludes to a particular form of degradation [243], [244].

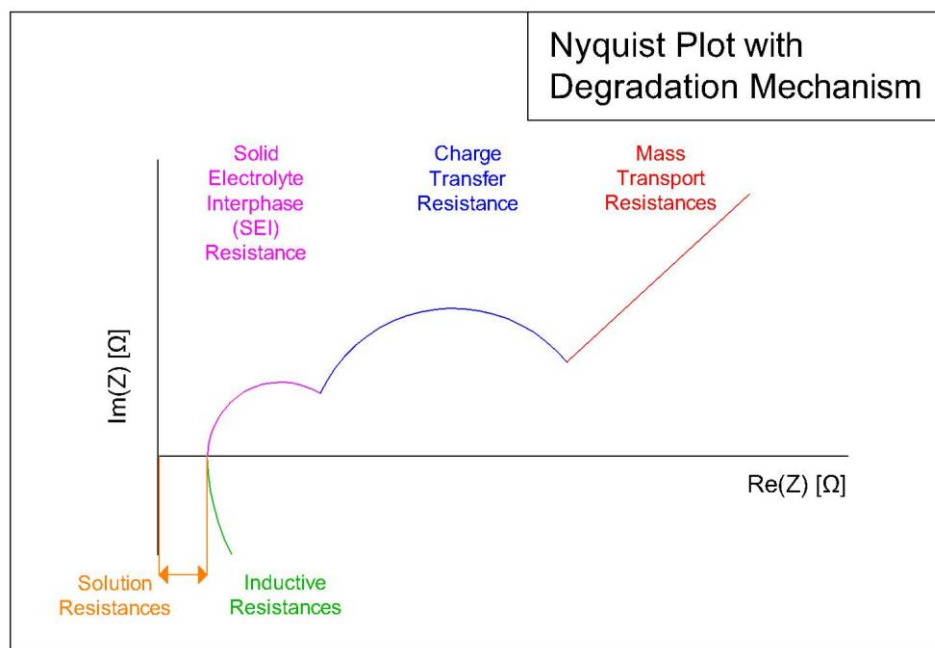


**Figure 2.0.9:** An example Nyquist plot, with examples of characteristic cell features and degradation mechanisms highlighted.

This plot can then be fitted to an equivalent electrical circuit with each electrical component describing the influence of impedance for each semicircle of the plot. There are five common

electrical components used, namely a resistor, inductor, capacitor, and a constant phase element (CPE) and the Warburg element. The Warburg element is used to establish the impedances related to the diffusivity of the bulk material. As with conventional electrical circuit calculations, where placed in series, the components are summed (*i.e.*  $Z_1 + Z_2 + Z_3 = Z_T$ ), whereas where components are in parallel, the inverse of the components are summed (*i.e.*  $Z_1^{-1} + Z_2^{-1} + Z_3^{-1} = Z_T^{-1}$ ). The semicircle features of a Nyquist plot typically consist of a resistor and capacitor/ CPE unit in parallel to form a Randles cell [243], [244], [245].

From an experimental perspective, impedance data can be collected by applying an AC signal over a wide range of frequencies, ranging from  $\mu\text{Hz}$  to MHz. Different impedance-sensitive elements of the cell applies the variation to the current and voltage sinusoidal curves, hence the development of the Lissajous figure and Nyquist plot. In the experiments conducted in this thesis, EIS procedures were carried out on a Biologic VMP-300 Potentiostat, with a frequency range of 100 mHz to 1 MHz. Cells were cycled at C/20 for two cycles followed by C/2 for 50 cycles, with EIS analysis occurring after cycle 0, 1, 5, 10, and every 5 cycles after that until cycle 50. The cycle was allowed to discharge to 3.0 V, followed by a 2-hour rest period before the EIS programme ran to allow the cell to come to equilibrium.

#### 2.4.3.4. – Galvanostatic Intermittent Titration Technique

Although the Warburg element described in EIS analysis can establish the diffusivity of the cathode material, a more accurate technique for calculating this was the Galvanostatic Intermittent Titration Technique (GITT). GITT is used to calculate the diffusion coefficients *in-situ* at various states of charge and involves the temporary charging of the cell at slow rate, known as ‘current pulses’ which increases the voltage to a certain potential, followed by a relaxation period with no current, where the potential plateaus to an equilibrium.

At a particular ‘initial’ voltage,  $E_{it}$ , a current pulse was applied, causing the voltage to increase instantaneously due to internal resistance (IR). After this, the voltage increases at an increasingly slower rate over the duration of this current pulse in order to maintain a constant concentration gradient as lithium ions deintercalate from the material. At the end of the pulse, the voltage achieved has a maximum voltage,  $E_t$ , and the current reduces to zero triggering a second IR drop before the relaxation period starts. During the relaxation period, lithium ions diffuse to reach a homogenous state at a potential less than  $E_t$  to a new equilibrium state,  $E_s$ , which becomes the new

$E_{it}$  for the next current pulse, as depicted in Figure 2.0.10 below. The reverse can be applied during the discharge phase of GITT experiments, with a negative current being applied causing a decrease in voltage to the corresponding  $E_t$  potential and the relaxation period causing a minor increase in potential to the homogenous  $E_s$  potential.

The potential drop during relaxation and the potential rise during the current pulse can be used to calculate chemical diffusivity at various states of charge. Using Fick's first law of diffusion, stating that the rate of diffusion is proportional to the concentration gradient with respect to the presence of lithium ions, the diffusion coefficient ( $D$ ) can be calculated using Equation 2.12 below.  $\tau$  represents the duration of the current pulse,  $n_{mol,B}$  represents the number of moles of the host material, ' $B$ ',  $V_{mol}$  is the volume occupied by one mole of the host material,  $\Delta E_s$  is the voltage change at steady state, and  $\Delta E_t$  was the total voltage change over the current pulse. ' $S$ ' is the electrode-electrolyte surface interface area, but due to inaccuracies in calculating this, the diffusion coefficient was commonly reported as 'diffusion per square-area' or ' $D s^2$ ' [246].

$$D = \frac{4}{\pi * \tau} \left( \frac{n_{mol,B} * V_M}{S} \right)^2 \left( \frac{\Delta E_s}{\Delta E_t} \right)^2 \quad \text{Equation 2.12.}$$

The GITT experiments conducted in this thesis are conducted over a voltage window of 3.0–4.5 V using a Biologic VMP-300 potentiostat. A 30-minute current pulse was applied at a C-rate of C/20, followed by a 2.5-hour relaxation period. Upon the upper cut-off voltage being achieved, a 3-hour relaxation period was undertaken prior to discharge.

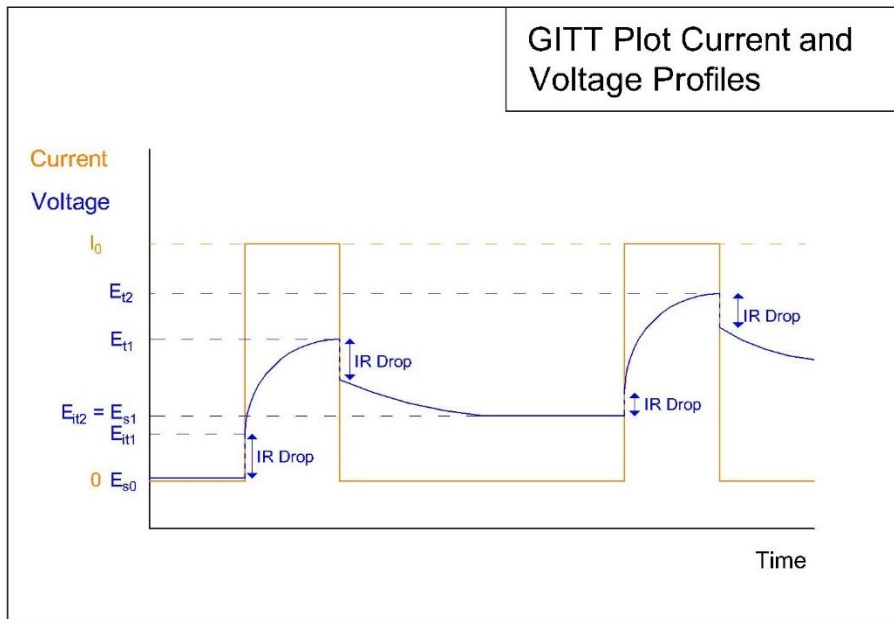


**Figure 2.0.10:** A GITT plot that demonstrates the current and voltage profiles over the course of 2 charging current pulses, with the gradual increase in potential observed.

#### 2.4.4. – Further Characterisation Techniques

##### 2.4.4.1. – Tap Density

In a bulk material, a material will occupy a volume consisting of voids between the particles. This ‘bulk density’ corresponds to a mass of material relative to the volume occupied by the randomly-coordinated particles. Disturbing this system can cause realignment of particles, with smaller particles occupying the voids and therefore reducing the voidage of the system and increasing the density of the sample. This is typically done *via* ‘taps’ on the container of material, coining the term ‘tap density’ for this disturbed system. If the original, bulk density volume for a mass of material was denoted  $V_o$ , and the tap density volume was denoted  $V_f$ , then a compression index can be determined through Equation 2.13.

$$\text{Compressability Index} = \frac{V_o - V_f}{V_o} * 100 \quad \text{Equation 2.13.}$$

Experimentally, the work in this thesis acquires this data using a Copley JV 200i Tap Density Tester, by measuring a particular mass of material into a measuring cylinder and recording the volume of

the material (bulk volume). The Copley JV 200i 'taps' the measuring cylinder by dropping it a short distance repeatedly. In these tests, the tapping protocol involved 1000 taps over a period of 5 minutes, with the tapped volume recorded after 1000, 3000 and 5000 taps until the volume plateaued.

#### 2.4.4.2. - Mechanical Testing

The mechanical strength of secondary particles is an indicator of the lifespan of the particles with electrochemical cycling due to the volumetric expansion and contraction exerting stresses on the secondary assembly that can be mimicked by mechanical testing *via* microindenter. NMC-811 samples were prepared by suspending the secondary particles in ethanol and drop casting them onto a silicon wafer, which was later mounted onto an SEM stub using superglue.

An Alemnis microindenter (Synton MDP, and Synton MDP with a diamond tip; Poisson's ratio of 0.07, Young's modulus of 1140 GPa) was mounted in an FEI Nova 450 SEM was used to apply a unidirectional load of  $0.1 \text{ mN s}^{-1}$  to the sample until fractured, when the tip was retracted. The SEM stub was mounted onto a translational stage, allowing the precise positioning of the microindenter above one secondary particle prior to indentation in order to ensure no neighbouring particles incurred direct contact. This procedure was conducted by Dr Laura Wheatcroft, with SEM imaging taken with a 5 kV electron beam, at an angle of  $70^\circ$  tilt to the indenter axis. Analysis involved the use of Alemnis AMMDA software, with each load curve needing a zero-correction at zero load, and a polynomial-fitted load drift correction. Indentation hardness was calculated by the load at the time of fracture per tip contact area [247].

### 3. Investigating oxygen-rich alternative calcination approaches for NMC-811 cathodes

The use of conventional conduction and convection-based heating during the calcination process of NMC cathode material synthesis is a lengthy process, with it taking up to 10-15 hours to complete [37], [88], [118], [167], excluding the cooling period and any intermediate grinding stages that be required. Microwave heating can provide more uniform heating, increase the rate of heating, and reduce the dwelling period of the material within the furnace, improving the throughput of the synthesis route [220]. Problems arise when considering the nickel-rich cathodes used in this work, where NMC-811 requires an oxygen-rich atmosphere during calcination to retain nickel in its trivalent oxidation state and promote the formation of the layered phase. An atmosphere rich enough in oxygen gas can form a plasma when exposed to microwaves, with the microwaves causing violent oscillations within the molecule, causing adjacent molecules to collide and increase the possibility of ionisation. This can lead to a significant increase in temperature above 1200 °C, which is above the temperature limit for the furnace and would cause a loss of lithium from the system in the form of Li<sub>2</sub>O [248], [249]. To overcome this, it is hypothesised that lithium peroxide can be utilised as a lithium source for the reaction, with it decomposing to form oxygen gas *via* Equation 3.1 below. This occurs at a low temperature of 280-400 °C, meaning Li<sub>2</sub>O<sub>2</sub> will thermally decompose at a lower temperature than the formation of the α-NaFeO<sub>2</sub> layered transition metal oxide phase at 650-850 °C, as discussed in Section 1.3.4 [104]. To minimise oxygen loss, samples calcined with lithium peroxide were placed in a closed crucible.



Here, optimisation of this procedure was investigated by studying the effect of lithium peroxide excess, temperature and duration of calcination and compared to benchmark samples prepared by conventional routes (a standard Li source, lithium hydroxide, in an oxygen-fed tube furnace).

#### 3.1. – The Ni<sub>0.8</sub>Mn<sub>0.1</sub>Co<sub>0.1</sub>(OH)<sub>2</sub> Precursor

Ni<sub>0.8</sub>Mn<sub>0.1</sub>Co<sub>0.1</sub>(OH)<sub>2</sub> was synthesised by Dr Nirmalesh Anthonisamy *via* a co-precipitation synthesis route in an Eppendorf BioFlo 320 stirred tank reactor with an optimised pH of 11.0 and temperature of 60 °C. The reaction was conducted over a total period of 41.5 hours, with a 13.5-hour addition time for the transition metal and ammonia solutions in a 1: 1.4 ratio followed by a 28-hour

‘maturation’ period. The resulting precipitant was washed and dried. XRD and SEM analysis was conducted on this sample prior to its use to optimise the calcination procedure in a microwave furnace. XRD analysis of the  $\text{Ni}_{0.8}\text{Mn}_{0.1}\text{Co}_{0.1}(\text{OH})_2$  precursor is shown in Figure 3.0.1, together with standard profiles from the Inorganic Crystal Structure Database (ICSD) for  $\text{Ni}(\text{OH})_2$  [250] and  $\text{Ni}_{0.6}\text{Mn}_{0.2}\text{Co}_{0.2}(\text{OH})_2$  [152]. An initial inspection confirms the layered brucite,  $\beta\text{-M}(\text{OH})_2$ , phase (Figure 3.0.1.a), with closer analysis of individual peaks revealing differences in the (001) and (102) peaks seen in Figure 3.0.1.b) and c).

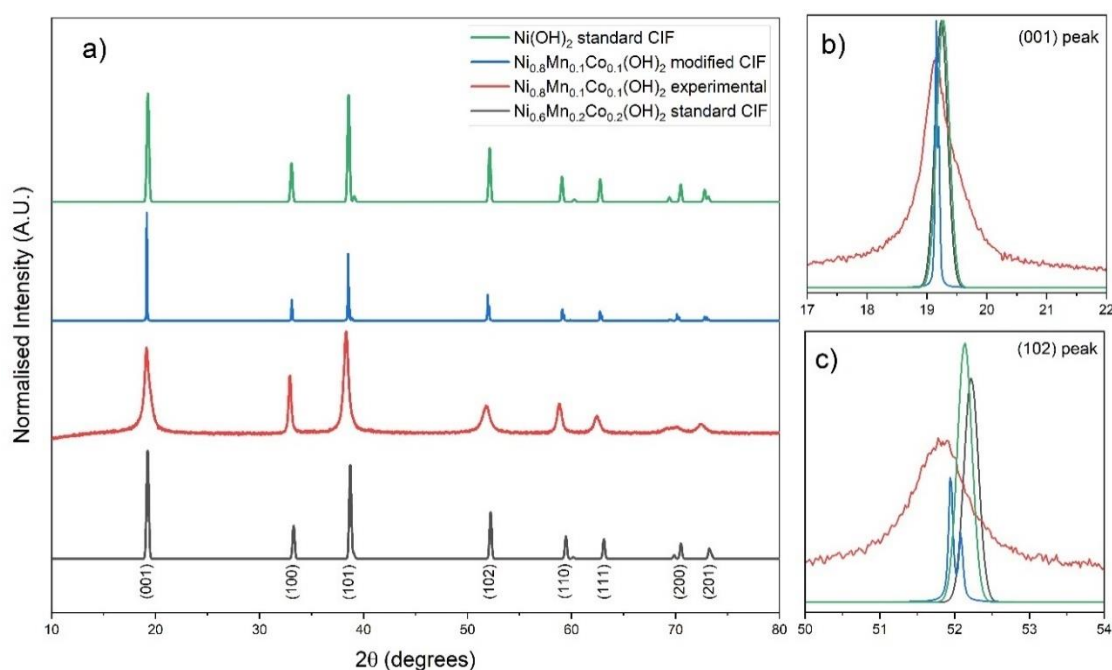


**Figure 3.0.1:** XRD profiles of experimentally acquired  $\text{Ni}_{0.8}\text{Mn}_{0.1}\text{Co}_{0.1}(\text{OH})_2$  (red), with ICSD standards of  $\text{Ni}(\text{OH})_2$  (green),  $\text{Ni}_{0.6}\text{Mn}_{0.2}\text{Co}_{0.2}(\text{OH})_2$  (black), and a manufactured CIF file of  $\text{Ni}_{0.8}\text{Mn}_{0.1}\text{Co}_{0.1}(\text{OH})_2$  (red). **a)** depicts the full range 10-80° XRD profile, with **b)** showing a close-up of the (001) peak between 17-22°, and **c)** showing the (102) peak at 50-54°.

Published crystallographic data exists for  $\text{Ni}(\text{OH})_2$  and  $\text{Ni}_{0.6}\text{Mn}_{0.2}\text{Co}_{0.2}(\text{OH})_2$  [152], [250]. Ying *et al.* have applied the  $\text{Ni}(\text{OH})_2$  model to experimentally-acquired  $\text{Ni}_{0.8}\text{Mn}_{0.1}\text{Co}_{0.1}(\text{OH})_2$  *via* Rietveld analysis [251]. Here, the published lattice parameters for  $\text{Ni}_{0.8}\text{Mn}_{0.1}\text{Co}_{0.1}(\text{OH})_2$  were used to modify the CIF file for  $\text{Ni}_{0.6}\text{Mn}_{0.2}\text{Co}_{0.2}(\text{OH})_2$  to better model and analyse the crystallographic data obtained in this thesis for  $\text{Ni}_{0.8}\text{Mn}_{0.1}\text{Co}_{0.1}(\text{OH})_2$ . The modified  $\text{Ni}_{0.8}\text{Mn}_{0.1}\text{Co}_{0.1}(\text{OH})_2$  CIF file is included in Figure 3.0.1 and shows that the correct  $\beta\text{-M}(\text{OH})_2$  phase is formed. Individual peak analysis reveals a smaller difference between angles for characteristic peaks, listed in Table 3.0.1, suggesting the modified CIF was a better approximation of lattice parameters. Peak splitting (likely associated with the  $\text{K}\alpha_1$  and

$K_{\alpha 2}$  peaks) was also observed for the modified  $\text{Ni}_{0.8}\text{Mn}_{0.1}\text{Co}_{0.1}(\text{OH})_2$  CIF file, with the angles recorded in Table 3.0.1 aligning to the largest intensity of the  $K_{\alpha 1}$  peak.

**Table 3.0.1:** A table of  $2\theta$  Bragg peaks for the  $\beta\text{-M}(\text{OH})_2$  phase and corresponding angles for each of the analysed  $\text{Ni}_{0.8}\text{Mn}_{0.1}\text{Co}_{0.1}(\text{OH})_2$  phases, with the difference to the experimental value in brackets.

	(001)	(100)	(101)	(102)	(110)	(111)	(200)	(201)
$\text{Ni}(\text{OH})_2$ CIF file $2\theta$ angles	19.27 (+0.15)	33.08 (+0.14)	38.56 (+0.24)	52.14 (+0.36)	59.08 (+0.28)	62.76 (+0.30)	70.50 (+0.44)	72.80 (+0.46)
$\text{Ni}_{0.6}\text{Mn}_{0.2}\text{Co}_{0.2}(\text{OH})_2$ CIF file $2\theta$ angles	19.24 (+0.12)	33.28 (+0.34)	38.72 (+0.40)	52.22 (+0.44)	59.46 (+0.66)	63.12 (+0.66)	70.52 (+0.46)	73.26 (+0.92)
$\text{Ni}_{0.8}\text{Mn}_{0.1}\text{Co}_{0.1}(\text{OH})_2$ CIF file $2\theta$ angles	19.16 (+0.04)	33.14 (+0.20)	38.52 (+0.20)	51.94 (+0.16)	59.11 (+0.31)	62.74 (+0.28)	70.14 (+0.08)	72.80 (+0.46)
$\text{Ni}_{0.8}\text{Mn}_{0.1}\text{Co}_{0.1}(\text{OH})_2$ experimental sample $2\theta$ angles	19.12 (-)	32.94 (-)	38.32 (-)	51.78 (-)	58.80 (-)	62.46 (-)	70.06 (-)	72.34 (-)

Rietveld refinement of experimentally-acquired  $\text{Ni}_{0.8}\text{Mn}_{0.1}\text{Co}_{0.1}(\text{OH})_2$  was conducted using the GSAS-II program against CIF files of  $\text{Ni}(\text{OH})_2$  acquired from ICSD,  $\text{Ni}_{0.8}\text{Mn}_{0.1}\text{Co}_{0.1}(\text{OH})_2$  acquired from ICSD, and the modified  $\text{Ni}_{0.8}\text{Mn}_{0.1}\text{Co}_{0.1}(\text{OH})_2$  CIF file, with the lattice parameters summarised in Table 3.0.2 [239]. The results indicate better fits for the  $\text{Ni}(\text{OH})_2$  and  $\text{Ni}_{0.8}\text{Mn}_{0.1}\text{Co}_{0.1}(\text{OH})_2$  models, due to the larger lattice parameters ( $a \approx 3.151 \text{ \AA}$ ,  $c \approx 4.653 \text{ \AA}$ ) and unit cell volumes ( $40.00\text{-}40.44 \text{ \AA}^3$ ). However, due to the increased  $\chi^2$  values of all results of 33.163-65.286, these results need more accurate crystallographic data from a synchrotron source to attain more accurate lattice parameters and generate a reliable CIF file for  $\text{Ni}_{0.8}\text{Mn}_{0.1}\text{Co}_{0.1}(\text{OH})_2$ .

**Table 3.0.2:** A table of lattice and model fitting parameters from the Rietveld refinement of experimentally acquired  $\text{Ni}_{0.8}\text{Mn}_{0.1}\text{Co}_{0.1}(\text{OH})_2$  compared to three different CIF files. Estimated standard deviations are included in brackets, where refined.

	Lattice parameter $a = b \text{ (\AA)}$	Lattice parameter $c \text{ (\AA)}$	Unit Cell Volume ( $\text{\AA}^3$ )	$\chi^2$ value
$\text{Ni}(\text{OH})_2$ CIF file	3.152(0)	4.653(7)	40.0(4)	33.163
$\text{Ni}_{0.6}\text{Mn}_{0.2}\text{Co}_{0.2}(\text{OH})_2$ CIF file	3.149(9)	4.652(1)	39.9(8)	65.286
$\text{Ni}_{0.8}\text{Mn}_{0.1}\text{Co}_{0.1}(\text{OH})_2$ CIF file	3.152(0)	4.654(2)	40.0(6)	38.369

The  $\text{Ni}_{0.8}\text{Mn}_{0.1}\text{Co}_{0.1}(\text{OH})_2$  precursor is made up of uniform, quasi-spherical secondary assemblies, consisting of randomly-oriented nanoplates, evidenced by SEM analysis in Figure 3.0.2 a)-c). Secondary particle size analysis using ImageJ is displayed as a histogram in Figure 3.0.3, and shows a modal average particle size of 8.5-9.0  $\mu\text{m}$ , which is similar to the desired diameter of 10  $\mu\text{m}$  [118], [157], [252]. The size of the primary particles was also analysed to find an average nanoplate diameter of 0.979  $\mu\text{m}$ .

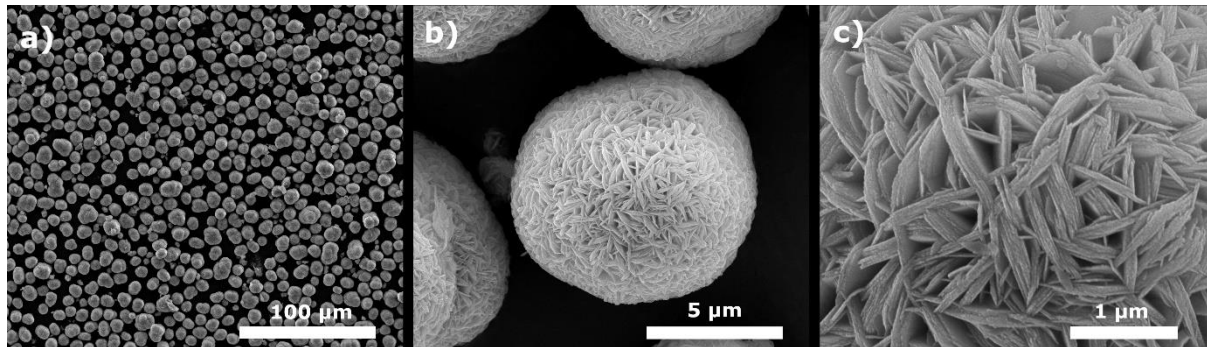


**Figure 3.0.2:** SEM images of  $\text{Ni}_{0.8}\text{Mn}_{0.1}\text{Co}_{0.1}(\text{OH})_2$  precursor at 1000x (a), 20,000x (b), and 120,000x (c) magnification.

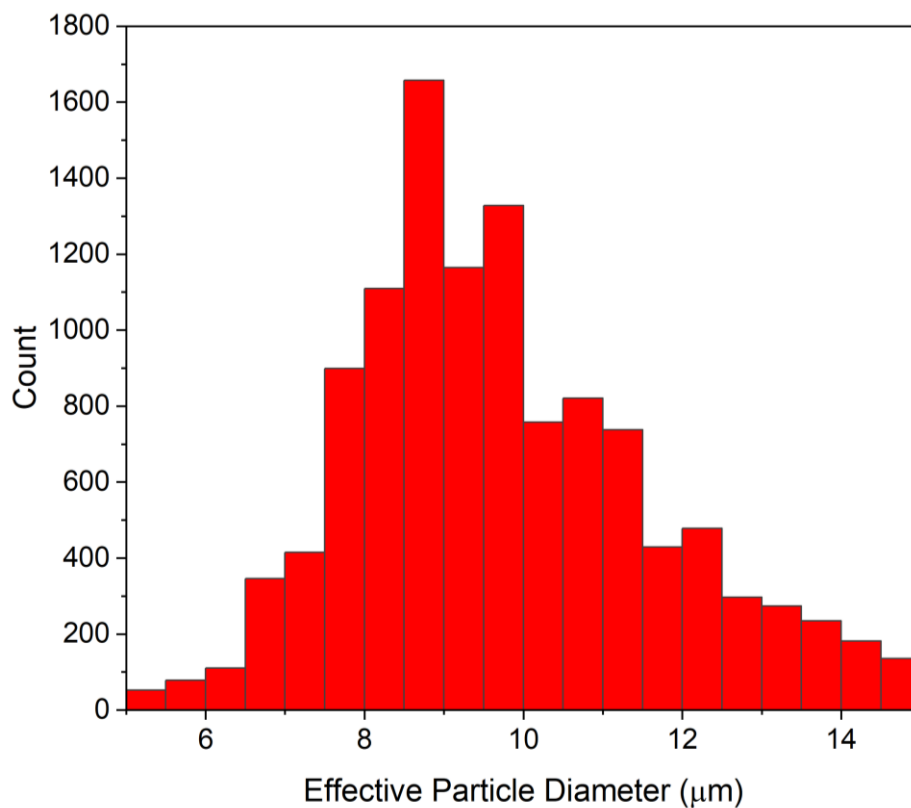


**Figure 3.0.3:** A histogram depicting the particle size distribution from the  $\text{Ni}_{0.8}\text{Mn}_{0.1}\text{Co}_{0.1}(\text{OH})_2$  sample, from a 200x SEM image with a population of 11,563 particles with at least 50% circularity.

### 3.2. – Lithiation of the $\text{Ni}_{0.8}\text{Mn}_{0.1}\text{Co}_{0.1}(\text{OH})_2$ Precursor

Prior to calcination, a lithium source is added to the  $\text{Ni}_{0.8}\text{Mn}_{0.1}\text{Co}_{0.1}(\text{OH})_2$  precursor, which involves the mixing of a lithium salt, typically lithium hydroxide (LiOH), and in this thesis lithium peroxide ( $\text{Li}_2\text{O}_2$ ). A small molar excess is added to account for the possible lithium loss at high temperature. Section 1.3.4. discussed the molar excess of LiOH was typically 3% and was by milled with  $\text{Ni}_{0.8}\text{Mn}_{0.1}\text{Co}_{0.1}(\text{OH})_2$  precursor in a pestle and mortar until homogenous. Here, the lithiation of  $\text{Ni}_{0.8}\text{Mn}_{0.1}\text{Co}_{0.1}(\text{OH})_2$  with  $\text{Li}_2\text{O}_2$  was examined as a potential dual Li and oxygen source. Lithium excess was investigated where the  $\text{Ni}_{0.8}\text{Mn}_{0.1}\text{Co}_{0.1}(\text{OH})_2$  precursor was mixed with 1, 3, 5 and 7% molar excess lithium peroxide before calcining in a microwave furnace at 750 °C for 5 hours.

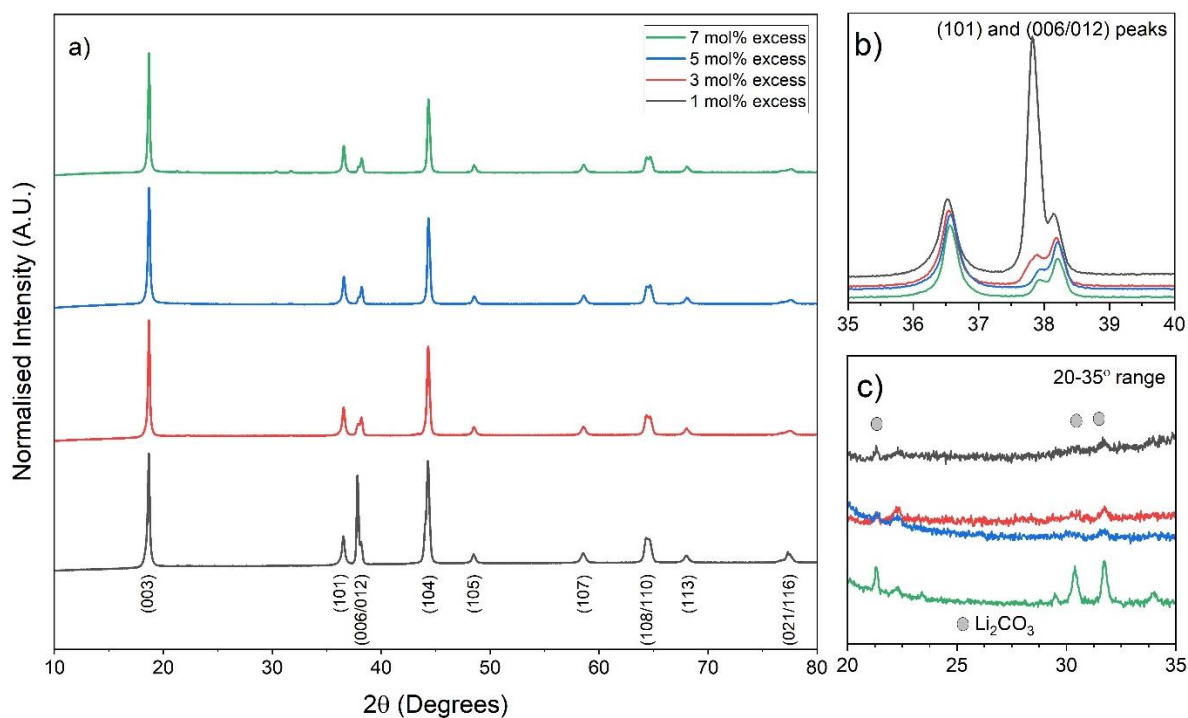


**Figure 3.0.4:** (a) XRD profiles of  $\text{LiNi}_{0.8}\text{Mn}_{0.1}\text{Co}_{0.1}\text{O}_2$  lithiated with 1, 3, 5 and 7 mol% excess  $\text{Li}_2\text{O}_2$  and calcined in a microwave furnace (750 °C for 5 hours); (b) an enlargement of the (101) and (006)/(012) doublet; (c) evidence of residual  $\text{Li}_2\text{CO}_3$  exhibited by the peaks in the 20-35°  $2\theta$  range, with peaks labelled with a grey circle.

Inspection of the XRD data obtained for all samples are displayed in Figure 3.0.4.a indicates the calcination reactions yielded the layered, hexagonal  $\alpha\text{-NaFeO}_2$  phase expected for  $\text{LiNi}_{0.8}\text{Mn}_{0.1}\text{Co}_{0.1}\text{O}_2$ , irrespective of the excess of  $\text{Li}_2\text{O}_2$  present. A greater (006) peak intensity is observed for the 1 mol% excess  $\text{Li}_2\text{O}_2$  sample (Figure 3.0.4.b). Combined with the low-angle shoulder on the (104) and (108) peaks, this could be indicative of the presence of a rocksalt impurity phase in

this sample. This coincides with the reduced presence of additional lithium phases in the 1 mol% sample (Figure 3.0.4.c). The 7 mol% excess sample displays the largest degree of additional lithium side phases, which aligns with  $\text{Li}_2\text{CO}_3$  peaks present at  $\approx 21^\circ$ ,  $\approx 30^\circ$  and  $\approx 32^\circ$   $2\theta$ , with a minor disparity in  $2\theta$  angle attributed to sample preparation. These peaks are not as intense in the 1, 3 and 5 mol% samples. Figure 3.0.5 identifies the additional lithium phase as lithium carbonate ( $\text{Li}_2\text{CO}_3$ ) by comparing the peaks between 20 and  $35^\circ$   $2\theta$  to ICSD standards for  $\text{Li}_2\text{CO}_3$ ,  $\text{LiOH}$  and  $\text{Li}_2\text{O}$  [253], [254], [255]. On the basis of the XRD results, the 3 mol% excess  $\text{Li}_2\text{O}_2$  was selected for further study.

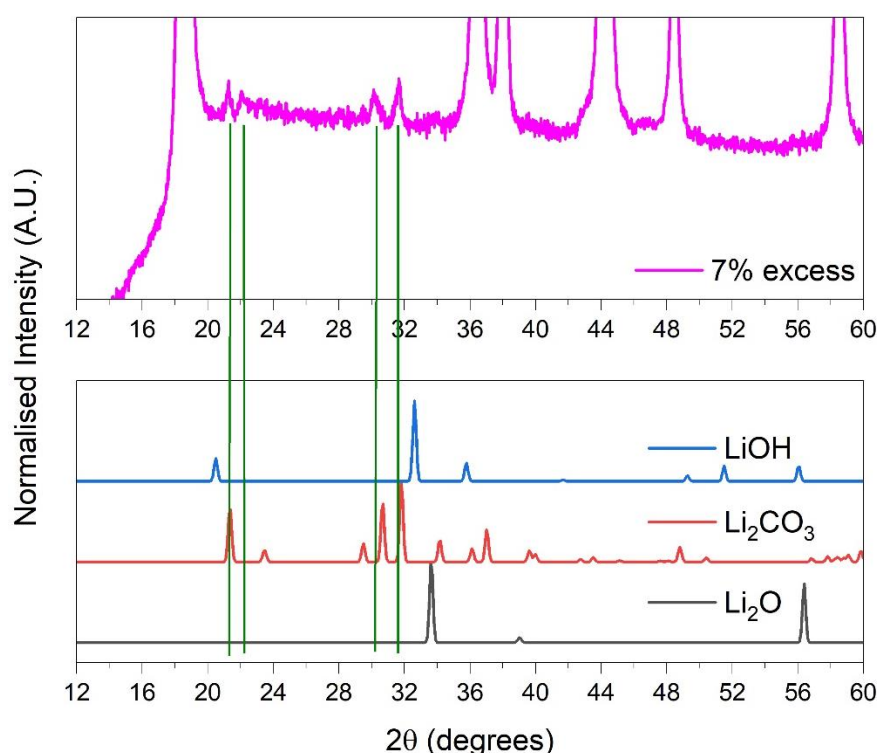


**Figure 3.0.5:** XRD profile of  $\text{LiNi}_{0.8}\text{Mn}_{0.1}\text{Co}_{0.1}\text{O}_2$  calcined with 7 mol% excess of  $\text{Li}_2\text{O}_2$ . Additional lithium peaks are compared to ICSD patterns for  $\text{LiOH}$ ,  $\text{Li}_2\text{CO}_3$  and  $\text{Li}_2\text{O}$  confirm the presence of  $\text{Li}_2\text{CO}_3$ .

### 3.3. – Optimisation of the Microwave Calcination Procedure

Calcination of the  $\text{Ni}_{0.8}\text{Mn}_{0.1}\text{Co}_{0.1}(\text{OH})_2$  by conventional  $\text{LiOH}$  or alternative  $\text{Li}_2\text{O}_2$  lithium sources was further investigated by microwave heating at constant power. Conventional calcination involves heating the  $\text{Ni}_{0.8}\text{Mn}_{0.1}\text{Co}_{0.1}(\text{OH})_2$  sample with  $\text{LiOH}$  for 10-15 hours and flowing oxygen gas through the furnace to promote the oxidation of transition metals in  $\text{Ni}_{0.8}\text{Mn}_{0.1}\text{Co}_{0.1}(\text{OH})_2$ , with a mechanism

described in Equation 3.2. Lithium peroxide was employed to generate oxygen gas *in-situ* in an attempt to replicate the flow of oxygen in a conventional tube furnace (Equations 3.3). The microwave dielectric heating effect permits rapid heating of the sample, allowing shorter reaction times (on the order of 4-6 hours), seen in Figure 3.0.6.

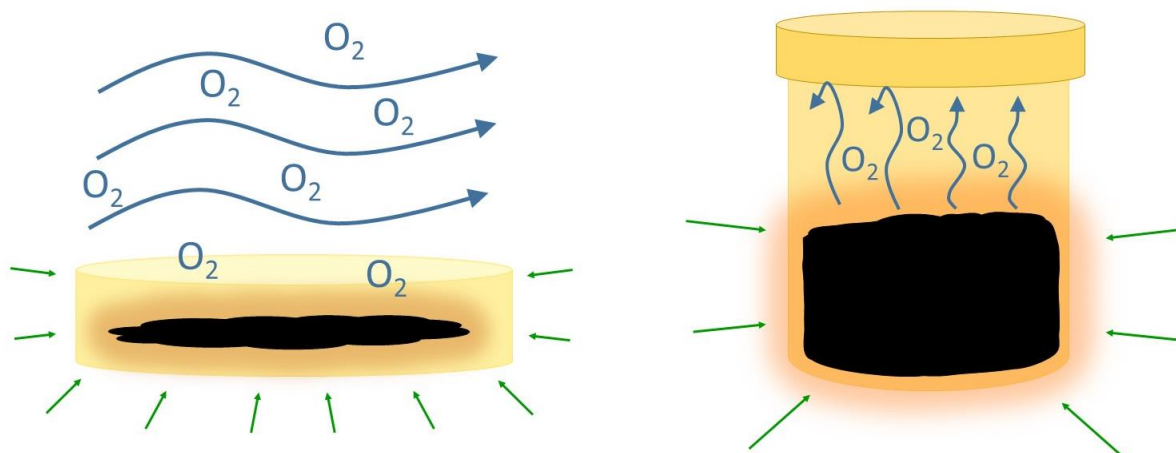
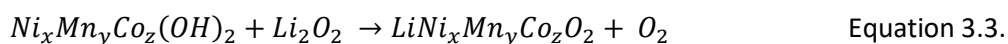


**Figure 3.0.6:** A depiction of the two calcination mechanisms within the conventional, oxygen-fed tube furnace (left) and microwave furnace with  $Ni_{0.8}Mn_{0.1}Co_{0.1}(OH)_2$  calcined with  $Li_2O_2$  with an added crucible lid to avoid oxygen loss (right).

The effect of microwave calcination with  $Li_2O_2$  was compared to the conventional procedure, which involves  $LiOH$  and an oxygen-fed tube furnace. A 10-hour calcination of  $Ni_{0.8}Mn_{0.1}Co_{0.1}(OH)_2$  precursor at  $850\text{ }^\circ\text{C}$  in an oxygen-fed tube furnace was compared with a 3-hour microwave calcination at  $850\text{ }^\circ\text{C}$ . For clarification, the microwave calcination is conducted in a CEM Phoenix furnace, which uses microwave heating to rapidly heat a silicon carbide (SiC) heating element, which in turn rapidly heats the insulated heating chamber through conduction and convection. Both reactions were conducted with  $LiOH$  or  $Li_2O_2$  to observe any differences, with the resulting XRD profiles for the four calcined samples shown in Figure 3.0.7.

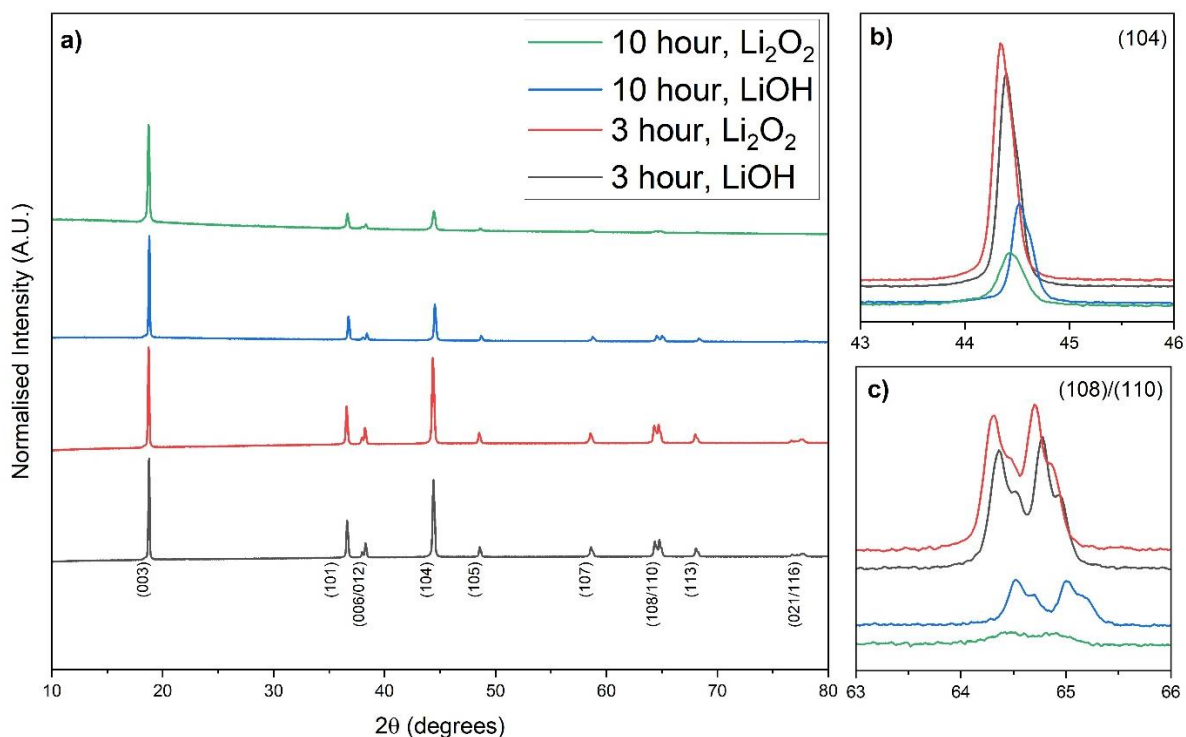


**Figure 3.0.7:** (a) XRD profiles for  $\text{LiNi}_{0.8}\text{Mn}_{0.1}\text{Co}_{0.1}\text{O}_2$  calcined at  $850^\circ\text{C}$  in a microwave furnace for 3 hours and an oxygen-fed tube furnace for 10 hours. Peak analysis of the (104) and (108)/(110) doublet are enclosed in (b) and (c) respectively.

Both furnace procedures produce the desired  $\alpha\text{-NaFeO}_2$  layered structure for  $\text{LiNi}_x\text{Mn}_y\text{Co}_z\text{O}_2$ , as observed in Figure 3.0.7.a). The (003)/(104) peak ratio was a qualitative indicator of cation ordering, with ratios larger than 1.2 suggesting greater degrees of ordering [37], [256], [257]. The XRD pattern is normalised against the most intense peak, (003), so it has a value of 1. Consequently, the height of the (104) peak can be a visual representation for the (003)/(104) peak ratio. A smaller (104) peak

observed

in

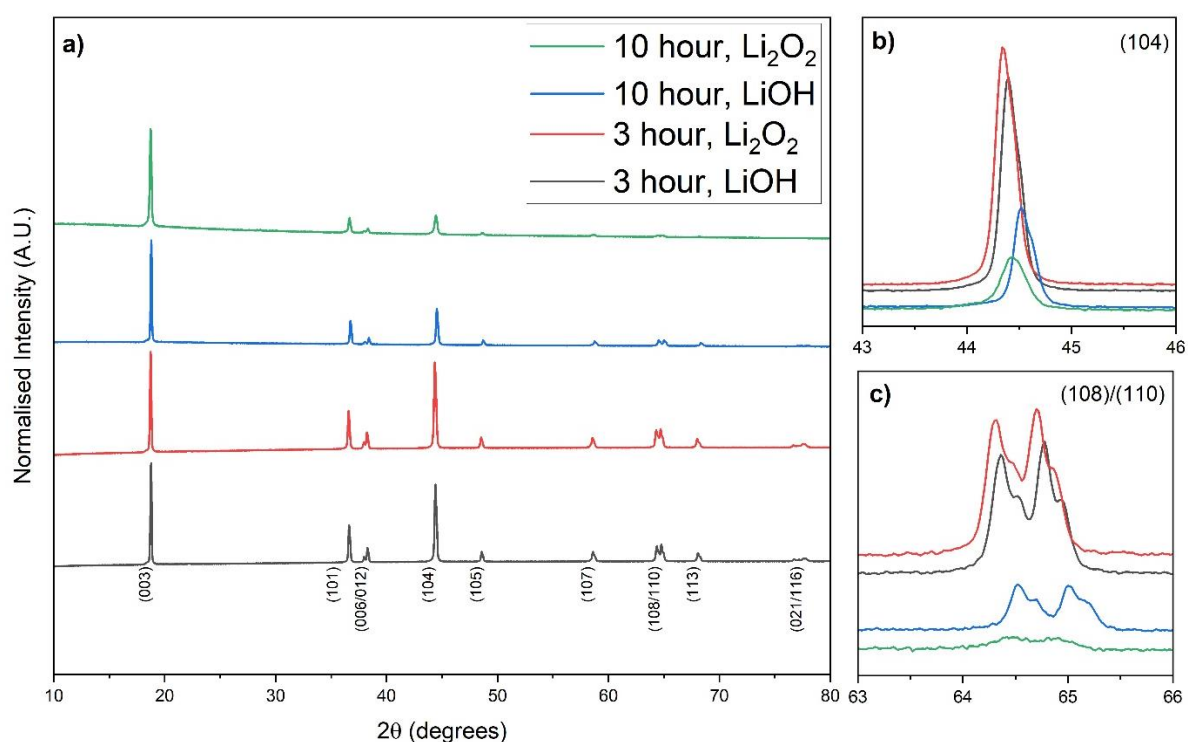


Figure 3.0.7.b) suggests that the 10-hour oxygen-fed tube furnace samples display a greater degree of cation ordering, due to their larger (003)/(104) ratios (2.595 and 4.464 for LiOH and Li<sub>2</sub>O<sub>2</sub>, respectively). The lower (003)/(104) peak ratio for the 3-hour microwave furnace reactions with LiOH and Li<sub>2</sub>O<sub>2</sub> of 1.241 and 1.107 respectively indicate a lower degree of cation ordering.

Figure 3.0.7.b) and 3.7.c) both show that microwave samples have an increased resolution in the (108)/(110) doublet peaks, with one possible cause for this pronunciation being a greater degree of crystallinity and layered ordering within the samples. One explanation for this is the faster formation of the crystal structure during microwave calcination forming more faceted particles, resulting in an increased intensity detected for the (108)/(110) peaks. The peak splitting observed in the (108)/(110) peak doublet is due to the absence of a monochromator on the Rigaku Miniflex diffractometer resulting in the presence of the K<sub>α1</sub> and K<sub>α2</sub> peaks. Sharper peaks in XRD are observed for the LiOH samples, which may indicate greater crystallinity, though further high-resolution experiments would be required to verify this. Optimisation of the temperature and duration was required in order to realise the potential of microwave calcination and lithium peroxide.

**Table 3.0.3:** Key values from the Rietveld refinement of LiNi<sub>0.8</sub>Mn<sub>0.1</sub>Co<sub>0.1</sub>O<sub>2</sub> calcined at 850 °C with LiOH or Li<sub>2</sub>O<sub>2</sub> in a microwave-assisted furnace for 3 hours; or an oxygen-fed tube furnace for 10 hours.

	<i>a</i> -, <i>b</i> - axis (Å)	<i>c</i> - axis (Å)	<i>c/a</i> ratio	Ni fraction in Li layer (%)	Unit Cell Volume (Å <sup>3</sup> )	Chi <sup>2</sup> value
MW furnace, 3 hours, LiOH at 850 °C	2.8782(5)	14.2222(3)	4.941(2)	9.2(1)	102.03(3)	3.800
MW furnace, 3 hours, Li <sub>2</sub> O <sub>2</sub> at 850 °C	2.8798(6)	14.2259(3)	4.940(2)	12.0(2)	102.18(4)	4.645
O <sub>2</sub> -fed furnace, 10 hours, LiOH at 850 °C	2.8681(1)	14.1939(7)	4.949(4)	0.9(3)	101.12(1)	6.600
O <sub>2</sub> -fed furnace, 10 hours, Li <sub>2</sub> O <sub>2</sub> at 850 °C	2.8722(4)	14.1902(4)	4.941(8)	0.9(4)	101.38(2)	6.389

This was reaffirmed quantitatively through Rietveld refinement, with the *c/a* unit cell ratio and the calculated value of nickel fraction in the lithium 3*a* layer being more accurate indicators of cation ordering (Appendix A.5). The *c/a* ratio of the oxygen-fed tube furnace samples were calculated to be 4.944 and 4.950 for LiOH and Li<sub>2</sub>O<sub>2</sub> respectively, with a cation mixing degree of 0.9% for both samples, as seen in **Table 3.0.3**. The *c/a* ratio yielded from the Rietveld refinement of the microwave samples were 4.941 and 4.940 for LiOH and Li<sub>2</sub>O<sub>2</sub> respectively, and the refinement gave feasible nickel fraction in the lithium layer values of 9.2% and 12.0% respectively (**Table 3.0.3**). This slightly smaller *c/a* ratio indicates smaller spacing between transition metal layers, suggesting an increase in cation mixing in the microwave treated samples, supported by the nickel fraction in the lithium layer values. There is also a marginal increase in *c/a* ratio for the LiOH samples relative to their Li<sub>2</sub>O<sub>2</sub>-calcined alternatives, which indicates a reduced degree of cation mixing in the Li<sub>2</sub>O<sub>2</sub> samples. Further examination by synchrotron X-ray or powder neutron analysis would give more accurate Ni and Li content, but this is beyond the scope of this thesis. However, for the purposes of optimising synthesis, these results were used as a basis for further reactions.

### 3.3.1. – Optimisation of the Calcination Temperature

Section 1.3.4 discussed the optimal temperature for the conventional (oxygen-fed tube furnace) calcination of NMC-811, which is reported to be 780-800 °C. To investigate the effect of temperature on the degree of cation mixing, calcination temperatures in the range of 650-850 °C were trialled in a microwave furnace. The Ni<sub>0.8</sub>Mn<sub>0.1</sub>Co<sub>0.1</sub>(OH)<sub>2</sub> precursor was milled with 3 mol% excess LiOH or Li<sub>2</sub>O<sub>2</sub> and calcined for 3 hours. This temperature range yielded the desired α-NaFeO<sub>2</sub> layered structure for

$\text{LiNi}_x\text{Mn}_y\text{Co}_z\text{O}_2$ , with the XRD patterns for the  $\text{Li}_2\text{O}_2$ -calcined samples shown in Figure 3.0.8.a). The (003)/(104) ratio, indicated by the height of the normalised (104) peak in Figure 3.0.8.b), shows that 825, 775 and 750 °C have the lowest relative intensity, indicating an increased order of cation ordering. This was confirmed through Rietveld refinement, with lower  $c/a$  ratios and nickel fraction in the lithium layer calculated for the samples calcined at these temperatures. These values, along with the (003)/(104) peak ratios, are shown in Table 3.0.4. Closer examination of the (108)/(110) peak doublet (Figure 3.0.8.c) shows an increased splitting in the doublet as samples are calcined above 750 °C. This indicates a larger degree of layered ordering within the structure, which is consistent with literature [9]. The largest peak splitting was prevalent in the 850 °C sample, but this sample also exhibits the largest degree of cation mixing, indicating that the ordering of the transition metal layers, and the cations are not always proportional.

**Table 3.0.4:** Key values from the Rietveld refinement of  $\text{LiNi}_{0.8}\text{Mn}_{0.1}\text{Co}_{0.1}\text{O}_2$  calcined with  $\text{Li}_2\text{O}_2$  at temperatures ranging from 650-850 °C in a 2.5 mL crucible.

Calcination temperature (°C)	$a$ -, $b$ - axis (Å)	$c$ - axis (Å)	$c/a$ ratio	Unit cell volume (Å <sup>3</sup> )	Ni fraction in the Li layer (%)	Chi <sup>2</sup>	(003)/(104) peak ratio
650	2.8797(3)	14.2247(2)	4.9396(1)	102.15(0)	8.0(4)	7.078	1.468
700	2.8800(1)	14.2237(8)	4.9387(5)	102.17(2)	10.3(2)	1.945	1.260
750	2.8781(1)	14.2164(1)	4.9396(5)	101.68(5)	5.3(4)	2.695	1.617
775	2.8778(1)	14.2192(4)	4.9411(3)	101.98(0)	5.9(1)	1.456	1.732
800	2.8772(1)	14.2191(6)	4.9420(4)	101.94(7)	3.1(3)	2.860	1.547
825	2.8773(1)	14.2191(6)	4.9418(4)	101.95(7)	1.0(2)	4.994	2.013
850	2.8799(6)	14.2259(3)	4.9398(2)	102.18(4)	12.0(2)	4.645	1.107

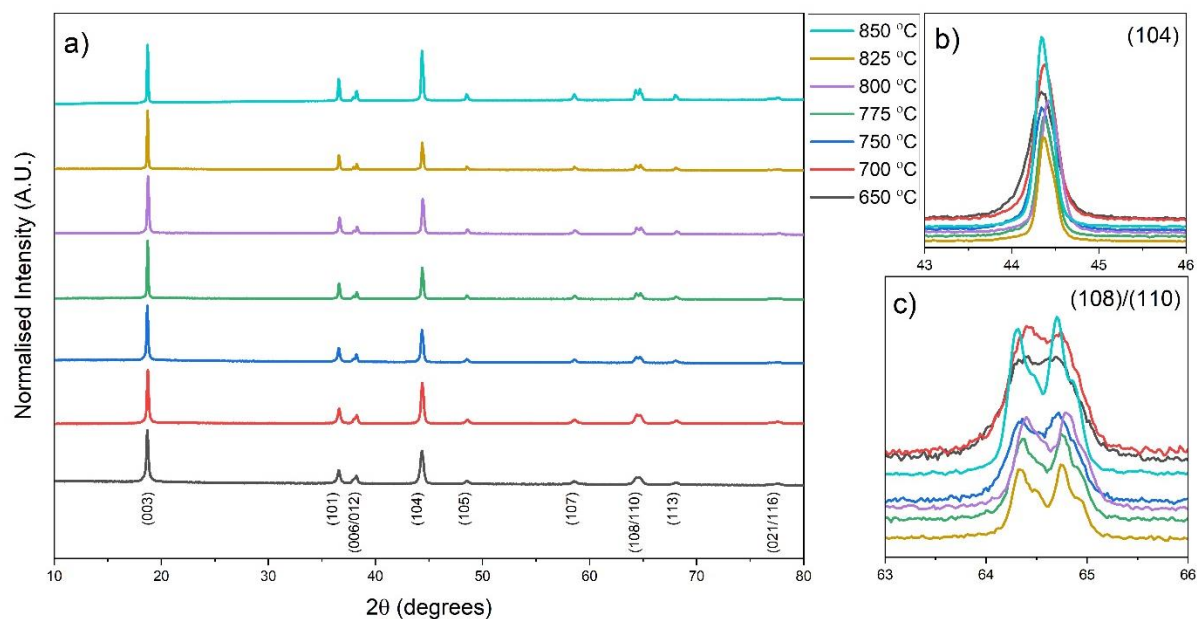


**Figure 3.0.8:** (a) XRD profiles for  $\text{LiNi}_{0.8}\text{Mn}_{0.1}\text{Co}_{0.1}\text{O}_2$  calcined with  $\text{Li}_2\text{O}_2$  for 3 hours at a range of temperatures 650-850 °C. The (104) and (108)/(110) peaks can be seen in (b) and (c) respectively.

Comparing the (003)/(104) peak ratio in Table 3.0.4 to the Rietveld refinement results confirms that an increase in ratio above 1.20 coincides with a decrease in nickel fraction in the lithium  $3a$  layer, indicating a higher degree of cation ordering. The Rietveld plots associated with Table 3.0.4 can be found in Appendix A.6. However, refining the nickel fraction for the 825 °C calcined sample did not provide a reliable result. The lattice parameter ratio ( $c/a$ ) and related unit cell volume provide more reliable parameters for evaluating these samples, with Table 3.0.4 showing an increase in  $c/a$  ratio and decrease in unit cell volume with a decrease in cation mixing, which is desirable. Optimal  $c/a$  values can be seen in the samples calcined at 775 and 800 °C. If these samples, calcined with  $\text{Li}_2\text{O}_2$ , were compared to the conventional lithium salt,  $\text{LiOH}$ , (Figure 3.0.10), it can be seen that all samples formed the desired  $\alpha\text{-NaFeO}_2$  layered structure with good (006)/(012) and (108)/(110) peak splitting, indicating good crystallinity and layered ordering.

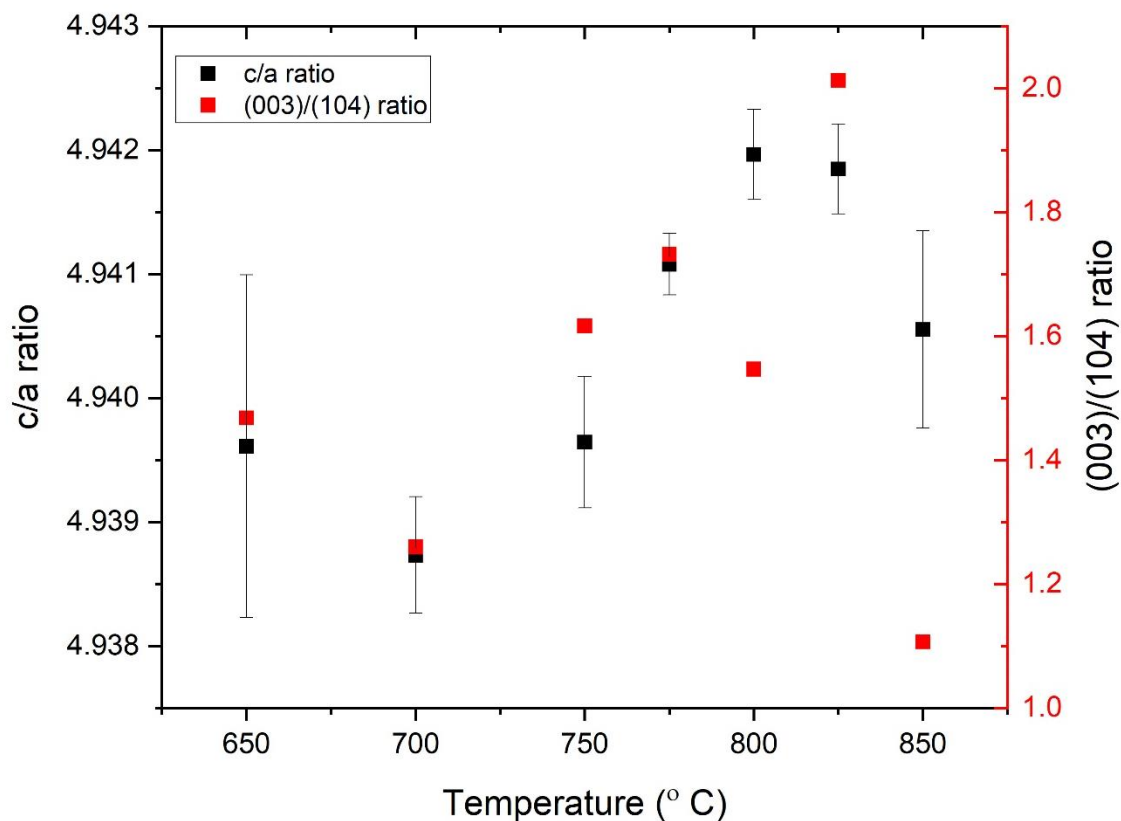


**Figure 3.9:** The variation in  $c/a$  ratio and (003)/(104) peak ratio for various microwave calcination temperatures (650-850 °C) when calcined with a  $\text{Li}_2\text{O}_2$  salt.

**Table 3.0.5:** Key values from the Rietveld refinement of  $\text{LiNi}_{0.8}\text{Mn}_{0.1}\text{Co}_{0.1}\text{O}_2$  calcined with LiOH or  $\text{Li}_2\text{O}_2$  at different temperatures 775-800 °C in a 2.5 mL crucible.

Calcination conditions temperature (°C), Li salt	$a$ -, $b$ - axis (Å)	$c$ - axis (Å)	$c/a$ ratio	Unit cell volume (Å <sup>3</sup> )	Ni fraction in the Li layer (%)	Chi <sup>2</sup>	(003)/(104) peak ratio
775, LiOH	2.8755(1)	14.2102(5)	4.9418(3)	101.76(6)	2.9(1)	1.891	1.753
775, $\text{Li}_2\text{O}_2$	2.8778(1)	14.2192(4)	4.9411(3)	101.98(0)	5.9(2)	1.456	1.732
800, LiOH	2.8826(1)	14.2326(5)	4.9374(3)	102.42(7)	9.1(2)	3.163	1.357
800, $\text{Li}_2\text{O}_2$	2.8772(1)	14.2191(6)	4.9420(4)	101.94(7)	3.1(3)	2.860	1.547

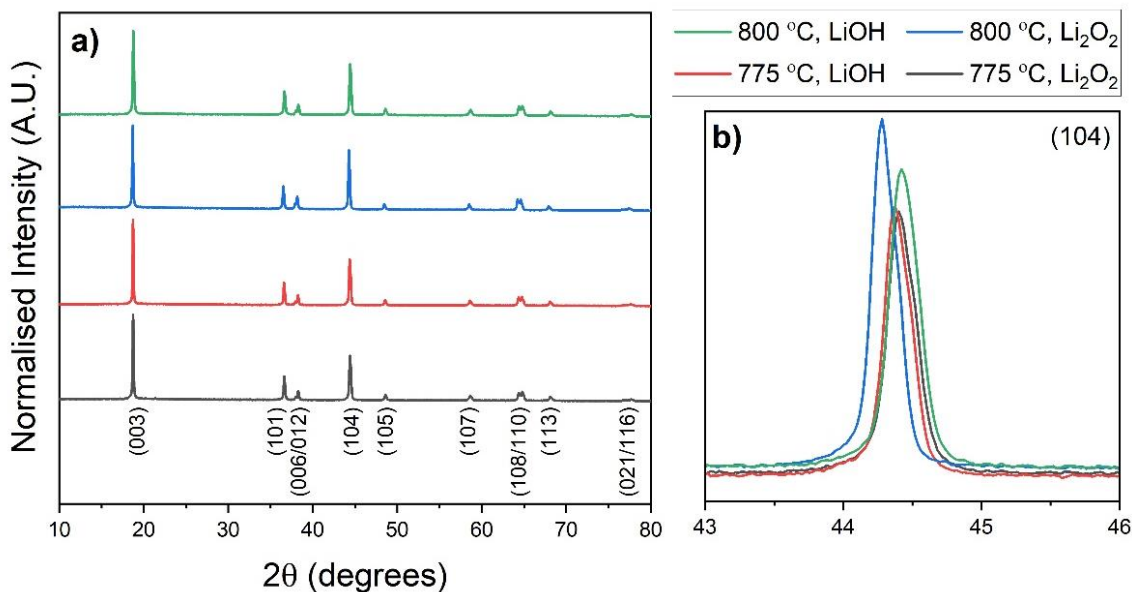


**Figure 3.0.10:** XRD profiles for  $\text{LiNi}_{0.8}\text{Mn}_{0.1}\text{Co}_{0.1}\text{O}_2$  calcined with  $\text{Li}_2\text{O}_2$  and  $\text{LiOH}$  for 3 hours at 775 and 800 °C. A full-range XRD pattern can be seen in **(a)**, with a magnification of the (104) peak in **(b)**.

From the XRD analysis, the main difference between the two lithium salts is the (104) peak (normalised against the (003) peak) for the 800 °C sample, with  $\text{LiOH}$  having a larger (003)/(104) ratio of 1.547 than  $\text{Li}_2\text{O}_2$  (1.357). At 775 °C the (003)/(104) peak ratios for  $\text{LiOH}$  and  $\text{Li}_2\text{O}_2$  have similar values of 1.753 and 1.732. This indicates that the 775 °C samples have less cation mixing than the 800 °C equivalents, confirmed *via* Rietveld refinement, with the degree of cation mixing found to be 2.9% and 5.9% for  $\text{LiOH}$  and  $\text{Li}_2\text{O}_2$  respectively (compared to 10.1% and 3.3% for the 800 °C samples respectively). The lattice parameters presented in Table 3.0.5 calculated by Rietveld refinement support this conclusion, with a  $c/a$  ratio for the samples calcined at 775 °C, 4.942 and 4.941, correlating with the results described above, with the 800 °C samples having values of 4.937 and 4.943. The associated Rietveld plots to these refinement values can be found in Appendix A.7.

### 3.3.2. – Optimisation of the Calcination Duration

An optimisation of the calcination duration was conducted concurrently with the calcination temperature described in Section 3.3.1. To preserve as much of the generated oxygen as possible from the thermal decomposition of the  $\text{Li}_2\text{O}_2$ , a single heating stage during the calcination was performed.  $\text{Ni}_{0.8}\text{Mn}_{0.1}\text{Co}_{0.1}(\text{OH})_2$  (2 mmol) was milled with 3 mol% excess  $\text{LiOH}$  or  $\text{Li}_2\text{O}_2$  and calcined at 750 °C in a 20 mL alumina crucible using a CEM Phoenix microwave furnace for time periods ranging from 90 minutes to 6 hours.

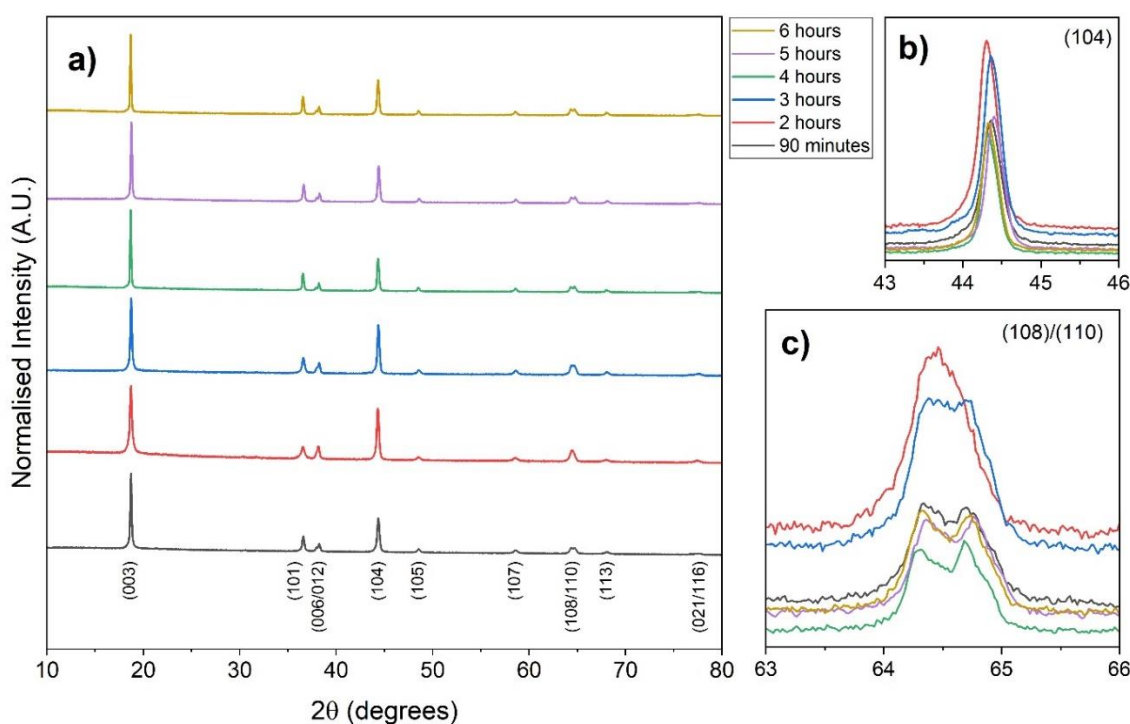


**Figure 3.0.11:** (a) XRD profiles of  $\text{LiNi}_{0.8}\text{Mn}_{0.1}\text{Co}_{0.1}\text{O}_2$  calcined with 3 mol% excess  $\text{Li}_2\text{O}_2$  in a microwave furnace over a range of durations, ranging from 90 minutes to 6 hours. The (104) peak (b) and (108)/(110) doublet peak (c) are magnified for analysis.

XRD analysis of  $\text{LiNi}_{0.8}\text{Mn}_{0.1}\text{Co}_{0.1}\text{O}_2$  calcined with 3 mol% excess  $\text{Li}_2\text{O}_2$  is shown in Figure 3.0.11.a) and reveals characteristic peaks that are consistent with the  $\alpha\text{-NaFeO}_2$  layered structure for all samples, with no phase impurities observed. Visual inspection of the (104) peak in Figure 3.0.11.b) shows that the 2 and 3 hour samples have larger intensities, smaller (003)/(104) ratios and a larger degree of cation mixing than the other calcination durations tested. This was confirmed *via* Rietveld refinement, with the samples calcined for 4-6 hours having larger  $c/a$  values of  $\sim 4.940$  and marginally smaller unit cell volumes ( $\sim 102.0$ ), shown in Table 3.0.6. The 90-minute sample also gave a low  $c/a$  ratio of 4.939 and unit cell size of  $102.084 \text{ \AA}^3$ . The (108)/(110) peak doublet, seen in Figure 3.0.11.c), shows clearer distinction of this peak doublet in the 90 minute, 4-, 5- and 6- hour samples indicating a greater degree of order within the crystal structure. The 3-hour sample has poor definition between the peaks, with the 2-hour sample displaying no indication of peak splitting. The Rietveld plots associated with Table 3.0.6 can be found in Appendix A.8.

**Table 3.0.6:** Key values from the Rietveld refinement of  $\text{LiNi}_{0.8}\text{Mn}_{0.1}\text{Co}_{0.1}\text{O}_2$  calcined with  $\text{Li}_2\text{O}_2$  at 750 °C for different durations, including the  $c/a$  lattice parameter ratio, the calculated nickel fraction in the lithium  $3a$  layer, and the (003)/(104) peak ratio calculated from the raw XRD data.

Calcination duration (h)	$a$ -, $b$ - axis (Å)	$c$ - axis (Å)	$c/a$ ratio	Unit cell volume (Å <sup>3</sup> )	Ni fraction in the Li layer (%)	Chi <sup>2</sup> value	(003)/(104) peak ratio
1.5 (90 minutes)	2.8792(2)	14.2198(1)	4.9389(7)	102.08(5)	4.6(2)	3.423	2.032
2	2.8827(3)	14.2098(2)	4.9294(1)	102.26(2)	10.1(3)	4.818	1.352
3	2.8800(1)	14.2151(9)	4.9358(6)	102.11(3)	9.0(2)	3.298	1.444
4	2.8786(2)	14.2194(7)	4.9397(4)	102.04(2)	9.2(2)	2.632	2.233
5	2.8797(1)	14.2278(8)	4.9407(5)	102.18(9)	4.3(2)	2.576	1.984
6	2.8784(1)	14.2193(6)	4.9399(4)	102.03(8)	5.9(1)	1.804	2.071

Variation in unit cell volumes over the range of durations was small, with no clear relationship with calculated nickel fraction in the lithium layer. The LiOH samples follow a similar trend, with an initial high  $c/a$  value of 4.940 for the 90-minute calcination, followed by an increasing  $c/a$  value from 2 hours (4.934) to 6 hours (4.942), depicted in Figure 3.0.12.c) and Table 3.0.7, correlating with a decrease in cation mixing. The reduced  $c/a$  ratio observed in both 2-hour samples is thought to be the result of phase alterations due to loss of the oxygen-rich environment between 90-minutes and 2 hours. It is thought that samples calcined longer than 2 hours stabilise to the oxygen-depleted environment, resulting in an increase in  $c/a$  ratio until it plateaus between 5- and 6- hours. The XRD profiles of two  $\text{Li}_2\text{O}_2$ -calcined samples with the largest  $c/a$  ratio (the 5- and 6- hour samples) are compared with their LiOH alternatives in Figure 3.0.12.a). The Rietveld plots associated with Table 3.0.7 can be found in Appendix A.9. All samples exhibit the  $\alpha$ - $\text{NaFeO}_2$  layered structure and good peak splitting in the (108)/(110) peak doublet, indicating a good degree of crystallinity and layered ordering. There is an increased (104) intensity for the 5-hour sample calcined with LiOH observed in Figure 3.0.12.b), coinciding with a reduction in the  $c/a$  value observed in Figure 3.0.12.c), but this was not observed in other samples. There appears to be an inverse relationship between the  $c/a$  ratio and Ni content in the Li layer (Table 3.0.8). Further synchrotron X-ray and neutron experiments would be useful in ascertaining accurate Ni and Li content values for these materials, but this is beyond the scope of this thesis.

**Table 3.0.7:** Key values from the Rietveld refinement of  $\text{LiNi}_{0.8}\text{Mn}_{0.1}\text{Co}_{0.1}\text{O}_2$  calcined with LiOH at 750 °C for different durations, including the  $c/a$  lattice parameter ratio, the calculated nickel fraction in the lithium  $3a$  layer, and the (003)/(104) peak ratio calculated from the raw XRD data.

Calcination duration (h)	$a$ -, $b$ - axis (Å)	$c$ - axis (Å)	$c/a$ ratio	Unit cell volume (Å <sup>3</sup> )	Ni fraction in the Li layer (%)	Chi <sup>2</sup> value	(003)/(104) peak ratio
1.5 (90 minutes)	2.8758(1)	14.2051(6)	4.9395(3)	101.74(7)	9.5(1)	1.789	2.032
2	2.8801(2)	14.2101(1)	4.9340(7)	102.08(1)	9.7(2)	2.577	1.352
3	2.8783(2)	14.2061(1)	4.9356(6)	101.92(1)	7.4(2)	2.757	1.444
4	2.8749(1)	14.2061(7)	4.9341(4)	101.68(9)	2.4(2)	2.500	2.233
5	2.8786(1)	14.2170(6)	4.9389(4)	102.02(7)	6.1(1)	1.615	1.984
6	2.8753(1)	14.2091(5)	4.9417(3)	101.74(6)	4.3(1)	1.779	2.071

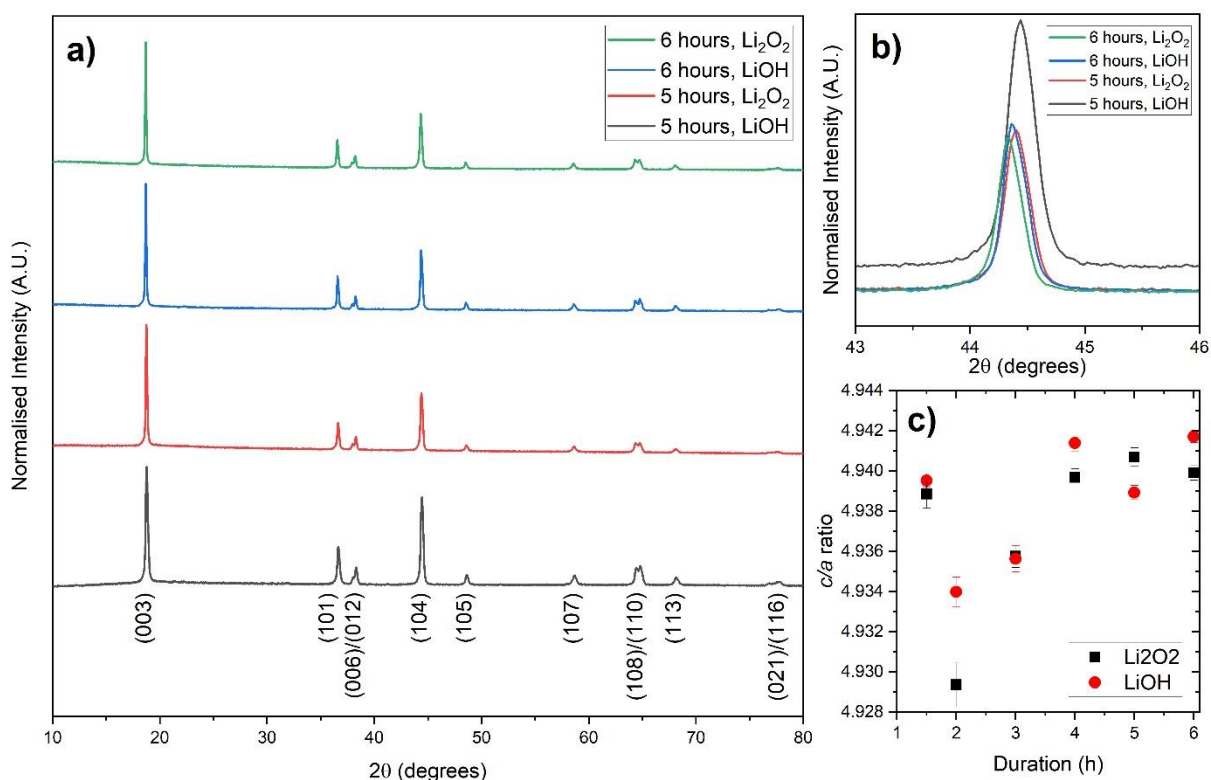


**Figure 3.0.12:** The XRD profile (a) and magnification of the (104) peak (b) of  $\text{LiNi}_{0.8}\text{Mn}_{0.1}\text{Co}_{0.1}\text{O}_2$  calcined with 3 mol% excess  $\text{Li}_2\text{O}_2$  or LiOH in a microwave furnace for 5-6 hours. The  $c/a$  ratios for both LiOH and  $\text{Li}_2\text{O}_2$  over the range of calcination durations and displayed in (c).

**Table 3.0.8:** Key values from the Rietveld refinement of  $\text{LiNi}_{0.8}\text{Mn}_{0.1}\text{Co}_{0.1}\text{O}_2$  calcined with  $\text{Li}_2\text{O}_2$  at 750 °C for 5 and 6 hours with LiOH or  $\text{Li}_2\text{O}_2$  in a microwave furnace. Estimated standard deviations are included in brackets, where refined.

Calcination conditions	$c/a$ ratio	Unit cell volume ( $\text{\AA}^3$ )	Nickel fraction in the lithium $3a$ layer (%)	$\chi^2$ value	(003)/(104) peak ratio
5 hours, LiOH	4.9389(4)	102.02(7)	6.1(1)	1.615	1.274
5 hours, $\text{Li}_2\text{O}_2$	4.9407(5)	102.18(9)	4.3(2)	2.576	1.985
6 hours, LiOH	4.9417(3)	101.74(7)	4.3(1)	1.779	1.928
6 hours, $\text{Li}_2\text{O}_2$	4.9399(4)	102.03(1)	5.9(1)	1.804	2.071

SEM images (Figure 3.0.13) indicate that the  $\sim 9 \mu\text{m}$  secondary precursor morphologies are maintained during the calcination procedure, yielding quasi-spherical secondary assemblies. This morphology and secondary particle size is within the desired range determined by literature [139], [140], [141]. Should secondary particle sizes get too large (for example above 20-30  $\mu\text{m}$ ), it inhibits the lithium-ion diffusion rate due to the greater distance travelled, but smaller particles ( $< 5 \mu\text{m}$ ) incurs a greater surface area to volume ratio, increasing the loss of active material to SEI formation per gram (of active material). The 2- and 3- hour calcination samples appear to produce larger, less spherical particles, coinciding with a reduction in  $c/a$  values for these samples. It would be expected that a lower specific capacity could be yielded from these samples due to the larger particle size, which is shown in Figure 3.0.14. No clear differences are observed between the two lithium salts. Larger primary particles are observed in the samples calcined for 4–6 hours, which have larger  $c/a$  ratios of  $\sim 4.940$ , compared to shorter calcination. From a primary particle perspective, all samples are similar, with small  $< 1 \mu\text{m}$  particles agglomerating with distinct boundaries between primary particles, resulting in ‘voids’ between them, which limits the ionic conductivity of lithium ions within the secondary particle compared to the ‘meatball’ model observed in literature (exemplified in Figure 1.8).

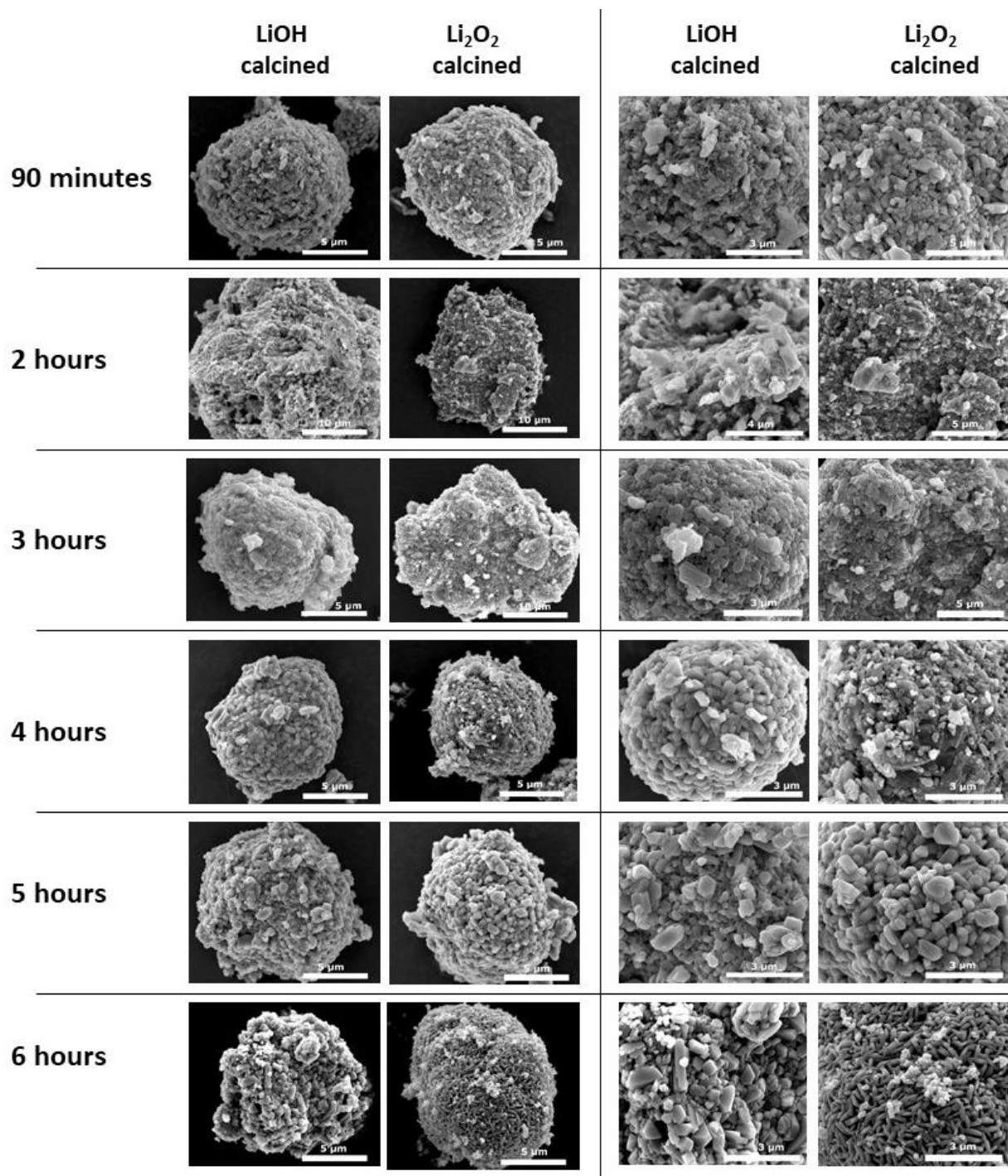


**Figure 3.0.13:** SEM images of LiNi<sub>0.8</sub>Mn<sub>0.1</sub>Co<sub>0.1</sub>O<sub>2</sub> calcined at 750 °C in a microwave furnace with 3 mol% excess LiOH or Li<sub>2</sub>O<sub>2</sub> that depict the secondary (left) and primary (right) morphology. The calcination periods for each calcination experiment are indicated on the left-hand side.

Electrochemical analysis was conducted on these samples, cycled at C/20 for two formation cycles followed by 98 cycles at C/2 with a voltage window of 3.0-4.2 V at room temperature. The capacity retention of these samples over the 100 cycles can be seen in Figure 3.0.14, where the highest discharge capacities are observed for samples calcined with LiOH for 1.5 and 4 hours (161.0 and

164.3 mAh g<sup>-1</sup> respectively at C/20). These cells were not cycled under controlled temperature, which accounts for the minor oscillations in capacity relating to temperature fluctuations during the day/night. One consistent trend observed from Figure 3.0.14 is that samples calcined with LiOH deliver a higher capacity compared to their Li<sub>2</sub>O<sub>2</sub> counterparts calcined for the same duration. This may indicate a reduction in lithium inventory during synthesis of the Li<sub>2</sub>O<sub>2</sub> samples. Additionally, there is a trend relating to the calcination durations and the *c/a* ratio of LiNi<sub>0.8</sub>Mn<sub>0.1</sub>Co<sub>0.1</sub>O<sub>2</sub>, with samples calcined at 1.5-, 4- and 5- hours experiencing a higher specific capacity than the 2- and 3- hour samples (Figure 3.0.12.c)), which supports the literature with respect to an increased *c/a* ratio having a more layered and ordered structure, which reduces cation mixing. The exception to this trend was the samples calcined for 6 hours, which yields a discharge capacity of approx. 80 mAh g<sup>-1</sup> at C/20 (when calcined with LiOH), approximately half of that of the equivalent samples calcined at 1.5- and 4- hours (161.0 and 164.3 mAh g<sup>-1</sup> respectively). This could be related to the particle morphology, where larger primary particles with greater voids between the particles may impede ion mobility. This may also explain the reduction in capacity for the 5-hour sample, which also shows a similar morphology (Figure 3.0.13).

Figure 3.0.14 reveals capacity drops for all samples as the C-rate is increased from C/20 to C/2, which is also observed in literature. The most pronounced capacity drop is noted for the Li<sub>2</sub>O<sub>2</sub> sample calcined for two hours, from approx. 70 to 10 mAh g<sup>-1</sup> after two C/20 formation cycles but retains this over the remaining cycles. The cells with the highest capacities (1.5-hour calcination with LiOH, Li<sub>2</sub>O<sub>2</sub>; and the 4-hour calcination with LiOH) experienced the highest capacity retention after 98 cycles of C/2, with capacity retention of 97.9%, 94.1% and 92.9% respectively. The other samples experienced a capacity retention of between 80.4-91.2%. Cells calcined with Li<sub>2</sub>O<sub>2</sub> generally yielded lower capacity retention over the 98 cycles relative to their LiOH counterparts.

The voltage profiles for all samples show a plateau at 3.6-3.8 V which coincides with the oxidation of Ni<sup>2+</sup> to Ni<sup>3+</sup>/Ni<sup>4+</sup> (Figure 3.0.15). An increase in the average voltage of this plateau in the charging profile indicates an increase in resistance or impedance within the cell, most likely from the formation/thickening of the SEI layers. An initial voltage peak ('hump' in the profile) is seen in the charge curve at *ca.* 3.7 V prior to delithiation, which is an overpotential that occurs due to a resistive layer formation at the surface of the particle, for example residual compounds such as LiOH and Li<sub>2</sub>CO<sub>3</sub> caused by excess lithium during preparation or incomplete lithiation of the cathode active material [258], [259]. This was commonly seen in samples on their 10<sup>th</sup>, 50<sup>th</sup> or 100<sup>th</sup> cycle, indicating

that the formation of these residual, resistive phases may occur during cycling rather than the pristine sample.

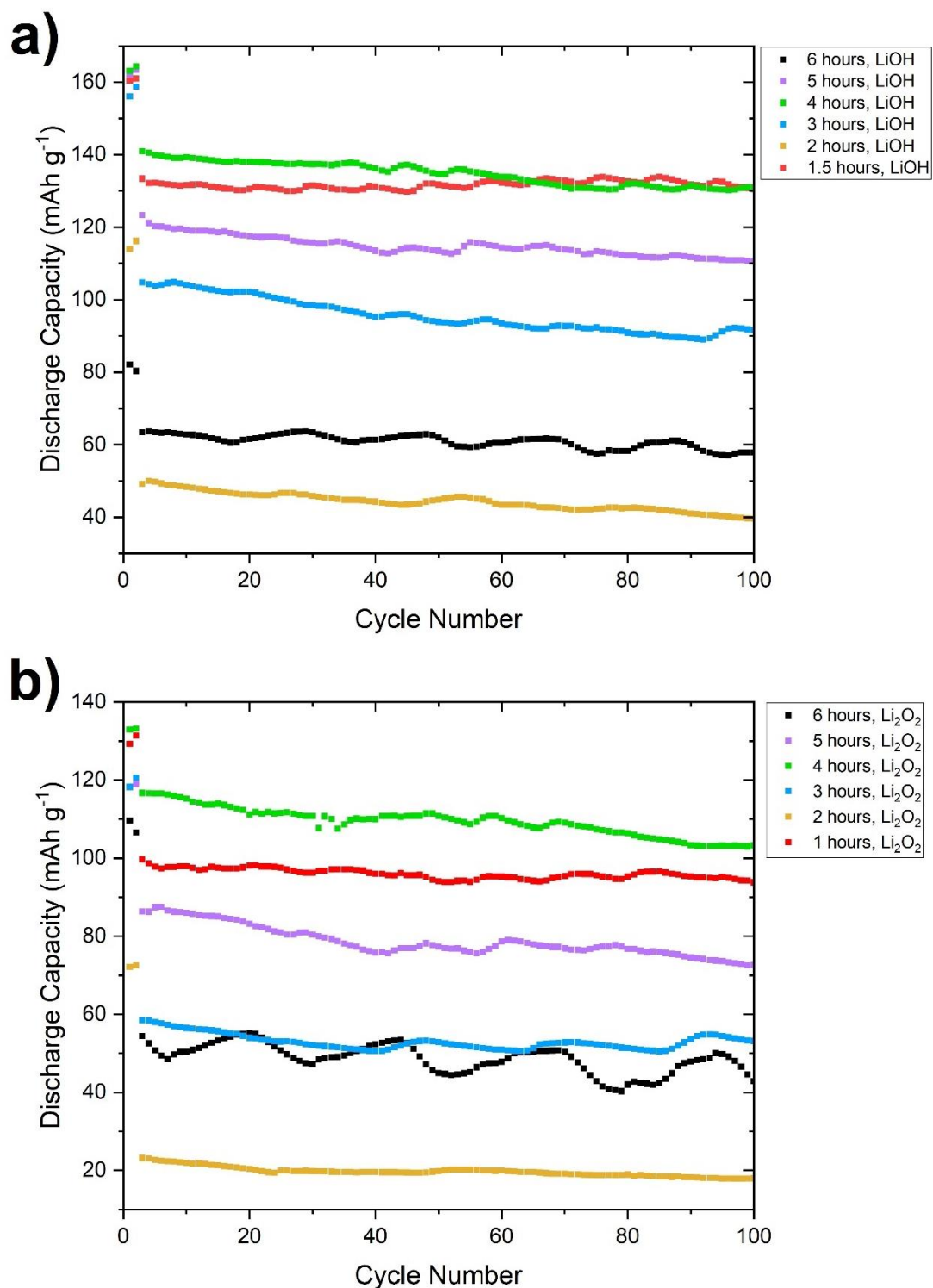


**Figure 3.0.14:** Capacity retention over 100 cycles of half-cells cycled with a voltage window of 3.0-4.2 V, with 2 cycles at C/20 followed by 98 cycles of C/2. The NMC-811 cathode active material was calcined for different durations with two lithium salts, LiOH **(a)** and  $\text{Li}_2\text{O}_2$  **(b)**.

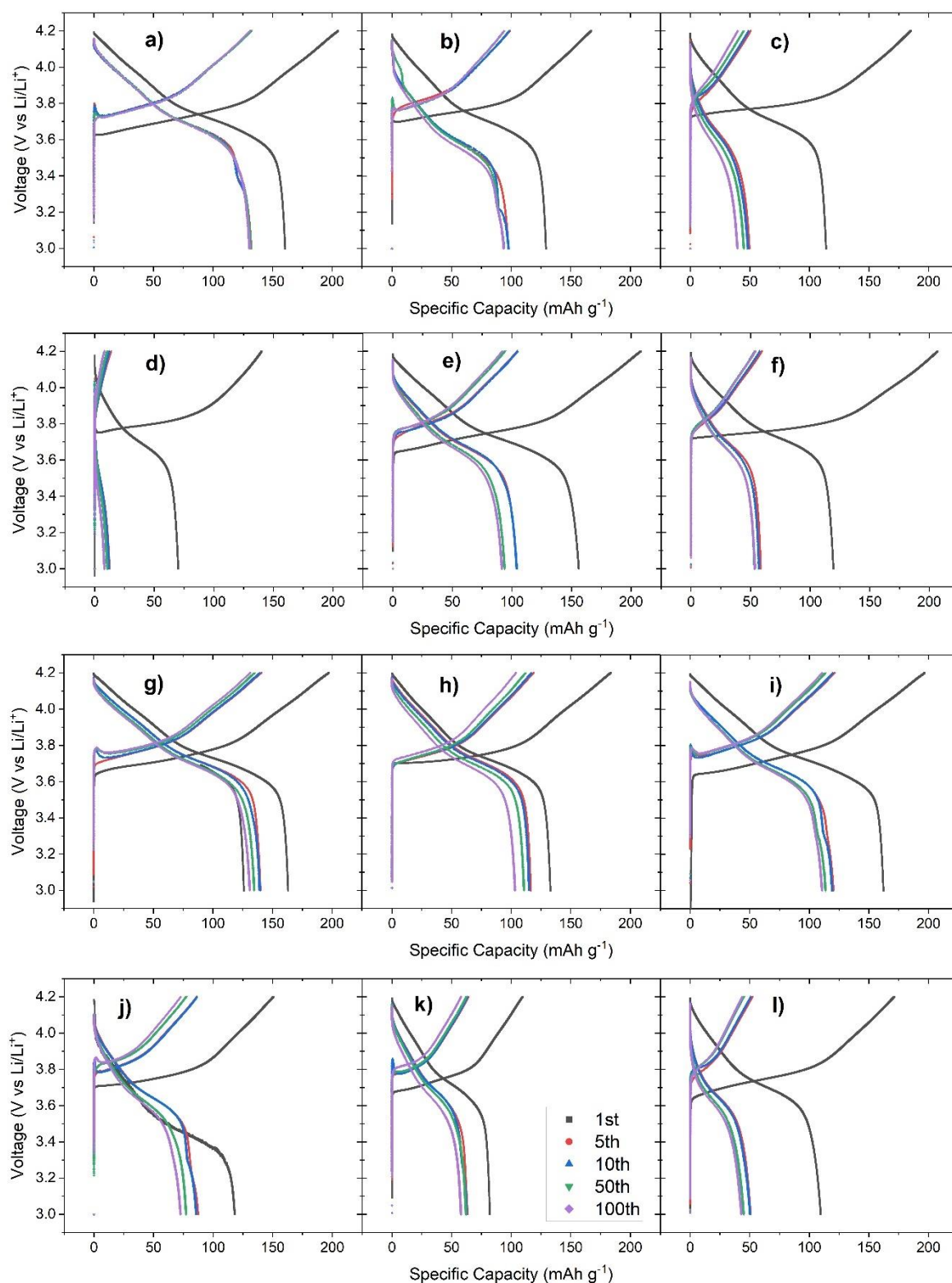


**Figure 3.0.15:** Voltage profiles for half-cells cycled at 3.0-4.2 V in their 1<sup>st</sup>, 5<sup>th</sup>, 10<sup>th</sup>, 50<sup>th</sup> and 100<sup>th</sup> cycle. **(a), (c), (e), (g), (i)** and **(k)** represent the cathode materials calcined with LiOH at 1.5, 2, 3, 4, 5 and 6 hours respectively; with their Li<sub>2</sub>O<sub>2</sub> counterparts seen in **(b), (d), (f), (h), (j)** and **(l)** respectively.

In the charging differential capacity profile (Figure 3.0.16), there is a main characteristic peak at *ca.* 3.6-3.8 V corresponding to the voltage plateau observed in Figure 3.0.15. It is established in literature that this characteristic peak was associated with the hexagonal to monoclinic (H1-M) phase change [33], [260]. There is a minor 'bump' that can be seen around the 4.0 V mark that was associated with the (M-H2) phase change. The shift in voltage from left to right in the 1.5-, 4-, 5- and 6- hour samples was implicit of a polarisation phenomenon, which is characterised by an increase in operational voltage above the equilibrium voltage as a result resistance between the electrolyte and cathode [261]. The discharge differential capacity profile mirrors the charging profile due to the reversibility of the H1-M and M-H2 transitions at *ca.* 3.7 V and *ca.* 3.95-4.0 V. The effect of polarisation can also be observed in these profiles, with subsequent cycles being shifted to a lower voltage. The area under the differential capacity profile represents the capacity delivered by the cathode, thus the first cycle has large area (as it was cycled at C/20) and subsequent cycles (conducted at C/2) had a smaller area under the profile, which decreased as the degradation of capacity occurred with cycling.

The electrochemical data reflects the conclusions drawn from the crystalline and morphological data. The higher electrochemical capacities yielded from the 1.5-, 4-, 5- and 6- hour calcined samples also had higher *c/a* crystalline ratio, which indicated a more layered, ordered structure, permitting the passage of lithium. The morphology of the 5- and 6- hour calcined samples indicated poorer contact between primary particles, which is mirrored in the lower capacity observed for these samples. It is unknown why the 1.5-hour calcined sample has a higher *c/a* ratio (and electrochemical capacity yield) than the 2- and 3- hour samples, but it was hypothesised that it could be related to the calcination mechanism and the oxygen evolution that occurs during the reaction. Further structural analysis, combined with full coin cell analysis, may deliver further insight into this but is beyond the scope of this thesis.

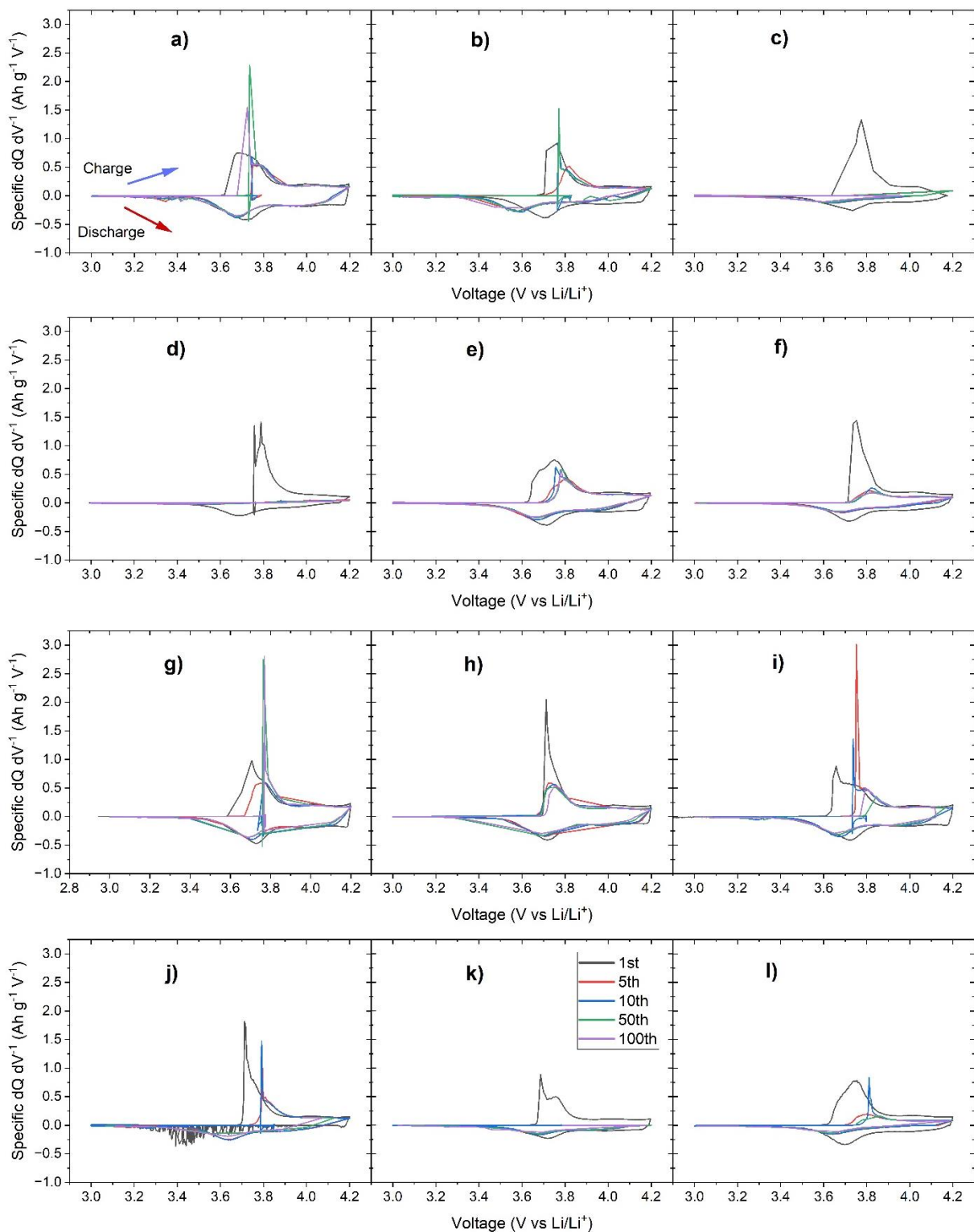


**Figure 3.0.16:** Differential capacity ( $dQ dV^{-1}$ ) profiles for the half-cells cycled at 3.0-4.2 V in their 1<sup>st</sup>, 5<sup>th</sup>, 10<sup>th</sup>, 50<sup>th</sup> and 100<sup>th</sup> cycle. **(a), (c), (e), (g), (i)** and **(k)** represent the cathode materials calcined with LiOH at 1.5, 2, 3, 4, 5 and 6 hours respectively; with their Li<sub>2</sub>O<sub>2</sub> counterparts seen in **(b), (d), (f), (h), (j)** and **(l)** respectively.

### 3.3.3. – *In-situ* XRD studies of the calcination of NMC-811

The calcination of nickel-rich hydroxide precursors proceeds *via* the formation of the spinel/rocksalt intermediate phase followed by the formation of the final  $\alpha$ -NaFeO<sub>2</sub> layered structure. The first phase transformation occurs at  $\sim 400$  °C and coincides with the decomposition of LiOH [152]. An investigation into how Li<sub>2</sub>O<sub>2</sub> reacts with this system was conducted using high-temperature XRD to examine intermediate and final phase formation as a function of temperature. Due to the *in-situ* XRD configuration, these calcination reactions were performed in air rather than an oxygen environment.

#### 3.3.3.1. – Investigation into the calcination of Ni<sub>0.8</sub>Mn<sub>0.1</sub>Co<sub>0.1</sub>(OH)<sub>2</sub> with LiOH

Ni<sub>0.8</sub>Mn<sub>0.1</sub>Co<sub>0.1</sub>(OH)<sub>2</sub> was calcined with LiOH in an air atmosphere. The hydroxide phase being dominant at temperatures below 300 °C, and a phase change to a rocksalt intermediate observed between 300-400 °C (Figure 3.0.17). Peaks observed at  $\sim 22^\circ$ ,  $\sim 30^\circ$  and  $\sim 32^\circ$ , indicates the presence of Li<sub>2</sub>CO<sub>3</sub>, formed from the reaction between lithium and CO<sub>2</sub> in air. As the temperature increases from 100-300 °C, the (101), (102), (110), and (111) hydroxide phase peaks experience a peak shift indicating an increase in unit cell volume, confirmed by Rietveld refinement (39.764 to 38.198 Å<sup>3</sup>).

Appendix A.10 shows that LiOH remains present at lower temperatures, with Li<sub>2</sub>CO<sub>3</sub> peaks at  $\sim 20$ - $21^\circ$  appearing above 300 °C. Li<sub>2</sub>O does not appear to be present in this temperature range. High temperature XRD experiments up to 850 °C (Figure 3.0.18) suggests LiNi<sub>0.8</sub>Mn<sub>0.1</sub>Co<sub>0.1</sub>O<sub>2</sub> is formed above 500 °C. The weak or absent (105), (107), (113), (116) peaks indicate the fully stacked unit cell seen in the fully-crystalline phase has not yet formed at this temperature. Additionally, small (111), (200) and (220) peaks labelled in green with the subscript 'R' indicate that above 750 °C, under these conditions, the rocksalt phase forms as a parasitic phase impurity. Figure 3.0.18 also shows an increased degree in peak splitting in the (006)/(012) and (108)/(110) peak doublets as temperature increases, indicating an increase in crystalline layered ordering. This coincides with the loss of Li<sub>2</sub>CO<sub>3</sub> from the system as the lithium species integrates with the transition metal at higher temperatures. There was evidence of Li<sub>2</sub>O in the system at higher temperatures (750-850 °C), which forms during Li<sub>2</sub>CO<sub>3</sub> degradation and lithium evolution, resulting in a loss of lithium from the system.

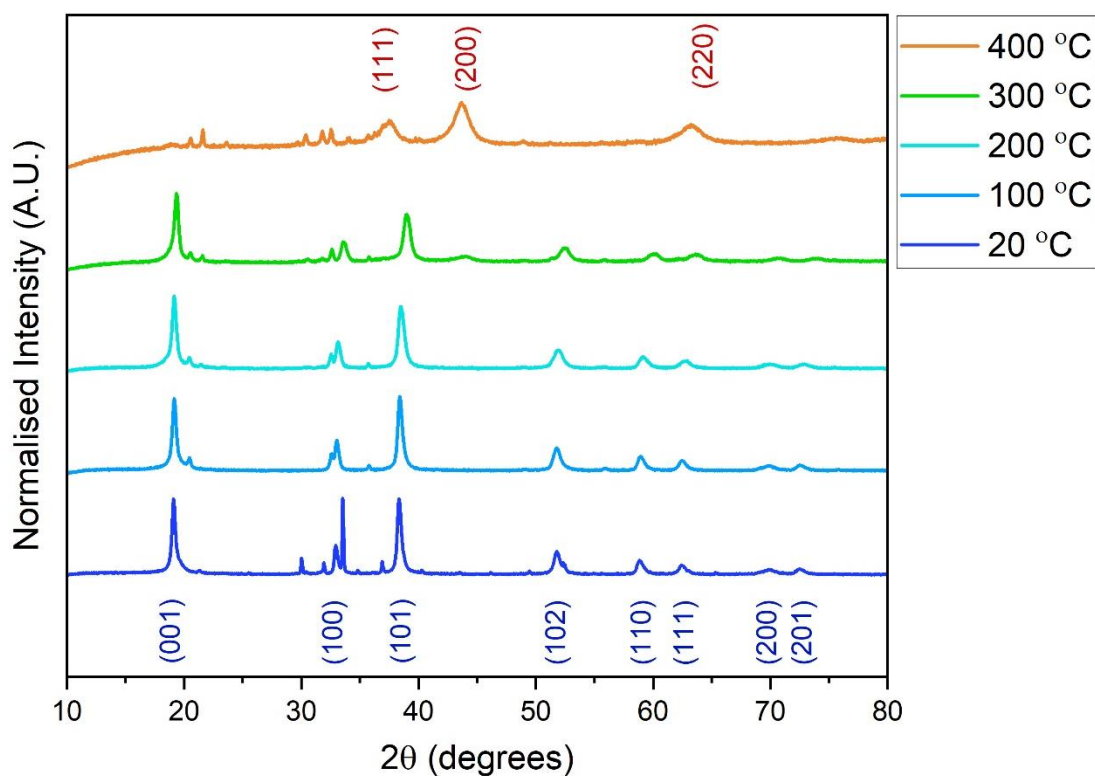


**Figure 3.0.17:** High temperature XRD of  $\text{Ni}_{0.8}\text{Mn}_{0.1}\text{Co}_{0.1}(\text{OH})_2$  heated with LiOH between 20-400 °C at 100 °C- intervals, captured using a Anton Parr BTS-500 XRD stage on a benchtop Rigaku Miniflex 6 diffractometer. Peaks are labelled for each potential phase (blue,  $M(\text{OH})_2$ ; green,  $M_3\text{O}_4$ ; red,  $\text{MO}$ ).

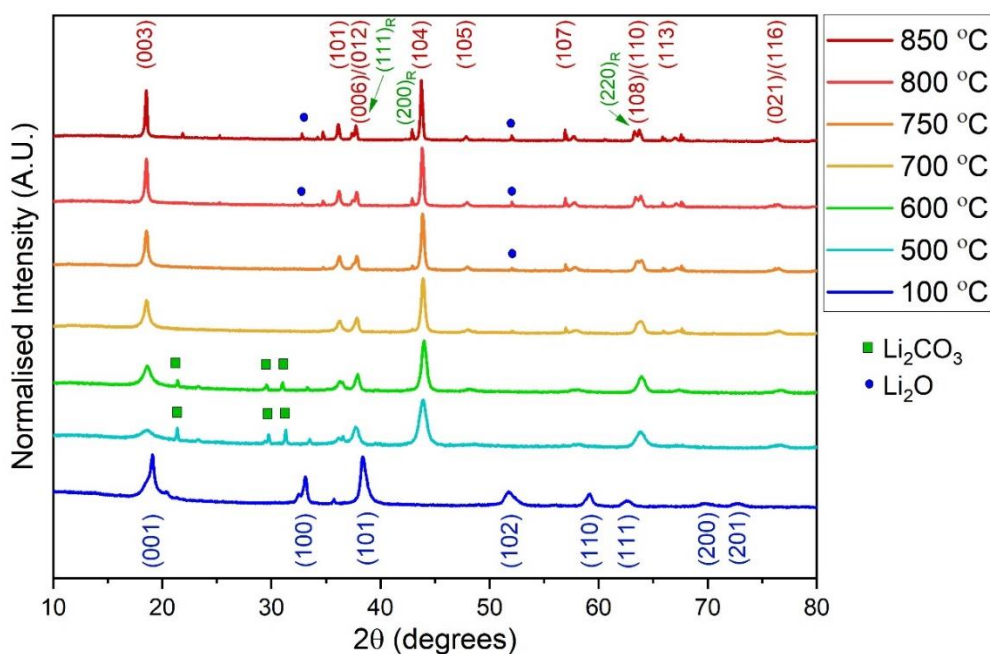


**Figure 3.0.18:** XRD patterns of  $\text{Ni}_{0.8}\text{Mn}_{0.1}\text{Co}_{0.1}(\text{OH})_2$  heated with LiOH in the 100-850 °C temperature range with  $\text{Li}_2\text{CO}_3$  indicated with a green square;  $\text{Li}_2\text{O}$  indicated with a blue circle. This was captured using a PANalytical X'Pert<sup>3</sup> X-ray diffractometer with a HTK 1200N high temperature stage.

### 3.3.3.2 – Investigation of the calcination of $\text{Ni}_{0.8}\text{Mn}_{0.1}\text{Co}_{0.1}(\text{OH})_2$ with $\text{Li}_2\text{O}_2$

XRD analysis into the calcination of  $\text{Ni}_{0.8}\text{Mn}_{0.1}\text{Co}_{0.1}(\text{OH})_2$  with  $\text{Li}_2\text{O}_2$  suggests the formation of a poorly-crystalline  $\alpha\text{-NaFeO}_2$  layered oxide phase between 300 and 400 °C (Figure 3.0.19). This evolution from the  $\text{Ni}_{0.8}\text{Mn}_{0.1}\text{Co}_{0.1}(\text{OH})_2$  phase occurs at a lower temperature of 200-300 °C rather than 300-400 °C observed with  $\text{LiOH}$ , owing to the lower thermal decomposition temperature of  $\text{Li}_2\text{O}_2$  [104]. The  $M(\text{OH})_2$  is phase dominant in the 20-200 °C and has peak asymmetry observed in the (001), (101) and (102) peaks, with a gradual high-angle peak shift suggesting a decrease in unit cell volume. This was confirmed by Rietveld refinement, which gives the degree in unit cell decrease from 41.581 to 37.856 Å<sup>3</sup> as the temperature increases from 20-200 °C. Interestingly, there appears to be a sharper phase transition for the sample calcined with  $\text{LiOH}$  (300-340 °C) compared to  $\text{Li}_2\text{O}_2$  (200-300 °C, Figure 3.0.20). This would suggest that the oxygen evolution during the calcination with  $\text{Li}_2\text{O}_2$  is gradual.

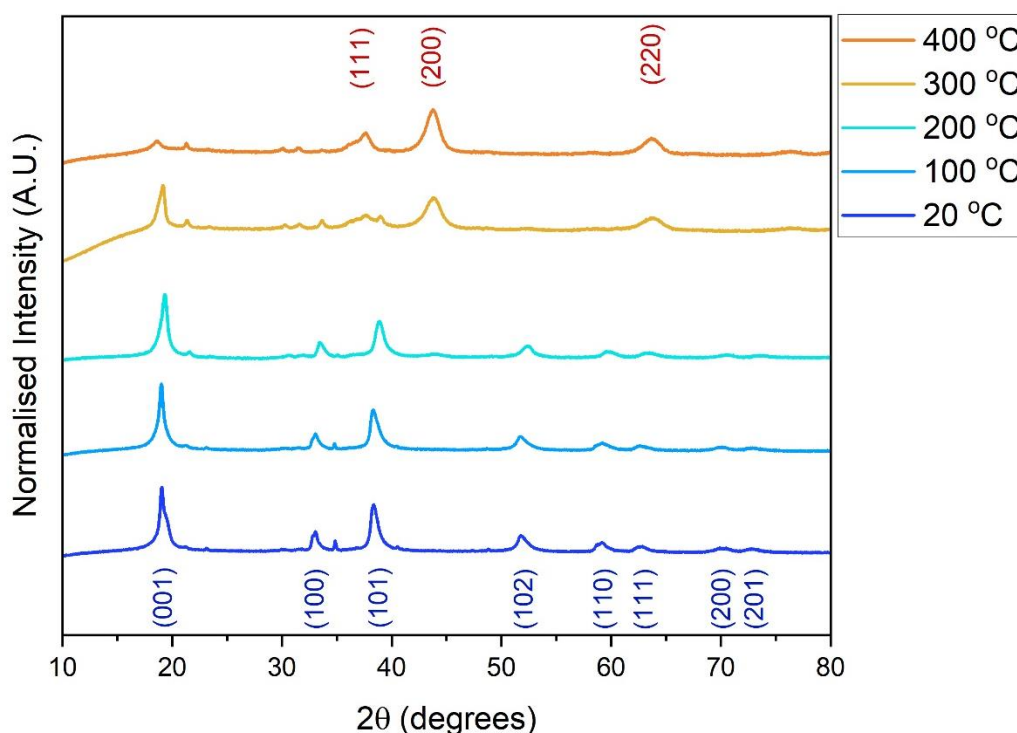


**Figure 3.0.19:** High temperature XRD study of  $\text{Ni}_{0.8}\text{Mn}_{0.1}\text{Co}_{0.1}(\text{OH})_2$  heated with  $\text{Li}_2\text{O}_2$  between 20-500 °C at 100 °C intervals, Peaks are labelled for each potential phase (blue,  $M(\text{OH})_2$ ; green,  $M_3\text{O}_4$ ; red,  $\text{MO}$ ).

Peaks observed at  $\sim 21^\circ$ ,  $\sim 31^\circ$  and  $32^\circ$   $2\theta$  grow in intensity from 200-300  $^\circ\text{C}$ , indicating the presence of  $\text{Li}_2\text{CO}_3$  (Figure 3.0.20). Both sets of high temperature XRD annealing experiments were carried out in air and the evolution of  $\text{Li}_2\text{CO}_3$  as a side product is not unexpected. The thermal decomposition of  $\text{Li}_2\text{O}_2$  and release of  $\text{O}_2$  stimulates a reaction with  $\text{CO}_2$  in air to form  $\text{Li}_2\text{CO}_3$  *via* the two-part mechanism seen below in Equations 3.4 and 3.5. There is no evidence of  $\text{Li}_2\text{O}$  Bragg peaks in the XRD patterns at any temperature, the  $\text{Li}_2\text{CO}_3$  peaks being more prominent. This indicates that the  $\text{Li}_2\text{O}$  intermediate phase readily reacts to form  $\text{Li}_2\text{CO}_3$ .

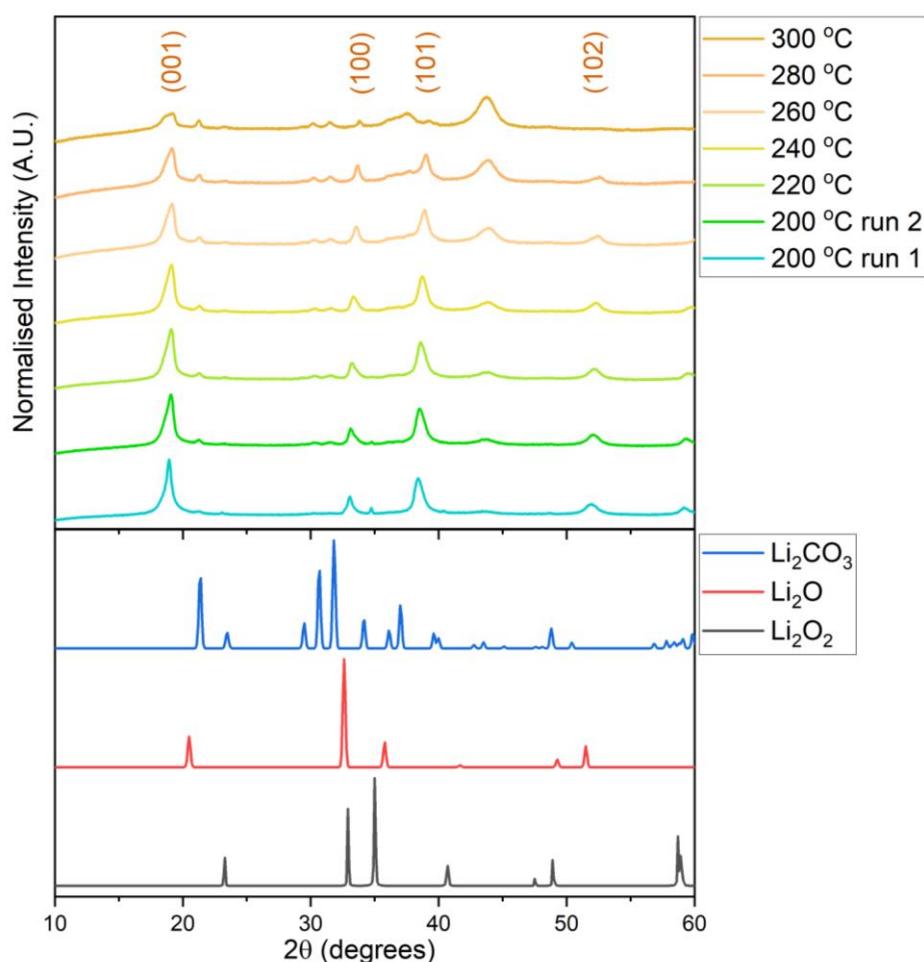


**Figure 3.0.20:** XRD patterns of  $\text{Ni}_{0.8}\text{Mn}_{0.1}\text{Co}_{0.1}(\text{OH})_2$  heated with  $\text{Li}_2\text{O}_2$  in the 200-300  $^\circ\text{C}$  temperature range with reference patterns of three common lithium species in the system:  $\text{Li}_2\text{O}_2$ ,  $\text{Li}_2\text{CO}_3$  and  $\text{LiOH}$  acquired from ICSD.

Upon heating to 850 °C, it can be seen that above 500 °C a poorly crystalline  $\alpha$ -NaFeO<sub>2</sub> layered phase is dominant, with peaks for the rocksalt intermediate phase appearing as an impurity at temperatures above 750 °C (Figure 3.0.21). A gradual increase in layer-order crystallinity can be observed through minor increases in peak splitting in the (108)/(110).

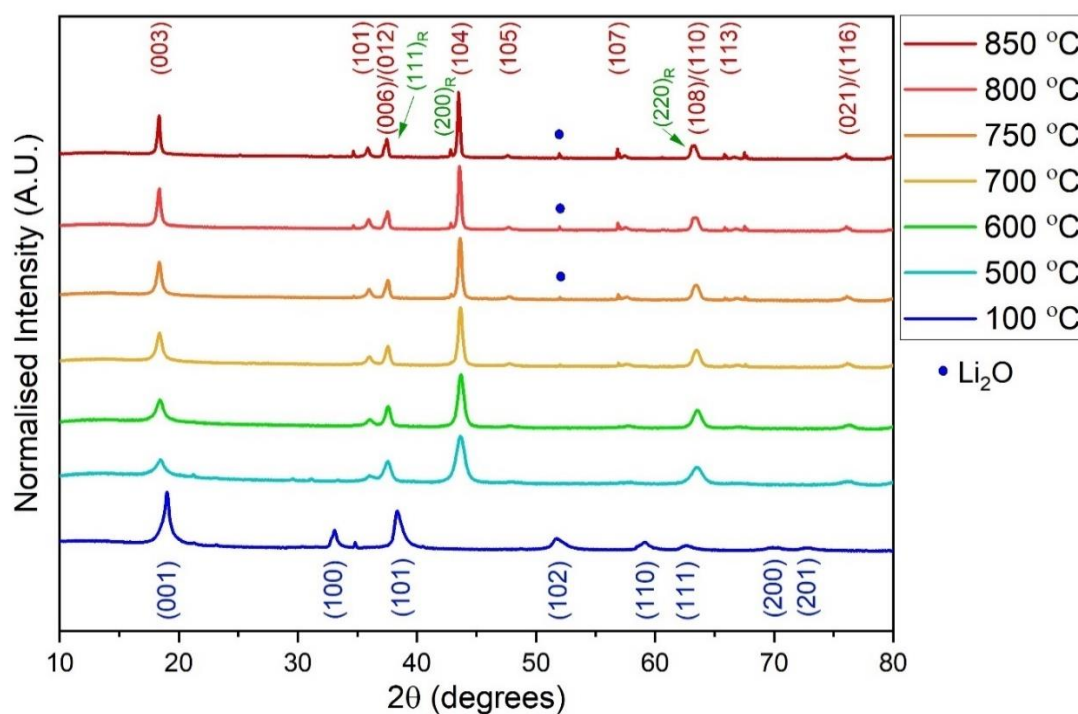


**Figure 3.0.21:** XRD patterns of Ni<sub>0.8</sub>Mn<sub>0.1</sub>Co<sub>0.1</sub>(OH)<sub>2</sub> heated with Li<sub>2</sub>O<sub>2</sub> between 100-850 °C, with the different Bragg peaks highlighted for each phase and the Li<sub>2</sub>O peaks indicated with a blue circle.

The PANalytical X'Pert<sup>3</sup> experiments conducted with LiOH and Li<sub>2</sub>O<sub>2</sub> suggests that a poorly-crystalline  $\alpha$ -NaFeO<sub>2</sub> layered LiNi<sub>0.8</sub>Mn<sub>0.1</sub>Co<sub>0.1</sub>O<sub>2</sub> phase is present at and above 500 °C. XRD analysis into Ni<sub>0.8</sub>Mn<sub>0.1</sub>Co<sub>0.1</sub>(OH)<sub>2</sub> heated with Li<sub>2</sub>O<sub>2</sub> suggests the formation of a disordered  $\alpha$ -NaFeO<sub>2</sub> layered LiNi<sub>0.8</sub>Mn<sub>0.1</sub>Co<sub>0.1</sub>O<sub>2</sub> phase at 400 °C, indicated by presence of the (003) peak at ~18°, whereas Ni<sub>0.8</sub>Mn<sub>0.1</sub>Co<sub>0.1</sub>(OH)<sub>2</sub> calcined with LiOH reveals the formation of a rocksalt intermediate phase at 300-400 °C. It is hypothesised that it is the decomposition of Li<sub>2</sub>O<sub>2</sub> at lower temperatures (250-400 °C) than LiOH (450-600 °C) facilitates the partial intercalation of Li<sup>+</sup> ions into the transition metal oxide structure, forming the disordered  $\alpha$ -NaFeO<sub>2</sub> layered phase in the Li<sub>2</sub>O<sub>2</sub> sample, but not the LiOH sample. Due to the overlap of the (001) peak of Ni<sub>0.8</sub>Mn<sub>0.1</sub>Co<sub>0.1</sub>(OH)<sub>2</sub> and the (003) peak of LiNi<sub>0.8</sub>Mn<sub>0.1</sub>Co<sub>0.1</sub>O<sub>2</sub>, it is possible the peak at ~18° consists of two phases. Further investigations utilising high-temperature synchrotron X-ray or powder neutron analysis would provide the necessary insight that cannot be achieved at a lab level.

### 3.3.4. – Increasing the Throughput for the Microwave Calcination of NMC-811

It was hypothesised that increasing the amount of  $\text{Ni}_{0.8}\text{Mn}_{0.1}\text{Co}_{0.1}(\text{OH})_2$  and  $\text{Li}_2\text{O}_2$  per volume of crucible would increase the partial pressure of oxygen within the crucible. This may further promote the formation of  $\text{Ni}^{3+}$  and  $\text{Ni}^{4+}$  ions within the system, thus reducing the presence of  $\text{Ni}^{2+}$  ions and the resultant cation mixing. The increase in NMC mass per crucible is also of interest in scaling up synthesis. Previous experiments in Chapter 3 described the calcination of 1-2 mmol of  $\text{NMC}(\text{OH})_2$  with a 3 mol% excess  $\text{Li}_2\text{O}_2$  in a 20 mL crucible, which equates to the formation of 46.1-92.2 mL of oxygen gas at 850 °C during the thermal decomposition of  $\text{Li}_2\text{O}_2$ . This would increase the oxygen content in the muffle furnace to 22.7% or 24.5% respectively (up from 21% at RTP). In this Section, 4 mmol of  $\text{NMC}(\text{OH})_2$  with 3 mol% excess  $\text{LiOH}$  or  $\text{Li}_2\text{O}_2$  was calcined in a 2.5 mL crucible, which would produce 184.3 mL of oxygen gas, increasing the oxygen content in the furnace to 28.0%. Increasing the oxygen content within the crucible and furnace would suggest a higher degree of cation ordering could be achieved. An optimisation experiment was conducted over a temperature and duration range of 750-850 °C and 3-5 hours. The optimisation of calcination temperature for  $\text{Ni}_{0.8}\text{Mn}_{0.1}\text{Co}_{0.1}(\text{OH})_2$  with a calcination period of 5 hours, with the XRD study seen in Figure 3.0.22 and Figure 3.0.23 for the  $\text{LiOH}$  and  $\text{Li}_2\text{O}_2$  respectively.

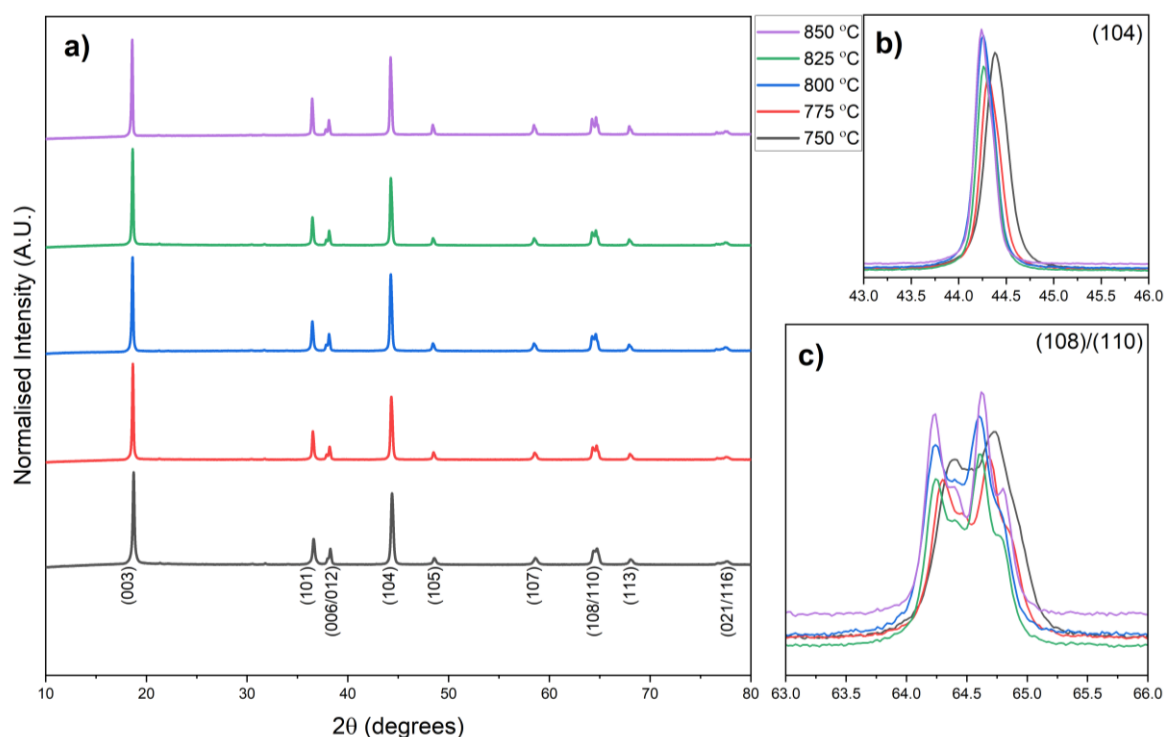


**Figure 3.0.22:** (a) XRD patterns of  $\text{LiNi}_{0.8}\text{Mn}_{0.1}\text{Co}_{0.1}\text{O}_2$ , calcined with  $\text{LiOH}$  in a 2.5 mL crucible for 5 hours at 750-850 °C. The (104) peak and (108)/(110) peak doublet are enclosed in (b) and (c).

All samples calcined from 750-850 °C yielded an  $\alpha$ -NaFeO<sub>2</sub> layered lithium transition metal oxide phase, irrespective of lithium salt (LiOH or Li<sub>2</sub>O<sub>2</sub>). X-ray diffraction data was collected for the NMC samples calcined with LiOH for 5 hours at 750-850 °C (Figure 3.0.22). All samples observed splitting of the (108)/(110) peak doublet, indicating a crystalline structure. The (104) peaks displayed in Figure 3.0.22.b) are normalised against the (003) peak, with (003)/(104) ratios of 1.32-1.64 observed for the samples calcined at 750-850 °C. The sample calcined at 775 °C having the highest ratio of 1.64. Similarly, the Ni<sub>0.8</sub>Mn<sub>0.1</sub>Co<sub>0.1</sub>(OH)<sub>2</sub> samples calcined with Li<sub>2</sub>O<sub>2</sub> displayed ordering within the layers through peak splitting in the (108)/(110) peak doublet in the 775, 800, 825 and 850 °C samples (Figure 3.0.23), albeit to a lesser degree. The (003)/(104) peak ratios (1.32-1.44) were marginally less than the equivalent samples calcined with LiOH, suggesting greater crystallographic structuring during calcination.

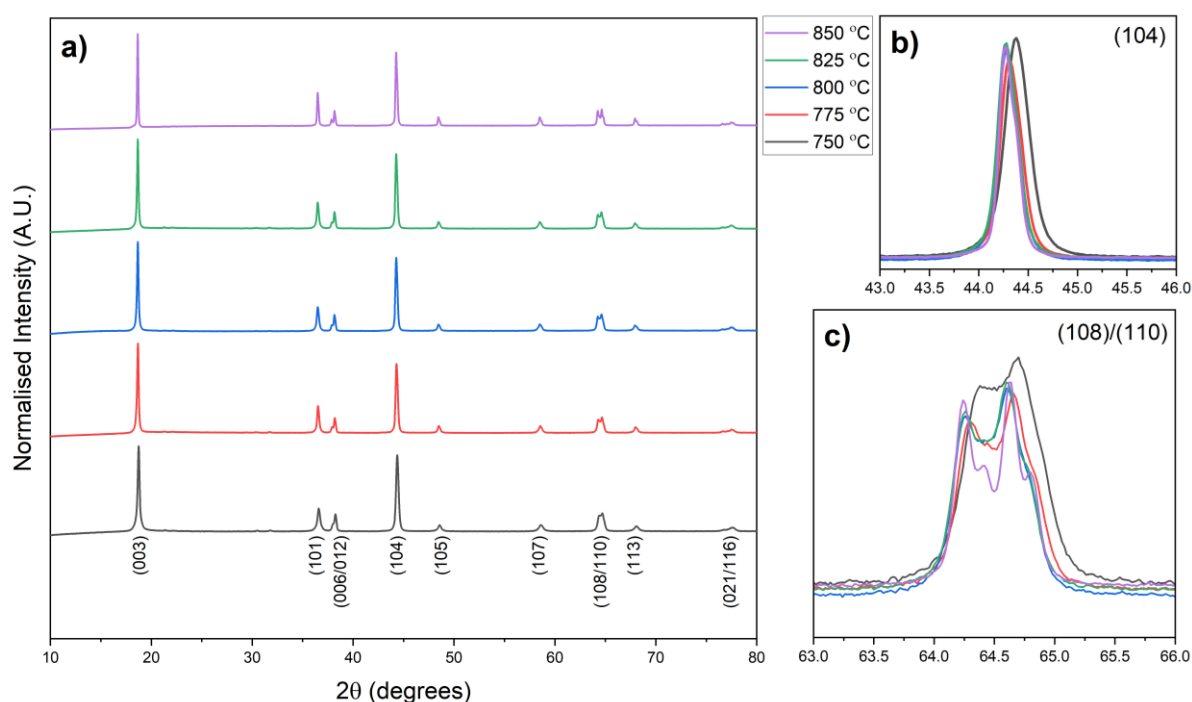


**Figure 3.0.23:** (a) XRD patterns of LiNi<sub>0.8</sub>Mn<sub>0.1</sub>Co<sub>0.1</sub>O<sub>2</sub>, calcined with Li<sub>2</sub>O<sub>2</sub> in a 2.5 mL crucible for 5 hours at 750-850 °C. The (104) peak and (108)/(110) peak doublet are enclosed in (b) and (c).

A calcination duration optimisation was conducted for 3-5 hours at 775 °C, with the XRD profiles for all LiOH and Li<sub>2</sub>O<sub>2</sub> samples yielding the  $\alpha$ -NaFeO<sub>2</sub> layered structure (Figure 3.0.24 and Figure 3.0.25). The (003)/(104) peak ratios for the LiOH and Li<sub>2</sub>O<sub>2</sub> samples reveal values of ~1.68 and ~1.43 respectively for all reaction durations trialled. A similar degree of peak splitting in the (108)/(110) doublet was observed for both LiOH and Li<sub>2</sub>O<sub>2</sub> samples over the 3-5 hour calcination periods,

indicating a similar degree of crystallinity. Rietveld refinement was conducted on all samples in order to gain further insight into the samples.

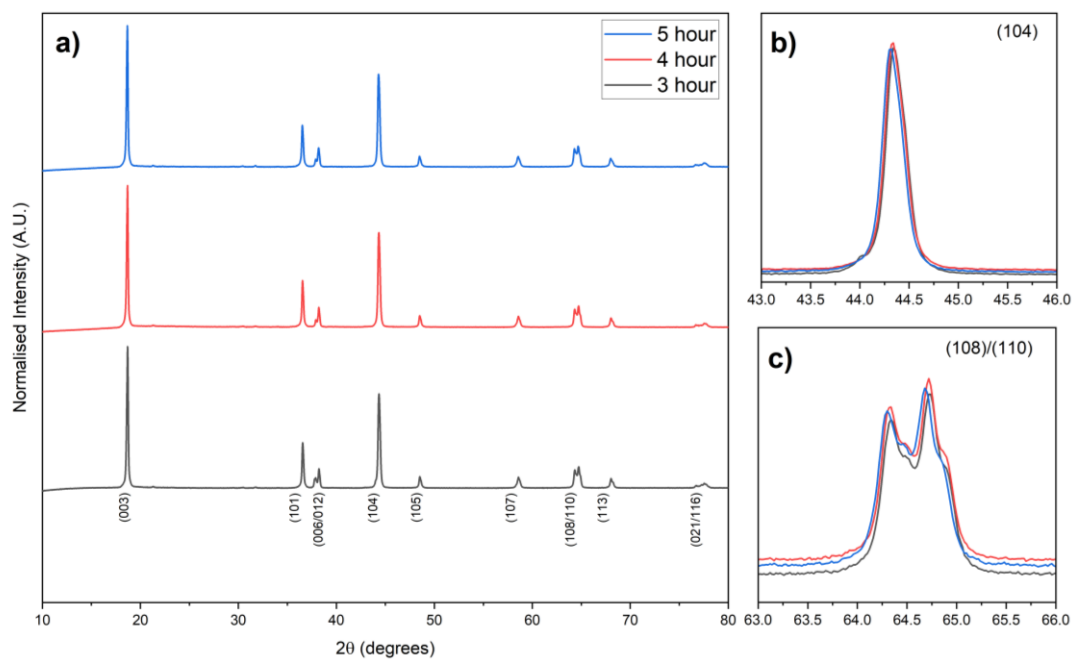


**Figure 3.0.24:** (a) XRD patterns of  $\text{LiNi}_{0.8}\text{Mn}_{0.1}\text{Co}_{0.1}\text{O}_2$ , calcined with  $\text{LiOH}$  in a 2.5 mL crucible for 3-5 hours at  $775^\circ\text{C}$ . The (104) peak and (108)/(110) peak doublet are enclosed in (b) and (c).

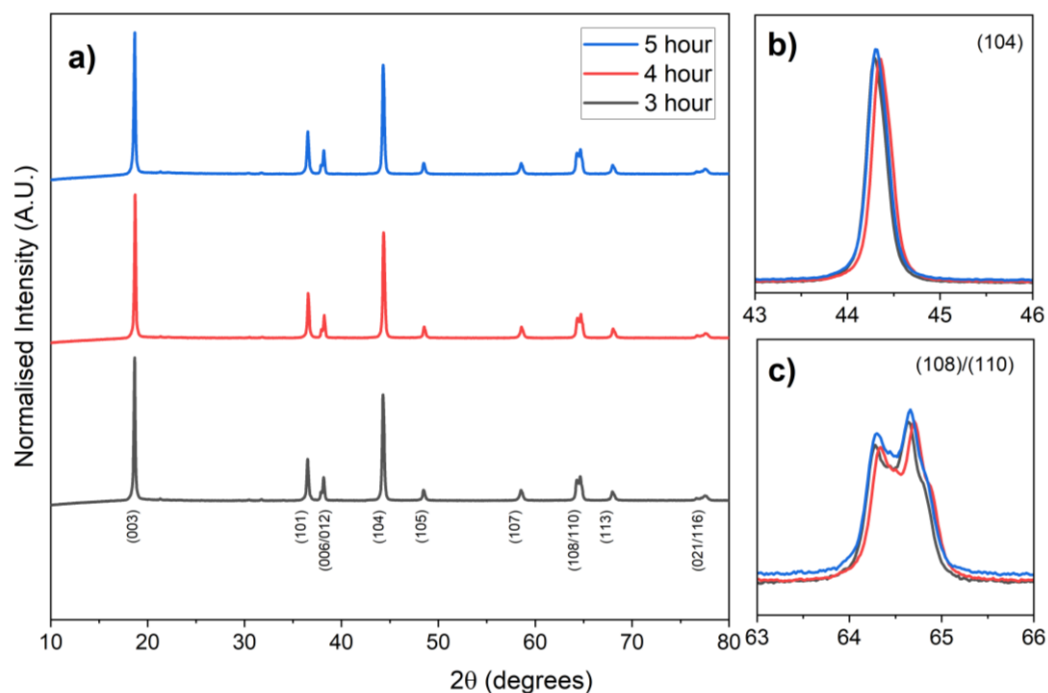


**Figure 3.0.25:** (a) XRD patterns of  $\text{LiNi}_{0.8}\text{Mn}_{0.1}\text{Co}_{0.1}\text{O}_2$ , calcined with  $\text{Li}_2\text{O}_2$  in a 2.5 mL crucible for 3-5 hours at  $775^\circ\text{C}$ . The (104) peak and (108)/(110) peak doublet are enclosed in (b) and (c).

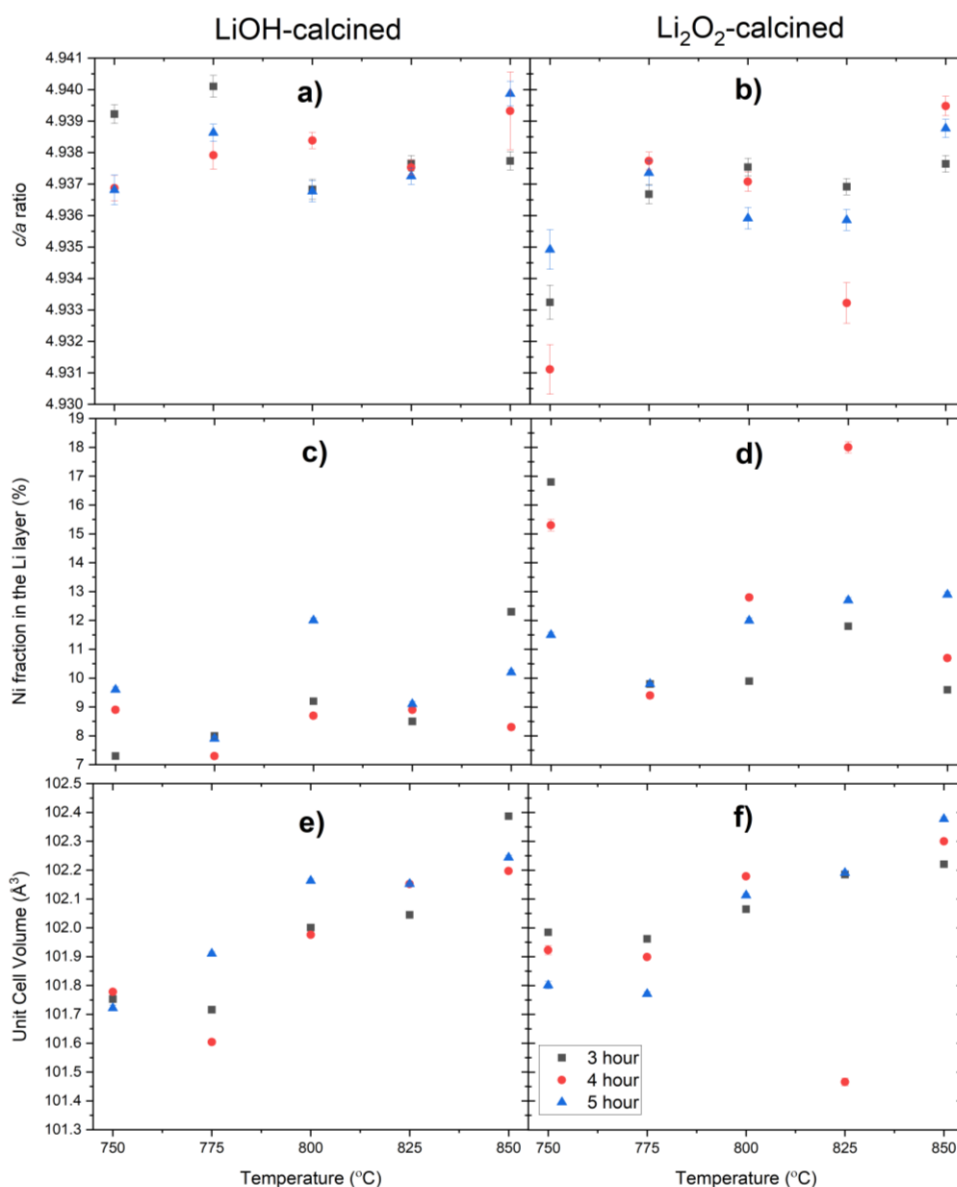


**Figure 3.0.26:** The Rietveld refinement results for the optimisation experiment conducted in the 2.5 mL alumina crucible, featuring the  $c/a$  ratio (**a, b**); the fraction of Ni in the Li layer (**c, d**); and the unit cell volume (**e, f**) for samples calcined with LiOH (**a, c, e**) and  $\text{Li}_2\text{O}_2$  (**b, d, f**). Error bars are present for all graphs but may not be visible due to the small magnitude of the standard deviation.

The Rietveld refinement results shown in Figure 3.0.26 indicates that samples calcined with LiOH have a consistently higher  $c/a$  ratio (4.937-4.940) than their equivalent  $\text{Li}_2\text{O}_2$ -calcined samples (4.931-4.940). The  $c/a$  ratios indicate that LiOH decreases the degree of cation mixing, confirmed by Figure 3.0.26.c) and d), with the degree of cation mixing quantified as 7.1-12.3% for the LiOH samples and 9.4-16.8% for the  $\text{Li}_2\text{O}_2$  samples. There is no clear relationship between the  $c/a$  ratio, the degree of cation mixing and calcination conditions (*i.e.* temperature and duration) from Figure 3.0.26.a)-d).

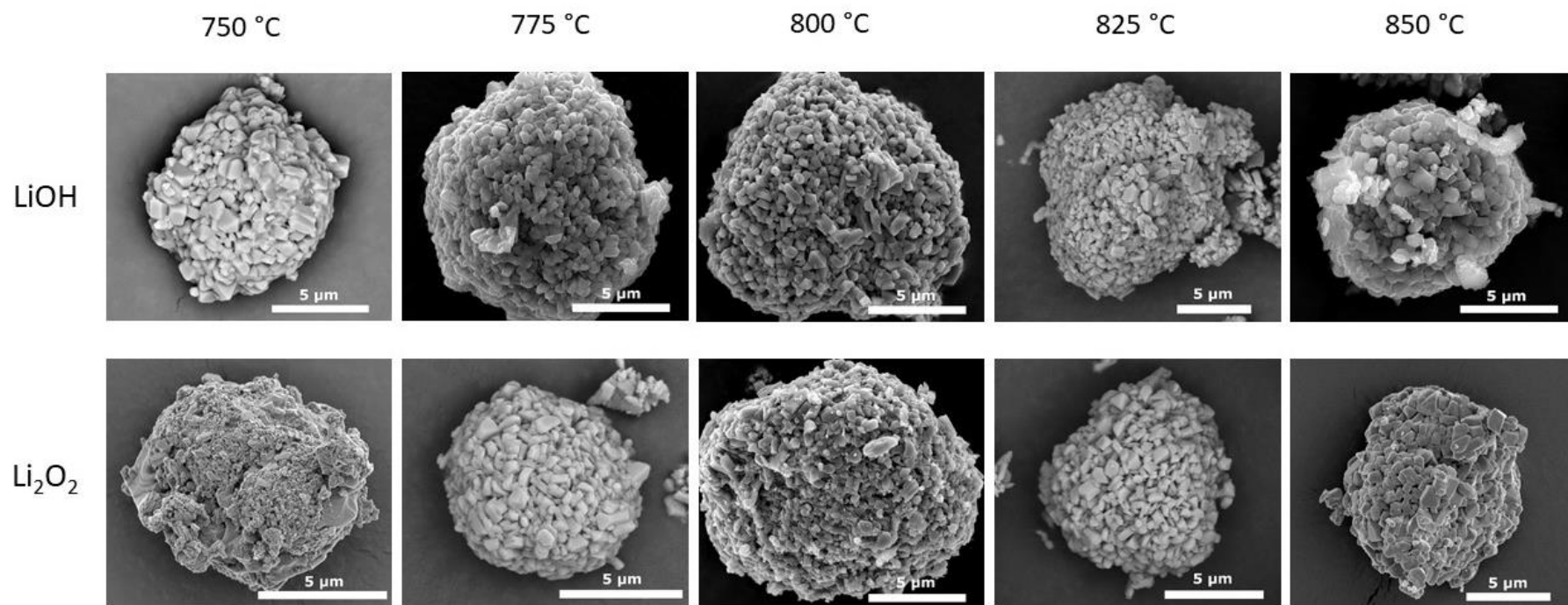


**Figure 3.0.27:** SEM images of  $\text{LiNi}_{0.8}\text{Mn}_{0.1}\text{Co}_{0.1}\text{O}_2$  secondary particles calcined with LiOH or  $\text{Li}_2\text{O}_2$  for 5 hours at a range of temperatures 750-850 °C.

The calculated unit cell volume for each sample is displayed in Figure 3.0.26.e) and f), and shows an increase in volume with temperature, regardless of calcination duration, with the exception of the 825 °C, 4-hour sample, which was found to have a reduced *c*- and *a*- axis, resulting in a reduced unit cell volume, which is thought to be a result of an abnormal .

Secondary particle assemblies were analysed *via* SEM and depicted in Figure 3.0.27. These secondary particles have a quasi-spherical morphology with a diameter of 9-12  $\mu\text{m}$ , which indicates that the secondary particle morphology was maintained from the  $\text{Ni}_{0.8}\text{Mn}_{0.1}\text{Co}_{0.1}(\text{OH})_2$  precursor. The primary particles appear to be a similar size for both Li salts, aside from the 850 °C samples which have marginally larger primary particles with evidence of a greater number of voids between the primary particles. XRD analysis Energy Dispersive Spectroscopy (EDS) analysis, shown in Figure 3.0.28, has carbon, Ni, Mn and Co mapped as purple, blue, yellow and green respectively suggests the presence of residual  $\text{Li}_2\text{CO}_3$  in the sample calcined at 750 °C (the thermal decomposition temperature of  $\text{Li}_2\text{CO}_3$  is 680-780 °C). The secondary particle assemblies depicted in Figure 3.0.29 show 8-12  $\mu\text{m}$ , quasi-spherical secondary particles of  $\text{LiNi}_{0.8}\text{Mn}_{0.1}\text{Co}_{0.1}\text{O}_2$  calcined for 3-5 hours at 775 or 800 °C. A similar degree of voids between primary particles is observed in all samples, with the exception of the samples calcined at 775 °C with LiOH, which had a smaller degree of voidage for all calcination durations trialled.

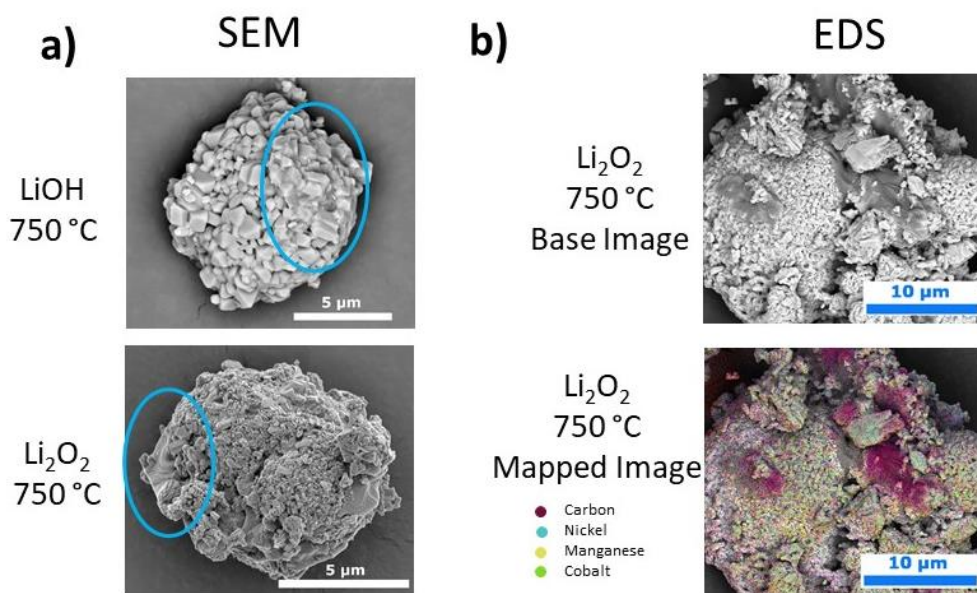


**Figure 3.0.28:** SEM and EDS images of  $\text{LiNi}_{0.8}\text{Mn}_{0.1}\text{Co}_{0.1}\text{O}_2$  secondary particles calcined with LiOH or  $\text{Li}_2\text{O}_2$  for 5 hours at 750 °C, with an amorphous material indicated by a blue oval in (a). EDS analysis was also conducted in (b), with each of the elements indicated by colour-key.

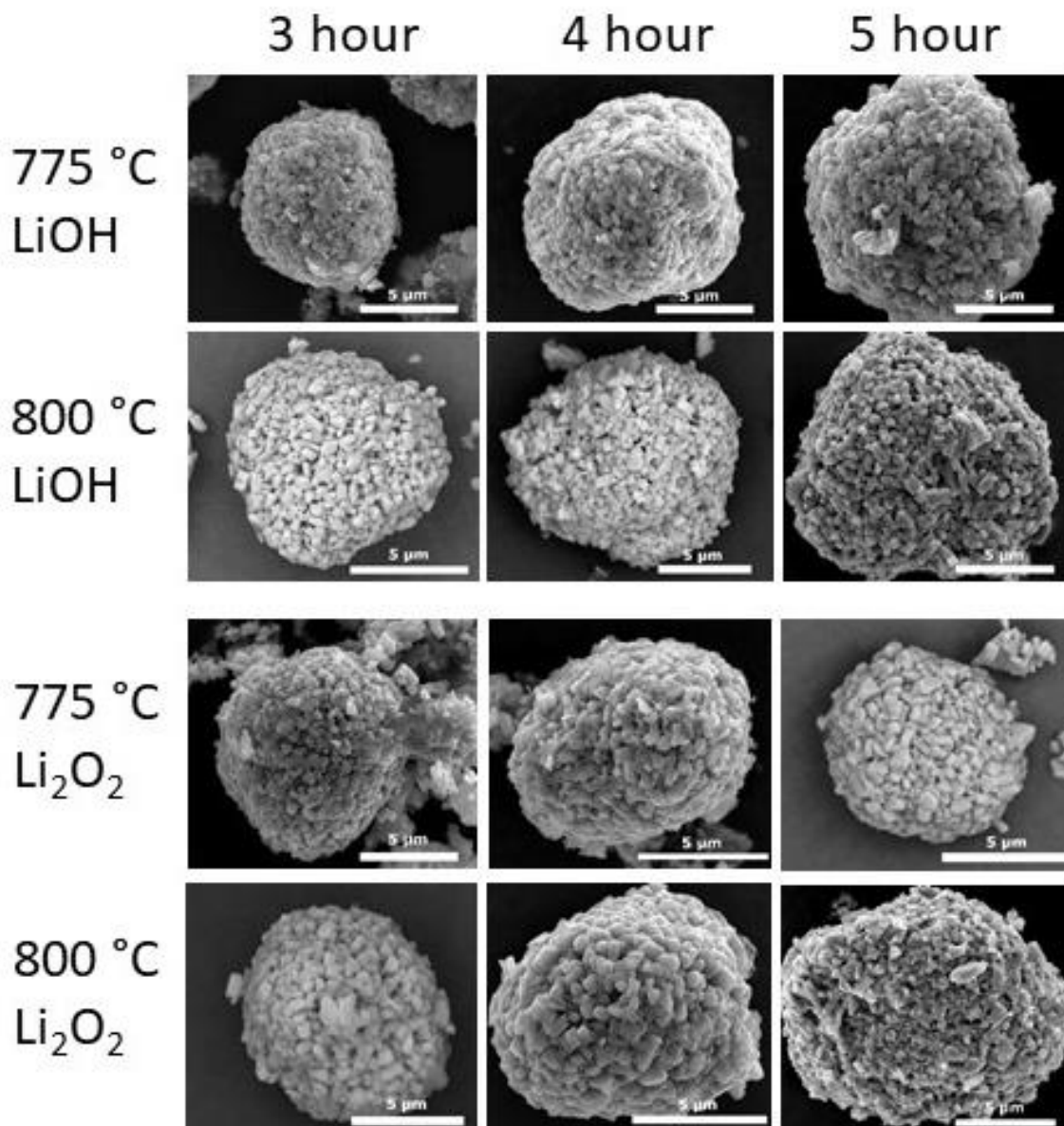


**Figure 3.0.29:** SEM images of  $\text{LiNi}_{0.8}\text{Mn}_{0.1}\text{Co}_{0.1}\text{O}_2$  secondary particles calcined with  $\text{LiOH}$  or  $\text{Li}_2\text{O}_2$  for 5 hours at a range of temperatures 750-850 °C, labelled.

Half-cells were constructed for samples calcined in the small, 2.5 mL crucible at 750, 775 and 800 °C for 4 hours. These half-cells were cycled at C/20 for two formation cycles followed by 98 cycles at a cycling rate of C/2. The capacity retention data (Figure 3.0.30) shows the sample calcined at 800 °C has a higher capacity than the 750 and 775 °C samples, with an initial C/20 discharge capacity of 202.6 mAh g<sup>-1</sup> (compared to 156.6 and 171.3 mAh g<sup>-1</sup>). However, when cycled at C/2, the capacity retention over the 98 cycles is 53.4% compared to 78.7 and 82.9% for 800, 750 and 775 °C-calcined samples. Cycling was conducted at room temperature so is exposed to temperature fluctuations, which result in capacity oscillations.

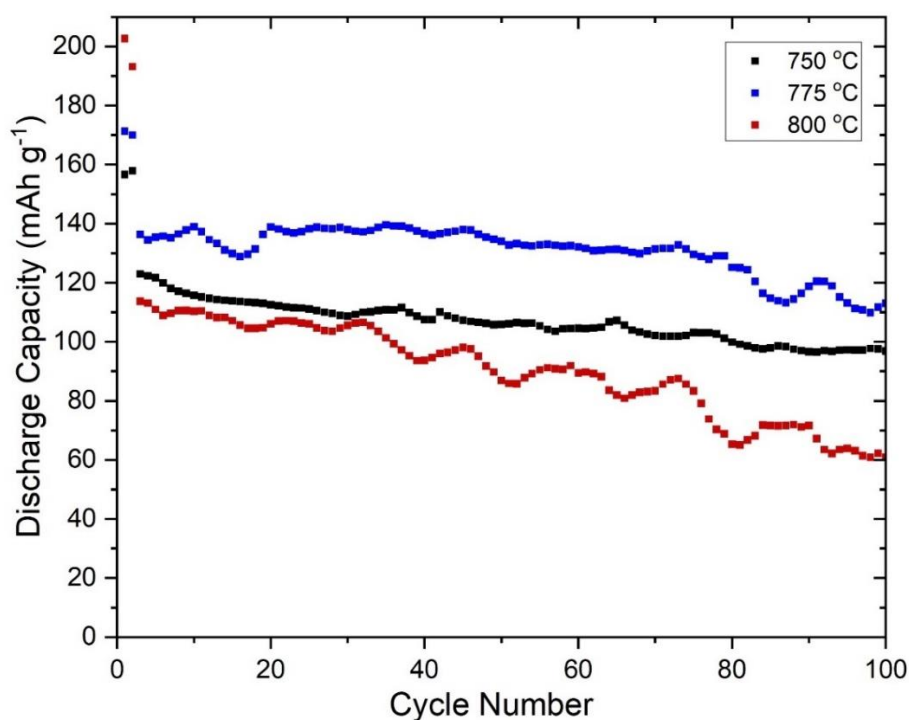


**Figure 3.0.30:** Capacity retention over 100 cycles of half-cells cycled with a voltage window of 3.0-4.3 V, the first two cycles at C/20, the following 98 conducted at C/2. The NMC-811 cathode material was calcined for 5 hours with a Li<sub>2</sub>O<sub>2</sub> lithium source at a temperature of 750, 775 or 800 °C.

The voltage profile (Figure 3.0.31) below shows a large voltage plateau in the first cycle profile at *ca.* 3.60-3.65 V in all samples, which raises to *ca.* 3.70-3.80 V in subsequent cycles, with the average voltage increasing with the number of cycles, indicative of an increase in resistance within the cell. There is also a small overpotential peak prior to delithiation seen in the later cycles of the 750 and 775 °C-calcined samples, which is theorised to be associated with the formation of surface lithium carbonate [75].

The differential capacity profiles (Figure 3.0.32) show that the 775 °C sample has a larger area under the curve than the 750 °C, reaffirming the larger charging and discharging capacity observed for this sample. There are two charging peaks at *ca.* 3.75 V and 4.05 V which are indicative of the H1-M and M-H2 phase transitions that occur during cycling. There is evidence for polarisation evolution between the first cycle (at C/20) and the subsequent cycles at C/2, observed *via* the shift in peak voltage of the peaks, but very little polarisation of the cycles when conducted at C/2. These observations are reflected for the discharge cycle, with peaks at 3.7 V, 4.0 V and 4.25 V, confirming the reduced degree of polarisation.

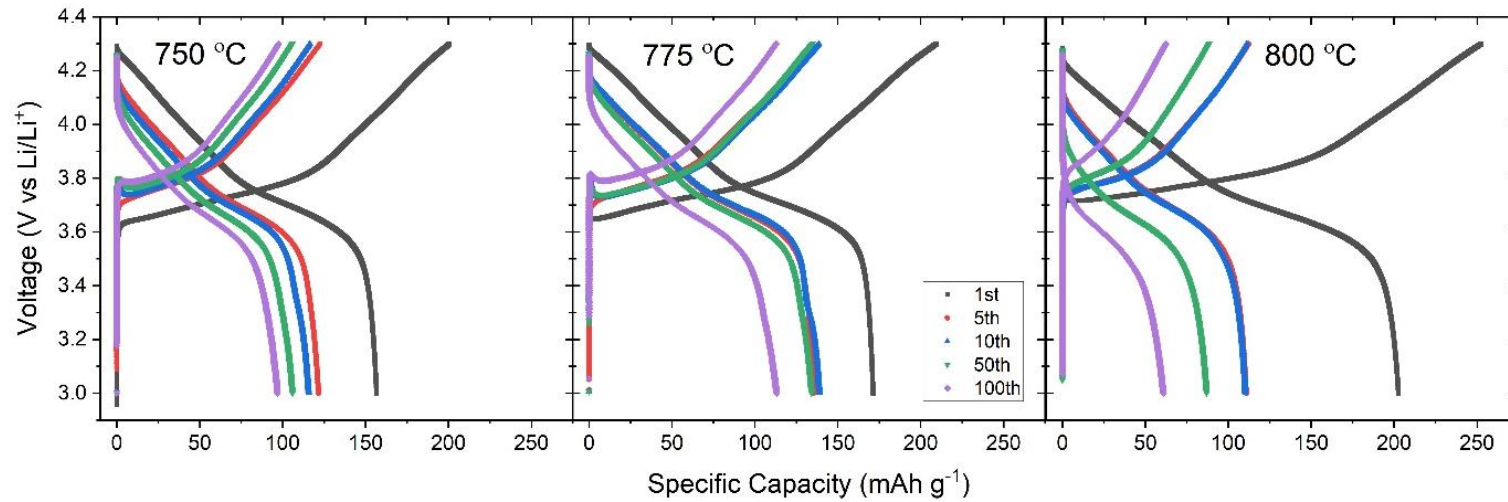


**Figure 3.0.31:** Voltage profiles of half-cells cycled at 3.0-4.3 V in their 1<sup>st</sup>, 5<sup>th</sup>, 10<sup>th</sup>, 50<sup>th</sup> and 100<sup>th</sup> cycle for samples calcined at 750, 775 and 800 °C with Li<sub>2</sub>O<sub>2</sub>.

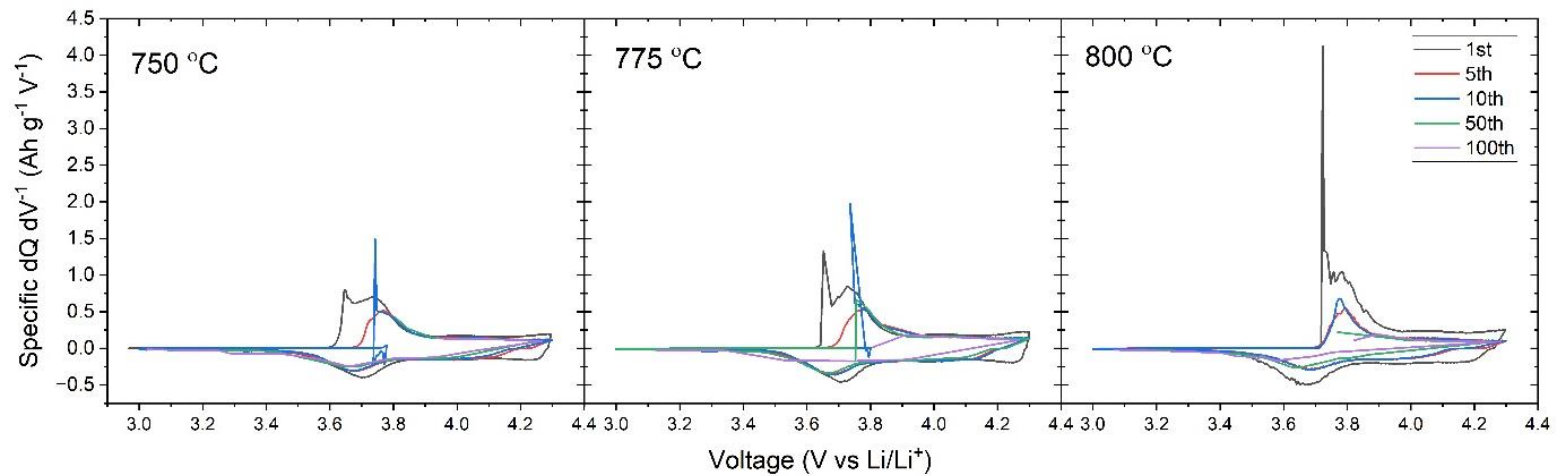


**Figure 3.0.32:** Differential capacity profiles of half-cells cycled at 3.0-4.3 V in their 1<sup>st</sup>, 5<sup>th</sup>, 10<sup>th</sup>, 50<sup>th</sup> and 100<sup>th</sup> cycle for samples calcined at 750, 775 and 800 °C with Li<sub>2</sub>O<sub>2</sub>.

The effect of calcination duration on electrochemical performance was also investigated by comparing NMC-811 samples calcined at 775 °C for 4- and 5- hours. These samples were cycled at 3.0-4.3 V in half-cells against a Li-metal anode for two formation cycles at C/20 followed by 98 cycles at C/2. The initial C/20 discharge capacity of the 5-hour calcined samples (170.2 and 171.3 mAh g<sup>-1</sup>) were higher than those of the 4-hour samples (181.6 and 160.5 mAh g<sup>-1</sup>) for both Li salts: LiOH and Li<sub>2</sub>O<sub>2</sub>. Samples calcined with LiOH had a higher capacity than those calcined with Li<sub>2</sub>O<sub>2</sub>, which was visualised with the dark red and black lines (compared to the pink and grey lines). This improved performance was extended to the capacity retention of the materials, with the samples calcined for 5 hours retaining 86.9% and 82.9% (for LiOH and Li<sub>2</sub>O<sub>2</sub>) of their capacity over 98 cycles at C/2 compared with 76.7% and 49.8% respectively for the 4-hour calcined samples.

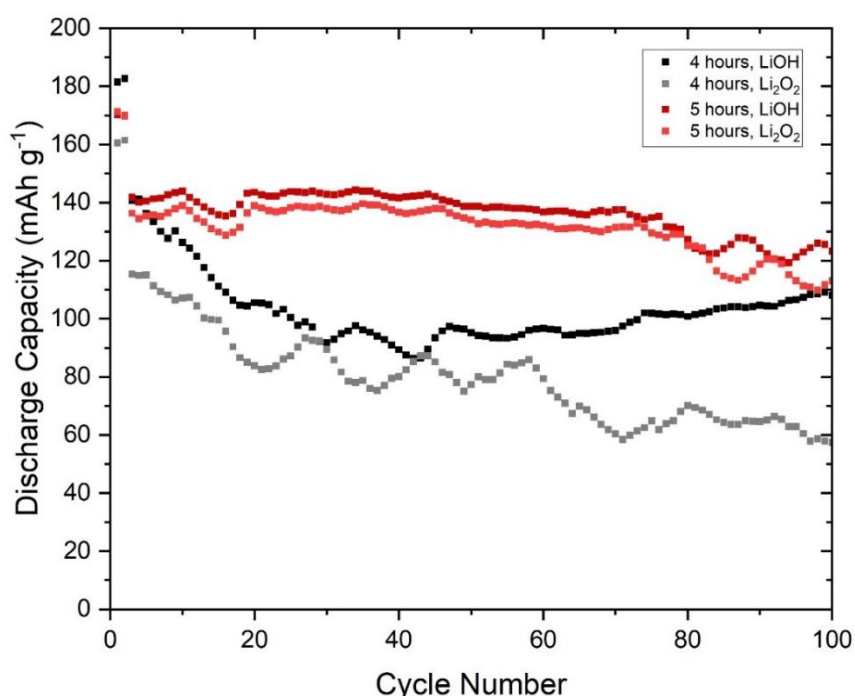


**Figure 3.0.33:** Capacity retention of two cycles at C/20 followed by 98 cycles at C/2 over a voltage window of 3.0-4.3 V. The NMC-811 cathode active material was calcined for 4-5 hours with either LiOH or Li<sub>2</sub>O<sub>2</sub> at a temperature of 775 °C.

The voltage profile (Figure 3.0.34) shows samples calcined for 4 hours (a) and 5 hours (b). The samples calcined for 4 hours experience a significant increase in delithiation voltage over the experiment, with the first cycle having a voltage of *ca.* 3.65 V, and subsequent cycles increasing from *ca.* 3.7-3.9 V. This is accompanied by a reduction in capacity and shorter initial voltage plateau, where the Ni<sup>2+</sup>/Ni<sup>3+</sup> and Ni<sup>2+</sup>/Ni<sup>4+</sup> oxidations would normally occur. This is indicative that the reversibility of nickel oxidation was compromised possibly by Ni<sup>2+</sup> migrating to the lithium layer. The

samples calcined for 5 hours appear to have a smoother voltage profile (Figure 3.0.34). An increase in delithiation voltage was observed, with the first cycle having a voltage of *ca.* 3.65 V (for both LiOH and Li<sub>2</sub>O<sub>2</sub> samples), which increases to *ca.* 3.7 V for the 5<sup>th</sup>, 10<sup>th</sup> and 50<sup>th</sup> cycles. For the 100<sup>th</sup> cycle, the sample calcined with LiOH has a lower delithiation voltage of *ca.* 3.7 V than the sample calcined with Li<sub>2</sub>O<sub>2</sub> (*ca.* 3.8 V). A small peak can be seen prior to delithiation in at *ca.* 3.7-3.8 V in the 5-hour sample calcined with Li<sub>2</sub>O<sub>2</sub> during the 10<sup>th</sup>, 50<sup>th</sup> and 100<sup>th</sup> cycle. This is indicative of the formation of Li<sub>2</sub>CO<sub>3</sub> or a similar residual lithium compound which likely adds to the internal resistance during (de)lithiation. The differential capacity plots (Figure 3.0.35) show the two characteristic peaks of H1-M and M-H2, occurring at *ca.* 3.75 V and 4.05 V during the charging profile. These peaks are also reflected in the discharge profile, occurring at *ca.* 3.7 V and 4.0 V. Polarisation was observed over the 100 cycles, with minor peak shifting observed for the 5-hour samples and notable high-voltage peak shifting observed in the 4-hour samples, most notably in the H1-M peaks.

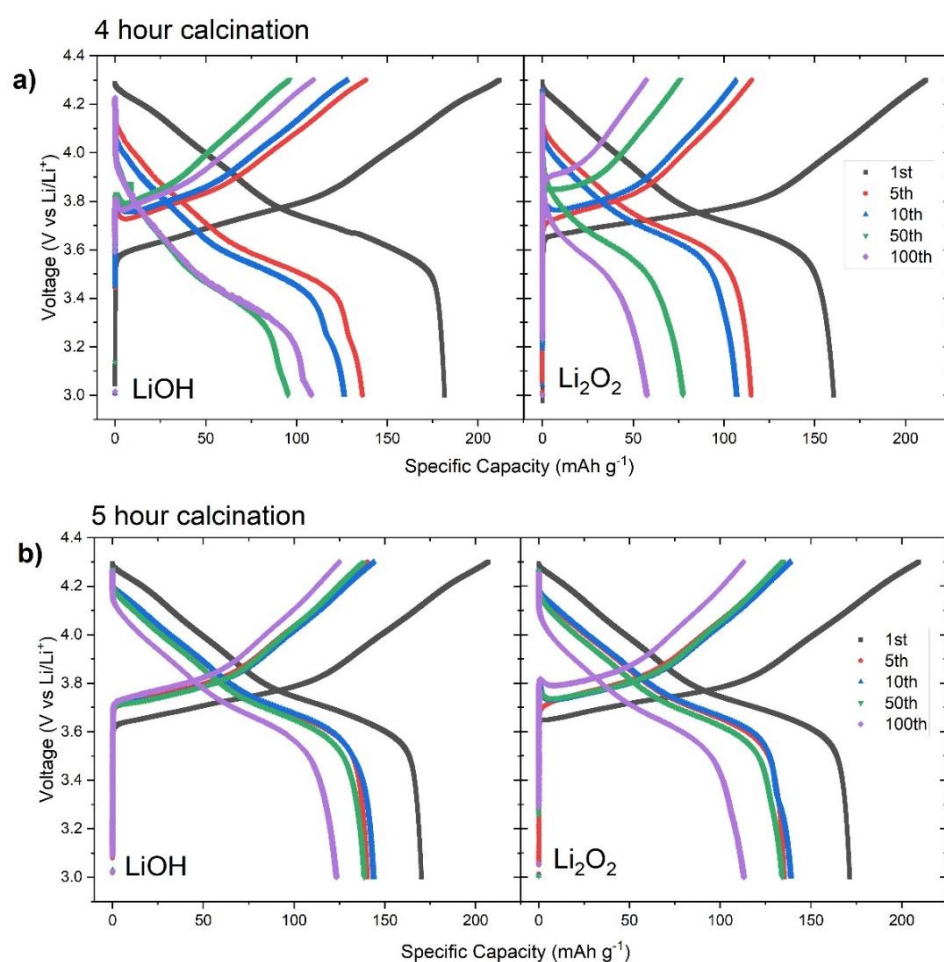


**Figure 3.0.34:** Voltage profiles of half-cells cycled over a voltage window of 3.0-4.3 V in their 1<sup>st</sup>, 5<sup>th</sup>, 10<sup>th</sup>, 50<sup>th</sup> and 100<sup>th</sup> cycle for samples calcined 775 °C with LiOH or Li<sub>2</sub>O<sub>2</sub>. Samples were calcined for 4 hours (a) and 5 hours (b).

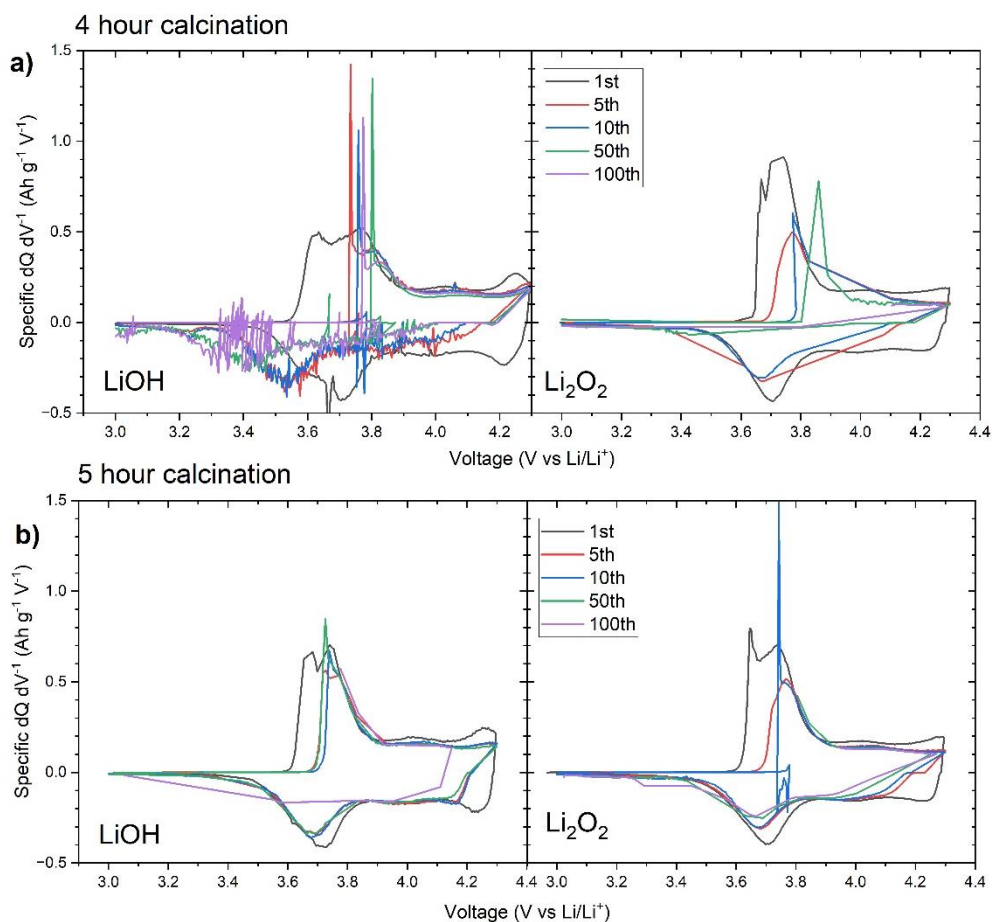


**Figure 3.0.35:** Differential capacity profiles of half-cells cycled over a voltage window of 3.0-4.3 V in their 1<sup>st</sup>, 5<sup>th</sup>, 10<sup>th</sup>, 50<sup>th</sup> and 100<sup>th</sup> cycle for samples calcined 775 °C with LiOH or Li<sub>2</sub>O<sub>2</sub>. Samples were calcined for 4 hours **(a)** and 5 hours **(b)**.

### 3.4. – Concluding Remarks for Chapter 3

The results presented in this chapter demonstrate that microwave-assisted heating can be employed successfully in the calcination of a Ni<sub>0.8</sub>Mn<sub>0.1</sub>Co<sub>0.1</sub>(OH)<sub>2</sub> precursor to reduce the reaction time compared to conventional furnace approaches. A secondary hypothesis was also tested, using an alternative lithium salt, Li<sub>2</sub>O<sub>2</sub>, to increase the partial pressure of oxygen within the crucible in an attempt to replicate the oxygen-rich atmosphere used in the conventional calcination of NMC-811.

Optimisation of the temperature and duration of the heating within the microwave-assisted furnace, was found to be 775 °C for 4 hours, with a heating time of 1 hour. This is a similar temperature to conventional heat treatments of NMC-811 but occurs over a shorter duration than the conventional 10-15 hour calcination [37], [118], [200]. The CEM Phoenix furnace used in this investigation utilises

microwaves to heat a heating element, with no direct coupling of microwaves and the sample occurring. Nevertheless, it is thought that the rapid heating of the heating element reduces the calcination duration with the rapid temperature change causing faster crystallisation and larger crystal growth, evidenced by the larger primary particles observed in SEM analysis. An increase in calcination duration from 3 to 5 hours saw no noticeable change in crystalline or morphological properties, supporting the theory that rapid temperature change causes faster crystallisation and 'maturation' of the lithium interaction and layered crystal structure. When  $\text{Li}_2\text{O}_2$  is used as the lithium source, a smaller 2.5 mL crucible formed more spherical secondary particle assemblies than samples calcined in the larger 20 mL crucible, with a more uniform primary particle size. This may suggest the smaller crucible increases the partial pressure of oxygen within the crucible and aids the formation of the faceted primary particles.

The investigation into the reaction mechanism between  $\text{Ni}_{0.8}\text{Mn}_{0.1}\text{Co}_{0.1}(\text{OH})_2$  and the conventional lithium source, LiOH, found that an intermediate rocksalt phase that arises at 300-400 °C, prior to the formation of the layered  $\alpha\text{-NaFeO}_2$  structure associated with NMC-811 at temperatures above 700 °C. The application of  $\text{Li}_2\text{O}_2$  formed this rocksalt phase at the lower temperature of 200-300 °C. The lower thermal degradation temperature of  $\text{Li}_2\text{O}_2$  (280-400 °C) relative to LiOH (400-650 °C) allowed the integration of lithium into the NMC-811 structure at a lower temperature, but results in a longer duration during which Ni/Li cation mixing can occur within the structure [104] This is evidenced by an increase in the cation mixing from 7.1-12.3% (LiOH samples) to 9.4-16.8% ( $\text{Li}_2\text{O}_2$  samples) and a reduction in the layered ordering of the crystalline structure, with less splitting of the (108)/(110) peak doublet.

An increased capacity was delivered by the 775 °C sample calcined with LiOH for 5 hours when cycled at a rate of C/2 at 3.0-4.3 V (136.3-141.8 mAh g<sup>-1</sup>) along with improved capacity retention (82.9%) compared to an equivalent sample calcined for 4 hours (86.4-140.7 mAh g<sup>-1</sup>, 76.7%). Despite the 4-hour calcination duration being optimal from crystallographic and morphological analysis, these results show that an extended calcination duration can mature the sample and improve its electrochemical performance. One explanation for this would be the additional heating period having an effect on the positioning of the primary particles, potentially increasing the packing density within the secondary particle. BET analysis could be conducted to determine the extent of this in future work.

When calcined with  $\text{Li}_2\text{O}_2$  as the lithium source, NMC-811 yielded similar capacities when calcined at 775 °C for 5 hours (123.8-141.5 mAh  $\text{g}^{-1}$ , at C/2, 3.0-4.3 V). This demonstrates that  $\text{Li}_2\text{O}_2$  is a viable alternative to LiOH as a lithium source for Ni-rich cathodes, but yields no discernible advantage, confirmed by the similar morphology when comparing the two lithium sources. The crystallographic results indicate that there is a larger degree of cation mixing in equivalent  $\text{Li}_2\text{O}_2$  samples compared to LiOH samples. This, combined with the knowledge of the lower thermal decomposition of  $\text{Li}_2\text{O}_2$  results in a longer period of lithiation within the calcination reaction, suggests that the oxygen gas generated by the thermal decomposition of  $\text{Li}_2\text{O}_2$  does not remain within the crucible, resulting in the same atmosphere for LiOH- and  $\text{Li}_2\text{O}_2$ - calcined samples. Further investigation on this is conducted in Chapter 4.

## 4. Validation of an Optimised Microwave Calcination Procedure

Chapter 3 demonstrated microwave heating as a viable means for calcining Ni-rich cathode materials. The conclusions drawn from Chapter 3 suggested that the optimal temperature of microwave calcination of  $\text{Ni}_{0.8}\text{Mn}_{0.1}\text{Co}_{0.1}(\text{OH})_2$  with either LiOH or  $\text{Li}_2\text{O}_2$  was 775 °C. The optimal calcination duration was between 4-5 hours, with both producing similar first-cycle discharge capacities of 160.5 and 171.3 mAh  $\text{g}^{-1}$  (cycled between 3.0-4.3 V at C/20). Morphologically, electron microscopy alluded greater voids between primary particles for samples calcined with  $\text{Li}_2\text{O}_2$ , which may impede ion mobility within the secondary assemblies. Chapter 4 focuses on comparing an optimised microwave calcination procedure (at 775 °C for 4 hours with either LiOH or  $\text{Li}_2\text{O}_2$ ) against a conventional furnace calcination procedure (at 775 °C for 4 hours with LiOH) to further validate the application of microwave technology and  $\text{Li}_2\text{O}_2$  as an alternative lithium source.

### 4.1. – Validation of Microwave Heating for the Calcination of $\text{Ni}_{0.8}\text{Mn}_{0.1}\text{Co}_{0.1}(\text{OH})_2$

To investigate the use of microwave heating as a route to faster calcination of NMC cathodes, samples were calcined at 775 °C for 4 hours using either LiOH or  $\text{Li}_2\text{O}_2$  as a lithium source and compared to equivalent samples calcined in an air-fed or oxygen-fed tube furnace with LiOH. Previous results in Section 3.3.4. indicates that oxygen gas evolved from the thermal decomposition of  $\text{Li}_2\text{O}_2$  was lost from the crucible. To mimic this, experiments were also conducted in a conventional air-fed tube furnace to compare against microwave heating where oxygen gas may be lost. The two conventionally heated conditions (in an air-fed or oxygen-fed tube furnace) were heated to 775 °C for 4 hours, to allow a direct, like-for-like comparison of the effect of microwave heating; and 12 hours, an average calcination duration for conventionally heated furnaces [37], [88], [118], [167].

XRD patterns of samples prepared using microwave, air-fed and oxygen-fed tube furnace samples are presented in Figure 4.0.1, where all profiles demonstrate an  $\alpha\text{-NaFeO}_2$  layered structure. While samples calcined in oxygen show no evidence for additional phases, samples prepared in the air-fed tube furnace and the microwave furnace indicate the presence of  $\text{Li}_2\text{CO}_3$ , with the small peaks between 20-35° 2 $\theta$ . The (003)/(104) peak ratio qualitatively suggests the oxygen-calcined samples have better cation ordering than the air- and microwave- calcined samples due to the increased

peak ratios of 1.859 and 1.946 for the 4- and 12- hour calcination procedures respectively (compared to 1.555-1.587 for the other samples). All samples have clear splitting of the (108)/(110) peak doublet, with the microwave-calcined and air-calcined samples having a smaller degree of peak splitting than the oxygen-calcined samples, indicating the latter has better ordering between layers.

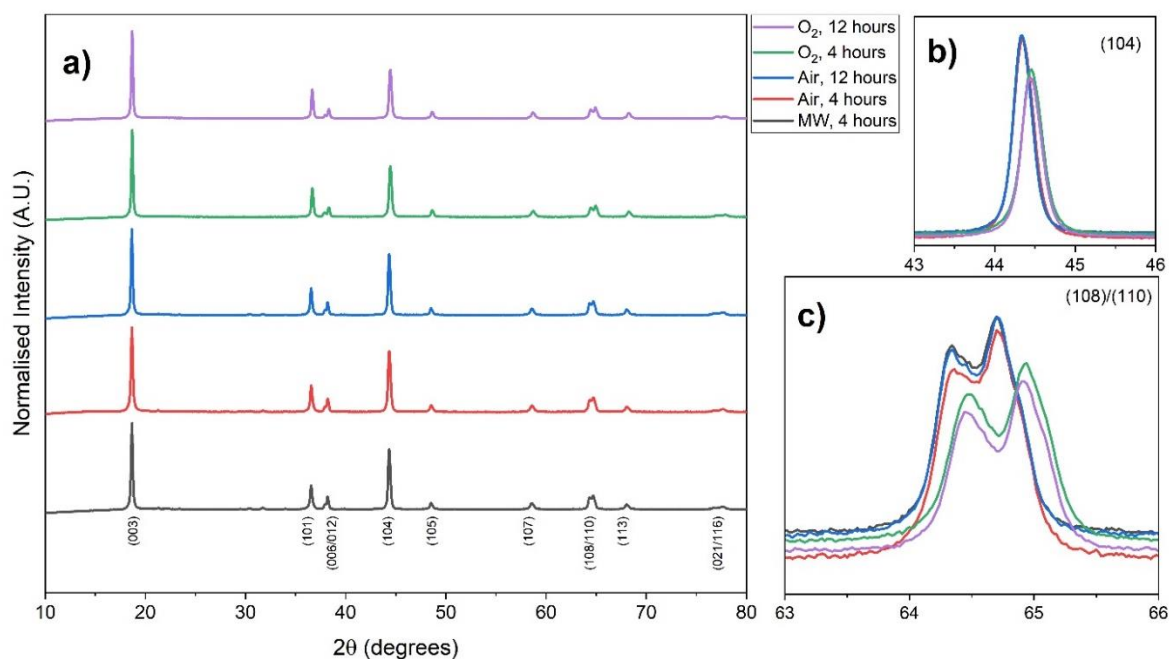


**Figure 4.0.1:** (a) XRD profiles of  $\text{LiNi}_{0.8}\text{Mn}_{0.1}\text{Co}_{0.1}\text{O}_2$  calcined with 3 mol% excess LiOH in a microwave furnace, air-fed tube furnace and oxygen-fed tube furnace at 775 °C for 4 or 12 hours. Magnification of the (104) peak (b) and (108)/(110) peak doublet (c) are included.

SEM revealed the morphology of the particles was similar regardless of the calcination procedure employed, as seen in Figure 4.0.2. The secondary particle assemblies have similar, quasi-spherical morphologies, with diameters of *ca.* 10  $\mu\text{m}$ . The 12-hour oxygen-calcined sample consists of primary particles of similar sizes and morphologies, with electron microscopy indicating good contact between primary particles. The microwave sample yields larger primary particles with more evidence for voids or gaps between primary particles, which may impede ion mobility within the secondary assemblies. It is thought that the larger nanobrick particles with larger voids between primary particles in the microwave sample is a result of the rapid heating experienced in the microwave furnace. The 4-hours samples calcined in air-supplied and oxygen-supplied tube furnaces show similar voids between primary particles when compared to their equivalent 12-hour calcined samples. SEM indicates a thickening of the primary particles as the calcination period increases from 4 hours to 12 hours, which may improve the grain boundary contact between these particles. The effect of oxygen on the calcination can be most clearly seen with respect to this, with primary

particles appearing to sinter together, with voids between primary particles reducing the 12- hour calcination.

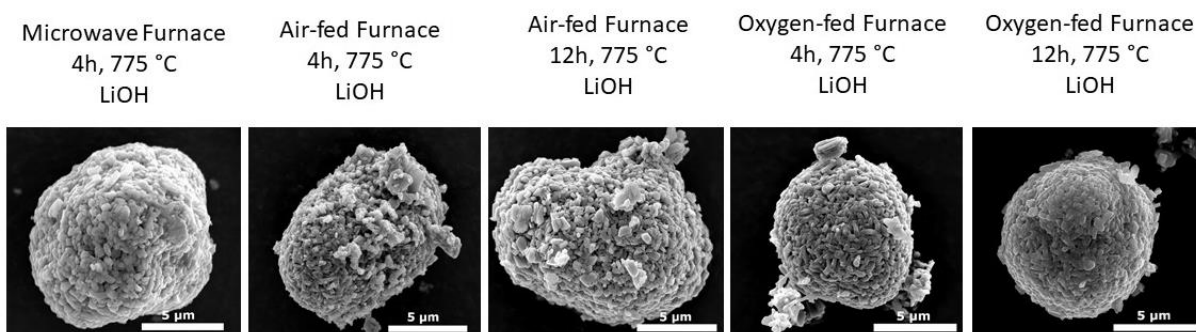


**Figure 4.0.2:** SEM images of  $\text{LiNi}_{0.8}\text{Mn}_{0.1}\text{Co}_{0.1}\text{O}_2$  calcined using different calcination procedures in a microwave furnace, air fed tube furnace or an oxygen fed tube furnace.

#### 4.2. – Validation of the Application of $\text{Li}_2\text{O}_2$ in the Calcination of $\text{Ni}_{0.8}\text{Mn}_{0.1}\text{Co}_{0.1}(\text{OH})_2$

$\text{Li}_2\text{O}_2$  has been demonstrated in Chapter 3 as a potential alternative Li source in the synthesis of Ni-rich cathodes. Here, application of  $\text{Li}_2\text{O}_2$  as a Li source is investigated during the microwave calcination of NMC-811 and compared conventionally-heated tube furnaces, with an air-supplied and oxygen-supplied atmosphere. The  $\text{Ni}_{0.8}\text{Mn}_{0.1}\text{Co}_{0.1}(\text{OH})_2$  precursor was calcined with LiOH or  $\text{Li}_2\text{O}_2$  in a microwave furnace (775 °C, 4 hours) or a conventional, air-supplied or oxygen-supplied tube furnace (775 °C, 12 hours). XRD profiles show all samples confirm the formation of the  $\alpha\text{-NaFeO}_2$  layered oxide structure of  $\text{LiNi}_{0.8}\text{Mn}_{0.1}\text{Co}_{0.1}\text{O}_2$  (Figure 4.0.3). The oxygen furnace produces a phase-pure  $\alpha\text{-NaFeO}_2$  layered oxide phase, whereas there is evidence of  $\text{Li}_2\text{CO}_3$  in the XRD patterns for samples calcined in the air and microwave XRD profiles, evidenced by small peaks in the 20-35° 2 $\theta$  range. Figure 4.0.3.b) shows the sample calcined in an oxygen-supplied tube furnace for 12 hours at 775 °C with LiOH has the largest (003)/(104) ratio with a value of 1.946, indicating a greater degree of cation ordering than the other samples, which have peak ratios of between 1.391 and 1.570. The samples calcined with  $\text{Li}_2\text{O}_2$  have smaller (003)/(104) peak ratios, indicating an increased degree of cation mixing. Most samples have a similar degree of (108)/(110) peak doublet splitting (Figure 4.0.3.c)), indicating a good degree of layered ordering. The exception was the air-calcined sample, which displays little peak splitting, which suggests poor layered ordering and coincides with the smallest (003)/(104) peak ratio observed, indicating this is a poor calcination route for NMC-811 which is to be expected.

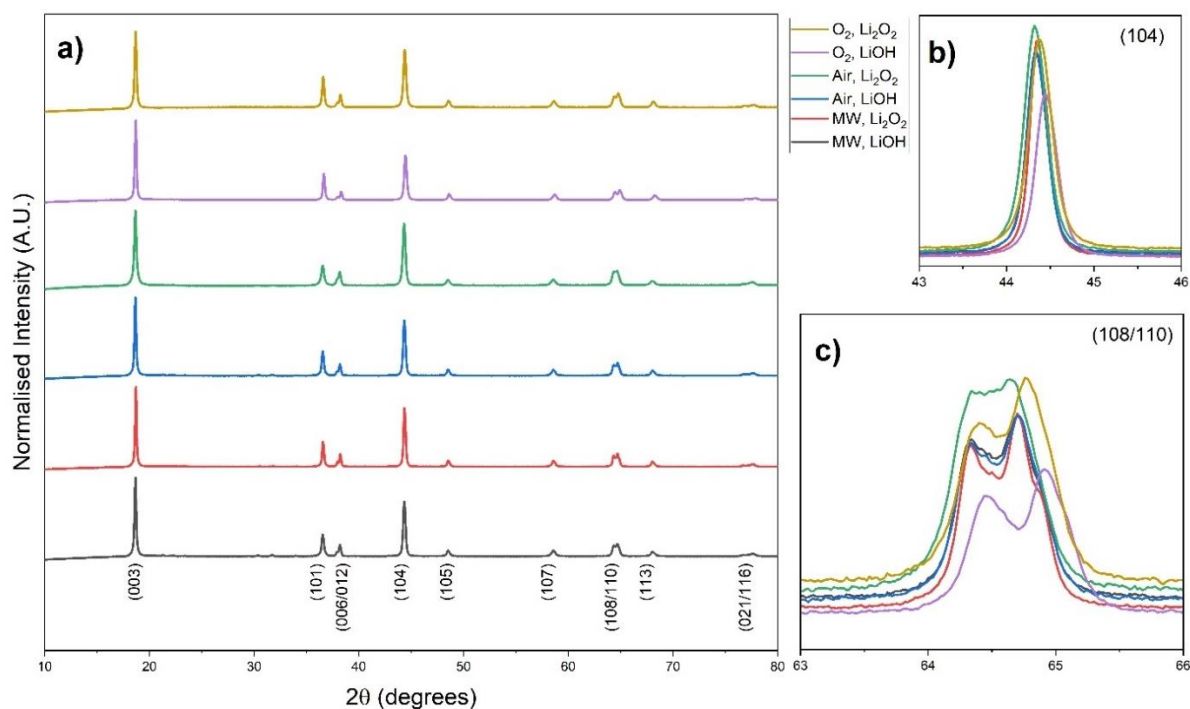


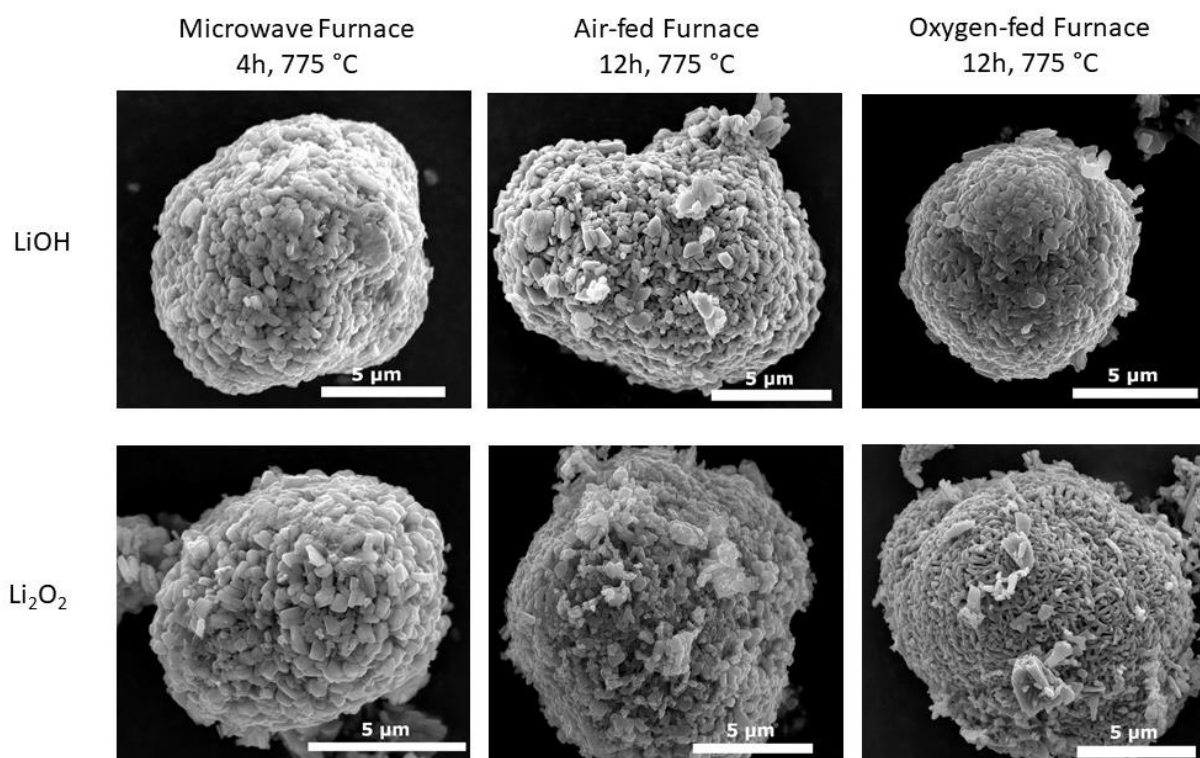
**Figure 4.0.3:** (a) XRD profiles of  $\text{LiNi}_{0.8}\text{Mn}_{0.1}\text{Co}_{0.1}\text{O}_2$  calcined with 3 mol% excess LiOH or  $\text{Li}_2\text{O}_2$  at  $775^\circ\text{C}$ . Microwave calcined samples were calcined for 4 hours, whereas an air-fed or oxygen-fed tube furnace samples were calcined for 12 hours. Magnification of the (104) peak (b) and the (108)/(110) doublet peaks (c) are also included.

Rietveld refinement confirms the use of lithium peroxide during calcination results in an increase in cation mixing (Table 4.0.1, plots in Appendix A.11). The oxygen-calcined sample with LiOH had the smallest value for cation mixing (2.9%) compared to other samples (7.4-9.8%). The  $c/a$  ratio was largest for the oxygen-calcined sample with LiOH (4.947), indicating increased layered ordering within the structure. The air-calcined sample with  $\text{Li}_2\text{O}_2$  was found to have the lowest  $c/a$  ratio of 4.936, whereas the other samples calcined had a  $c/a$  of between 4.938-4.941.

SEM analysis revealed no significant differences in the secondary particle size or morphology, with all samples being quasi-spherical and having a secondary particle diameter of *ca.*  $10\ \mu\text{m}$  (Figure 4.0.4). Similarities between the primary particles of samples calcined in the microwave furnace and the air-fed tube furnace are notable, where larger, faceted particles are observed. The primary particles of the oxygen-calcined sample with LiOH display more densely packed assemblies. In the microwave-calcined samples, the primary particle morphology is similar for both Li sources (LiOH and  $\text{Li}_2\text{O}_2$ ) with large, faceted particles agglomerating to form the secondary particle assembly.  $\text{Li}_2\text{O}_2$  samples calcined in the air-fed and oxygen-fed tube furnace appear to have smaller primary particle sizes compared with their LiOH equivalent samples.

**Table 4.0.1:** Lattice parameters from the Rietveld refinement of  $\text{LiNi}_{0.8}\text{Mn}_{0.1}\text{Co}_{0.1}\text{O}_2$  calcined using a microwave, air-supplied and oxygen-supplied furnace. Estimated standard deviations are included in brackets, where refined.

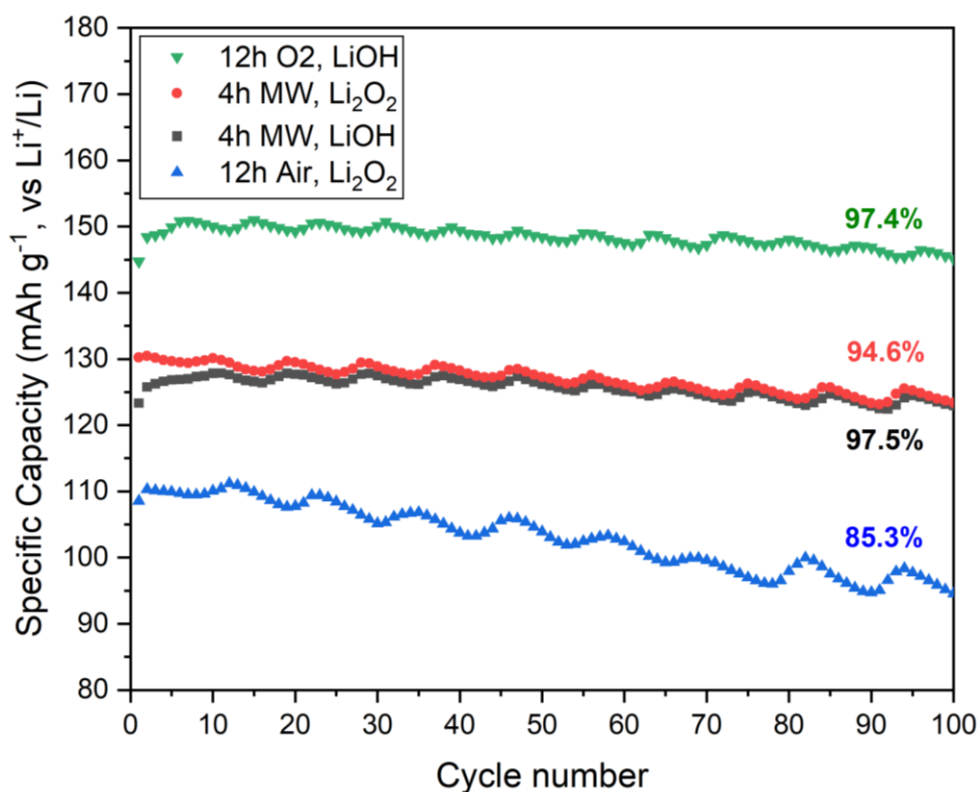
	$a$ -, $b$ - axis (Å)	$c$ - axis (Å)	$c/a$ ratio	Unit cell volume (Å <sup>3</sup> )	Ni fraction in the Li layer (%)	Chi <sup>2</sup> value
Microwave Calcined, 775 °C, 4 hours, LiOH	2.8768(1)	14.2096(3)	4.9395(3)	101.84(6)	7.4(1)	7.340
Microwave Calcined, 775 °C, 4 hours, Li <sub>2</sub> O <sub>2</sub>	2.8776(1)	14.2090(3)	4.9377(3)	101.90(6)	9.4(1)	5.864
Air Calcined, 775 °C, 12 hours, LiOH	2.8754(1)	14.2009(4)	4.9387(4)	101.68(8)	7.4(1)	6.399
Air Calcined, 775 °C, 12 hours, Li <sub>2</sub> O <sub>2</sub>	2.8738(2)	14.1845(7)	4.9357(6)	101.45(1)	9.8(1)	9.466
Oxygen Calcined, 775 °C, 12 hours, LiOH	2.8673(1)	14.1851(5)	4.9472(4)	101.00(8)	2.9(1)	6.628
Oxygen Calcined, 775 °C, 12 hours, Li <sub>2</sub> O <sub>2</sub>	2.8745(1)	14.2044(6)	4.9414(4)	101.65(9)	8.1(1)	7.156



**Figure 4.0.4:** SEM images of  $\text{LiNi}_{0.8}\text{Mn}_{0.1}\text{Co}_{0.1}\text{O}_2$  calcined with LiOH and  $\text{Li}_2\text{O}_2$  using an optimised microwave-heated calcination procedure and equivalent air-fed and oxygen-fed conventionally-heated calcination procedures.

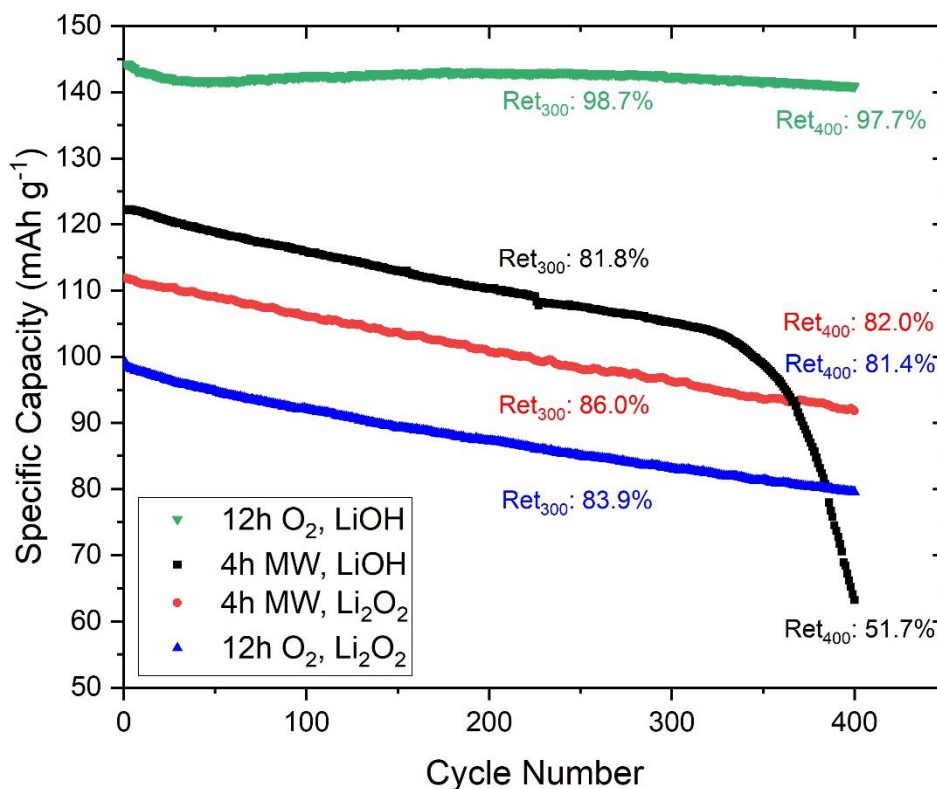
#### 4.3. – Electrochemical Analysis of Microwave Calcination Procedures

Figure 4.0.5 shows the oxygen-calcined sample has the highest discharge capacity over 100 cycles in a voltage window of 3.0-4.2 V at a rate of  $C/2$  (144.6-151.0  $\text{mAh g}^{-1}$ ), with a 100-cycle retention of 97.4%. The two microwave furnace samples (calcined with LiOH or  $\text{Li}_2\text{O}_2$ ) had similar capacities of 122.7-127.5  $\text{mAh g}^{-1}$  and 123.4-130.5  $\text{mAh g}^{-1}$  respectively, achieving a capacity retention of 97.5% and 94.6% over 100 cycles. The similarities in the capacities and capacity retention indicate  $\text{Li}_2\text{O}_2$  can be applied as a lithium source, but little difference in capacity suggests further optimisation is required for the oxygen gas environment generated. The air-calcined sample delivered the smallest a capacity of 94.1-111.2  $\text{mAh g}^{-1}$  and a 100-cycle capacity retention of 85.3%. The electrochemical data suggests that particles where good contact exists between primary particles (as observed in SEM) results in a higher specific capacity. Larger primary particles also tend to yield and retain capacity better than the smaller particles.



**Figure 4.0.5:** Capacity retention data for the half-cell cycling of  $\text{LiNi}_{0.8}\text{Mn}_{0.1}\text{Co}_{0.1}\text{O}_2$  over 100 cycles at 3.0-4.2 V at a rate of  $C/2$ . Oxygen-fed furnace with LiOH (green), microwave furnace with a LiOH or  $\text{Li}_2\text{O}_2$  salt (black and red respectively), and air-fed furnace with  $\text{Li}_2\text{O}_2$  (blue) are compared.

Long-term cycling of half-cells over 400 cycles at 3.0-4.2 V in a 25 °C temperature-controlled chamber was conducted (Figure 4.0.6). The oxygen-calcined sample yields the largest specific capacity of 140.8-144.2  $\text{mAh g}^{-1}$ , retaining 98.7% of its capacity after 300 cycles ( $\text{Ret}_{300}$ ) and 97.7% of its capacity after 400 cycles ( $\text{Ret}_{400}$ ). The microwave sample calcined with LiOH displayed an initial capacity of 122.3  $\text{mAh g}^{-1}$ , which dropped to 105.2  $\text{mAh g}^{-1}$  after 300 cycles ( $\text{Ret}_{300} = 81.8\%$ ), and 63.2  $\text{mAh g}^{-1}$  after 400 cycles ( $\text{Ret}_{400} = 51.7\%$ ). The drop-off in capacity is a result of the lifetime fade in that particular cell, not related to the chemistry specifically. The microwave-calcined sample with the  $\text{Li}_2\text{O}_2$  salt yielded an initial discharge capacity of 111.9  $\text{mAh g}^{-1}$  but retained 86.0% of its capacity after 300 cycles (96.2  $\text{mAh g}^{-1}$ ), and 82.0% of its capacity after 400 cycles (91.8  $\text{mAh g}^{-1}$ ). The air-calcined sample again yielded the smallest capacities over the 100 cycles, with an initial capacity of 99.1  $\text{mAh g}^{-1}$  and a capacity after 400 cycles of 79.5  $\text{mAh g}^{-1}$  ( $\text{Ret}_{400} = 81.4\%$ ). It should be noted that these long-term cycling tests are carried out in half coin cells cycled against a Li metal reference electrode. The results give a very useful indication of capacity performance, but future experiments in full coin and pouch cells would provide greater insight into degradation mechanisms and lifetime analysis of these cathode materials.



**Figure 4.0.6:** Long-term capacity retention data for half-cells consisting of  $\text{LiNi}_{0.8}\text{Mn}_{0.1}\text{Co}_{0.1}\text{O}_2$  cycled over 400 cycles at 3.0-4.2 V at a rate of C/2. Oxygen-fed furnace with LiOH (green), microwave furnace with a LiOH or  $\text{Li}_2\text{O}_2$  salt (black and red respectively), and an air-fed furnace with  $\text{Li}_2\text{O}_2$  (blue) are compared.

Half-cells were cycled over a voltage window of 3.0-4.3 V for 100 cycles, with two formation cycles of C/20 followed by 98 cycles of C/2 (Figure 4.0.7). The microwave-calcined samples yielded an initial (C/20) capacity of 156.6 and 160.5  $\text{mAh g}^{-1}$  for samples calcined with LiOH and  $\text{Li}_2\text{O}_2$  respectively. This capacity dropped to 123.0 and 115.4  $\text{mAh g}^{-1}$  respectively when cycled at a rate of C/2, with a retention of 78.8% and 49.8% achieved after 100 cycles. The sample calcined in an air-supplied tube furnace yielded an initial C/20 capacity of 165.8  $\text{mAh g}^{-1}$ , with a 100-cycle capacity retention of 79.2%. The oxygen-calcined samples with LiOH or  $\text{Li}_2\text{O}_2$  had the largest initial capacity when cycled at C/20, delivering a capacity of 190.7 and 205.1  $\text{mAh g}^{-1}$  respectively. The capacity of the samples drops to 160.2 and 167.8  $\text{mAh g}^{-1}$  when cycled at C/2 respectively with a capacity retention of 94.5% and 75.0% after the 100 cycles.

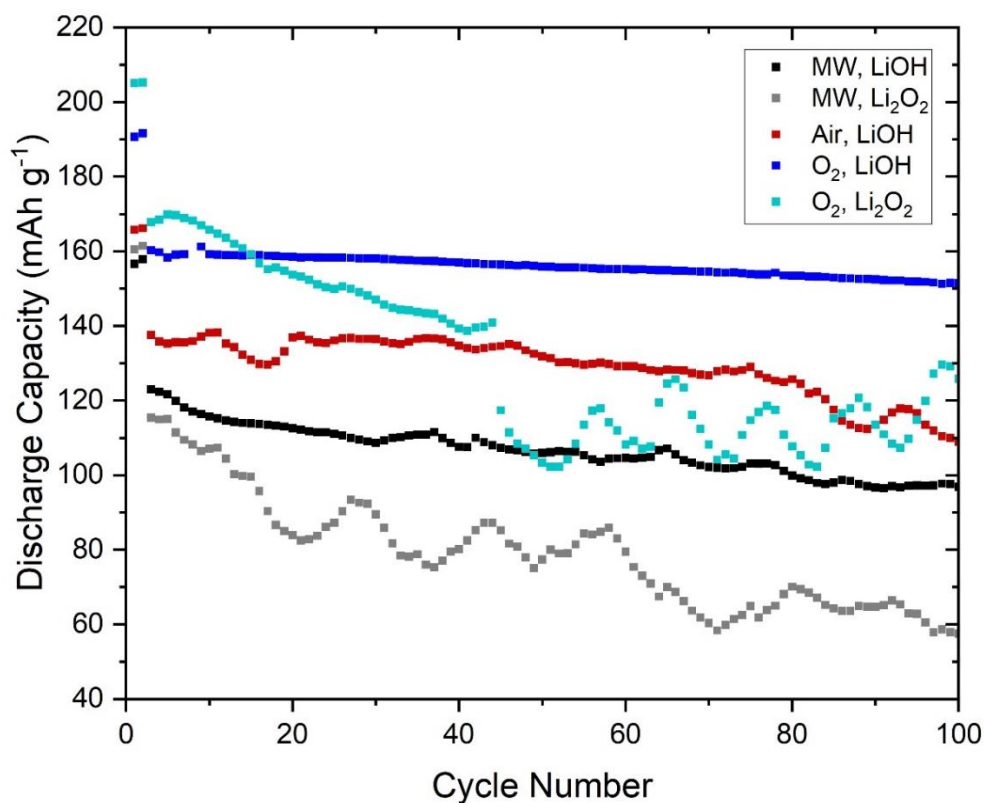


**Figure 4.0.7:** Capacity retention data for the half-cells of  $\text{LiNi}_{0.8}\text{Mn}_{0.1}\text{Co}_{0.1}\text{O}_2$  cycled twice at a rate of  $C/20$  followed by 98 cycles at  $C/2$ , over a voltage window of 3.0-4.3 V. Microwave-calcined samples with LiOH or  $\text{Li}_2\text{O}_2$  salt (black and grey respectively), an air-fed sample calcined with LiOH (red) and oxygen-fed calcination samples with LiOH and  $\text{Li}_2\text{O}_2$  (blue and cyan respectively) are compared.

The voltage profiles seen in Figure 4.0.8 show that the initial delithiation voltage plateau occurred at approx. 3.60-3.65 V for all samples, but gradually increased with cycle number. The microwave sample calcined with  $\text{Li}_2\text{O}_2$  observing an increase from 3.7–3.9 V over 100 cycles, compared to the microwave-calcined LiOH sample, which increased from 3.7-3.8 V. The air-calcined sample with LiOH and oxygen-calcined sample with  $\text{Li}_2\text{O}_2$  experienced an increase in delithiation voltage from 3.7-3.8 V, whereas the oxygen-calcined sample with LiOH had a consistent delithiation voltage of ca. 3.7 V. All samples have an overpotential ‘hump’ prior to delithiation in the 10<sup>th</sup>, 50<sup>th</sup> and 100<sup>th</sup> cycle for samples calcined with both salts, likely related to the presence of residual lithium on the surface causing an overpotential within the system. The overpotential is most prevalent in the  $\text{Li}_2\text{O}_2$  samples, which may indicate a reduction in lithium inventory in these samples with cycling.

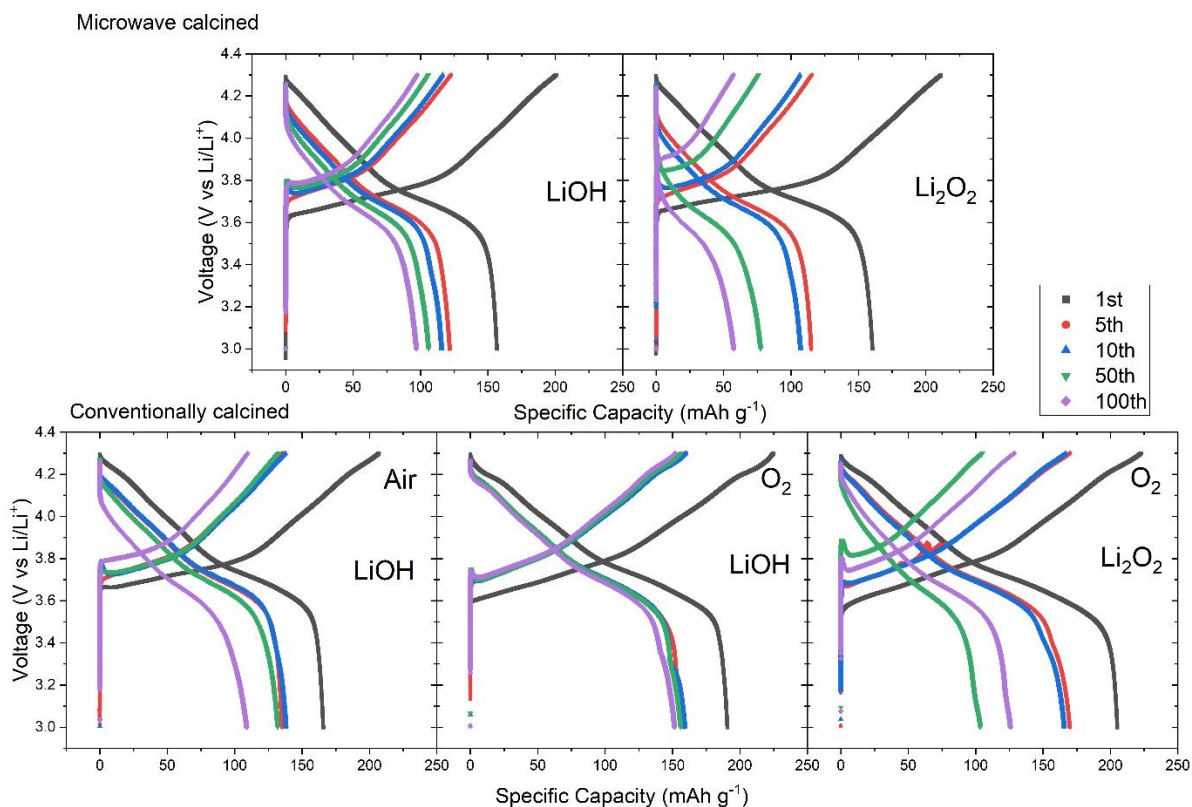


**Figure 4.0.8:** Voltage profiles of half-cells cycled over a voltage window of 3.0-4.3 V. The 1<sup>st</sup>, 5<sup>th</sup>, 10<sup>th</sup>, 50<sup>th</sup> and 100<sup>th</sup> cycles are included for samples calcined 775 °C with LiOH or Li<sub>2</sub>O<sub>2</sub>, in either a microwave furnace for 4 hours (top row) or 12 hours in a conventional furnace (bottom row).

The differential capacity profiles displayed in Figure 4.0.9 confirms the presence of the peaks associated with the H1-M and M-H2 phase transitions at *ca.* 3.7 V and 4.05 V respectively. Peak shifting was observed in the samples calcined with Li<sub>2</sub>O<sub>2</sub>, with both the microwave and oxygen-calcined samples showing a high-voltage peak shift from *ca.* 3.7 V to 3.85 V in the H1-M peak during the charging cycle associated with polarisation within the half-cell. Interestingly, the microwave sample calcined with LiOH observed a low-voltage H1-M peak shift after the first cycle (from *ca.* 3.85 V to 3.75 V).

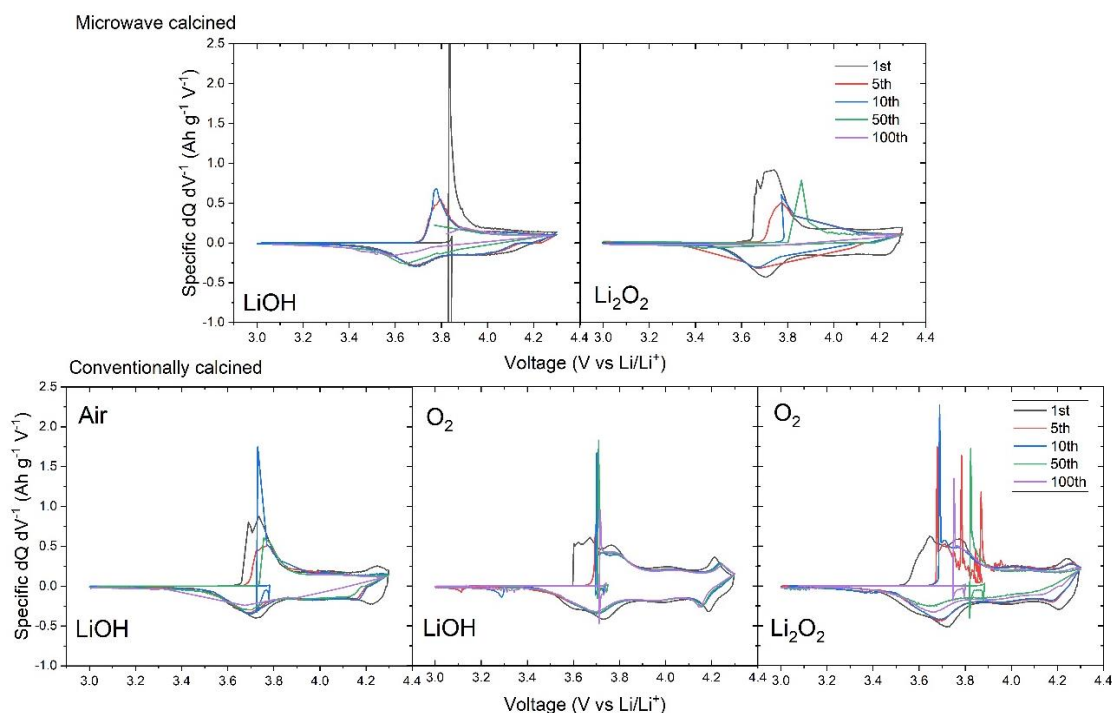


**Figure 4.0.9:** Differential capacity profiles of half-cells cycled at 3.0-4.3 V. The 1<sup>st</sup>, 5<sup>th</sup>, 10<sup>th</sup>, 50<sup>th</sup> and 100<sup>th</sup> cycles for samples calcined 775 °C with LiOH or Li<sub>2</sub>O<sub>2</sub> in either a microwave furnace for 4 hours (top row) or 12 hours in a conventional furnace (bottom row).

To examine changes in crystal structure with cycling, *operando* XRD experiments were conducted on the optimised microwave calcination sample (775 °C, 4 hours) with Li<sub>2</sub>O<sub>2</sub>. This was performed using a half-cell with a 180 µm Kapton window (**Error! Reference source not found.**) which is X-ray transparent. The *operando* XRD experiment was conducted by Dr Laurence Middlemiss using a silver sourced X-ray diffractometer with the coin cell cycled at C/20. The XRD profile was recorded at 0.1 V intervals over the voltage profile, from open circuit voltage (OCV) to 4.3 V (Figure 4.0.10), with aluminium peaks indicated by a silver circle. In agreement with reports in the literature, the (003) peak position shifts to lower  $^{\circ}2\theta$  during initial charge which indicates an increase in the *c* lattice parameter as Li<sup>+</sup> departs the cathode (Figure 4.11.b) [59], [61]. This reflection then shifts to higher  $^{\circ}2\theta$  with further cycling as the *c* lattice parameter decreases at higher states of charge, coinciding with the redox process observed in differential capacity plots. Shifts in (101) and (110) are also observed and these peak shifts are most clearly represented in Figure 4.0.11.

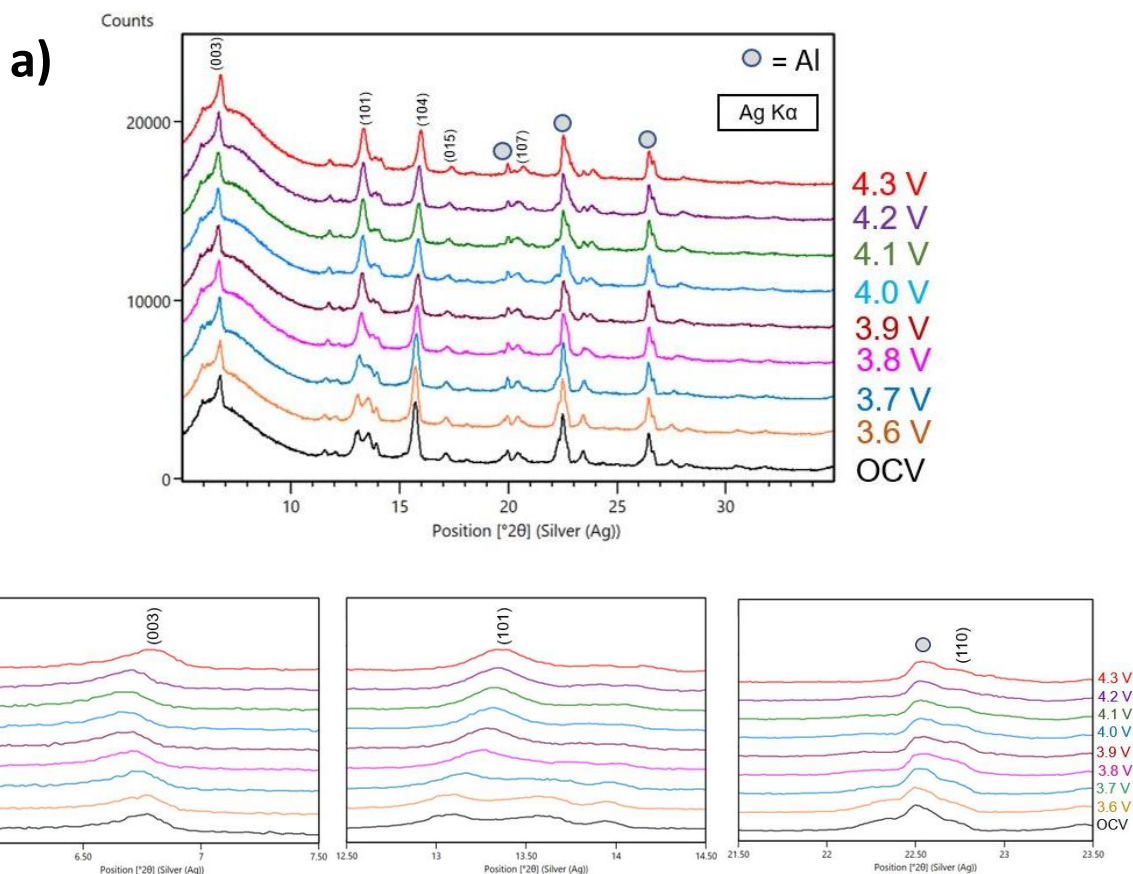


**Figure 4.0.10:** (a) XRD profiles of a  $\text{LiNi}_{0.8}\text{Mn}_{0.1}\text{Co}_{0.1}\text{O}_2$  cathode calcined in a microwave furnace at  $775^\circ\text{C}$  for 4 hours with  $\text{Li}_2\text{O}_2$ . Magnification of the (003), (101), and (110) peaks are seen in (b).

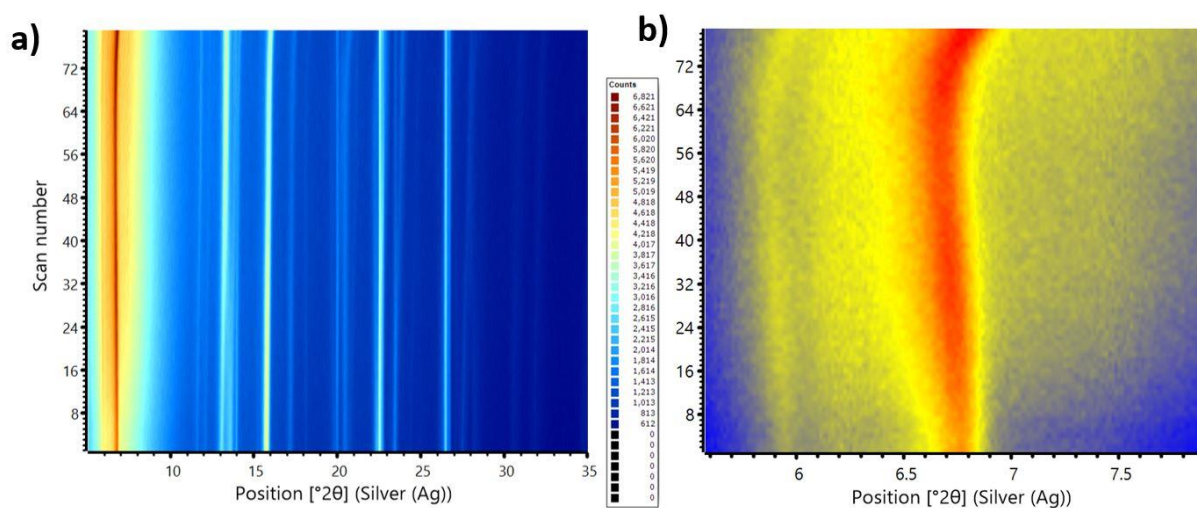


**Figure 4.0.11:** A chromatic 'heat map' of the XRD profile for the  $\text{LiNi}_{0.8}\text{Mn}_{0.1}\text{Co}_{0.1}\text{O}_2$  cathode analysed *via* XRD *in-operando* over a voltage range of 3.0-4.3 V. (a) depicts the whole angle range ( $0\text{-}35^\circ$ ) of the XRD profile, with (b) showing a magnification of the (003) peak at  $6\text{-}7^\circ$ .  $\theta$

Electrochemical Impedance Spectroscopy (EIS) conducted on the optimised microwave- and oxygen-calcined samples (Figure 4.0.12.a) and b) respectively) shows that in the first cycle there is the clear

appearance of multiple semi-circle contributions to the impedance. This indicates the overall impedance has contributions from more than one cell component. Semi-circles appearing at higher frequencies indicate processes occurring on a shorter timescale, for example ion migration in the liquid electrolyte. Semi-circle contributions at lower frequencies, and hence longer timescales, can be attributed to charge transfer within or between particles. A qualitative assessment of the EIS data collected indicates a growth in resistance as the battery cycles for both samples. This may be due to SEI growth on the cathode, which could be exacerbated by particle cracking with further cycling. These results are in agreement with previous observations from galvanostatic cycling and SEM.

GITT analysis can be employed to investigate changes in ion diffusion dynamics as a function of state of charge. The extracted results from GITT for the first charge of the optimised microwave-calcined sample with  $\text{Li}_2\text{O}_2$  and oxygen-calcined sample with  $\text{LiOH}$  are shown in Figure 4.0.13. Previous reports indicate that at  $x < 0.1$ , the ion diffusion can be overestimated due to the cell not being fully relaxed prior to the current pulse being applied [59]. The  $\text{Li}^+$  mobility increases for both samples from  $x = 0.1$  to a maximum of  $x \sim 0.5$ . The microwave-calcined sample typically observes a higher ionic conductivity than the oxygen-calcined sample, with a conductivity of *ca.*  $1.5 \times 10^{-10} \text{ cm}^6 \text{ s}^{-1}$  at  $\sim 50\%$  state of charge compared to *ca.*  $5.5 \times 10^{-10} \text{ cm}^6 \text{ s}^{-1}$ .

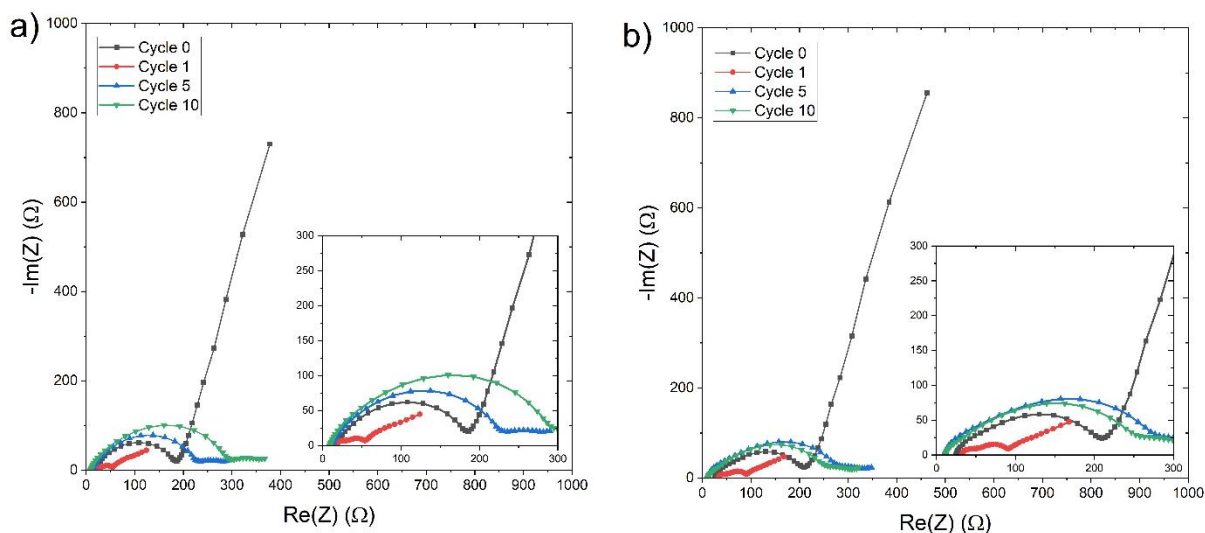


**Figure 4.0.12:** Nyquist plots for uncycled, 1<sup>st</sup>, 5<sup>th</sup>, 10<sup>th</sup> cycles of  $\text{LiNi}_{0.8}\text{Mn}_{0.1}\text{Co}_{0.1}\text{O}_2$  calcined using the optimised microwave calcination **(a)** and oxygen-fed calcination procedures **(b)** cycled over a voltage window of 3.0 – 4.3 V, with two cycles at C/20 followed by 8 cycles at a rate of C/2.

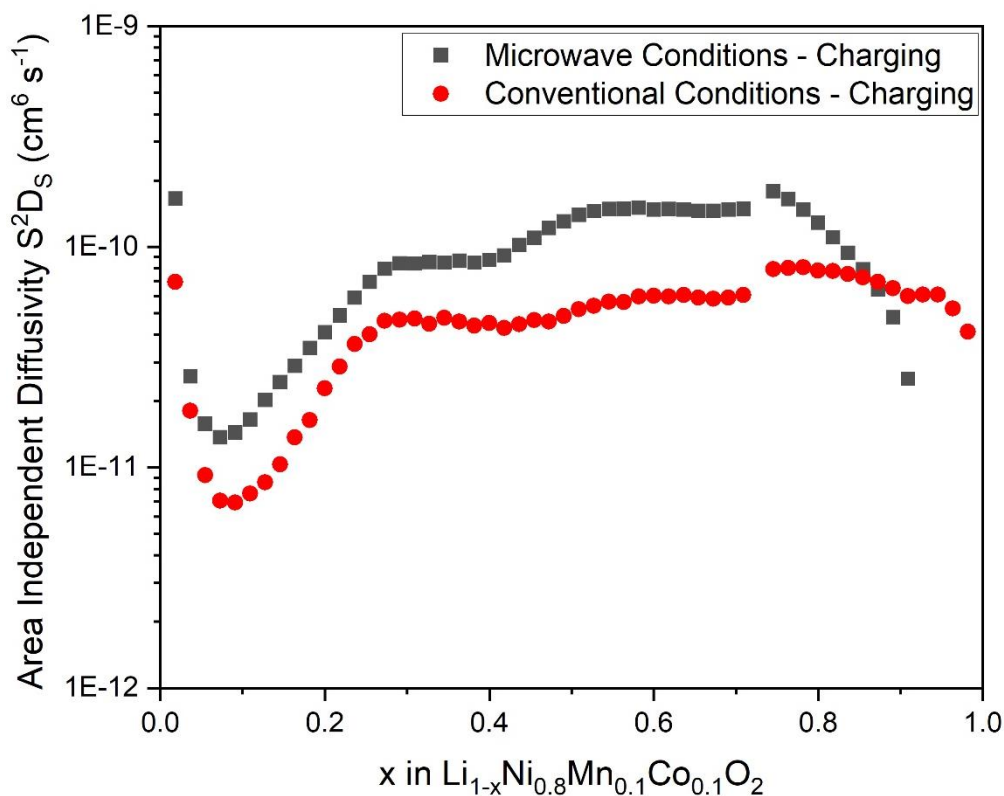


**Figure 4.0.13:** GITT analysis of the optimised microwave and oxygen-fed calcination procedures during the charge profile, cycled between 3.0–4.5 V at a rate of C/20.

Rate capability analysis was conducted on the optimised microwave-calcined oxygen-calcined samples (Figure 4.0.14), with a C-rate increasing from C/20 to 10C over a voltage window of 3.0-4.3 V. The oxygen-calcined sample shows a higher initial capacity of 177.7-177.9 mAh g<sup>-1</sup> over the first 5 cycles (C/10), followed by a capacity of 180.8-186.0 mAh g<sup>-1</sup> (C/20). This capacity decreases gradually to *ca.* 155.1, 147.5, 121.3 and 79.4 mAh g<sup>-1</sup> as the rate increases from C/2 to 5C, with no capacity recorded when cycled at 10C. The final 5 cycles yielded a capacity of 173.6-179.4 mAh g<sup>-1</sup> (C/20) meaning that approximately 96% of the capacity was retained. In comparison, the microwave-calcined sample yielded an initial capacity of 152.8-155.2 mAh g<sup>-1</sup> (C/10) and 159.1-164.0 mAh g<sup>-1</sup> (C/20), which is 20-25 mAh g<sup>-1</sup> lower than the oxygen-calcined sample. The capacity yielded at higher capacity rates also dropped with increased cycling rates with C/2, 1C, 2C and 5C cycling rates yielding capacities of 124.9, 105.9, 83.3 and 42.4 mAh g<sup>-1</sup> respectively, with no capacity delivered at 10C. Voltage profiles for the rate capability test show similar profiles for the microwave-calcined and oxygen-calcined samples, included in Appendix A.12. An overpotential peak prior to delithiation increases in magnitude as the cycling rate increases for both samples, indicating a potential increase in resistive surface phases. The higher capacities observed for the oxygen calcined sample compared with the microwave sample may be a result of the particle morphology.

SEM images revealed greater void spacing between larger primary particles for the microwave calcined sample. This may influence the ion mobility at higher C-rates compared with smaller, more compact primary particles found for the oxygen calcined sample.

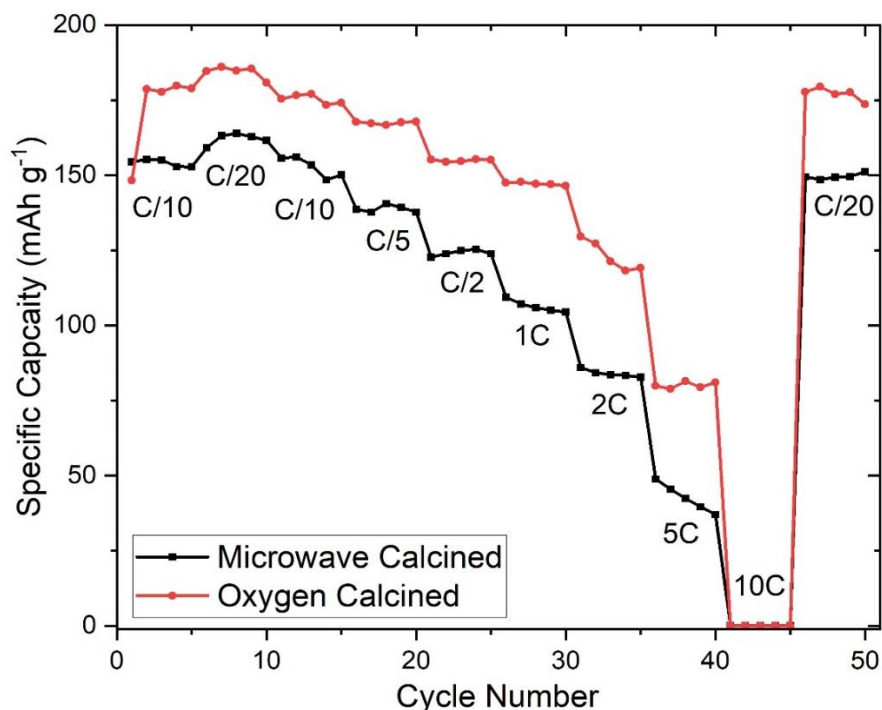


**Figure 4.0.14:** A rate capability test of the optimised microwave-calcined oxygen-calcined samples via a series of rates: C/20, C/10/ C/5, C/2, 1C, 2C, 5C and 10C; cycled at 3.0-4.3 V.

#### 4.4. – Post-Mortem Analysis of Microwave-calcined Cells

Analysing the cathode material after cycling was conducted to investigate the mechanical impact of cycling on microwave calcined samples compared with conventionally calcination samples. The half-cells cycled in Figure 4.0.5 (*i.e.* cycled 100 times at C/2) were deconstructed and XRD and SEM analysis was conducted under inert conditions to preserve the materials extracted from the cell as much as possible.

A high-energy molybdenum source X-ray transmission diffractometer was used, with the cathode sealed between two acetate sheets. The transmittance of the X-rays through the cathode meant both NMC and aluminium data was recorded, resulting in overlapping of the characteristic Bragg peaks. Due to the increased intensity of the aluminium peak compared to the NMC file, multiphase

refinement was unsuccessful. To isolate the NMC data from the aluminium peaks, an XRD pattern for aluminium was subtracted from the NMC/Al foil dataset, leaving the phase-pure NMC pattern. To do this, the CIF file for aluminium was refined using GSAS-II to fit an aluminium specific peak in the NMC/Al foil data at  $28.6^\circ$  [239]. This revealed a linear scale factor that could be applied to the NMC/Al phase to ascertain the intensity of the aluminium foil within the NMC/Al phase. An accurate intensity of the aluminium peaks could then be subtracted from the NMC/Al phase without impacting the intensity of the NMC phase, leaving the NMC characteristic peaks. This procedure is highlighted in Figure 4.0.15.a) and b) below.

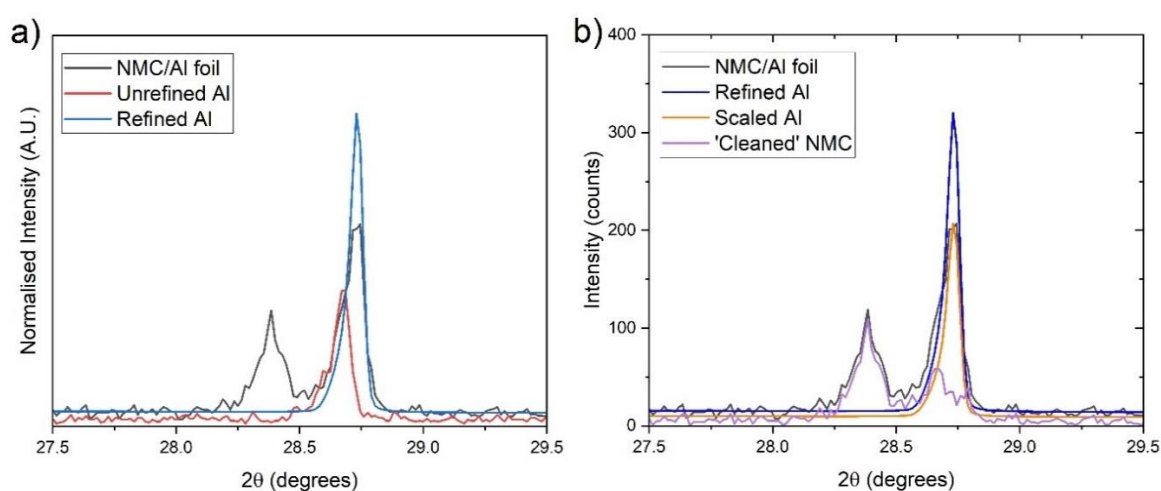


**Figure 4.0.15:** XRD profiles of a  $\text{LiNi}_{0.8}\text{Mn}_{0.1}\text{Co}_{0.1}\text{O}_2$  cathode disc with aluminium foil. **(a)** depicts the effects of refining the sample displacement of crystalline Al; **(b)** demonstrates how scaling a peak can remove aluminium peaks without impacting the intensity of the NMC peaks.

XRD analysis was conducted on the cycled cathodes of the optimised microwave-calcined samples (calcined with  $\text{LiOH}$  or  $\text{Li}_2\text{O}_2$ ), and the equivalent air- and oxygen- calcined samples (calcined with  $\text{Li}_2\text{O}_2$  and  $\text{LiOH}$  respectively). Each sample was directly compared to the 'pristine' (uncycled)  $\text{LiNi}_{0.8}\text{Mn}_{0.1}\text{Co}_{0.1}\text{O}_2$  powder attained from a Cu-sourced X-ray diffractometer (Figure 4.0.16). The uncycled powder reveals significant changes in the (003)/(104) peak ratios and (006)/(012) peak intensities in all samples due to the incomplete removal of the aluminium from the (006)/(012) peak. This hinders the accurate Rietveld refinement of the XRD pattern. There are no additional peaks, suggesting that the  $\alpha\text{-NaFeO}_2$  layered oxide structure remained dominant throughout cycling. The abnormal (006)/(012) peak intensity has affected the (003) and (104) peaks equally, therefore the (003)/(104) peak ratio can be considered a reasonable qualitative estimation of the degree of cation mixing for the cathode samples. The oxygen-calcined sample saw the largest (003)/(104) ratio of 1.776, indicating a good degree of cation ordering, which reduced to 1.568 over the 100 cycles,

indicating an increase in cation mixing. The microwave-calcined samples had initial (003)/(104) peak ratios of 1.407 and 1.345 for samples calcined with LiOH and Li<sub>2</sub>O<sub>2</sub> respectively, which reduced to 1.056 and 1.103 after cycling. The air-calcined sample had the smallest (003)/(104) ratio of 1.198, which reduced to 1.058 after the 100 cycles.

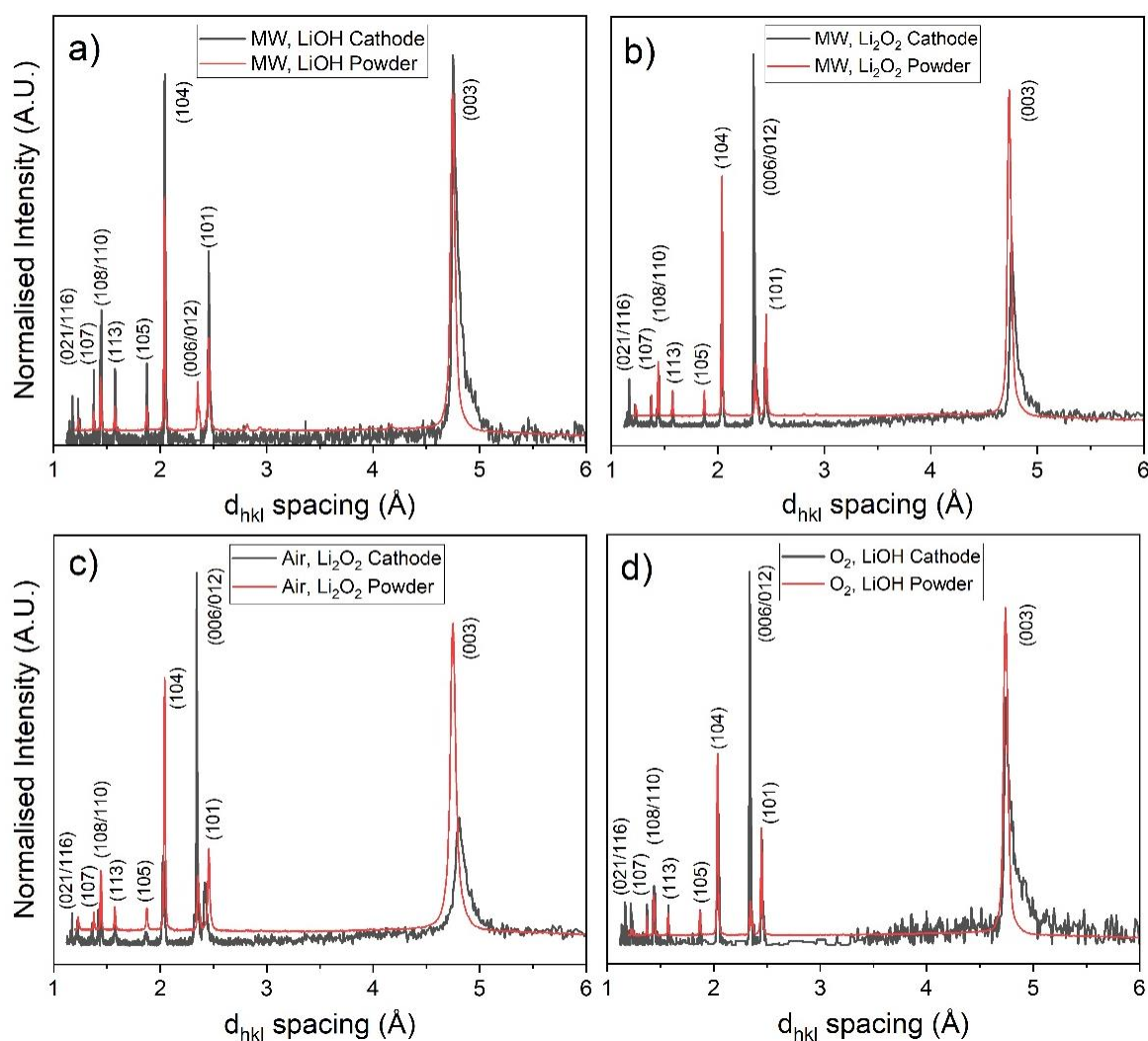


**Figure 4.0.16:** XRD profiles of the microwave-calcined samples with LiOH or Li<sub>2</sub>O<sub>2</sub> (**a and b**), air-calcined sample with Li<sub>2</sub>O<sub>2</sub> (**c**), and the oxygen-calcined sample with LiOH (**d**). Two profiles are included for the uncycled powder (red) and cycled cathode (black).

SEM analysis was conducted on the cycled samples after 100 cycles, with the secondary particle size and shape remaining quasi-spherical in morphology and *ca.* 10  $\mu\text{m}$  in diameter (Figure 4.0.17). There is evidence for particle cracking in the cycled microwave-calcined samples in Figure 4.0.17.c and d). All particles undergo unit cell expansion and contraction during (de)lithiation which results in an increase particle size and subsequent strain between adjacent particles, most prevalent within the

core of the particle. In oxygen-calcined samples, it is thought that the alignment of the particles allows greater inter-particle strength, mitigating the formation and propagation of a cracks within the secondary particle. In the microwave-calcined sample, it is thought the rapid formation of the primary particles forms harder individual particles that agglomerate with weaker inter-particle interactions. The weaker inter-particle interactions mean that as the primary particles expand during lithiation there is greater strain on the particle-particle interfaces, resulting in greater strain between particles and less room to expand into, resulting in the formation of cracks as the particles expand outwards, eventually resulting in the expulsion of material from the particle, as seen in Figure 4.0.17.c) and d). This event is not present in all particles, but the loss of active material would contribute to the degradation of capacity in microwave-calcined materials.

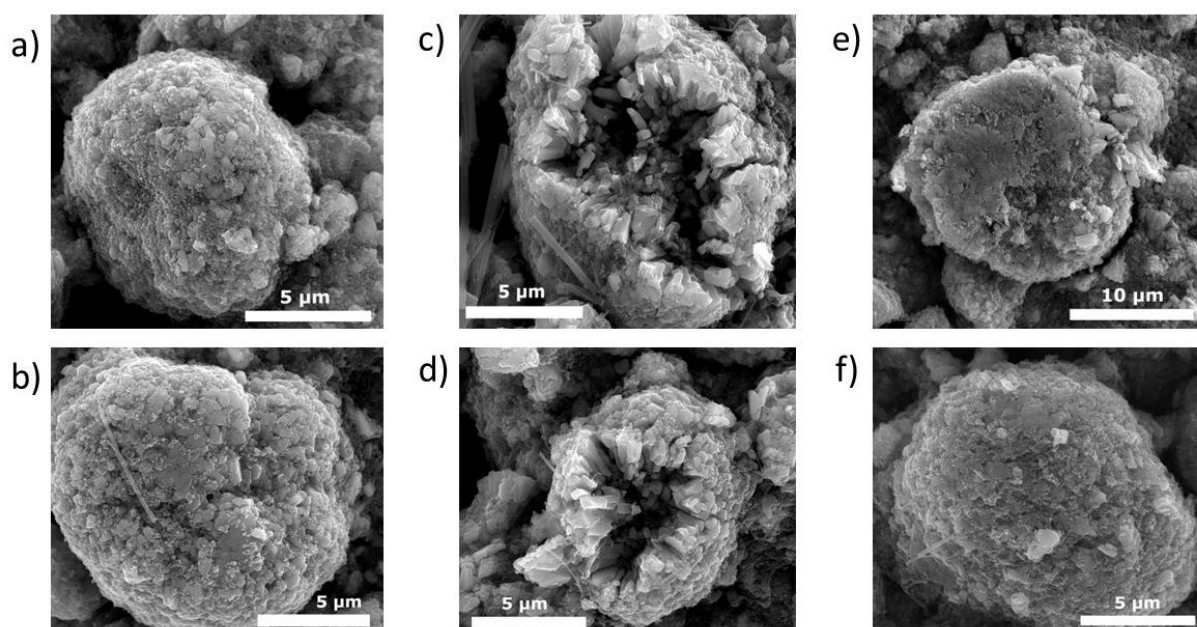


**Figure 4.0.17:** SEM images of the cycled cathode materials, featuring the two microwave samples calcined with LiOH **(a)**, **(c)**, and Li<sub>2</sub>O<sub>2</sub> **(b)**, **(d)**; the air-calcined sample with Li<sub>2</sub>O<sub>2</sub> **(e)**, and the oxygen-calcined sample with LiOH **(f)**. Images **(c)** and **(d)** depict the extreme cracking event that some microwave-calcined particles underwent during cycling.

This analysis concludes that the oxygen-calcined sample has an increased degree of crystalline and morphological stability after cycling, with less cation mixing and morphological cracking observed compared to the microwave-calcined samples. The microwave samples appear to crack after prolonged cycling due to increased strain within the secondary particle assemblies from unit cell volume expansion and contraction during (de)lithiation resulting in extreme cracking events in some

particles as the material was cycled and the unit cell volume expands and contracts during (de)lithiation.

#### 4.5. – Mechanical Testing of oxygen- and microwave- calcined particles

The strength of a particle, defined as the maximum pressure it can withhold before failing, was determined using micro-indentation in conjunction with SEM imaging. It was hypothesised that the larger particles observed for the microwave calcined samples may influence their mechanical strength properties, which could provide some insight into particle resilience, e.g. during volume expansion/ contraction or during calendaring. Two samples,  $\text{LiNi}_{0.8}\text{Mn}_{0.1}\text{Co}_{0.1}\text{O}_2$  calcined *via* the optimised microwave procedure (4 hours at 775 °C), or equivalent oxygen procedure (12 hours at 775 °C) were loaded with pressure until failure (Figure 4.0.18). It can be seen that the cracking propagates along the primary particle grain boundaries in a similar manner for both samples.

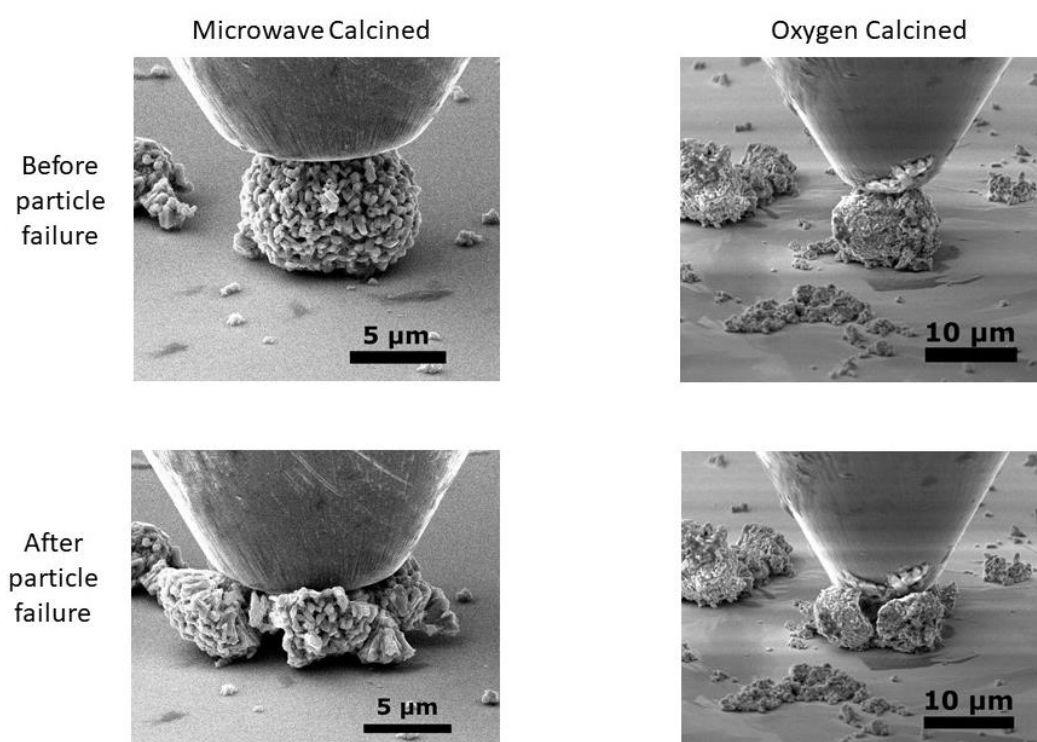


**Figure 4.0.18:** SEM images of  $\text{LiNi}_{0.8}\text{Mn}_{0.1}\text{Co}_{0.1}\text{O}_2$  calcined *via* a microwave procedure (left) or oxygen-calcined procedure (right). The micro-indenter applies pressure, with images depicting the secondary particles before (top) and after (bottom) particle failure.

Six samples were tested in this manner and yielded similar visual failure mechanisms, with the particle fragmenting into multiple pieces around a central, vertical axis (Figure 4.0.19). It is noted that the conventional, oxygen-fed calcined samples fragmented into more pieces than the microwave samples, but this is more likely a comment on the assembly of the secondary particle rather than its strength. Figure 4.0.19 shows both calcination procedures yield secondary particles with similar mechanical strength, with the oxygen-calcined samples being marginally more size-dependent than the microwave-calcined samples, with larger particles being weaker than smaller particles.

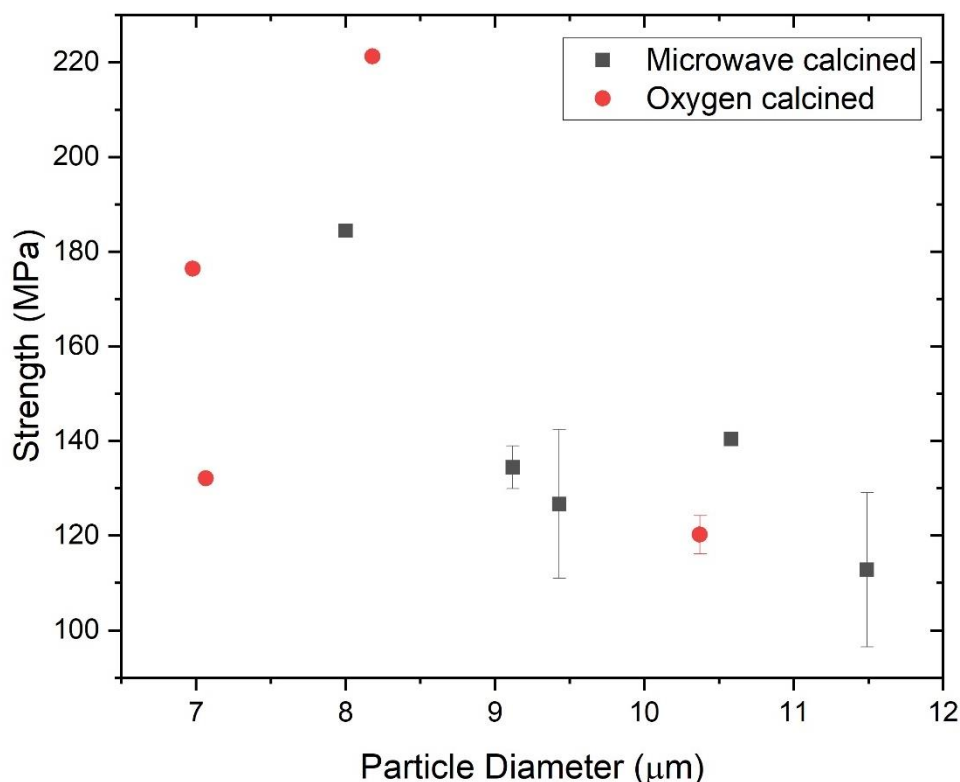


**Figure 4.0.19:** The mechanical strength of  $\text{LiNi}_{0.8}\text{Mn}_{0.1}\text{Co}_{0.1}\text{O}_2$  secondary particles relative to the particle diameter. Error bars are included for all datapoints, but some are too small to be visible.

The testing conducted comments on the strength of the calcined secondary particles, not the primary particles. The synthesis and testing of single-crystal  $\text{LiNi}_{0.8}\text{Mn}_{0.1}\text{Co}_{0.1}\text{O}_2$  particles will provide a clearer insight into the effects of microwave calcination on the strength of the  $\text{LiNi}_{0.8}\text{Mn}_{0.1}\text{Co}_{0.1}\text{O}_2$  crystallites.

#### 4.5. – Concluding remarks for Chapter 4

In order to validate the optimised microwave calcination procedure, it (775 °C for 4 hours) was compared to equivalent conventional procedures, namely an air-supplied tube furnace (775 °C for 12 hours) and an oxygen-supplied tube furnace (775 °C for 12 hours). It was found that the microwave-calcined samples yielded more capacity (122.7-130.5 mAh g<sup>-1</sup>, 3.0-4.2 V at C/2) than conventionally heated air-calcined samples (94.1-111.2 mAh g<sup>-1</sup>, 3.0-4.2 V at C/2), which was thought to be related to the rapid heating of the microwave-assisted promoting crystal growth within the NMC material. This is evidenced by increased XRD peak splitting in the (108)/(110) doublet and larger, more faceted primary particle morphologies observed under SEM analysis. The more faceted particles are thought to have increased lithium-ion conductivity properties compared to the air-calcined samples, possibly related to the rapid crystallisation that occurs under the rapid heating in the microwave furnace. There are similarities between the microwave- and conventional air-calcined samples, suggesting that the formation of oxygen during the thermal decomposition of Li<sub>2</sub>O<sub>2</sub> was quickly dissipated and any increase in partial pressure is minimal. It is suggested that the lower thermal decomposition temperature of Li<sub>2</sub>O<sub>2</sub> (280-400 °C) compared to LiOH (400-650 °C) allows a longer period for lithium intercalation during calcination in a reductive (air) atmosphere, thus an increased degree of Li/Ni cation mixing is observed in the resultant LiNi<sub>0.8</sub>Mn<sub>0.1</sub>Co<sub>0.1</sub>O<sub>2</sub> [104].

The oxygen-calcined samples outperformed the microwave-calcined samples with respect to the capacity, yielding 144.6-151.0 mAh g<sup>-1</sup> compared to 122.7-130.5 mAh g<sup>-1</sup> (cycled at 3.0-4.2 V at a rate of C/2). An increased capacity retention was observed for the oxygen-calcined sample over long-term cycling at 3.0-4.2 V (97.7% retention compared to 82.0% for the microwave-calcined sample). The similarities between the LiOH and Li<sub>2</sub>O<sub>2</sub> lithium sources when compared to the oxygen-calcined sample further supports the theory that the oxygen generated from the thermal decomposition of Li<sub>2</sub>O<sub>2</sub> does not increase the partial pressure of oxygen within the crucible. This experiment further demonstrates the importance of an oxygen-rich atmosphere when calcining Ni-rich cathodes that has been described in literature and Section 1.3.4. The microwave-calcined samples yielded similar mechanical strength properties to the oxygen-calcined counterpart and GITT analysis showed higher diffusivity coefficients in these samples. This indicates that if an oxygen-rich atmosphere can be safely applied to a microwave furnace, then the capacity deficiencies described could be overcome and coupled with improved diffusivity properties and minimal impact on secondary particle structure and mechanical properties.

## 5. Optimising a Microwave-Assisted Hydrothermal Synthesis Pathway for $\text{Ni}_{0.8}\text{Mn}_{0.1}\text{Co}_{0.1}(\text{OH})_2$

Prior investigation into the hydrothermal synthesis of  $\text{Ni}_{0.5}\text{Mn}_{0.3}\text{Co}_{0.2}\text{O}_2$  was conducted by Shi *et al.* using urea as a precipitating agent [150]. Here, this was adapted for the synthesis of the  $\beta$ -polymorph  $\text{Ni}_{0.8}\text{Mn}_{0.1}\text{Co}_{0.1}(\text{OH})_2$  *via* a microwave-assisted hydrothermal procedure. Optimisation of this procedure is conducted with respect to temperature, duration, transition metal: urea ratio, and the pressure within the hydrothermal vessel. It is hypothesised that milder reaction conditions within the hydrothermal vessel may result in the weaker hydrolysis of urea and thus formation of the less-ordered  $\alpha$ - $\text{Ni}_{0.8}\text{Mn}_{0.1}\text{Co}_{0.1}(\text{OH})_2$  precursor, with water or anions intercalating between the interlayer galleries. These impurities may impact the crystallinity of  $\text{LiNi}_{0.8}\text{Mn}_{0.1}\text{Co}_{0.1}\text{O}_2$  post calcination. An investigation into the  $\alpha$ - $\text{Ni}_{0.8}\text{Mn}_{0.1}\text{Co}_{0.1}(\text{OH})_2$  and calcined  $\text{LiNi}_{0.8}\text{Mn}_{0.1}\text{Co}_{0.1}\text{O}_2$  properties is conducted to evaluate the effect on electrochemical cycling. A high temperature XRD study is also presented which investigates the evolution of the  $\alpha$ - $\text{Ni}_{0.8}\text{Mn}_{0.1}\text{Co}_{0.1}(\text{OH})_2$  upon heating.

### 5.1. Optimisation of the microwave-assisted hydrothermal methodology

#### 5.1.1. Optimisation of the Reaction Duration

The conventional synthesis of  $\text{Ni}_{0.5}\text{Mn}_{0.3}\text{Co}_{0.2}\text{CO}_3$  described by Shi *et al.* found that a reaction for 24 hours at 200 °C in a hydrothermal vessel was optimal [150]. The dielectric nature of microwave heating can shorten the reaction duration. These reactions were conducted in a CEM Mars6 Synthesis. Reactions were performed at 200 °C for different time durations: 30 minutes, 45 minutes, 1 hour, 2 hours and 3 hours.

Four individual hydrothermal vessels hosted the reaction concurrently, with the vessels rotating around the microwave cavity. An XRD study shows the formation of the desired  $\beta$ - $\text{Ni}_{0.8}\text{Mn}_{0.1}\text{Co}_{0.1}(\text{OH})_2$  polymorph phase (Figure 5.0.1). A phase impurity was identified *via* four Bragg peaks at 30.5°, 35.8°, 43.5° and 57.6° 2 $\theta$ , highlighted with vertical lines on Figure 5.0.1. Comparisons with ICSD standards of  $(\text{Ni}_{0.6}\text{Mn}_{0.2}\text{Co}_{0.2})_3\text{O}_4$  spinel and  $\text{Ni}_{0.6}\text{Mn}_{0.2}\text{Co}_{0.2}\text{O}$  rocksalt phases identified the phase impurity as spinel [152]. One possible origin of this spinel phase is through the oxidation of manganese to form the  $\text{Mn}_3\text{O}_4$  phase is possible if the reaction solvent is not sufficiently deoxygenated [144].

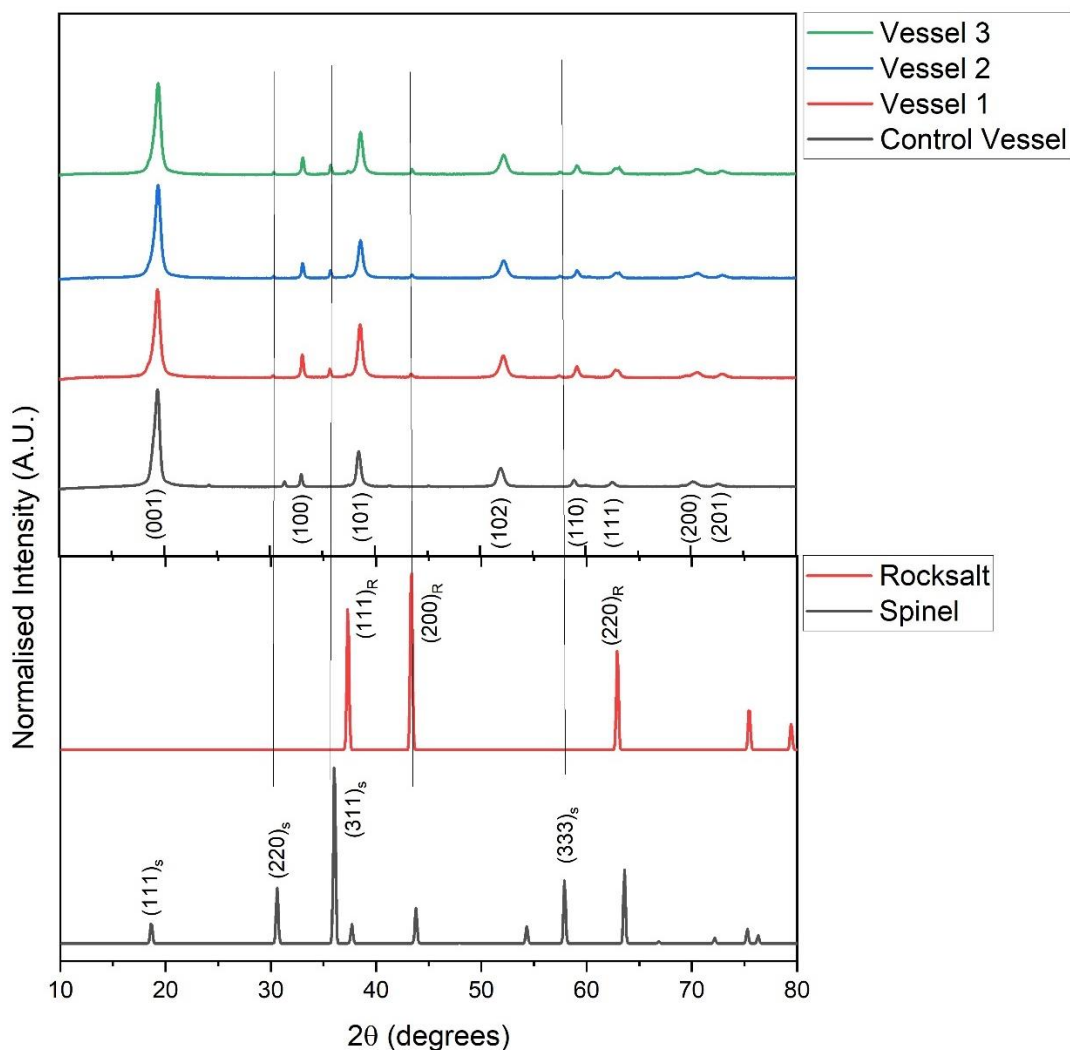


**Figure 5.0.1:** XRD profiles of  $\text{Ni}_{0.8}\text{Mn}_{0.1}\text{Co}_{0.1}(\text{OH})_2$  samples synthesised in four hydrothermal vessels within the Mars6 Synthesis (200 °C, 3 hours), with labelled Bragg peaks. The potential phase impurities,  $(\text{Ni}_{0.6}\text{Mn}_{0.2}\text{Co}_{0.2})_3\text{O}_4$  spinel and  $\text{Ni}_{0.6}\text{Mn}_{0.2}\text{Co}_{0.2}\text{O}$  rocksalt, are also included.

The desired  $\beta$ -polymorph of  $\text{Ni}_{0.8}\text{Mn}_{0.1}\text{Co}_{0.1}(\text{OH})_2$  was identified for all samples from the XRD profiles displayed in Figure 5.0.2. The peak intensities differ between each sample which may indicate some preferred orientation in these samples. The presence of a spinel impurity phase is found in all samples. SEM analysis shows all samples gave quasi-spherical secondary assemblies (Figure 5.0.3). The secondary particles depicted have a diameter of approximately 10  $\mu\text{m}$  (with the exception of the 120- minute sample, which has a typical particle diameter of 40  $\mu\text{m}$ ).

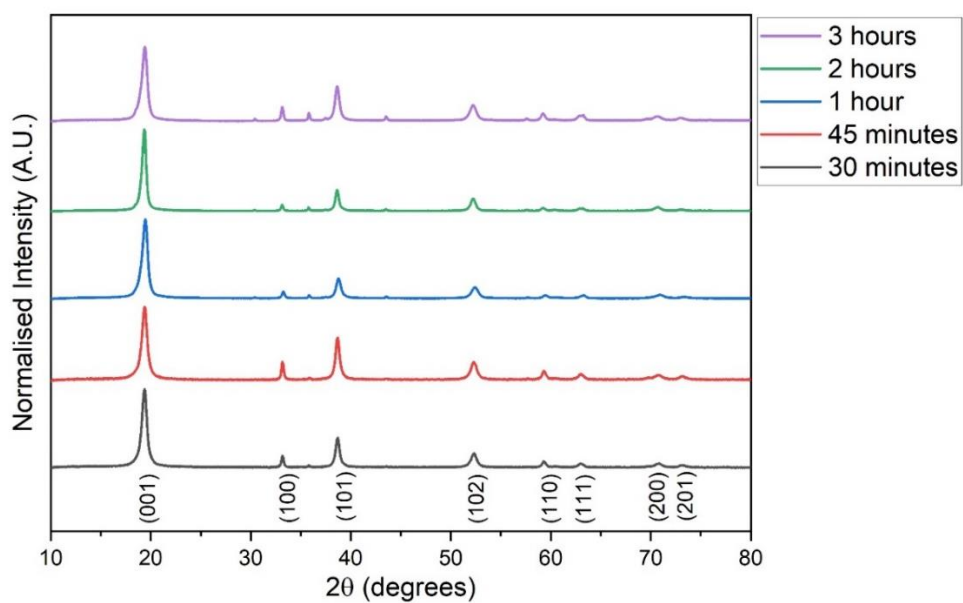


**Figure 5.0.2:** XRD profiles of  $\text{Ni}_{0.8}\text{Mn}_{0.1}\text{Co}_{0.1}(\text{OH})_2$  synthesised *via* a microwave-assisted hydrothermal method at 200 °C with a reaction period of 30 minutes, 45 minutes, 1 hour, 2 hours and 3 hours.

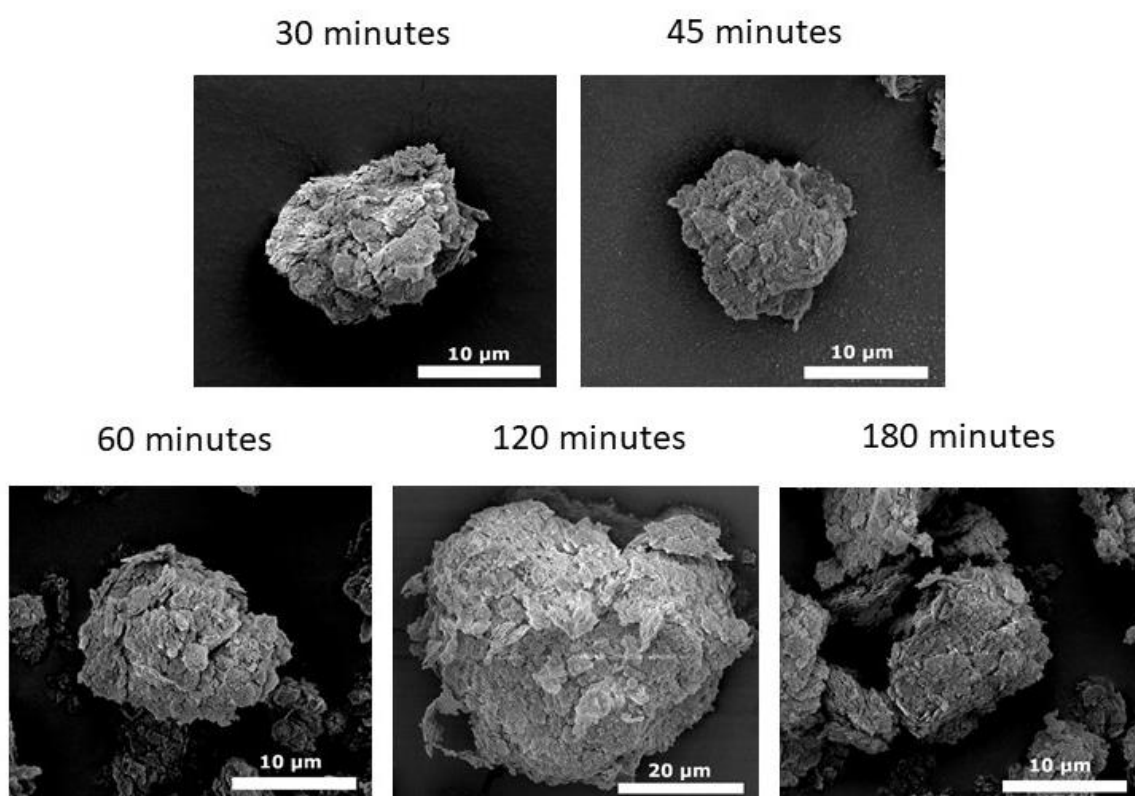


**Figure 5.0.3:** SEM images of  $\text{Ni}_{0.8}\text{Mn}_{0.1}\text{Co}_{0.1}(\text{OH})_2$  synthesised *via* a microwave-assisted hydrothermal method at 200 °C with a reaction duration of 30 minutes, 45 minutes, 1 hour, 2 hours and 3 hours.

Calcination of the  $\text{Ni}_{0.8}\text{Mn}_{0.1}\text{Co}_{0.1}(\text{OH})_2$  precursor was conducted using an oxygen-fed tube furnace for 12 hours at 775 °C. XRD analysis revealed all samples formed the desired  $\alpha\text{-NaFeO}_2$   $\text{LiNi}_{0.8}\text{Mn}_{0.1}\text{Co}_{0.1}\text{O}_2$  transition metal layered structure (Figure 5.0.4). The (003)/(104) peak ratios suggested the smallest degree of cation mixing for the 45-minute reaction (2.736), whereas the 30- and 120- minute samples have the highest degree (1.660 and 1.806 respectively). Rietveld refinement determined the proportion of nickel in the lithium layer to be as 4.5%, 3.4%, 1.5%, 3.1%, and 5.8% for the 30-, 45-, 60-, 120- and 180- minute reactions respectively, as shown in Table 5.0.1 (associated plots in Appendix A.13). This suggests that the 60-minute sample has the least cation mixing but confirms the 30- and 180- minute samples have the most. The layered ordering of the samples is indicated by the (108)/(110) peak splitting seen in Figure 5.0.4.c) and shows all samples having a similar degree of peak splitting. SEM analysis of the calcined  $\text{LiNi}_{0.8}\text{Mn}_{0.1}\text{Co}_{0.1}\text{O}_2$  showed the 60-, 120- and 180- minute samples form quasi-spherical secondary particles with a particle diameter of 10-20  $\mu\text{m}$  (Figure 5.0.5).

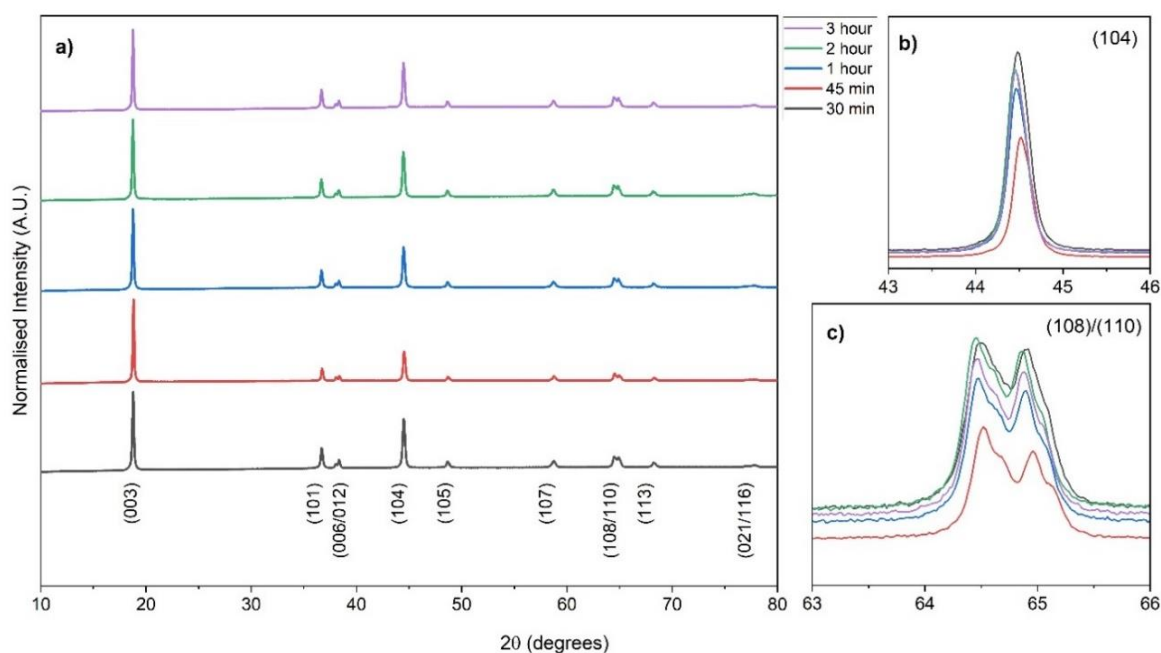


**Figure 5.0.4:** (a) XRD profiles of  $\text{LiNi}_{0.8}\text{Mn}_{0.1}\text{Co}_{0.1}\text{O}_2$ , calcined in an oxygen-fed tube furnace with LiOH (775 °C, 12 hours). The (104) peak (b) and (108)/(110) peak doublet (c) are enclosed.

**Table 5.0.1:** Key values from the Rietveld refinement of  $\text{LiNi}_{0.8}\text{Mn}_{0.1}\text{Co}_{0.1}\text{O}_2$  calcined with LiOH in an oxygen-rich atmosphere at 775 °C for 12 hours, including the lattice parameters, the calculated nickel fraction in the lithium  $3a$  layer, and the (003)/(104) peak ratio. The  $\text{Ni}_{0.8}\text{Mn}_{0.1}\text{Co}_{0.1}(\text{OH})_2$  precursors were synthesised in a microwave reactor at 200 °C for 30 minutes – 3 hours.

Reaction duration	$a$ -, $b$ - axis (Å)	$c$ - axis (Å)	$c/a$ ratio	Unit cell volume (Å <sup>3</sup> )	Ni fraction in the Li layer (%)	Chi <sup>2</sup> value	(003)/(104) peak ratio
30 minutes	2.8722(1)	14.1947(4)	4.9421(3)	101.41(5)	4.5(1)	5.690	1.660
45 minutes	2.8718(1)	14.1959(3)	4.9432(2)	101.29(3)	3.4(1)	5.894	2.736
1 hour	2.8726(1)	14.1939(6)	4.9411(3)	101.44(7)	1.5(1)	12.938	1.998
2 hours	2.8734(1)	14.1977(5)	4.9410(3)	101.52(6)	3.1(1)	8.846	1.806
3 hours	2.8729(1)	14.1967(4)	4.9416(2)	101.48(4)	5.8(1)	5.863	1.822

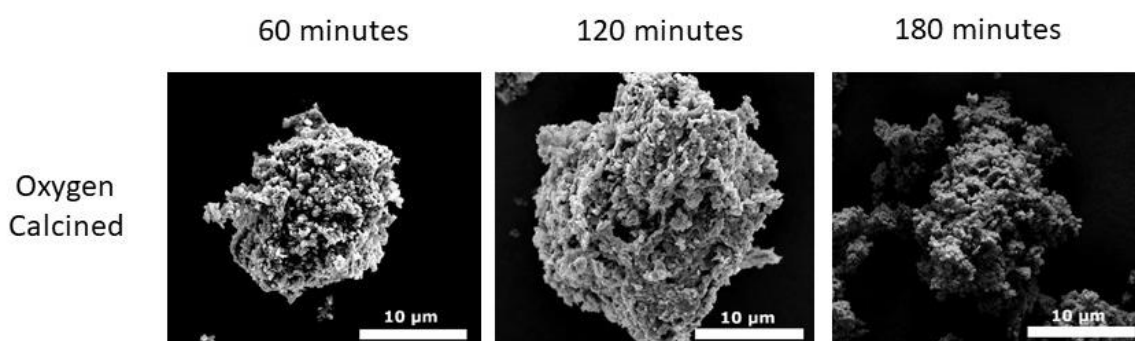


**Figure 5.0.5:** SEM images of  $\text{LiNi}_{0.8}\text{Mn}_{0.1}\text{Co}_{0.1}\text{O}_2$  calcined in an oxygen-fed tube furnace (775 °C, 12 hours). Samples were synthesised using a microwave-assisted hydrothermal method at 200 °C for 1 hour, 2 hours and 3 hours.

### 5.1.2. Optimisation of the Reaction Temperature

The reaction temperature can affect the internal pressure of the vessel depending on the boiling point of the solvent and Charles's law. Temperatures of 180, 200 and 220 °C were investigated for a reaction duration of 2 hours. XRD analysis shows the formation of  $\beta\text{-Ni}_{0.8}\text{Mn}_{0.1}\text{Co}_{0.1}(\text{OH})_2$  for all temperatures (Figure 5.0.6). There is a minor spinel phase impurity observed in all samples which is qualitatively identified due the unknown orientation of the spinel phase. SEM analysis of the synthesised  $\text{Ni}_{0.8}\text{Mn}_{0.1}\text{Co}_{0.1}(\text{OH})_2$  shows the formation of a quasi-spherical morphology with a secondary particle diameter of 10-20  $\mu\text{m}$  (Figure 5.0.7).

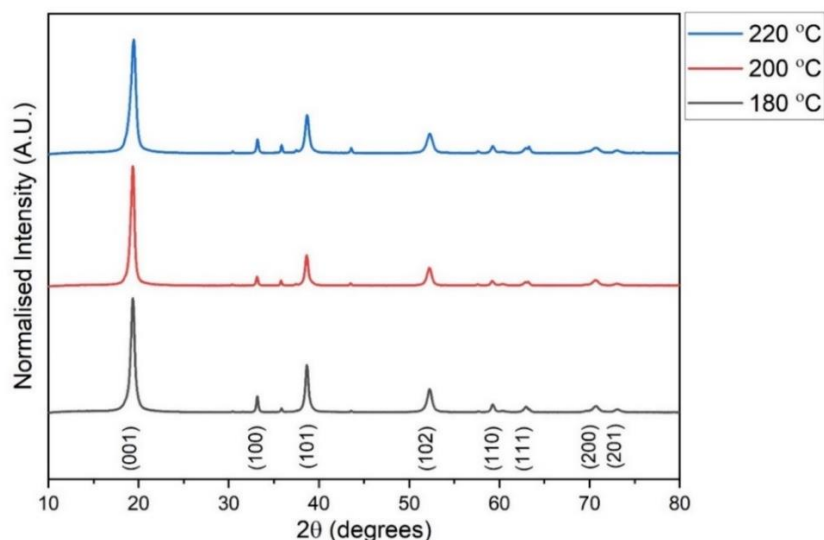


**Figure 5.0.6:** XRD profiles of  $\text{Ni}_{0.8}\text{Mn}_{0.1}\text{Co}_{0.1}(\text{OH})_2$  synthesised *via* a microwave-assisted hydrothermal method at 180, 200 and 220 °C for 2 hours, with labelled Bragg peaks.

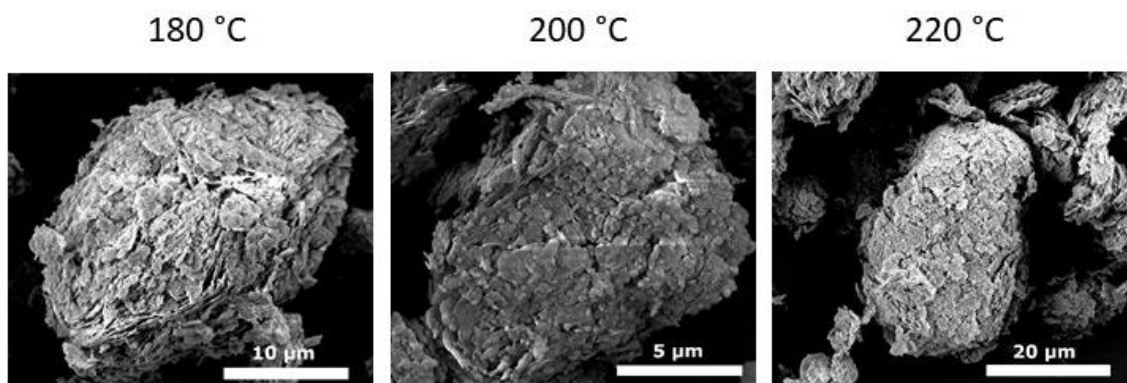


**Figure 5.0.7:** SEM images of  $\text{Ni}_{0.8}\text{Mn}_{0.1}\text{Co}_{0.1}(\text{OH})_2$  synthesised *via* a microwave-assisted hydrothermal method for 2 hours at 180, 200 and 220 °C.

**Table 5.0.2:** Key values from the Rietveld refinement of  $\text{LiNi}_{0.8}\text{Mn}_{0.1}\text{Co}_{0.1}\text{O}_2$  calcined with LiOH in an oxygen-rich atmosphere at 775 °C for 12 hours, including the lattice parameters, the calculated nickel fraction in the lithium  $3a$  layer, and the (003)/(104) peak ratio. The  $\text{Ni}_{0.8}\text{Mn}_{0.1}\text{Co}_{0.1}(\text{OH})_2$  precursors were synthesised in a microwave reactor at 180-220 °C for 2 hours.

Reaction temperature (°C)	$a$ -, $b$ - axis (Å)	$c$ - axis (Å)	$c/a$ ratio	Unit cell volume (Å <sup>3</sup> )	Ni fraction in the Li layer (%)	Chi <sup>2</sup> value	(003)/(104) peak ratio
180 °C	2.8728(1)	14.1948(4)	4.9412(3)	101.45(5)	4.4(1)	6.503	1.670
200 °C	2.8734(1)	14.1977(5)	4.9410(3)	101.52(6)	3.1(1)	8.846	1.806
220 °C	2.8726(1)	14.1953(5)	4.9416(3)	101.45(5)	3.7(1)	8.518	1.839

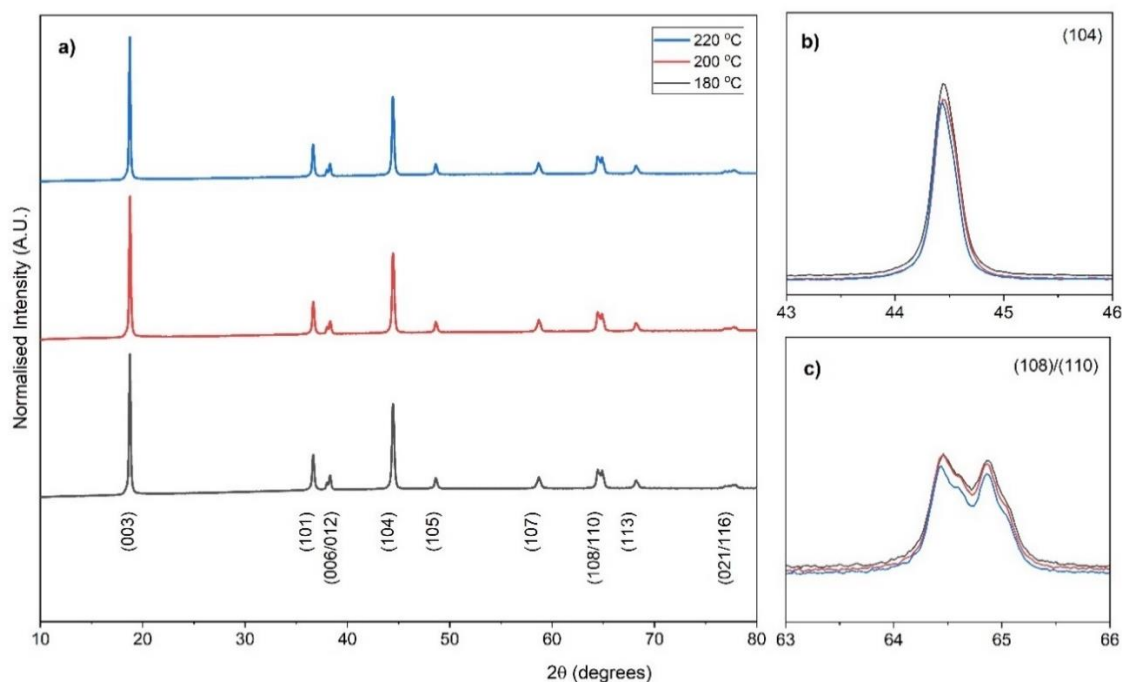


**Figure 5.0.8: (a)** XRD profiles of  $\text{LiNi}_{0.8}\text{Mn}_{0.1}\text{Co}_{0.1}\text{O}_2$ , calcined with LiOH for 12 hours in an oxygen-fed tube furnace at 775 °C. The (104) peak and (108)/(110) peak doublet are enclosed in **(b)** and **(c)**.

The  $\text{Ni}_{0.8}\text{Mn}_{0.1}\text{Co}_{0.1}(\text{OH})_2$  precursor were calcined in an oxygen-fed tube furnace. XRD analysis showed the resultant  $\text{LiNi}_{0.8}\text{Mn}_{0.1}\text{Co}_{0.1}\text{O}_2$  formed the desired  $\alpha\text{-NaFeO}_2$  layered oxide structure (Figure 5.0.8). The (003)/(104) peak ratios indicate the degree of cation mixing within the samples, with all temperatures having similar peak ratios of *ca.* 1.81. Rietveld refinement confirmed the similar degree of cation mixing, with 4.4%, 3.1% and 3.7% nickel in the lithium layer for the 180 °C, 200 °C and 220 °C samples respectively, as described in Table 5.0.2 (associated plots are included in Appendix A.14). The crystallinity of the samples is also similar across all samples, with a similar degree of peak splitting observed in the (108)/(110) peak doublet. SEM analysis of the calcined  $\text{LiNi}_{0.8}\text{Mn}_{0.1}\text{Co}_{0.1}\text{O}_2$  samples shows the quasi-spherical secondary particle assembly remains after calcination, with no change in the 10-20  $\mu\text{m}$  particle size (Figure 5.0.9).

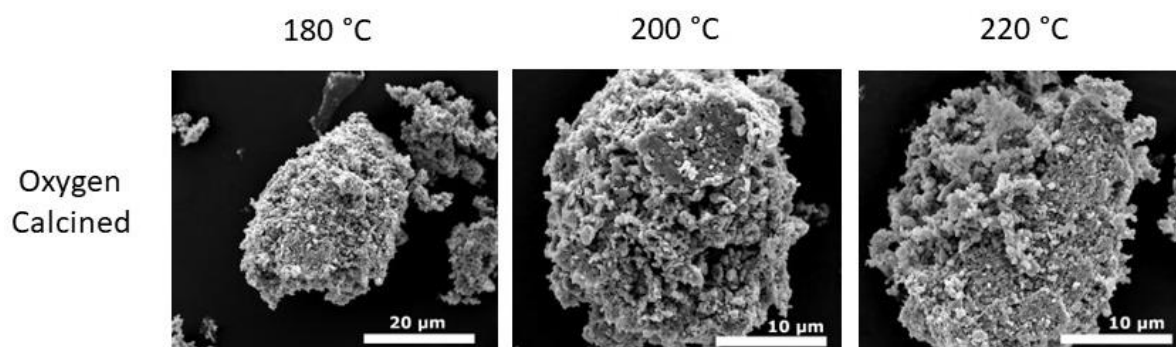


**Figure 5.0.9:** SEM images of  $\text{LiNi}_{0.8}\text{Mn}_{0.1}\text{Co}_{0.1}\text{O}_2$  calcined at  $775\text{ }^\circ\text{C}$  for 12 hours. These samples were synthesised using a microwave-assisted hydrothermal method for 2 hours at 180, 200 and  $220\text{ }^\circ\text{C}$ .

### 5.1.3. Investigating the Effect of Pressure on the Reaction

To evaluate the effect of pressure on the synthesis of  $\text{Ni}_{0.8}\text{Mn}_{0.1}\text{Co}_{0.1}(\text{OH})_2$ , reactions were carried out in solvent volumes of 20 mL and 40 mL at  $200\text{ }^\circ\text{C}$  to examine the effect of head space pressure on the reaction outcome. This also provides insight into the scalability of the process. An alternative trial controlled the pressure of the hydrothermal vessel to 400 PSI for a 20 mL reaction. This increased the ramp time to 5 minutes compared to the temperature-controlled ( $200\text{ }^\circ\text{C}$ ) trials which took 20 minutes.

XRD analysis revealed the formation of the  $\beta\text{-Ni}_{0.8}\text{Mn}_{0.1}\text{Co}_{0.1}(\text{OH})_2$ . The 20 mL and 400 PSI samples have similar crystallographic profiles, demonstrating the synthesis of  $\beta\text{-Ni}_{0.8}\text{Mn}_{0.1}\text{Co}_{0.1}(\text{OH})_2$ , with evidence of a minor spinel impurity. The samples prepared with 40 mL of solvent displays the  $\beta\text{-Ni}_{0.8}\text{Mn}_{0.1}\text{Co}_{0.1}(\text{OH})_2$  with no evidence for phase impurities (Figure 5.0.10). SEM analysis of synthesised  $\text{Ni}_{0.8}\text{Mn}_{0.1}\text{Co}_{0.1}(\text{OH})_2$  shows the samples prepared with 40 mL of solvent comprises secondary particles with lower density agglomeration compared with more densely-packed, quasi-spherical secondary structures observed for samples prepared with 20 L of solvent at  $200\text{ }^\circ\text{C}$  or 400 PSI (Figure 5.0.11), indicating it is the result of increased pressure within the system. This increase in pressure has little impact on the primary particle formation, as all samples have the similar primary particles sizes.

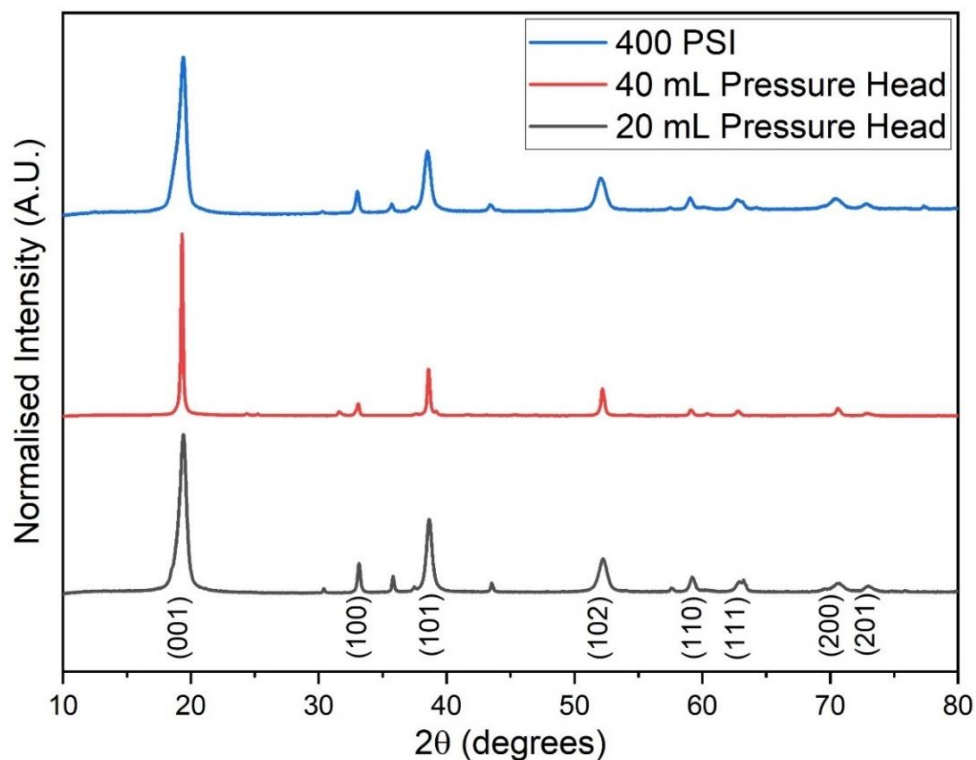


**Figure 5.0.10:** XRD profiles of  $\text{Ni}_{0.8}\text{Mn}_{0.1}\text{Co}_{0.1}(\text{OH})_2$  synthesised *via* a microwave-assisted hydrothermal method for 3 hours at a variety of pressures: 200 °C with a volume of 20 mL, 200 °C with a volume of 40 mL; and at 400 PSI.

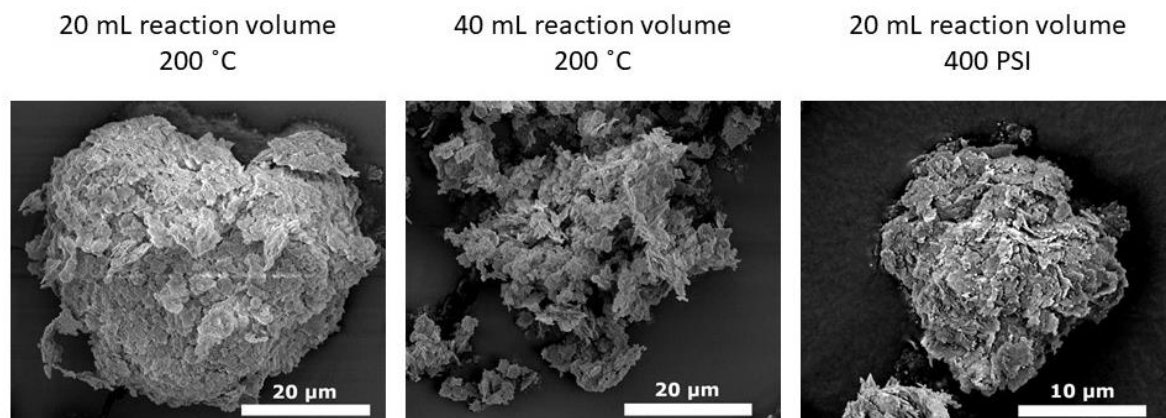


**Figure 5.0.11:** SEM images of  $\text{Ni}_{0.8}\text{Mn}_{0.1}\text{Co}_{0.1}(\text{OH})_2$  synthesised *via* a microwave-assisted hydrothermal method for 3 hours in 20 mL of solvent (left), 40 mL of solvent (centre), and in 20 mL solvent at a fixed pressure of 400 PSI with variable temperature.

The  $\text{Ni}_{0.8}\text{Mn}_{0.1}\text{Co}_{0.1}(\text{OH})_2$  samples were calcined under an oxygen environment. XRD analysis shows the formation of the  $\alpha\text{-NaFeO}_2$  layered  $\text{LiNi}_{0.8}\text{Mn}_{0.1}\text{Co}_{0.1}\text{O}_2$  (Figure 5.0.12). The (003)/(104) peak ratio is a qualitative indicator for the degree of cation mixing, with 400 PSI sample having the smallest ratio of 1.41, indicating the most cation mixing, whereas the two temperature-controlled (20 mL and 40 mL) samples have ratios of 1.81 and 1.71 respectively. Rietveld refinement confirmed this with the degree of cation mixing calculated to be 6.8%, 6.2% and 5.8% respectively, as shown in Table 5.0.3 (associated plots are depicted in Appendix A.15). The two temperature-controlled samples (20 mL and 40 mL) observed (108)/(110) peak doublet splitting, indicating a good degree of layered ordering within the structure, whereas the 400 PSI sample observed a reduced degree of splitting. SEM analysis of the calcined  $\text{LiNi}_{0.8}\text{Mn}_{0.1}\text{Co}_{0.1}\text{O}_2$  showing quasi-spherical secondary particle assemblies with a particle diameter of *ca.* 10-25  $\mu\text{m}$  Figure 5.0.13.

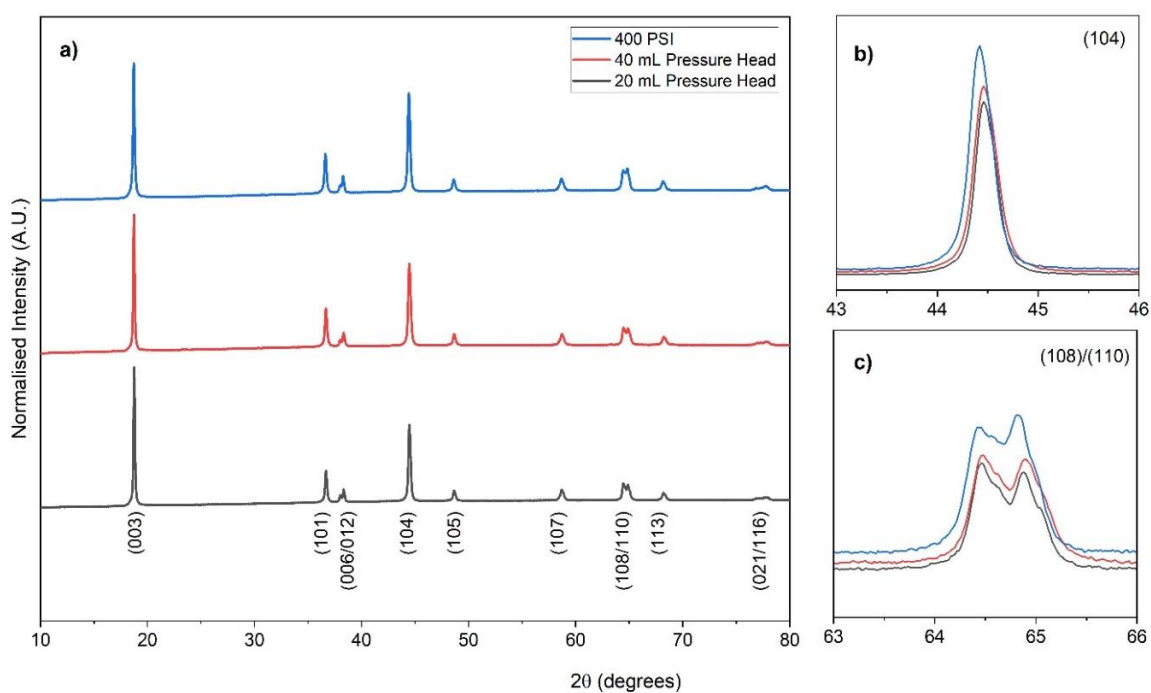


**Figure 5.0.12: (a)** XRD profiles of  $\text{LiNi}_{0.8}\text{Mn}_{0.1}\text{Co}_{0.1}\text{O}_2$ , calcined with LiOH for 12 hours in an oxygen-fed tube furnace at 775 °C. The (104) peak and (108)/(110) peak doublet are enclosed in **(b)** and **(c)**.

**Table 5.0.3:** Key values from the Rietveld refinement of  $\text{LiNi}_{0.8}\text{Mn}_{0.1}\text{Co}_{0.1}\text{O}_2$  calcined with LiOH in an oxygen-rich atmosphere at 775 °C for 12 hours, including the lattice parameters, the calculated nickel fraction in the lithium  $3a$  layer, and the (003)/(104) peak ratio. The  $\text{Ni}_{0.8}\text{Mn}_{0.1}\text{Co}_{0.1}(\text{OH})_2$  precursors were synthesised in a microwave reactor for 3 hours at conditions to provoke different pressures within the hydrothermal vessels.

Reaction conditions	$a$ -, $b$ - axis (Å)	$c$ - axis (Å)	$c/a$ ratio	Unit cell volume (Å <sup>3</sup> )	Ni fraction in the Li layer (%)	Chi <sup>2</sup> value	(003)/(104) peak ratio
200 °C, 20 mL	2.8729(1)	14.1967(4)	4.9416(2)	101.47(4)	5.8(1)	5.863	1.822
200 °C, 40 mL	2.8709(1)	14.1905(4)	4.9428(3)	101.29 (5)	6.2(1)	5.863	1.683
400 PSI, 20 mL	2.8735(1)	14.1911(4)	4.9386(2)	101.48(4)	6.8(1)	5.072	1.406

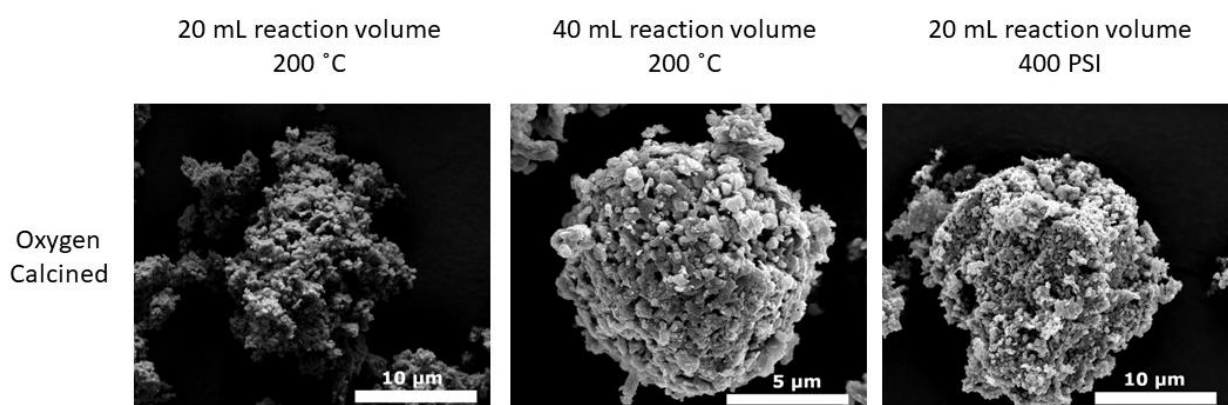


**Figure 5.0.13:** SEM images of  $\text{LiNi}_{0.8}\text{Mn}_{0.1}\text{Co}_{0.1}\text{O}_2$  synthesised *via* a microwave-assisted hydrothermal method for 3 hours at different pressures: the hydrostatic pressure head for a 20 mL reaction (left) and 40 mL (centre), as well as a fixed pressure of 400 PSI with variable temperature. Samples calcined in an oxygen-supplied tube furnace at 775 °C for 12 hours.

#### 5.1.4. Optimisation of the urea ratio

Shi *et al.* discusses the role of urea in the hydrothermal reaction, with an increasing urea: transition metal ratio resulting in the formation of more  $\text{NH}_4^+$  ions and  $[\text{M}(\text{NH}_3)_n]^{2+}$  ligands [150]. XRD analysis of  $\text{Ni}_{0.8}\text{Mn}_{0.1}\text{Co}_{0.1}(\text{OH})_2$  synthesised with a urea: transition metal ratios ranging from 1: 1 to 5: 1 show the formation of a desirable  $\beta$ -polymorph hydroxide phase after a 45-minute reaction at 200 °C (Figure 5.0.14). A low-angle shoulder of the (001) peak in the 1: 1 urea: transition metal sample is observed, which could indicate a stacking fault in the  $c$ -axis of the parallel transition metal layers or

phase impurity. This stacking fault is thought to be a result of the carboxyl or carbonate ions that reside within the interplanar gallery, which results in the splitting of the (001) peak, as seen in the  $\alpha$ - polymorph of the transition metal hydroxide phase described in Section 1.2.4. Additional peaks can be observed in samples is attributed a spinel phase, possibly caused by the oxidation of manganese to form a  $Mn_3O_4$  spinel phase.

SEM analysis of the  $Ni_{0.8}Mn_{0.1}Co_{0.1}(OH)_2$  precursor show the formation of secondary particle assemblies for all urea: transition metal ratio samples (Figure 5.0.15). The 1:1, 2.5:1 and 2.9:1 samples show densely agglomerated primary particles that form quasi-spherical secondary constructions. The 3:1 sample also has a quasi-spherical secondary particle morphology but with poor primary particle packing. The 5: 1 urea ratio also has a secondary particle arrangement but was not a uniform spherical structure and the primary particles appear smaller than other samples. The typical secondary particle size is  $\sim 12 \mu m$  for all samples apart from the 1:1 urea ratio sample, which has a particle diameter of  $\sim 40 \mu m$ .

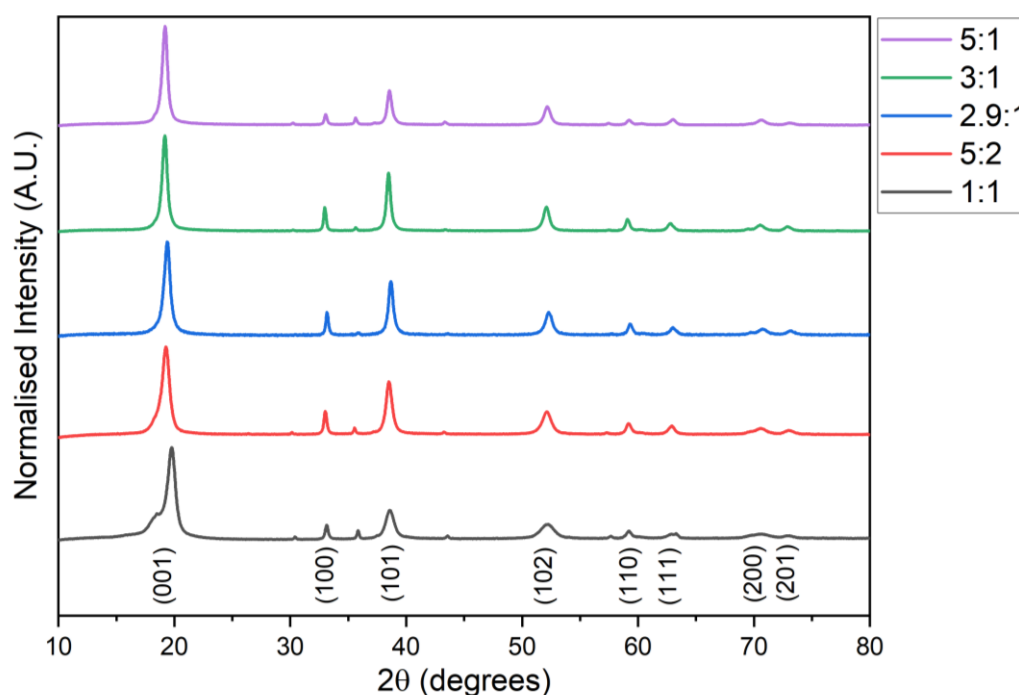


**Figure 5.0.14:** XRD profiles of  $Ni_{0.8}Mn_{0.1}Co_{0.1}(OH)_2$  synthesised *via* a microwave-assisted hydrothermal method at 200 °C for 45 minutes using a range of urea: transition metal ratios (1: 1, 5: 2, 2.9: 1, 3: 1 and 5: 1). The Bragg's peaks for the  $\beta$ -polymorph  $Ni_{0.8}Mn_{0.1}Co_{0.1}(OH)_2$  are labelled.

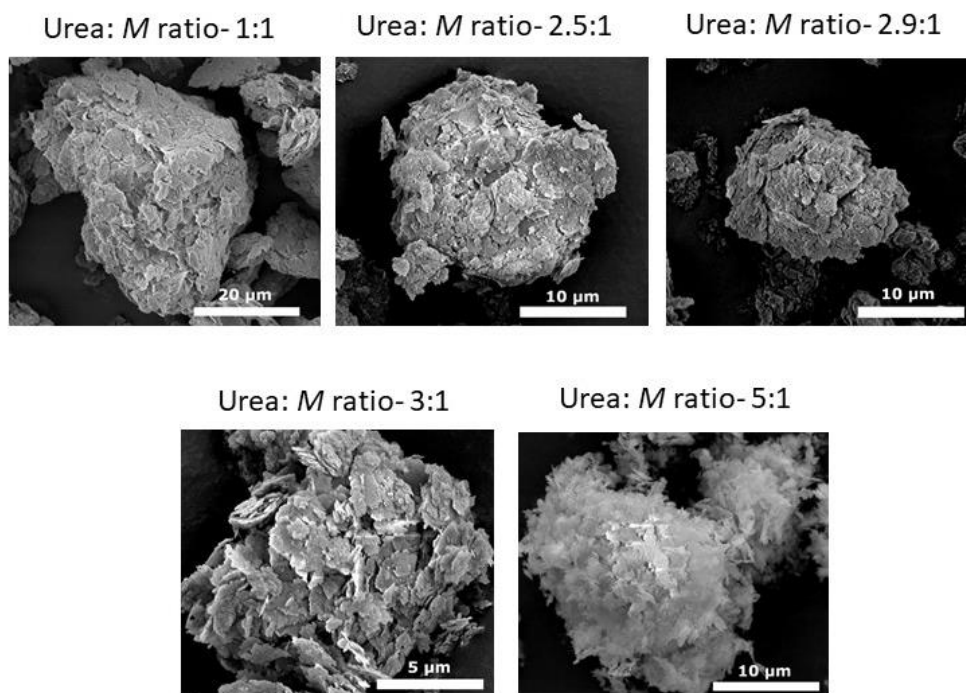


**Figure 5.0.15:** SEM images of  $\text{Ni}_{0.8}\text{Mn}_{0.1}\text{Co}_{0.1}(\text{OH})_2$  synthesised *via* a microwave-assisted hydrothermal method for 45 minutes at 200 °C using a variety of urea: transition metal (*M*) ratios, ranging from 1:1 to 5:1.

The  $\text{Ni}_{0.8}\text{Mn}_{0.1}\text{Co}_{0.1}(\text{OH})_2$  precursor samples were calcined under oxygen XRD analysis reveals the formation of the desired  $\alpha\text{-NaFeO}_2$  layered  $\text{LiNi}_{0.8}\text{Mn}_{0.1}\text{Co}_{0.1}\text{O}_2$  phase in all samples (Figure 5.0.16). The 5: 1 and 5: 2 samples have similar, small (003)/(104) peak ratios of 1.13-1.15, indicating poor cation mixing. Rietveld refinement supports this, with cation mixing values of 19.6% and 20.4%, compared to values of 4.8%, 3.4% and 2.3% for the 1:1, 2.9:1 and 3:1 samples respectively, as shown in Table 5.0.4 (associated plots depicted in Appendix A.16). The 5: 1 and 5: 2 *M*: urea samples do not have splitting of the (108)/(110) peak doublet, indicating poor layered ordering, whereas the 1:1, 2.9:1 and 3:1 samples have the peak doublet splitting, indicating better crystallinity.

**Table 5.0.4:** Key values from the Rietveld refinement of  $\text{LiNi}_{0.8}\text{Mn}_{0.1}\text{Co}_{0.1}\text{O}_2$  calcined with LiOH in an oxygen-rich atmosphere at 775 °C for 12 hours, including the lattice parameters, the calculated nickel fraction in the lithium  $3a$  layer, and the (003)/(104) peak ratio. The  $\text{Ni}_{0.8}\text{Mn}_{0.1}\text{Co}_{0.1}(\text{OH})_2$  precursors were synthesised in a microwave reactor at 200 °C for 45 minutes using a range of Urea: transition metal ratios.

Urea ratio in the reaction	$a$ -, $b$ - axis (Å)	$c$ - axis (Å)	$c/a$ ratio	Unit cell volume (Å <sup>3</sup> )	Ni fraction in the Li layer (%)	Chi <sup>2</sup> value	(003)/(104) peak ratio
1.0:1	2.8721(1)	14.1918(4)	4.9413(2)	101.38(4)	4.8(1)	6.081	1.660
2.5:1	2.8880(1)	14.2353(1)	4.9282(2)	102.81(7)	19.6(1)	9.191	2.736
2.9:1	2.8718(5)	14.1959(3)	4.9432(2)	101.39(3)	3.4(1)	5.864	1.998
3.0:1	2.8730(1)	14.1968(4)	4.9414(3)	101.48(5)	2.3(1)	8.754	1.806
5.0:1	2.8879(1)	14.2319(7)	4.9281(4)	102.79(8)	20.4(2)	9.196	1.822

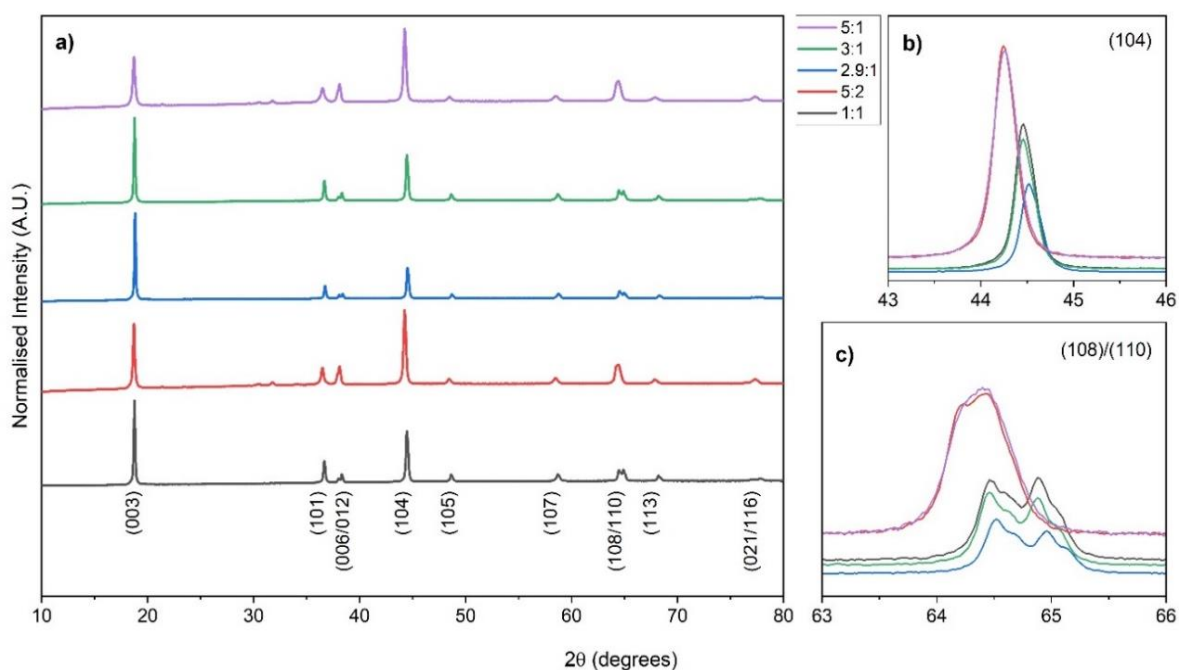


**Figure 5.0.16:** (a) XRD profiles of  $\text{LiNi}_{0.8}\text{Mn}_{0.1}\text{Co}_{0.1}\text{O}_2$ , calcined with LiOH for 12 hours in an oxygen-fed tube furnace at 775 °C. The (104) peak and (108)/(110) peak doublet are enclosed in (b) and (c).

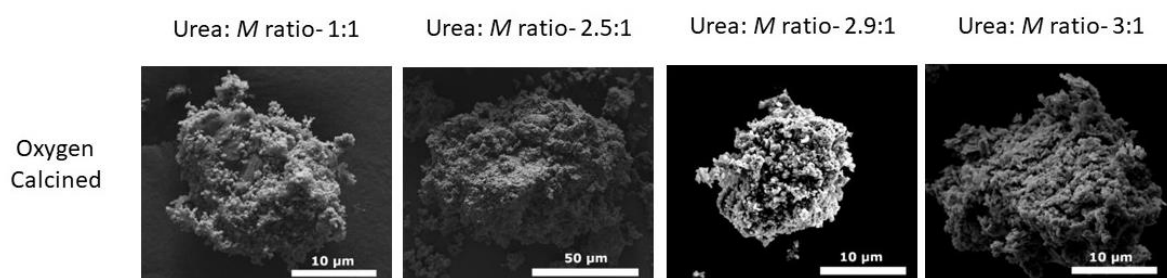


**Figure 5.0.17:** SEM images of  $\text{LiNi}_{0.8}\text{Mn}_{0.1}\text{Co}_{0.1}\text{O}_2$  synthesised *via* a microwave-assisted hydrothermal method for 45 minutes at 200 °C using a range of urea: transition metal (*M*) ratios, 1:1 to 5:1.

SEM analysis of the  $\text{LiNi}_{0.8}\text{Mn}_{0.1}\text{Co}_{0.1}\text{O}_2$  samples showed the formation of quasi-spherical secondary particle assemblies with similar primary particle sizes and morphologies (Figure 5.0.17). Variation in secondary particle size was observed, with particle sizes ranging from approximately 10-100  $\mu\text{m}$ .

## 5.2. Electrochemical Analysis of Hydrothermally Synthesised $\text{LiNi}_{0.8}\text{Mn}_{0.1}\text{Co}_{0.1}\text{O}_2$

### 5.2.1. Effect of Temperature and Duration on the Electrochemical Performance

$\text{LiNi}_{0.8}\text{Mn}_{0.1}\text{Co}_{0.1}\text{O}_2$  synthesised at 200 and 220 °C, for 1, 2 and 3 hours were cycled in half-cells between 3.0-4.3 V, at a rate of C/20 for two formation cycles followed by 50 cycles at a rate of C/2. The capacity and capacity retention data in Figure 5.0.18 indicates that samples synthesised at 220 °C yield higher capacities than samples synthesised at 200 °C (205.0-223.4  $\text{mAh g}^{-1}$  compared to 192.5-194.5  $\text{mAh g}^{-1}$  for the 2-hour reaction sample, cycled at C/20). The 2-hour reaction samples yield higher capacities (184.7  $\text{mAh g}^{-1}$ , cycled at C/2) than the 3-hour reaction samples (175.9  $\text{mAh g}^{-1}$ , cycled at C/2) and 1-hour samples (177.3  $\text{mAh g}^{-1}$ , cycled at C/2). The capacity retention over 50 cycles for the 220 °C samples indicated the 2-hour reaction samples had the largest retention of 91.5% compared to the 3-hour reaction (90.7%) and 1-hour reaction (74.2%)

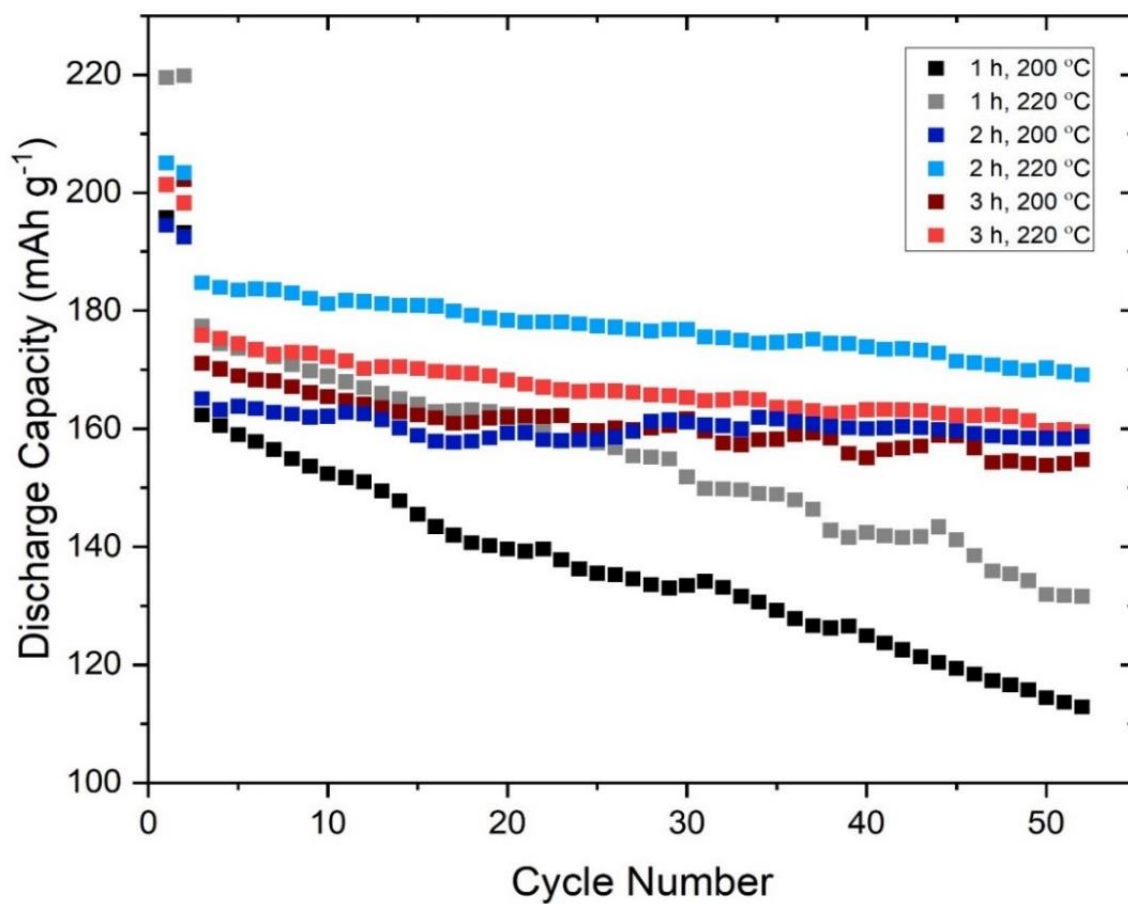


**Figure 5.0.18:** Capacity retention plot for the  $\text{LiNi}_{0.8}\text{Mn}_{0.1}\text{Co}_{0.1}\text{O}_2$  samples with a precursor synthesis reaction duration of 1-, 2- and 3- hours and a reaction temperature of 200 and 220 °C. The half-cells were cycled at 3.0-4.3 V for 52 cycles (2 cycles of C/20, 50 cycles of C/2).

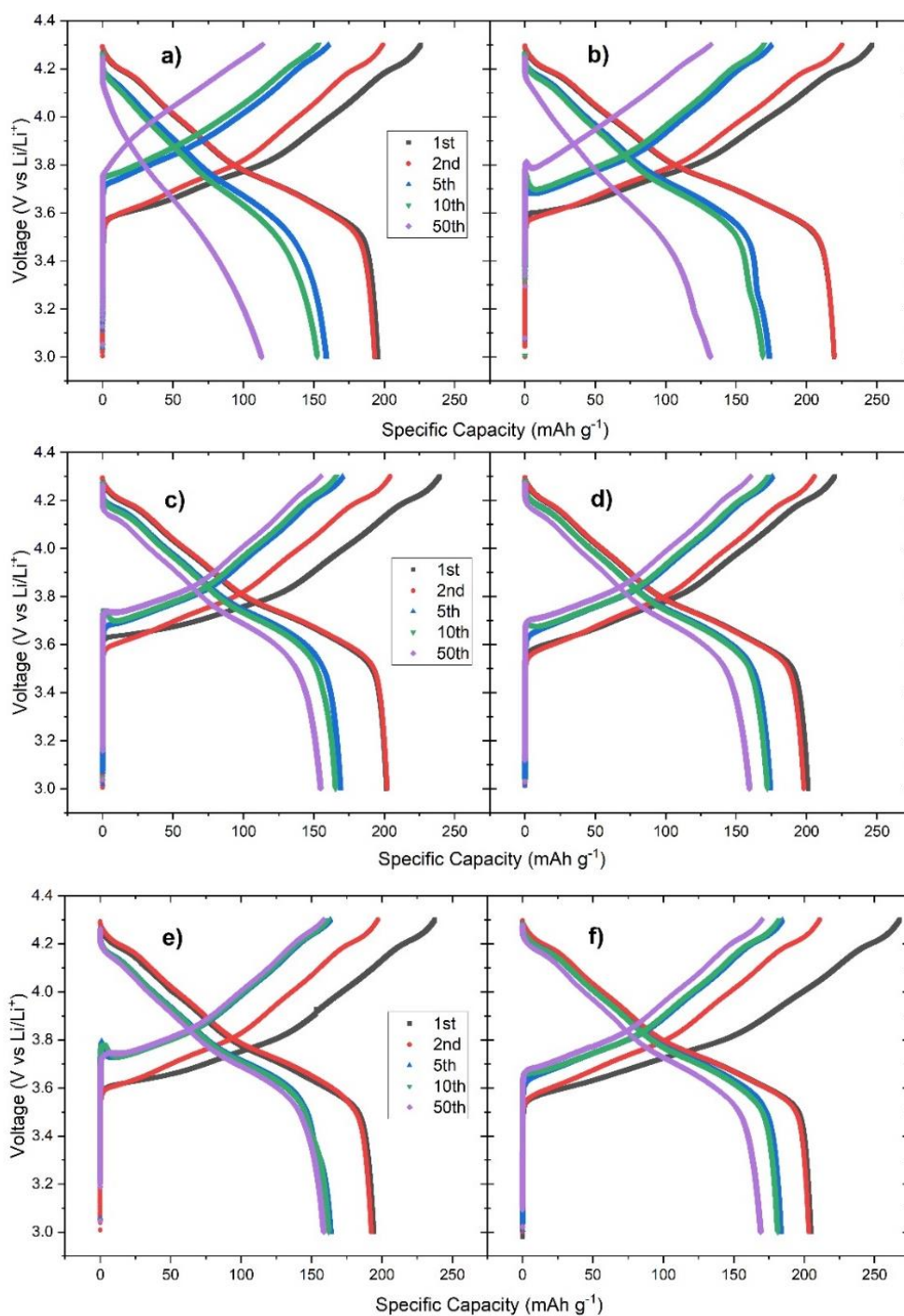


**Figure 5.0.19:** Voltage profile plots of the  $\text{LiNi}_{0.8}\text{Mn}_{0.1}\text{Co}_{0.1}\text{O}_2$  samples with a precursor synthesis reaction duration of 1- (a-b), 2- (c-d) and 3- (e-f) hours and a reaction temperature of 200 °C (a, c, e) and 220 °C (b, d, f). The voltage profiles include the 1<sup>st</sup>, 2<sup>nd</sup>, 5<sup>th</sup>, 10<sup>th</sup> and 50<sup>th</sup> cycles.

Voltage profiles show the delithiation voltage C/20 discharge voltage is *ca.* 3.5-3.6 V, which increases to *ca.* 3.65-3.8 V as the cycling rate increases to C/2 (Figure 5.0.19). An overpotential is also observed in some later cycles, represented as a 'hump' prior to discharge, which is thought to be

related to the build-up of lithium-containing materials at the surface of the particles. The voltage profiles for each sample appear to have similar characteristics, with two distinct gradients, one below *ca.* 3.8 V, one between 3.8-4.2 V. Differential capacity plots (Figure 5.0.20) reveal redox processes at *ca.* 3.6-3.8 V and 4.0 V. Polarisation can be observed by the high-voltage shift in the positive, charging  $dQ/dV$  profile and low-voltage shift in the discharge, negative profile.

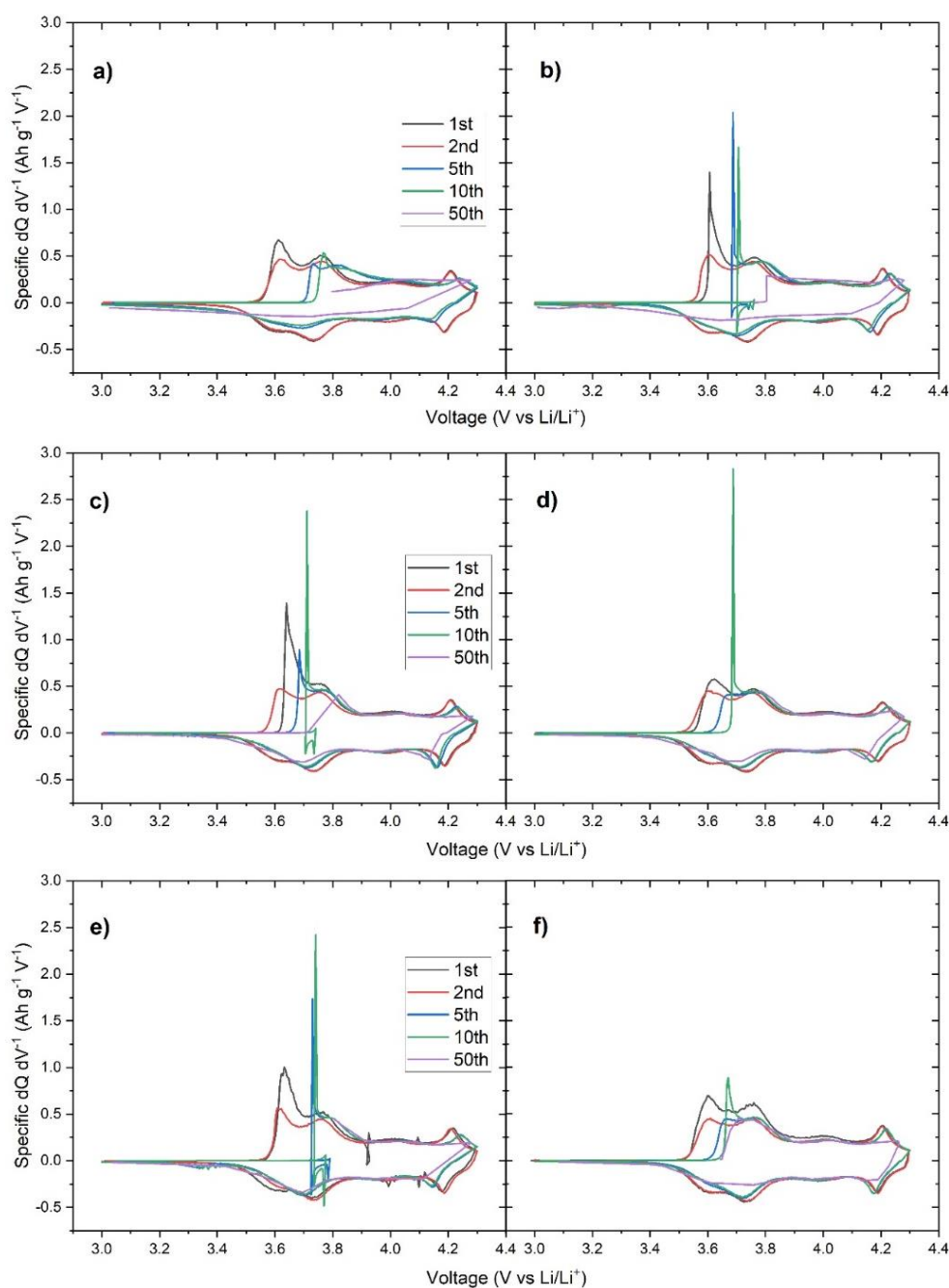


**Figure 5.0.20:** Differential capacity profiles for the  $\text{LiNi}_{0.8}\text{Mn}_{0.1}\text{Co}_{0.1}\text{O}_2$  samples with a precursor synthesis reaction duration of 1- (a-b), 2- (c-d) and 3- (e-f) hours and a reaction temperature of 200 °C (a, c, e) and 220 °C (b, d, f). The profiles for the 1<sup>st</sup>, 2<sup>nd</sup>, 5<sup>th</sup>, 10<sup>th</sup> and 50<sup>th</sup> cycles are included.

### 5.2.2. Effect of pressure on the capacity of microwave-assisted hydrothermal $\text{LiNi}_{0.8}\text{Mn}_{0.1}\text{Co}_{0.1}\text{O}_2$

The 20 mL and 40 mL volume samples for the 1-, 2- and 3- hour samples were reacted at 200 °C and compared with a sample that reacted for 3 hours at 400 PSI. Half-cells were cycled between 3.0-4.3 V for 2 cycles at C/20 and C/2 for 50 cycles. The initial C/20 discharge capacity delivered by the 20 mL samples (*i.e.* the 1-, 2-, 3- hour samples and the 400 PSI sample) was 192.5-202.2 mAh g<sup>-1</sup>. The 40 mL samples that reacted for 1-, 2- and 3- hours had discharge capacities of 170.6-174.0, 163.5-164.2, and 194.2-196.1 mAh g<sup>-1</sup> respectively at C/20 (Figure 5.0.21). When cycled at C/2, a capacity retention of 96.1%, 90.4% and 93.9% is observed over 50 cycles for the 20 mL, 2- and 3- hour samples, and the 40 mL, 3- hour sample respectively. The 40 mL samples with reaction durations of 1- and 2- hours achieved a capacity retention of 91.7% and 89.2% respectively. The 400 PSI sample retained 70.5% of its capacity over 50 cycles.

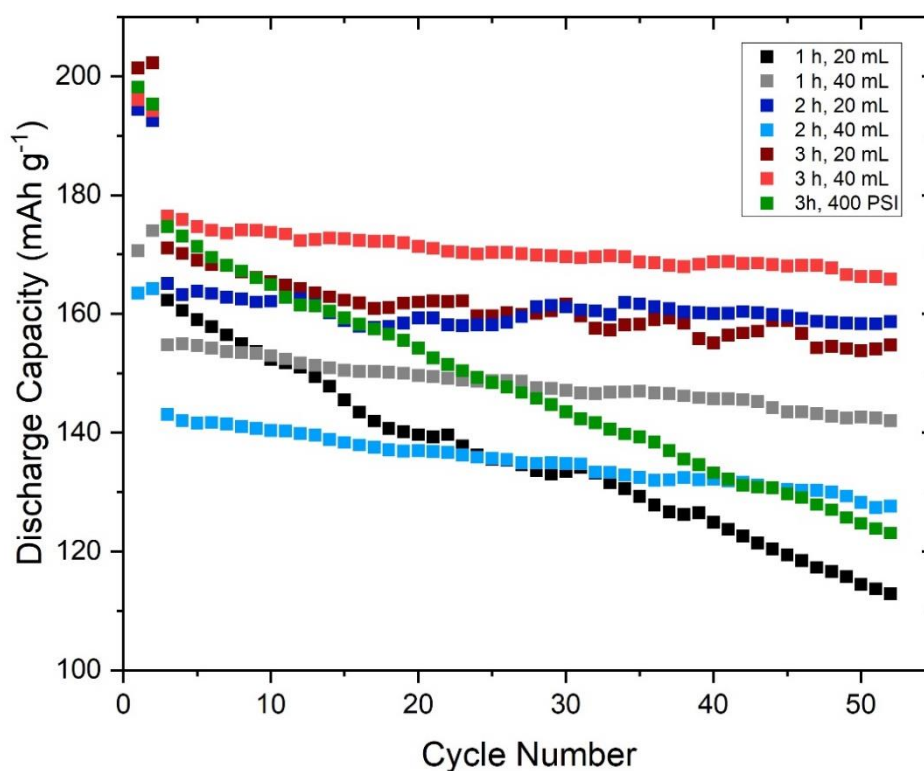


**Figure 5.0.21:** Capacity retention plot for the  $\text{LiNi}_{0.8}\text{Mn}_{0.1}\text{Co}_{0.1}\text{O}_2$  samples with a precursor synthesis reaction duration of 1-, 2- and 3- hours, reaction temperature of 200 °C and a reaction volume of 20 or 40 mL. This was also compared to a 20 mL sample that was reacted at 400 PSI for 3 hours. The half-cells were cycled over a voltage window of 3.0-4.3 V, with 2 cycles of C/20, 50 cycles of C/2.

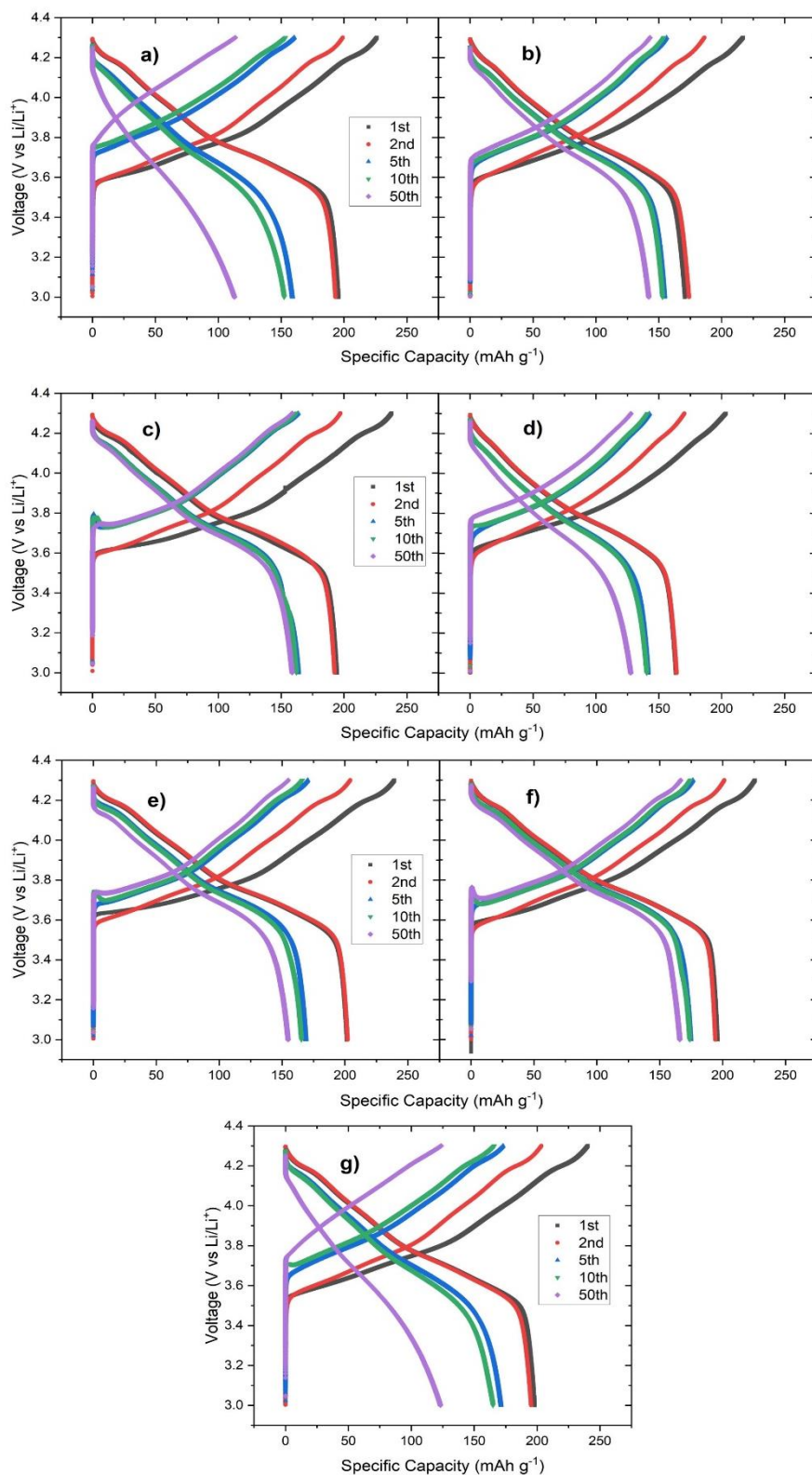


**Figure 5.0.22:** Voltage profile plots of the 1<sup>st</sup>, 2<sup>nd</sup>, 5<sup>th</sup>, 10<sup>th</sup> and 50<sup>th</sup> cycles for LiNi<sub>0.8</sub>Mn<sub>0.1</sub>Co<sub>0.1</sub>O<sub>2</sub> samples with a precursor synthesis reaction duration of 1- **(a-b)**, 2- **(c-d)** and 3- **(e-f)** hours with a reaction volume of 20 mL **(a, c, e)** and 40 mL **(b, d, f)**. The sample that was synthesised at 400 PSI for 3 hours is included in part **(g)**.

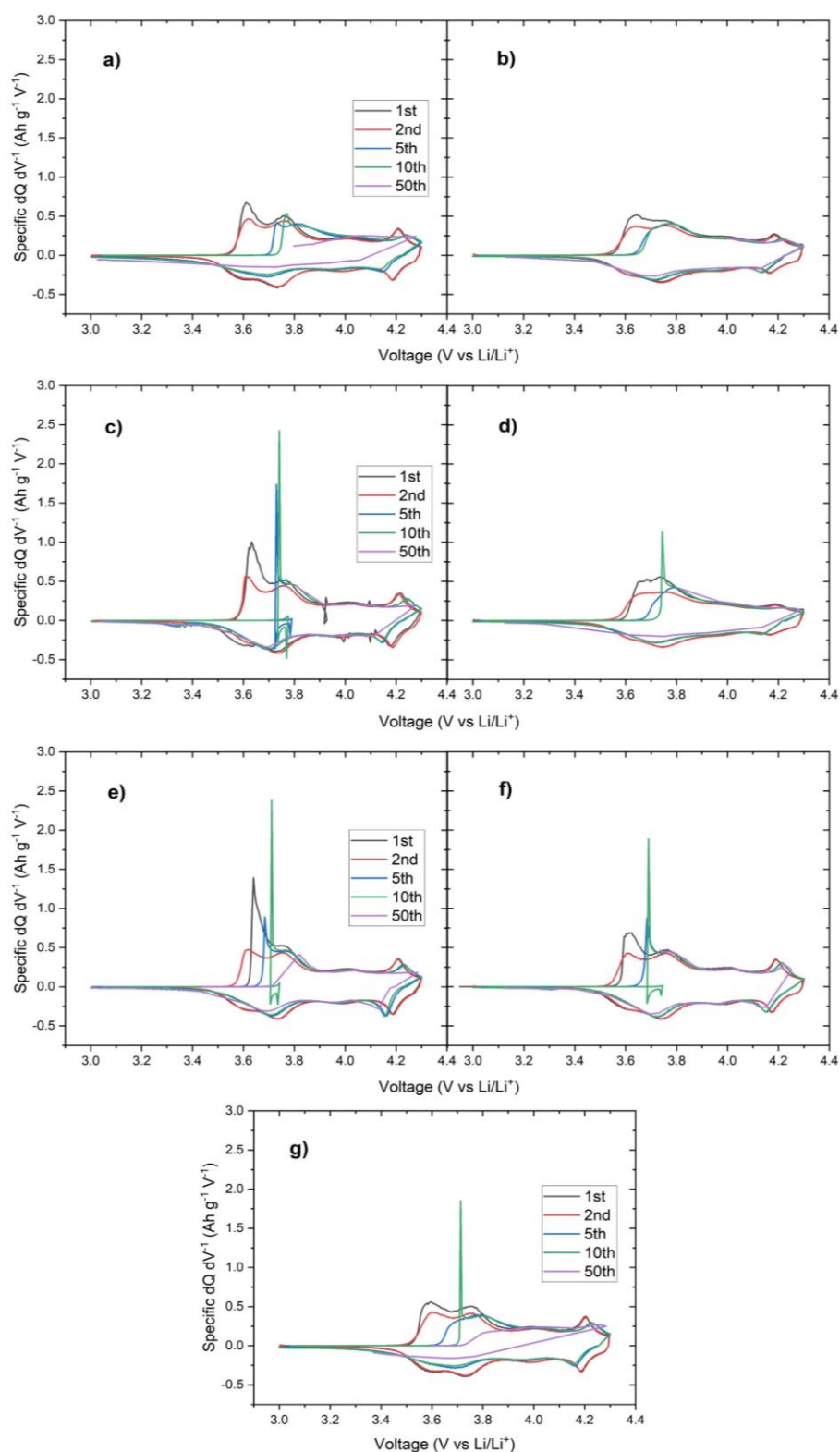


**Figure 5.0.23:** Differential capacity profile plots for the 1<sup>st</sup>, 2<sup>nd</sup>, 5<sup>th</sup>, 10<sup>th</sup> and 50<sup>th</sup> cycles of  $\text{LiNi}_{0.8}\text{Mn}_{0.1}\text{Co}_{0.1}\text{O}_2$  samples with a precursor synthesis reaction duration of 1- **(a-b)**, 2- **(c-d)** and 3- **(e-f)** hours with a reaction volume of 20 mL **(a, c, e)** and 40 mL **(b, d, f)**. The sample that was synthesised at 400 PSI for 3 hours is included in part **(g)**.

Voltage profiles show a delithiation voltage of *ca.* 3.55-3.6 V when cycled at C/20, with subsequent C/2 cycles increasing to *ca.* 3.65-3.8 V (Figure 5.0.22). The differential capacity profiles again reveal two redox processes at 3.6-3.8 V and *ca.* 4.0 V (Figure 5.0.23). These peaks see a high-voltage shift in the charging (positive) profile and low-voltage shift in the discharge (negative) profile associated with polarisation, which increases the operational voltage of the cell and thus decreases the electrochemical efficiency of the reaction, reducing the energy yield from the cell.

### 5.3. Synthesis of the $\alpha$ -Ni<sub>0.8</sub>Mn<sub>0.1</sub>Co<sub>0.1</sub>(OH)<sub>2</sub> polymorph

The microwave-assisted synthesis of Ni<sub>0.8</sub>Mn<sub>0.1</sub>Co<sub>0.1</sub>(OH)<sub>2</sub> can yield both  $\alpha$ - and  $\beta$ - polymorphs of the hydroxide precursor. To investigate the synthesis of the  $\alpha$ -Ni<sub>0.8</sub>Mn<sub>0.1</sub>Co<sub>0.1</sub>(OH)<sub>2</sub> polymorph, reactions were carried out with 40 mL of solvent for 45 minutes at 200 °C. XRD analysis in Figure 5.0.24 shows that both  $\alpha$ - and  $\beta$ - hydroxide polymorphs form desired layered LiNi<sub>0.8</sub>Mn<sub>0.1</sub>Co<sub>0.1</sub>O<sub>2</sub> phase after calcination in an oxygen-fed tube furnace at 775 °C for 12 hours. Both  $\alpha$ - and  $\beta$ - samples display similar (108)/(110) peak splitting, indicating that intercalated foreign species the formation of parallel transition metal layers and a good degree of transition metal layer ordering was achieved. The (003)/(104) peak ratio suggests the beta polymorph has an increased degree of cation ordering, with a ratio of 1.96 compared to 1.54 for the alpha polymorph.

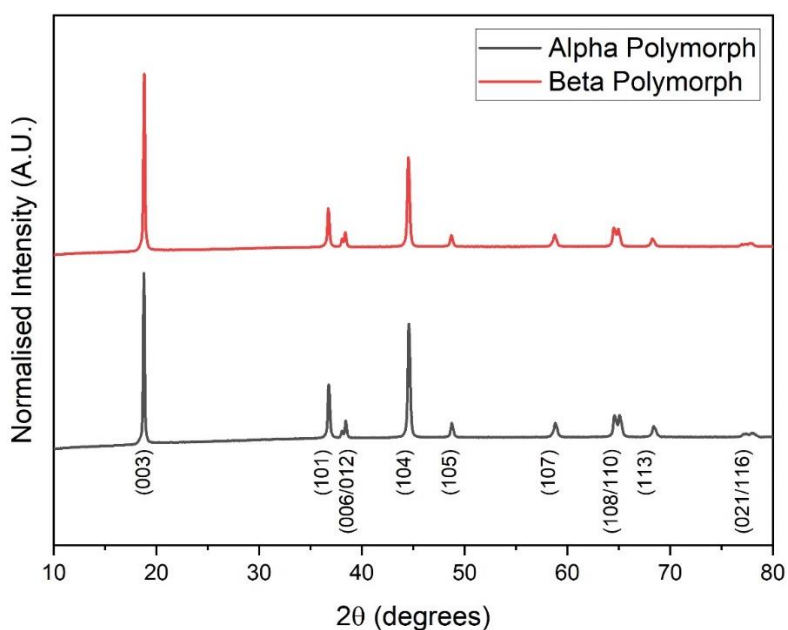


**Figure 5.0.24:** The XRD profiles of the LiNi<sub>0.8</sub>Mn<sub>0.1</sub>Co<sub>0.1</sub>O<sub>2</sub> samples calcined from the  $\alpha$ - and  $\beta$ - Ni<sub>0.8</sub>Mn<sub>0.1</sub>Co<sub>0.1</sub>(OH)<sub>2</sub> precursors, with the Bragg peaks labelled accordingly below the profiles.

$\text{LiNi}_{0.8}\text{Mn}_{0.1}\text{Co}_{0.1}\text{O}_2$  was obtained from the  $\alpha$ - and  $\beta$ -  $\text{Ni}_{0.8}\text{Mn}_{0.1}\text{Co}_{0.1}(\text{OH})_2$  samples and cycled over a voltage window of 3.0-4.3 V for 52 cycles (two formation cycles at C/20 followed by 50 cycles at C/2). The capacity delivered by the  $\alpha$ - $\text{Ni}_{0.8}\text{Mn}_{0.1}\text{Co}_{0.1}(\text{OH})_2$  yields a lower discharge capacity at C/20 (165.0-165.7 mAh g<sup>-1</sup>) compared to the  $\beta$ - $\text{Ni}_{0.8}\text{Mn}_{0.1}\text{Co}_{0.1}(\text{OH})_2$  alternative (193.3-195.8 mAh g<sup>-1</sup>). Cycling at C/2 indicated that the  $\alpha$ -polymorph sample has a higher stability than that of the  $\beta$ -polymorph, with a 50-cycle capacity retention of 93.7% compared to 69.5% (Figure 5.0.25).

The voltage profiles depicted in Figure 5.0.26 show similar initial delithiation voltages for both the  $\alpha$ - and  $\beta$ - polymorphs, with a voltage of *ca.* 3.6 V observed when cycled at a rate of C/20, and a potential of *ca.* 3.7-3.8 V observed when cycled at a rate of C/2. Differential capacity plots reveal redox processes at *ca.* 3.6-3.8 V and 4.0 V respectively (Figure 5.0.27). Polarisation is observed in both the  $\alpha$ - and  $\beta$ - polymorphs, evidenced by high-voltage shifting of the peaks during the positive charging profiles and the low-voltage peak shifting of the negative discharge profiles.

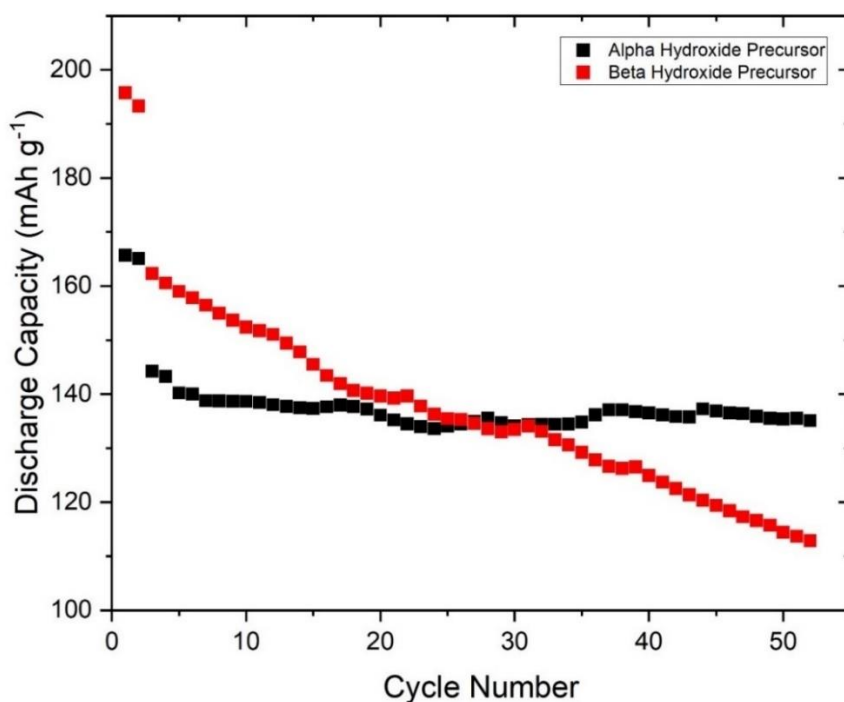


**Figure 5.0.25:** A capacity retention plot for the  $\text{LiNi}_{0.8}\text{Mn}_{0.1}\text{Co}_{0.1}\text{O}_2$  samples with the  $\alpha$ - and  $\beta$ -  $\text{Ni}_{0.8}\text{Mn}_{0.1}\text{Co}_{0.1}(\text{OH})_2$  precursor. Half-cells were cycled over a voltage window of 3.0-4.3 V for 52 cycles (2 cycles of C/20, 50 cycles of C/2).

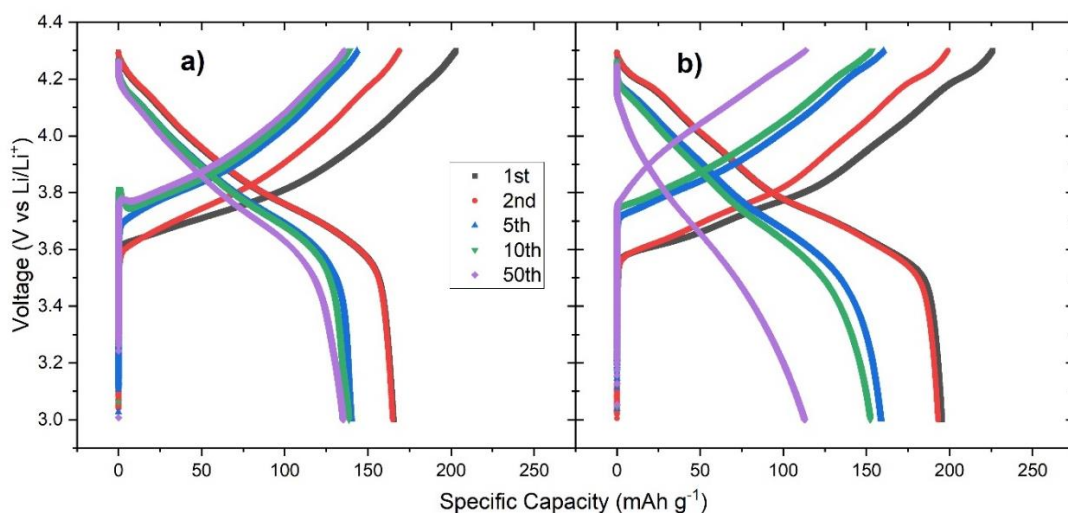


**Figure 5.0.26:** Voltage profiles of the  $\text{LiNi}_{0.8}\text{Mn}_{0.1}\text{Co}_{0.1}\text{O}_2$  calcined from with the  $\alpha$ - or  $\beta$ - $\text{Ni}_{0.8}\text{Mn}_{0.1}\text{Co}_{0.1}(\text{OH})_2$  polymorphs represented in parts (a) and (b) respectively. The voltage profiles include the 1<sup>st</sup>, 2<sup>nd</sup>, 5<sup>th</sup>, 10<sup>th</sup> and 50<sup>th</sup> cycles.

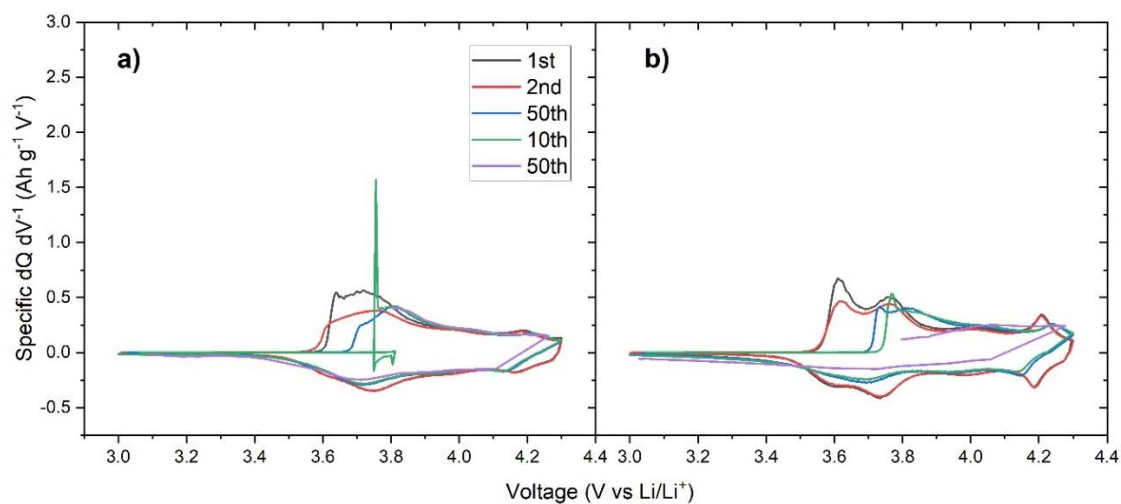


**Figure 5.0.27:** Differential capacity profiles of the  $\text{LiNi}_{0.8}\text{Mn}_{0.1}\text{Co}_{0.1}\text{O}_2$  calcined from with the  $\alpha$ - or  $\beta$ - $\text{Ni}_{0.8}\text{Mn}_{0.1}\text{Co}_{0.1}(\text{OH})_2$  polymorphs represented in parts (a) and (b) respectively. The voltage profiles include the 1<sup>st</sup>, 2<sup>nd</sup>, 5<sup>th</sup>, 10<sup>th</sup> and 50<sup>th</sup> cycles.

An *in-situ* high temperature XRD study to investigate the reaction between  $\alpha$ - $\text{Ni}_{0.8}\text{Mn}_{0.1}\text{Co}_{0.1}(\text{OH})_2$  and 3 mol% excess LiOH at temperatures up to 500 °C. XRD analysis the  $\alpha$ - $\text{Ni}_{0.8}\text{Mn}_{0.1}\text{Co}_{0.1}(\text{OH})_2$  phase showed a transformation to an intermediate rocksalt phase above 300 °C (Appendix A.17).

#### 5.4. Concluding remarks

This work presented the development of the microwave-assisted hydrothermal synthesis of  $\text{Ni}_{0.8}\text{Mn}_{0.1}\text{Co}_{0.1}(\text{OH})_2$  using urea as a complexing agent. Reaction times of 2-3 hours at temperatures of 200-220 °C yielded  $\beta\text{-Ni}_{0.8}\text{Mn}_{0.1}\text{Co}_{0.1}(\text{OH})_2$  with the smallest degree of cation mixing (<5%) and delivered the highest capacity of 203.4-205.1 mAh g<sup>-1</sup> when cycled at C/20 (3.0-4.3 V). The application of a microwave reactor to facilitate this reaction significantly reduced the reaction time from 24 hours to 2-3 hours, most likely the result of the rapid heating from the direct coupling of microwaves with the reactants to causing crystallisation to occur as opposed to the precipitation mechanism previously proposed [150]. Increasing the pressure within the vessel by increasing the reaction volume from 20 mL to 40 mL led to an increase in capacity from 170.6 to 196.1 mAh g<sup>-1</sup>, which supports this theory, as increased pressure increases the rate of crystallisation. The effect of urea was investigated by analysing a range of ratios (1:1 – 5:1), with an optimal urea: transition metal ratio of 2.9:1–3:1 determined. Although the stoichiometry for the reaction mechanism proposed suggests a 1:1 ratio of urea to transition metals is necessary, an excess is required to ensure reaction completion, however it is thought that too much urea can increase the pH of the system such that the transition metals do not crystallise or precipitate out of the solution.

During this investigation,  $\alpha\text{-Ni}_{0.8}\text{Mn}_{0.1}\text{Co}_{0.1}(\text{OH})_2$  was formed, thus an investigation into its calcination mechanism was conducted, finding that the polymorph formed a rocksalt intermediate phase formed when calcined with LiOH before forming the desired  $\alpha\text{-NaFeO}_2$  layered phase. This is suggestive that any intercalated species within the interplanar gallery of the  $\text{Ni}_{0.8}\text{Mn}_{0.1}\text{Co}_{0.1}(\text{OH})_2$  structure does not impede the formation of the desired  $\alpha\text{-NaFeO}_2$  layered  $\text{LiNi}_{0.8}\text{Mn}_{0.1}\text{Co}_{0.1}\text{O}_2$  phase. Electrochemical cycling of these samples showed that samples prepared from the  $\alpha\text{-Ni}_{0.8}\text{Mn}_{0.1}\text{Co}_{0.1}(\text{OH})_2$  precursor delivered a capacity of 165.1-165.7 mAh g<sup>-1</sup> when cycled at C/20 (compared to 193.3-195.8 mAh g<sup>-1</sup> for samples obtained from the  $\beta$ - polymorph), but retained 93.7% of its capacity after 50 cycles at C/2, compared to 69.5% retention in the  $\beta$ -polymorph sample. The capacity retention plots, and resolution of the differential capacity profiles suggest that  $\beta$ -polymorph sample has fewer crystal structure defects, allowing more capacity to be yielded, but the capacities yielded from the samples are too similar to conclude one polymorph is better than the other.

## 6. The development of a co-precipitation synthesis pathway for NMC-811 in a microwave reactor

The use of microwave heating to synthesise  $\text{Ni}_{0.8}\text{Mn}_{0.1}\text{Co}_{0.1}(\text{OH})_2$  has been established in Chapter 5, with a hydrothermal procedure producing the  $\beta$ -polymorph. Here, a microwave-assisted co-precipitation synthesis pathway for NMC-811 is presented that would scale up and improve control over the precipitation process. This synthetic route can take up to 40 hours conventionally, but it was theorised that the microwave dielectric heating mechanism can reduce this reaction time.

The microwave environment poses many challenges, as many features of the conventional stirred tank reactor (STR) contain metal, which interacts with microwaves and superheats. A reactor system needed to be designed to withstand not only the microwave reactor, but the harsh chemical conditions the co-precipitation of NMC-811 requires (pH 11, use of ammonia and sodium hydroxide). It was decided that 3D printing a reactor vessel would produce a tailor-made vessel that could satisfy both requirements. The microwave stirred tank reactor (MiSTR) system was based around a CEM Mars6 Synthesis Microwave reactor, with a 3D-printed STR used within the Mars6 Synthesis in cohesion with external pH probes and peristaltic pumps to synthesise  $\text{Ni}_{0.8}\text{Mn}_{0.1}\text{Co}_{0.1}(\text{OH})_2$  *via* a semi-batch co-precipitation methodology. This was calcined in either an oxygen-supplied tube furnace or a microwave furnace to investigate the crystalline, morphological, and electrochemical properties of the desired  $\text{LiNi}_{0.8}\text{Mn}_{0.1}\text{Co}_{0.1}\text{O}_2$  product.

### 6.1. – Design of the Microwave Stirred Tank Reactor (MiSTR) System

The design of the microwave stirred tank reactor (MiSTR) system was based on the Eppendorf BioFlo 320 stirred tank reactor, which consists of a hemispherical metal base with a cylindrical glass upper. The BioFlo 320 (STR) has 4 equally-spaced baffles, an overhead stirrer, and was heated through the hemispherical stainless-steel base, which provides a heat-transfer surface through a constant supply of heated water. The BioFlo STR also has a temperature sensor and pH sensor to monitor the temperature and pH respectively in real-time, with the ability to incorporate these into a real-time feedback control loop to maintain these parameters at pre-set values.

### 6.1.1. Design of the stirred tank reactor vessel

A non-metal STR needed to be designed to ensure the reactor was microwave-transparent, with glass or plastic being two material options. The reactor vessel required a customised design, meaning its manufacture should be completed using a glass-blower or by 3D printer with a plastic composite material. The 3D printed reactor was chosen due to the shorter manufacturing times for the prototype, and subsequent reactor vessels should a vessel failure occur.

The dimensions of the 3D printer limited the height of the MiSTR vessel to a maximum of 20 cm. The geometry of a STR features a cylindrical section and hemispherical base, with the equation for the volume of the reactor vessel being represented in Equation 6.1. STRs are typically designed such that the height of the fluid in the vessel should equal the diameter of the vessel to promote an equal proportion of axial and radial mixing. One safety heuristic is that the maximum operational volume should not exceed 80% of the total reactor volume. A total reactor volume ( $V$ ) of 1 L was chosen, equating to a radius ' $x$ ' of 5.34 cm, which was rounded down to 5.0 cm to improve the success of the printing. Baffles within the reactor vessel prevent the formation of vortices during agitation. These are typically 10% of the diameter of the vessel and protrude 1 cm from the inner circumference along the cylindrical part of the reactor vessel. In this reactor vessel, 4 baffles are employed equidistant along the circumference, which are depicted in Figure 6.0.1.

$$V = (\pi * x^3) + \left(\frac{2}{3} * \pi * x^3\right) \quad \text{Equation 6.1.}$$

There are two types of 3D printing: filament or resin. The filament material (polypropylene 30% glass fibre) PPGF-30 was chemical and temperature resistant. The resin alternative, 'Formlabs Tough 1500 V1' had no evidence that it was chemically resistant to ammonia on the data sheet, but previous experience with this material indicated some chemical resistivity. The resultant vessels were pictured in Figure 6.0.2. The filament-printed vessel had gaps between adjacent filaments, leading to vessel structure being porous. The vessel was washed with ethyl acetate in an attempt to chemically cure the vessel, but the vessel remained porous. The resin-printed reactor vessel was not porous but had a few stalagmites of resin on the hemispherical base remaining from printing, which caused difficulties with vessel cleaning in order to prevent cross-contamination between experiments. The resin vessel was chosen to conduct the synthesis of NMC-811 and had a wall-thickness of 2.5 mm, as seen in Figure 6.0.1.

The chemical resistance of the 3D-printed reactor vessel was described as ‘chemically resistant’ but failed to detail its resistance to ammonia and pH levels >11.0 in its technical documents. To ensure the resin was compatible with the harsh chemical conditions employed during the co-precipitation reaction, a 3D-printed sample was soaked in pH 12 NaOH for 12 hours with no observable discolouration and no weakening or warping of the structure. Additionally, the first reaction conducted in the 3D-printed vessel reaction was conducted in a 2 L beaker, so if the vessel failed, the contents would be safely contained. After the three commissioning reactions, there was no sign of vessel weakening, degradation or failure.

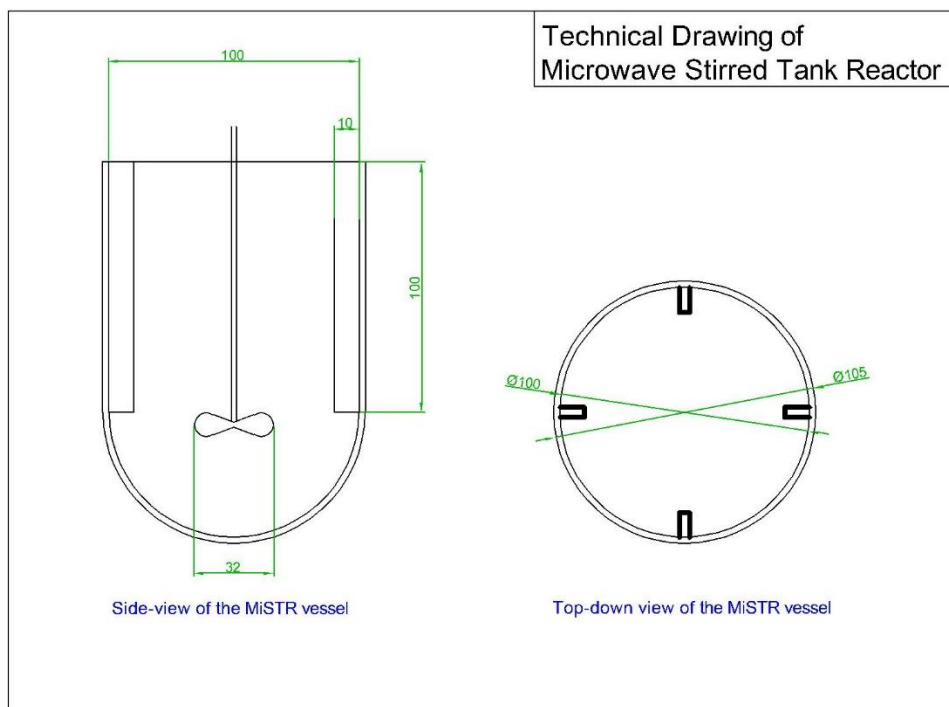


**Figure 6.0.1:** A technical drawing of the Microwave stirred tank reactor (MiSTR) vessel design, including the baffles and agitator, as an overhead stirrer. All dimensions are in millimetres (mm).

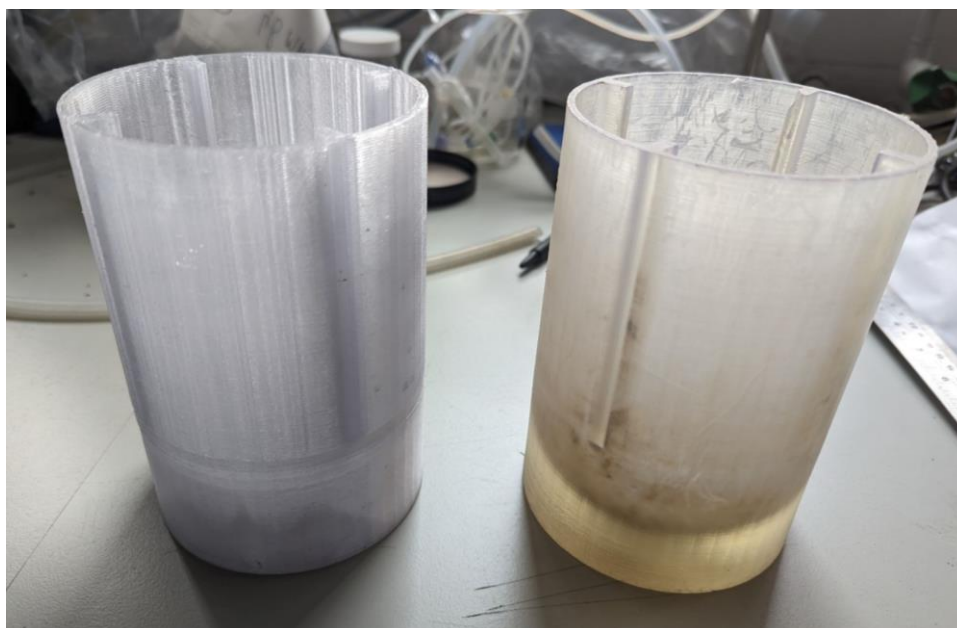


**Figure 6.0.2:** A photo of the two 3D-printed stirred tank reactor vessels: the filament-printed vessel (left) and resin-printed vessel (right).

#### 6.1.2. Agitator design – Stirrer bar vs Overhead stirrer

Agitation of a stirred tank reactor is most conventionally conducted *via* an overhead stirrer, due to its accurate control of its rotational speed. For quasi-water viscosity systems, a common heuristic for the diameter of the agitator is it should be one-third of the vessel diameter to provide good mixing properties. The overhead stirrer is powered by a stirrer unit on a benchtop, with a flexible drivetrain suspended above the Mars6 Synthesis to minimise the wobble caused by centrifugal force of the mass of the stirrer unit suspended at height. The shape of the impeller blade also has an impact on the agitation rate and regime, with both axial and radial mixing being desired. Zhu *et al.* found that a pitched propeller increased the particle size, tap density, and formed needle-like primary particles when synthesising NMC-622 [262]. Consequently, an impeller with three equidistant pitched propeller blades was designed with an angle of  $45^\circ$  around the shaft (diameter 6 mm), emulating the design of the BioFlo 320. The impeller blade is depicted as a 3D model in Figure 6.0.3, with the blades having a length of 13 mm (based on the one-third tank diameter heuristic described above) and a perpendicular height of 8 mm.

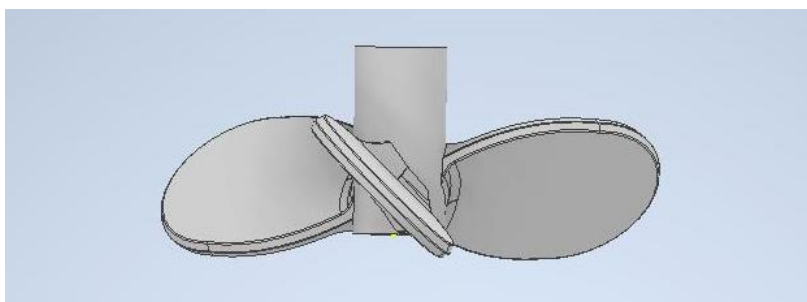


**Figure 6.0.3:** A 3D visualisation of the design for the MiSTR impellor blade using Autodesk Inventor.

There is a practical problem with the overhead stirrer however, with the agitator shaft needing to be plastic and in excess of 40 cm long due to the long I/O port of the CEM Mars6 Synthesis. This results in the agitator shaft to start ‘whipping’ (deviating from a straight axis of rotation) upon high revolution speeds of *ca.* 200 rpm, which is significantly below the optimal agitation rate of 800-1000 rpm found in literature [118], [156]. During the commissioning of the MiSTR system, stirring *via* a magnetic stirrer bar was conducted using pre-set arbitrary values of ‘low’, ‘medium’ and ‘high’ on the CEM Mars6 Synthesis.

A safe revolution speed of 100 rpm was observed to be appropriate to maximise mixing without causing the whipping of the agitator shaft. The flow regime for this agitation rate was determined by calculating the Reynolds number, seen in Equation 6.2. It is assumed the dynamic viscosity of the NMC reactor solution is within the same order of magnitude as water, thus a value of 0.001 Pa s was used. The density of the NMC reactor solution was calculated to be 1.107 kg m<sup>-3</sup>. The Reynolds number was calculated to be 1889.3, indicating the flow regime for this impellor blade would be in the transition phase between the laminar flow ( $Re < 10$ ), and turbulent ( $Re > 10^4$ ) regimes, indicating some degree of mixing [207].

$$Re = \frac{\rho * N * D_I^2}{\mu} = \frac{1107 * \left(\frac{100}{60}\right) * 0.032^2}{0.001} = 1889.3 \quad \text{Equation 6.2.}$$

To determine whether the agitation rate was sufficient to suspend the precipitated Ni<sub>0.8</sub>Mn<sub>0.1</sub>Co<sub>0.1</sub>(OH)<sub>2</sub> particles, the Froude number (Equation 6.3) was calculated to be 32.6, indicating the inertial forces allowed the suspension of the precipitated particles. The Zwietering *et al.* model (Equation 6.4) was employed to determine the minimum velocity required to maintain a suspension. The concentration of particulates in the solution (*B*) was estimated to be 0.083 wt% under the assumption that there was an overall transition metal concentration of 1 M in the 800 mL solution.

The particle density ( $\rho_p$ ) was estimated to be 2,000 kg m<sup>-3</sup> based on high-density literature values [143], [144], with their diameter ( $D_p$ ) being estimated to be 10  $\mu$ m. The minimum velocity ( $N_{min}$ ) was 0.751 revolutions per second (45 rpm), indicating the particles will be suspended at speeds of 100 rpm employed during the reaction. The Fox and Gex model (Equation 6.5) was used to calculate a dimensionless mixing time factor ( $Nt_t$ ) of 122.88, which equates to a mixing time ( $t_t$ ) of 73.7 seconds with a rotational mixing speed of 100 rpm.

$$Fr = \frac{n^2 * D_I}{g} = \frac{100^2 * 0.032}{9.81} = 32.619 \quad \text{Equation 6.3.}$$

$$N_{min} = \frac{B^{0.125} \mu_L^{0.17} [g(\rho_p - \rho_L)^{0.42}] D_p^{0.14}}{\rho_L^{0.58} D_I^{0.89}} = 0.751 \text{ rps} \quad \text{Equation 6.4.}$$

$$Nt_t = 16.9 \left(\frac{D_T}{D_I}\right)^{10/6} \left(\frac{H}{D_T}\right)^{1/2} = 122.884 \quad \text{Equation 6.5.}$$

The narrow I/O port, which has an internal diameter of 42 mm, needs to have multiple tubes, the fibre optic temperature sensor and the overhead stirrer shaft in it without the rotating shaft tangling the tubes and wires. A tube separator was designed to isolate the overhead stirrer rod from the sensors and tubes in the I/O port, with a 3D model for this included in Figure 6.0.4.

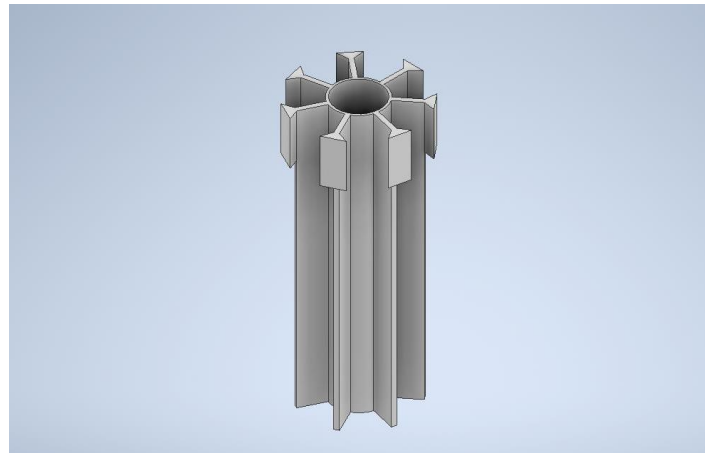


**Figure 6.0.4:** A 3D model rendered in Autodesk Inventor for the tube separator device designed for the throat of the I/O port of the CEM Mars6 Synthesis. The model was shortened to 100 mm in length for clarity, but was printed to a length of 300 mm.

## 6.2. – Operation of the Microwave Stirred Tank Reactor (MiSTR) System

The Microwave stirred tank reactor (MiSTR) system consists of the 3D-printed reactor vessel situated in the Mars6 Synthesis cavity. The piping and instrumentation diagram (P&ID) in Figure 6.0.5 visualises the MiSTR system configuration, with peristaltic pumps being used to transition metal and basic solutions from storage beakers and extract the product once the reaction has completed. Additionally, the overhead stirrer, if selected, and fibre optic temperature sensor are also inserted through the throat of the Mars6 Synthesis's I/O port. The peristaltic pumps are controlled by an Eppendorf BioFlo 320 control station, that allows the measurement and control of pH *via* an electronic pH sensor (Mettler Toledo 3250i). This contains a platinum reference electrode, this cannot be inserted directly into the MiSTR vessel or microwave cavity, so there must be an external feedback loop in order to monitor and/or control the pH.

The pH sensor was pumped along 4 m of tubing to and from the pH sensor (2 m in each direction), which had an internal diameter of 4.8 mm equates to a volume of 72.4 mL. The maximum flow rate of 15 mL min<sup>-1</sup> was employed, resulting in a 5-minute delay within the feedback loop. This resulted in the pH of the system oscillating between a pH of 10.0 and 12.4 with the automated cascade feedback loop of the BioFlo Control system. In an attempt to dampen this, the NaOH solution was diluted from 5 M to 3 M, with the pH oscillation reducing to between 10.0 and 12. Manual control of the base solution was conducted in the final trial, which controlled the pH to 10.9-11.1.

The lid of the MiSTR vessel was not air-tight, resulting in the oxygenation of the solution and loss of water *via* evaporation for the duration of the reaction. Sparging the reactor solution with nitrogen gas would be ineffective due to the absence of a nitrogen head above the solution and potentially dangerous due to the venting of the nitrogen into the local atmosphere around the CEM Mars6 Synthesis. Additionally, tests were conducted to measure the rate of water loss due to evaporation by heating a vessel of water to 60 °C in the reactor vessel. It was found that water was lost at a rate of 50 mL h<sup>-1</sup>. To compensate for this, the transition metal solution was diluted with an appropriate amount of water to maintain a constant reactor vessel volume.

The P&ID displayed in Figure 6.0.5 depicts the two reactant storage mixing tanks M-101 and M-102 which host the transition metal solution and basic solution respectively. Lines 0.1-0.3 represent the addition of the nickel, manganese sulphate powders to the vessel, with line 0.4 representing the deionised water solvent used to form the solution. Similarly, lines 0.5 and 0.6 are the sodium hydroxide solution and ammonia solutions that form the basic solution of M-102. The manual valves

represent the non-mechanical manual addition of substances to the reactant mixing tanks. Peristaltic pumps P-101 and P-102 supply the stirred tank reactor (R-201) with the contents of the reactant storage tanks, with the flow controlled by the BioFlo control system. The microwave cavity and I/O port throat was also included to aid the visualisation of the system. The pH feedback loop was depicted through the loop featuring P-103, P-104 and M-201, which represent the peristaltic pumps pumping the reactor to and from the reactor, and the beaker that holds reactor fluid and pH sensor respectively. A stirrer hotplate can be seen as part of the M-201 unit, with a temperature control loop implemented *via* a temperature indicator (TI) and temperature controller (TC). The pH meter is represented by the ME instrument, which controls the flow rate of P-102 and the basic solution to the stirred tank reactor in the pH feedback loop described above.

For clarity and simplicity, the P&ID depicted in Figure 6.0.5 represents the Mars6 Synthesis as a black box with the I/O port acting as a conduit for the tubing. Reactor R-201 is positioned inside with a magnetic stirrer bar acting as an agitator, as this was utilised in the initial commissioning trials reported in this work. The temperature control loop within the reactor system is represented by the control loop connecting R-201 and the heater unit H-201, which represents the magnetron that emits the microwaves used in the heating of the reactor contents. Finally, peristaltic pump P-201 was used to pump the reacted products out of the reactor system. A picture of the system in operation is included in Figure 6.0.6.

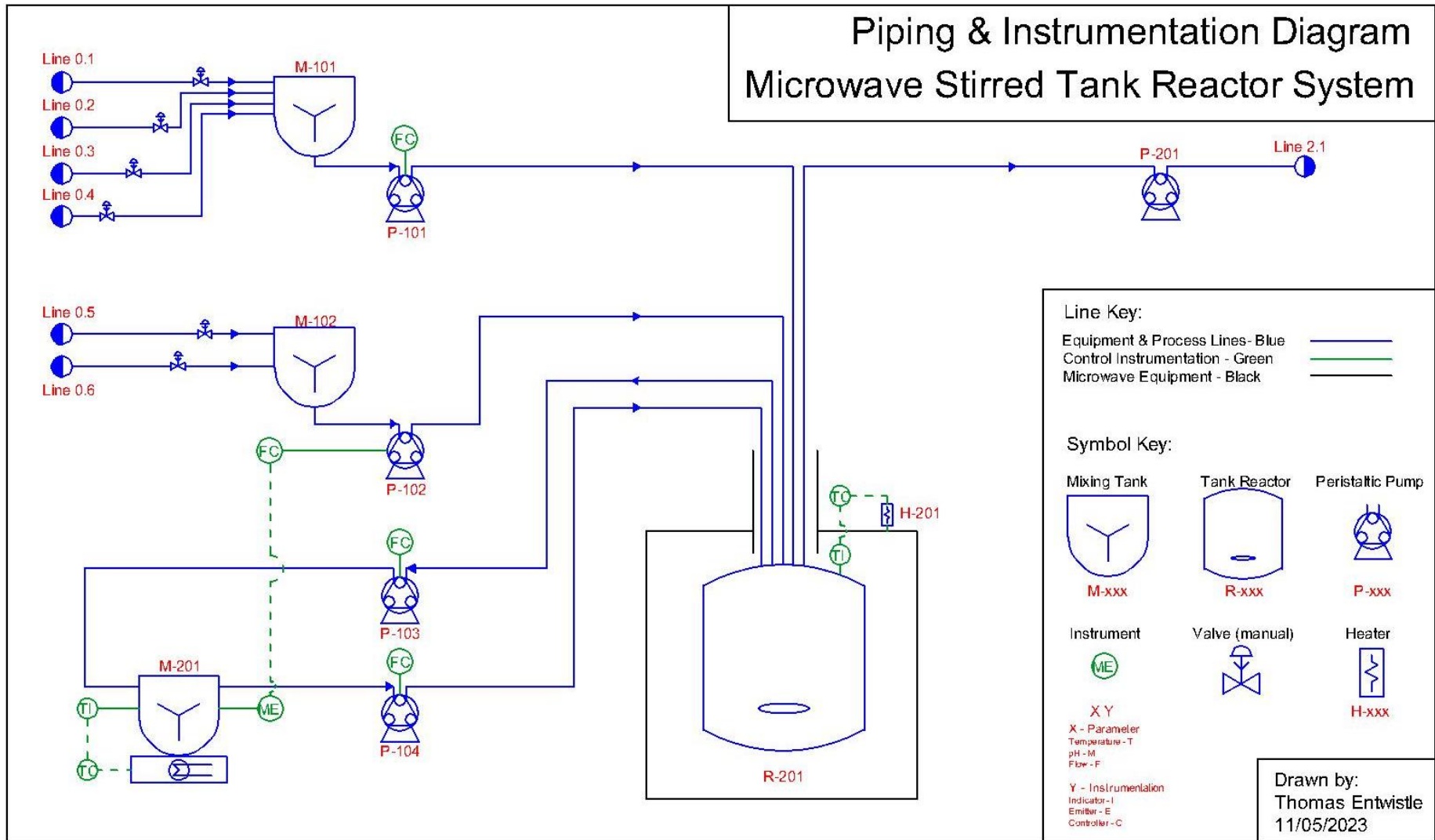
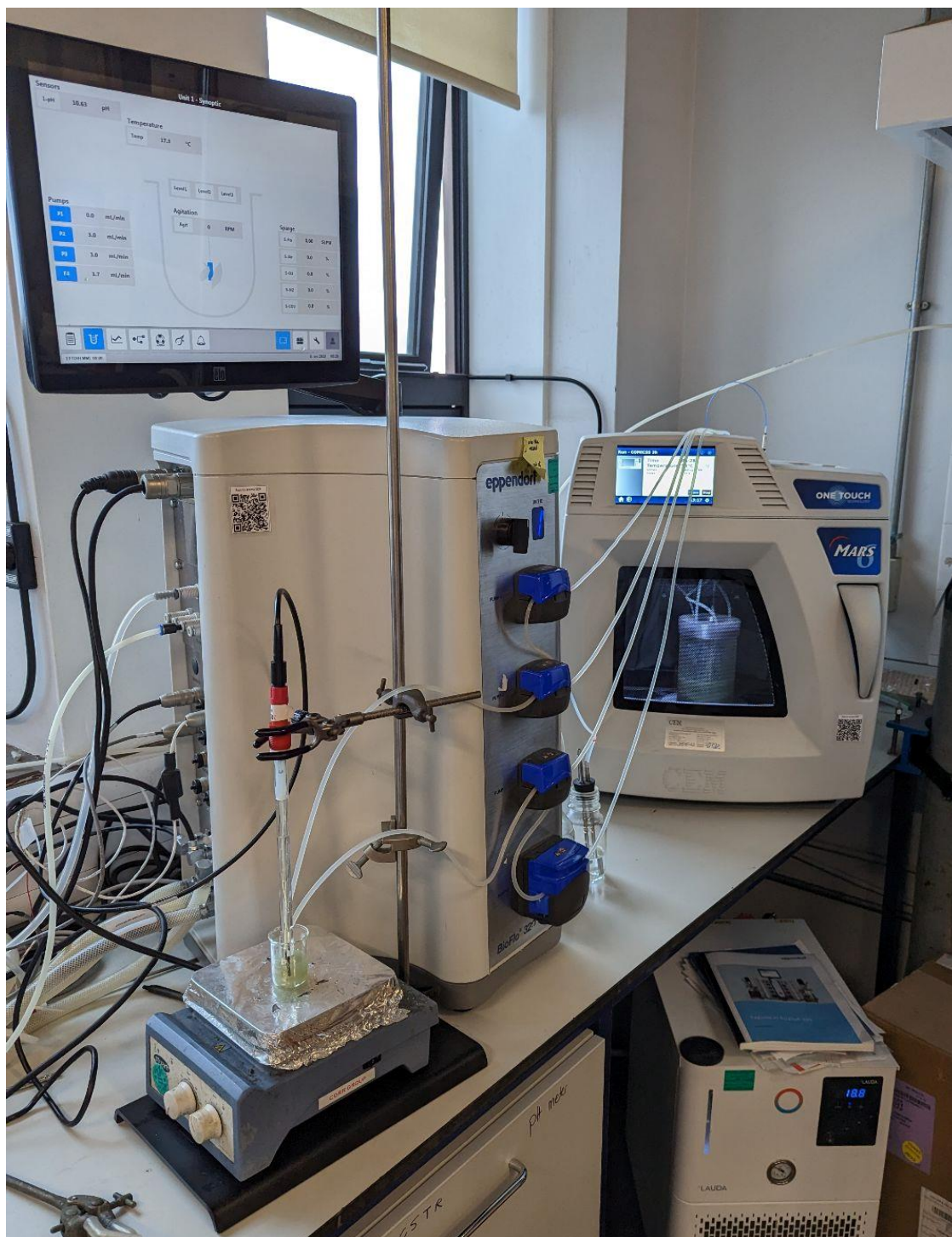


Figure 6.0.5: A piping and instrumentation diagram (P&ID) of the microwave stirred tank reactor (MiSTR) system.



**Figure 6.0.6:** A picture of the microwave stirred tank reactor (MiSTR) system during a reaction.

### 6.3. – Evaluation of the co-precipitation synthesis product synthesised from the MiSTR system

Three trial “commissioning” experiments were conducted in the MiSTR system, which aimed to test the feasibility of the microwave co-precipitation synthesis of  $\text{Ni}_{0.8}\text{Mn}_{0.1}\text{Co}_{0.1}(\text{OH})_2$ . The presence of oxygen during the reaction is expected to oxidise the transition metals to their trivalent and tetravalent states; potentially forming phase impurities within the desired layered  $\text{Ni}_{0.8}\text{Mn}_{0.1}\text{Co}_{0.1}(\text{OH})_2$  structure. Here, crystallographic, morphological, and electrochemical analysis of the synthesised  $\text{Ni}_{0.8}\text{Mn}_{0.1}\text{Co}_{0.1}(\text{OH})_2$  and calcined  $\text{LiNi}_{0.8}\text{Mn}_{0.1}\text{Co}_{0.1}(\text{OH})_2$  cathode active material is examined.

#### 6.3.1. Material Characterisation of $\text{Ni}_{0.8}\text{Mn}_{0.1}\text{Co}_{0.1}(\text{OH})_2$

An XRD study of the three trial experiments indicated the formation of a  $\beta$ - $\text{Ni}_{0.8}\text{Mn}_{0.1}\text{Co}_{0.1}(\text{OH})_2$  layered structure (Figure 6.0.7). Comparing the three trials to a benchmark sample synthesised in-house using a conventional stirred tank reactor, the presence of a low-angle shoulder on the (001) peak was observed, which may be the result of stacking faults. Samples with the most (001) asymmetry saw a larger high-angle peak shift in the (101) and (110) peak, as seen in Figure 6.0.7.b) and c).

Visually, the  $\text{Ni}_{0.8}\text{Mn}_{0.1}\text{Co}_{0.1}(\text{OH})_2$  yielded from the MiSTR co-precipitation reactions were dark brown in colour upon drying, and the supernatant filtered from the reactor vessel was clear, indicating no unreacted  $\text{Ni}[(\text{NH}_4)_x(\text{H}_2\text{O})_y]$  complexes remain (which appear blue in colour upon dissolution in water). SEM analysis showed the formation of secondary assemblies that were not spherical in morphology in initial trials (Figure 6.0.8). Trial 3 was spherical than the other two samples, suggesting the pH control improves the agglomeration of primary particles.

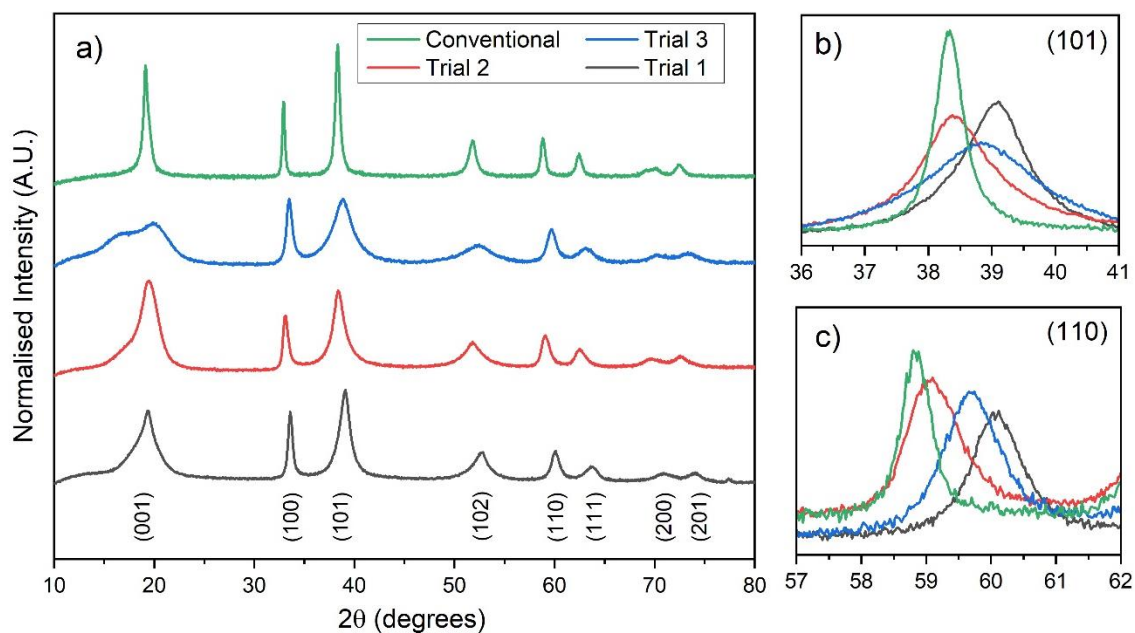


**Figure 6.0.7:** (a) XRD profiles for the  $\text{Ni}_{0.8}\text{Mn}_{0.1}\text{Co}_{0.1}(\text{OH})_2$  precursors synthesised in the (MiSTR) system, featuring three MISTR trial runs and a benchmark sample. (b) and (c) depicts the (104) peak and (108)/(110) peak doublet respectively.

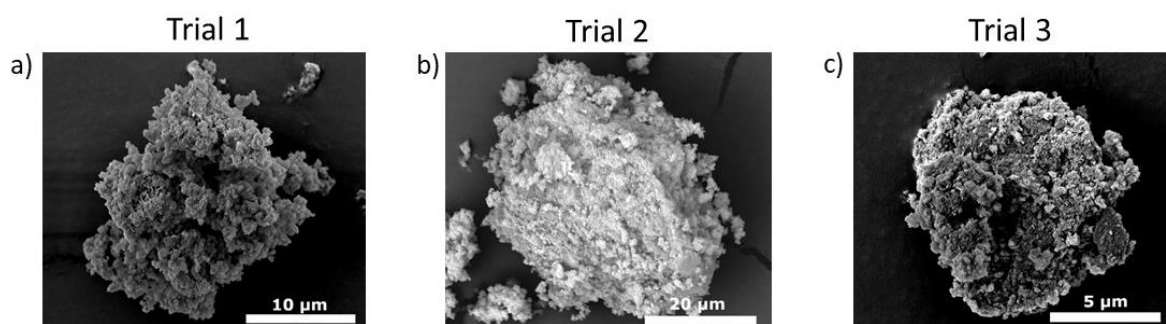


**Figure 6.0.8:** SEM images of the  $\text{Ni}_{0.8}\text{Mn}_{0.1}\text{Co}_{0.1}(\text{OH})_2$  during trials 1, 2 and 3 (depicted in a, b, and c respectively).

The tap density of these  $\text{Ni}_{0.8}\text{Mn}_{0.1}\text{Co}_{0.1}(\text{OH})_2$  suggests that the control of reaction pH is critical for a high tap density, with trial 3 (with the most pH control) having a tap density of  $1.239 \text{ g cm}^{-3}$ , whereas trials 1 and 2 (which had poor pH control) had values of  $0.352$  and  $0.594 \text{ g cm}^{-3}$  respectively. The compressibility ratio of these samples was 21.6%, 11.6% and 19.7% for trials 1, 2, and 3 respectively.

### 6.3.2. Material Characterisation of $\text{LiNi}_{0.8}\text{Mn}_{0.1}\text{Co}_{0.1}\text{O}_2$

The calcination of the  $\text{Ni}_{0.8}\text{Mn}_{0.1}\text{Co}_{0.1}(\text{OH})_2$  powder was conducted in an oxygen-supplied tube furnace with 3 mol% excess LiOH to attain the desired  $\text{LiNi}_{0.8}\text{Mn}_{0.1}\text{Co}_{0.1}\text{O}_2$  product.

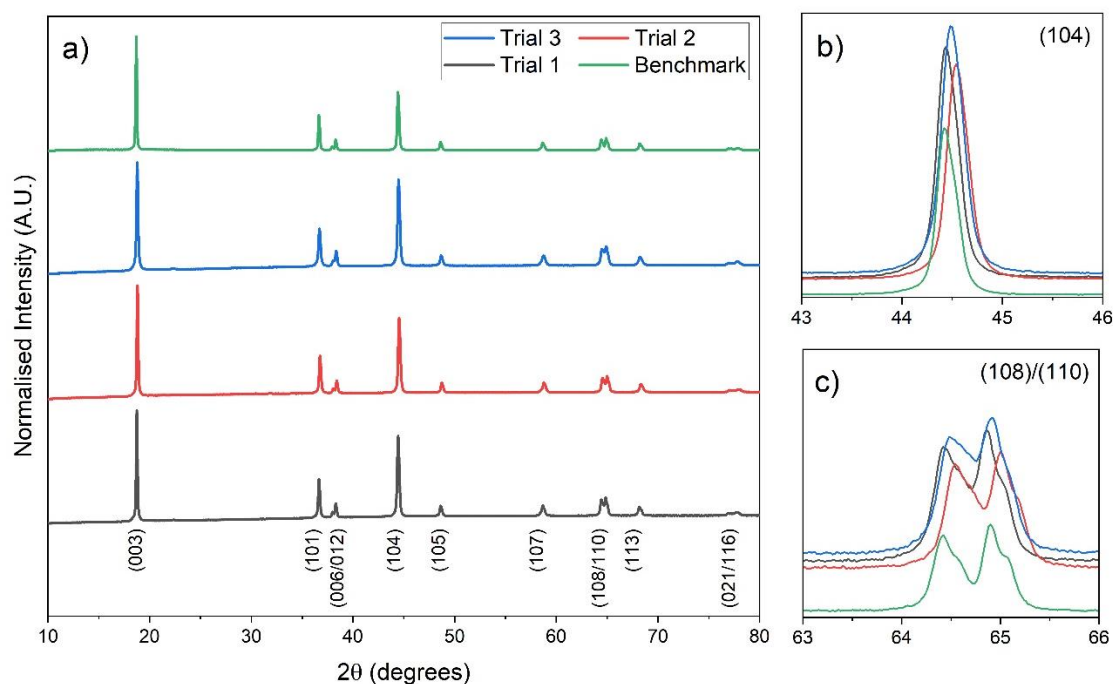


**Figure 6.0.9:** X-ray diffraction profiles of  $\text{LiNi}_{0.8}\text{Mn}_{0.1}\text{Co}_{0.1}\text{O}_2$ , synthesised from the calcination of the three MiSTR trials conducted in an oxygen-supplied tube furnace, compared to a benchmark sample. **(a)** depicts the full XRD profile range of 10-80° with labelled  $hkl$  planes, with **(b)** and **(c)** depicting peak analysis of the (104) peak and (108)/(110) peak doublet respectively.

XRD profiles for the synthesised  $\text{LiNi}_{0.8}\text{Mn}_{0.1}\text{Co}_{0.1}\text{O}_2$  revealed the formation of the desired  $\alpha\text{-NaFeO}_2$  layered structure in Figure 6.0.9.a). The (003)/(104) peak ratios are 1.260, 1.355 and 1.162 for trials 1-3 respectively, compared to the benchmark sample (1.811). Rietveld refinement confirms trials 1-3 have a degree of cation mixing equivalent of 9.3%, 6.7%, and 8.5% respectively, with the benchmark material having a value of 2.5%, as seen in Table 6.0.1 (associated plots are included in Appendix A.18). This may indicate the addition time of the reactants during the co-precipitation reaction impacts the degree of cation mixing, with trial 2 having the longest addition time and lowest degree of cation mixing. The degree of layered ordering was indicated by the (108)/(110) peak doublet splitting, depicted in Figure 6.0.9.c), with all trials having a similar degree of peak double splitting and thus similar degree of layered ordering.

**Table 6.0.1:** Key values from the Rietveld refinement of  $\text{LiNi}_{0.8}\text{Mn}_{0.1}\text{Co}_{0.1}\text{O}_2$  calcined with LiOH in an oxygen-rich atmosphere at 775 °C for 12 hours, including the lattice parameters, the calculated nickel fraction in the lithium 3a layer, and the (003)/(104) peak ratio. The  $\text{Ni}_{0.8}\text{Mn}_{0.1}\text{Co}_{0.1}(\text{OH})_2$  precursors were synthesised in the MiSTR reactor, which occurred over three trials and then compared to a benchmark sample.

Trial Number	$a$ -, $b$ - axis (Å)	$c$ - axis (Å)	$c/a$ ratio	Unit cell volume (Å <sup>3</sup> )	Ni fraction in the Li layer (%)	Chi <sup>2</sup> value	(003)/(104) peak ratio
Trial 1	2.8731(1)	14.2016(5)	4.9430(3)	101.52(5)	9.3(1)	10.682	1.415
Trial 2	2.8697(1)	14.1922(4)	4.9456(3)	101.22(5)	6.7(1)	8.197	1.524
Trial 3	2.8727 (1)	14.1957(4)	4.9416(2)	101.45(5)	8.5(1)	6.762	1.310
Benchmark	2.8664(1)	14.1851(3)	4.9488(2)	100.93(4)	2.5(1)	8.614	2.098

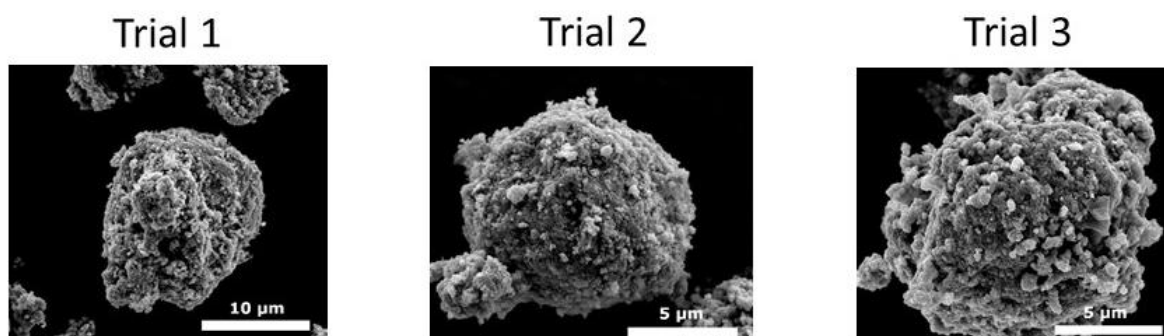


**Figure 6.0.10:** SEM images of calcined  $\text{LiNi}_{0.8}\text{Mn}_{0.1}\text{Co}_{0.1}\text{O}_2$  secondary particles in an oxygen-atmosphere tube furnace. The three trials (1-3) are included left to right.

The SEM analysis of the calcined  $\text{LiNi}_{0.8}\text{Mn}_{0.1}\text{Co}_{0.1}\text{O}_2$  samples show quasi-spherical secondary assemblies that have an approximate particle diameter of 10-12  $\mu\text{m}$ , as displayed in Figure 6.0.10. The particles have a small, similarly-sized primary particles. Trial 2 formed the most spherical secondary assemblies, suggesting that a slow addition rate may impact the secondary assemblies. The sample with the best pH control and short addition time of 3.5 hours, trial 3, displayed quasi-spherical particles.

Energy dispersive spectroscopy (EDS) visualised distribution of elements within the three samples (Figure 6.0.11). EDS mapping showed an even distribution of nickel, manganese, and cobalt across

the depicted particles, suggesting the three transition metals co-precipitated to form  $\text{LiNi}_{0.8}\text{Mn}_{0.1}\text{Co}_{0.1}\text{O}_2$ , as opposed to separately precipitating to form single-transition metal oxides. Due to the similar atomic number of nickel, manganese and cobalt, it is possible that there is an overlapping of signals, thus any quantification of elemental proportions within the samples cannot be accurately reported through this method.

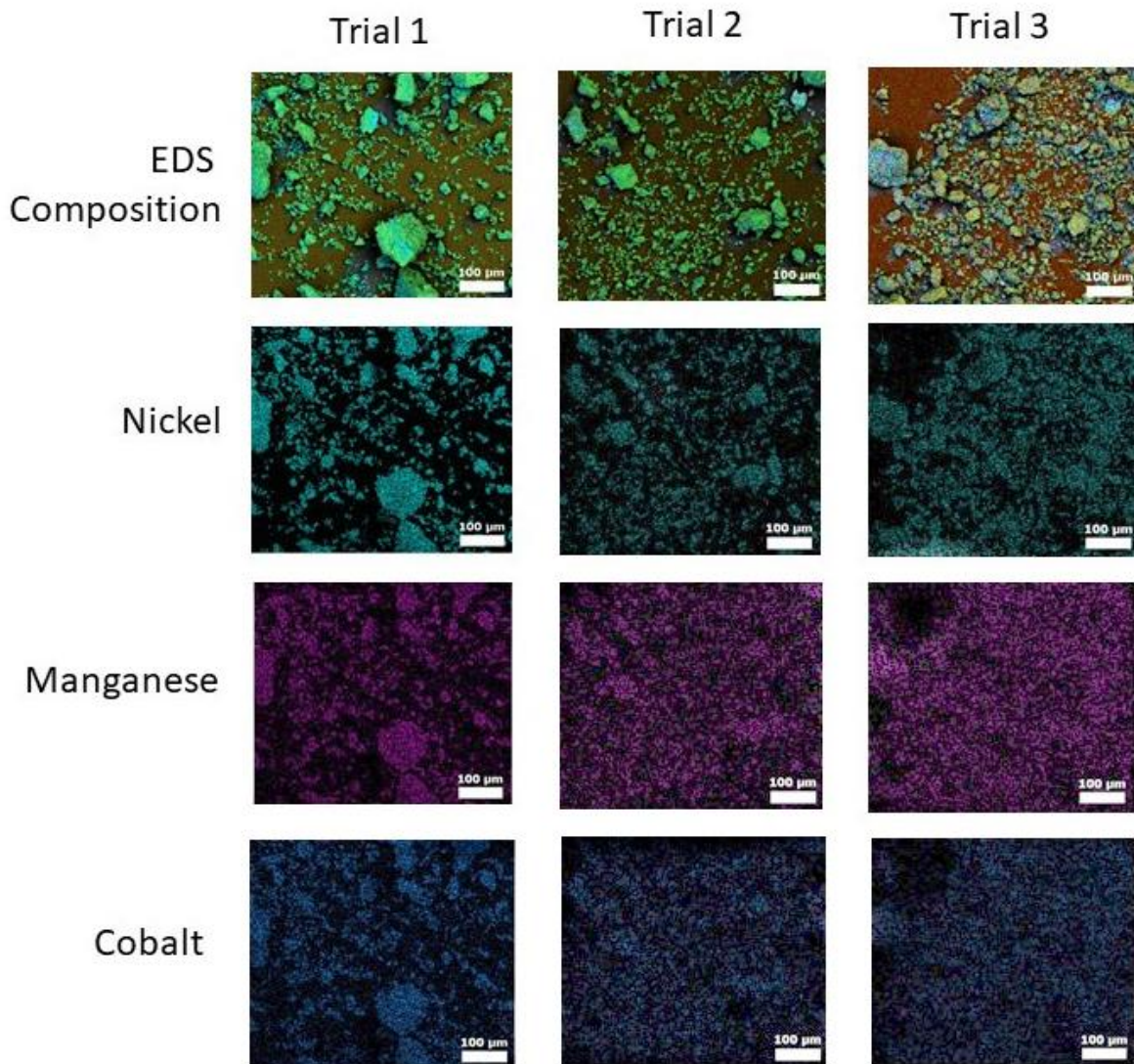


**Figure 6.0.11:** SEM/EDS images of the three MiSTR trial experiment samples (1-3, left to right), with an elemental overlay as well as individual images for nickel, manganese and cobalt EDS mapping.

### 6.3.3. Electrochemical Characterisation of $\text{LiNi}_{0.8}\text{Mn}_{0.1}\text{Co}_{0.1}\text{O}_2$

Galvanostatic cycling was conducted on half cells cycled over a voltage window 3.0-4.3 V, with two formation cycles at C/2 conducted followed by 98 cycles at C/2. A C/20 capacity of 188.7, 173.3 and 187.2 mAh g<sup>-1</sup> was delivered by trials 1-3 respectively (Figure 6.0.12). At C/2, trials 2 and 3 yielded similar capacities (152.6 and 159.6 mAh g<sup>-1</sup> respectively) compared to trial 1, (117.4 mAh g<sup>-1</sup>). The capacity retention over the 98 cycles at C/2 were calculated to be 92.0%, 89.0% and 84.1% for trials 1-3 respectively. Small fluctuations in capacity can be observed every 10-12 cycles which accounts for the day-night variations in temperature affecting the capacity yielded.

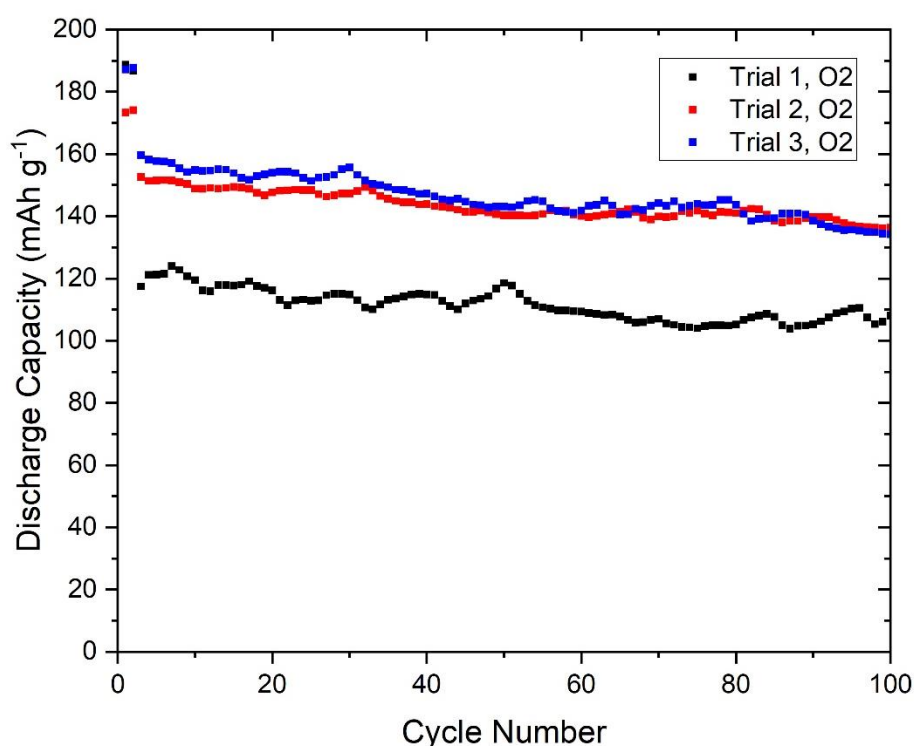


**Figure 6.0.12:** Capacity retention plot for the three MiSTR commissioning trials calcined in an oxygen-fed tube furnace. The half-cells were cycled over a voltage window of 3.0-4.3 V for 100 cycles (2 cycles of C/20, 98 cycles of C/2).

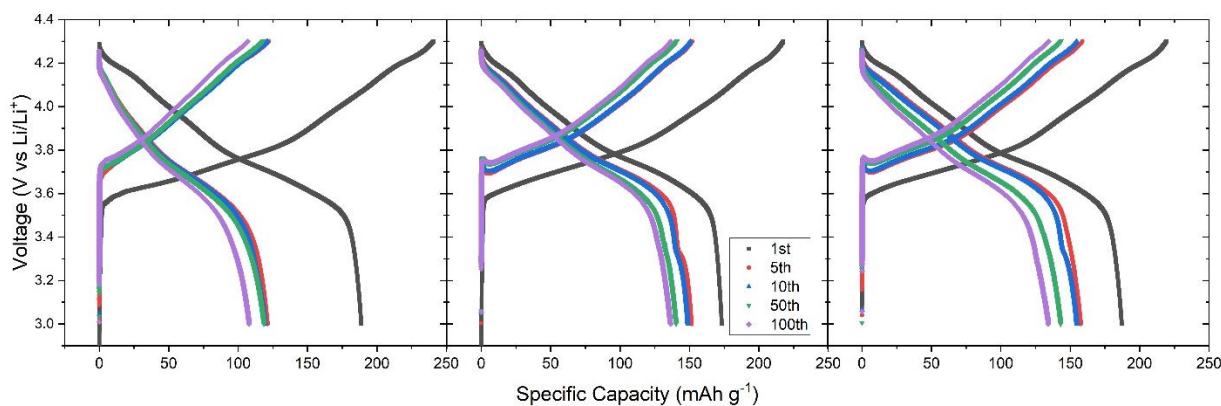


**Figure 6.0.13:** Voltage profile of the three MiSTR commissioning trials (1-3), calcined using an oxygen-fed tube furnace (left to right respectively). Profiles of cycles 1, 5, 10, 50 and 100 displayed.

Voltage profiles for the oxygen-calcined samples shows an initial C/20 delithiation voltage of 3.55-3.6 V, increasing to *ca.* 3.7 V when cycled at C/2 (Figure 6.0.13). A minor change in gradient above 3.8 V is observed in all samples. The C/2 cycles experiences an overpotential ‘hump’ prior to delithiation, attributed to residual lithium compounds on the surface of the particles causing increased resistance. Differential capacity of the oxygen-calcined samples shows two distinct redox processes occurring at *ca.* 3.7 V and 4.0 V respectively (Figure 6.0.14). Polarisation is observed between the 1<sup>st</sup> and 5<sup>th</sup> cycle, with a low-voltage shift in the negative discharge peaks observed and high-voltage shift in the positive, charging peaks. Minimal polarisation observed in the C/2 cycles (5<sup>th</sup>-100<sup>th</sup> cycles).

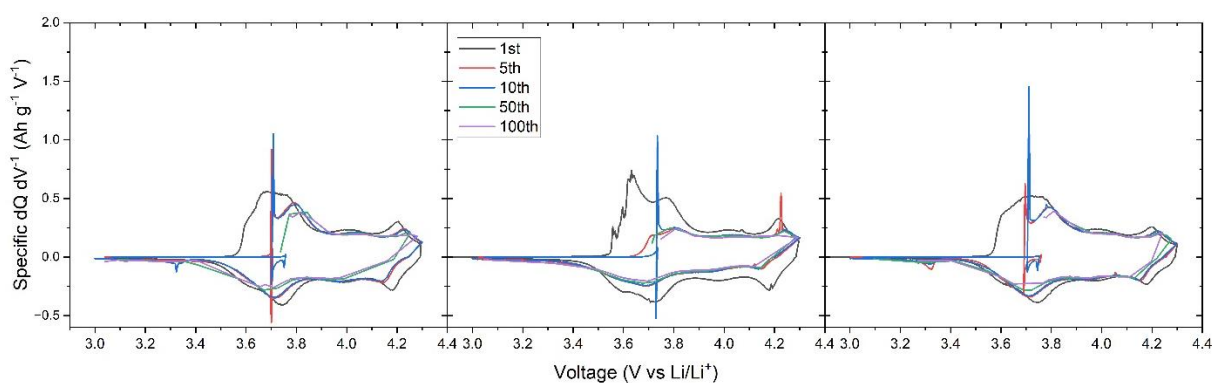


**Figure 6.0.14:** Differential capacity profiles for the three MiSTR commissioning trials (1-3) calcined in an oxygen-fed tube furnace, displayed left to right respectively. Profiles of cycles 1, 5, 10, 50 and 100 displayed.

#### 6.4. Concluding remarks

In this research, the development and commissioning of a microwave stirred tank reactor (MiSTR) system was presented as a pathway to facilitate the high-throughput co-precipitation synthesis of  $\text{Ni}_{0.8}\text{Mn}_{0.1}\text{Co}_{0.1}(\text{OH})_2$  cathode material. The use of microwave technology during the synthesis pathway aims to reduce the reaction time from 41.5 hours described in the conventional synthesis of  $\text{Ni}_{0.8}\text{Mn}_{0.1}\text{Co}_{0.1}(\text{OH})_2$  in Chapter 3 to approximately 5 hours (with optimisation on this value required in further research) without sacrificing electrochemical performance with respect to capacity and capacity retention. Additionally, the shorter reaction durations have the potential for economic savings due to less energy consumed during the reaction, with the Mars6 microwave having a smaller power consumption of 200-300 W compared to the conventional stirred tank reactor (approximately 2970 W).

The application of microwave radiation during the reaction presented several design constraints with respect to the reactor material and pH monitoring, due to the typical use of metals within these pieces of equipment. To overcome this, a 3D-printed, plastic composite reactor was designed, and an external pH feedback loop configured. Three trial experiments were conducted to establish the feasibility of the synthesis of  $\beta\text{-Ni}_{0.8}\text{Mn}_{0.1}\text{Co}_{0.1}(\text{OH})_2$ , focussing on controlling the pH of the system *via* the external feedback loop. Results showed the 2<sup>nd</sup> trial, which had longer addition time of 5 hours and a dilute base solution of 2.0 M, had the highest degree of cation ordering (6.7% Li/Ni cation mixing compared to 9.3% and 8.5% for trials 1 and 3 respectively), more spherical particles, and a high specific capacity yielded (of  $152.6 \text{ mAh g}^{-1}$ , compared to  $117.4$  and  $159.6 \text{ mAh g}^{-1}$  respectively, cycled at  $C/2$ , over a voltage window of 3.0-4.3 V) when calcined in an oxygen atmosphere. This suggests that the particle growth aspect of LaMer's principle is equally reliant on the reaction duration with respect to the formation of a uniform, quasi-spherical secondary particle assembly as the chemical conditions, and there will be limits to how short the microwave-heated co-precipitation reaction duration can feasibly be without sacrificing electrochemical performance.

This investigation proved the potential for the MiSTR system as a viable microwave-assisted co-precipitation synthesis route for  $\text{Ni}_{0.8}\text{Mn}_{0.1}\text{Co}_{0.1}(\text{OH})_2$ , with initial trials indicating significantly reduced reaction times, and capacities that are comparable to conventionally-synthesised NMC-811. Consequently, this system should be considered for further investigation and optimisation either for the synthesis of Ni-rich cathode active materials or alternative chemistries and systems that desire scale-up syntheses.

## 7. Conclusions

The research conducted in this thesis investigates the potential applications of microwave heating technology on the synthesis of the  $\text{LiNi}_{0.8}\text{Mn}_{0.1}\text{Co}_{0.1}\text{O}_2$  cathode active material and its precursor,  $\text{Ni}_{0.8}\text{Mn}_{0.1}\text{Co}_{0.1}(\text{OH})_2$ . Microwave heating revolves around the direct interaction and heating of polar molecules and causes homogenous and rapid heating at an atomic level. This can reduce reaction times and consequently save time and energy by being more energy efficient than conventional heating (e.g. conduction, convection).

Conventional calcination of  $\text{Ni}_{0.8}\text{Mn}_{0.1}\text{Co}_{0.1}(\text{OH})_2$  involves milling it with 3 mol% excess LiOH and heating the mixture in a conventionally heated, oxygen-fed tube furnace. The microwave furnace used in this work is a box furnace, which does not allow for an oxygen feed into its heated cavity. An alternative lithium salt,  $\text{Li}_2\text{O}_2$ , was investigated because it thermally decomposes to form oxygen gas, which hypothetically would decompose to form a localised oxygen-rich environment within the crucible, replicating the conditions of an oxygen-fed tube furnace. The formation of the desired  $\text{LiNi}_{0.8}\text{Mn}_{0.1}\text{Co}_{0.1}\text{O}_2$  layered oxide phase was proved for both lithium salts *via* the same reaction mechanism, thus an optimisation on the procedure was conducted. A range of temperatures, calcination durations and crucible volumes were investigated to investigate their effect on the  $\text{LiNi}_{0.8}\text{Mn}_{0.1}\text{Co}_{0.1}\text{O}_2$  crystallographic, morphological, and electrochemical properties. It was found that calcining  $\text{Ni}_{0.8}\text{Mn}_{0.1}\text{Co}_{0.1}(\text{OH})_2$  at 775-800 °C for 4 hours in a microwave furnace was optimal, with temperatures above this yielding higher degrees of cation mixing. Compared to conventional calcination procedures for NMC-811 (750-800 °C, 10-15 hours), the notable advantage of the microwave-assisted method is the reduced calcination duration, which is thought to be related to the rapid heating induced by the microwave furnace, which rapidly heats a silicon carbide heating element that in turn rapidly heats the sample and increases the rate of crystal growth.

This optimised microwave calcination procedure (heated at 775 °C for 4 hours) was used as a basis to compare the two lithium salts, LiOH and  $\text{Li}_2\text{O}_2$ , with an equivalent conventionally-heated oxygen-fed tube furnace procedure of 775 °C for 12 hours. It was found that the LiOH and  $\text{Li}_2\text{O}_2$  salts yielded similar specific capacities of 130.5 and 127.5 mAh g<sup>-1</sup> respectively when calcined using the microwave furnace (at a rate of C/2, 3.0-4.2 V), which was lower than the oxygen-fed tube furnace sample, which yielded a capacity of 151.0 mAh g<sup>-1</sup> over the same cycling conditions. This suggested that there was no additional benefit to using  $\text{Li}_2\text{O}_2$  over LiOH, with both salts yielding less capacity than the oxygen-rich atmosphere sample, indicating that the release of oxygen gas during the

calcination of  $\text{Li}_2\text{O}_2$  does not remain within the crucible and thus the atmosphere in both the  $\text{LiOH}$ - and  $\text{Li}_2\text{O}_2$ - calcined microwave furnace samples are air-rich.

An investigation into the applicability of microwave heating on the hydrothermal synthesis of the  $\text{Ni}_{0.8}\text{Mn}_{0.1}\text{Co}_{0.1}(\text{OH})_2$  precursor was conducted with a range of synthesis conditions investigated, including the temperature, reaction duration, pressure, complexing agent concentration and pH. It was found that increasing the temperature to 200-220 °C, increasing the reaction duration to 2-3 hours and increasing the pressure of the system (by increasing the volume of the reactants) improved primary particle packing within the secondary particles and electrochemical discharge capacity yielded from the samples. This is likely due to the increased degree of crystallisation with increased pressure and temperature; with a prolonged reaction duration allowing greater crystal growth. During this investigation, it was found that reactions with high volume and short reaction times yielded the  $\alpha$ - $\text{Ni}_{0.8}\text{Mn}_{0.1}\text{Co}_{0.1}(\text{OH})_2$  polymorph rather than the more desirable  $\beta$ - $\text{Ni}_{0.8}\text{Mn}_{0.1}\text{Co}_{0.1}(\text{OH})_2$  polymorph, most likely relating to the rapid nature of the reaction over a short period creating disorder within the system and allowing foreign species to intercalate within the interplanar galleries. The alternative  $\alpha$ - polymorph had no impact on the formation of layered  $\text{LiNi}_{0.8}\text{Mn}_{0.1}\text{Co}_{0.1}\text{O}_2$  and yielded slightly reduced capacities of 165.0-165.7  $\text{mAh g}^{-1}$  when cycled at C/20 (3.0-4.3 V), compared to the equivalent  $\beta$ - polymorph sample (193.3-195.8  $\text{mAh g}^{-1}$  over the same cycling conditions).

Finally, a microwave co-precipitation stirred tank reactor (MiSTR) system was developed to synthesise  $\text{Ni}_{0.8}\text{Mn}_{0.1}\text{Co}_{0.1}(\text{OH})_2$  in a controlled environment with reduced reaction times. This system involved a 3D-printed stirred tank reactor vessel being placed in a microwave reactor cavity with materials being pumped into the vessel from external peristaltic pumps. The desired  $\beta$ - $\text{Ni}_{0.8}\text{Mn}_{0.1}\text{Co}_{0.1}(\text{OH})_2$  polymorph was yielded in initial experiments that had a residence time of 5-6 hours, compared to the conventional co-precipitation reaction that occurs over a period of up to 40 hours. Calcination was conducted in a conventionally-heated oxygen-fed tube furnace, with the  $\text{LiNi}_{0.8}\text{Mn}_{0.1}\text{Co}_{0.1}\text{O}_2$  forming quasi-spherical secondary particles with a degree of cation mixing of 6.7-9.3%. The electrochemical performance of the synthesised samples yielded 173.2-188.7  $\text{mAh g}^{-1}$  at C/20, with a capacity retention of 84.1-92.0% over 98 cycles at C/2 (with a voltage window of 3.0-4.3 V). This proved the concept that microwave-assisted co-precipitation reaction can synthesise  $\text{Ni}_{0.8}\text{Mn}_{0.1}\text{Co}_{0.1}(\text{OH})_2$  with a quasi-spherical morphological and electrochemical properties comparable to the conventionally synthesised  $\text{LiNi}_{0.8}\text{Mn}_{0.1}\text{Co}_{0.1}\text{O}_2$ , providing scope for further investigation and optimisation into this methodology.

## 8. Future Work

The results and conclusions drawn from this work permits the scope for further research on the application of microwave technology on the synthesis of nickel-rich cathodes such as NMC-811 and its precursor  $\text{Ni}_{0.8}\text{Mn}_{0.1}\text{Co}_{0.1}(\text{OH})_2$ . This work has focused on the formation of poly-crystalline NMC-811 based on previous work conducted within the research group, future work could investigate this as a route to single crystal Ni-rich cathodes which are reported to reduce cracking phenomena associated with polycrystalline counterparts.

In order to bridge the gap in capacity between the microwave-calcined samples and the conventionally heated oxygen-fed samples observed in Chapter 3, an oxygen atmosphere needs to be present in the microwave in order to facilitate the oxidation of the electrochemically active nickel to its less stable  $\text{Ni}^{4+}$  state. Attempting to generate an oxygen-rich environment within a crucible was unsuccessful, with the hypothetical thermal degradation of  $\text{Li}_2\text{O}_2$  releasing oxygen gas, but the results presented here indicate a loss of oxygen. This indicates that a continuous feed of oxygen was required to oxidise the transition metals. To enable this, a microwave-heated tube furnace would need to be developed, with a similar configuration to that developed by Negari *et al.* as seen in Figure 8.0.1 [263].

An overview of the design shows that a commercial 2.45 GHz, 1 kW microwave oven was used as a microwave source with a post-market mullite tube added to the oven that would host the sample. Due to the wavelength of a 2.45 GHz microwave being approximately 12.4 cm, the length of tubing outside the microwave furnace should be longer than this to prevent the propagation of microwaves along the tubing. Silicon carbide heating elements are used in close proximity to the insulated heating zone, which absorb microwaves and rapidly heat to high temperatures, acting as the heat source for the sample. If oxygen gas was supplied within the tube in order to facilitate the transition metal oxidation, consideration should be made to the flow rate, as it was possible for microwaves to interact with oxygen to form a plasma. The  $\text{Ni}_{0.8}\text{Mn}_{0.1}\text{Co}_{0.1}(\text{OH})_2$  precursor and LiOH lithium salt are not flammable, therefore the risk of an ignition was limited, but the precise effect on the mullite tubing, microwave oven/ reactor or sample was unknown. Should the flow rate of oxygen be sufficiently high, the oxygen gas could oxidise the transition metal without forming excessive, if any, plasma.

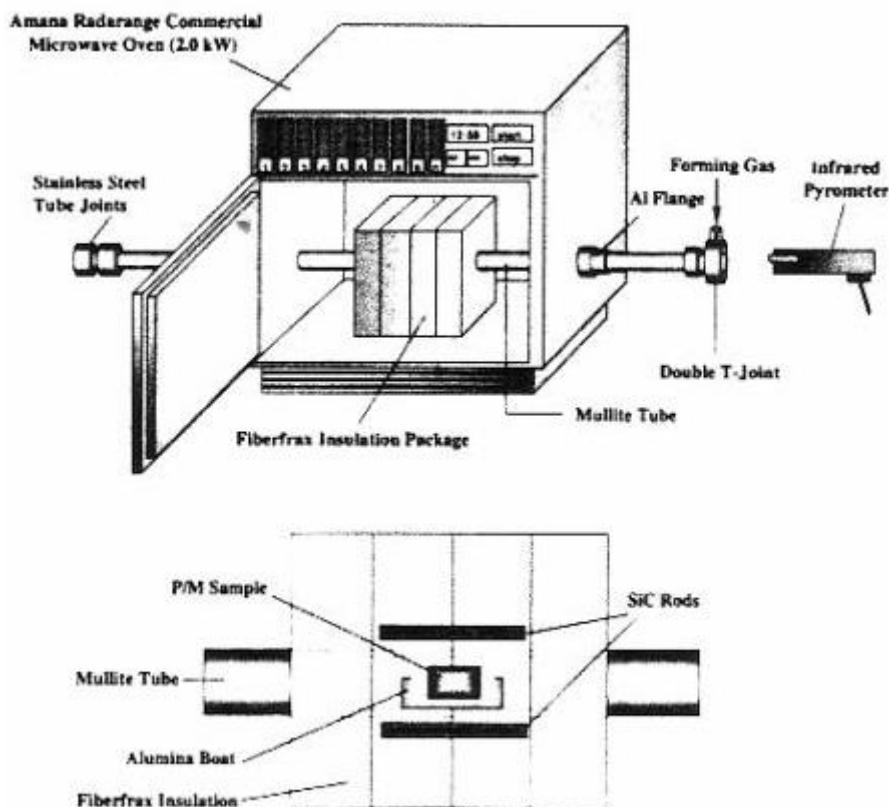


**Figure 8.0.1:** A schematic of a microwave tube furnace, comprised of a commercial microwave with a mullite tube and fibrefrax insulation package with silicon carbide rods to facilitate the high-temperature heating [263]. Reproduced with permissions from Springer Nature, 2023.

If successful, this would synthesise  $\text{LiNi}_{0.8}\text{Mn}_{0.1}\text{Co}_{0.1}\text{O}_2$  in an oxygen environment and hypothetically increase the specific capacity yielded from these samples to within a competitive range of the conventionally calcined  $\text{LiNi}_{0.8}\text{Mn}_{0.1}\text{Co}_{0.1}\text{O}_2$ , although the reaction time would be a shorter *ca.* 5-hour duration as opposed to *ca.* 20-hour duration.

The microwave-assisted hydrothermal synthesis of  $\text{Ni}_{0.8}\text{Mn}_{0.1}\text{Co}_{0.1}(\text{OH})_2$  presented in this work confirms the formation of the  $\beta\text{-Ni}_{0.8}\text{Mn}_{0.1}\text{Co}_{0.1}(\text{OH})_2$  polymorph was desirable to maximise the capacity yielded from the samples. The synthesis conditions discussed suggest that increasing the temperature and duration generally improve the capacity yielded from the samples as well as forming well-packed, quasi-spherical secondary particles. These particles are not always spherical nor uniform, leaving scope for further investigation and optimisation. The reaction time was limited to 3 hours based on the manufacturer's recommendation to prevent the magnetron from overheating. The power usage of the magnetron was lower than first anticipated, therefore there was scope to conduct the reaction for longer periods, particularly if a lower temperature of 180-200 °C was used, which would alleviate the work done by the magnetron. Further investigation

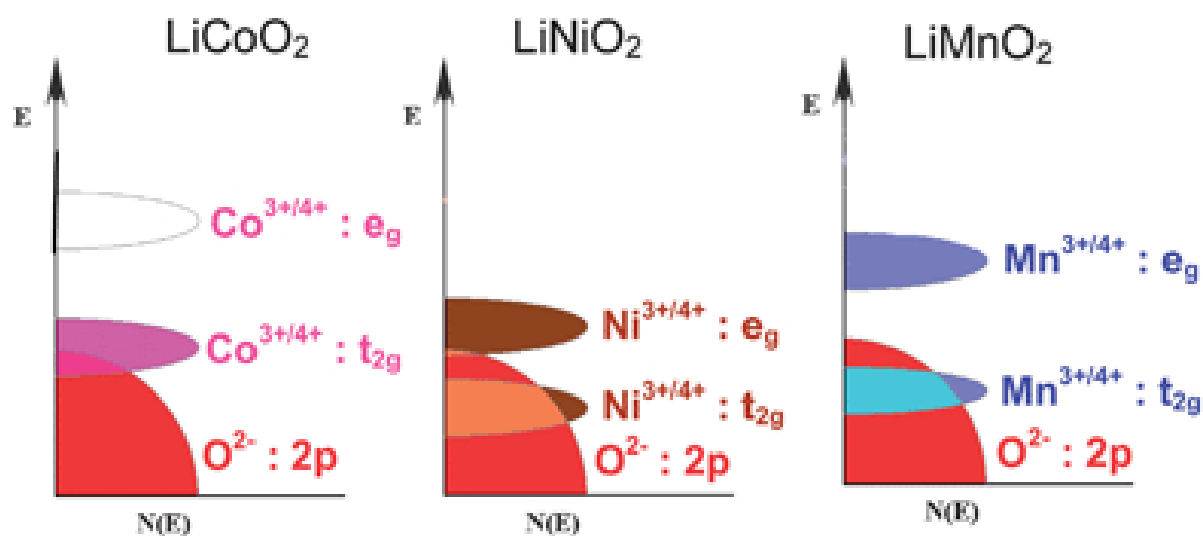
into the optimal urea: transition metal ratio could also be conducted to ascertain the effect of urea: transition metal ratio between the values of 5: 2 and 3: 1. Considerations should be made to mitigate the presence of the spinel phase impurity with the exploration of new synthesis conditions and its effect on the electrochemical capacity. Due to the successful synthesis of  $\beta\text{-Ni}_{0.8}\text{Mn}_{0.1}\text{Co}_{0.1}(\text{OH})_2$  with the high-throughput reaction volume of 40 mL within the 100 mL reactor, further optimisation, and exploration of the high-throughput capabilities of the microwave-assisted hydrothermal method could also be investigated, either through the increase of reaction volume or shortening of the reaction duration.

A new microwave continuous stirred tank reactor (MiSTR) system has been demonstrated for the synthesis of  $\beta\text{-Ni}_{0.8}\text{Mn}_{0.1}\text{Co}_{0.1}(\text{OH})_2$  which upon calcination and electrochemical cycling yielded a maximum capacity of  $188.7 \text{ mAh g}^{-1}$  when cycled at C/20 over a voltage window of 3.0-4.3 V. The experimental and operational control during the commissioning tests reported was poor, with poor control over the stirring, pH, and addition of materials. The stirring was conducted using a magnetic stirrer bar with arbitrary 'low', 'medium' and 'high' stirring rate, not controlled to a specific stirring rate. An overhead stirrer has been developed with control over the stirring rate as revolutions per minute, but considerations should be made to prevent the whipping of the agitator rod. This could be installed, tested, and the agitator head redesigned should it not provide adequate mixing at the stirring rate deemed safe.

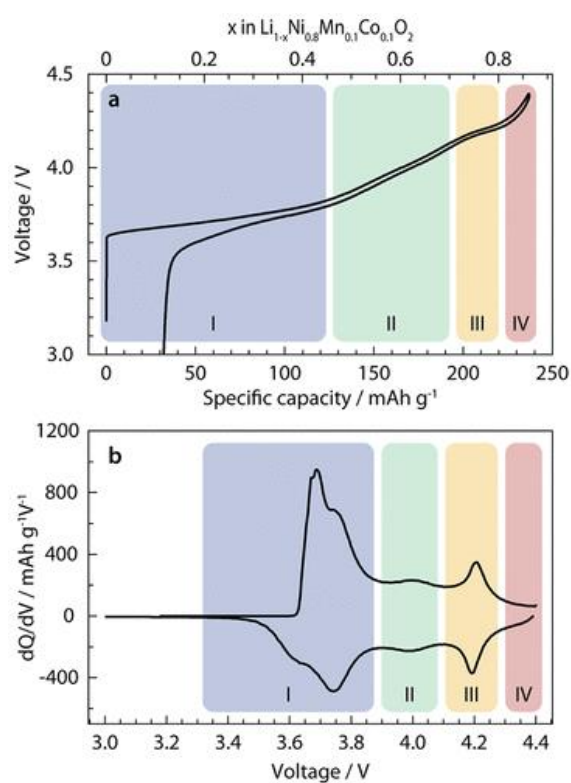
Optimisation of the reaction conditions can also be conducted. The pH sensors used have a platinum electrode and thus cannot be inserted in the microwave reactor. In the commissioning tests the pH sensor was implemented as a feedback loop in a satellite station outside of the reactor, with the addition of the sodium hydroxide and ammonia solution used to control the pH being controlled automatically by a control station. The feedback delay caused the pH to oscillate erratically, limiting the control capability of the system. Alternative control systems could be investigated to overcome this challenge and control the pH to a more uniform value. The utilisation of additional pumps during a reaction that would facilitate the separate addition of the ammonia and sodium hydroxide, which would mean the ammonia: transition metal ratio within the reaction would be independent of the pH control. Other reaction conditions such as the reaction duration, which encompasses the addition and maturation time, could also be investigated to investigate the optimal reaction conditions needed to synthesise uniform secondary particles with respect to size, morphology and density.

The optimisation of the semi-batch operation of the MiSTR system through the synthesis of uniform, dense particles with a high specific capacity yielded from Galvanostatic cycling would result in a reduction in the synthesis time of  $\text{Ni}_{0.8}\text{Mn}_{0.1}\text{Co}_{0.1}(\text{OH})_2$  from approximately 40 hours to 5-6 hours. Additionally, the power consumption and operational costs would also be reduced, as discussed in Chapter 6. This would make this MiSTR process desirable for industry and high-throughput synthesis of  $\text{Ni}_{0.8}\text{Mn}_{0.1}\text{Co}_{0.1}(\text{OH})_2$ . Consequently, given the geometry of the MiSTR vessel being identical to a continuous stirred tank reactor (CSTR), the processes could be adapted for continuous operation, further increasing the throughput of the system. This continuous microwave synthesis (COMICS) system would require a rebuild or redesign of the reactor vessel and overhead stirrer to construct more mechanically robust equipment during the reaction.

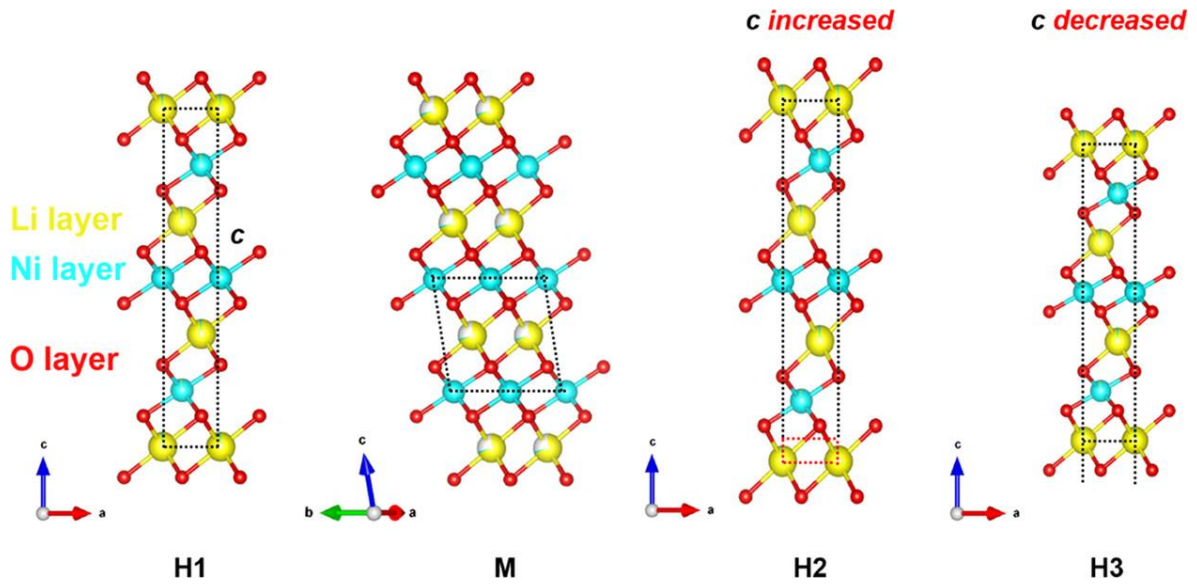
## 9. Appendices



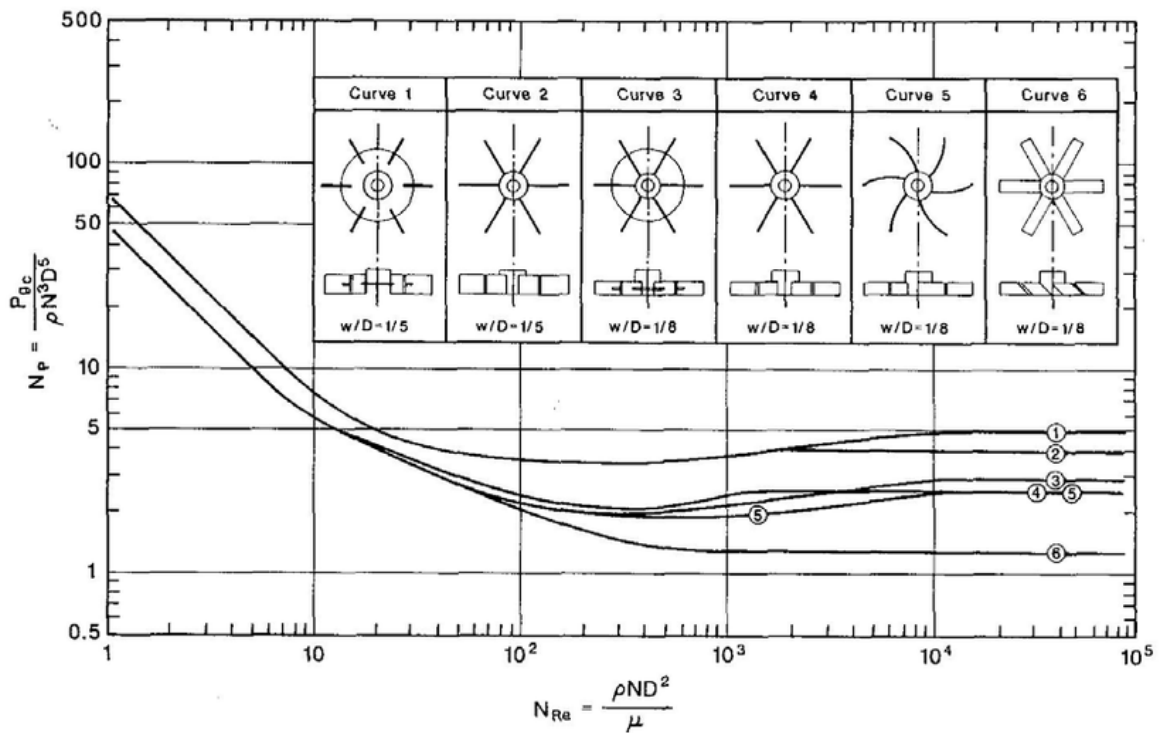
**Appendix A.1:** A density of states diagram of layered transition metal oxides  $\text{LiCoO}_2$ ,  $\text{LiNiO}_2$ ,  $\text{LiMnO}_2$ . Reproduced with permission from Royal Society of Chemistry, 2021 [31].



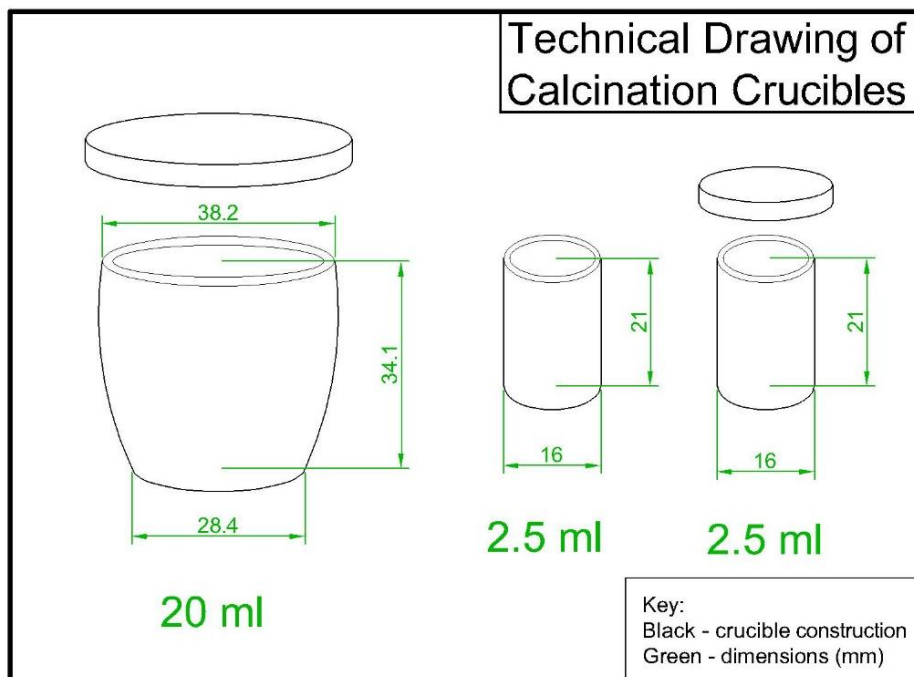
**Appendix A.2.a):** An example voltage plot and differential capacity profile that depicts the four phase transitions during (de)lithiation: H1, M, H2, H3. Reproduced with permission of the American Chemical Society, 2011.



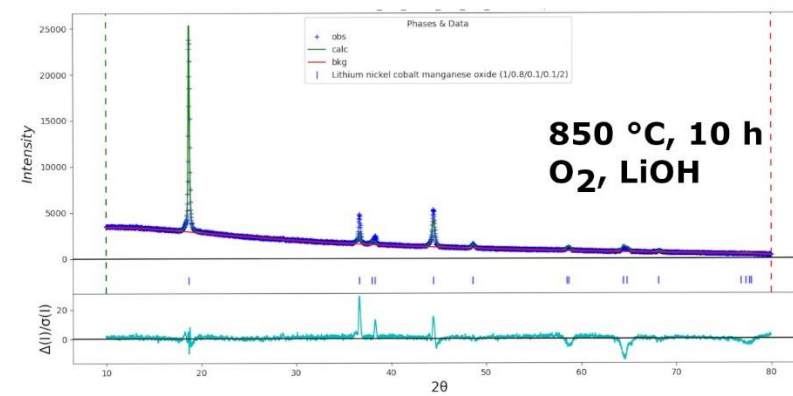
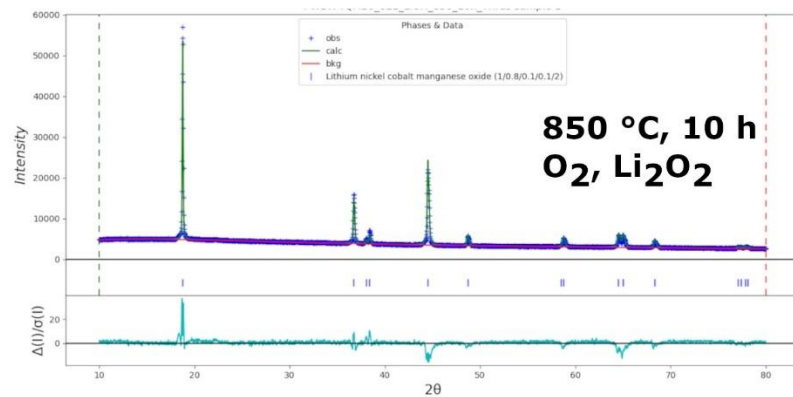
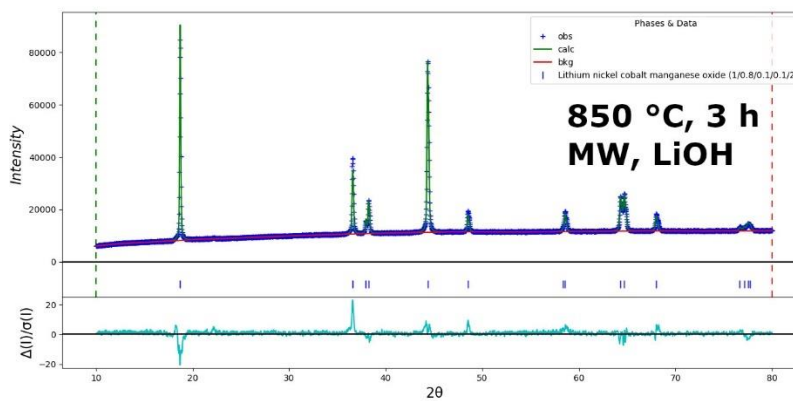
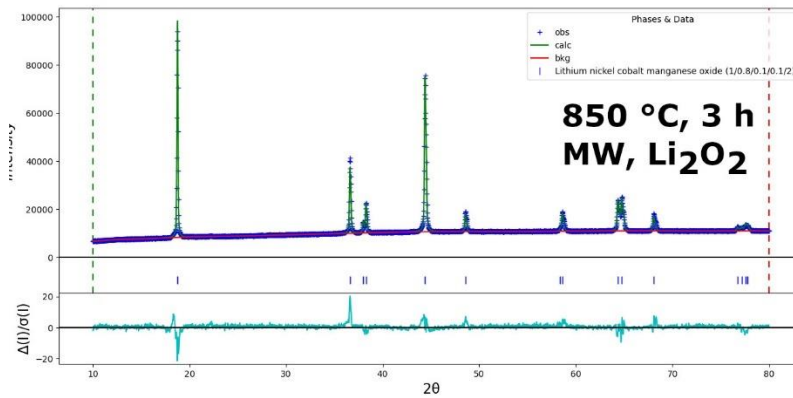
**Appendix A.2.b):** The crystallographic structure of the four phases (H1, M, H2, H3) during (de)lithiation of a layered transition metal material, with Ni representing the transition metals [60]. Reproduced with permission of the American Chemical Society, 2021.



**Appendix A.3:** A Power number- Reynolds number profile for a Newtonian fluid describing various impellers in a baffled STR. Reproduced with permission from the American Chemical Society, 1963 [264].

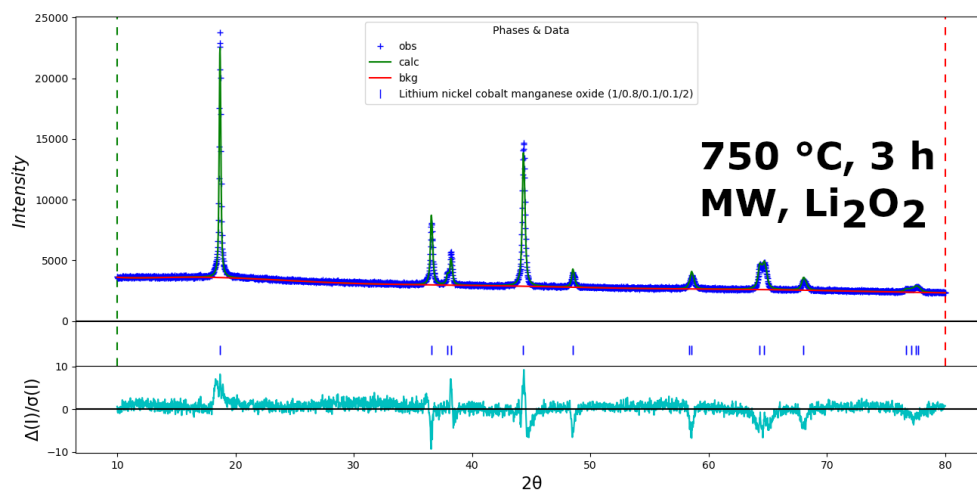
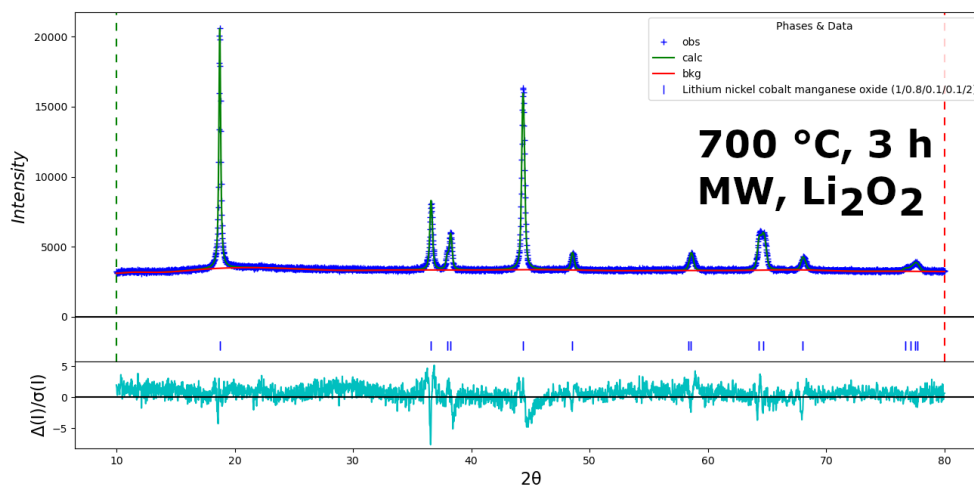
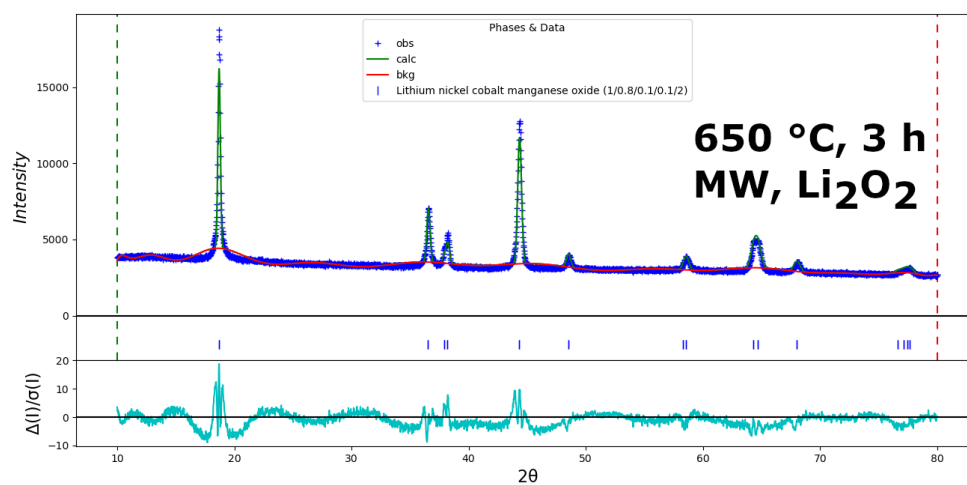


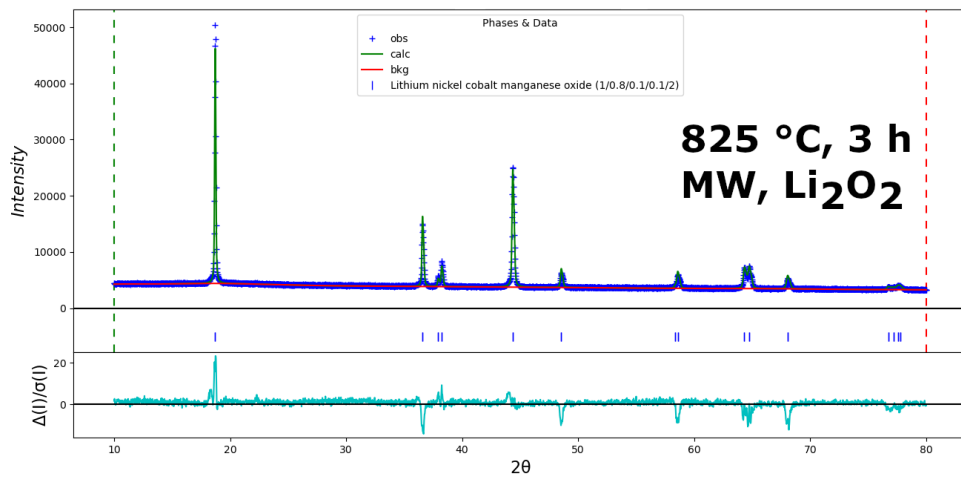
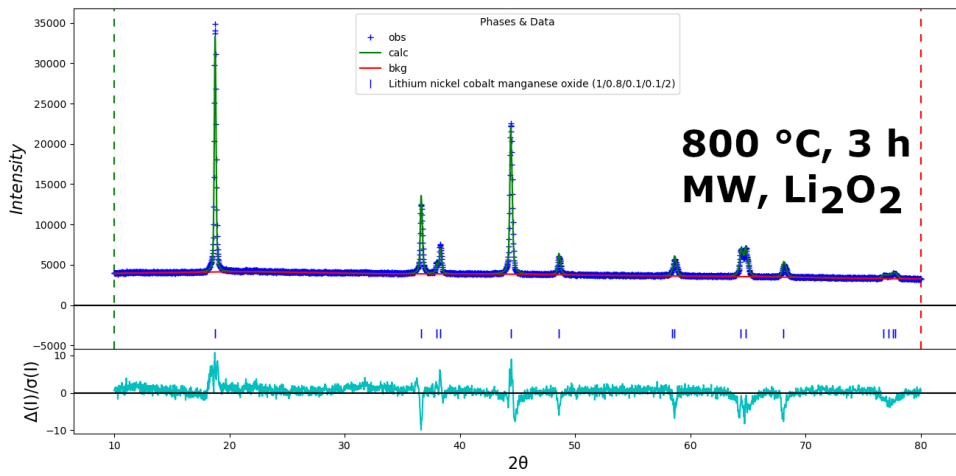
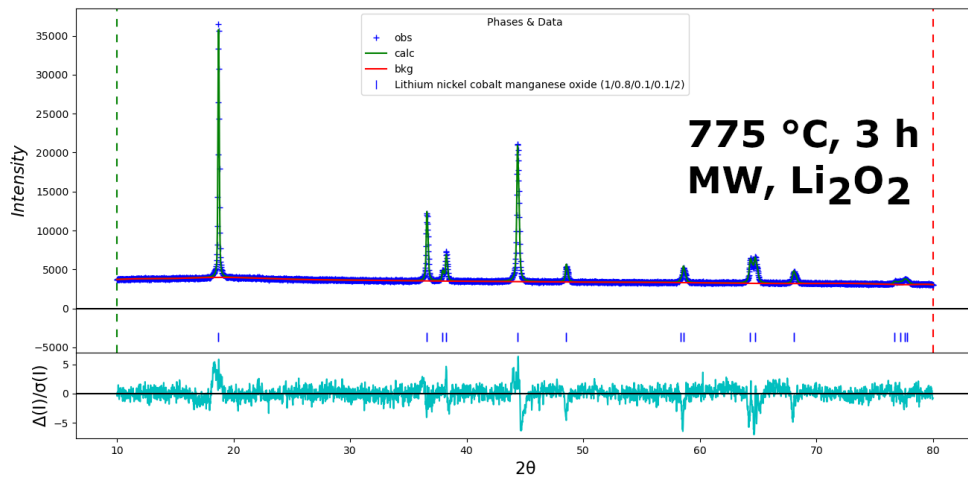
**Appendix A.4:** Images of the three crucible configurations used throughout the optimisation of NMC 811(OH)<sub>2</sub> in a microwave furnace. A large 20 mL crucible (left) was used with a lid on, a small 2.5 mL crucible (centre) with no lid, and a small crucible with a lid on (right).

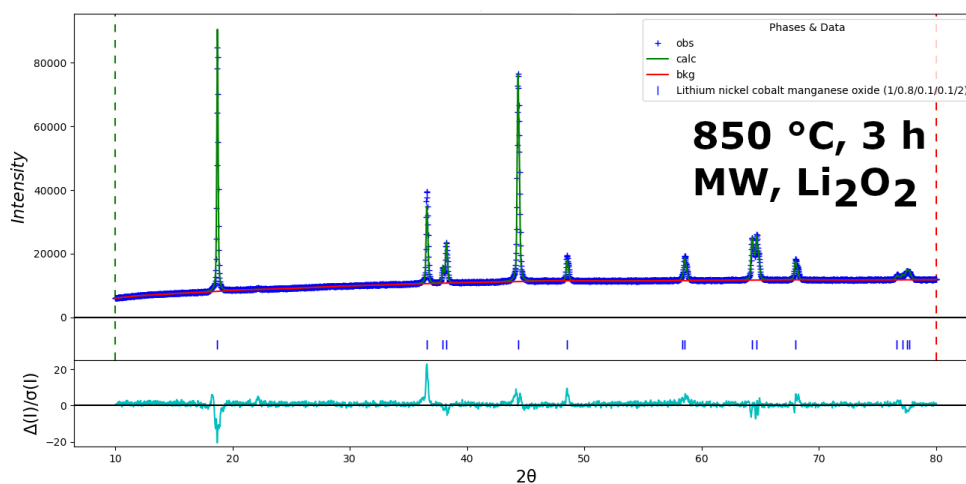


**Appendix A.5:** The Rietveld refinement fittings for the  $\text{LiNi}_{0.8}\text{Mn}_{0.1}\text{Co}_{0.1}\text{O}_2$  samples represented in **Table 3.0.3:** Key values from the Rietveld refinement of  $\text{LiNi}_{0.8}\text{Mn}_{0.1}\text{Co}_{0.1}\text{O}_2$  calcined at  $850\text{ }^\circ\text{C}$  with

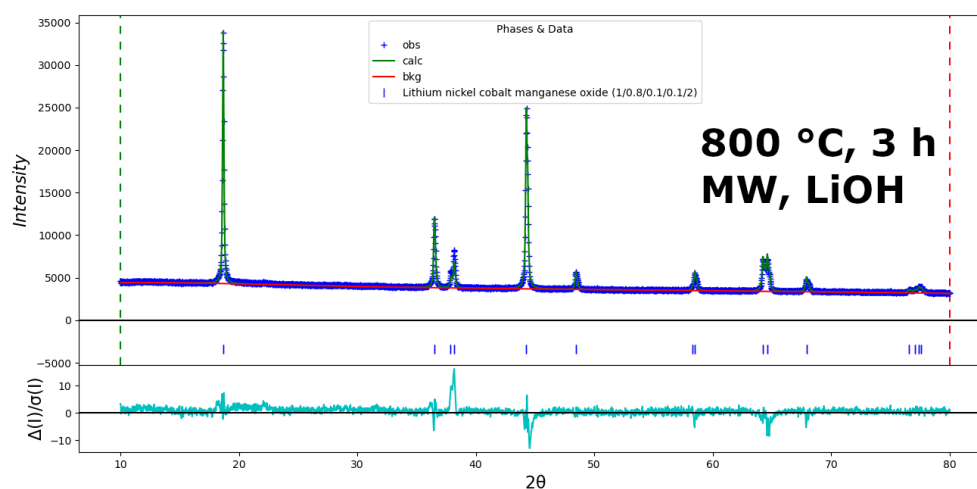
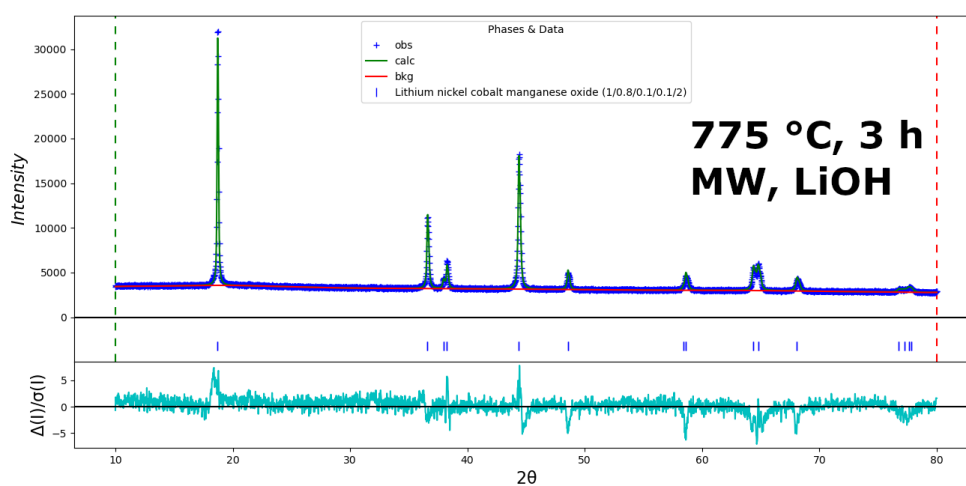
LiOH or  $\text{Li}_2\text{O}_2$  in a microwave-assisted furnace for 3 hours; or an oxygen-fed tube furnace for 10 hours. **Table 3.0.3**, refined in GSAS-II software, with the sample descriptions included for each plot.

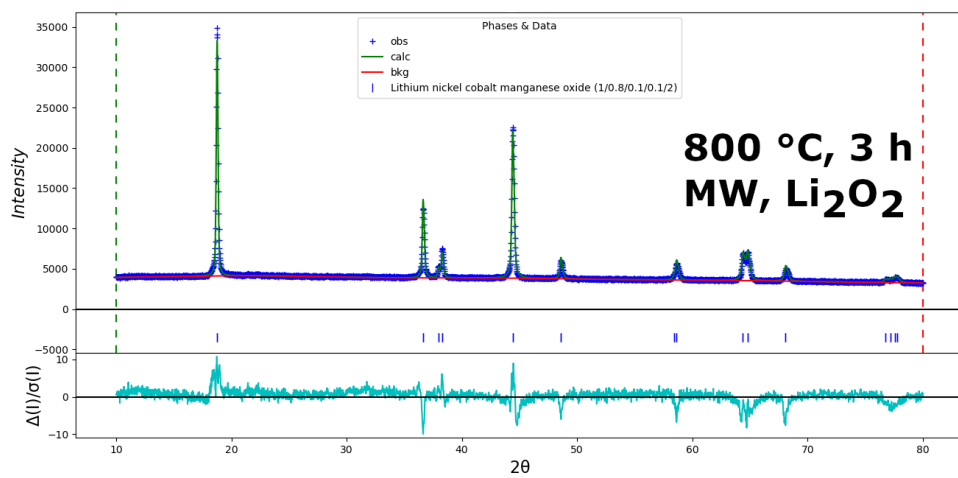
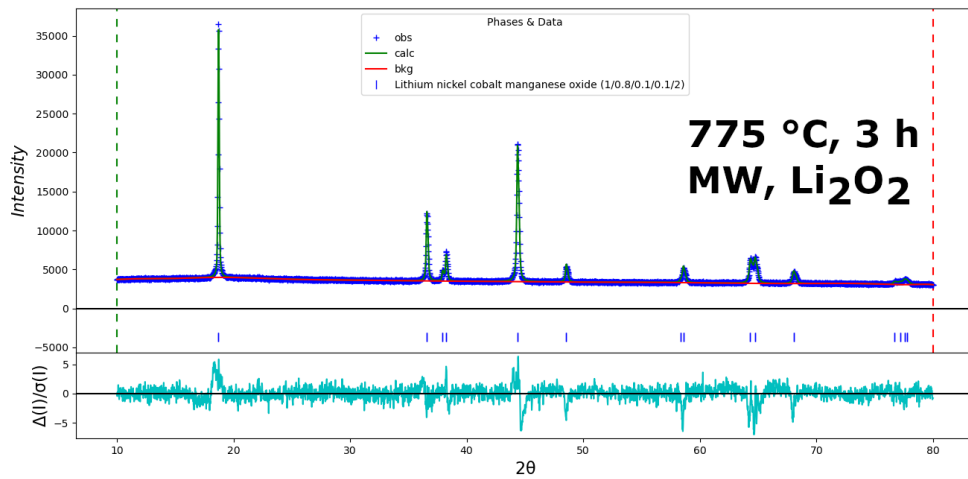




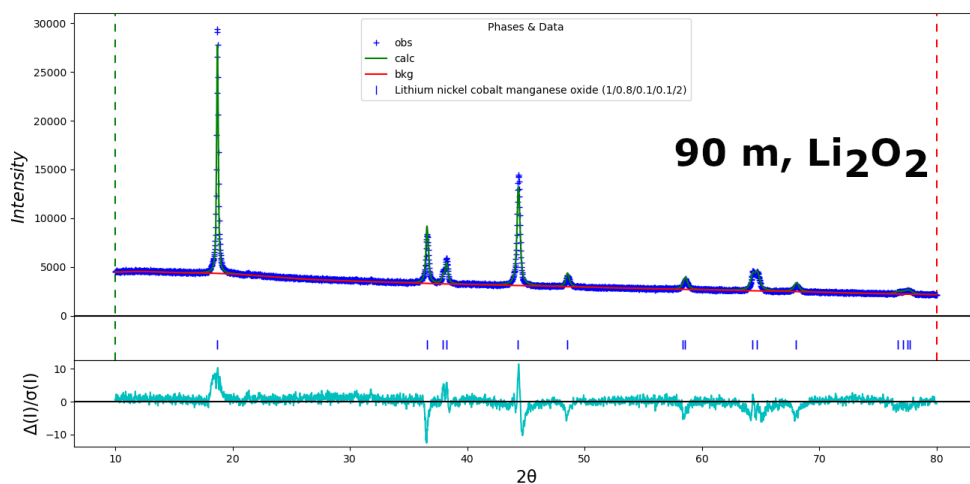


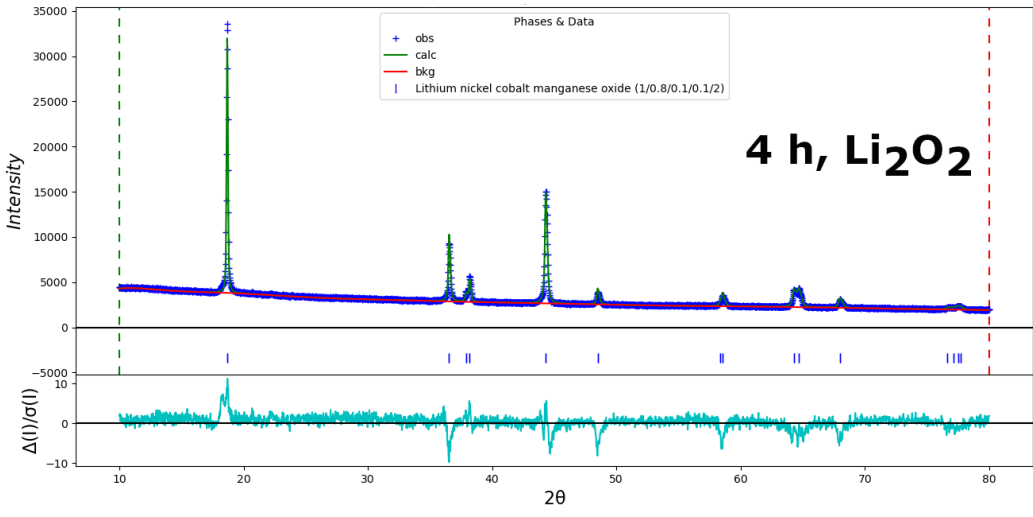
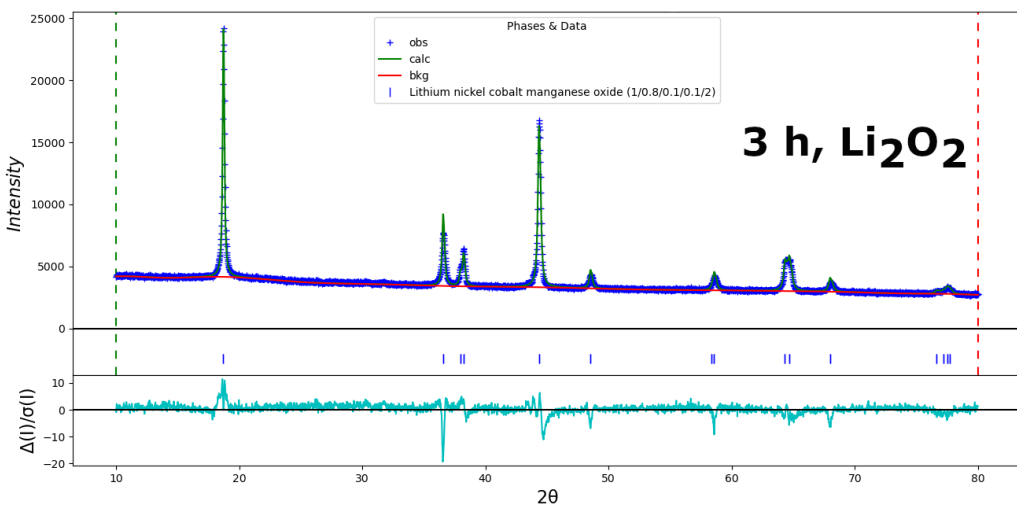
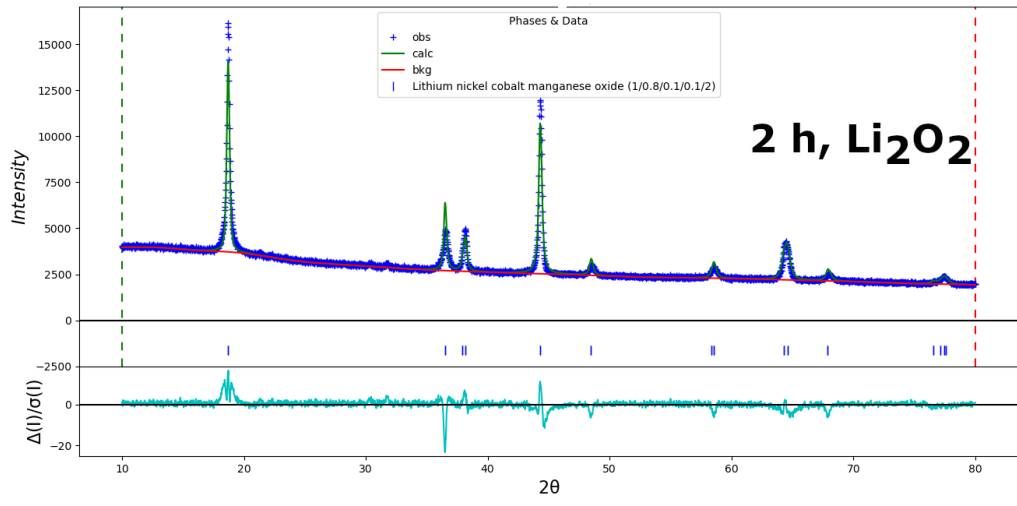
**Appendix A.6:** The Rietveld refinement fittings for the  $\text{LiNi}_{0.8}\text{Mn}_{0.1}\text{Co}_{0.1}\text{O}_2$  samples represented in **Table 3.0.3:** Key values from the Rietveld refinement of  $\text{LiNi}_{0.8}\text{Mn}_{0.1}\text{Co}_{0.1}\text{O}_2$  calcined at 850 °C with LiOH or  $\text{Li}_2\text{O}_2$  in a microwave-assisted furnace for 3 hours; or an oxygen-fed tube furnace for 10 hours. Table 3.0.4, refined in GSAS-II software, with the sample descriptions included for each plot.

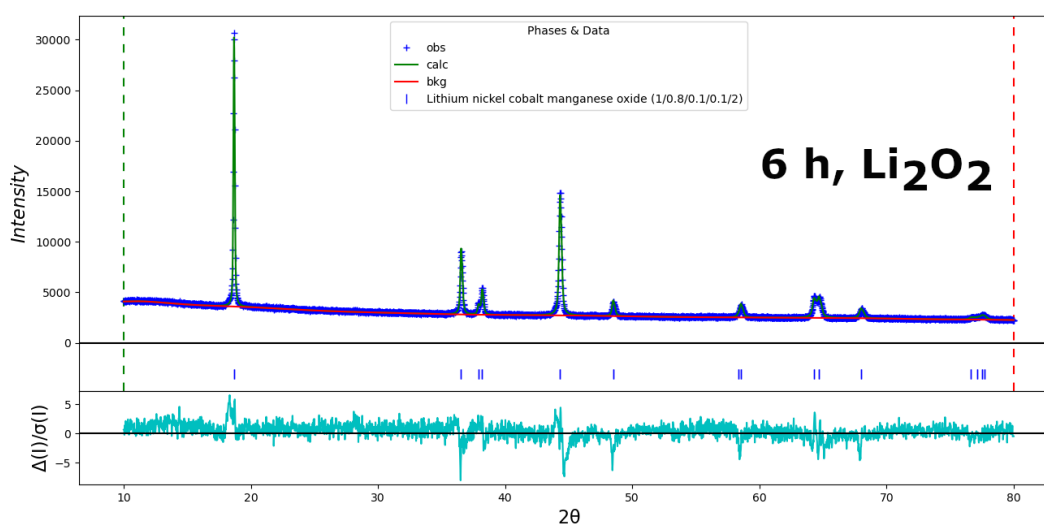
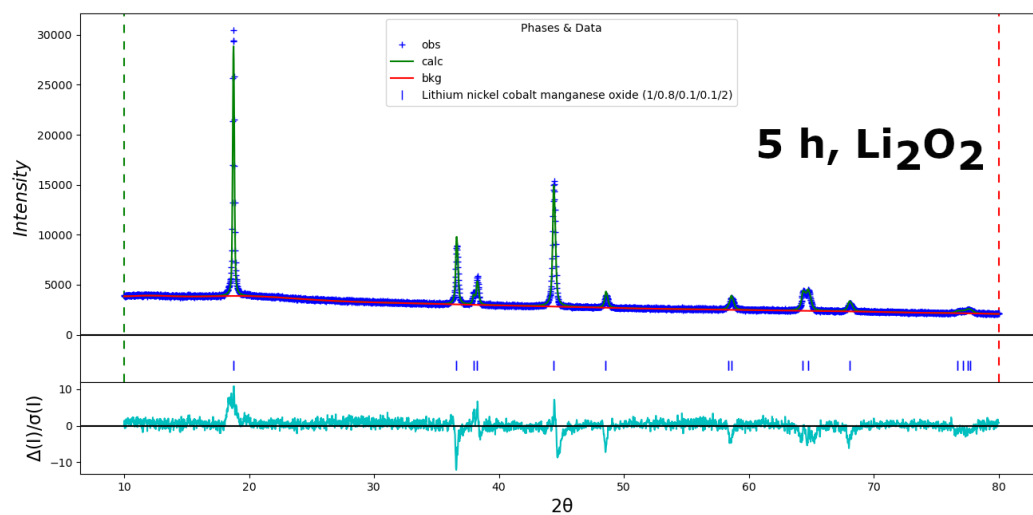




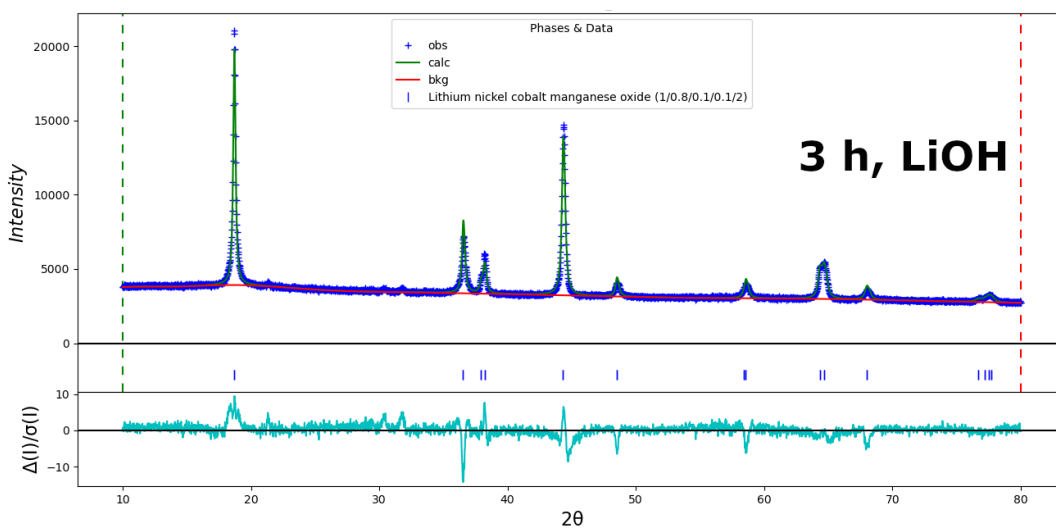
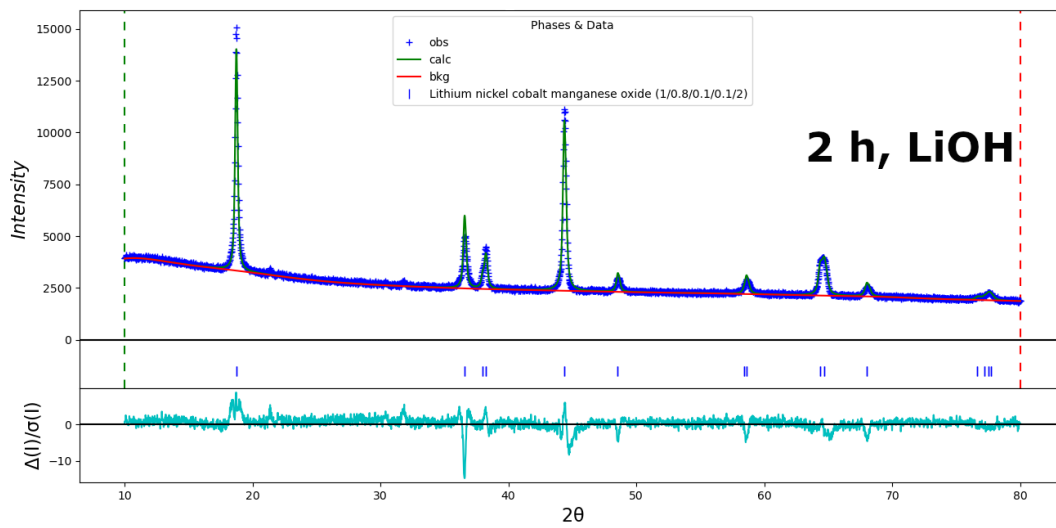
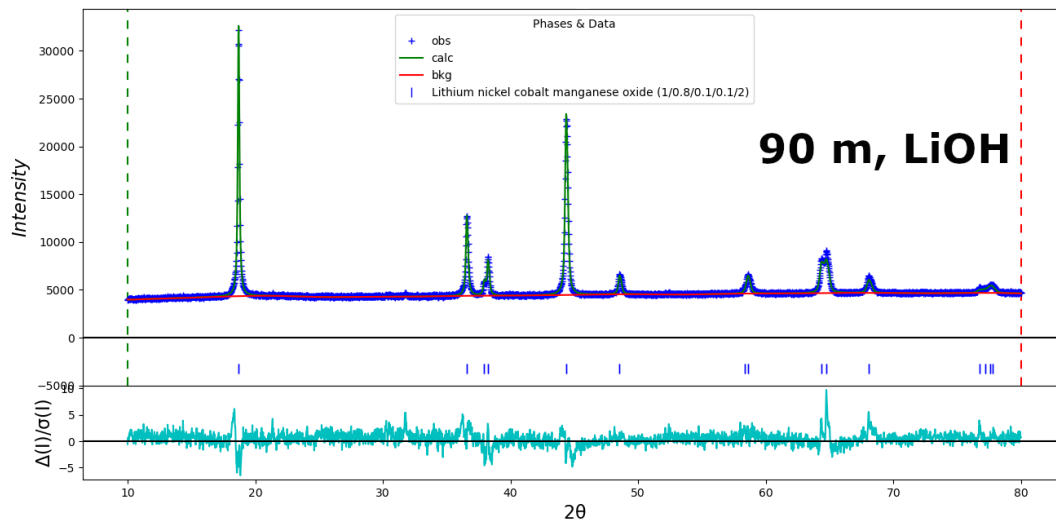
**Appendix A.7:** The Rietveld refinement fittings for the  $\text{LiNi}_{0.8}\text{Mn}_{0.1}\text{Co}_{0.1}\text{O}_2$  samples represented in **Table 3.0.3:** Key values from the Rietveld refinement of  $\text{LiNi}_{0.8}\text{Mn}_{0.1}\text{Co}_{0.1}\text{O}_2$  calcined at 850 °C with LiOH or  $\text{Li}_2\text{O}_2$  in a microwave-assisted furnace for 3 hours; or an oxygen-fed tube furnace for 10 hours. Table 3.0.5, refined in GSAS-II software, with the sample descriptions included for each plot.

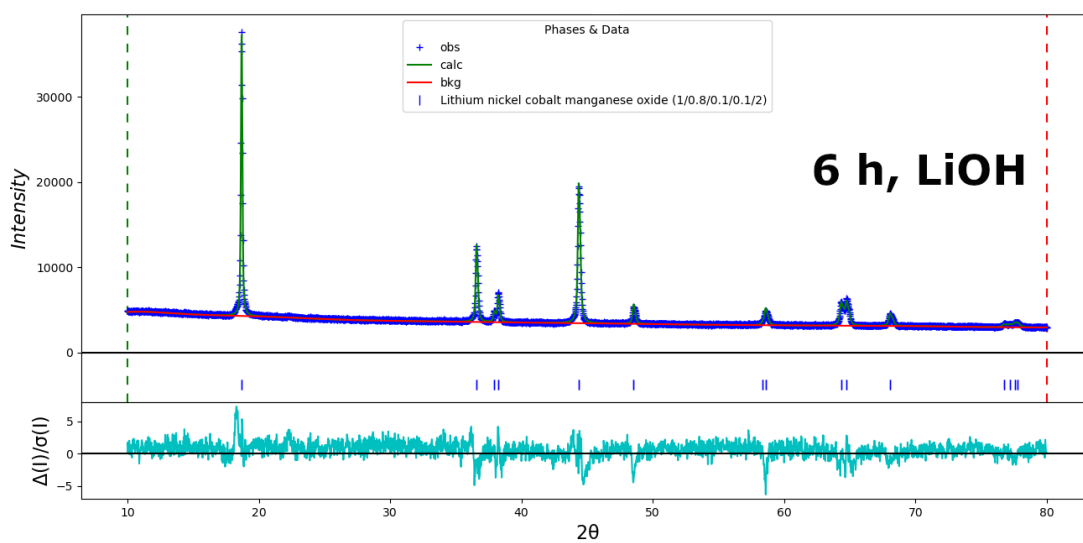
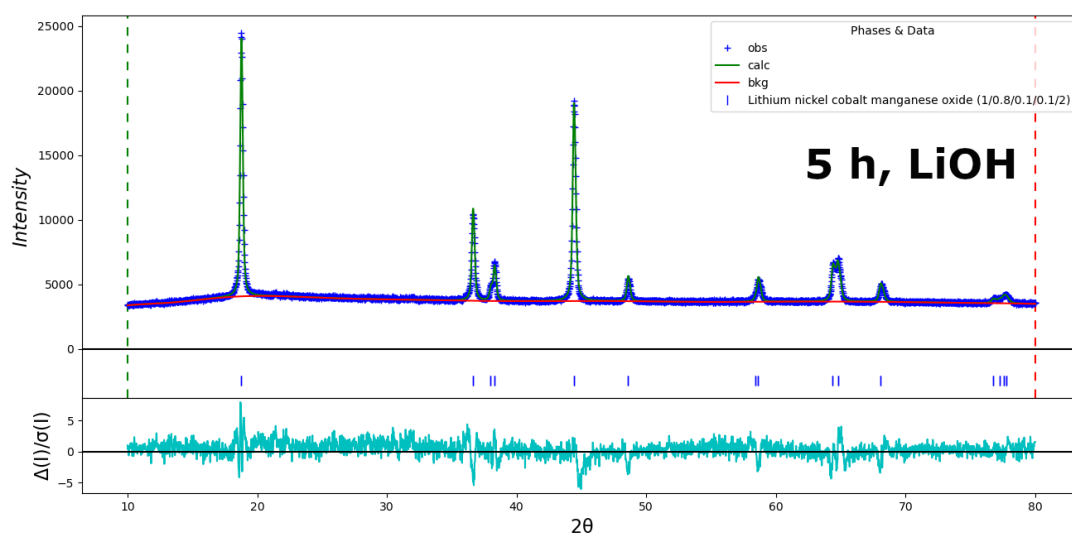
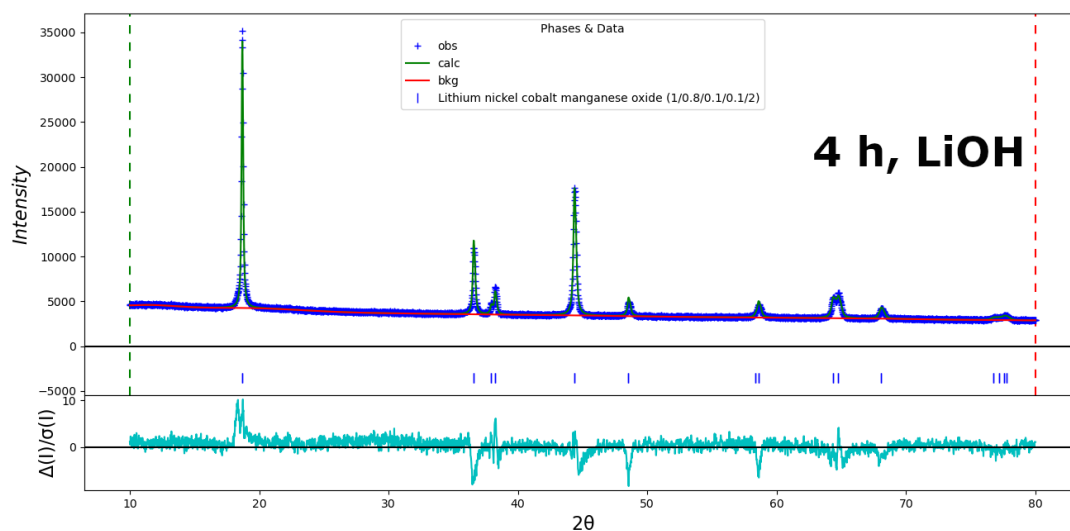






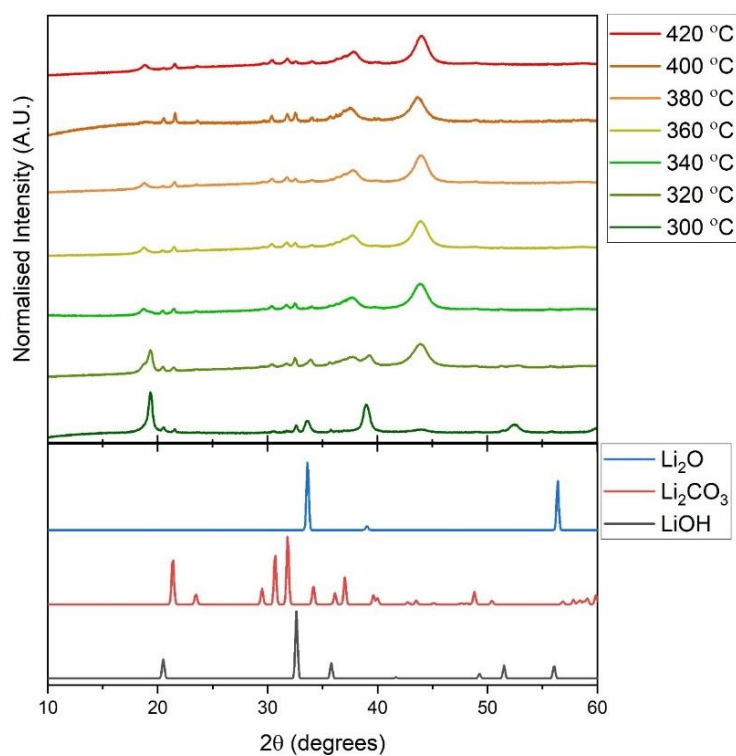
**Appendix A.8:** The Rietveld refinement fittings for the  $\text{LiNi}_{0.8}\text{Mn}_{0.1}\text{Co}_{0.1}\text{O}_2$  samples represented in **Table 3.0.3:** Key values from the Rietveld refinement of  $\text{LiNi}_{0.8}\text{Mn}_{0.1}\text{Co}_{0.1}\text{O}_2$  calcined at  $850^\circ\text{C}$  with  $\text{LiOH}$  or  $\text{Li}_2\text{O}_2$  in a microwave-assisted furnace for 3 hours; or an oxygen-fed tube furnace for 10 hours. Table 3.0.6, refined in GSAS-II software, with the sample descriptions included for each plot.



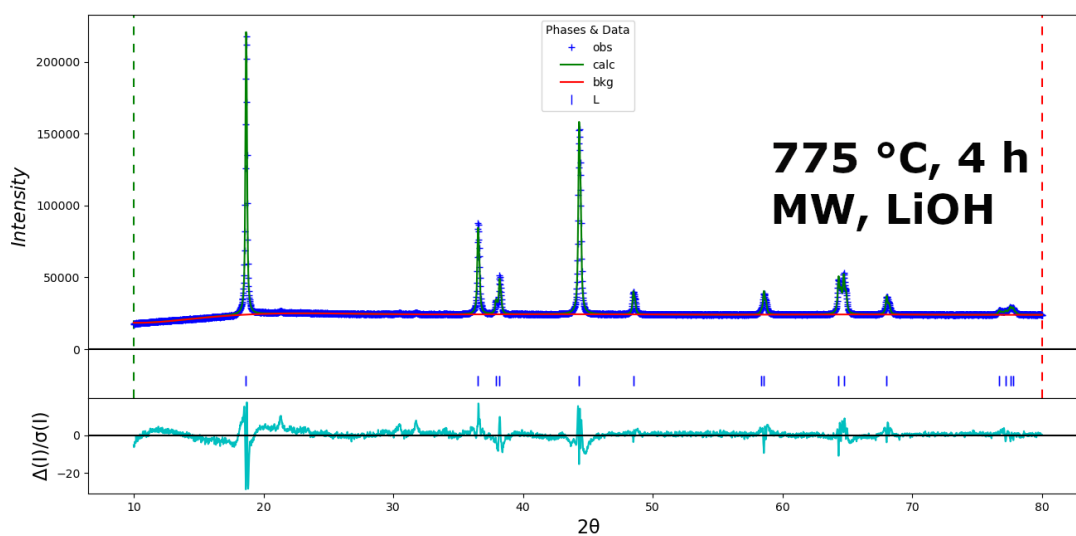


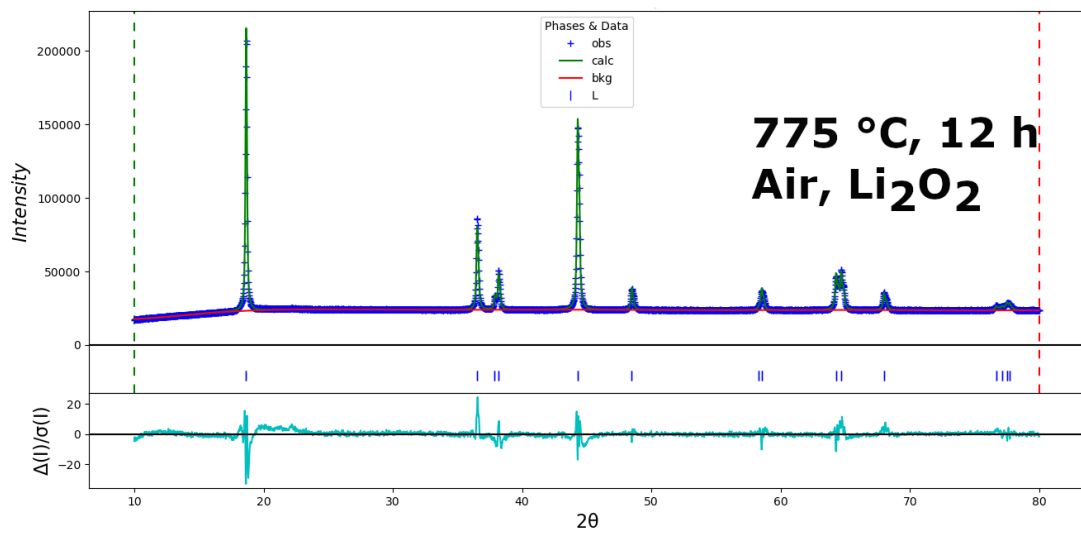
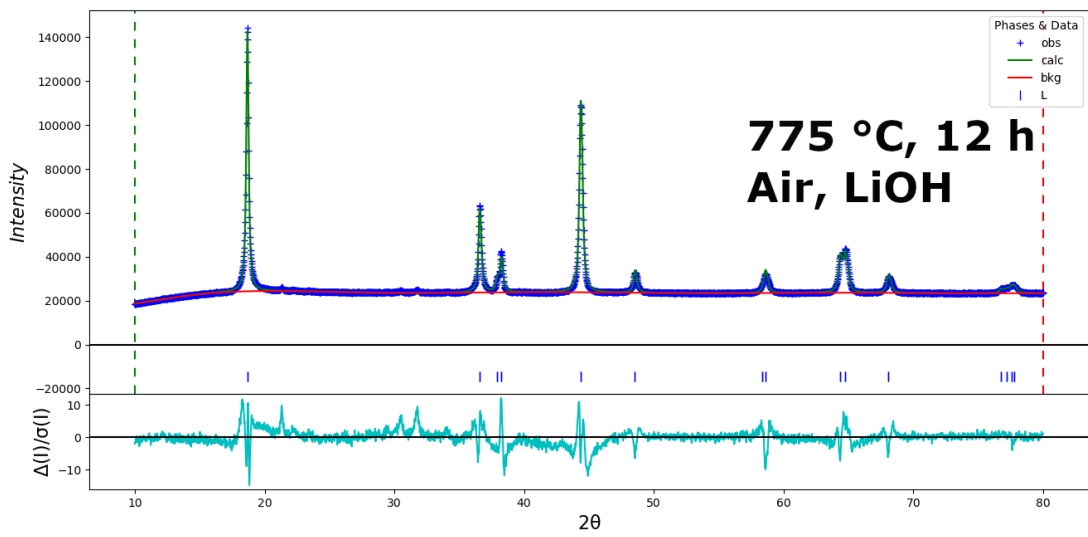
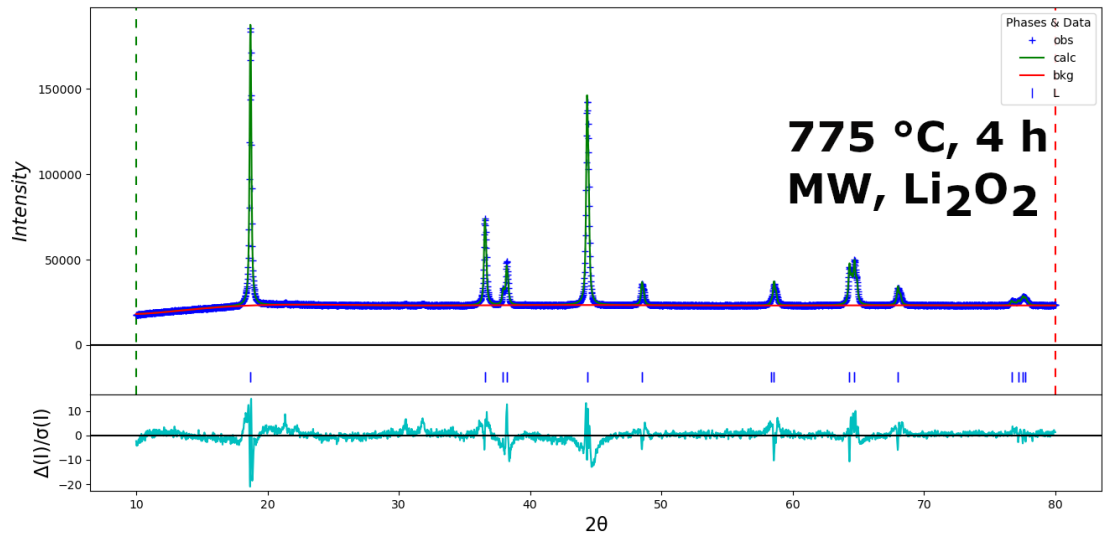
**Appendix A.9:** The Rietveld refinement fittings for the  $\text{LiNi}_{0.8}\text{Mn}_{0.1}\text{Co}_{0.1}\text{O}_2$  samples represented in **Table 3.0.3:** Key values from the Rietveld refinement of  $\text{LiNi}_{0.8}\text{Mn}_{0.1}\text{Co}_{0.1}\text{O}_2$  calcined at  $850^\circ\text{C}$  with

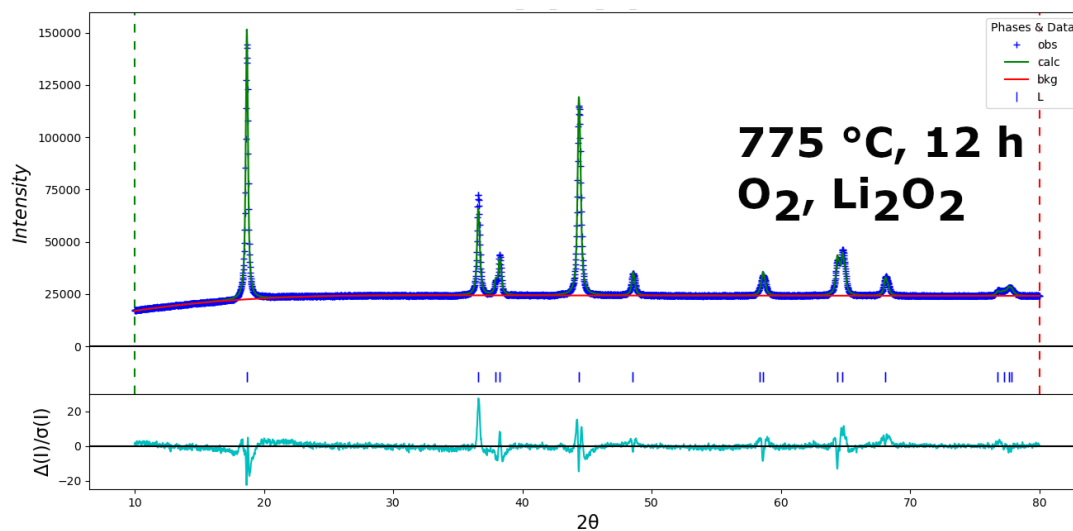
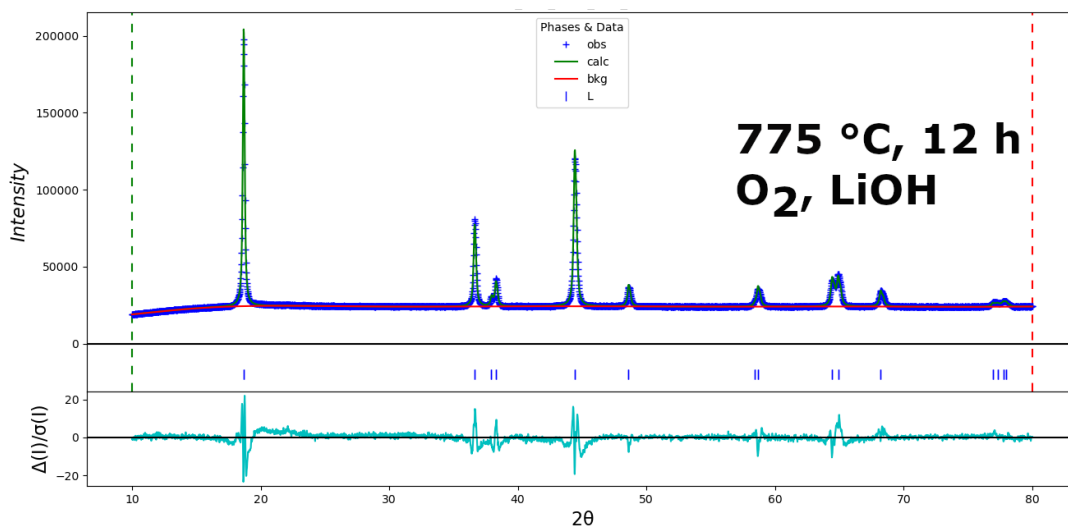
LiOH or Li<sub>2</sub>O<sub>2</sub> in a microwave-assisted furnace for 3 hours; or an oxygen-fed tube furnace for 10 hours. Table 3.0.7, refined in GSAS-II software, with the sample descriptions included for each plot.



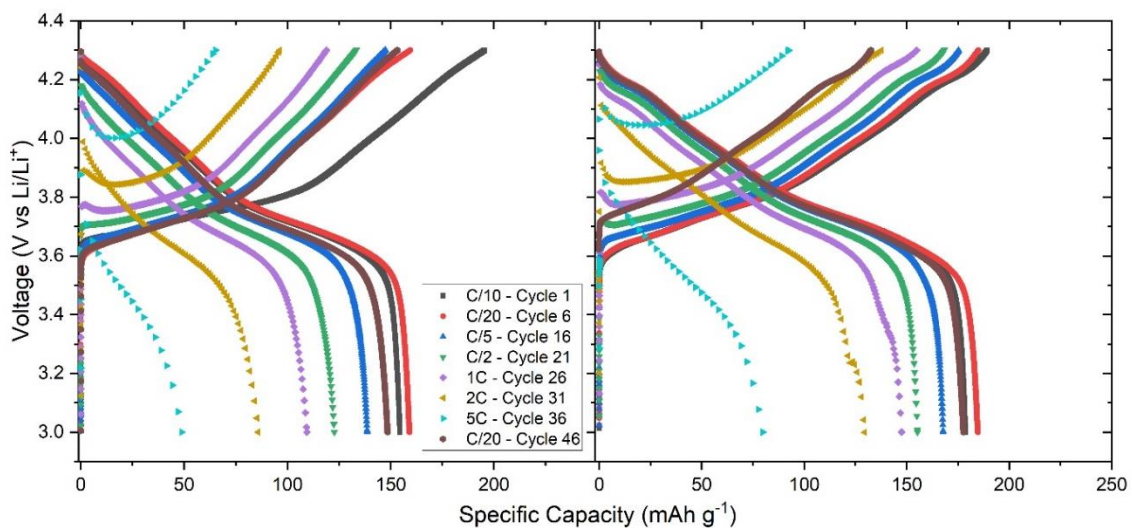
**Appendix A.10:** XRD patterns of Ni<sub>0.8</sub>Mn<sub>0.1</sub>Co<sub>0.1</sub>(OH)<sub>2</sub> heated with LiOH in the 300-420 °C temperature range with reference patterns of three common lithium species in the system: Li<sub>2</sub>O, Li<sub>2</sub>CO<sub>3</sub> and LiOH acquired from ICSD.



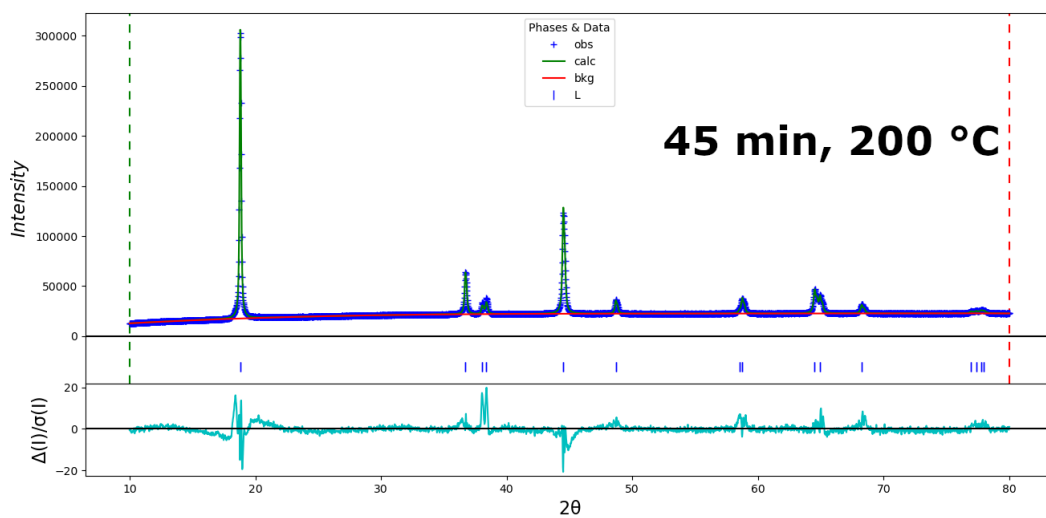
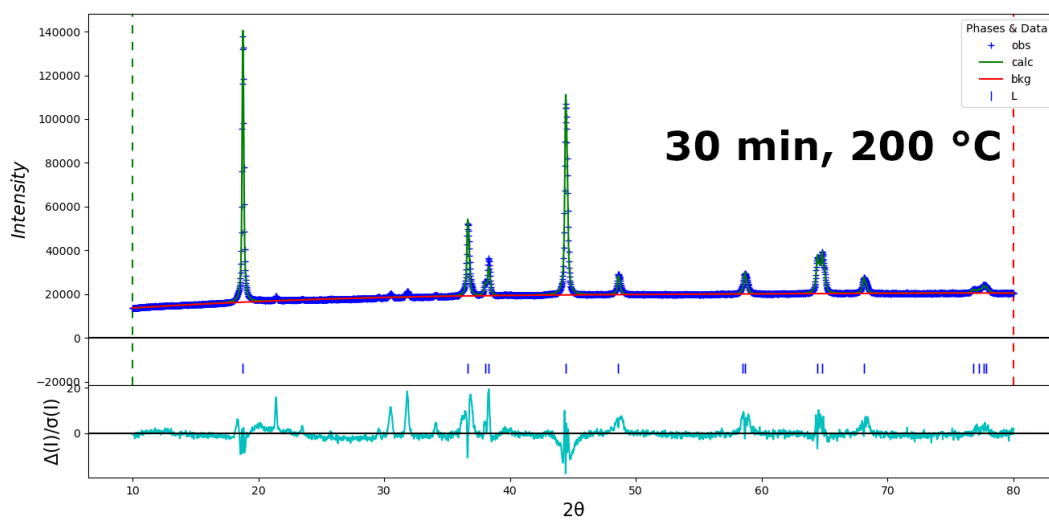


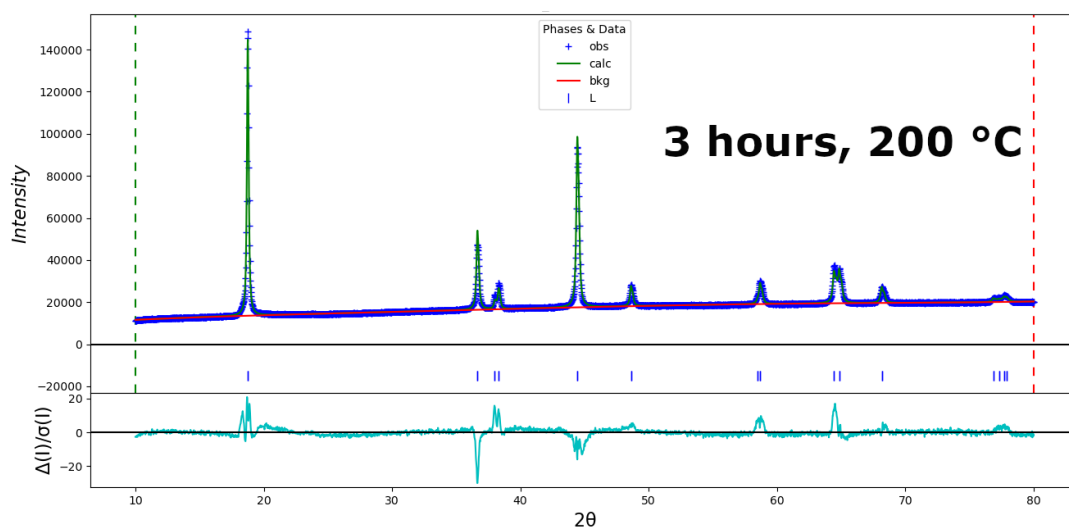
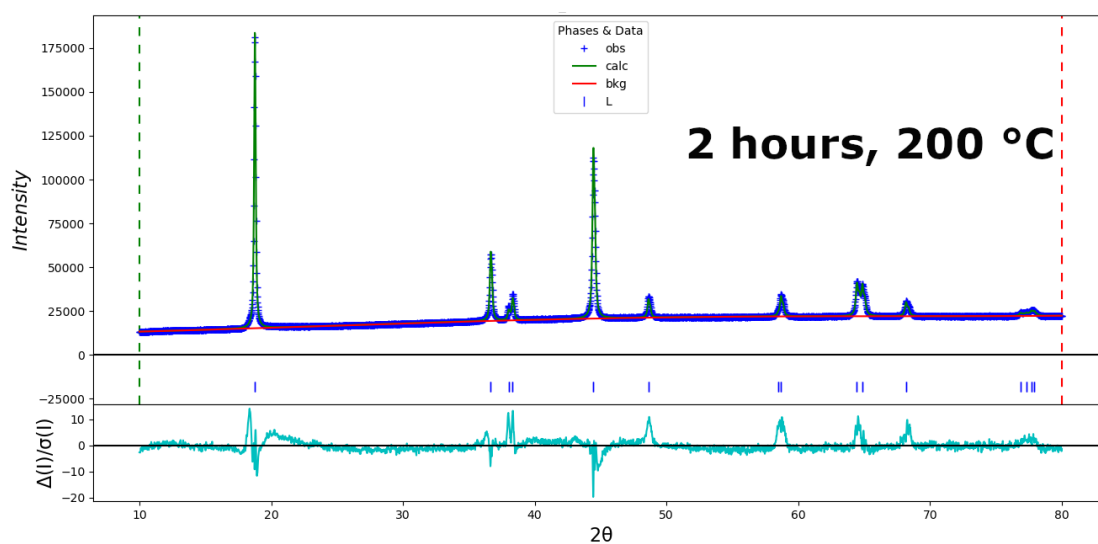
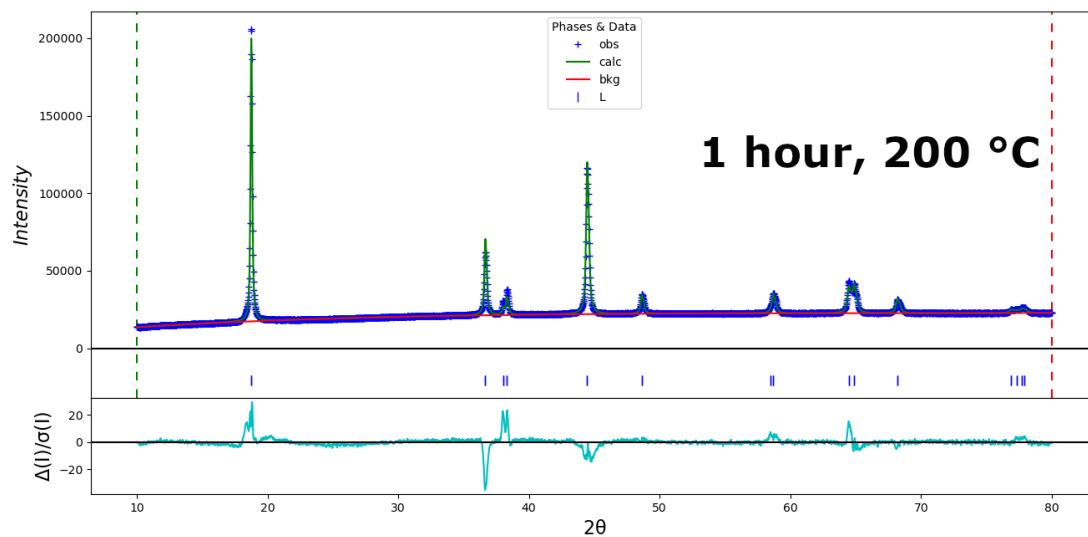


**Appendix A.11:** The Rietveld refinement fittings for the  $\text{LiNi}_{0.8}\text{Mn}_{0.1}\text{Co}_{0.1}\text{O}_2$  samples represented in **Table 3.0.3**: Key values from the Rietveld refinement of  $\text{LiNi}_{0.8}\text{Mn}_{0.1}\text{Co}_{0.1}\text{O}_2$  calcined at 850 °C with LiOH or  $\text{Li}_2\text{O}_2$  in a microwave-assisted furnace for 3 hours; or an oxygen-fed tube furnace for 10 hours. Table 4.0.1, refined in GSAS-II software, with the sample descriptions included for each plot.



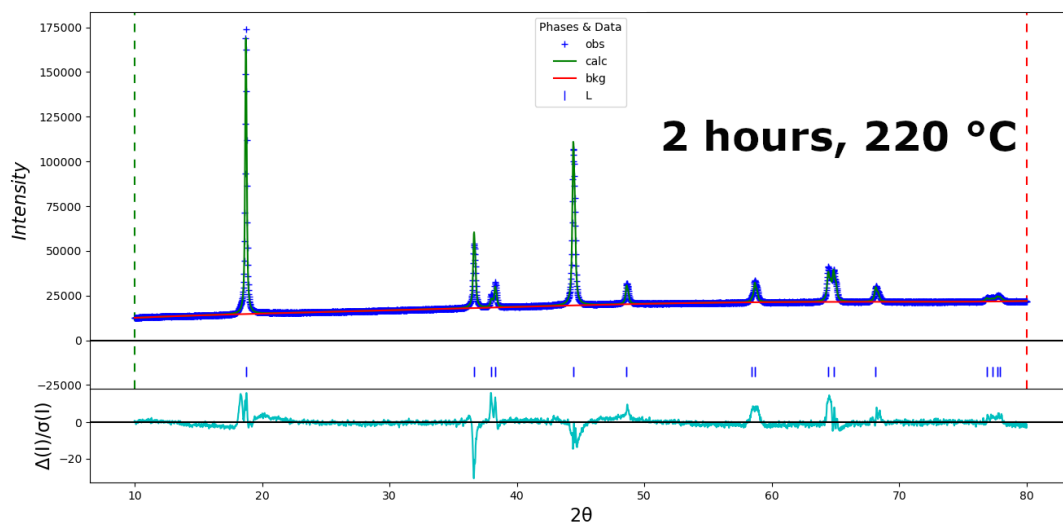
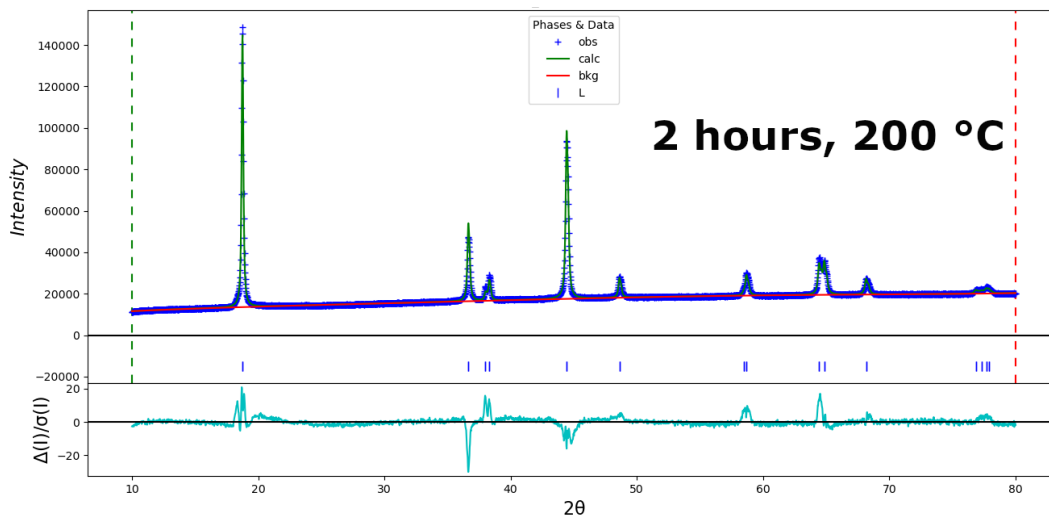
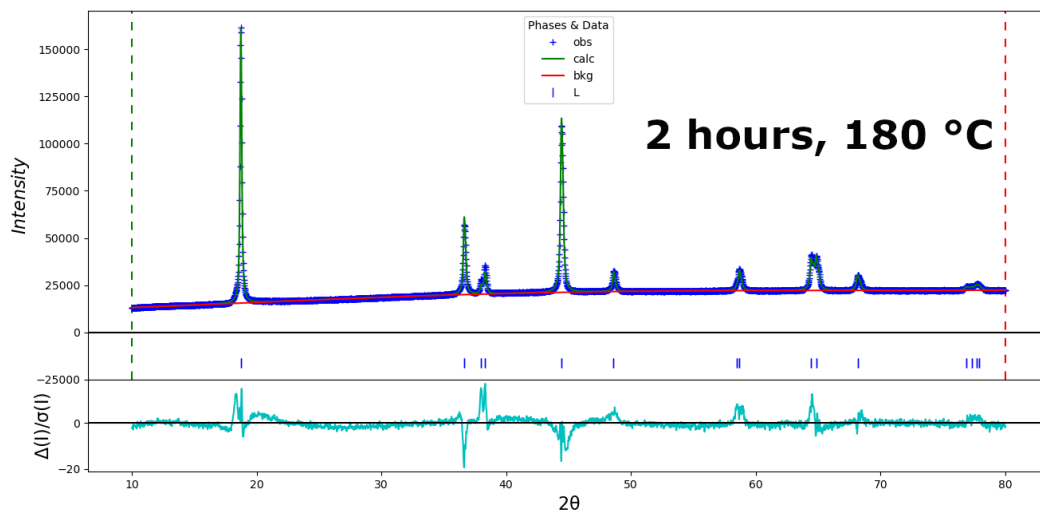
**Appendix A.12:** Voltage profiles of the optimised microwave-calcined sample (left) and equivalent oxygen-calcined sample (right) for the rate capability test.



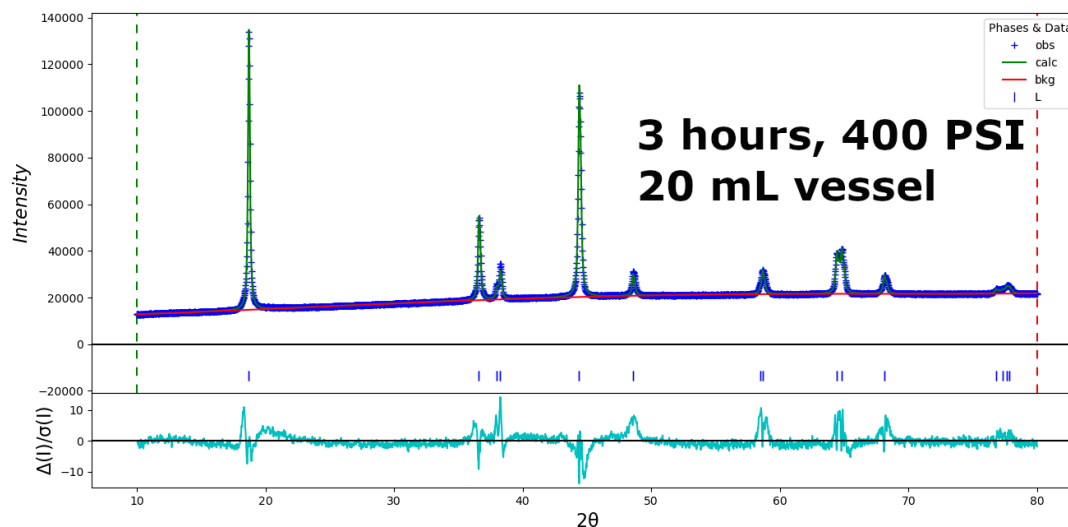
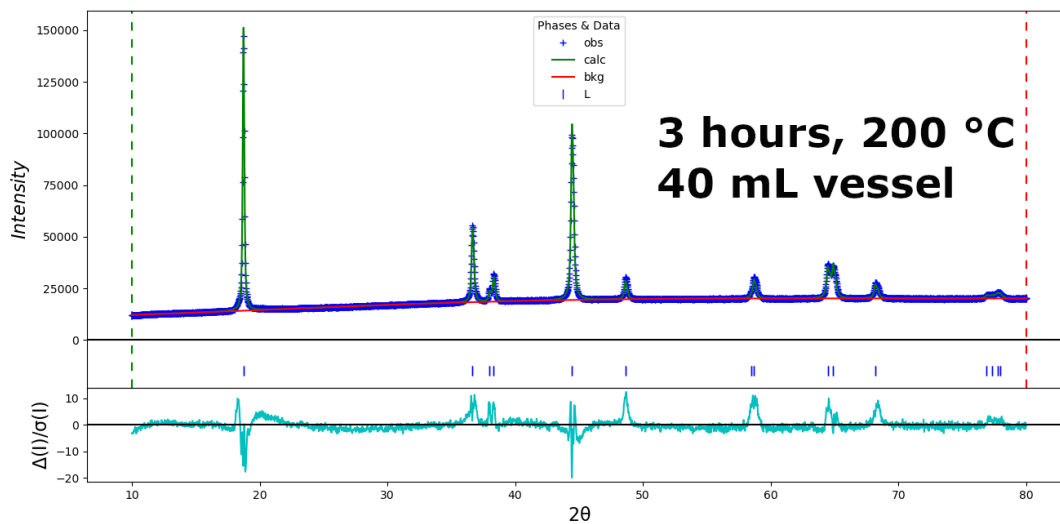
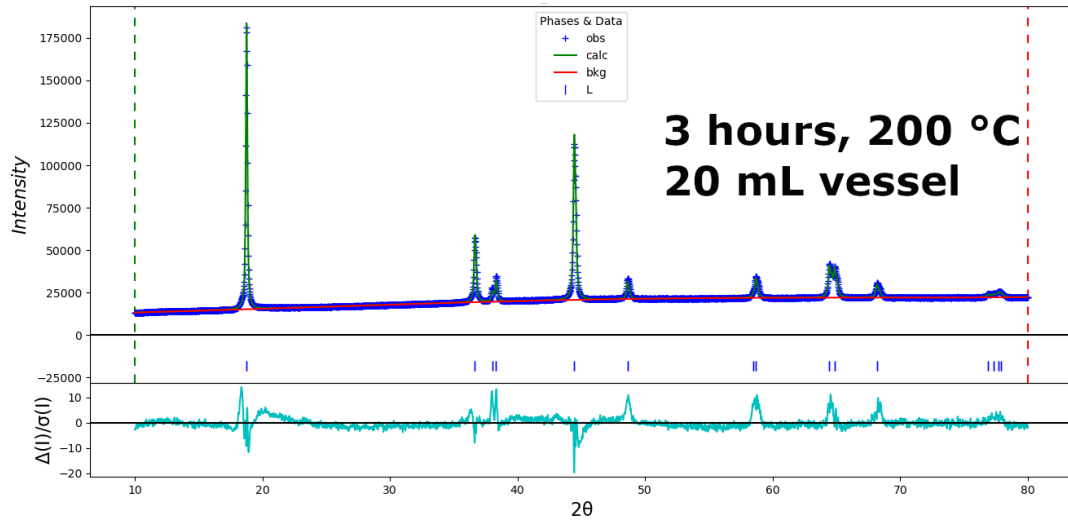


**Appendix A.13:** The Rietveld refinement fittings for the  $\text{LiNi}_{0.8}\text{Mn}_{0.1}\text{Co}_{0.1}\text{O}_2$  samples represented in **Table 3.0.3:** Key values from the Rietveld refinement of  $\text{LiNi}_{0.8}\text{Mn}_{0.1}\text{Co}_{0.1}\text{O}_2$  calcined at 850 °C with

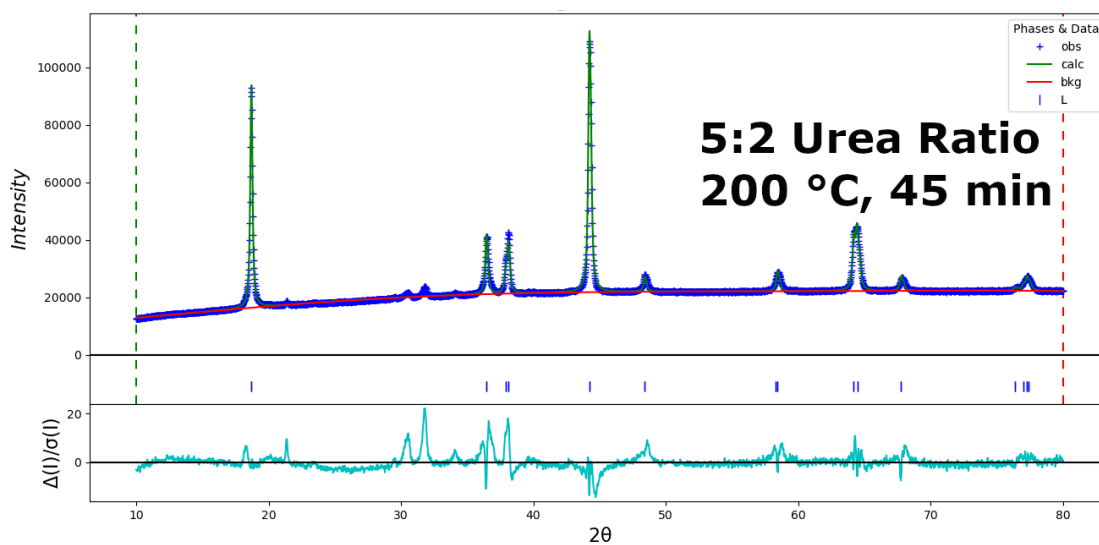
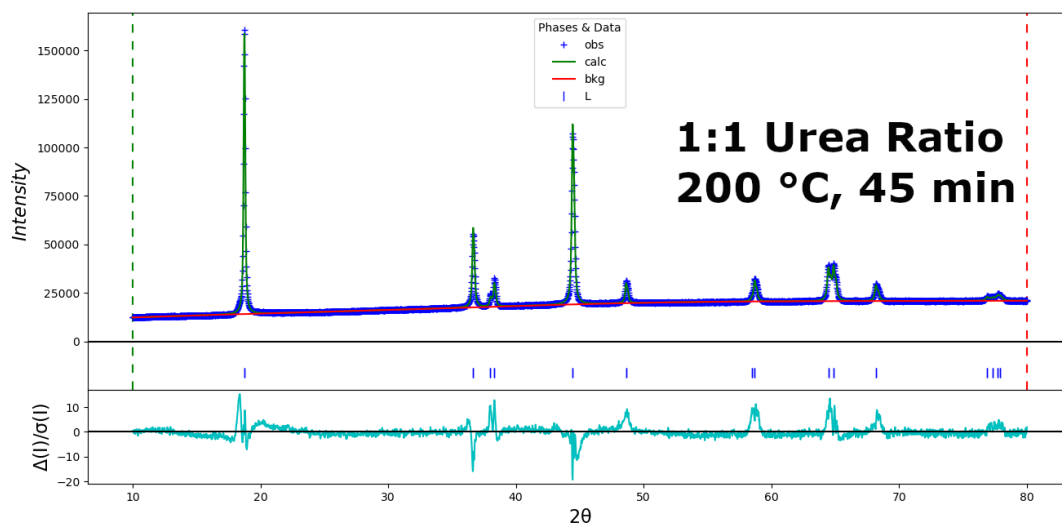
LiOH or Li<sub>2</sub>O<sub>2</sub> in a microwave-assisted furnace for 3 hours; or an oxygen-fed tube furnace for 10 hours. Table 5.0.1, refined in GSAS-II software, with the sample descriptions included for each plot.

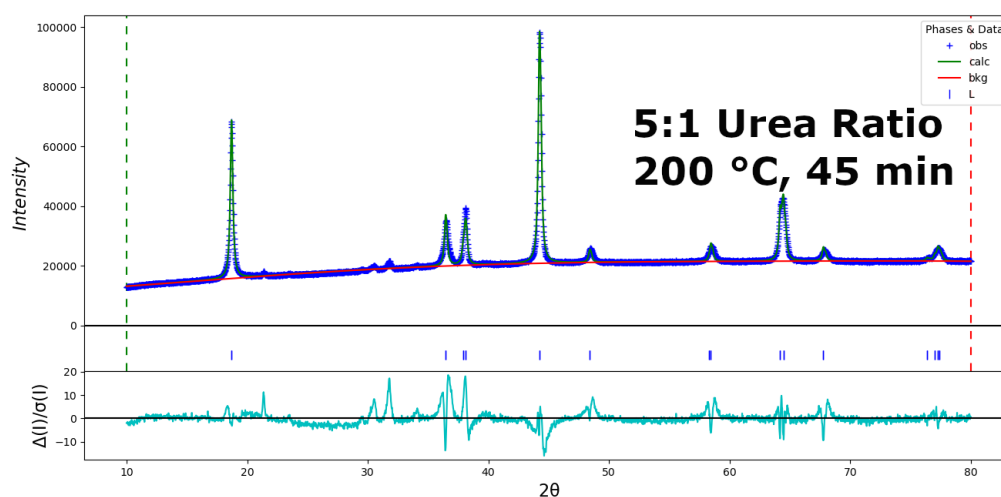
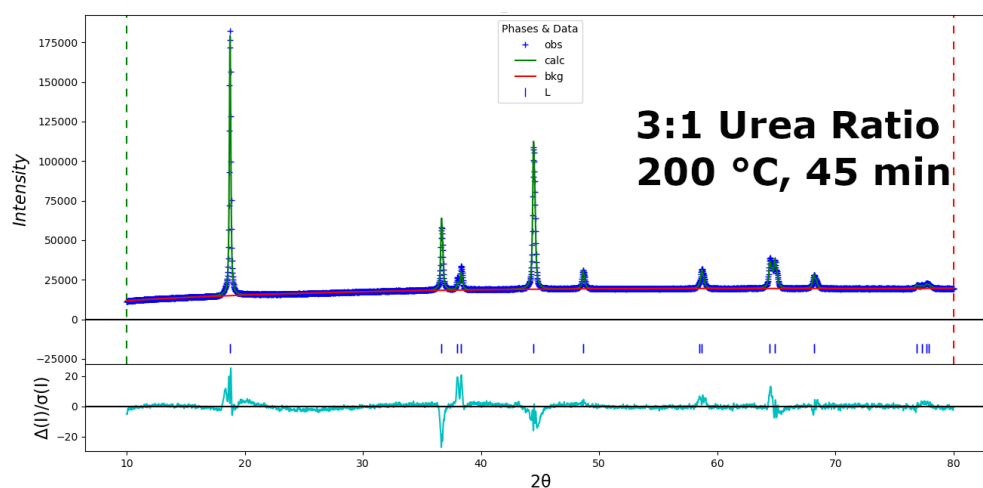
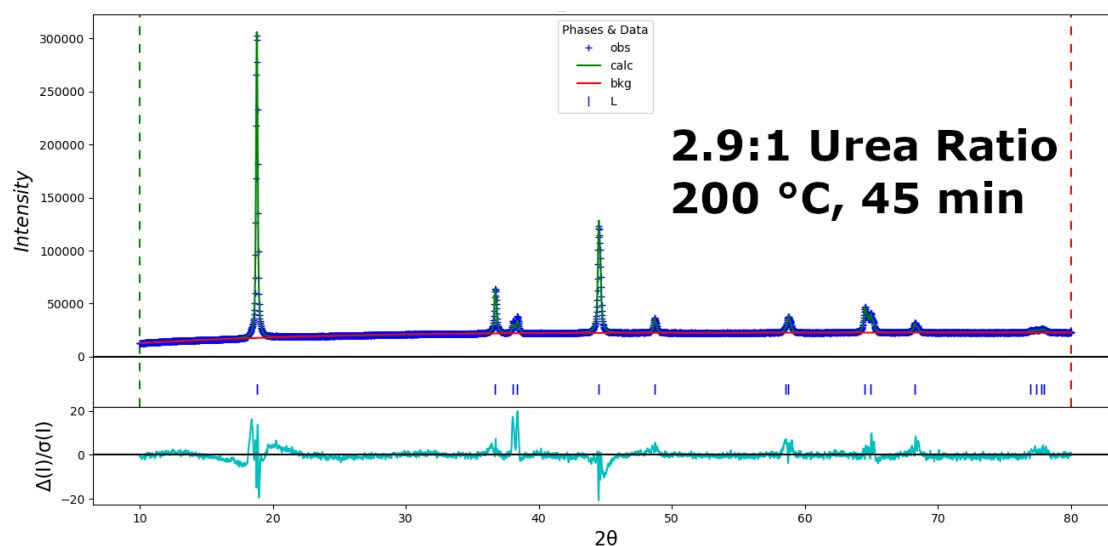


**Appendix A.14:** The Rietveld refinement fittings for the  $\text{LiNi}_{0.8}\text{Mn}_{0.1}\text{Co}_{0.1}\text{O}_2$  samples represented in **Table 3.0.3:** Key values from the Rietveld refinement of  $\text{LiNi}_{0.8}\text{Mn}_{0.1}\text{Co}_{0.1}\text{O}_2$  calcined at  $850\text{ }^\circ\text{C}$  with  $\text{LiOH}$  or  $\text{Li}_2\text{O}_2$  in a microwave-assisted furnace for 3 hours; or an oxygen-fed tube furnace for 10 hours. Table 5.0.2, refined in GSAS-II software, with the sample descriptions included for each plot.

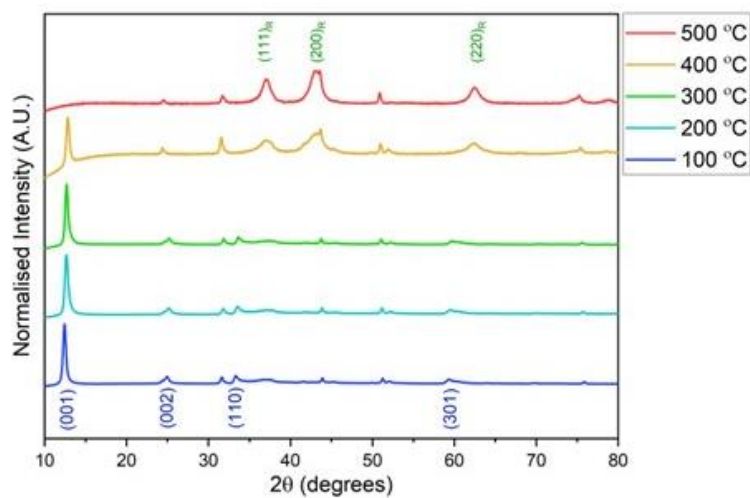


**Appendix A.15:** The Rietveld refinement fittings for the  $\text{LiNi}_{0.8}\text{Mn}_{0.1}\text{Co}_{0.1}\text{O}_2$  samples represented in **Table 3.0.3:** Key values from the Rietveld refinement of  $\text{LiNi}_{0.8}\text{Mn}_{0.1}\text{Co}_{0.1}\text{O}_2$  calcined at  $850\text{ }^\circ\text{C}$  with  $\text{LiOH}$  or  $\text{Li}_2\text{O}_2$  in a microwave-assisted furnace for 3 hours; or an oxygen-fed tube furnace for 10 hours. Table 5.0.3, refined in GSAS-II software, with the sample descriptions included for each plot.

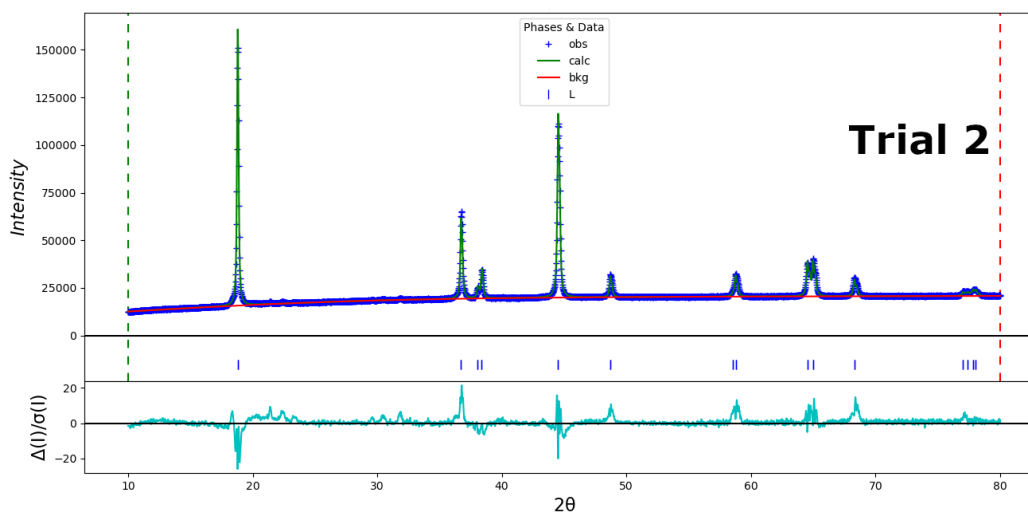
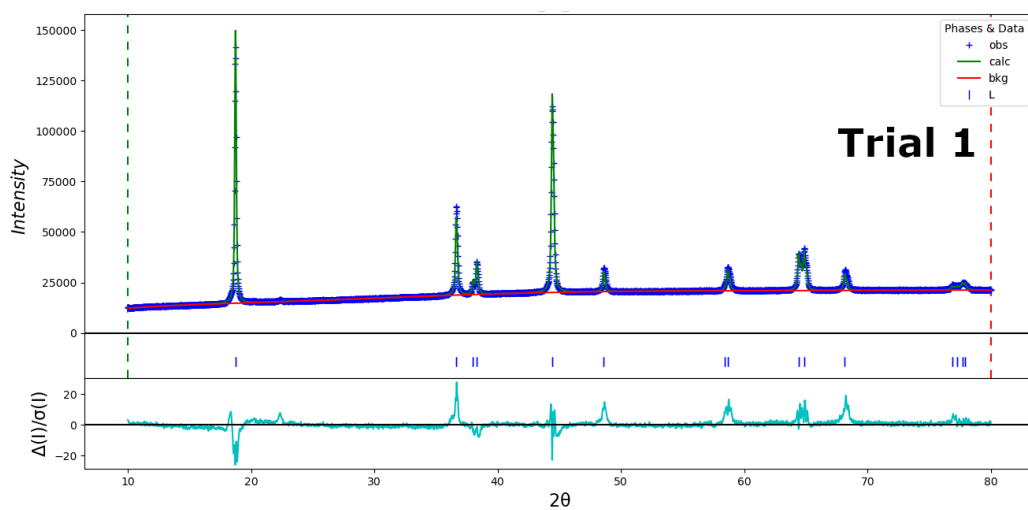


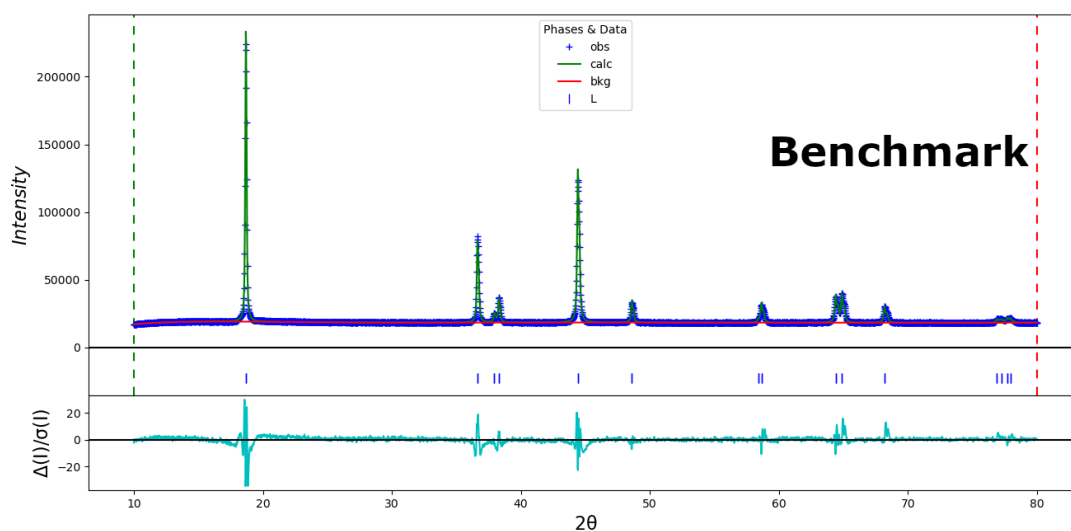
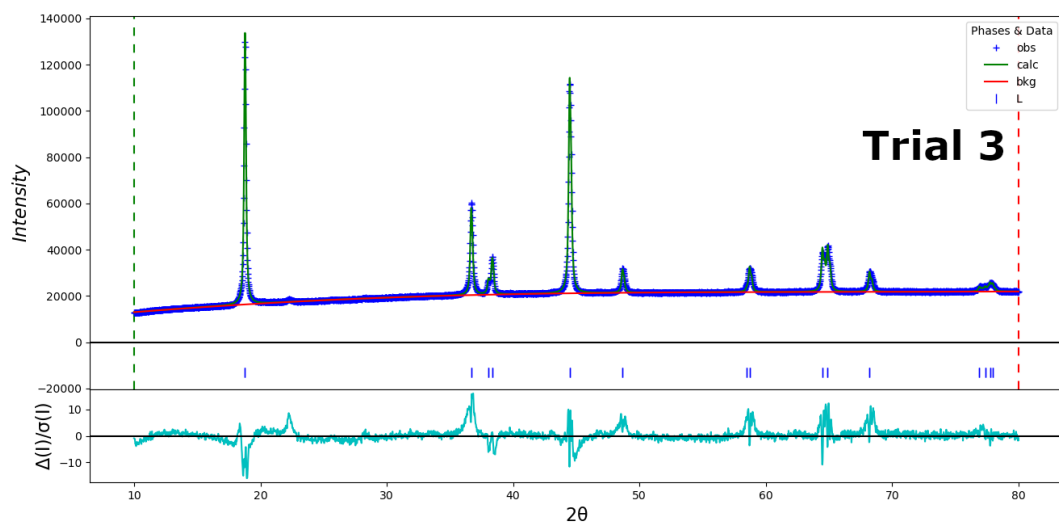


**Appendix A.16:** The Rietveld refinement fittings for the  $\text{LiNi}_{0.8}\text{Mn}_{0.1}\text{Co}_{0.1}\text{O}_2$  samples represented in **Table 3.0.3:** Key values from the Rietveld refinement of  $\text{LiNi}_{0.8}\text{Mn}_{0.1}\text{Co}_{0.1}\text{O}_2$  calcined at  $850\text{ }^\circ\text{C}$  with  $\text{LiOH}$  or  $\text{Li}_2\text{O}_2$  in a microwave-assisted furnace for 3 hours; or an oxygen-fed tube furnace for 10 hours. Table 5.0.4, refined in GSAS-II software, with the sample descriptions included for each plot.



**Appendix A.17:** High temperature XRD of  $\alpha\text{-Ni}_{0.8}\text{Mn}_{0.1}\text{Co}_{0.1}(\text{OH})_2$  heated with LiOH. Bragg peaks are included for each phase (blue,  $\alpha\text{-M}(\text{OH})_2$ ; green,  $\text{MO}$ ), and the  $\text{Li}_2\text{CO}_3$  impurity (green square).





**Appendix A.18:** The Rietveld refinement fittings for the  $\text{LiNi}_{0.8}\text{Mn}_{0.1}\text{Co}_{0.1}\text{O}_2$  samples represented in Table 6.1 **Table 3.0.3:** Key values from the Rietveld refinement of  $\text{LiNi}_{0.8}\text{Mn}_{0.1}\text{Co}_{0.1}\text{O}_2$  calcined at 850 °C with LiOH or  $\text{Li}_2\text{O}_2$  in a microwave-assisted furnace for 3 hours; or an oxygen-fed tube furnace for 10 hours., refined in GSAS-II software, with the sample descriptions included for each plot.

## References

- [1] International Energy Agency, "World Energy Outlook 2022." [Online]. Available: [www.iea.org/t&c/](http://www.iea.org/t&c/)
- [2] Vattenfall, "Vattenfall."
- [3] Anesco, "Anesco TM."
- [4] A. J. Hutchinson and D. T. Gladwin, "Techno-economic assessment of novel hybrid energy storage control strategies for Dynamic Frequency Response," *J Energy Storage*, vol. 55, p. 105694, Nov. 2022, doi: 10.1016/J.EST.2022.105694.
- [5] Deloitte, "Unplugged: Electric vehicle realities versus consumer expectations," p. 32, 2011.
- [6] I. Beyers, A. Bensmann, and R. Hanke-Rauschenbach, "Ragone plots revisited: A review of methodology and application across energy storage technologies," *J Energy Storage*, vol. 73, p. 109097, Dec. 2023, doi: 10.1016/J.EST.2023.109097.
- [7] S. Ahmed, P. A. Nelson, K. G. Gallagher, N. Susarla, and D. W. Dees, "Cost and energy demand of producing nickel manganese cobalt cathode material for lithium ion batteries," *J Power Sources*, vol. 342, pp. 733–740, Feb. 2017, doi: 10.1016/J.JPOWSOUR.2016.12.069.
- [8] P. J. W. and J. B. G. K. Mizushima, P.C. Jones, "Li<sub>x</sub>CoO<sub>2</sub> (0 < x < 1): A NEW CATHODE MATERIAL FOR BATTERIES OF HIGH ENERGY DENSITY," *Material Research Bulletin*, vol. 15, pp. 783–789, 1980.
- [9] M. Bianchini, M. Roca-Ayats, P. Hartmann, T. Brezesinski, and J. Janek, "There and Back Again—The Journey of LiNiO<sub>2</sub> as a Cathode Active Material," *Angewandte Chemie - International Edition*, vol. 58, no. 31, pp. 10434–10458, 2019, doi: 10.1002/anie.201812472.
- [10] K. M. Abraham, "Prospects and limits of energy storage in batteries," *Journal of Physical Chemistry Letters*, vol. 6, no. 5, pp. 830–844, 2015, doi: 10.1021/jz5026273.
- [11] X. Wang, Y. L. Ding, Y. P. Deng, and Z. Chen, "Ni-Rich/Co-Poor Layered Cathode for Automotive Li-Ion Batteries: Promises and Challenges," *Adv Energy Mater*, vol. 10, no. 12, Mar. 2020, doi: 10.1002/AENM.201903864.
- [12] W. Li, E. M. Erickson, and A. Manthiram, "High-nickel layered oxide cathodes for lithium-based automotive batteries," *Nat. Energy*, vol. 5, no. 1, p. 26, Jan. 2020, doi: 10.1038/s41560-019-0513-0.
- [13] D. Becker, R. Haberkorn, and G. Kickelbick, "Reactive Milling Induced Structure Changes in Phenylphosphonic Acid Functionalized LiMn<sub>2</sub>O<sub>4</sub> Nanocrystals – Synthesis, Rietveld Refinement, and Thermal Stability," *Eur J Inorg Chem*, vol. 2019, no. 45, pp. 4835–4845, Dec. 2019, doi: 10.1002/EJIC.201900946.
- [14] K. Momma and F. Izumi, "VESTA 3 for three-dimensional visualisation of crystal, volumetric and morphology data." pp. 1272–1276, 2011.
- [15] J. Asenbauer, T. Eisenmann, M. Kuenzel, A. Kazzazi, Z. Chen, and D. Bresser, "The success story of graphite as a lithium-ion anode material – fundamentals, remaining challenges, and

- recent developments including silicon (oxide) composites," *Sustain Energy Fuels*, vol. 4, no. 11, pp. 5387–5416, Oct. 2020, doi: 10.1039/D0SE00175A.
- [16] M. Winter, J. O. Besenhard, M. E. Spahr, and P. Novák, "Insertion Electrode Materials for Rechargeable Lithium Batteries\*\*," *Advanced Materials*, vol. 10, no. 10, pp. 725–763, 1998, doi: 10.1002/(SICI)1521-4095(199807)10:10.
- [17] A. Bhandari, C. Peng, J. Dziejczak, J. R. Owen, D. Kramer, and C. K. Skylaris, "Li nucleation on the graphite anode under potential control in Li-ion batteries," *J Mater Chem A Mater*, vol. 10, no. 21, pp. 11426–11436, May 2022, doi: 10.1039/D2TA02420A.
- [18] B. Rowden and N. Garcia-Araez, "Estimating lithium-ion battery behavior from half-cell data," *Energy Reports*, vol. 7, pp. 97–103, 2021, doi: 10.1016/j.egy.2021.02.048.
- [19] B. Son, M. H. Ryou, J. Choi, S. H. Kim, J. M. Ko, and Y. M. Lee, "Effect of cathode/anode area ratio on electrochemical performance of lithium-ion batteries," *J Power Sources*, vol. 243, pp. 641–647, Dec. 2013, doi: 10.1016/J.JPOWSOUR.2013.06.062.
- [20] S. Krueger, R. Kloepsch, J. Li, S. Nowak, S. Passerini, and M. Winter, "How Do Reactions at the Anode/Electrolyte Interface Determine the Cathode Performance in Lithium-Ion Batteries?," *J Electrochem Soc*, vol. 160, no. 4, pp. A542–A548, Jan. 2013, doi: 10.1149/2.022304JES/XML.
- [21] K. Long *et al.*, "High interfacial capacitance enabled stable lithium metal anode for practical lithium metal pouch cells," *Energy Storage Mater*, vol. 58, pp. 142–154, Apr. 2023, doi: 10.1016/J.ENSM.2023.02.039.
- [22] J. Hu, B. Wu, S. Chae, J. Lochala, Y. Bi, and J. Xiao, "Achieving highly reproducible results in graphite-based Li-ion full coin cells," *Joule*, vol. 5, no. 5, pp. 1011–1015, May 2021, doi: 10.1016/J.JOULE.2021.03.016.
- [23] J.-G. Zhang *et al.*, "Silicon-Based Anodes for Li-Ion Batteries," *Encyclopedia of Sustainability Science and Technology*, pp. 9293–9316, 2012, doi: 10.1007/978-1-4419-0851-3\_496.
- [24] H. Flåten Andersen *et al.*, "Silicon-carbon composite anodes from industrial battery grade silicon", doi: 10.1038/s41598-019-51324-4.
- [25] K. H. Kim, J. Shon, H. Jeong, H. Park, S. J. Lim, and J. S. Heo, "Improving the cyclability of silicon anodes for lithium-ion batteries using a simple pre-lithiation method," *J Power Sources*, vol. 459, p. 228066, May 2020, doi: 10.1016/J.JPOWSOUR.2020.228066.
- [26] H. M. Woolley and N. M. Vargas-Barbosa, "Hybrid solid electrolyte-liquid electrolyte systems for (almost) solid-state batteries: Why, how, and where to?," *J Mater Chem A Mater*, 2022, doi: 10.1039/D2TA02179J.
- [27] H. J. Lee *et al.*, "Li-ion conductivity in Li<sub>2</sub>OHCl<sub>1-x</sub>Br<sub>x</sub> solid electrolytes: grains, grain boundaries and interfaces," *J Mater Chem A Mater*, vol. 10, no. 21, pp. 11574–11586, Apr. 2022, doi: 10.1039/D2TA01462A.
- [28] S. S. Zhang, "Design aspects of electrolytes for fast charge of Li-ion batteries," *InfoMat*, vol. 3, no. 1, pp. 125–130, Jan. 2021, doi: 10.1002/INF2.12159.
- [29] A. Manthiram, "An Outlook on Lithium Ion Battery Technology," *ACS Cent Sci*, vol. 3, no. 10, pp. 1063–1069, Oct. 2017, doi: 10.1021/ACSCENTSCI.7B00288/ASSET/IMAGES/LARGE/OC-2017-002885\_0004.JPEG.

- [30] C. M. Julien, A. Mauger, K. Zaghib, and H. Groult, "Comparative Issues of Cathode Materials for Li-Ion Batteries," *Inorganics* 2014, Vol. 2, Pages 132-154, vol. 2, no. 1, pp. 132–154, Mar. 2014, doi: 10.3390/INORGANICS2010132.
- [31] A. Manthiram, A. Vadivel Murugan, A. Sarkar, and T. Muraliganth, "Nanostructured electrode materials for electrochemical energy storage and conversion," *Energy Environ Sci*, vol. 1, no. 6, pp. 621–638, Dec. 2008, doi: 10.1039/B811802G.
- [32] W. Kong *et al.*, "Tailoring Co3d and O2p Band Centers to Inhibit Oxygen Escape for Stable 4.6 V LiCoO<sub>2</sub> Cathodes," *Angewandte Chemie International Edition*, vol. 60, no. 52, pp. 27102–27112, Dec. 2021, doi: 10.1002/ANIE.202112508.
- [33] R. Jung, M. Metzger, F. Maglia, C. Stinner, and H. A. Gasteiger, "Oxygen Release and Its Effect on the Cycling Stability of LiNi<sub>x</sub>Mn<sub>y</sub>Co<sub>z</sub>O<sub>2</sub> (NMC) Cathode Materials for Li-Ion Batteries," *J Electrochem Soc*, vol. 164, no. 7, pp. A1361–A1377, 2017, doi: 10.1149/2.0021707jes.
- [34] Y. N. Zhou *et al.*, "Tuning charge-discharge induced unit cell breathing in layer-structured cathode materials for lithium-ion batteries," *Nat Commun*, vol. 5, pp. 1–8, 2014, doi: 10.1038/ncomms6381.
- [35] S. Watanabe, M. Kinoshita, T. Hosokawa, K. Morigaki, and K. Nakura, "Capacity fade of LiAl<sub>y</sub>Ni<sub>1-x-y</sub>CoxO<sub>2</sub> cathode for lithium-ion batteries during accelerated calendar and cycle life tests (surface analysis of LiAl<sub>y</sub>Ni<sub>1-x-y</sub>CoxO<sub>2</sub> cathode after cycle tests in restricted depth of discharge ranges)," *J Power Sources*, vol. 258, pp. 210–217, Jul. 2014, doi: 10.1016/J.JPOWSOUR.2014.02.018.
- [36] J. Li, J. Harlow, N. Stakheiko, N. Zhang, J. Paulsen, and J. Dahn, "Dependence of Cell Failure on Cut-Off Voltage Ranges and Observation of Kinetic Hindrance in LiNi<sub>0.8</sub>Co<sub>0.15</sub>Al<sub>0.05</sub>O<sub>2</sub>," *J Electrochem Soc*, vol. 165, no. 11, pp. A2682–A2695, Aug. 2018, doi: 10.1149/2.0491811JES/XML.
- [37] H. J. Noh, S. Youn, C. S. Yoon, and Y. K. Sun, "Comparison of the structural and electrochemical properties of layered Li[Ni<sub>x</sub>Co<sub>y</sub>Mn<sub>z</sub>]O<sub>2</sub> (x = 1/3, 0.5, 0.6, 0.7, 0.8 and 0.85) cathode material for lithium-ion batteries," *J Power Sources*, vol. 233, pp. 121–130, 2013, doi: 10.1016/j.jpowsour.2013.01.063.
- [38] J. E. Harlow *et al.*, "A Wide Range of Testing Results on an Excellent Lithium-Ion Cell Chemistry to be used as Benchmarks for New Battery Technologies," *J Electrochem Soc*, vol. 166, no. 13, pp. A3031–A3044, 2019, doi: 10.1149/2.0981913jes.
- [39] N. Ikeda, I. Konuma, H. B. Rajendra, T. Aida, and N. Yabuuchi, "Why is the O<sub>3</sub> to O<sub>1</sub> phase transition hindered in LiNiO<sub>2</sub> on full delithiation?," *J Mater Chem A Mater*, vol. 9, no. 29, pp. 15963–15967, Aug. 2021, doi: 10.1039/D1TA03066C.
- [40] Z. Ruff *et al.*, "O<sub>3</sub> to O<sub>1</sub> Phase Transitions in Highly Delithiated NMC811 at Elevated Temperatures," *Chemistry of Materials*, Jun. 2023, doi: 10.1021/ACS.CHEMMATER.3C00307.
- [41] S. Wang *et al.*, "Enabling stable and high-rate cycling of a Ni-rich layered oxide cathode for lithium-ion batteries by modification with an artificial Li<sup>+</sup>-conducting cathode-electrolyte interphase," *J Mater Chem A Mater*, vol. 9, no. 19, pp. 11623–11631, May 2021, doi: 10.1039/D1TA02563E.

- [42] J. Li *et al.*, "Correlated biphasic features of improved rate capability upon Ga doping in  $\text{LiNi}_0.6\text{Mn}_0.2\text{Co}_0.2\text{O}_2$ ," *J Mater Chem A Mater*, vol. 9, no. 41, pp. 23323–23334, Nov. 2021, doi: 10.1039/D1TA05676J.
- [43] D. Zhuang and M. Z. Bazant, "Theory of Layered-Oxide Cathode Degradation in Li-ion Batteries by Oxidation-Induced Cation Disorder," *J Electrochem Soc*, vol. 169, no. 10, p. 100536, Oct. 2022, doi: 10.1149/1945-7111/AC9A09.
- [44] H. L. Guo, H. F. Lin, Y. C. Yang, C. H. Cheng, Y. R. Tsai, and F. M. Wang, "Modification of  $\text{LiCoO}_2$  through rough coating with lithium lanthanum zirconium tantalum oxide for high-voltage performance in lithium ion batteries," *Journal of Solid State Electrochemistry*, vol. 25, no. 1, pp. 105–115, 2021, doi: 10.1007/s10008-020-04529-x.
- [45] X. Ren *et al.*, "Designing Advanced In Situ Electrode/Electrolyte Interphases for Wide Temperature Operation of 4.5 V  $\text{Li}|\text{LiCoO}_2$  Batteries," *Advanced Materials*, vol. 32, no. 49, p. 2004898, Dec. 2020, doi: 10.1002/ADMA.202004898.
- [46] M. S. Whittingham, "Lithium batteries and cathode materials," *Chem Rev*, vol. 104, no. 10, pp. 4271–4301, 2004, doi: 10.1021/cr020731c.
- [47] M. D. Radin *et al.*, "Narrowing the Gap between Theoretical and Practical Capacities in Li-Ion Layered Oxide Cathode Materials," *Adv Energy Mater*, vol. 7, no. 20, pp. 1–33, 2017, doi: 10.1002/aenm.201602888.
- [48] M. Chen, "The Democratic Republic of Congo's Other Crisis," *The Nation*, 2019. [Online]. Available: <https://www.thenation.com/article/archive/congo-china-mining-electronics/>
- [49] L. Mu *et al.*, "Dopant Distribution in Co-Free High-Energy Layered Cathode Materials," *Chemistry of Materials*, vol. 31, no. 23, pp. 9769–9776, 2019, doi: 10.1021/acs.chemmater.9b03603.
- [50] L. Croguennec, C. Poullierie, and C. Delmas, "Structural characterization of new metastable  $\text{NiO}_2$  phases," *Solid State Ion*, vol. 135, no. 1–4, pp. 259–266, 2000, doi: 10.1016/S0167-2738(00)00441-0.
- [51] H. Arai, S. Okada, H. Ohtsuka, M. Ichimura, and J. Yamaki, "Characterization and cathode performance of  $\text{Li}_{1-x}\text{Ni}_{1+x}\text{O}_2$  prepared with the excess lithium method," *Solid State Ion*, vol. 80, no. 3–4, pp. 261–269, 1995, doi: 10.1016/0167-2738(95)00144-U.
- [52] C. S. Yoon, D. W. Jun, S. T. Myung, and Y. K. Sun, "Structural Stability of  $\text{LiNiO}_2$  Cycled above 4.2 v," *ACS Energy Lett*, vol. 2, no. 5, pp. 1150–1155, 2017, doi: 10.1021/acsenergylett.7b00304.
- [53] X. LIU, G. Xu, L. Yin, I. Hwang, M. Ouyang, and K. Amine, "The Role of Cobalt and Manganese for the Safety of Ni-Rich NMC Cathode," *ECS Meeting Abstracts*, vol. MA2021-01, no. 5, p. 304, May 2021, doi: 10.1149/MA2021-015304MTGABS.
- [54] H. Li, M. Cormier, N. Zhang, J. Inglis, J. Li, and J. R. Dahn, "Is Cobalt Needed in Ni-Rich Positive Electrode Materials for Lithium Ion Batteries?," *J Electrochem Soc*, vol. 166, no. 4, pp. A429–A439, 2019, doi: 10.1149/2.1381902jes.
- [55] T. Entwistle, E. Sanchez-Perez, G. J. Murray, N. Anthonisamy, and S. A. Cussen, "Co-precipitation synthesis of nickel-rich cathodes for Li-ion batteries," *Energy Reports*, vol. 8, pp. 67–73, Nov. 2022, doi: 10.1016/J.EGYR.2022.06.110.

- [56] J. Zheng, W. H. Kan, and A. Manthiram, "Role of Mn content on the electrochemical properties of Nickel-Rich layered  $\text{LiNi}_{0.8-x}\text{Co}_{0.1}\text{Mn}_{0.1+x}\text{O}_2$  ( $0.0 \leq x \leq 0.08$ ) cathodes for lithium-ion batteries," *ACS Appl Mater Interfaces*, vol. 7, no. 12, pp. 6926–6934, 2015, doi: 10.1021/acsami.5b00788.
- [57] W. Li, H. Y. Asl, Q. Xie, and A. Manthiram, "Collapse of  $\text{LiNi}_{1-x-y}\text{Co}_x\text{Mn}_y\text{O}_2$  Lattice at Deep Charge Irrespective of Nickel Content in Lithium-Ion Batteries," *J Am Chem Soc*, vol. 141, no. 13, pp. 5097–5101, 2019, doi: 10.1021/jacs.8b13798.
- [58] R. Robert, C. Villevieille, and P. Novák, "Enhancement of the high potential specific charge in layered electrode materials for lithium-ion batteries," *J Mater Chem A Mater*, vol. 2, no. 23, pp. 8589–8598, May 2014, doi: 10.1039/C3TA12643A.
- [59] K. Märker, P. J. Reeves, C. Xu, K. J. Griffith, and C. P. Grey, "Evolution of Structure and Lithium Dynamics in  $\text{LiNi}_{0.8}\text{Mn}_{0.1}\text{Co}_{0.1}\text{O}_2$  (NMC811) Cathodes during Electrochemical Cycling," *Chemistry of Materials*, vol. 31, no. 7, pp. 2545–2554, Apr. 2019, doi: 10.1021/ACS.CHEMMATER.9B00140/ASSET/IMAGES/LARGE/CM-2019-00140H\_0007.JPEG.
- [60] H. Li *et al.*, "New Insights into Lithium Hopping and Ordering in  $\text{LiNiO}_2$  Cathodes during Li (De)intercalation," *Chemistry of Materials*, vol. 33, no. 24, pp. 9546–9559, Dec. 2021, doi: 10.1021/ACS.CHEMMATER.1C02680/ASSET/IMAGES/LARGE/CM1C02680\_0012.JPEG.
- [61] C. Xu *et al.*, "Bulk fatigue induced by surface reconstruction in layered Ni-rich cathodes for Li-ion batteries," *Nature Materials* 2020 20:1, vol. 20, no. 1, pp. 84–92, Aug. 2020, doi: 10.1038/s41563-020-0767-8.
- [62] J. L. White, F. S. Gittleson, M. Homer, and F. El Gabaly, "Nickel and Cobalt Oxidation State Evolution at Ni-Rich NMC Cathode Surfaces during Treatment," *Journal of Physical Chemistry C*, vol. 124, no. 30, pp. 16508–16514, Jul. 2020, doi: 10.1021/ACS.JPCC.0C04794/ASSET/IMAGES/LARGE/JP0C04794\_0004.JPEG.
- [63] T. Liu *et al.*, "Rational design of mechanically robust Ni-rich cathode materials via concentration gradient strategy," *Nature Communications* 2021 12:1, vol. 12, no. 1, pp. 1–10, Oct. 2021, doi: 10.1038/s41467-021-26290-z.
- [64] J. Zahnow *et al.*, "Impedance Analysis of NCM Cathode Materials: Electronic and Ionic Partial Conductivities and the Influence of Microstructure," *Applied Energy Materials*, vol. 4, no. 2, pp. 1335–1345, Jan. 2021.
- [65] H. Li *et al.*, "Investigation of Structural and Electronic Changes Induced by Postsynthesis Thermal Treatment of  $\text{LiNiO}_2$ ," *Chemistry of Materials*, vol. 34, no. 18, pp. 8163–8177, Sep. 2022, doi: 10.1021/ACS.CHEMMATER.2C00995/ASSET/IMAGES/LARGE/CM2C00995\_0011.JPEG.
- [66] H. Gupta and R. K. Singh, "High-Voltage Nickel-Rich NMC Cathode Material with Ionic-Liquid-Based Polymer Electrolytes for Rechargeable Lithium-Metal Batteries," *ChemElectroChem*, vol. 7, no. 17, pp. 3597–3605, Sep. 2020, doi: 10.1002/CELC.202000608.
- [67] N. Zhang *et al.*, "Structural, Electrochemical, and Thermal Properties of Nickel-Rich  $\text{LiNi}_x\text{Mn}_y\text{Co}_z\text{O}_2$  Materials," *Chemistry of Materials*, vol. 30, no. 24, pp. 8852–8860, Dec. 2018, doi: 10.1021/ACS.CHEMMATER.8B03827/ASSET/IMAGES/LARGE/CM-2018-038277\_0010.JPEG.

- [68] A. Liu *et al.*, "Investigating the Effects of Magnesium Doping in Various Ni-Rich Positive Electrode Materials for Lithium Ion Batteries," *J Electrochem Soc*, vol. 166, no. 16, pp. A4025–A4033, 2019, doi: 10.1149/2.1101915jes.
- [69] H. Li, P. Zhou, F. Liu, H. Li, F. Cheng, and J. Chen, "Stabilizing nickel-rich layered oxide cathodes by magnesium doping for rechargeable lithium-ion batteries," *Chem Sci*, vol. 10, no. 5, pp. 1374–1379, 2019, doi: 10.1039/c8sc03385d.
- [70] H. H. Ryu, K. J. Park, D. R. Yoon, A. Aishova, C. S. Yoon, and Y. K. Sun, "Li[Ni<sub>0.9</sub>Co<sub>0.09</sub>W<sub>0.01</sub>]O<sub>2</sub>: A New Type of Layered Oxide Cathode with High Cycling Stability," *Adv Energy Mater*, vol. 9, no. 44, pp. 0–6, 2019, doi: 10.1002/aenm.201902698.
- [71] Y. Wei *et al.*, "Kinetics Tuning of Li-Ion Diffusion in Layered Li(NixMnyCoz)O<sub>2</sub>," *J Am Chem Soc*, vol. 137, no. 26, pp. 8364–8367, Jul. 2015, doi: 10.1021/JACS.5B04040/SUPPL\_FILE/JA5B04040\_SI\_001.PDF.
- [72] A. Van Der Ven and G. Ceder, "Lithium Diffusion in Layered Li<sub>x</sub>CoO<sub>2</sub>," *Electrochemical and Solid-State Letters*, vol. 3, no. 7, 2000.
- [73] K. Kang and G. Ceder, "Factors that affect Li mobility in layered lithium transition metal oxides," *Phys Rev B*, vol. 74, p. 094105, 2006, doi: 10.1103/PhysRevB.74.094105.
- [74] C. Xu *et al.*, "Operando visualization of kinetically induced lithium heterogeneities in single-particle layered Ni-rich cathodes," *Joule*, vol. 6, no. 11, pp. 2535–2546, Nov. 2022, doi: 10.1016/J.JOULE.2022.09.008.
- [75] A. J. Smith, J. C. Burns, X. Zhao, D. Xiong, and J. R. Dahn, "A High Precision Coulometry Study of the SEI Growth in Li/Graphite Cells," *J Electrochem Soc*, vol. 158, no. 5, p. A447, Mar. 2011, doi: 10.1149/1.3557892/XML.
- [76] E. W. C. Spotte-Smith *et al.*, "Toward a Mechanistic Model of Solid-Electrolyte Interphase Formation and Evolution in Lithium-Ion Batteries," *ACS Energy Lett*, vol. 7, no. 4, pp. 1446–1453, 2022, doi: 10.1021/acsenergylett.2c00517.
- [77] A. O. Kondrakov *et al.*, "Anisotropic Lattice Strain and Mechanical Degradation of High- and Low-Nickel NCM Cathode Materials for Li-Ion Batteries," *Journal of Physical Chemistry C*, vol. 121, no. 6, pp. 3286–3294, Feb. 2017, doi: 10.1021/ACS.JPCC.6B12885/ASSET/IMAGES/LARGE/JP-2016-12885A\_0006.JPEG.
- [78] R. Jung, M. Metzger, F. Maglia, C. Stinner, and H. A. Gasteiger, "Chemical versus electrochemical electrolyte oxidation on NMC111, NMC622, NMC811, LNMO, and conductive carbon," *Journal of Physical Chemistry Letters*, vol. 8, no. 19, pp. 4820–4825, 2017, doi: 10.1021/acs.jpcllett.7b01927.
- [79] S. Ma *et al.*, "Temperature effect and thermal impact in lithium-ion batteries: A review," *Progress in Natural Science: Materials International*, vol. 28, no. 6, pp. 653–666, Dec. 2018, doi: 10.1016/J.PNSC.2018.11.002.
- [80] S. J. An, J. Li, C. Daniel, D. Mohanty, S. Nagpure, and D. L. Wood, "The state of understanding of the lithium-ion-battery graphite solid electrolyte interphase (SEI) and its relationship to formation cycling," *Carbon N Y*, vol. 105, pp. 52–76, Aug. 2016, doi: 10.1016/J.CARBON.2016.04.008.

- [81] S. Y. Luchkin, S. A. Lipovskikh, N. S. Katorova, A. A. Savina, A. M. Abakumov, and K. J. Stevenson, "Solid-electrolyte interphase nucleation and growth on carbonaceous negative electrodes for Li-ion batteries visualized with in situ atomic force microscopy," *Scientific Reports* 2020 10:1, vol. 10, no. 1, pp. 1–10, May 2020, doi: 10.1038/s41598-020-65552-6.
- [82] M. Shang, X. Chen, and J. Niu, "Nickel-rich layered LiNi<sub>0.8</sub>Mn<sub>0.1</sub>Co<sub>0.1</sub>O<sub>2</sub> with dual gradients on both primary and secondary particles in lithium-ion batteries," *Cell Rep Phys Sci*, vol. 3, no. 2, p. 100767, Feb. 2022, doi: 10.1016/J.XCRP.2022.100767.
- [83] P. S. Grant *et al.*, "Roadmap on Li-ion battery manufacturing research," *Journal of Physics: Energy*, vol. 4, no. 4, p. 042006, Nov. 2022, doi: 10.1088/2515-7655/AC8E30.
- [84] D. Andre *et al.*, "Future generations of cathode materials: An automotive industry perspective," *J Mater Chem A Mater*, vol. 3, no. 13, pp. 6709–6732, 2015, doi: 10.1039/c5ta00361j.
- [85] S. T. Myung *et al.*, "Nickel-Rich Layered Cathode Materials for Automotive Lithium-Ion Batteries: Achievements and Perspectives," *ACS Energy Lett*, vol. 2, no. 1, pp. 196–223, Jan. 2017, doi: 10.1021/ACSENERGYLETT.6B00594/ASSET/IMAGES/LARGE/NZ-2016-00594B\_0017.JPEG.
- [86] C. S. Yoon, D. W. Jun, S. T. Myung, and Y. K. Sun, "Structural Stability of LiNiO<sub>2</sub> Cycled above 4.2 v," *ACS Energy Lett*, vol. 2, no. 5, pp. 1150–1155, May 2017, doi: 10.1021/ACSENERGYLETT.7B00304/ASSET/IMAGES/LARGE/NZ-2017-00304E\_0006.JPEG.
- [87] K.-J. Park *et al.*, "Improved Cycling Stability of Li[Ni<sub>0.90</sub>Co<sub>0.05</sub>Mn<sub>0.05</sub>]O<sub>2</sub> Through Microstructure Modification by Boron Doping for Li-Ion Batteries," *Adv Energy Mater*, vol. 8, no. 25, p. 1801202, Sep. 2018, doi: 10.1002/AENM.201801202.
- [88] H. H. Ryu, K. J. Park, C. S. Yoon, and Y. K. Sun, "Capacity fading of ni-rich li [ni x co y mn1-x-y] o2 (0.6 ≤ x ≤ 0.95) cathodes for high-energy-density lithium-ion batteries: bulk or surface degradation?," *Chemistry of materials*, vol. 30, no. 3, p. 1155, Feb. 2018, doi: 10.1021/acs.chemmater.7b05269.
- [89] T. Sasaki, V. Godbole, Y. Takeuchi, Y. Ukyo, and P. Novák, "Morphological and Structural Changes of Mg-Substituted Li(Ni,Co,Al)O<sub>2</sub> during Overcharge Reaction," *J Electrochem Soc*, vol. 158, no. 11, p. A1214, 2011, doi: 10.1149/2.025111jes.
- [90] B. Namkoong *et al.*, "High-Energy Ni-Rich Cathode Materials for Long-Range and Long-Life Electric Vehicles," *Adv Energy Mater*, vol. 12, no. 21, Jun. 2022, doi: 10.1002/AENM.202200615.
- [91] Q. Xie, W. Li, A. Dolocan, and A. Manthiram, "Insights into boron-based polyanion-tuned high-nickel cathodes for high-energy-density Lithium-Ion Batteries," *Chemistry of Materials*, 2019, doi: 10.1021/acs.chemmater.9b02916.
- [92] D. Becker *et al.*, "Surface Modification of Ni-Rich LiNi<sub>0.8</sub>Co<sub>0.1</sub>Mn<sub>0.1</sub>O<sub>2</sub> Cathode Material by Tungsten Oxide Coating for Improved Electrochemical Performance in Lithium-Ion Batteries," *ACS Appl Mater Interfaces*, vol. 11, no. 20, pp. 18404–18414, 2019, doi: 10.1021/acsami.9b02889.

- [93] F. Schipper *et al.*, “Stabilizing nickel-rich layered cathode materials by a high-charge cation doping strategy: Zirconium-doped  $\text{LiNi}_0.6\text{Co}_0.2\text{Mn}_0.2\text{O}_2$ ,” *J Mater Chem A Mater*, vol. 4, no. 41, pp. 16073–16084, 2016, doi: 10.1039/c6ta06740a.
- [94] S. J. An, J. Li, C. Daniel, D. Mohanty, S. Nagpure, and D. L. Wood, “The state of understanding of the lithium-ion-battery graphite solid electrolyte interphase (SEI) and its relationship to formation cycling,” *Carbon N Y*, vol. 105, pp. 52–76, 2016, doi: 10.1016/j.carbon.2016.04.008.
- [95] S. Hy, H. Liu, M. Zhang, D. Qian, B. J. Hwang, and Y. S. Meng, “Performance and design considerations for lithium excess layered oxide positive electrode materials for lithium ion batteries,” *Energy Environ Sci*, vol. 9, no. 6, pp. 1931–1954, 2016, doi: 10.1039/c5ee03573b.
- [96] Z. Chang, Y. Qiao, H. Deng, H. Yang, P. He, and H. Zhou, “A stable high-voltage lithium-ion battery realized by an in-built water scavenger,” *Energy Environ Sci*, vol. 13, no. 4, pp. 1197–1204, 2020, doi: 10.1039/d0ee00060d.
- [97] C. H. Jo, D. H. Cho, H. J. Noh, H. Yashiro, Y. K. Sun, and S. T. Myung, “An effective method to reduce residual lithium compounds on Ni-rich  $\text{Li}[\text{Ni}_0.6\text{Co}_0.2\text{Mn}_0.2]\text{O}_2$  active material using a phosphoric acid derived  $\text{Li}_3\text{PO}_4$  nanolayer,” *Nano Res*, vol. 8, no. 5, pp. 1464–1479, May 2015, doi: 10.1007/s12274-014-0631-8/METRICS.
- [98] P. Y. Hou, L. Q. Zhang, and X. P. Gao, “A high-energy, full concentration-gradient cathode material with excellent cycle and thermal stability for lithium ion batteries,” *J Mater Chem A Mater*, vol. 2, no. 40, pp. 17130–17138, Sep. 2014, doi: 10.1039/c4ta03158j.
- [99] K. Liu, Y. Liu, D. Lin, A. Pei, and Y. Cui, “Materials for lithium-ion battery safety,” *Sci Adv*, vol. 4, no. 6, 2018, doi: 10.1126/sciadv.aas9820.
- [100] M. Guilmard, L. Croguennec, D. Denux, and C. Delmas, “Thermal Stability of Lithium Nickel Oxide Derivatives. Part I:  $\text{Li}_x\text{Ni}_{1-0.2}\text{O}_2$  and  $\text{Li}_x\text{Ni}_{0.89}\text{Al}_{0.16}\text{O}_2$  ( $x = 0.50$  and  $0.30$ ),” *Chemistry of Materials*, vol. 15, no. 23, pp. 4476–4483, Nov. 2003, doi: 10.1021/cm030059f/ASSET/IMAGES/LARGE/cm030059ff00012.jpeg.
- [101] W. Li, S. Lee, and A. Manthiram, “High-Nickel NMA: A Cobalt-Free Alternative to NMC and NCA Cathodes for Lithium-Ion Batteries,” *Advanced Materials*, vol. 32, no. 33, pp. 1–6, 2020, doi: 10.1002/adma.202002718.
- [102] L. Wang, T. Maxisch, and G. Ceder, “A first-principles approach to studying the thermal stability of oxide cathode materials,” *Chemistry of Materials*, vol. 19, no. 3, pp. 543–552, 2007, doi: 10.1021/cm0620943.
- [103] A. C. Martinez *et al.*, “High reactivity of the nickel-rich  $\text{LiNi}_{1-x-y}\text{Mn}_x\text{Co}_y\text{O}_2$  layered materials surface towards  $\text{H}_2\text{O}/\text{CO}_2$  atmosphere and  $\text{LiPF}_6$ -based electrolyte,” *J Power Sources*, vol. 468, no. April, pp. 1–10, 2020, doi: 10.1016/j.jpowsour.2020.228204.
- [104] H. Beyer, S. Meini, N. Tsiouvaras, M. Piana, and H. A. Gasteiger, “Thermal and electrochemical decomposition of lithium peroxide in non-catalyzed carbon cathodes for Li–air batteries,” *Phys. Chem. Chem. Phys*, vol. 15, p. 11025, 2013, doi: 10.1039/c3cp51056e.
- [105] U. H. Kim, E. J. Lee, C. S. Yoon, S. T. Myung, and Y. K. Sun, “Compositionally Graded Cathode Material with Long-Term Cycling Stability for Electric Vehicles Application,” *Adv Energy Mater*, vol. 6, no. 22, pp. 1–8, 2016, doi: 10.1002/aenm.201601417.

- [106] G. Shang *et al.*, “Enhancing structural stability unto 4.5 V of Ni-rich cathodes by tungsten-doping for lithium storage,” *J Power Sources*, vol. 423, no. January, pp. 246–254, 2019, doi: 10.1016/j.jpowsour.2019.03.072.
- [107] H. H. Ryu, G. T. Park, C. S. Yoon, and Y. K. Sun, “Suppressing detrimental phase transitions via tungsten doping of LiNiO<sub>2</sub> cathode for next-generation lithium-ion batteries,” *J Mater Chem A Mater*, vol. 7, no. 31, pp. 18580–18588, 2019, doi: 10.1039/c9ta06402h.
- [108] M. Eilers-Rethwisch *et al.*, “Comparative study of Sn-doped Li[Ni<sub>0.6</sub>Mn<sub>0.2</sub>Co<sub>0.2-x</sub>Sn<sub>x</sub>]O<sub>2</sub> cathode active materials (x = 0–0.5) for lithium ion batteries regarding electrochemical performance and structural stability,” *J Power Sources*, vol. 397, no. June, pp. 68–78, 2018, doi: 10.1016/j.jpowsour.2018.06.072.
- [109] T. Weigel, F. Schipper, E. M. Erickson, F. A. Susai, B. Markovsky, and D. Aurbach, “Structural and Electrochemical Aspects of LiNi<sub>0.8</sub>Co<sub>0.1</sub>Mn<sub>0.1</sub>O<sub>2</sub> Cathode Materials Doped by Various Cations,” *ACS Energy Lett*, vol. 4, no. 2, pp. 508–516, Feb. 2019, doi: 10.1021/ACSENERGYLETT.8B02302/ASSET/IMAGES/LARGE/NZ-2018-02302T\_0004.JPEG.
- [110] Metalary, “Metalary.” Accessed: Aug. 22, 2022. [Online]. Available: <https://www.metalary.com/>
- [111] X. Tan, M. Zhang, J. Li, D. Zhang, Y. Yan, and Z. Li, “Recent progress in coatings and methods of Ni-rich LiNi<sub>0.8</sub>Co<sub>0.1</sub>Mn<sub>0.1</sub>O<sub>2</sub> cathode materials: A short review,” *Ceram Int*, vol. 46, no. 14, pp. 21888–21901, 2020, doi: 10.1016/j.ceramint.2020.06.091.
- [112] W. Yan, S. Yang, Y. Huang, Y. Yang, and Guohui Yuan, “A review on doping/coating of nickel-rich cathode materials for lithium-ion batteries,” *J Alloys Compd*, vol. 819, p. 153048, 2020, doi: 10.1016/j.jallcom.2019.153048.
- [113] Y. Shi, M. Zhang, D. Qian, and Y. S. Meng, “Ultrathin Al<sub>2</sub>O<sub>3</sub> Coatings for Improved Cycling Performance and Thermal Stability of LiNi<sub>0.5</sub>Co<sub>0.2</sub>Mn<sub>0.3</sub>O<sub>2</sub> Cathode Material,” *Electrochim Acta*, vol. 203, pp. 154–161, 2016, doi: 10.1016/j.electacta.2016.03.185.
- [114] X. Xu *et al.*, “Progressive concentration gradient nickel-rich oxide cathode material for high-energy and long-life lithium-ion batteries,” *J Mater Chem A Mater*, vol. 7, no. 13, pp. 7728–7735, 2019, doi: 10.1039/C9TA00224C.
- [115] Y. K. Sun, S. T. Myung, H. S. Shin, Y. C. Bae, and C. S. Yoon, “Novel core - Shell-structured Li[(Ni<sub>0.8</sub>Co<sub>0.2</sub>)<sub>0.8</sub>(Ni<sub>0.5</sub>Mn<sub>0.5</sub>)<sub>0.2</sub>]O<sub>2</sub> via coprecipitation as positive electrode material for lithium secondary batteries,” *Journal of Physical Chemistry B*, vol. 110, no. 13, pp. 6810–6815, May 2006, doi: 10.1021/JP0571473/ASSET/IMAGES/LARGE/JP0571473F00011.JPEG.
- [116] P. Hou, H. Zhang, Z. Zi, L. Zhang, and X. Xu, “Core-shell and concentration-gradient cathodes prepared via co-precipitation reaction for advanced lithium-ion batteries,” *J Mater Chem A Mater*, vol. 5, no. 9, pp. 4254–4279, Feb. 2017, doi: 10.1039/C6TA10297B.
- [117] Y. Zhang, H. Cao, J. Zhang, and B. Xia, “Synthesis of LiNi<sub>0.6</sub>Co<sub>0.2</sub>Mn<sub>0.2</sub>O<sub>2</sub> cathode material by a carbonate co-precipitation method and its electrochemical characterization,” *Solid State Ion*, vol. 177, no. 37–38, pp. 3303–3307, Dec. 2006, doi: 10.1016/J.SSI.2006.09.008.
- [118] D. L. Vu and J. won Lee, “Properties of LiNi<sub>0.8</sub>Co<sub>0.1</sub>Mn<sub>0.1</sub>O<sub>2</sub> as a high energy cathode material for lithium-ion batteries,” *Korean Journal of Chemical Engineering*, vol. 33, no. 2, pp. 514–526, 2016, doi: 10.1007/s11814-015-0154-3.

- [119] D. S. Hall, D. J. Lockwood, C. Bock, and B. R. MacDougall, "Nickel hydroxides and related materials: A review of their structures, synthesis and properties," *Proceedings of the Royal Society A: Mathematical, Physical and Engineering Sciences*, vol. 471, no. 2174, 2015, doi: 10.1098/rspa.2014.0792.
- [120] K. Lawson, S. P. Wallbridge, A. E. Catling, C. A. Kirk, and S. E. Dann, "Determination of layered nickel hydroxide phases in materials disordered by stacking faults and interstratification," *J Mater Chem A Mater*, Dec. 2022, doi: 10.1039/D2TA07655A.
- [121] X. Zhao, F. Zhou, J. R. Dahn, and in Ni, "Phases Formed in Al-Doped Ni<sub>1/3</sub>Mn<sub>1/3</sub>Co<sub>1/3</sub>(OH)<sub>2</sub> Prepared by Coprecipitation: Formation of Layered Double Hydroxide," *J Electrochem Soc*, vol. 155, no. 9, p. A642, Jul. 2008, doi: 10.1149/1.2949405.
- [122] S. Bette, B. Hinrichsen, D. Pfister, and E. Dinnebier, Robert, "A routine for the determination of the microstructure of stacking-faulted nickel cobalt aluminium hydroxide precursors for lithium nickel cobalt aluminium oxide battery materials Microstructure determination for NCA precursors," *J Appl Crystallogr*, vol. 53, pp. 76–87, 2020, doi: <https://doi.org/10.1107/S1600576719016212>.
- [123] C. Tessier, P. H. Haumesser, P. Bernard, and C. Delmas, "The Structure of Ni(OH)<sub>2</sub>: From the Ideal Material to the Electrochemically Active One," *J Electrochem Soc*, vol. 146, no. 6, p. 2059, 1999.
- [124] C. Didier, W. K. Pang, Z. Guo, S. Schmid, and V. K. Peterson, "Phase Evolution and Intermittent Disorder in Electrochemically Lithiated Graphite Determined Using in Operando Neutron Diffraction," *Chemistry of Materials*, vol. 32, no. 6, pp. 2518–2531, Mar. 2020, doi: 10.1021/ACS.CHEMMATER.9B05145/SUPPL\_FILE/CM9B05145\_SI\_001.PDF.
- [125] Y. Wang, D. Cao, G. Wang, S. Wang, J. Wen, and J. Yin, "Spherical clusters of β-Ni(OH)<sub>2</sub> nanosheets supported on nickel foam for nickel metal hydride battery," *Electrochim Acta*, vol. 56, no. 24, pp. 8285–8290, Oct. 2011, doi: 10.1016/J.ELECTACTA.2011.06.098.
- [126] D. Wang *et al.*, "Morphology-controlled synthesis of hierarchical mesoporous α-Ni(OH)<sub>2</sub> microspheres for high-performance asymmetric supercapacitors," *J Alloys Compd*, vol. 737, pp. 238–247, Mar. 2018, doi: 10.1016/J.JALLCOM.2017.12.095.
- [127] H. Chen, J. M. Wang, T. Pan, Y. L. Zhao, J. Q. Zhang, and C. N. Cao, "The structure and electrochemical performance of spherical Al-substituted α-Ni(OH)<sub>2</sub> for alkaline rechargeable batteries," *J Power Sources*, vol. 143, no. 1–2, pp. 243–255, Apr. 2005, doi: 10.1016/J.JPOWSOUR.2004.11.041.
- [128] J. R. Dahn and C. A. Michal, "Structure and electrochemistry of Li<sub>1±y</sub>NiO<sub>2</sub> and a new Li<sub>2</sub>NiO<sub>2</sub> phase with the Ni(OH)<sub>2</sub> structure," *Solid State Ion.*, vol. 44, pp. 87–97, 1990.
- [129] A. Rougier, P. Gravereau, and C. Delmas, "Optimization of the Composition of the Li<sub>1-z</sub>Ni<sub>1+z</sub>O<sub>2</sub> Electrode Materials: Structural, Magnetic, and Electrochemical Studies," *J Electrochem Soc*, vol. 143, no. 4, pp. 1168–1175, Apr. 1996, doi: 10.1149/1.1836614/XML.
- [130] C. Nithya, R. Thirunakaran, A. Sivashanmugam, G. V. M. Kiruthika, and S. Gopukumar, "High-capacity sol-gel synthesis of LiNi<sub>x</sub>Co<sub>y</sub>Mn<sub>1-x-y</sub>O<sub>2</sub> (0 ≤ x, y ≤ 0.5) cathode material for use in lithium rechargeable batteries," *Journal of Physical Chemistry C*, vol. 113, no. 41, pp. 17936–17944, 2009, doi: 10.1021/jp907036a.

- [131] W. Zhou *et al.*, "Perspective on the Preparation Methods of Single Crystalline High Nickel Oxide Cathode Materials," *Adv Energy Mater*, p. 2300378, Jul. 2023, doi: 10.1002/AENM.202300378.
- [132] J. Kim, H. Lee, H. Cha, M. Yoon, M. Park, and J. Cho, "Prospect and Reality of Ni-Rich Cathode for Commercialization," *Adv. Energy Mater.*, vol. 8, no. 6, p. 1702028, Feb. 2018, doi: 10.1002/aenm.201702028.
- [133] S. Shi *et al.*, "Full microwave synthesis of advanced Li-rich manganese based cathode material for lithium ion batteries," *J Power Sources*, vol. 337, pp. 82–91, 2017, doi: 10.1016/j.jpowsour.2016.10.107.
- [134] L. Mu *et al.*, "Dopant Distribution in Co-Free High-Energy Layered Cathode Materials," *Chemistry of Materials*, vol. 31, no. 23, pp. 9769–9776, Dec. 2019, doi: 10.1021/ACS.CHEMMATER.9B03603/ASSET/IMAGES/LARGE/CM9B03603\_0005.JPEG.
- [135] J. Xu, F. Lin, M. M. Doeff, and W. Tong, "A review of Ni-based layered oxides for rechargeable Li-ion batteries," *J Mater Chem A Mater*, vol. 5, no. 3, pp. 874–901, 2017, doi: 10.1039/C6TA07991A.
- [136] J. Zhu and G. Chen, "Single-crystal based studies for correlating the properties and high-voltage performance of Li[NixMnyCo1-x-y]O2 cathodes," *J Mater Chem A Mater*, vol. 7, no. 10, pp. 5463–5474, Mar. 2019, doi: 10.1039/C8TA10329A.
- [137] V. Pimenta *et al.*, "Synthesis of Li-Rich NMC: A Comprehensive Study," *Chemistry of Materials*, vol. 29, no. 23, pp. 9923–9936, 2017, doi: 10.1021/acs.chemmater.7b03230.
- [138] Ltd. Ningbo Ronbay New Energy Technology Co., "Initial public offering and listing on the Science and Technology Innovation Board - Prospectus," China International Trust Investment Corporation, 2019.
- [139] O. Capron, R. Gopalakrishnan, J. Jaguemont, P. Van Den Bossche, N. Omar, and J. Van Mierlo, "On the Ageing of High Energy Lithium-Ion Batteries—Comprehensive Electrochemical Diffusivity Studies of Harvested Nickel Manganese Cobalt Electrodes," *Materials 2018, Vol. 11, Page 176*, vol. 11, no. 2, p. 176, Jan. 2018, doi: 10.3390/MA11020176.
- [140] S. Aldrich, "Lithium nickel manganese cobalt oxide," 2020. [Online]. Available: <https://www.sigmaaldrich.com/catalog/product/aldrich/761001?lang=en&region=GB>
- [141] M. N. Obrovac, L. Zheng, and M. D. L. Garayt, "Engineered Particle Synthesis by Dry Particle Microgranulation," *Cell Rep Phys Sci*, vol. 1, no. 6, p. 100063, Jun. 2020, doi: 10.1016/J.XCRP.2020.100063.
- [142] C. Julien, A. Mauger, K. Zaghib, and H. Groult, "Optimization of layered cathode materials for lithium-ion batteries," *Materials*, vol. 9, no. 7, 2016, doi: 10.3390/MA9070595.
- [143] A. van Bommel and J. R. Dahn, "Synthesis of Spherical and Dense Particles of the Pure Hydroxide Phase Ni<sub>1/3</sub>Mn<sub>1/3</sub>Co<sub>1/3</sub>(OH)<sub>2</sub>," *J Electrochem Soc*, vol. 156, no. 5, p. A362, 2009, doi: 10.1149/1.3079366.
- [144] F. Zhou, X. Zhao, A. Van Bommel, A. W. Rowe, and J. R. Dahn, "Coprecipitation synthesis of NixMn<sub>1-x</sub>(OH)<sub>2</sub> Mixed Hydroxide," *Chemistry of Materials*, vol. 22, no. 3, pp. 1015–1021, Feb. 2010, doi: 10.1021/CM9018309/ASSET/IMAGES/LARGE/CM-2009-018309\_0001.JPEG.

- [145] N. T. K. Thanh, N. Maclean, and S. Mahiddine, "Mechanisms of nucleation and growth of nanoparticles in solution," *Chem Rev*, vol. 114, no. 15, pp. 7610–7630, 2014, doi: 10.1021/cr400544s.
- [146] H. Dong, A. Wang, G. Smart, D. Johnson, and G. M. Koenig, "In-situ analysis of nucleation and growth of transition metal oxalate battery precursor particles via time evolution of solution composition and particle size distribution," *Colloids Surf A Physicochem Eng Asp*, vol. 558, no. June, pp. 8–15, 2018, doi: 10.1016/j.colsurfa.2018.08.047.
- [147] J. R. Shimpi, D. S. Sidhaye, and B. L. V. Prasad, "Digestive Ripening: A Fine Chemical Machining Process on the Nanoscale," *Langmuir*, vol. 33, no. 38, pp. 9491–9507, Sep. 2017, doi: 10.1021/ACS.LANGMUIR.7B00193/ASSET/IMAGES/LARGE/LA-2017-00193U\_0021.JPEG.
- [148] A. Desiraju, Gautam R; Vittal, Jagadese J; Ramanan, *Crystal Engineering A Testbook*. Singapore: World Scientific Publishing Co. Pte. Ltd., 2011.
- [149] E. C. Vreeland *et al.*, "Enhanced Nanoparticle Size Control by Extending LaMer's Mechanism," *Chemistry of Materials*, vol. 27, no. 17, pp. 6059–6066, Sep. 2015, doi: 10.1021/ACS.CHEMMATER.5B02510/ASSET/IMAGES/LARGE/CM-2015-025108\_0002.JPEG.
- [150] Y. Shi, M. Zhang, C. Fang, and Y. S. Meng, "Urea-based hydrothermal synthesis of LiNi<sub>0.5</sub>Co<sub>0.2</sub>Mn<sub>0.3</sub>O<sub>2</sub> cathode material for Li-ion battery," *J Power Sources*, vol. 394, pp. 114–121, Aug. 2018, doi: 10.1016/J.JPOWSOUR.2018.05.030.
- [151] C. Delmas *et al.*, "An overview of the Li(Ni,M)O<sub>2</sub> systems: syntheses, structures and properties," *Electrochim Acta*, vol. 45, no. 1–2, pp. 243–253, Sep. 1999, doi: 10.1016/S0013-4686(99)00208-X.
- [152] W. Hua *et al.*, "Chemical and Structural Evolution during the Synthesis of Layered Li(Ni,Co,Mn)O<sub>2</sub> Oxides," *Chemistry of Materials*, vol. 32, no. 12, pp. 4984–4997, 2020, doi: 10.1021/acs.chemmater.9b05279.
- [153] P. Singh, M. Sunder, E. Campbell, and L. Palmer, "A Case Study of Nickel Dendritic Growth on Printed-Circuit Boards," *2020 Pan Pacific Microelectronics Symposium, Pan Pacific 2020*, Feb. 2020, doi: 10.23919/PANPACIFIC48324.2020.9059398.
- [154] A. Bordbar-Khiabani, S. Bahrampour, M. Mozafari, and M. Gasik, "Surface functionalization of anodized tantalum with Mn<sub>3</sub>O<sub>4</sub> nanoparticles for effective corrosion protection in simulated inflammatory condition," *Ceram Int*, vol. 48, no. 3, pp. 3148–3156, Feb. 2022, doi: 10.1016/J.CERAMINT.2021.10.088.
- [155] A. C. Fisher, *Electrode Dynamics*. Oxford University Press, 2009.
- [156] M. H. Lee, Y. J. Kang, S. T. Myung, and Y. K. Sun, "Synthetic optimization of Li[Ni<sub>1/3</sub>Co<sub>1/3</sub>Mn<sub>1/3</sub>]O<sub>2</sub> via co-precipitation," *Electrochim Acta*, vol. 50, no. 4, pp. 939–948, 2004, doi: 10.1016/j.electacta.2004.07.038.
- [157] A. Van Bommel and J. R. Dahn, "Analysis of the growth mechanism of coprecipitated spherical and dense nickel, manganese, and cobalt-containing hydroxides in the presence of aqueous ammonia," *Chemistry of Materials*, vol. 21, no. 8, pp. 1500–1503, Apr. 2009, doi: 10.1021/CM803144D/ASSET/IMAGES/CM-2008-03144D\_M005.GIF.

- [158] D. Wang *et al.*, "Synthesis of high capacity cathodes for lithium-ion batteries by morphology-tailored hydroxide co-precipitation," *J Power Sources*, vol. 274, pp. 451–457, 2015, doi: 10.1016/j.jpowsour.2014.10.016.
- [159] Z. Feng *et al.*, "In Situ Monitoring of the Growth of Nickel, Manganese, and Cobalt Hydroxide Precursors during Co-Precipitation Synthesis of Li-Ion Cathode Materials," *J Electrochem Soc*, vol. 165, no. 13, pp. 3077–3083, 2018, doi: 10.1149/2.0511813jes.
- [160] L. Liang *et al.*, "Co-precipitation synthesis of Ni<sub>0.6</sub>Co<sub>0.2</sub>Mn<sub>0.2</sub>(OH)<sub>2</sub> precursor and characterization of LiNi<sub>0.6</sub>Co<sub>0.2</sub>Mn<sub>0.2</sub>O<sub>2</sub> cathode material for secondary lithium batteries," *Electrochim Acta*, vol. 130, pp. 82–89, Jun. 2014, doi: 10.1016/J.ELECTACTA.2014.02.100.
- [161] D. Wang, I. Belharouak, G. M. Koenig, G. Zhou, and K. Amine, "Growth mechanism of Ni<sub>0.3</sub>Mn<sub>0.7</sub>CO<sub>3</sub> precursor for high capacity Li-ion battery cathodes," *J Mater Chem*, vol. 21, no. 25, pp. 9290–9295, Jun. 2011, doi: 10.1039/C1JM11077B.
- [162] K. K. Cheralathan *et al.*, "Preparation of spherical LiNi<sub>0.80</sub>Co<sub>0.15</sub>Mn<sub>0.05</sub>O<sub>2</sub> lithium-ion cathode material by continuous co-precipitation," *J Power Sources*, vol. 195, no. 5, pp. 1486–1494, Mar. 2010, doi: 10.1016/J.JPOWSOUR.2009.08.101.
- [163] Q. Zhu, H. Xiao, R. Zhang, S. Geng, and Q. Huang, "Effect of impeller type on preparing spherical and dense Ni<sub>1-x-y</sub>CoxMny(OH)<sub>2</sub> precursor via continuous co-precipitation in pilot scale: A case of Ni<sub>0.6</sub>Co<sub>0.2</sub>Mn<sub>0.2</sub>(OH)<sub>2</sub>," *Electrochim Acta*, vol. 318, pp. 1–13, 2019, doi: 10.1016/j.electacta.2019.06.008.
- [164] C. S. Yoon, H. H. Ryu, G. T. Park, J. H. Kim, K. H. Kim, and Y. K. Sun, "Extracting maximum capacity from Ni-rich Li[Ni<sub>0.95</sub>Co<sub>0.025</sub>Mn<sub>0.025</sub>]O<sub>2</sub> cathodes for high-energy-density lithium-ion batteries," *J Mater Chem A Mater*, vol. 6, no. 9, pp. 4126–4132, Feb. 2018, doi: 10.1039/C7TA11346C.
- [165] M. Eilers-Rethwisch, M. Winter, and F. M. Schappacher, "Synthesis, electrochemical investigation and structural analysis of doped Li[Ni<sub>0.6</sub>Mn<sub>0.2</sub>Co<sub>0.2-x</sub>Mx]O<sub>2</sub> (x = 0, 0.05; M = Al, Fe, Sn) cathode materials," *J Power Sources*, vol. 387, no. March, pp. 101–107, 2018, doi: 10.1016/j.jpowsour.2018.02.080.
- [166] C. S. Yoon, H. H. Ryu, G. T. Park, J. H. Kim, K. H. Kim, and Y. K. Sun, "Extracting maximum capacity from Ni-rich Li[Ni<sub>0.95</sub>Co<sub>0.025</sub>Mn<sub>0.025</sub>]O<sub>2</sub> cathodes for high-energy-density lithium-ion batteries," *J Mater Chem A Mater*, vol. 6, no. 9, pp. 4126–4132, 2018, doi: 10.1039/c7ta11346c.
- [167] K.-J. Park *et al.*, "Improved Cycling Stability of Li[Ni<sub>0.90</sub>Co<sub>0.05</sub>Mn<sub>0.05</sub>]O<sub>2</sub> Through Microstructure Modification by Boron Doping for Li-Ion Batteries," *Adv Energy Mater*, vol. 8, no. 25, p. 1801202, Sep. 2018, doi: 10.1002/AENM.201801202.
- [168] A. Liu *et al.*, "Investigating the Removal of Layered Double Hydroxides in [Ni<sub>0.80</sub>Co<sub>0.15</sub>]O<sub>2</sub> Prepared by Coprecipitation," *J Electrochem Soc*, vol. 165, no. 11, pp. A2781–A2791, Aug. 2018, doi: 10.1149/2.0731811JES/XML.
- [169] U. H. Kim *et al.*, "Pushing the limit of layered transition metal oxide cathodes for high-energy density rechargeable Li ion batteries," *Energy Environ Sci*, vol. 11, no. 5, pp. 1271–1279, May 2018, doi: 10.1039/C8EE00227D.

- [170] J. Zhu and G. Chen, "Single-crystal based studies for correlating the properties and high-voltage performance of Li[NixMnyCo1-x-y]O2 cathodes," *J Mater Chem A Mater*, vol. 7, no. 10, pp. 5463–5474, Mar. 2019, doi: 10.1039/C8TA10329A.
- [171] H. Widiyandari, A. Nadya Sukmawati, H. Sutanto, C. Yudha, and A. Purwanto, "Synthesis of LiNi0.8Mn0.1Co0.1O2 cathode material by hydrothermal method for high energy density lithium ion battery," *J Phys Conf Ser*, vol. 1153, no. 1, p. 012074, Feb. 2019, doi: 10.1088/1742-6596/1153/1/012074.
- [172] H. Hayashi and Y. Hakuta, "Hydrothermal Synthesis of Metal Oxide Nanoparticles in Supercritical Water," *Materials 2010, Vol. 3, Pages 3794-3817*, vol. 3, no. 7, pp. 3794–3817, Jun. 2010, doi: 10.3390/MA3073794.
- [173] S. C. Moldoveanu and V. David, "Mobile Phases and Their Properties," in *Essentials in Modern HPLC Separations*, Elsevier, 2013, pp. 363–447. doi: 10.1016/B978-0-12-385013-3.00007-0.
- [174] W. H. Ryu, S. J. Lim, W. K. Kim, and H. Kwon, "3-D dumbbell-like LiNi1/3Mn1/3Co1/3O2 cathode materials assembled with nano-building blocks for lithium-ion batteries," *J Power Sources*, vol. 257, pp. 186–191, Jul. 2014, doi: 10.1016/J.JPOWSOUR.2014.02.003.
- [175] S. Shi, T. Wang, M. Cao, J. Wang, M. Zhao, and G. Yang, "Rapid Self-Assembly Spherical Li1.2Mn0.56Ni0.16Co0.08O2 with Improved Performances by Microwave Hydrothermal Method as Cathode for Lithium-Ion Batteries," *ACS Appl Mater Interfaces*, vol. 8, no. 18, pp. 11476–11487, 2016, doi: 10.1021/acsami.6b01683.
- [176] L. Wang *et al.*, "Single-crystal LiNi0.6Co0.2Mn0.2O2 as high performance cathode materials for Li-ion batteries," *J Alloys Compd*, vol. 674, pp. 360–367, 2016, doi: 10.1016/j.jallcom.2016.03.061.
- [177] S. Ashoka, G. Nagaraju, K. V. Thipperudraiah, and G. T. Chandrappa, "Controlled synthesis of cadmium carbonate nanowires, nanoribbons, nanorings and sphere like architectures via hydrothermal method," *Mater Res Bull*, vol. 45, no. 11, pp. 1736–1740, Nov. 2010, doi: 10.1016/J.MATERRESBULL.2010.06.055.
- [178] M. Jiang *et al.*, "Synthesis of Ni-Rich Layered-Oxide Nanomaterials with Enhanced Li-Ion Diffusion Pathways as High-Rate Cathodes for Li-Ion Batteries," *ACS Appl Energy Mater*, vol. 3, no. 7, pp. 6583–6590, Jul. 2020, doi: 10.1021/ACSAEM.0C00765/ASSET/IMAGES/LARGE/AE0C00765\_0006.JPEG.
- [179] R. Essehli *et al.*, "Hydrothermal synthesis of Co-free NMA cathodes for high performance Li-ion batteries," *J Power Sources*, vol. 545, p. 231938, Oct. 2022, doi: 10.1016/J.JPOWSOUR.2022.231938.
- [180] R. Essehli *et al.*, "Hydrothermal synthesis of Co-free NMA cathodes for high performance Li-ion batteries," *J Power Sources*, vol. 545, p. 231938, Oct. 2022, doi: 10.1016/J.JPOWSOUR.2022.231938.
- [181] S. T. Myung, S. Komaba, and N. Kumagai, "Synthetic optimization of orthorhombic LiMnO2 by emulsion-drying method and cycling behavior as cathode material for Li-ion battery," *Solid State Ion*, vol. 150, no. 3–4, pp. 199–205, Oct. 2002, doi: 10.1016/S0167-2738(02)00520-9.
- [182] J. Li, J. Camardese, S. Glazier, and J. R. Dahn, "Structural and electrochemical study of the Li-Mn-Ni oxide system within the layered single phase region," *Chemistry of Materials*, vol. 26,

- no. 24, pp. 7059–7066, Dec. 2014, doi:  
10.1021/CM503505B/SUPPL\_FILE/CM503505B\_SI\_001.PDF.
- [183] Y. Zhou, B. Shi, J. Zhang, and W. Li, “Multiple Chelation-Assisted Lithiation Improves the Performance of Phosphate-Modified  $\text{LiNi}_{0.8}\text{Co}_{0.1}\text{Mn}_{0.1}\text{O}_2$ ,” *J Electrochem Soc*, vol. 170, no. 1, p. 010525, Jan. 2023, doi: 10.1149/1945-7111/ACAF43.
- [184] W. M. Seong *et al.*, “Controlling Residual Lithium in High-Nickel (90 %) Lithium Layered Oxides for Cathodes in Lithium-Ion Batteries,” *Angewandte Chemie - International Edition*, vol. 59, no. 42, pp. 18662–18669, Oct. 2020, doi: 10.1002/ANIE.202007436.
- [185] J. Eom, M. G. Kim, and J. Cho, “Storage Characteristics of  $\text{LiNi}_{0.8}\text{Co}_{0.1} + x\text{Mn}_{0.1} - x\text{O}_2$  ( $x = 0, 0.03$ , and  $0.06$ ) Cathode Materials for Lithium Batteries,” *J Electrochem Soc*, vol. 155, no. 3, p. A239, Jan. 2008, doi: 10.1149/1.2830946.
- [186] C. H. Jo, D. H. Cho, H. J. Noh, H. Yashiro, Y. K. Sun, and S. T. Myung, “An effective method to reduce residual lithium compounds on Ni-rich  $\text{Li}[\text{Ni}_{0.6}\text{Co}_{0.2}\text{Mn}_{0.2}]\text{O}_2$  active material using a phosphoric acid derived  $\text{Li}_3\text{PO}_4$  nanolayer,” *Nano Res*, vol. 8, no. 5, pp. 1464–1479, May 2015, doi: 10.1007/S12274-014-0631-8/METRICS.
- [187] P. Kurzhals, F. Riewald, M. Bianchini, H. Sommer, H. A. Gasteiger, and J. Janek, “The  $\text{LiNiO}_2$  Cathode Active Material: A Comprehensive Study of Calcination Conditions and their Correlation with Physicochemical Properties. Part I. Structural Chemistry,” *J Electrochem Soc*, vol. 168, no. 11, p. 110518, Nov. 2021, doi: 10.1149/1945-7111/AC33E5.
- [188] H. Zhang, H. Liu, L. F. J. Piper, M. S. Whittingham, and G. Zhou, “Oxygen Loss in Layered Oxide Cathodes for Li-Ion Batteries: Mechanisms, Effects, and Mitigation,” *Chem Rev*, vol. 122, no. 6, pp. 5641–5681, Mar. 2022, doi:  
10.1021/ACS.CHEMREV.1C00327/ASSET/IMAGES/LARGE/CR1C00327\_0023.JPEG.
- [189] S. P. Lin, K. Z. Fung, Y. M. Hon, and M. H. Hon, “Crystallization kinetics and mechanism of the  $\text{Li}_x\text{Ni}_{2-x}\text{O}_2$  ( $0 < x \leq 1$ ) from  $\text{Li}_2\text{CO}_3$  and  $\text{NiO}$ ,” *J Cryst Growth*, vol. 234, no. 1, pp. 176–183, Jan. 2002, doi: 10.1016/S0022-0248(01)01669-4.
- [190] M. C. Biesinger, B. P. Payne, A. P. Grosvenor, L. W. M. Lau, A. R. Gerson, and R. S. C. Smart, “Resolving surface chemical states in XPS analysis of first row transition metals, oxides and hydroxides: Cr, Mn, Fe, Co and Ni,” *Appl Surf Sci*, vol. 257, no. 7, pp. 2717–2730, Jan. 2011, doi: 10.1016/J.APSUSC.2010.10.051.
- [191] M. S. Idris and A. R. West, “The Effect on Cathode Performance of Oxygen Non-Stoichiometry and Interlayer Mixing in Layered Rock Salt  $\text{LiNi}_{0.8}\text{Mn}_{0.1}\text{Co}_{0.1}\text{O}_{2-\delta}$ ,” *J Electrochem Soc*, vol. 159, no. 4, pp. A396–A401, Jan. 2012, doi: 10.1149/2.037204JES/XML.
- [192] J. H. Shim *et al.*, “Effects of heat-treatment atmosphere on electrochemical performances of Ni-rich mixed-metal oxide ( $\text{LiNi}_{0.80}\text{Co}_{0.15}\text{Mn}_{0.05}\text{O}_2$ ) as a cathode material for lithium ion battery,” *Electrochim Acta*, vol. 138, pp. 15–21, Aug. 2014, doi:  
10.1016/J.ELECTACTA.2014.06.079.
- [193] J. Choi, L. Dong, C. Y. Yu, C. O’Meara, E. Lee, and J. H. Kim, “Relationship of Chemical Composition and Moisture Sensitivity in  $\text{LiNi}_x\text{Mn}_y\text{Co}_{1-x-y}\text{O}_2$  for Lithium-Ion Batteries,” *Journal of Electrochemical Energy Conversion and Storage*, vol. 18, no. 4, Nov. 2021, doi: 10.1115/1.4051208/1109444.

- [194] K. S. Park, S. H. Park, Y. K. Sun, K. S. Nahm, Y. S. Lee, and M. Yoshio, "Effect of oxygen flow rate on the structural and electrochemical properties of lithium nickel oxides synthesized by the sol-gel method," *J Appl Electrochem*, vol. 32, no. 11, pp. 1229–1233, Nov. 2002, doi: 10.1023/A:1021606712486/METRICS.
- [195] M. Wolfman *et al.*, "The Importance of Surface Oxygen for Lithiation and Morphology Evolution during Calcination of High-Nickel NMC Cathodes," *Adv Energy Mater*, vol. 12, no. 16, p. 2102951, Apr. 2022, doi: 10.1002/AENM.202102951.
- [196] D. Caurant, N. Baffier, B. Garcia, and J. P. Pereira-Ramos, "Synthesis by a soft chemistry route and characterization of  $\text{LiNi}_x\text{Co}_{1-x}\text{O}_2$  ( $0 \leq x \leq 1$ ) cathode materials," *Solid State Ion.*, vol. 91, no. 1–2, p. 45, Oct. 1996, doi: 10.1016/s0167-2738(96)00418-3.
- [197] G. Shang *et al.*, "Enhancing structural stability unto 4.5 V of Ni-rich cathodes by tungsten-doping for lithium storage," *J Power Sources*, vol. 423, pp. 246–254, May 2019, doi: 10.1016/j.jpowsour.2019.03.072.
- [198] J. V. Laveda *et al.*, "Stabilizing Capacity Retention in NMC811/Graphite Full Cells via TMSPi Electrolyte Additives," *ACS Appl Energy Mater*, vol. 2, no. 10, pp. 7036–7044, Oct. 2019, doi: 10.1021/ACSAEM.9B00727/ASSET/IMAGES/LARGE/AE9B00727\_0007.JPEG.
- [199] A. Habibi, M. Jalaly, R. Rahmanifard, and M. Ghorbanzadeh, "The effect of calcination conditions on the crystal growth and battery performance of nanocrystalline  $\text{Li}(\text{Ni}_{1/3}\text{Co}_{1/3}\text{Mn}_{1/3})\text{O}_2$  as a cathode material for Li-ion batteries," *New Journal of Chemistry*, vol. 42, no. 23, pp. 19026–19033, 2018, doi: 10.1039/c8nj05007d.
- [200] I. McClelland *et al.*, "Direct Observation of Dynamic Lithium Diffusion Behavior in Nickel-Rich,  $\text{LiNi}_{0.8}\text{Mn}_{0.1}\text{Co}_{0.1}\text{O}_2$  (NMC811) Cathodes Using *Operando* Muon Spectroscopy," *Chemistry of Materials*, May 2023, doi: 10.1021/ACS.CHEMMATER.2C03834.
- [201] M. Bianchini, F. Fauth, P. Hartmann, T. Brezesinski, and J. Janek, "An: In situ structural study on the synthesis and decomposition of  $\text{LiNiO}_2$ ," *J Mater Chem A Mater*, vol. 8, no. 4, pp. 1808–1820, 2020, doi: 10.1039/c9ta12073d.
- [202] Riewald, Felix, P. Kurzahls, M. Bianchini, H. Sommer, J. Janek, and H. A. Gasteiger, "The  $\text{LiNiO}_2$  Cathode Active Material: A Comprehensive Study of Calcination Conditions and their Correlation with Physicochemical Properties Part II. Morphology," *J Electrochem Soc*, vol. 169, no. 2, p. 020529, Feb. 2022, doi: 10.1149/1945-7111/AC4BF3.
- [203] J. Zheng, P. Yan, L. Estevez, C. Wang, and J. G. Zhang, "Effect of calcination temperature on the electrochemical properties of nickel-rich  $\text{LiNi}_{0.76}\text{Mn}_{0.14}\text{Co}_{0.10}\text{O}_2$  cathodes for lithium-ion batteries," *Nano Energy*, vol. 49, pp. 538–548, Jul. 2018, doi: 10.1016/j.nanoen.2018.04.077.
- [204] L. Xu, F. Zhou, J. Kong, Z. Chen, and K. Chen, "Synthesis of  $\text{Li}(\text{Ni}_{0.6}\text{Co}_{0.2}\text{Mn}_{0.2})\text{O}_2$  with sodium DL-lactate as an eco-friendly chelating agent and its electrochemical performances for lithium-ion batteries," *Ionics (Kiel)*, vol. 24, no. 8, pp. 2261–2273, 2018, doi: 10.1007/s11581-017-2363-8.
- [205] Y. Zhu *et al.*, "Calcined Mg/Al layered double hydroxides as efficient adsorbents for polyhydroxy fullerenes," *Appl Clay Sci*, vol. 151, pp. 66–72, Jan. 2018, doi: 10.1016/j.clay.2017.10.018.

- [206] I. S. Metcalfe, *Chemical Reaction Engineering*. Oxford: Oxford University Press, 2011.
- [207] J. M. Coulson, J. F. Richardson, J. R. Backhurst, and J. H. Harker, *Coulson & Richardson's Chemical Engineering Volume 1: Fluid Flow, Heat Transfer and Mass Transfer*, Sixth. Oxford: Elsevier, 1999.
- [208] P. M. Doran, *Bioprocess Engineering Principles*. Elsevier, 2013. [Online]. Available: <https://www.sciencedirect.com/book/9780122208515/bioprocess-engineering-principles?via=ihub=>
- [209] G. Baldi, R. Conti, and E. Alaria, "Complete suspension of particles in mechanically agitated vessels," *Chem Eng Sci*, vol. 33, no. 1, pp. 21–25, Jan. 1978, doi: 10.1016/0009-2509(78)85063-5.
- [210] T. N. Zwietering, "Suspending of solid particles in liquid by agitators," *Chem Eng Sci*, vol. 8, no. 3–4, pp. 244–253, Jun. 1958, doi: 10.1016/0009-2509(58)85031-9.
- [211] R. H. Perry, *PERRY'S Chemical Engineering Handbook*. McGraw-Hill, 2007. [Online]. Available: <http://books.google.com/books?id=X1wIW9TrqXMC&pgis=1>
- [212] S. S. Deshpande, K. K. Kar, J. Walker, J. Pressler, and W. Su, "An experimental and computational investigation of vortex formation in an unbaffled stirred tank," *Chem Eng Sci*, vol. 168, pp. 495–506, Aug. 2017, doi: 10.1016/J.CES.2017.04.002.
- [213] R. K. Sinnott, *Coulson and Richardson's Chemical Engineering Volume 6: Design*. Butterworth-Heinemann Ltd, 1996.
- [214] J. R. Cooper, W. R. Penney, J. R. Fair, and S. M. Walas, *Chemical Process Equipment Selection and Design*, Second Edi. Gulf Professional Publishing, 2004.
- [215] M. Shah and Anchor Insitute, "Process Engineering: Agitation & Mixing." [Online]. Available: <https://dokumen.tips/documents/course-material-process-engineering-agitation-mixing.html?page=163>
- [216] E. A. Fox and V. E. Gex, "Single-phase blending of liquids," *AIChE Journal*, vol. 2, no. 4, pp. 539–544, 1956, doi: 10.1002/AIC.690020422.
- [217] K. J. Rao, B. Vaidhyanathan, M. Ganguli, and P. A. Ramakrishnan, "Synthesis of inorganic solids using microwaves," *Chemistry of Materials*, vol. 11, no. 4, pp. 882–895, 1999, doi: 10.1021/CM9803859/ASSET/IMAGES/LARGE/CM9803859F00012.JPEG.
- [218] S. Balaji, D. Mutharasu, N. S. Subramanian, and K. Ramanathan, "A review on microwave synthesis of electrode materials for lithium-ion batteries," *Ionics (Kiel)*, vol. 15, no. 6, pp. 765–777, 2009, doi: 10.1007/s11581-009-0350-4.
- [219] M. Nüchter, B. Ondruschka, W. Bonrath, and A. Gum, "Microwave assisted synthesis – a critical technology overview," *Green Chemistry*, vol. 6, no. 3, pp. 128–141, Mar. 2004, doi: 10.1039/B310502D.
- [220] G. D. Stefanidis, A. N. Muñoz, G. S. J. Sturm, and A. Stankiewicz, "A helicopter view of microwave application to chemical processes: Reactions, separations, and equipment concepts," *Reviews in Chemical Engineering*, vol. 30, no. 3, pp. 233–259, Jun. 2014, doi: 10.1515/REVCE-2013-0033/ASSET/GRAPHIC/REVCE-2013-0033\_CV4.JPG.

- [221] C. Ke, T. Liu, Y. Zhang, and Q. Xiong, "Energy absorption performances of silicon carbide particles during microwave heating process," *Chemical Engineering and Processing - Process Intensification*, vol. 172, p. 108796, Feb. 2022, doi: 10.1016/J.CEP.2022.108796.
- [222] O. Długosz and M. Banach, "Continuous synthesis of metal and metal oxide nanoparticles in microwave reactor," *Colloids Surf A Physicochem Eng Asp*, vol. 606, p. 125453, Dec. 2020, doi: 10.1016/J.COLSURFA.2020.125453.
- [223] S. Shi, T. Wang, M. Cao, J. Wang, M. Zhao, and G. Yang, "Rapid Self-Assembly Spherical Li<sub>1.2</sub>Mn<sub>0.56</sub>Ni<sub>0.16</sub>Co<sub>0.08</sub>O<sub>2</sub> with Improved Performances by Microwave Hydrothermal Method as Cathode for Lithium-Ion Batteries," *ACS Appl Mater Interfaces*, vol. 8, no. 18, pp. 11476–11487, May 2016, doi: 10.1021/ACSAMI.6B01683/ASSET/IMAGES/LARGE/AM-2016-016839\_0012.JPEG.
- [224] L. Nie, K. Deng, S. Yuan, W. Zhang, and Q. Tan, "Microwave-assisted hydrothermal synthesis of hierarchically porous  $\gamma$ -Al<sub>2</sub>O<sub>3</sub> hollow microspheres with enhanced Cu<sup>2+</sup> adsorption performance," *Mater Lett*, vol. 132, pp. 369–372, Oct. 2014, doi: 10.1016/J.MATLET.2014.06.095.
- [225] J. Li, M. K. Aslam, and C. Chen, "One-Pot Hydrothermal Synthesis of Porous  $\alpha$ -Ni(OH)<sub>2</sub>/C Composites and Its Application in Ni/Zn Alkaline Rechargeable Battery," *J Electrochem Soc*, vol. 165, no. 5, pp. A910–A917, Mar. 2018, doi: 10.1149/2.0721805JES/XML.
- [226] Y. Liu, W. Yao, C. Lei, Q. Zhang, S. Zhong, and Z. Yan, "Ni-Rich Oxide LiNi<sub>0.85</sub>Co<sub>0.05</sub>Mn<sub>0.1</sub>O<sub>2</sub> for Lithium Ion Battery: Effect of Microwave Radiation on Its Morphology and Electrochemical Property," *J Electrochem Soc*, vol. 166, no. 8, pp. A1300–A1309, Apr. 2019, doi: 10.1149/2.0151908JES/XML.
- [227] Omega, "How Do Infrared Thermometers Work?" [Online]. Available: <https://www.omega.com/en-us/resources/infrared-thermometer-how-work#:~:text=Working of Infrared Thermometers&text=When the infrared radiation falls,gets displayed on the screen.>
- [228] F. Technologies, "Technology Introduction GaAs," Quebec, 2018. [Online]. Available: <https://fiso.com/wp-content/uploads/2018/10/Technology-introduction-GaAs-MC-00244.pdf>
- [229] C. Corporation, "CEM Mars 5 Manual," 2001. [Online]. Available: <http://www.iproweb.fr/test/0 - MATOS GUILLAUME/CEM - IPO technology - MARS 5/MARS5.pdf>
- [230] I. B. Butler, M. A. A. Schoonen, and D. T. Rickard, "Removal of dissolved oxygen from water: A comparison of four common techniques," *Talanta*, vol. 41, no. 2, pp. 211–215, 1994, doi: 10.1016/0039-9140(94)80110-X.
- [231] M. Buerkle and Y. Asai, "Thermal conductance of Teflon and Polyethylene: Insight from an atomistic, single-molecule level," *Scientific Reports 2017 7:1*, vol. 7, no. 1, pp. 1–7, Feb. 2017, doi: 10.1038/srep41898.
- [232] W. H. R. Shaw and J. J. Bordeaux, "The Decomposition of Urea in Aqueous Media," *J Am Chem Soc*, vol. 77, no. 18, pp. 4729–4733, 1955, doi: 10.1021/JA01623A011/ASSET/JA01623A011.FP.PNG\_V03.

- [233] Formlabs, "Formlabs Safety Data Sheet - Clear Resin," 2022. [Online]. Available: <https://formlabs-media.formlabs.com/datasheets/1801037-SDS-ENEU-0.pdf>
- [234] C. Hammond, *The Diffraction of X-rays: The Basics of Crystallography and Diffraction*. Oxford: Oxford University Press, 2015.
- [235] "X-Ray Emission – PhysicsOpenLab." Accessed: Apr. 02, 2024. [Online]. Available: <https://physicsopenlab.org/2018/02/13/x-ray-emission/>
- [236] W. Massa, *Crystal Structure Determination*. Berlin Heidelberg: Springer-Verlag, 2004.
- [237] H. M. Rietveld and IUCr, "A profile refinement method for nuclear and magnetic structures," *urn:issn:0021-8898*, vol. 2, no. 2, pp. 65–71, Jun. 1969, doi: 10.1107/S0021889869006558.
- [238] B. H. Toby, "R factors in Rietveld analysis: How good is good enough?," *Powder Diffr*, vol. 21, no. 1, pp. 67–70, 2006, doi: 10.1154/1.2179804.
- [239] B. H. Toby and R. B. Von Dreele, "GSAS-II: the genesis of a modern open-source all purpose crystallography software package," *urn:issn:0021-8898*, vol. 46, no. 2, pp. 544–549, Mar. 2013, doi: 10.1107/S0021889813003531.
- [240] J. J. Hren, J. I. Goldstein, and D. C. Joy, *Introduction to analytical electron microscopy*. Springer New York, 1979.
- [241] P. J. Goodhew, J. Humphreys, and R. Beanland, *Electron Microscopy and Analysis*, Third Edit. Taylor & Francis, 2001.
- [242] C. A. Schneider, W. S. Rasband, and K. W. Eliceiri, "NIH Image to ImageJ: 25 years of image analysis," *Nature Methods* 2012 9:7, vol. 9, no. 7, pp. 671–675, Jun. 2012, doi: 10.1038/nmeth.2089.
- [243] G. Instruments, "Basics of Electrochemical Impedance Spectroscopy." [Online]. Available: <https://www.gamry.com/assets/Application-Notes/Basics-of-EIS.pdf>
- [244] Middlemiss *et al.*, "Characterisation of batteries by electrochemical impedance spectroscopy," *Energy Reports*, vol. 6, pp. 232–241, 2019, doi: 10.1016/j.egy.2020.03.029.
- [245] M. E. Orazem and B. Tribollet, *Electrochemical Impedance Spectroscopy*, 2nd Editio. Wiley, 2017.
- [246] J. Kim, S. Park, S. Hwang, and W.-S. Yoon, "Principles and Applications of Galvanostatic Intermittent Titration Technique for Lithium-ion Batteries," *J. Electrochem. Sci. Technol*, vol. 2022, no. 1, pp. 19–31, doi: 10.33961/jecst.2021.00836.
- [247] L. Wheatcroft *et al.*, "Fracture Testing of Lithium-Ion Battery Cathode Secondary Particles in-situ inside the Scanning Electron Microscope," *Batter Supercaps*, vol. 6, no. 5, p. e202300032, May 2023, doi: 10.1002/BATT.202300032.
- [248] M. Baeva *et al.*, "The effect of oxygen admixture on the properties of microwave generated plasma in Ar–O<sub>2</sub>: a modelling study," *J Phys D Appl Phys*, vol. 54, no. 35, p. 355205, Jun. 2021, doi: 10.1088/1361-6463/AC08CC.
- [249] Y. H. Chou, N. Hondow, C. I. Thomas, R. Mitchell, R. Brydson, and R. E. Douthwaite, "Microwave plasma synthesis of lanthanide zirconates from microwave transparent oxides," *Dalton Transactions*, vol. 41, no. 8, pp. 2472–2476, Feb. 2012, doi: 10.1039/C2DT12269C.

- [250] V. Y. Kazimirov *et al.*, "Atomic structure and lattice dynamics of Ni and Mg hydroxides," *Solid State Ion*, vol. 181, no. 39–40, pp. 1764–1770, Dec. 2010, doi: 10.1016/J.SSI.2010.10.002.
- [251] B. Ying *et al.*, "Monitoring the Formation of Nickel-Poor and Nickel-Rich Oxide Cathode Materials for Lithium-Ion Batteries with Synchrotron Radiation," *Chemistry of Materials*, Jan. 2023, doi: 10.1021/ACS.CHEMMATER.2C02639.
- [252] M. Thanh Tung and V. Duc Luong, "Electrochemical properties of LiNi<sub>0.8</sub>Co<sub>0.1</sub>Mn<sub>0.1</sub>O<sub>2</sub> synthesized by sol-gel and co-precipitation methods," *Vietnam Journal of Chemistry*, vol. 54, no. 6, pp. 724–729, 2016, doi: 10.15625/0866-7144.2016-00394.
- [253] C. M. Skaggs *et al.*, "Iridate Li<sub>8</sub>IrO<sub>6</sub>: An Antiferromagnetic Insulator," *Inorg Chem*, vol. 60, no. 22, pp. 17201–17211, Nov. 2021, doi: 10.1021/ACS.INORGCHEM.1C02535/SUPPL\_FILE/IC1C02535\_SI\_001.PDF.
- [254] S. L. Mair and IUCr, "The electron distribution of the hydroxide ion in lithium hydroxide," *urn:issn:0567-7394*, vol. 34, no. 4, pp. 542–547, Jul. 1978, doi: 10.1107/S0567739478001151.
- [255] Y. Idemoto, J. W. Richardson, N. Koura, S. Kohara, and C. K. Loong, "Crystal structure of (Li<sub>x</sub>K<sub>1-x</sub>)<sub>2</sub>CO<sub>3</sub> (x = 0, 0.43, 0.5, 0.62, 1) by neutron powder diffraction analysis," *Journal of Physics and Chemistry of Solids*, vol. 59, no. 3, pp. 363–376, Mar. 1998, doi: 10.1016/S0022-3697(97)00209-6.
- [256] J. Li *et al.*, "Addressing cation mixing in layered structured cathodes for lithium-ion batteries: A critical review," *Nano Materials Science*, Oct. 2022, doi: 10.1016/J.NANOMS.2022.09.001.
- [257] W. Liu *et al.*, "Nickel-Rich Layered Lithium Transition-Metal Oxide for High-Energy Lithium-Ion Batteries," *Angewandte Chemie International Edition*, vol. 54, no. 15, pp. 4440–4457, Apr. 2015, doi: 10.1002/ANIE.201409262.
- [258] H. Liu, A. J. Naylor, A. S. Menon, W. R. Brant, K. Edström, and R. Younesi, "Understanding the Roles of Tris(trimethylsilyl) Phosphite (TMSPi) in LiNi<sub>0.8</sub>Mn<sub>0.1</sub>Co<sub>0.1</sub>O<sub>2</sub> (NMC811)/Silicon–Graphite (Si–Gr) Lithium-Ion Batteries," *Adv Mater Interfaces*, vol. 7, no. 15, p. 2000277, Aug. 2020, doi: 10.1002/ADMI.202000277.
- [259] A. Grenier *et al.*, "Reaction Heterogeneity in LiNi<sub>0.8</sub>Co<sub>0.15</sub>Al<sub>0.05</sub>O<sub>2</sub> Induced by Surface Layer," *Chemistry of Materials*, vol. 29, no. 17, pp. 7345–7352, Sep. 2017, doi: 10.1021/ACS.CHEMMATER.7B02236/SUPPL\_FILE/CM7B02236\_SI\_001.PDF.
- [260] J. Z. Olson, C. M. López, and E. J. F. Dickinson, "Differential Analysis of Galvanostatic Cycle Data from Li-Ion Batteries: Interpretative Insights and Graphical Heuristics," *Chemistry of Materials*, Feb. 2023, doi: 10.1021/ACS.CHEMMATER.2C01976.
- [261] A. Nyman, T. G. Zavalis, R. Elger, M. Behm, and G. Lindbergh, "Analysis of the Polarization in a Li-Ion Battery Cell by Numerical Simulations," *J Electrochem Soc*, vol. 157, no. 11, p. A1236, Sep. 2010, doi: 10.1149/1.3486161/XML.
- [262] Q. Zhu, H. Xiao, R. Zhang, S. Geng, and Q. Huang, "Effect of impeller type on preparing spherical and dense Ni<sub>1-x-y</sub>Co<sub>x</sub>Mn<sub>y</sub>(OH)<sub>2</sub> precursor via continuous co-precipitation in pilot scale: A case of Ni<sub>0.6</sub>Co<sub>0.2</sub>Mn<sub>0.2</sub>(OH)<sub>2</sub>," *Electrochim Acta*, vol. 318, pp. 1–13, Sep. 2019, doi: 10.1016/J.ELECTACTA.2019.06.008.
- [263] A. N. M. Negari, R. S. Mamoory, A. Simchi, and N. Ehsani, "Determination of the physical and mechanical properties of iron-based powder materials produced by microwave sintering,"

*Powder Metallurgy and Metal Ceramics*, vol. 46, no. 9–10, pp. 423–428, Sep. 2007, doi:  
10.1007/S11106-007-0066-9/METRICS.

- [264] R. L. Bates, P. L. Fondy, and R. R. Corpstein, “An examination of some geometric parameters of impeller power,” *Industrial and Engineering Chemistry Process Design and Development*, vol. 2, no. 4, pp. 310–314, Oct. 1963, doi:  
10.1021/I260008A011/ASSET/I260008A011.FP.PNG\_V03.